Samer H. Hamdar
Editor

Traffic and Granular Flow '17

Springer

Traffic and Granular Flow ’17

Samer H. Hamdar
Editor

Traffic and Granular Flow '17

Springer

Editor
Samer H. Hamdar
Dept. of Civil & Environ. Engineering
George Washington University
Washington, DC, USA

ISBN 978-3-030-11439-8 ISBN 978-3-030-11440-4 (eBook)
https://doi.org/10.1007/978-3-030-11440-4

Cover image: By courtesy of Samer H. Hamdar

This Springer imprint is published by the registered company Springer Nature Switzerland AG.
The registered company address is: Gewerbestrasse 11, 6330 Cham, Switzerland

Preface

In its 12th edition, the "Traffic and Granular Flow" (TGF) conference was held for the first time on the North American continent with a setup facilitating the exchange of scientific ideas between professionals, academicians/researchers and students. The conference took place between July 19 and July 22, 2017. The venue was the Science and Engineering Hall, home of the George Washington University (GW) School of Engineering and Applied Science (SEAS). The conference was organized by the GW Transportation Engineering Program that is part of the Civil and Environmental Engineering Department.

Originally conceived to facilitate new ideas by considering the similarities of traffic and granular flow, the latest TGF conference covered a broad range of topics related to particle and transport systems. Such topics included granular flow and dynamics of granular materials, pedestrian and highway traffic interactions, and the collective motion in biological systems.

The TGF'17 comes at a time when the field of traffic and granular flow is experiencing a major development seen in the participation of new researchers and professionals from different disciplines (e.g., electrical engineers, computer scientists, mathematicians, and economists). Such participation has led to the adoption of new theories and approaches (e.g.: game theory and artificial intelligence) and the utilization of new technologies (e.g., LIDAR technologies, smartphone devices, and supercomputers) with multiple new contributions and breakthroughs. In line with such development, the 2017 TGF's theme was:

> From Molecular Interactions to Internet of Things and Smart Cities: The Role of Technology in the Understanding and the Evolution of Particle Dynamics.

Accordingly, further attention was dedicated to the latest research efforts in connected and automated vehicles (CAVs), intermodal integrated urban traffic, pedestrian detection and artificial intelligence, complex networks, intelligent transportation systems, and big-data analytics.

In total, 81 researchers/students attended the conference. The program consisted of one plenary session, seven parallel lectern sessions, and two poster sessions. These sessions allowed for 99 total presentations consisting of 3 plenary presen-

tations, 60 oral podium presentations, and 36 poster presentations. The attendees produced 56 high-quality research chapters included in this book. These chapters do not represent all the contributions included in the TGF'17 program. All chapters in this book were reviewed by up to three members of the international scientific committee. Out of the 56 chapters, 17 chapters were invited to be extended and submitted for consideration for publication in the *Journal of Transportation and Traffic Engineering*. 16 different chapters were invited for extension and consideration for publication in the *Journal of Intelligent Transportation Systems*.

The success of this conference and the resulting contributions were made possible because of the TGF research community, the authors, and the attendees. Special appreciation is extended to the conference international scientific committee for the review and selection process of the chapters included in this book.

I am also grateful to the members of the local organizing committee (Ms. Claire Silverstein, Ms. Joyce Randolph, Mr. Shiju Varghese, Mr. Adam Casper, Mr. Raoul Gabian, Ms. Edna Aguilar, and Ms. Madison Haley) for translating our conference plans into a reality. Last but not least, I thank Ms. Anne Comment and the Springer publication team members for their efforts in the final preparation of this book.

The conference series will continue with the next conference being held in Pamplona, Spain, in 2019.

Washington, DC, USA Samer H. Hamdar
July 2018

International Scientific Committee

Soyoung Ahn, University of Wisconsin, Madison, USA
Cécile Appert-Rolland, Paris Sud University, Orsay, France
Jean-Michel Auberlet, IFSTTAR, France
Stefania Bandini, University of Milano, Bicocca, Italy
Robert Bertini, University of South Florida, USA
Nikolai Bode, University of Bristol, UK
Christine Buisson, IFSTTAR, France
Alexander Buslaev, Moscow Automobile and Road State Technical University, Russia
Mohcine Chraibi, Forschungszentrum Jülich, Germany
Benjamin Coifman, Ohio State University, USA
Winnie Daamen, Delft University of Technology, Netherlands
Bart de Schutter, Delft University of Technology, Netherlands
Vikash Gayah, Pennsylvania State University, USA
Timon Idema, Delft University of Technology, Netherlands
Boris Kerner, University of Duisburg-Essen, Germany
Victor Knoop, Delft University of Technology, Netherlands
Gerta Köster, University of Applied Sciences Munich, Germany
Valery Kozolv, Steklov mathematical Institute of Russian Academy of Science, Russia
Tobias Kretz, PTV Group, Germany
Sylvain Lassare, IFSTTAR, France
Jean-Patrick Lebacque, IFSTTAR, France
Seung Jae Lee, Florida International University, USA
Xiaopeng Li, University of South Florida, USA
Reinhard Mahnke, University of Rostock, Germany
Monica Menendez, ETH Zurich, Switzerland
Katsuhiro Nishinari, University of Tokyo, Japan
Vincenzo Punzo, University of Naples Federico II, Italy
K Ramachandra Rao, Indian Institute of Technology (IIT) Delhi, India
Meead Saberi, Monash University, Australia

Majid Sarvi, Monash University, Australia
Andreas Schadschneider, University of Cologne, Germany
Dingena Schott, Delft University of Technology, Netherlands
Armin Seyfried, Forschungszentrum Jülich, Germany
WeiGuo Song, University of Science and Technology of China, China
Albert Steiner, Zürich University of Applied Sciences, Switzerland
Alireza Talebpour, University of Texas A&M, USA
Guy Théraulaz, University of Toulouse, France
Martin Treiber, Technical University of Dresden, Germany
Dixit Vinayak, University of New South Wales, Australia
Peter Vortisch, Karlsruhe Institute of Technology, Germany
Peter Wagner, German Aerospace Center, Germany
Eddie Wilson, Bristol University, UK
Marina Yashina, Moscow Technical University of Communications and Informatics, Russia

Contents

Part I Roadway Vehicular Flow: Data Collection, Modeling and Simulation

Exact Formula of Time-Headway Distribution for TASEP with Random-Sequential Update 3
Pavel Hrabák

Impact of Next-Nearest Leading Vehicles on Followers' Driving Behaviours in Mixed Traffic 11
Akihito Nagahama, Daichi Yanagisawa, and Katsuhiro Nishinari

Higher-Order Continuum Model and Its Numerical Solutions for Heterogeneous Traffic Flow with Non-lane Discipline 19
Hari Krishna Gaddam and K. Ramachandra Rao

Static Traffic Assignment on Ensembles of Synthetic Road Networks 29
Alonso Espinosa Mireles de Villafranca, Richard D. Connors, and R. Eddie Wilson

The Effect of Traffic Signals on the Macroscopic Fundamental Diagram 37
Boudewijn Zwaal, Victor L. Knoop, and Hans van Lint

Braess Paradox in Networks of Stochastic Microscopic Traffic Models ... 45
Stefan Bittihn and Andreas Schadschneider

Dynamical Universality Class of the Nagel–Schreckenberg and Related Models 53
Andreas Schadschneider, Johannes Schmidt, Jan de Gier, and Gunter M. Schütz

Prediction of Moving Bottleneck and Associated Traffic Phenomena for Automated Driving 61
Dominik Wegerle, Boris S. Kerner, Sergey L. Klenov, and Michael Schreckenberg

F → S → F Transitions in Vehicle Probe Data 71
Sven-Eric Molzahn, Boris S. Kerner, Hubert Rehborn, Sergey L. Klenov, and Micha Koller

Microscopic Jam Tail Warning for Automated Driving 79
Sven-Eric Molzahn, Boris S. Kerner, and Hubert Rehborn

Study of Vehicle-Following Behavior Under Heterogeneous Traffic Conditions 87
Narayana Raju, Shriniwas Arkatkar, and Gaurang Joshi

Development of a Decision-Making Model for Merging Maneuvers: A Game Theoretical Approach 97
Kyungwon Kang and Hesham A. Rakha

Macroscopic Fundamental Diagram Validation for Collision Formation on Freeway Networks 107
Claire E. Silverstein, Samer H. Hamdar, Seungmo Kang, and Kitae Jang

Towards a More Stable Traffic Flow Performance: Applying and Calibrating the Intelligent Driver Model 117
Dong Pan, Samer H. Hamder, and Antonio J. Caamaño

Numerical Comparison Between Traffic Flow Models with and Without Adaptation Behavior 125
Alma Rosa Méndez, Rosa María Velasco, and Wilson Marques Jr.

A Game-Theoretic Approach for Minimizing Delays in Autonomous Intersections 131
Robert P. Adkins, David M. Mount, and Alice A. Zhang

Part II Pedestrian Traffic: Analytical and Empirical Studies

Empirical Evaluation of Crowds Using Automated Methods 143
Muhammad Baqui, Michelle Isenhour, and Rainald Löhner

Micro and Macro Pedestrian Dynamics in Counterflow: The Impact of Social Groups 151
Luca Crociani, Andrea Gorrini, Claudio Feliciani, Giuseppe Vizzari, Katsuhiro Nishinari, and Stefania Bandini

Pedestrian Flow Through Complex Infrastructure, Experiments, and Mass-Transport Processes 159
Pavel Hrabák, Marek Bukáček, Peter M. Kielar, and André Borrmann

Mining the Social Media Data for a Bottom-Up Evaluation of Walkability 167
Christian Berzi, Andrea Gorrini, and Giuseppe Vizzari

Experimental Investigation of Pedestrian Queuing Behaviour 177
Jiahua Zhang, Miho Iryo-Asano, and Charitha Dias

Safety Training Through Educational Online Computer Games on Crowd Evacuations? 187
Nikolai W. F. Bode

Hybrid Tracking System for Pedestrians in Dense Crowds 195
Jette Schumann, Maik Boltes, and Armin Seyfried

Investigating the Effect of Social Groups in Uni-directional Pedestrian Flow 205
Luca Crociani, Yiping Zeng, Andrea Gorrini, Giuseppe Vizzari, and Weiguo Song

Towards Microscopic Calibration of Pedestrian Simulation Models Using Open Trajectory Datasets: The Case Study of the Edinburgh Informatics Forum 215
Ruggiero Lovreglio, Charitha Dias, Xiang Song, and Lucia Ballerini

Influence of Gender on the Fundamental Diagram and Gait Characteristics 225
Jiayue Wang, Maik Boltes, Armin Seyfried, Antoine Tordeux, Jun Zhang, Verena Ziemer, and Wenguo Weng

Evaluation of Pedestrian Density Distribution with Respect to the Velocity Response 235
Marek Bukáček and Jana Vacková

Using Raspberry Pi for Measuring Pedestrian Visiting Patterns via WiFi-Signals in Uncontrolled Field Studies 245
Peter M. Kielar, Pavel Hrabák, Marek Bukáček, and André Borrmann

Group Parameters for Social Groups in Evacuation Scenarios 255
Cornelia von Krüchten and Andreas Schadschneider

Simulating Assisted Evacuation Using Unity3D 265
Anass Rahouti, Ruggiero Lovreglio, Charitha Dias, and Sélim Datoussaïd

An Application of New Pedestrian Tracking Sensors for Evaluating Platform Safety Risks at Swiss and Dutch Train Stations 277
Jeroen van den Heuvel, Jasmin Thurau, Martin Mendelin, Rik Schakenbos, Marcel van Ofwegen, and Serge P. Hoogendoorn

Influence of Pedestrian Density on the Use of the Danger Zone at Platforms of Train Stations 287
Jasmin Thurau, Jeroen van den Heuvel, Nicolas Keusen, Marcel van Ofwegen, and Serge P. Hoogendoorn

Detecting Competitive Behaviors in Conflicts 297
Daichi Yanagisawa and Keisuke Yamazaki

Towards Faster Navigation Algorithms on Floor Fields 307
Benedikt Zönnchen, Matthias Laubinger, and Gerta Köster

Automated Quality Assessment of Space-Continuous Models for Pedestrian Dynamics 317
Valentina Kurtc, Mohcine Chraibi, and Antoine Tordeux

Prediction of Pedestrian Speed with Artificial Neural Networks 327
Antoine Tordeux, Mohcine Chraibi, Armin Seyfried, and Andreas Schadschneider

Noise-Induced Stop-and-Go Dynamics 337
Antoine Tordeux, Andreas Schadschneider, and Sylvain Lassarre

Evacuation Simulation and Experiment Without Exit Information 347
Yusuke Miyoshi, Daichi Yanagisawa, and Katsuhiro Nishinari

Fluctuations in Pedestrian Evacuation Times: Going One Step Beyond the Exit Capacity Paradigm for Bottlenecks 357
Alexandre Nicolas

Macroscopic Fundamental Diagram for Train Platforms 365
Winnie Daamen, Jeroen van den Heuvel, Victor L. Knoop, and Serge P. Hoogendoorn

Towards Safer Pedestrian Traffic: Investigation of the Impact of Social Field Characteristic on Crowd Dynamics 373
Jingwan Fu, Boxiao Cao, Samer H. Hamdar, and Tianshu Li

Defining the Pedestrian Fundamental Diagram 383
Ernst Bosina and Ulrich Weidmann

Part III From Individual Interactions to Complex Systems: Airplanes, Bicycles, Mixed Flow, Particles and Traveler Behavior

Simulating Ground Traffic on Airports Using Cellular Automata: The CAMAT-Model 395
Florian Mazur and Michael Schreckenberg

Investigating Passengers' Seating Behavior in Suburban Trains 405
Jakob Schöttl, Michael J. Seitz, and Gerta Köster

How Long Does It Take to Board an Airplane? 415
Jevgenijs Kaupužs, Reinhard Mahnke, Eitan Bachmat, and Vidar Frette

Assessment of Pedestrian Fatality Risk at Unsignalized Crosswalks by Means of Simulation 423
Claudio Feliciani, Luca Crociani, Andrea Gorrini, Giuseppe Vizzari, Katsuhiro Nishinari, and Stefania Bandini

Algebraic and Geometric Aspects of Flow Modeling and Prospects of Natural Science Applications 433
Valery V. Kozlov, Boris N. Chetverushkin, Alexander P. Buslaev, Alexander G. Tatashev, and Marina V. Yashina

Crossing Behaviour of Social Groups: Insights from Observations at Non-signalised Intersection 443
Andrea Gorrini, Luca Crociani, Giuseppe Vizzari, and Stefania Bandini

Modeling and Solving of Multiple Conflict Situations in Shared Spaces 451
Chris Schiermeyer, Federico Pascucci, Nils Rinke, Volker Berkhahn, and Bernhard Friedrich

Vibration Driven Vehicles Flowing Through Bottlenecks 459
Germán A. Patterson, Federico Sangiuliano Jimka, Pablo G. König, Luis A. Pugnaloni, Angel Garcimartín, Iker Zuriguel, Pablo I. Fierens, and Daniel R. Parisi

Conflict Model of Evacuees and Vehicles on Pedestrian Crossing in the Aftermath of Disaster 467
Kentaro Kumagai and Kenji Ono

Social Force Model Describing Pedestrian and Cyclist Behaviour in Shared Spaces 477
Yufei Yuan, Bernat Goñi-Ros, Tim P. van Oijen, Winnie Daamen, and Serge P. Hoogendoorn

Multi-Attribute, Multi-Class, Trip-Based, Multi-Modal Traffic Network Equilibrium Model: Application to Large-Scale Network 487
Mostafa Ameli, Jean-Patrick Lebacque, and Ludovic Leclercq

Microscopic Cycling Behavior Model Using Differential Game Theory ... 497
Alexandra Gavriilidou, Yufei Yuan, Haneen Farah, and Serge P. Hoogendoorn

Simulating Bicycle Traffic by the Intelligent-Driver Model: Reproducing the Traffic-Wave Characteristics Observed in a Bicycle-Following Experiment 507
Valentina Kurtc and Martin Treiber

Large-Scale Modeling of VANET and Transportation Systems 517
Ahmed Elbery, Hesham A. Rakha, and Mustafa ElNainay

Activity Location Recommendation Using a Decentralized Proportional Feedback Mechanism 527
Tim P. van Oijen, Winnie Daamen, and Serge P. Hoogendoorn

Contributors

Robert P. Adkins Department of Computer Science, University of Maryland, College Park, MD, USA

Mostafa Ameli Universite Paris-Est, IFSTTAR, GRETTIA, Champs-sur-Marne, France

Université de Lyon, ENTPE, IFSTTAR, LICIT, Lyon, France

Shriniwas Arkatkar Sardar Vallabhbhai National Institute of Technology, Department of Civil Engineering, Surat, India

Eitan Bachmat Department of Computer Science, Ben-Gurion University, Beer-Sheva, Israel

Lucia Ballerini Department of Neuroimaging Sciences, University of Edinburgh, Edinburgh, UK

Stefania Bandini CSAI Research Center, University of Milano-Bicocca, Milan, Italy

RCAST, The University of Tokyo, Tokyo, Japan

Muhammad Baqui George Mason University, Fairfax, VA, USA

Volker Berkhahn Leibniz Universität Hannover, Institute for Risk and Reliability, Hannover, Germany

Christian Berzi CSAI-Complex Systems and Artificial Intelligence Research Centre, Department of Informatics, Systems and Communications, University of Milano-Bicocca, Milan, Italy

Stefan Bittihn University of Cologne, Institute for Theoretical Physics, Köln, Germany

Nikolai W. F. Bode University of Bristol, Department of Engineering Mathematics, Bristol, UK

Maik Boltes Jülich Supercomputing Centre, Jülich Research Centre, Jülich, Germany

André Borrmann Technische Universität München, Munich, Germany

Ernst Bosina ETH Zurich, Institute for Transport Studies and Systems (IVT), Zurich,Switzerland

Marek Bukáček Faculty of Information Technology, Czech Technical University in Prague, Prague 6, Czech Republic

Alexander P. Buslaev Moscow State Automobile and Road Tech. Univ. (MADI), High Mathematics Department, Moscow, Russia

Antonio J. Caamaño Rey Juan Carlos University, Móstoles, Spain

Boxiao Cao The George Washington University, Washington, DC, USA

Boris N. Chetverushkin Keldysh Institute of Applied Mathematics, Russian Academy of Sciences, Moscow, Russia

Mohcine Chraibi Forschungszentrum Jülich, Jülich, Germany

Richard D. Connors University of Leeds, Leeds, UK

Luca Crociani CSAI Research Center, University of Milano-Bicocca, Milan, Italy

Winnie Daamen Delft University of Technology, Delft, The Netherlands

Sélim Datoussaïd Architectural Engineering Department, Risks Institute, University of Mons, Mons, Belgium

Jan de Gier ARC Centre of Excellence for Mathematical and Statistical Frontiers (ACEMS), School of Mathematics and Statistics, The University of Melbourne, Melbourne, VIC, Australia

Alonso Espinosa Mireles de Villafranca University of Bristol, Bristol, UK

Charitha Dias Institute of Industrial Science, The University of Tokyo, Tokyo, Japan

Ahmed Elbery Department of Computer Science, Virginia Tech, Blacksburg, VA, USA

Mustafa ElNainay Department of Computer and Systems Engineering, Alexandria University, Alexandria, Egypt

Haneen Farah Delft University of Technology, Delft, The Netherlands

Claudio Feliciani Department of Advanced Interdisciplinary Studies, The University of Tokyo, Tokyo, Japan

Pablo I. Fierens Instituto Tecnológico de Buenos Aires, CONICET, Buenos Aires, Argentina

Vidar Frette Department of Engineering, Stord/Haugesund College, Haugesund, Norway

Bernhard Friedrich Technische Universität Braunschweig, Institute for Transportation and Urban Engineering, Braunschweig, Germany

Jingwan Fu School of Engineering and Applied Science Department of Civil and Environmental Engineering, The George Washington University Science and Engineering Hall, Washington, DC, USA

Hari Krishna Gaddam Department of Civil Engineering, IIT Delhi, New Delhi, India

Angel Garcimartín Departamento de Física y Matemática Aplicada, Facultad de Ciencias, Universidad de Navarra, Pamplona, Spain

Alexandra Gavriilidou Delft University of Technology, Delft, The Netherlands

Bernat Goñi-Ros Delft University of Technology, Delft, The Netherlands

Andrea Gorrini CSAI-Complex Systems and Artificial Intelligence Research Centre, Department of Informatics, Systems and Communications, University of Milano-Bicocca, Milan, Italy

Samer H. Hamdar George Washington University, Washington, DC, USA

Serge P. Hoogendoorn Delft University of Technology, Delft, The Netherlands

Pavel Hrabák Faculty of Information Technology, Czech Technical University in Prague, Prague 6, Czech Republic

Miho Iryo-Asano Department of Environmental Engineering and Architecture, Nagoya University, Nagoya, Japan

Michelle Isenhour Naval Post Graduate School, Monterey, CA, USA

Kitae Jang Korea Advanced Institute of Science and Technology, Daejeon, South Korea

Gaurang Joshi Sardar Vallabhbhai National Institute of Technology, Surat, India

Kyungwon Kang Virginia Polytechnic Institute and State University, The Charles E. Via, Jr. Department of Civil and Environmental Engineering, Blacksburg, VA, USA

Seungmo Kang Korea University, Seoul, South Korea

Jevgenijs Kaupužs Institute of Technical Physics, Riga Technical University, Faculty of Materials Science and Applied Chemistry, Riga, Latvia

Institute of Mathematical Sciences and Information Technologies, University of Liepaja, Liepaja, Latvia

Boris S. Kerner Physics of Transportation and Traffic, University of Duisburg-Essen, Duisburg, Germany

Nicolas Keusen Bundesamt für Verkehr BAV, Ittigen, Switzerland

Peter M. Kielar Technische Universität München, Munich, Germany

Sergey L. Klenov Department of Physics, Moscow Institute of Physics and Technology, Moscow, Russia

Victor L. Knoop Delft University of Technology, Delft, The Netherlands

Micha Koller Daimler AG, Sindelfingen, Germany

Pablo G. König Instituto Tecnológico de Buenos Aires, Buenos Aires, Argentina

Gerta Köster Munich University of Applied Sciences, Munich, Germany

Valery V. Kozlov Steklov Mathematical Institute, Russian Academy of Sciences, Moscow, Russia

Kentaro Kumagai Disaster Prevention Research Institute, Kyoto University, Kyoto, Japan

Valentina Kurtc Peter the Great St. Petersburg Polytechnic University, Department of Applied Mathematics, St. Petersburg, Russia

Sylvain Lassarre IFSTTAR COSYS GRETTIA, Marne la Vallée Cedex 2, France

Matthias Laubinger Munich University of Applied Sciences, Munich, Germany

Jean-Patrick Lebacque Universite Paris-Est, IFSTTAR, GRETTIA, Champs-sur-Marne, France

Ludovic Leclercq Université Lyon, ENTPE, IFSTTAR, LICIT, Lyon, France

Tianshu Li The George Washington University, Washington, DC, USA

Rainald Löhner George Mason University, Fairfax, VA, USA

Ruggiero Lovreglio School of Built Environment, Massey University, Auckland, New Zealand

Reinhard Mahnke Rostock University, Institute of Physics, Rostock, Germany

Wilson Marques Departamento de Física, Universidade Federal do Paraná, Curitiba, Brazil

Florian Mazur University of Duisburg-Essen, Physics of Transport and Traffic, Duisburg, Germany

Martin Mendelin Swiss Federal Railways AG (SBB), Bern, Switzerland

Alma Rosa Méndez Departamento de Matemáticas Aplicadas y Sistemas, Universidad Autónoma Metropolitana, Cuajimalpa, Mexico

Yusuke Miyoshi Department of Aeronautics and Astronautics, School of Engineering, The University of Tokyo, Tokyo, Japan

Sven-Eric Molzahn Daimler AG, Sindelfingen, Germany

David M. Mount Department of Computer Science, University of Maryland, College Park, MD, USA

Akihito Nagahama Department of Advanced Interdisciplinary Studies, Graduate School of Engineering, University of Tokyo, Tokyo, Japan

Alexandre Nicolas LPTMS, CNRS, Université Paris-Sud, Université Paris-Saclay, Orsay, France

Katsuhiro Nishinari Research Center for Advanced Science and Technology, University of Tokyo, Tokyo, Japan

Kenji Ono Port and Airport Research Institute, Yokosuka, Kanagawa, Japan

Dong Pan Department of Civil and Environmental Engineering, George Washington University, Washington, DC, USA

Daniel R. Parisi Instituto Tecnológico de Buenos Aires, CONICET, Buenos Aires, Argentina

Federico Pascucci Technische Universität Braunschweig, Institute for Transportation and Urban Engineering, Braunschweig, Germany

Germán A. Patterson Instituto Tecnológico de Buenos Aires, CONICET, Buenos Aires, Argentina

Luis A. Pugnaloni Departamento de Ingeniería Mecánica, Facultad Regional La Plata, Universidad Tecnológica Nacional, CONICET, La Plata, Argentina

Anass Rahouti University of Mons, Civil Engineering and Structural Mechanics Department, Mons, Belgium

Narayana Raju Sardar Vallabhbhai National Institute of Technology, Surat, India

Hesham A. Rakha Virginia Polytechnic Institute and State University, The Charles E. Via, Jr. Department of Civil and Environmental Engineering, Blacksburg, VA, USA

Bradley Department of Electrical and Computer Engineering, Virginia Tech, Blacksburg, VA, USA

K. Ramachandra Rao Department of Civil Engineering and Transportation Research and Injury Prevention Programme (TRIPP), IIT Delhi, New Delhi, India

Hubert Rehborn Daimler AG, Sindelfingen, Germany

Nils Rinke Leibniz Universität Hannover, Institute for Risk and Reliability, Hannover, Germany

Federico Sangiuliano Jimka Instituto Tecnológico de Buenos Aires, Buenos Aires, Argentina

Andreas Schadschneider Institute for Theoretical Physics, University of Cologne, Köln, Germany

Rik Schakenbos NS Stations, Netherlands Railways (NS), Utrecht, The Netherlands

Chris Schiermeyer Leibniz Universität Hannover, Institute for Risk and Reliability, Hannover, Germany

Johannes Schmidt Institut für Theoretische Physik, Universität zu Köln, Köln, Germany

Jakob Schöttl Munich University of Applied Sciences, Munich, Germany

Michael Schreckenberg University of Duisburg-Essen, Physics of Transport and Traffic, Duisburg, Germany

Jette Schumann Forschungszentrum Jülich, Jülich Supercomputing Centre, Jülich, Germany

Gunter M. Schütz Institute of Complex Systems, Forschungszentrum Jülich, Jülich, Germany

Michael J. Seitz Munich University of Applied Sciences, Munich, Germany

Armin Seyfried Jülich Supercomputing Centre, Jülich Research Centre, Jülich, Germany

Faculty of Architecture and Civil Engineering, University of Wuppertal, Wuppertal, Germany

Claire E. Silverstein George Washington University, Washington, DC, USA

Weiguo Song State Key Laboratory of Fire Science, University of Science and Technology of China, Hefei, China

Xiang Song Department of Civil and Environmental Engineering, Massachusetts Institute of Technology, Cambridge, MA, USA

Alexander G. Tatashev Moscow Tech. Univ. of Communications and Informatics (MTUCI), Moscow, Russia

Jasmin Thurau Swiss Federal Railways AG (SBB), Bern, Switzerland

Antoine Tordeux Forschungszentrum Jülich, Jülich, Germany

University of Wuppertal, Wuppertal, Germany

Martin Treiber Technische Universität Dresden, Institute for Transport and Economics, Dresden, Germany

Jana Vacková Czech Technical University, Prague, Czech Republic

Jeroen van den Heuvel Department of Transport and Planning, Faculty of Civil Engineering and Geosciences, Delft University of Technology, Delft, The Netherlands

NS Stations, Netherlands Railways (NS), Utrecht, The Netherlands

Hans van Lint Delft University of Technology (TU Delft), Delft, The Netherlands

Marcel van Ofwegen ProRail, Utrecht, The Netherlands

Tim P. van Oijen Delft University of Technology, Department of Transport and Planning, Delft, The Netherlands

Rosa María Velasco Departamento de Física, Universidad Autónoma Metropolitana, Iztapalapa, Mexico

Giuseppe Vizzari CSAI-Complex Systems and Artificial Intelligence Research Centre, Department of Informatics, Systems and Communications, University of Milano-Bicocca, Milan, Italy

Cornelia von Krüchten Institut für Theoretische Physik, Universität zu Köln, Köln, Germany

Jiayue Wang Institute of Public Safety Research, Department of Engineering Physics, Tsinghua University, Beijing, China

Center for Capital Social Safety, People's Public Security University of China, Beijing, China

Juelich Supercomputing Centre, Juelich Research Centre, Juelich, Germany

Dominik Wegerle Physics of Transportation and Traffic, University of Duisburg-Essen, Duisburg, Germany

Ulrich Weidmann ETH Zurich, Institute for Transport Studies and Systems (IVT), Zurich, Switzerland

Wenguo Weng Institute of Public Safety Research, Department of Engineering Physics, Tsinghua University, Beijing, China

R. Eddie Wilson University of Bristol, Bristol, UK

Keisuke Yamazaki The Artificial Intelligence Research Center, National Institute of Advanced Industrial Science and Technology, Tokyo, Japan

Daichi Yanagisawa Research Center for Advanced Science and Technology, University of Tokyo, Tokyo, Japan

Marina V. Yashina Moscow Technical University of Communications and Informatics (MTUCI), Moscow, Russia

Yufei Yuan Delft University of Technology, Department of Transport and Planning, Delft, The Netherlands

Yiping Zeng Complex Systems and Artificial Intelligence Research Center, University of Milano-Bicocca Milano, Italy

State Key Laboratory of Fire Science, University of Science and Technology of China, Hefei, China

Alice A. Zhang Montgomery Blair High School, Silver Spring, MD, USA

Jiahua Zhang Graduate School of Engineering, The University of Tokyo, Tokyo, Japan

Jun Zhang State Key Laboratory of Fire Science, University of Science and Technology of China, Hefei, China

Verena Ziemer Jülich Supercomputing Centre, Jülich Research Centre, Jülich, Germany

Faculty of Architecture and Civil Engineering, University of Wuppertal, Wuppertal, Germany

Benedikt Zönnchen Munich University of Applied Sciences, Munich, Germany

Technical University of Munich, Garching, Germany

Iker Zuriguel Departamento de Física y Matemática Aplicada, Facultad de Ciencias, Universidad de Navarra, Pamplona, Spain

Boudewijn Zwaal Delft University of Technology, Delft, The Netherlands

Part I
Roadway Vehicular Flow: Data Collection, Modeling and Simulation

Exact Formula of Time-Headway Distribution for TASEP with Random-Sequential Update

Pavel Hrabák

Abstract The analytical derivation of time-headway distribution for random-sequential totally asymmetric simple exclusion process (TASEP) with periodic boundaries is presented. The finite and periodic nature of the lattice together with the lattice-size-dependent hopping probability related to the random-sequential update does not allow to use common method for the derivation of the time-headway distribution. Another method is presented in this article. The exact derivation of the time-headway distribution leads to several interesting combinatorial tasks. Further, after proper time scaling and using the large L limit we obtain the approximation of the distribution, which can be considered as exact result for TASEP with continuous time.

1 Introduction

The distribution of the spatial and temporal headway serves as a useful tool for traffic engineering since it may reflect microscopic properties of vehicular/traffic flow as, e.g., repulsion forces between vehicles and uncertainty/stochasticity of driver's reactions. A systematic review of vehicle headway studies can be found in [4].

The aim of this paper is to investigate analytically the temporal-headway distribution for the well-known totally asymmetric simple exclusion process (TASEP) with the random-sequential update. Such study completes the studies on the time-headway distribution of parallel [2], generalized backward-sequential, and continuous update [3].

P. Hrabák (✉)
Faculty of Information Technology, Czech Technical University in Prague, Prague 6, Czech Republic
e-mail: pavel.hrabak@fit.cvut.cz; hrabapav@fit.cvut.cz

S. H. Hamdar (ed.), *Traffic and Granular Flow '17*,
https://doi.org/10.1007/978-3-030-11440-4_1

The TASEP can be considered as the simplest model of traffic and vehicular flow. Despite its simplicity the model evinces complex properties of collective motion. The model belongs to the class of interacting or hopping particle systems, the overview applicability of such processes in traffic flow modelling can be found in [6].

The TASEP can be considered as Markov chain or process and is usually investigated in stationary/steady state. The stationary-state properties of TASEP with variety of updates are investigated in [5] and well summarized in [1]. The main result used in this article is the fact that the stationary measure of TASEP with random-sequential update is the Bernoulli measure, i.e., in the periodic boundary case all configurations have uniform probability.

2 Model Definition

For simplicity the periodic boundary conditions are considered. The model consists in N particles moving along the lattice consisting of L sites by hopping from one site to the neighbouring site in one given direction, i.e., a particle sitting in site x can hop to the neighbouring site $x + 1$ with probability $p \in (0, 1]$, if the target site is empty. The periodicity means that the neighbouring site to the last site is the first site of the lattice. For illustration see Fig. 1. The periodic boundary conditions preserve the number of particles on the lattice defining the particle density as $\rho = N/L$.

In the random-sequential update, during each time step of the algorithm one site is chosen at random (uniformly, i.e., with probability $1/L$). If the chosen site is occupied by a particle, the particle hops according to the above-mentioned rules. Under this update the value of hopping probability p does effect only the temporal scaling of the model dynamics [5] and therefore can be set equal to one without loss of generality. Due to the dependence of the dynamics on the lattice size it is convenient (and even necessary) to scale the time in the way that one algorithm step corresponds to $1/L$ of the time unit.

It is worth noting that the random-sequential dynamics simplifies the derivation of the stationary-state distribution and therefore simplifies the derivation of spatial quantities in comparison to the parallel updates, under which all particles hop simultaneously. However, the derivation of temporal related quantities is then rather more difficult due to the dependency of the motion of individual particles on the lattice.

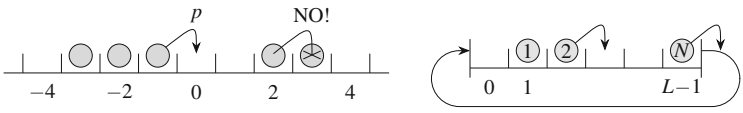

Fig. 1 To the definition of TASEP dynamics

3 Time-Headway Distribution

The time headway between two consecutive vehicles is defined as the length Δt of the time interval between the passing of the vehicles through given detector. In the case of lattice hopping models, the role of the detector is played by the reference site, which can be chosen arbitrarily due to the periodic nature of the dynamics. In the following, the time measured in algorithm steps will be denoted by letter k. The transition to the time t measured in time units is performed by means of the time-scaling transformation $t = k/L$.

Let us consider two consecutive particles. For purposes of the derivation let us denote the first particle as *leading* particle (abbr. L) and the second as *following* particle (abbr. F). The step-headway between these two particles is the time interval

$$\Delta k = k_{\mathrm{F}}^{\mathrm{out}} - k_{\mathrm{L}}^{\mathrm{out}}\,, \tag{1}$$

where k_i^{in} denotes the arrival time of particle i to the reference site (denoted as 0) and k_i^{out} denotes the departure time of i from site 0. For illustration see the space-time diagram in Fig. 2.

The investigated quantity called step-headway distribution is then characterized by the probability density function f, i.e.,

$$f(k; L, N) = \mathrm{P}(\Delta k = k \mid L, N). \tag{2}$$

Here, the number of sites L and the number of particles N are parameters of the distribution and are often omitted in the notation.

The common concept of calculating the temporal headway distribution, introduced in [2], is to decompose the probability with respect to the time interval between the departure of the leading particle and the arrival of the following particle, i.e.,

$$\mathrm{P}(\Delta k = k) = \sum_{k_1} \mathrm{P}\left(k_{\mathrm{F}}^{\mathrm{in}} - k_{\mathrm{L}}^{\mathrm{out}} = k_1\right) \mathrm{P}\left(k_{\mathrm{F}}^{\mathrm{out}} - k_{\mathrm{F}}^{\mathrm{in}} = k - k_1 \,\middle|\, k_{\mathrm{F}}^{\mathrm{in}} - k_{\mathrm{L}}^{\mathrm{out}} = k_1\right). \tag{3}$$

k	$\cdots$	-4	-3	-2	-1	0	1	2	3	4	$\cdots$	
-1	$\cdots$	0	F	0	0	L	0	1	1	0	$\cdots$	
0	$\cdots$	0	F	0	0	0	L	1	1	0	$\cdots$	$k_{\mathrm{LP}}^{\mathrm{out}}$
1	$\cdots$	0	0	F	0	0	L	1	0	1	$\cdots$	
2	$\cdots$	0	0	0	F	0	L	0	1	0	$\cdots$	
3	$\cdots$	1	0	0	0	F	0	L	0	1	$\cdots$	$k_{\mathrm{FP}}^{\mathrm{in}}$
4	$\cdots$	1	0	0	0	F	0	0	L	0	$\cdots$	
5	$\cdots$	0	1	0	0	F	0	0	0	L	$\cdots$	
6	$\cdots$	0	1	0	0	0	F	0	0	L	$\cdots$	$k_{\mathrm{FP}}^{\mathrm{out}}$

Fig. 2 Illustration to the step-headway notation. The space-time diagram is presented, F, L, and 1 denote the position of following, leading, and other particle, respectively

This concept works for updates under which the motion of leading and following particle is independent during the time interval between $k_{\mathrm{L}}^{\mathrm{out}}$ and $k_{\mathrm{F}}^{\mathrm{in}}$. But this is not the case of the random-sequential update, since at most one particle can move within given algorithm step.

4 Calculation for Random-Sequential Update

The dependence of the motion of leading and following particle induces us to consider the situation of both particles at ones. The first step is to decompose the problem to situations with given number m of empty sites in front of the following particle F and the number n of occupied sites in front of the leading particle L, i.e.,

$$f(k) = \sum_{m,n} P(m,n)\mathrm{P}(\Delta k = k \mid m,n)\,, \tag{4}$$

where

$$P(m,n) = \mathrm{P}(m \text{ sites in front of } F \wedge n \text{ particles in front of } L) \tag{5}$$

$$= \binom{L-n-m-2}{N-m-1}\binom{L-2}{N-1}^{-1}. \tag{6}$$

The latter equality holds because all configurations have the same probability. The situation is depicted in Fig. 3.

In such situation, the following particle has to hop m-times to reach the reference site 0, there is cluster of n leading particles, which need to hop sequentially by one site to empty the site 1, and then the following particle needs to hop at exactly k-th step. This means that there are $z = k - m - n - 1$ steps, during which none of the involved particles hops. And this is the crucial moment of the derivation. Let us code the process trajectories by letters F, L, and 0 denoting the hop of following particle, the hop of particle in cluster in front of the leading particle, and not hopping of involved particles. Three possible situations have to be distinguished:

1. Following particle still did not reach site 0 and leading particle is still in site 1, i.e., both can hop. Then the symbol 0 appears with probability $(1 - 2/L)$.
2. Following particle still did not reach site 0 and leading particle already left site 1. Then the symbol 0 appears with probability $(1 - 1/L)$.
3. Following particle already reached site 0 and leading particle is still in site 1. Then the symbol 0 appears with probability $(1 - 1/L)$.

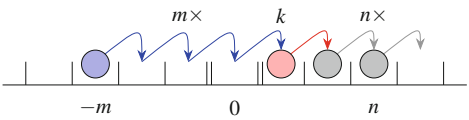

Fig. 3 Illustration to the situation of the type (m, n)

The situation when following particle reached 0 and leading particle left 1 is not interesting, because then 0 appears with probability 1 or 0 depending on the number of 0s in the trajectory before.

The conditional probability $\mathrm{P}(\Delta k = k \mid m, n)$ can be then decomposed with respect to the number of zeros appearing before the last F or the last L, i.e.,

$$\mathrm{P}(\Delta k = k \mid m, n) = \sum_{j=0}^{z} \left(\frac{1}{L}\right)^{k-z} \left(1 - \frac{2}{L}\right)^{j} \left(1 - \frac{1}{L}\right)^{z-j} C_{n,m,z}(j)\,, \tag{7}$$

where $C_{n,m,z}(j)$ is the number of trajectories in which there are exactly j zeros before the last F or the last L given that there are m symbols F, n symbols L, and z symbols 0. This leads to the following combinatorial task:

- I have a bag with m F-balls, n L-balls, and z 0-balls.
- I drag sequentially all balls from the sack.
- What is the probability that I dragged exactly j 0-balls before the last F-ball?

The solution of this combinatorial task is provided in Appendix. We obtain that

$$\begin{aligned} C_{n,m,z}(j) = &\binom{j+n-1}{j}\left[\binom{z+n+m}{m} - \binom{j+n+m-1}{m}\right] + \\ &+ \binom{j+m-1}{j}\left[\binom{z+n+m}{n} - \binom{j+n+m-1}{n}\right]. \end{aligned} \tag{8}$$

Before the final formula can be presented, one situation is to be discussed. So far, we have assumed that the motion of the first particle in the cluster and the motion of following particle are dependent only because of the random-sequential update. However, in case that $k \geq L$, we have to calculate with the situation that all particles are in one cluster and therefore the following particle is actually the first particle of the cluster in front of the leading particle. In such a case, we will "wait" until the first particle hops one site further and then we can proceed in the same way as above.

The final formula is then

$$\begin{aligned} f(k; L, N) = &\sum_{n}\sum_{m} \frac{P_{L,N}(n,m)}{L^{n+m+1}} \sum_{j=0}^{z} C_{n,m,z}(j) \left(1 - \frac{2}{L}\right)^{j} \left(1 - \frac{1}{L}\right)^{z-j} \\ &+ \mathbf{1}_{\{k \geq L\}} \binom{L-2}{N-1}^{-1} L^{-L} \sum_{w}\sum_{i} C_{N-1,L-N-1,k-w-L}(i) \left(1 - \frac{2}{L}\right)^{i} \left(1 - \frac{1}{L}\right)^{k-L-i}, \end{aligned} \tag{9}$$

where $z = k - 1 - n - m$, $n = 1, \ldots, \min\{k-1, N-1\}$, $m = 1, \ldots, \min\{k-1-n, L-N-1\}$, $w = 0, \ldots, k-L$, and $i = 1, \ldots, k-w-L$.

Here it is important to note that the time t measured in time units in random-sequential update scales by the factor $1/L$, i.e., one algorithm step corresponds to $1/L$ time unit. In Fig. 4, the exact values of scaled time headways $f(t) := f(k/L)$

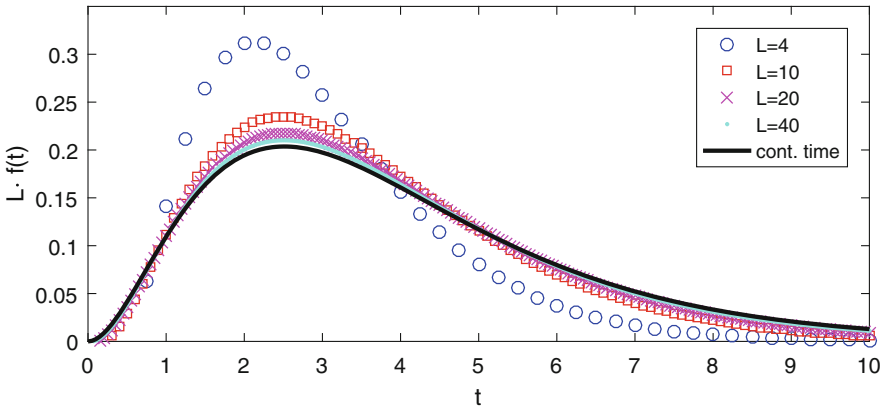

Fig. 4 Step headway for random-sequential TASEP for $\rho = 1/2$. Values $f(t)$ are multiplied by the lattice size L to visually compensate the fact that one time unit contains L values k/L

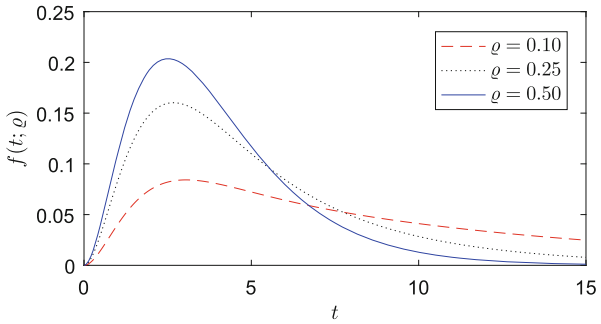

Fig. 5 Time headway for continuous time TASEP

are plotted. It is obvious that the exact formula converges to the continuous time approximation quite fast.

Expected value of the time-headway distribution $f(k/L)$ is reciprocal to the flow $J = \frac{N}{L}\left(1 - \frac{N}{L}\right)\frac{L}{L-1}$. Denoting by $\rho = N/L$ the particle density, we get $\mathrm{E}\Delta t = \frac{1}{\rho\bar{\rho}}\frac{L-1}{L}$.

To obtain the large L limit it is convenient to use the result for parallel update [2]. The limiting distribution is then

$$f(t;\rho) = \frac{\rho}{\bar{\rho}}\left(\mathrm{e}^{-\rho t} - \mathrm{e}^{-t}\right) + \frac{\bar{\rho}}{\rho}\left(\mathrm{e}^{-\bar{\rho} t} - \mathrm{e}^{-t}\right) - t\mathrm{e}^{-t}\,, \quad t \geq 0\,, \tag{10}$$

where ρ is the parameter preserving the density of particles, i.e., $N = \lfloor \rho L \rfloor$, and $\bar{\rho} = 1 - \rho$. Expected value and variation of the distribution are $\mathrm{E}\Delta t = \frac{1}{J} = \frac{1}{\rho\bar{\rho}}$ and $\mathrm{var}\Delta t = \frac{1-2\rho\bar{\rho}-2(\rho\bar{\rho})^2}{(\rho\bar{\rho})^2}$. We refer the reader for more details to [3]. The distribution $f(t)$ is for illustration plotted in Fig. 5.

5 Conclusions

The main goal of this paper was to complete the studies on temporal headway distribution of the TASEP model under variety of updates by the exact derivation of the random-sequential update.

The exact derivation illustrates that several problems appear due to the dependency of the motion of leading and following particle caused by the random-sequential update. Despite the solution of augmented combinatorial tasks the exact formula is still given in the form of "not summed" sums, which lead to hypergeometric functions. However, for small lattice size L, this formula can be used for precise calculation of the distribution. This seems to be sufficient, since the distribution quickly converges to the distribution of the continuous time TASEP, which is provided in more pleasant form.

Acknowledgement This work was supported by the Czech Science Foundation under grant GA15-15049S.

Appendix

Lemma 1 *For $n, m \geq 1$ and $z \geq 0$ it holds*

$$C_{n,m,z}(j) = \binom{j+n-1}{j}\left[\binom{z+n+m}{m} - \binom{j+n+m-1}{m}\right] + \\ + \binom{j+m-1}{j}\left[\binom{z+n+m}{n} - \binom{j+n+m-1}{n}\right] \tag{11}$$

Proof This combinatorial task leads to the expression

$$C_{n,m,z}(j) = \sum_{d=0}^{z-j}\sum_{r_L=0}^{m-1}\binom{z-j-d+r_L}{r_m}\frac{(j+m+n-r_L-2)!}{k!(n-1)!(m-1-r_L)!} \\ + \sum_{d=0}^{z-j}\sum_{r_F=0}^{n-1}\binom{z-j-d+r_F}{r_n}\frac{(j+m+n-r_F-2)!}{j!(m-1)!(n-1-r_F)!}\,, \tag{12}$$

as can be seen from Fig. 6. This can be summed using combinatorial Lemmas 2 and 3 shown below.

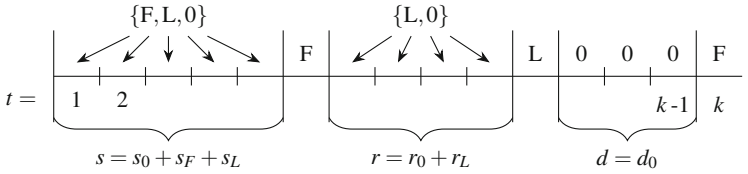

Fig. 6 To the derivation of $C_{n,m,z}(j)$, where $s_0 = j, r_0 = z-j-d, r_L+s_L = m-1, s_F = n-1$. Exchanging F and L leads to the second sum of (12)

Lemma 2 *For $a, b, m \geq 0$ it holds*

$$\sum_{k=0}^{m} \binom{a+k}{k} \binom{b+m-k}{m-k} = \binom{a+b+m+1}{m}. \tag{13}$$

Proof

$$\sum_{m=0}^{+\infty} \binom{a+b+m+1}{m} z^m = (1-z)^{-(a+1)-(b+1)} = \sum_{m=0}^{+\infty} \sum_{k=0}^{m} \binom{a+k}{k} \binom{b+m-k}{m-k} z^m . \tag{14}$$

Lemma 3 *For $a > b \geq 0$ and $m \geq 0$ it holds*

$$\sum_{d=0}^{m} \binom{a+d}{b} = \binom{a+m+1}{b+1} - \binom{a}{b+1}. \tag{15}$$

Proof The relation can be directly derived using

$$\binom{a+d}{b} = \binom{a+d+1}{b+1} - \binom{a+d}{b+1}. \tag{16}$$

References

1. Blythe, R., Evans, M.: Nonequilibrium steady states of matrix-product form: a solver's guide. J. Phys. A Math. Theor. **40**(46), R333–R441 (2007). https://doi.org/10.1088/1751-8113/40/46/R01
2. Chowdhury, D., Pasupathy, A., Sinha, S.: Distributions of time- and distance-headways in the Nagel-Schreckenberg model of vehicular traffic: effects of hindrances. Eur. Phys. J. B **5**(3), 781–786 (1998). https://doi.org/10.1007/s100510050502
3. Hrabák, P., Krbálek, M.: Time-headway distribution for periodic totally asymmetric exclusion process with various updates. Phys. Lett. A **380**(9–10), 1003–1011 (2016). https://doi.org/10.1016/j.physleta.2016.01.013
4. Li, L., Chen, X.M.: Vehicle headway modeling and its inferences in macroscopic/microscopic traffic flow theory: a survey. Transp. Res. C Emerg. Technol. **76**, 170–188 (2017). https://doi.org/10.1016/j.trc.2017.01.007
5. Rajewsky, N., Santen, L., Schadschneider, A., Schreckenberg, M.: The asymmetric exclusion process: comparison of update procedures. J. Stat. Phys. **92**(1–2), 151–194 (1998). https://doi.org/10.1023/A:1023047703307
6. Schadschneider, A., Chowdhury, D., Nishinari, K.: Stochastic Transport in Complex Systems: From Molecules to Vehicles. Elsevier Science B.V., Amsterdam (2010). https://doi.org/10.1016/B978-0-444-52853-7.00016-6

Impact of Next-Nearest Leading Vehicles on Followers' Driving Behaviours in Mixed Traffic

Akihito Nagahama, Daichi Yanagisawa, and Katsuhiro Nishinari

Abstract The number of vehicles on the road is increasing across all vehicle types, especially in developing countries. The rise of heterogeneity in traffic causes greater mixed traffic congestion. This study focuses on the impact of next-nearest leading vehicles on the driving of following drivers in mixed traffic. Although previous studies reported that traffic stability can be improved with the introduction of followers' anticipatory driving that references multiple leaders, these works did not consider whether anticipatory driving occurred in mixed traffic. Using data collected in experiments with groups of two and three vehicles, we found that the operational delay and the maximum acceleration and deceleration of the followers were affected by the presence of next-nearest leaders. In addition, we also found that the height of the next-nearest leading vehicles affected followers' deceleration. These findings imply that model parameters for determining the deceleration of following vehicles should take the height of the next-nearest leading vehicle into account.

1 Introduction

The number of vehicles being driven on roads is increasing across all vehicle sectors and types, and traffic heterogeneity is particularly pronounced in developing countries [6]. This leads to greater traffic congestion, which causes problems such as economic losses and traffic accidents.

This study focuses on the impact of next-nearest leading vehicles on followers' drivings in mixed traffic. Although whether the followers refer the next-nearest leaders' driving is still unclear [4, 5], several studies have reported that in homogeneous

A. Nagahama (✉)
Department of Advanced Interdisciplinary Studies, Graduate School of Engineering, The University of Tokyo, Tokyo, Japan
e-mail: nagahama0814@g.ecc.u-tokyo.ac.jp

D. Yanagisawa · K. Nishinari
Research Center for Advanced Science and Technology, The University of Tokyo, Tokyo, Japan
e-mail: tDaichi@mail.ecc.u-tokyo.ac.jp; tknishi@mail.ecc.u-tokyo.ac.jp

S. H. Hamdar (ed.), *Traffic and Granular Flow '17*,
https://doi.org/10.1007/978-3-030-11440-4_2

traffic flow comprising one type of vehicles, stability improves if the followers anticipate driving of the nearest leaders with reference to next-nearest leaders' driving [3]. In heterogeneous traffic, anticipation can also improve stability because visibility of the next-nearest leaders can be improved due to the varying vehicle sizes, e.g. heights and lengths.

In this study, using data collected on a test course, we applied a statistical test to compare the driving characteristics of the followers with and without next-nearest leaders present. These observations clarified which driving characteristics of the followers were affected by the presence of the next-nearest leaders. In addition, we also developed regression models for these affected characteristics and found factors that affect the next-nearest leaders. From these comparisons, we suggest guidelines for how to determine parameters in car-following models under the assumption that followers refer to multiple leaders in heterogeneous traffic.

2 Experiment

To investigate the effects of the next-nearest leaders as well as effective factors of vehicle and driving characteristics, we observed following behaviours in groups comprising two and three vehicles as shown in Fig. 1. A group with two vehicles comprised a follower and a nearest leader. A group with three vehicles included a follower, a nearest leader and a next-nearest leader. We refer to measurements with two vehicles and those with three vehicles as Type A and Type B, respectively. Vehicles were chosen from motorcycles, normal passenger cars and container trucks. The motorcycles were 50-cc scooters. For the normal passenger cars, Toyota Corolla Axios were used. For the trucks, Isuzu Elfs with a container were used.

In the test course, three types of cones instructed the leading vehicles to start, brake or stop. We instructed the leading front end vehicles to commence acceleration from the start cones. After reaching 50 or 60 km/h, the front end vehicles maintained constant velocity. The front end vehicles were instructed to brake starting at the braking cones to stop at the stop cones. In contrast, we did not give any instructions to the followers and next-nearest leaders other than telling them to follow the vehicles in front of them. While these vehicles were driving based on our instructions, the positions of the vehicles were recorded to an accuracy of 60 cm

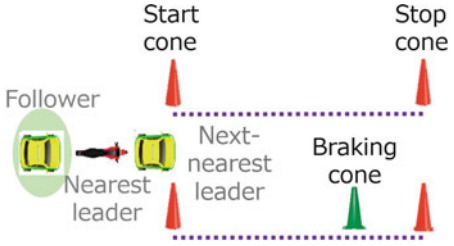

Fig. 1 Configuration of the test course

Table 1 Vehicle combinations and measured sample numbers in experiments for Type A and Type B

Test type	Follower	Nearest leader	Next-nearest leader	Trial number
Type A (two vehicles)	MC	MC	–	2
	Car	MC	–	16
	Truck	MC	–	11
Type B (three vehicles)	MC	MC	MC	4
			Car	4
			Truck	4
	Car	MC	MC	3
			Car	18
			Truck	3
	Truck	MC	MC	10
			Car	4
			Truck	10

MC denotes for motorcycle

by GPS antennas (Hemisphere A100) on top of the vehicles. The details of our measurement methods were the same as those in [7].

We conducted our experiments in December 2015 ($Day1$) and September 2016 ($Day2$) to obtain sufficient trial numbers. We utilised test courses of the Japan Automobile Research Institute on both days. On $Day1$, the experiments were held on a straight course. On $Day2$, an oval course was used. The oval course was divided into several sections. Some of these sections were not used due to their sags and curves.

Table 1 shows the numbers of trials that we performed for vehicle combinations. By fixing the nearest leaders as motorcycles, we can ignore the effects from the type of the nearest leaders. All drivers participating in the experiment were males between the ages of 20 and 50 and had at least 3 years of driving experience.

3 Driving and Vehicle Characteristics

To compare differences in driving behaviour, we need to introduce the characteristic features of driving behaviour. Additionally, the physical and performance characteristics of each vehicle need to be considered to explain the changes in the followers' driving. We selected characteristic features from the velocities and accelerations of the leaders and followers as well as the distance gaps between vehicles. V, a

and S denote the velocities, accelerations and distance gaps, respectively. From the velocities, we chose the maximum value, i.e. $V_{\max}$. From the accelerations, the maximum and the minimum values denoted as $a_{\max}$ and $a_{\min}$ were chosen. From the distance gaps, the initial and maximum values (S_{start} and $S_{\max}$) were chosen. In addition the ϵ_{a} was considered as operational delay, and it represents the difference of emerging times of the maximum accelerations between the followers and the nearest leaders, and the nearest leaders and the next-nearest leaders. We refer to these variables as driving characteristics. Note that we use superscripts "f", "1st l" and "2nd l" to indicate the followers, the nearest leaders and next-nearest leaders, respectively. For example, $a_{\max}^{\text{2nd l}}$ indicates the next-nearest leaders' maximum acceleration and $V_{\max}^{\text{f}}$ indicates the followers' maximum velocity. The superscripts of "1st" and "2nd" represent the relationships between the followers and the nearest leaders, and the nearest leaders and the next-nearest leaders, respectively. In following sections, we analyse $\epsilon_{\text{a}}^{\text{1st}}$, $V_{\max}^{\text{f}}$, $a_{\max}^{\text{f}}$, $a_{\min}^{\text{f}}$, $S_{\text{start}}^{\text{1st}}$ and $S_{\max}^{\text{1st}}$ one by one.

For vehicle characteristics, we applied the vehicle longitudinal length, height (including the drivers for motorcycles) and the maximum power divided by the weight, i.e. the power-to-weight ratio (PWR). L, TH and P stand for the length, the height and the PWR, respectively. Note that the same superscripts, i.e. "f", "1st l" and "2nd l", are used to indicate the relations between vehicles.

In addition to these characteristics, we initially considered whether the vehicle weight, width, height or torque-to-weight ratio should be included to the vehicle characteristics. However, we finally removed these parameters because they were strongly correlated with other characteristics, at least in our datasets. Such strong correlations could cause problems of multi-collinearity in the analysis that we present in Sect. 5. In Sect. 5, we develop regression models of the driving characteristics of followers using these vehicle characteristics along with other driving characteristics.

4 Impact of Next-Nearest Leaders' Presence

In this section we consider whether or not $\epsilon_{\text{a}}^{\text{1st}}$, $V_{\max}^{\text{f}}$, $a_{\max}^{\text{f}}$, $a_{\min}^{\text{f}}$, $S_{\text{start}}^{\text{1st}}$ and $S_{\max}^{\text{1st}}$ are affected by the presence of next-nearest leaders. If we statistically conclude that these characteristics are different with and without next-nearest leaders present, we will find that follower driving is affected by the presence of next-nearest leaders. Therefore, we applied a statistical test for whether driving characteristics are different with two (Type A) or three vehicles (Type B) in a group. To evaluate only the effect of next-nearest leaders' presence, we compared only the data when the follower is the car for Type A and the data when the follower is a car and the next-nearest leader is the car for Type B.

We applied the Wilcoxon–Mann–Whitney test because the parameters we measured could not be necessarily assumed to follow a Gauss distribution. The p-values of $S_{\text{start}}^{\text{1st}}$ and $S_{\max}^{\text{1st}}$ were over 20%. We could not conclude that the distance gaps were

affected by the presence of a next-nearest leader. As the p-value of ϵ_a^{1st} was less than 0.1%, ϵ_a^{1st} was affected by the next-nearest leaders. The maximum acceleration and deceleration of the followers returned p-values of 16% and 13%, respectively. These values leave possibility that these characteristics are driven by the leaders' behaviour open. Therefore, we focus more closely on effects of next-nearest leaders in the next section

5 Effective Factors of Next-Nearest Leaders

In this section, we compare differences between linear regression models for Type A and Type B to clarify which characteristics of the next-nearest leaders affect the followers' behaviour. We assume that explanatory variables included in the regression model for Type A are also included in the model for Type B for the same follower driving behaviours.

Figure 2 shows how we developed our models. We refer to the procedures to develop models for Type A and Type B as Step A and Step B, respectively. To obtain the models for Type A datasets, we first calculated the relative importance of

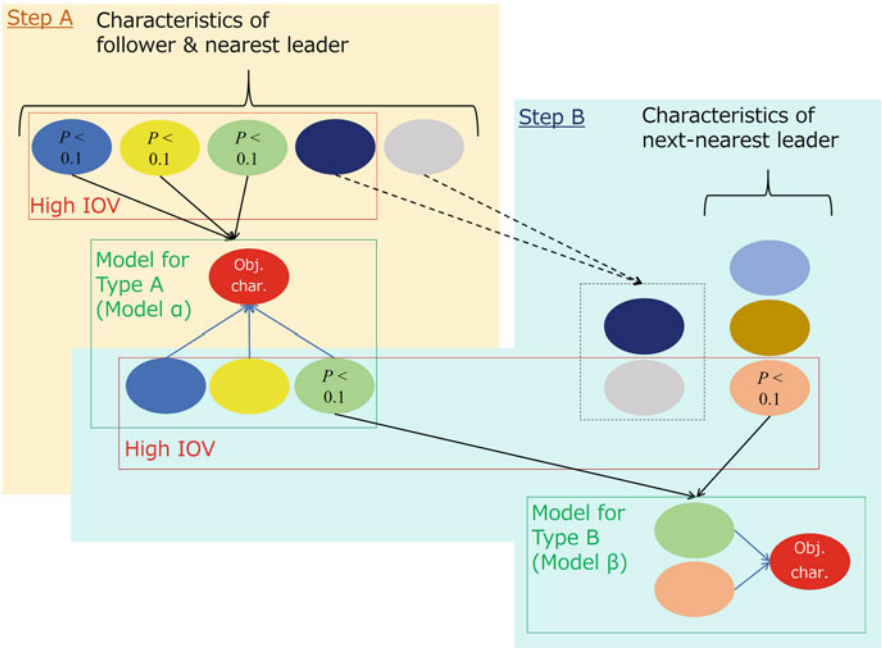

Fig. 2 Selection procedure for models for Type A and Type B (two- and three-driver groups). Respective coloured ellipses represent driving and vehicle characteristics, i.e. explanatory and objective variables

variable candidates, i.e. IOV. Variable candidates included all vehicle characteristics, dummy variables for Day and test drivers and related driving characteristics from the perspective of the timing of emergence. The IOV is a value from 0 to 1 and is often used to practically check which explanatory variables play important roles in candidate models. IOV can be obtained by summing up the Akaike weights [2, 8] for possible models using every combination of explanatory variables. Since the Akaike weight of a certain model grows large when the model is close to the best model from the perspective of the Akaike information criterion (AIC) [1], large IOVs for each variable mean that the explanatory variable is frequently included in better models from the AIC perspective. Here we summed up the Akaike weights of models within 2.0 of AIC difference from the best model.

Using all the variables with high IOVs, a regression model to explain the objective variable can be constructed. Although it is common in practice to apply a threshold IOV of 0.8 as the standard for variable importance, we eliminated variables for which the IOV became small suddenly. As each variable has a p-value whether its regression coefficient is significant or not, we finally developed a regression model for Type A, i.e. Model α with variables with p-values less than 0.1.

Next, we explain Step B. Using the explanatory variables in Model α, excluding the characteristics in Step A and characteristics of next-nearest leaders, we calculated IOVs again. Note that we only summed up the Akaike weights of models including all variables in Model α. Once we obtained a set of variables with high IOVs, we made a model that included all of these variables. Based on the p-values in the model, we collected variables with p-values less than 0.1 and developed a model for Type B, i.e. Model β. Although we assumed that the variables in Model α would also be included in Model β, some variables in Model α were eliminated in Step B due to their p-values.

Models β of respective driving characteristics are shown in Fig. 3. Characteristics with red font indicate that they were added in Model β and not present in Model α. The characteristics marked with chequered pattern indicate that they were eliminated in Step B due to their statistical significance. The numbers shown next to the explanatory variables are their regression coefficients in standardised regression models. In other words, we can evaluate degree of effectiveness of variables based on their regression coefficients. In Fig. 3, we do not display the effects of the dummy variables that represent the Day and which test drivers operated the variable.

Regarding operational delay, i.e. $\epsilon_{\mathrm{a}}^{1\mathrm{st}}$, no effects were detected except for $TD3$ in model β. The follower length, i.e. L^{f}, included in Model α was removed due to its significance in Model β. In Fig. 3b, the maximum velocity of the next-nearest leaders, i.e. $V_{\mathrm{max}}^{2\mathrm{nd\,l}}$, was added to Model β. From the regression coefficients, we recognised that effectiveness of $V_{\mathrm{max}}^{2\mathrm{nd\,l}}$ was more strong than that of $V_{\mathrm{max}}^{1\mathrm{st\,l}}$. In contrast, regarding the acceleration in Fig. 3c, the effect of nearest leaders' behaviour seemed to be larger than that of the next-nearest leaders. In Fig. 3d, the vehicle characteristics of the next-nearest leaders are included. The model implies that the followers' deceleration decreases as the height of the next-nearest leader

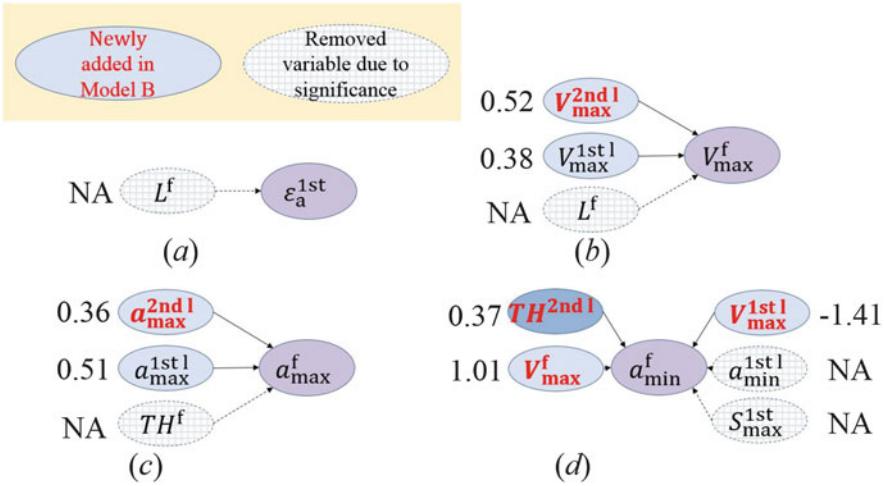

Fig. 3 Obtained Model β for each driving characteristic of the followers. Characteristics printed in red indicate that they were newly added in Model β and not included in Model α. The characteristics marked with a chequered pattern indicate that they were eliminated in Step B due to statistical significance. (**a**) Delay. (**b**) Velocity. (**c**) Acceleration. (**d**) Deceleration

increases. This seems to be a natural effect from the perspective of driver safety and anticipatory behaviours.

6 Conclusion

In this study, we investigated the factors of next-nearest leaders that affect followers' driving as well as what driving behaviours of the followers are affected by the presence of next-nearest leaders.

We conducted experiments with groups comprising of two and three vehicles on a test course. While varying the collection of vehicle types in the groups, we observed the following behaviours of each driver. Our experimental context enabled us to measure differences in car-following behaviour without any interference such as lane changes.

From the statistical tests, we conclude that the initial and maximum distance gaps were not affected by the presence of next-nearest leaders. In contrast, we suggest that the maximum velocity, acceleration, deceleration and operational delay of the followers were affected by the presence of next-nearest leaders.

In addition, we developed regression models to explain follower behaviours in terms of other drivers' behaviour and vehicle characteristics. By comparing the statistical models of experimental data from groups of two and three vehicles, we conclude that the maximum velocity and acceleration of the followers are both

affected by those of the nearest leaders and the next-nearest leaders. These effects naturally appear from car-following models that consider multiple leading vehicles. We also conclude that the maximum deceleration of the followers was affected by the height of the next-nearest leading vehicles. This implies that the height of the next-nearest leading vehicles should be considered when we fit parameters dedicated to reproducing following drivers' deceleration.

Acknowledgements This work was supported by JSPS KAKENHI Grant Numbers 25287026 and 15K17583.

References

1. Akaike, H.: Information theory and an extension of the maximum likelihood principle. In: Selected Papers of Hirotugu Akaike, pp. 199–213. Springer, New York (1998)
2. Burnham, K.P., Anderson, D.R.: Model Selection and Multimodel Inference: A Practical Information-Theoretic Approach. Springer, New York (2003)
3. Ge, H., Dai, S., Dong, L., Xue, Y.: Stabilization effect of traffic flow in an extended car-following model based on an intelligent transportation system application. Phys. Rev. E **70**(6), 066134 (2004)
4. Helbing, D., Hennecke, A., Shvetsov, V., Treiber, M.: Master: macroscopic traffic simulation based on a gas-kinetic, non-local traffic model. Transp. Res. B Methodol. **35**(2), 183–211 (2001)
5. Herman, R., Rothery, R.W.: Car following and steady state flow. In: Proceedings of the Second International Symposium on the Theory of Road Traffic Flow London 1963, pp. 1–11. Organisation for Economic Co-operation and Development, Paris (1965)
6. Hsu, T.P., Sadullah, A.F.M., Dao, N.X.: A comparison study on motorcycle traffic development in some Asian countries–case of Taiwan, Malaysia and Vietnam. In: The Eastern Asia Society for Transportation Studies (EASTS), International Cooperative Research Activity, Washington (2003)
7. Nagahama, A., Yanagisawa, D., Nishinari, K.: Dependence of driving characteristics upon follower–leader combination. Physica A **483**, 503–516 (2017)
8. Wagenmakers, E.J., Farrell, S.: AIC model selection using Akaike weights. Psychon. Bull. Rev. **11**(1), 192–196 (2004)

Higher-Order Continuum Model and Its Numerical Solutions for Heterogeneous Traffic Flow with Non-lane Discipline

Hari Krishna Gaddam and K. Ramachandra Rao

Abstract The aim of this study is to capture the behaviour of non-lane based heterogeneous traffic flow which is predominantly occupied by vehicles with varying physical and dynamical characteristics and their staggered car following behaviour. In order to describe this behaviour, the study presents the higher-order heterogeneous continuum model considering the effect of roadway width and the lateral friction offered by sideways movement. Further, the model also incorporates the viscosity term by considering the higher-order terms. The eigenvalues of the system show that the new model overcomes the non-physical solutions such as isotropic behaviour and wrong way travel which can be seen in other higher-order models. The numerical simulation results show that the proposed model is able to capture complex traffic flow patterns such as shock and rarefaction waves, stop-and-go, local cluster effect, etc. One-sided lateral gap in the model improves the stability region of the traffic flow and able to dissipate the perturbation quickly when compared to other models. The results obtained are consistent with the empirical observations.

1 Introduction

A considerable amount of literature is available on higher-order macroscopic continuum models representing the traffic flow on homogeneous car following traffic environment [3, 7]. These models are either phenomenological in nature or derived from car following theories. The main assumption behind these theories is that the vehicles strictly travel at the center of the lane and they assign leadership fully to the front vehicle. The follower vehicle response strictly depends on the

H. K. Gaddam
Department of Civil Engineering, IIT Delhi, New Delhi, India

K. Ramachandra Rao (✉)
Department of Civil Engineering and Transportation Research and Injury Prevention Programme (TRIPP), IIT Delhi, New Delhi, India
e-mail: rrkalaga@civil.iitd.ac.in

S. H. Hamdar (ed.), *Traffic and Granular Flow '17*,
https://doi.org/10.1007/978-3-030-11440-4_3

relative distance and a relative speed between the leader and follower vehicles and lane changing is strictly prohibited. However, in developing countries such as India, vehicles do not follow lane discipline, and they always deviate from its center-line positions. Moreover, each vehicle has multiple leaders ahead, and disruptive lane changing can also be observed. Further, complexity increases due to the presence of slow and fast moving vehicles and their wide range of physical and dynamical characteristics. Therefore continuum models developed from the lane based car following models will poorly represent the dynamics of non-lane heterogeneous traffic (NLHT) and cannot be applied directly. Even though few researchers [8, 9, 11] attempted to model the traffic in NLHT environment, they are successful only to some extent. Gupta and Dhiman [1] proposed a non-lane based continuum model using one-sided lateral gap car following model [5]. However, their model does not take into account the interactions between slow moving and fast moving vehicles and driver memory is absent. The present study attempts to improve the one-sided lateral gap continuum model by incorporating vehicle heterogeneity, frictional effects of slow moving vehicles on fast moving vehicles and driver memory.

2 Development of New Dynamic Model

Modified non-lane based car following model for heterogeneous traffic on a single lane road is presented in Eq. (1):

$$\begin{aligned} a_n(t) = \alpha\{U[\Delta x_{n,n+1}(t), \Delta x_{n,n+2}(t), \Delta x_{n,n+3}(t)] - V_n(t)\} \\ +\kappa G[\Delta V_{n,n+1}(t), \Delta V_{n,n+2}(t), \Delta V_{n,n+3}(t)] \end{aligned} \tag{1}$$

Here $\Delta x^i_{n,n+1}(t) = \sum_{j=1}^{n} P_{ij}(x^j_{n+1}(t) - x^i_n(t))$, $\Delta V^i_{n,n+1}(t) = \sum_{j=1}^{n} P_{ij}(V^j_{n+1}(t) - V^i_n(t))$ are the space headway and speed of vehicle class i, respectively. N is the number of vehicle classes, and P_{ij} is the number of times vehicle class i followed vehicle class j. $\alpha_i = \frac{1}{T_i}$ and $\kappa_i = \frac{1}{\tau_i}$ are the driver reactive coefficients of vehicle class i. The next step is to develop the macroscopic continuum model for NLHT stream from the improved car following model, given in Eq. (1). In order to develop macroscopic continuum model, suitable transformation technique must be used to convert discrete variables into the continuous variables. The method suggested in Eq. (2) is applied to transfer the variables from microscopic to macroscopic ones:

$$\begin{aligned} &V[(1-p_n)\Delta x^i_{n,n+1}(t) + p_n \Delta x^i_{n,n+2}(t)] \to V_{ie}\left(\frac{K(x,t)}{1+\delta_i}\right), V^i_n(t) \to V_i(x,t), \\ &V^j_{n+2}(t) \to V_j(x+2\Delta x, t), P_{ij} \to P_{ij}(x+\Delta x, t), \alpha_i = \frac{1}{T_i}, \kappa_i = \frac{1}{\tau_i}, p_i \to \delta_i \end{aligned} \tag{2}$$

where $V_{ie}(.)$ is the equilibrium speed of vehicle class i with respect to density K $\left(\sum_{i=1}^{n} K_i\right)$ and LSD parameter (δ_i) of same vehicle class. $K_i(x,t)$ and $V_i(x,t)$ are the density and speed of vehicle class i, respectively, at point (x,t). T_i and τ_i are the drivers relaxation coefficient and reactive coefficient at macrolevel, respectively. $P_{ij}(x+\Delta x,t)$ is the proportion of jth vehicle classes present in front of ith vehicle class in section $x+\Delta x$ at time t and can be simplified as $P_j(x,t)$. Substituting transformation variables (Eq. (2)) into Eq. (1) and after applying Taylor expansion series and considering the higher-order terms, the final form of the model is shown below:

$$\frac{\partial V_i}{\partial t}+V_i\frac{\partial V_i}{\partial x}=\frac{1}{T_i}\left[V_{ie}\left(\frac{K}{1+\delta_i}\right)-V_i\right]+\frac{1}{\tau_i}(1+\delta_i)\sum_{j=1}^{n}P_j\Delta x\frac{\partial V_j}{\partial x}+$$
$$\frac{1}{\tau_i}\left(\frac{1+3\delta_i}{2}\right)\sum_{j=1}^{n}P_j\Delta x^2\frac{\partial^2 V_j}{\partial x}+\frac{1}{\tau_i}\sum_{j=1}^{n}P_j(V_j(x,t)-V_i(x,t)) \tag{3}$$

Even though the macroscopic continuum model present in Eq. (3) is logically sound, some engineering corrections need to be applied to capture complex driving behaviour present in Indian driving environment. The interaction between different vehicle classes has been observed to obtain the suitable macroscopic parameters and those observations are incorporated into the model. The final form of the proposed model is given in Eq. (4):

$$\frac{\partial V_i}{\partial t}+V_i\frac{\partial V_i}{\partial x}=\frac{1}{T_i}\left[V_{ie}\left(\frac{K}{1+\delta_i}\right)-V_i\right]+(1+\delta_i)\sum_{j=1}^{n}P_jc_j(K)\frac{\partial V_j}{\partial x}+$$
$$\left(\frac{1+3\delta_i}{2}\right)\sum_{j=1}^{n}P_jc_j^2(K)\tau_i\frac{\partial^2 V_j}{\partial x^2}+\sum_{j(\neq i)}^{n}\mu_{ij}\frac{P_j}{\tau_i}(V_j-V_i)\qquad\forall\, i,j=1,2,3\ldots n \tag{4}$$

Here, V_{it} and V_{ix} are the average speed of ith-class vehicle with respect to time and space, and V_{ie} is the equilibrium speed of the ith-class vehicle. K is the vehicle density, $P_j(x,t)$ is the proportion of jth-class vehicle at (x,t) and T_i and τ_i are the driver reactive coefficients. Further, $c_{ij}=\frac{\Delta x}{\tau i}$, $c_j^2(K)*\tau_i=\left(\frac{\Delta x}{\tau_i}\right)^2=\left(-k*V'_{je}(k)\right)^2*\tau_i$. In the present model, $\delta_i=0$ if $K>\frac{2}{3}K_{jam}$;$\mu_{ij}=1$ if $V_{if}>V_{jf}$, otherwise zero. $\mu_{ij}=0$ for density greater than $K>\frac{2}{3}K_{jam}$ for all vehicle classes. The first term in the right-hand side of the equation represents the relaxation term; the second term represents the driver reactions to sudden change in the density. The third term considers the effect of slow moving vehicles on fast moving vehicles in the non-lane heterogeneous traffic. Disturbance propagation

speed $c_j(K) = -K * V_{je}^{'}(K)$ and $c_j^2(K) = \left(-K * V_{je}^{'}(K)\right)^2$. Modified lateral separation distance (LSD) factor for heterogeneous traffic $\delta_{ij} = \frac{LSD_{ij}}{3.5}$ and $\delta_i = \sum_{j=1}^{n} P_{ij}\delta_{ij}$.

3 Mathematical Properties

Mathematical properties such as hyperbolicity and anisotropy have been studied using eigenvalues of the system. The combination of dynamic velocity equations given in Eq. (4) and vehicle conservation equation produces the heterogeneous continuum model for the non-lane based system. The quasi-linear form of the model is

$$U_t + A(U)U_x = S(U) \tag{5}$$

Here **A**(**U**) is the Jacobian matrix and for N vehicle classes. However, it is difficult to obtain the eigenvalues for more than two vehicle classes. Therefore system matrix for N = 2 vehicle classes is chosen for estimation. The mathematical formulation for two vehicle classes is

$$U = [K_1\ V_1\ K_2\ V_2]^T$$

$$\mathbf{A(U)} = \begin{bmatrix} V_1 & K_1 & 0 & 0 \\ 0 & V_1 + P_1(1+\delta_1)KV_1(K)^{'} & 0 & P_2(1+\delta_2)KV_2(K)^{'} \\ 0 & 0 & V_2 & K_2 \\ 0 & P_1(1+\delta_1)KV_1(K)^{'} & 0 & V_2 + P_2(1+\delta_2)KV_2(K)^{'} \end{bmatrix}$$

$$S(U) = \begin{bmatrix} 0 \\ \frac{1}{T_1}\left[V_{1e}\left(\frac{k}{1+\delta_1}\right) - V_1\right] + \left(\frac{1+3\delta_1}{2}\right)\sum_{j=1}^{2} P_j c_j^2(k)\tau_1 \frac{\partial^2 V_j}{\partial x^2} + \sum_{j(\neq i)}^{2} \mu_{1j}\frac{P_j}{\tau_1}(V_j - V_1) \\ 0 \\ \frac{1}{T_2}\left[V_{2e}\left(\frac{k}{1+\delta_2}\right) - V_2\right] + \left(\frac{1+3\delta_2}{2}\right)\sum_{j=1}^{2} P_j c_j^2(k)\tau_2 \frac{\partial^2 V_j}{\partial x^2} + \sum_{j(\neq i)}^{2} \mu_{2j}\frac{P_j}{\tau_2}(V_j - V_2) \end{bmatrix}$$

The eigenvalues are: $\lambda_1 = V_1$, $\lambda_2 = V_2$, $\lambda_3 = \frac{1}{2}(A - \sqrt{B})$, $\lambda_4 = \frac{1}{2}(A + \sqrt{B})$, where $A = V_1 + V_2 + (1+\delta_1)KP_1V_1(K)^{'} + (1+\delta_2)KP_2V_2(K)^{'}$ and $B = (-V_1 - V_2 - (1+\delta_1)KP_1V_1(K)^{'} - (1+\delta_2)KP_2V_2(K)^{'})^2 - 4(V_1V_2 + (1+\delta_1)KP_1V_2V_1(K)^{'} + (1+\delta_2)KP_2V_1V_2(K)^{'})$.

Eigenvalues $[\lambda_1, \lambda_2, \lambda_3, \lambda_4]$ of the system are real and distinct. It shows that the model is strictly hyperbolic in nature. The analysis also proves that the proposed model overcomes the isotropic problem where vehicles only respond to the frontal stimuli. The in-homogeneous system (Eq. (4)) behaves more or less similar to that

of its corresponding homogeneous system. However, the additional viscosity term introduced in the model further smoothing out the shock fronts, frictional term considers the effect of slow moving vehicles on traffic stream and the relaxation term drives the system to the equilibrium state.

4 Numerical Simulation

To explore the full potential of the new model and to avoid the numerical instabilities at large gradients, the present study adopted first order finite difference scheme to discretize the model (Eq. (4)).The numerical schema of the model is given below:

$$K_{i,m}^{r+1} = K_{i,m}^{r} - \left(\frac{\Delta t}{\Delta x}\right)[(V_{i,m}^{r})(K_{i,m}^{r} - K_{i-1,m}^{r}) + K_{i,m}^{r}(V_{i+1,m}^{r} - V_{i,m}^{r})] \tag{6}$$

If $V_{i,m}^{r} < c_m(K)$

$$V_{i,m}^{r+1} = V_{i,m}^{r} - \left(\frac{\Delta t}{\Delta x}\right)(V_{i,m}^{r})(V_{i+1,m}^{r} - V_{i,m}^{r}) + \left(\frac{\Delta t}{\Delta x}\right)(1+\delta_m)\sum_{j=1}^{n} P_j c_j(K)(V_{i+1,j}^{r} - V_{i,j}^{r}) +$$
$$\frac{\Delta t}{T_m}(V_{me}(K_i^{r}) - V_{i,m}^{r}) + \sum_{j(\neq m)}^{n} \mu_{mj}\frac{P_j}{\tau_m}(V_{i+1,j}^{r} - V_{i,m}^{r}) +$$
$$\left(\frac{\Delta t}{\Delta x^2}\right)\left(\frac{1+3\delta_m}{2}\right)\sum_{j=1}^{n} P_j c_j^2(K)\tau_m(V_{i+2,j}^{r} - 2V_{i+1,j}^{r} + V_{i,j}^{r}) \tag{7}$$

If $V_{i,m}^{r} > c_m(K)$

$$V_{i,m}^{r+1} = V_{i,m}^{r} - \left(\frac{\Delta t}{\Delta x}\right)(V_{i,m}^{r})(V_{i,m}^{r} - V_{i-1,m}^{r}) + \left(\frac{\Delta t}{\Delta x}\right)(1+\delta_m)\sum_{j=1}^{n} P_j c_j(K)(V_{i,j}^{r} - V_{i-1,j}^{r}) +$$
$$\frac{\Delta t}{T_m}(V_{me}(K_i^{r}) - V_{i,m}^{r}) + \sum_{j(\neq m)}^{n} \mu_{mj}\frac{P_j}{\tau_m}(V_{i,j}^{r} - V_{i-1,m}^{r}) +$$
$$\left(\frac{\Delta t}{\Delta x^2}\right)\left(\frac{1+3\delta_m}{2}\right)\sum_{j=1}^{n} P_j c_j^2(K)\tau_m(V_{i-2,j}^{r} - 2V_{i-1,j}^{r} + V_{i,j}^{r}) \tag{8}$$

Here $K_{i,m}^{r}$, $V_{i,m}^{r}$ are, respectively, the density and speed of the mth-class vehicle at point (i, r), K_i^{r} is the total density of vehicles at point (i, r) on the road and i, r, Δt, Δx are the spatial index, time index, time step and spatial step, respectively. The homogeneous version of the scheme is used for the analysis.

4.1 Shock and Rarefaction Waves

The numerical simulations will be carried out to show the formation of shock fronts between congested and free flow traffic using the following Riemann initial conditions:

$$K_u = 0.04 \;\; veh/m, K_d = 0.18 \;\; veh/m \tag{9}$$

$$K_u = 0.18 \;\; veh/m, K_d = 0.04 \;\; veh/m \tag{10}$$

Here K_u and K_d are the upstream and downstream conditions, respectively. Condition (9) represents the shock wave situations where free flow vehicles meet a congested portion of the road. Condition (10) represents the dissipation of traffic jams where vehicles from stopped position were catching up with the freely moving traffic stream; it leads to the formation of rarefaction waves. Initial speeds of vehicles on the road are

$$V_u^{1,2} = V_e\left(\frac{K_u^{1,2}}{1+\delta}\right), V_d^{1,2} = V_e\left(\frac{K_d^{1,2}}{1+\delta}\right) \tag{11}$$

Free boundary conditions, i.e. $\frac{\partial K}{\partial x} = 0$ and $\frac{\partial V}{\partial x} = 0$, are used for the simulation on both sides of the road stretch. The equilibrium speed–density relationship used for the simulation is

$$V = \frac{V_f\left[1 - \left(\frac{K}{K_j}\right)^a\right]^b}{1 + E\left(\frac{K}{K_j}\right)^\theta} \tag{12}$$

Here V_f is the free flow speed;K_j is the jam density and E, a, b are the shape parameters. The length of the test road considered is 20 km and it is divided into 100 equal sections. The simulation time step is 1 s. The parameter values used in the simulation are $V_f = 30$ m/s, $K_j = 0.2$ veh/m, E = 10.30, = 2.14, a = 4, b = 1, T = 10 s, c = 11 m/s, = 7.5 s. The simulation results are shown in Fig. 1. The results show that the proposed model successfully predicts the formation of shock waves and rarefaction waves under the given traffic conditions.

4.2 Perturbation

The numerical simulations will be carried out to localized perturbation assumed in an initially homogeneous traffic environment. The initial distribution of the density and mean speed of the traffic stream are given in Eq. (13):

$$K(x,0) = K_0 + \Delta K(x), x \in [0, L], V(x,0) = V_{KK}(K(x,0)), x \in [0, L] \tag{13}$$

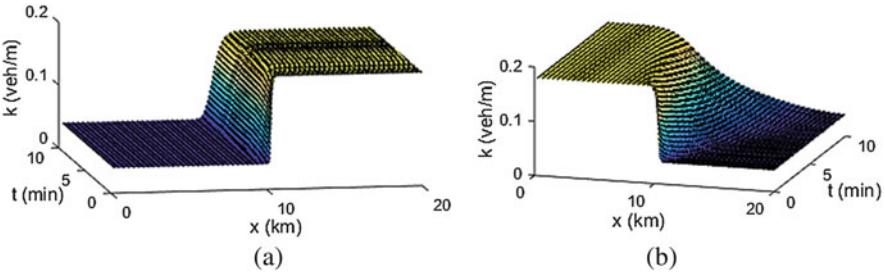

Fig. 1 (**a**) Shock waves and (**b**) rarefaction waves under Riemann initial conditions

Here $\Delta K(x)$ is the localized perturbation caused due to the sudden stopping of vehicles, unexpected changing of lanes, etc. The shape of the localized perturbation $\Delta K(x)$ assumed for the numerical investigation is estimated using Eq. (14) [2]:

$$\Delta K(x) = \Delta K_0 \left\{ cosh^{-2}\left[\frac{160}{L}\left(x - \frac{5L}{16}\right)\right] - \frac{1}{4} cosh^{-2}\left[\frac{40}{L}\left(X - \frac{11L}{32}\right)\right]\right\} \tag{14}$$

Here L is the circumference of the circular road section under consideration. In this study, we assume L = 30 km as a circumference of a ring road. Periodic boundary conditions (Eq. (15)) are used for the numerical simulation:

$$q(0,t) = q(L,t), V(0,t) = V(L,t), \frac{\partial V(0,t)}{\partial x} = \frac{\partial V(L,t)}{\partial x} \tag{15}$$

Equilibrium equation $V_{KK}(K)$ [6] used for the analysis is

$$V_{KK}(K) = V_f \left\{ \left[1 + exp\left(\frac{\frac{K}{K_j} - 0.25}{0.06} \right) \right]^{-1} - 3.72 * 10^{-6} \right\} \tag{16}$$

Let $\Delta K_0 = 0.01$ veh/m and the circumference of road section is divided into 300 equal sections, i.e. $\Delta x = 100$ m, and the simulation time step, i.e. $\Delta t = 1$ s. The other parameters selected for the study are: $V_f = 30$ m/s, $K_j = 0.2$ veh/m, T = 10 s, c = 11 m/s and $\tau = 7.5$ s. The simulation is carried out for $\delta = 0.15$ without viscosity term. The results are compared with speed gradient (SG) model [4] (Fig. 2).

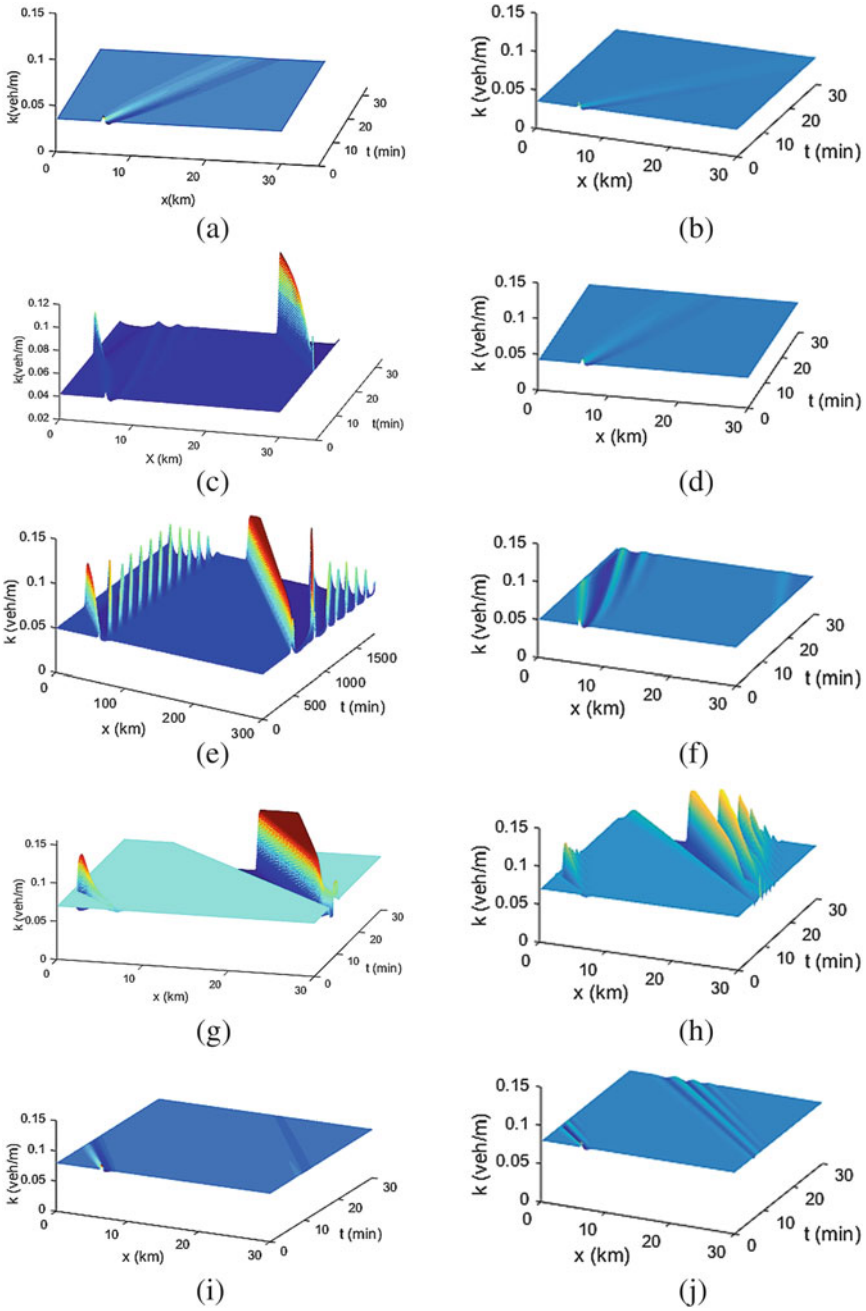

Fig. 2 Spatio-temporal evolution of density on a 30 km ring road for 30 min time where (**a**), (**c**), (**e**), (**g**), (**i**) are outputs from the SG model (where $\delta = 0$) [4] and (**b**), (**d**), (**f**), (**h**), (**j**) are the outputs from the one-sided lateral gap model with viscosity term (where $\delta = 0.15$) with $K_0 = 0.035$, 0.042, 0.05, 0.07 and 0.08 and amplitude $\Delta K_0 = 0.01$

5 Conclusions

The new model presented in the study considers the effect of lateral separation characteristics of drivers, frictional resistance offered by slow moving vehicles and viscosity. The model captures all the complex interactions of vehicles on single lane road without lane discipline. It is a general form of SG [4] and Tang et al. [10] models. The model overcomes several non-physical solutions such as isotropy and wrong way travel. Moreover, it is able to replicate many complex traffic flow phenomenon such as local traffic perturbations, phantom traffic jams and queue dissipations. Comparison with SG model [4] implies that one-sided lateral gap parameter in the model dissipates the small traffic perturbation quickly and thus improves the stability. It is expected that the presented model will help in studying alternative transport policy measures in future.

References

1. Gupta, A.K., Dhiman, I.: Analyses of a continuum traffic flow model for a nonlane-based system. Int. J. Mod. Phys. C **25**(10), 1450045 (2014)
2. Herrmann, M., Kerner, B.S.: Local cluster effect in different traffic flow models. Physica A **255**(1), 163–188 (1998)
3. Hoogendoorn, S.P., Bovy, P.H.: State-of-the-art of vehicular traffic flow modelling. Proc. Inst. Mech. Eng. I J. Syst. Control. Eng. **215**(4), 283–303 (2001)
4. Jiang, R., Wu, Q.S., Zhu, Z.J.: A new continuum model for traffic flow and numerical tests. Transp. Res. B Methodol. **36**(5), 405–419 (2002)
5. Jin, S., Wang, D., Tao, P., Li, P.: Non-lane-based full velocity difference car following model. Physica A **389**(21), 4654–4662 (2010)
6. Kerner, B.S., Konhäuser, P.: Structure and parameters of clusters in traffic flow. Phys. Rev. E **50**(1), 54 (1994)
7. Mohan, R., Ramadurai, G.: State-of-the art of macroscopic traffic flow modelling. Int. J. Adv. Eng. Sci. Appl. Math. **5**(2–3), 158–176 (2013)
8. Mohan, R., Ramadurai, G.: Heterogeneous traffic flow modelling using second-order macroscopic continuum model. Phys. Lett. A **381**(3), 115–123 (2017)
9. Nair, R., Mahmassani, H.S., Miller-Hooks, E.: A porous flow approach to modeling heterogeneous traffic in disordered systems. Proc. Soc. Behav. Sci. **17**, 611–627 (2011)
10. Tang, T., Huang, H., Zhao, S., Shang, H.: A new dynamic model for heterogeneous traffic flow. Phys. Lett. A **373**(29), 2461–2466 (2009)
11. Thankappan, A., Vanajakshi, L., Subramanian, S.C.: Significance of incorporating heterogeneity in a non-continuum macroscopic model for density estimation. Transport **29**(2), 125–136 (2014)

Static Traffic Assignment on Ensembles of Synthetic Road Networks

Alonso Espinosa Mireles de Villafranca, Richard D. Connors, and R. Eddie Wilson

Abstract We present a systematic approach for studying how performance of road networks is affected by changes in their geometry. We develop a new family of random planar graphs that models road networks and interpolates between a square grid and the β-skeleton of uniformly random points. The capacities of streets are set according to a rule that models a fixed provision of total resources. Ensembles of graphs are generated for different geometric parameter choices and the static traffic assignment problem is solved for a range of traffic demands. We find that variations in network efficiency, measured by the price of anarchy, are small both across demand values and geometric parameters. However, the best-performing networks are those which preserve some grid structure. We find that the price of anarchy does not correlate well with standard network statistics.

1 Introduction

An open question is how to compare the road network performance of cities of different shapes and sizes. Youn et al. [8] calculate a performance metric known as the *price of anarchy* [5] (PoA) for networks representing the street maps of the cities of New York, London and Boston—as well as for regular lattices and ensembles of standard random graph models (small-world, Erdos–Renyi and Barabasi–Albert). These networks have clear structural differences and this is reflected in their PoA metrics. They find that networks with shortcuts tend to have poorer PoA metrics and while they find that the PoA does not vary greatly for different types of networks, their method for choosing cost parameters does not take into account the geometry of the networks.

A. Espinosa Mireles de Villafranca (✉) · R. E. Wilson
University of Bristol, Bristol, UK
e-mail: alonso.espinosa@bristol.ac.uk; R.E.Wilson@bristol.ac.uk

R. D. Connors
University of Leeds, Leeds, UK
e-mail: R.D.Connors@its.leeds.ac.uk

S. H. Hamdar (ed.), *Traffic and Granular Flow '17*,
https://doi.org/10.1007/978-3-030-11440-4_4

The aim of this paper is to develop a systematic approach for studying the topological dependence of the PoA and in this light re-examine the claims of Youn et al. [8]. We generate a parameterised continuum of proximity graphs that homotopes between a regular square lattice and the β-skeleton [2] of a set of uniformly random points. In contrast to [8], we take special care to ensure that the total road capacity in each network is the same, so that the comparison between networks is fair and differences in PoA relate only to topology.

Traffic routing is done by solving the standard *static traffic assignment problem* (STAP) which we review in Sect. 2. In Sect. 3 we describe our model for generating the graph ensembles and allocating cost parameters to edges. From the numerical results showing the dependence of the PoA across network ensembles in Sect. 4, we conclude in Sect. 5 that the results of Youn et al. [8] for PoA fail to capture fully the role that network structure plays in the efficiency of road networks.

2 Review of Static Traffic Assignment

The *static traffic assignment problem* (STAP) describes how traffic demand distributes itself across the routes and edges (i.e. streets) of a network in a time-independent setting [6]. The key inputs are:

- Cost functions c_i for each edge i that describe how the travel time on that edge increases with the flow x_i. Here we use the affine choice $c_i(x_i) = a_i + b_i x_i$, where a_i represents the free-flow travel time and b_i (a kind of inverse capacity) models the congestibility of the edge.
- An origin–destination demand matrix that describes the flows per unit time that begin and end journeys at all possible pairs of nodes. Here for simplicity we use a single origin node and a single destination node with demand d in vehicles per unit time.

Our approach throughout is to work in terms of flows on edges (rather than on routes) because the edge flow solutions $\mathbf{x}$ are unique. In this setting, all valid assignments (solutions) satisfy

$$\mathbf{x} \geq \mathbf{0} \tag{1}$$

and a set of linear constraints

$$\mathbf{E}\mathbf{x} = \mathbf{d} \tag{2}$$

that model flow conservation at nodes (i.e. at street intersections). Here $\mathbf{E}$ is the matrix

$$E_{ij} = \begin{cases} -1, & \text{if edge } j \text{ is outgoing at node } i, \\ +1, & \text{if edge } j \text{ is incoming at node } i, \\ 0, & \text{otherwise,} \end{cases} \tag{3}$$

and the demand vector $\mathbf{d}$ takes the form

$$d_i = \begin{cases} -d, & \text{if node } i \text{ is the origin,} \\ +d, & \text{if node } i \text{ is the destination,} \\ 0, & \text{otherwise.} \end{cases} \tag{4}$$

There are then two assignments of interest. The *system optimal* (SO) assignment $\mathbf{x}_{\mathrm{SO}}$ minimises the network's total cost

$$F_{\mathrm{SO}}(\mathbf{x}) = \sum_i c_i(x_i)x_i = \mathbf{a}^{\mathrm{T}}\mathbf{x} + \mathbf{x}^{\mathrm{T}}\mathbf{B}\mathbf{x} \tag{5}$$

per unit time and models the best that a 'benevolent dictator' could achieve. Here $\mathbf{B} = \mathrm{diag}\,\{b_i\}$.

In contrast, the *user equilibrium* (UE) assignment $\mathbf{x}_{\mathrm{UE}}$ models a Nash game where individual drivers are self-optimising, so that the cost of used routes is equal and less than or equal to the cost of unused routes. Although UE is naturally expressed as a complementarity problem in route flow variables, the Beckmann transformation [1] shows that edge flows $\mathbf{x}_{\mathrm{UE}}$ minimise a functional that (in our affine cost setting) takes the form

$$F_{\mathrm{UE}}(\mathbf{x}) = \mathbf{a}^{\mathrm{T}}\mathbf{x} + \frac{1}{2}\mathbf{x}^{\mathrm{T}}\mathbf{B}\mathbf{x}. \tag{6}$$

Note that minimising (5) or (6) with respect to (1) and (2) gives a quadratic optimisation problem with linear constraints which can be solved numerically using widely available packages.

The price of anarchy (PoA) [7]

$$\mathrm{PoA} := \frac{F_{\mathrm{SO}}(\mathbf{x}_{\mathrm{UE}})}{F_{\mathrm{SO}}(\mathbf{x}_{\mathrm{SO}})} \tag{7}$$

measures the efficiency of the UE assignment by benchmarking its total network cost against the best achievable. Clearly $\mathrm{PoA} \geq 1$ and (non-trivially [7]) $\mathrm{PoA} \leq 4/3$. The PoA is known to depend upon the structural configuration [3] of available routes in a network and higher values of PoA represent a greater loss of efficiency due to free will.

3 Network Synthesis Model

Our model for synthesising road networks consists of three steps. The first two generate the network geometry by sampling the nodes and wiring the edges. The third step models cost functions for the edges.

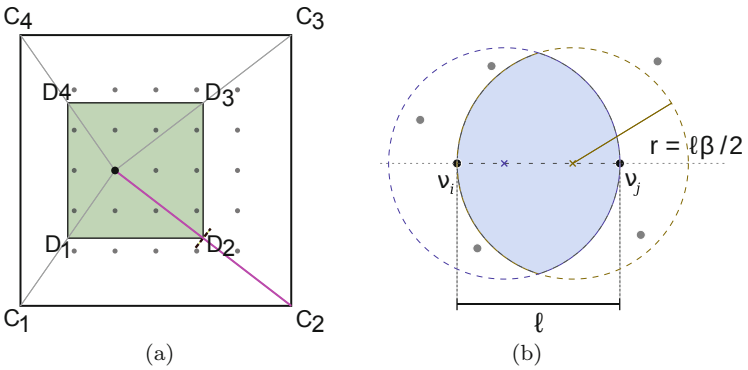

Fig. 1 Construction diagrams for generating our synthetic networks: (**a**) illustrates the construction of re-sampling boxes from the primitive square lattice; (**b**) shows the construction of proximity neighbourhoods for β-skeletons. For different values of β, well-known graphs can be recovered: as $\beta \to 0$ the Delaunay triangulation is recovered; for $\beta = 1$, we have the Gabriel graph; for $\beta = 2$, we have the relative neighbourhood graph. For $\beta \in [1, 2]$ the skeleton also contains the minimum spanning tree

See Fig. 1. We start with a square lattice of n points contained inside the unit square. Consecutive points in a row (or column) have a spacing of $1/\sqrt{n}$ and the distance between the outer points and the boundary of the square is $1/2\sqrt{n}$. From each lattice point P we trace straight lines to each corner of the unit square $C_1C_2C_3C_4$. We then construct a smaller re-sampling box $D_1D_2D_3D_4$ by choosing corners points on the lines PC_i $(i = 1, \ldots, 4)$ that split the line PC_i such that $\alpha = PD_i/PC_i$. A node is then generated by choosing a random point uniformly from $D_1D_2D_3D_4$.

For $\alpha = 0$, the original lattice points are the nodes. For $\alpha = 1$, the nodes are distributed uniformly over the unit square since it coincides with all of the re-sampling boxes. Intermediate values of α result in an increasingly perturbed lattice that loses regularity as α grows past α_{crit}, where

$$\alpha_{\text{crit}} := \frac{1}{\sqrt{n}+1}, \tag{8}$$

at which point the re-sampling boxes begin to overlap.

Streets (edges) are placed by constructing the lune-based β-skeleton (a type of proximity graph [2] that is useful for reconstructing road networks [4]) of the nodes as generated above. Proximity graphs are constructed by associating a neighbourhood $U(v_1, v_2) \subset \Re^2$ to each possible pair of nodes (v_i, v_j) in a vertex set V. If $U(v_i, v_j)$ is empty of all other $v_k \in V$ (with $v_k \neq v_i, v_j$), an edge connecting v_i with v_j is placed. For β-skeletons in particular, the neighbourhood for a pair of points is the intersection of two disks whose centres lie on the line segment $\overline{v_i v_j}$, with radii $r = \beta d(v_i, v_j)/2$, each containing one of the points of the pair in its boundary. To construct a directed graph, we replace each existing edge

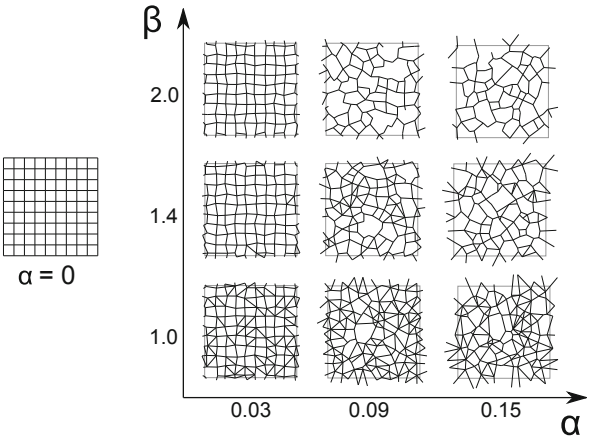

Fig. 2 Examples showing the topology of synthesised networks for different values of α and β. To visualise nodes that are adjacent through the periodic boundaries, edges have been drawn leaving the square

by two directed edges with opposite orientations. Finally, during the β-skeleton construction process, we associate the edges of the unit square toroidally with each other to achieve periodic boundaries so that edge effects are eliminated. Example networks for different parameter values can be seen in Fig. 2.

At this point, the three parameters n, α and β have defined (together with random sampling) a road network geometry. We now set the free-flow parameters a_i equal to the Euclidean length of the corresponding edges. However, the congestibility parameters b_i require more thought. We may consider each $1/b_i$ as a kind of capacity, which in simplistic terms scales with the width (or number of lanes) of the corresponding street.

To enable a fair comparison between different networks, we suppose they have an equal infrastructure budget achieved in the form of equal road surface area. In re-scaled form, we thus impose

$$\sum_i \frac{a_i}{b_i} = 1. \tag{9}$$

To determine unique values of b_i, we suppose each node ν has the same constant 'intersection capacity' λ that is shared equally between its incoming edges $i \in \mathcal{I}_\nu$ so that

$$\frac{1}{b_i} = \frac{\lambda}{k_\nu}, \tag{10}$$

where $k_v := |\mathcal{I}_v|$ is the in-degree. By substituting (10) in (9), we obtain

$$\lambda = \frac{1}{\sum_{v \in V} \frac{1}{k_v} \sum_{i \in \mathcal{I}_v} a_i}, \tag{11}$$

so that the b_i may be determined by (10).

4 Results

Figure 3 shows the traffic assignments of one network instance and the corresponding PoA as demand is varied. As demand increases, traffic distributes itself across the whole network, with the toroidal boundaries generally enabling an even spread except in close proximity to the origin and destination.

Figure 4a, b show the dependence of the ensemble-averaged PoA across the demand range for different ensembles. In both figures, the best-performing networks (with lower PoA) are the ones with $\alpha < \alpha_{\text{crit}}$ that preserve some of the grid structure. This is consistent with the findings of Youn et al. [8] that networks with 'shortcuts' (such as small-world networks), which are absent in lattices, tend to perform worse. The change in PoA with respect to β, while less remarkable, is detectable in the tail of the PoA traces.

To measure how the ensemble performs across the demand range, we integrate the area under the PoA curve. How this changes with (α, β) is compared in Fig. 5 to the mean degree of the ensemble, the mean algebraic connectivity (which broadly reflects how well connected networks are) and the total street length. Note the mean degree of a planar graph is strongly related to its topological structure and is well-known to be bounded above by six. In contrast, the algebraic connectivity is

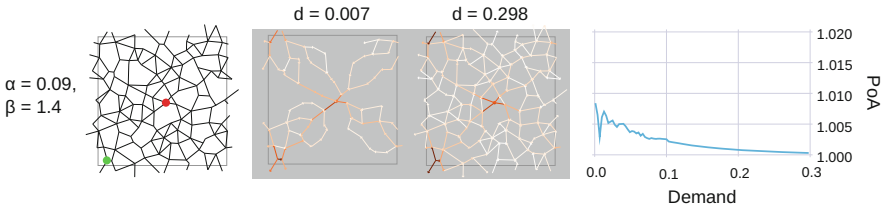

Fig. 3 The traffic flow patterns of a network instance with $\alpha = 0.009$ and $\beta = 1.4$ are shown. The leftmost column shows the network structure, with the green (bottom left) and red (middle) dots marking the origin and destination, respectively. The middle two columns show the used roads for different values of demand: the darker shades of orange indicate higher traffic volumes. The rightmost column shows the PoA profile as demand increases. With the resource allocation heuristic, the peak in the PoA for different networks tends to occur at a similar demand value even for different parameters α and β

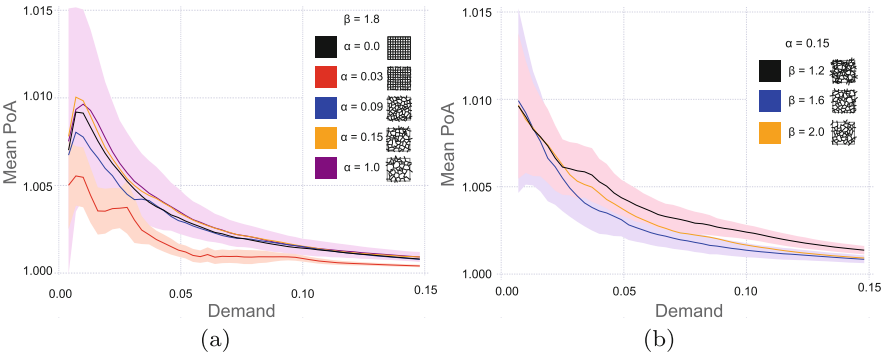

Fig. 4 (**a**) The ensemble-averaged variation of PoA with demand is shown for ensembles with $\beta = 1.8$ and different values of α. The ribbons for the traces corresponding to $\alpha = 1.0$ and $\alpha = 0.03$ show one standard deviation above and below the mean. (**b**) The ensemble-averaged PoA as a function of demand for ensembles of different values of β for $\alpha = 0.15$. The ribbons show a standard deviation above and below the mean for $\beta = 1.2$ and $\beta = 2.0$. For all (α, β) pairs the ensemble average for 100 networks was computed, and the demand range was sampled at intervals of length 0.003. The inlays show individual instances of the networks

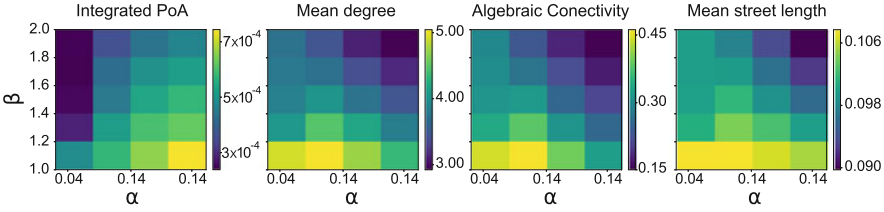

Fig. 5 Different averaged graph metrics and integrated PoA over the demand range for ensembles with different (α, β). The best-performing networks have large β and small α, which from Fig. 2 can be seen are the ones that preserve the grid-like structure the most

typically used to analyse dynamical processes such as diffusive-like phenomena on the networks.

We can see that while some standard network metrics correlate with each other, namely the mean degree of the ensemble and the mean algebraic connectivity, the PoA shows completely different behaviour. This suggests that the properties of the traffic equilibria depend more on the extraneous structure imposed on the network by the modelling parameters than perhaps on the shape of the network itself.

5 Conclusions

The family of random planar graphs that we have constructed allows for the network topology to be controlled by the (α, β) parameter pair. The order of magnitude of the variations in the price of anarchy metric was found consistent with [8]; however,

there are two main differences in our model to the ensembles used there. Firstly, our networks are planar, which is a significantly better approximation to real-world urban street plans than can be achieved with small-world or scale-free models. Secondly, edge parameters are informed by geometry and by a resource allocation model that is naturally parsimonious (in fact, parameter-free) and allows networks with very different topologies and sizes to be compared fairly.

We have found that the total loss of efficiency across demand levels, as measured by the integrated PoA, does not directly correlate with standard network topology metrics such as the mean degree, total edge length or the algebraic connectivity. Therefore it is not sufficient to consider network topology alone in order to understand the efficiency (relative to system optimal) of transportation networks. Rather, the choice of cost functions for the edges seems to play a more important role.

Acknowledgement The first author would like to acknowledge funding from the Mexican Council of Science and Technology (CONACYT).

References

1. Beckmann, M.J., McGuire, C.B., Winsten, C.B.: Studies in the Economics of Transportation. Yale University Press, New Haven (1956)
2. Jaromczyk, J., Toussaint, G.: Relative neighborhood graphs and their relatives. Proc. IEEE **80**(9), 1502–1517 (1992)
3. O'Hare, S.J., Connors, R.D., Watling, D.P.: Mechanisms that govern how the price of anarchy varies with travel demand. Transp. Res. B Methodol. **84**, 55–80 (2016)
4. Osaragi, T., Hiraga, Y.: Street network created by proximity graphs: its topological structure and travel efficiency. In: 17th Conference of the Association of Geographic Information Laboratories for Europe on Geographic Information Science (AGILE2014), pp. 1–5. AGILE Digital Editions, Aalborg (2014)
5. Papadimitriou, C.: Algorithms, games, and the internet. In: Proceedings of the Thirty-Third Annual ACM Symposium on Theory of Computing, STOC 01, pp. 749–753. ACM, New York (2001)
6. Patriksson, M.: The Traffic Assignment Problem: Models and Methods. Courier Dover Publications, Mineola (2015)
7. Roughgarden, T.: The price of anarchy is independent of the network topology. J. Comput. Syst. Sci. **67**(2), 341–364 (2003)
8. Youn, H., Gastner, M.T., Jeong, H.: Price of anarchy in transportation networks: efficiency and optimality control. Phys. Rev. Lett. **101**(12), 128701–128704 (2008)

The Effect of Traffic Signals on the Macroscopic Fundamental Diagram

Boudewijn Zwaal, Victor L. Knoop, and Hans van Lint

Abstract Since the recent empirical evidence of the existence of the macroscopic fundamental diagram (MFD), there are already numerous applications for it, ranging from traffic management to traffic flow modelling. However, little is known what effect internal network control has on the shape of the MFD. This research will investigate the shape of an MFD on a regular network with and without traffic lights. To this end, we consider a regular grid network of infinite length. This is represented in a microscopic traffic simulation model as a two-ring network. We compare the situation without traffic lights to the situation with traffic lights with fixed timing. The uncontrolled case shows a higher flow for lower densities, while the controlled case shows a higher flow for higher densities. Analysis of the underlying process shows that this is due to the fact that traffic lights keep the vehicles spread more homogeneously over a network. In contrast, uncontrolled intersections result in an unstable situation where one part of the network becomes fully congested and the other part almost empty. This shows that traffic lights are reducing the performance for the low-density situations, but improving the traffic performance in high-density situation. In particular, the stability of a homogeneous spatial traffic distribution can be improved, even with fixed traffic light settings.

1 Introduction

The idea of describing traffic dynamics within a neighbourhood, or zone, by means of a single function is very recent. This macroscopic fundamental diagram (MFD) relates traffic production (i.e., the average flow) to traffic density within an urban network and can therefore be used in traffic flow models for large urban areas. Introduced by Godfrey [11], the MFD has been shown to exist empirically [9], where they averaged loop-detector data from the city of Yokohama in Japan. This

B. Zwaal · V. L. Knoop (✉) · H. van Lint
Delft University of Technology, Delft, The Netherlands
e-mail: v.l.knoop@tudelft.nl

S. H. Hamdar (ed.), *Traffic and Granular Flow '17*,
https://doi.org/10.1007/978-3-030-11440-4_5

concave relationship appears to have one value for the density at which the flow in the network is maximal, which is called the critical density. Increasing the density beyond this value decreases the flow and this is where we speak of congestion. Daganzo [1] proposed that a necessary condition for the existence of an MFD is that the spatial distribution of traffic (and therefore of congestion) is homogeneous over the network. While Geroliminis et al. [10] indeed showed that the spatial distribution has an important impact on the shape and the amount of scatter in the MFD, Knoop et al. [12] showed that the MFD is actually a cross-section of a generalized MFD. This GMFD is a continuous three-dimensional function relating density and inhomogeneity to average flow, therefore suggesting that there is no single MFD for every traffic state. Another condition often considered as necessary to have an MFD is that the demand changes slowly over time. Daganzo [2] states that in rapidly changing demand situations, the MFD may exhibit too much scatter. Next to these conditions, little is known about network-specific properties that influence the MFD.

The most common urban-network elements are intersections, with or without traffic lights. A first step to find the influence of specific urban elements on the MFD would therefore be to investigate the effect of traffic lights at intersections on the MFD. Gayah et al. [6] propose a simple network of two one-way roads with periodic boundary conditions, which intersect each other at one location. At this location it is possible to change from one road to the other road, see Fig. 1. While the authors study the flow using different densities and turn fractions, therefore creating an MFD, they do this using kinematic wave theory. This means that they assume a fundamental diagram (FD) for each road.

The shape of an MFD considering (adaptive) traffic lights has already been researched with microscopic simulations [4, 8]. Both papers conclude that the network outflow is higher when the traffic signals are adapted such that they prevent gridlock from happening, especially in the uncontrolled parts of the network. Both studies test this however on a relatively large network with multiple intersections,

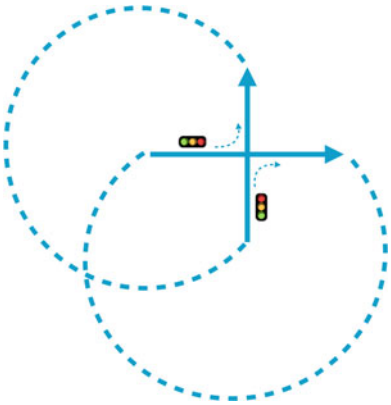

Fig. 1 The network

where we will try to bring the shape of the MFD back to the very basics by means of one single intersection.

The research as presented in this paper is therefore to investigate the impact of traffic lights on the shape of the macroscopic fundamental diagram, using a microscopic traffic simulation on the simple double ring road as presented in Fig. 1. The results show a more stable traffic state for the controlled intersection, which can be used in determining the layout of an aggregated network for which we assume an MFD, which in turn can be used in large-scale traffic models that utilize the MFD.

The outline of this paper is as follows. We first present the methodology in Sect. 2, stating the simulation set-up, the calculation of the MFD, the model parameters, traffic light and turn fraction settings in respectively Sects. 2.1–2.3. We then present the analyses that we have performed in Sect. 2.4. The results of these analyses are shown in Sect. 3, and we discuss and conclude these results in, respectively, Sects. 4 and 5.

2 Methodology

2.1 Simulation Set-Up

To study the effect of traffic lights on the MFD, we use a simple intersection where two one-way roads cross, see Fig. 1. Here, the vehicles that exit the intersection on road 1 return to the intersection on road 1, so there are periodic boundary conditions. We assume that both roads have the same length (1 km in our simulations) and that all vehicles have the same probability to turn according to predetermined turning probabilities. The model includes the intelligent driver model for the car-following behaviour of the vehicles.[1] At the start of the simulation, a predetermined number of vehicles are evenly spread along the two roads, and all start with a speed of zero. The simulation is run for 10,000 s, or 2.8 h, with a time step of 0.1 s, after which it terminates. To compute the average flow we use Edie's generalized definitions [5] for $t = 5000$–$10,000$ s, yielding one observation.

2.2 Car-Following Parameters

For the intelligent driver model, we aimed to choose the most appropriate and realistic parameters. A list is given in Table 1. For an explanation of these parameters, see [13].

[1] See, for example, [13, chapter 2].

Table 1 Parameters used in the intelligent driver model

Free-flow speed	15 m/s
Safe time headway	1.6 s
Maximum acceleration	0.73 m/s^2
Comfortable deceleration	1.67 m/s^2
Acceleration exponent	4
Length of car	4 m
Linear jam distance	2 m
Non-linear jam distance	3 m

2.3 Traffic Lights and Turn Fractions

The intersection consists of a simple traffic management system which allows vehicles on one road to pass through (where vehicles either continue on the same road or change roads) while the vehicles on the other road have to wait for red. During all simulations we use a cycle time of 60 s with a green time of 30 s. Every vehicle in the simulation chooses to either stay on their road or turn to the other road at the intersection. The four probabilities are thus: p_{11} to stay on road 1, $p_{12} = 1 - p_{11}$ to change from road 1 to road 2, and in a same manner p_{22} to stay on road 2 and p_{21} to change from road 2 to road 1. During all simulations we set $p_{11} = p_{22} = 0.5$ since this is required for a stable situation, at least stable as a result of the turning fractions. We should remark here that in the uncontrolled situation, the priority rules are such that the vehicles cross the intersection alternately, which is equivalent to an all-stop intersection as is often used in the USA and Canada.

2.4 Analyses

The analyses we will perform with this model consist of the comparison between the uncontrolled intersection and the controlled intersection. We will compute the average flow as described above for all total number of vehicles between 0 vehicles and 160 vehicles (jam accumulation) per road, using an interval of 10 vehicles, for both scenarios. Notice that this results in 256 simulations per scenario. These 256 number of average flows will be visualized in an MFD and a contour plot, where the latter helps to visualize the impact of the initial distribution among the two roads. As described above, we will use the same cycle time and turning fractions for all simulations.

3 Results

In this section we will present the results of the analyses. Both MFDs from the uncontrolled and controlled simulation are shown in Fig. 2. Here all data points are shown, where one point is based on one simulation. The white line represents the median, the dark blue filling represents the first and third quartiles, and the light blue filling represents the outliers. Both the uncontrolled and the controlled MFD show a linear increase of flow for densities lower than 50 vehicles, which is the case where all or nearly all vehicles can drive at free-flow speed. Then we see in both figures a line representing the capacity, which in the case of the uncontrolled simulation is higher (380 veh/h) than the controlled case (260 veh/h). The uncontrolled MFD starts to decrease when exceeding an accumulation of 100 vehicles, where the controlled declines after 140 vehicles, allowing some simulations up to an accumulation of 200 vehicles to keep their flow at the high value of 260 veh/h. The fact that there are different outcomes of different initial accumulation distributions that have the same total number of vehicles can be seen in Fig. 3. When the initial spatial distribution is more balanced in the controlled situation, i.e., a total number of 200 vehicles consisting of 100 on the first road and 100 on the second road in contrary to, for example, 140 and 60, the flow will remain higher. This is not seen in the uncontrolled case, visible through the straight diagonals in Fig. 3a. This 'plateau extension' of high flows in initially unbalanced high-accumulation situations on the controlled intersection, visible between a total accumulation of 150–200 vehicles and a total accumulation of 240–300 vehicles, is the biggest difference between the controlled and uncontrolled designs.

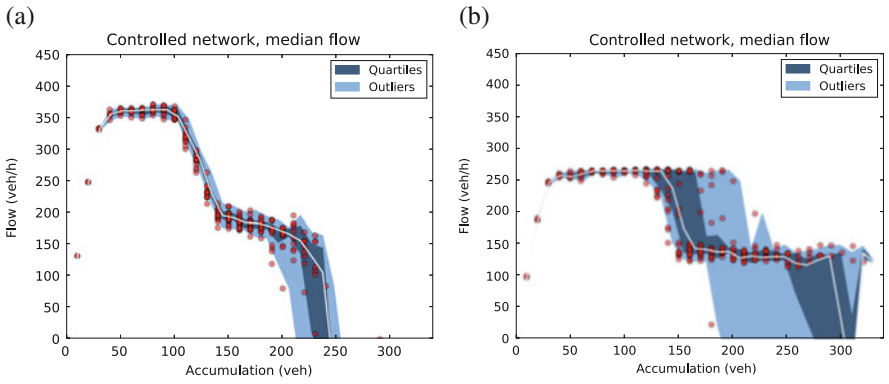

Fig. 2 Macroscopic fundamental diagrams. (**a**) Without traffic lights. (**b**) With traffic lights

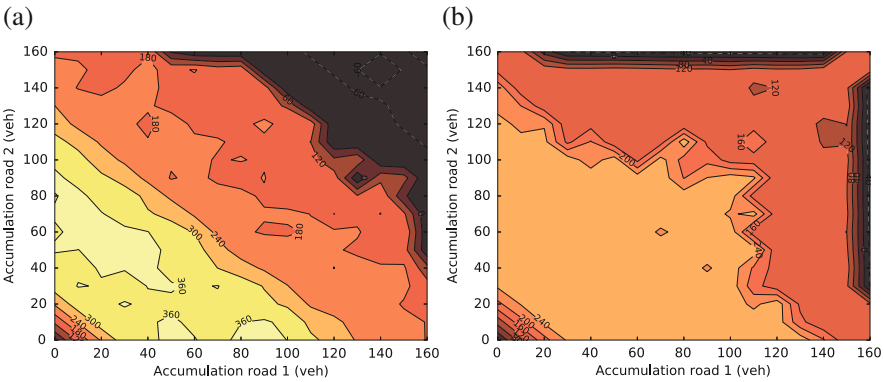

Fig. 3 Average flow (in colours). (**a**) Without traffic lights. (**b**) With traffic lights

4 Discussion

In this research we studied the effect of a simple intersection with and without traffic lights on the shape of the corresponding macroscopic fundamental diagram. We used a microscopic simulation on a double ring road with an increasing number of vehicles on both roads. For each case we computed the average flow which we plotted against the accumulation in an MFD graph. We showed that both situations lead to a concave MFD. The uncontrolled case had a higher peak at lower densities but a steeper and sharper decline after the peak, while the controlled case had a lower flow at lower densities but was able to maintain this flow also for higher densities. In the controlled scenario, it is interesting to see that there are two 'plateaus' in the MFD. The first plateau is the one which has a flow of 260 veh/h, which corresponds to the situation where most of the cars are driving at free-flow speed, while a part of them is standing in a queue to wait for green. The second plateau in the controlled MFD has a flow of 130 veh/h, and is especially interesting because it extends up until a total accumulation of 300 vehicles. These are situations where there are almost no vehicles driving at free-flow, and most vehicles are driving in a stop-and-go manner with the same frequency as the traffic light cycle. As long as there is space for such a stop-and-go wave to exist, the flow remains at a relatively high value of 130 veh/h. This shows that for higher densities, a traffic management system increases the throughput at a basic intersection such as the one used in this simulation, and thus that it would be interesting to turn the traffic lights off at lower densities, and on at higher densities.

When we investigate the different simulations from the uncontrolled case, we notice that after the critical accumulation of 100 vehicles in total, the system became unstable. Here we mean that there always will be one road filling up almost completely while the other roads empty itself. The system is unable to recover from this, and the flow therefore becomes remarkably low from an accumulation of 130 and onwards. It causes the flow to rapidly decline after an accumulation

of 200 vehicles, and this is an important difference between the uncontrolled and the controlled case. The controlled intersection is much better at abiding a stable configuration where the flow remains at a higher level. This also has the consequence that the vehicles are more homogeneously spread along the network, which is what we generally accept as a necessary condition for a low-scatter MFD.

Drawbacks of our approach are obviously that both the network and the intersection itself are very simplistic. While this does gives us interesting insights in very basic situations, the applicability of this research to real urban networks is limited and therefore extending this research to larger networks is vital for our understanding of the macroscopic fundamental diagram. Another drawback is that the car-following model, the intelligent driver model (IDM), is very sensitive to its parameters and although we attempted to choose the parameters as realistic as possible, further research using different car-following models might give us more feedback on the effect of the model on the MFD.

Another interesting application of the double ring road is the two-bin model presented firstly by Daganzo et al. [3] and extended by Gayah et al. [7]. Here they start with a square-grid network, which they divide into two halves, each represented by a bin, i.e., the aggregated accumulation of that half of the network. They assume a homogeneous spread in accumulation and model each bin with an MFD, investigating the dynamics and more specifically the instability of the dynamics considering different densities. They conclude that the recovery of congested areas is relatively slow causing an unstable situation in which this hardly recovers at all. In Gayah et al. [8] the authors extend upon this research by comparing it with a network that uses adaptive traffic lights, giving green time according to the upstream demand. This showed to improve the stability. They did not, however, used static traffic lights as well in their comparison, which could be interesting as our study shows that they already improve the stability by quite a margin. Their network size is also relatively large, which makes the comparison with our results difficult.

5 Conclusions

Our study shows that the spatial distribution of traffic on a small network with at least one intersection using (static) traffic lights is much more homogeneous and stable than without any form of traffic control. This shows that when partitioning a network into reservoirs for which an MFD is assumed, this assumption might be invalid if the reservoir contains mostly un-signalized intersection, since this may lead to a more unstable and heterogeneous distribution of vehicles.

References

1. Daganzo, C.F.: Urban gridlock: macroscopic modeling and mitigation approaches. Transp. Res. Part B **41**(1), 49–62 (2007). https://doi.org/10.1016/j.trb.2006.03.001
2. Daganzo, C.F., Geroliminis, N.: An analytical approximation for the macroscopic fundamental diagram of urban traffic. Transp. Res. Part B **42**(9), 771–781 (2008). https://doi.org/10.1016/j.trb.2008.06.008
3. Daganzo, C.F., Gayah, V.V., Gonzales, E.J.: Macroscopic relations of urban traffic variables: bifurcations, multivaluedness and instability. Transp. Res. Part B Methodol. **45**(1), 278–288 (2011). http://dx.doi.org/10.1016/j.trb.2010.06.006
4. De Jong, D., Knoop, V.L., Hoogendoorn, S.P.: The effect of signal settings on the macroscopic fundamental diagram and its applicability in traffic signal driven perimeter control strategies. In: IEEE Conference on Intelligent Transportation Systems, Proceedings, ITSC (ITSC), 1010–1015 (2013). https://doi.org/10.1109/ITSC.2013.6728364
5. Edie, L.: Discussion of traffic stream measurements and definitions. In: Organisation for Economic Co-operation and Development Proceedings, p. 139 (1965)
6. Gayah, V., Daganzo, C.: Effects of turning maneuvers and route choice on a simple network. Transp. Res. Rec. J. Transp. Res. Board **2249**(1), 15–19 (2011). http://dx.doi.org/10.3141/2249-03
7. Gayah, V.V., Daganzo, C.F.: Clockwise hysteresis loops in the Macroscopic Fundamental Diagram: an effect of network instability. Transp. Res. Part B **45**, 643–655 (2011). https://doi.org/10.1016/j.trb.2010.11.006
8. Gayah, V.V., Gao, X., Nagle, A.S.: On the impacts of locally adaptive signal control on urban network stability and the Macroscopic Fundamental Diagram. Transp. Res. Part B **70**, 255–268 (2014). https://doi.org/10.1016/j.trb.2014.09.010
9. Geroliminis, N., Daganzo, C.F.: Existence of urban-scale macroscopic fundamental diagrams: some experimental findings. Transp. Res. Part B **42**(9), 759–770 (2008). https://doi.org/10.1016/j.trb.2008.02.002
10. Geroliminis, N., Sun, J.: Properties of a well-defined macroscopic fundamental diagram for urban traffic. Transp. Res. Part B **45**, 605–617 (2011). https://doi.org/10.1016/j.trb.2010.11.004
11. Godfrey, J.: The mechanism of a road network. Traffic Eng. Control **11**, 323–327 (1969)
12. Knoop, V.L., van Lint, H., Hoogendoorn, S.P.: Traffic dynamics: its impact on the Macroscopic Fundamental Diagram. Physica A Stat. Mech. Appl. **438**, 236–250 (2015). http://dx.doi.org/10.1016/j.physa.2015.06.016. http://www.sciencedirect.com/science/article/pii/S0378437115005695
13. Malinauskas, R.: The Intelligent Driver Model: Analysis and Application to Adaptive Cruise Control (2014). http://tigerprints.clemson.edu/all_theses

Braess Paradox in Networks of Stochastic Microscopic Traffic Models

Stefan Bittihn and Andreas Schadschneider

Abstract The Braess Paradox describes a counterintuitive situation that can arise in traffic networks which are used by selfish drivers who want to minimize their own traveltimes. For specific combinations of demand and traveltime functions of the roads in such networks the addition of a new road, resulting in a per se faster origin–destination connection, can lead to higher traveltimes for all network users. As an important addition to previous research on the paradox which focused on deterministic macroscopic models of traffic in road networks, we study its occurrence employing a stochastic microscopic traffic model—the totally asymmetric exclusion process (TASEP). We find that the paradox also occurs in these more realistic traffic models and that, depending on the degree of stochasticity, it dominates large parts of the phase space.

1 Introduction

The Braess Paradox was first found by D. Braess in 1968 [4, 5]. He introduced a mathematical model of a transport network which is used by selfish drivers. In his model all drivers want to go from the same origin to the same destination and they can choose between two equivalent routes. Then a new road is built, resulting in a third possible origin–destination route which is shorter than the two former ones. Braess showed that for specific demands and traveltime functions of the roads, this additional road leads to a stable network state in which all drivers have higher traveltimes than in the stable state of the network without the new road. The stable network states correspond to so-called user optima of the systems in which the drivers distribute onto the routes such that all used routes have the same traveltime which is smaller than that of any unused routes [17]. The fact that an

S. Bittihn (✉) · A. Schadschneider
Institute for Theoretical Physics, University of Cologne, Köln, Germany
e-mail: bittihn@thp.uni-koeln.de; as@thp.uni-koeln.de

S. H. Hamdar (ed.), *Traffic and Granular Flow '17*,
https://doi.org/10.1007/978-3-030-11440-4_6

additional *faster* origin–destination connection can actually render the situation of all network users worse sparked the interest of traffic researchers because of its significant consequences for road network design: Building new roads, inducing not only monetary but also environmental and other costs, can in some cases render the road network's situation worse. This implies that traffic congestion problems could in some cases be relieved by closing roads instead of building new ones.

Since its first discovery a lot of effort went into understanding the paradox in more general terms. It was shown that its occurrence is prevalent in congested networks [15]. The regions of its occurrence in certain models were determined [11, 12] and the paradox was also observed in the real world [8]. Furthermore, analogues were found, e.g., in mechanical networks [13], energy networks [18] and pedestrian dynamics [6]. Most studies focused on deterministic macroscopic models of the transport in the networks where the individual roads are treated as being uncorrelated and the functions employed to describe the road traveltimes are linear in the number of road users. This results in an overall rather unrealistic modelling of traffic. While nevertheless many insights on the paradox were obtained already in these previous works, we consider it important to extend the studies by employing more realistic traffic models. By doing this, we hope to gain a deeper understanding of the paradox and try to work towards the aim of being able to predict its occurrence in real road networks and thus contributing to the efficiency of future infrastructure planning. As first steps, we considered the same network that Braess addressed in his original work but with modelling the traffic using totally asymmetric exclusion processes (TASEPs) [9]. The TASEP is basically the $v_{\max} = 1$ version of the Nagel–Schreckenberg model [10]. It is a cellular automaton which includes microscopic exclusion dynamics, jamming effects and inter-road correlations. We studied the network of TASEPs with two levels of stochasticity [1, 2] and could determine the phase diagrams of both systems. We proved that the paradox not only occurs in both systems but even dominates large parts of their phase spaces.

2 The Model

In this section we briefly introduce the TASEP which is used to model all the roads in our network before presenting the network itself and its two different levels of stochasticity. Then the possible states that can occur in the comparison of the network with and without the new road are discussed.

2.1 The Totally Asymmetric Exclusion Process

As already stated in Sect. 1, the individual roads of our network are given by TASEPs. The TASEP is a simple cellular automaton which was originally introduced to describe protein translation [9] and is now renowned as the paradigmatic

Fig. 1 The TASEP consists of L cells, which are either empty or occupied by maximally one particle. If a site is chosen to be updated and is occupied by a particle, the particle can jump to the next site, if the next site is empty. The case of open boundary conditions is shown, where site 1 feeds from a reservoir which is occupied with probability α and site L exits into a reservoir which is empty with probability β

model for single-lane traffic. A sketch of a single (open boundary) TASEP segment is depicted in Fig. 1. A TASEP segment consists of L cells (L is also called the length of a TASEP), which are either empty or occupied by a single particle. All particles move in the same direction (here: left to right).

In the case of open boundary conditions, particles are fed onto the first site of the system from a reservoir which is occupied with the entrance probability α. Particles can jump out of the last site of the system into a reservoir which is empty with exit probability β. In the case of periodic boundary conditions, site $L + 1$ is identified with site 1. Then the total number of particles is constant and the system becomes effectively a ring.

In our analysis we employed the so-called random sequential update procedure: One of the sites[1] is chosen with uniform probability. If the chosen site contains a particle, the particle can jump to the next site, iff the next site is empty. After L or $L+1$ (periodic or open boundary conditions) such updates, a time step is completed.

In the case of periodic boundary conditions, the stationary state is always given by a flat density profile, where all sites have an average density which is equal to the global density. For the case of open boundary conditions, the stationary state depends on α and β. The TASEP with open boundary conditions can be solved analytically [3, 7, 14]; high density, low density and maximum current phases develop, depending on the values of α and β. For the special cases $\alpha = \beta < 1/2$, a so-called domain wall phase develops, in which a domain wall which separates a low density phase on the left and a high density phase on the right performs a random walk through the TASEP segment.

2.2 *The Braess Network*

We consider the same network Braess analysed in his original work, as shown in Fig. 2. All cars want to go from the origin, which is at junction site j_1 to the destination at junction site j_4. They can choose between the three different routes

[1]For periodic boundary conditions one of the L sites is chosen. For open boundary conditions the entrance-reservoir is included into the update procedure. Then one of the total $L+1$ sites is chosen.

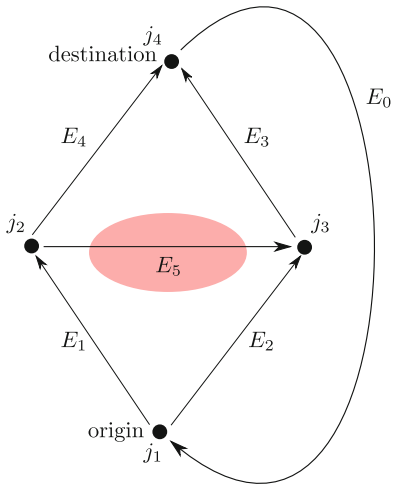

Fig. 2 The network consists of edges $E_i, i \in \{0, \ldots, 5\}$, which are given by TASEPs of length L_i and are connected through junction sites $j_k, k \in \{1, \ldots, 4\}$. Periodic boundary conditions are achieved through E_0 with $L_0 = 1$. All particles want to go from the same origin at j_1 to the same destination at j_4. They can choose between routes 14, 23 and the new route 153, resulting from the new edge E_5. When reaching the destination, they are fed back to the origin via E_0

14, 23 and 153. Edge E_5 (note: from here on the terms 'road' and 'edge' are used interchangeably) is considered the *new road/edge* which is added to the system. Thus route 153 is *the new route*.

In his original work, Braess assigned deterministic, linear traveltime functions to all roads and showed the occurrence of his paradox in this model. In our case, all the roads $E_i, i \in \{0, \ldots, 5\}$, are given by TASEPs of lengths L_i and are connected through junction sites $j_k, k \in \{1, \ldots, 4\}$, which can take upto one particle. Additionally, we added periodic boundary conditions through E_0 of length $L_0 = 1$. Thus the total number of particles M (note: from here on the terms particles, drivers and cars are used interchangeably), also called the demand, in the network is constant. The network without the new road is chosen to be symmetric with $L_1 = L_3$ and $L_2 = L_4$. The two routes 14 and 23 are of equal lengths. The length of the new road is chosen to be

$$L_5 \leq L_2 - L_1 - 1, \tag{1}$$

which results in the new route 153 being shorter than routes 14 and 23:

$$\hat{L}_{153} = 5 + L_1 + L_3 + L_5 \leq 4 + L_1 + L_2 = \hat{L}_{14} = \hat{L}_{23}. \tag{2}$$

Lengths of routes are indicated as $\hat{L}_i$. We thus end up with a network that consists of two equal-length origin–destination routes and an additional shorter (and thus faster route, if routes are used by a single particle) route which is added to the system. We look at two versions of the system with different levels of stochasticity that differ in the route choice mechanism.

Drivers with Fixed Strategies In the version of the model with less stochasticity a network state is given by the amounts N_{14}, N_{23}, N_{153} of drivers choosing route 14, 23 and 153, respectively. These amounts are then the tunable parameters for each

combination of the L_i and M. The stochasticity is in this case limited to the random sequential update mechanism which is described in Sect. 2.1.

Network with Turning Probabilities In the model version with higher stochasticity the route choices are given by turning probabilities γ and δ which are the probabilities of drivers turning left on junctions j_1 and j_2, respectively. In this version, individual drivers do not have individual fixed strategies. Only on average the same amounts of drivers keep choosing the same routes. The turning probabilities γ and δ are the tunable parameters for each combination of the L_i and M in this version of the model.

2.3 Possible States in Our Networks

A network state is given by the distribution of the particles onto the different routes. In the model with fixed strategies it is thus given by the N_{14}, N_{23}, N_{153} and in the model with turning probabilities it is given by γ and δ (Sect. 2.2). Two different states are the most important ones when analysing network transport. The first one is the stable state of a network of selfish users, the so-called user optimum (uo). This has to be distinguished from the system optimum (so), which optimizes the system's performance but is not necessarily stable [17]. The uo is the state in which traveltimes (traveltime of route i is denoted as T_i and describes the number of time steps, a particle needs to get from origin to destination via this route) on all used routes are equal and smaller than those of any unused routes. If this, and the fact that all drivers have knowledge about traveltimes of all possible routes (which is assumed in the context of Braess paradox), is the case, no driver will change to a different route since this change would increase their traveltime. Thus this state is stable for selfish drivers. The so, on the other hand, does not have to be stable. It is the state in which the maximum traveltime out of all routes is minimized compared to all other possible distributions of drivers. Thus it optimizes the system as a whole. Note that throughout literature, different definitions of so are considered, e.g. the state minimizing the total traveltime [16]. We chose this definition since it is the same as the one that Braess used in his original work.

To analyse whether Braess paradox occurs in our model one has to find the user and system optima of the systems with and without E_5 for the same demand (same total number of particles M) and compare their representative traveltimes. The systems with and without E_5 are also referred to as 5link or 4link system and corresponding variables are indicated by superscripts (5)/(4). The traveltimes to be compared are those of the uo, i.e. $T(uo)$, where all roads have the same traveltime and the maximum traveltime in the so, i.e. $T_{max}(so)$. In our network the states depicted in Fig. 3 are possible. In the states "E_5 optimal" and "E_5 improves", the new road leads to lower traveltimes in the user optimum of the system. In the "Braess 1/2" states, it increases the traveltimes in the user optimum. In the "E_5 not used" state, the new road will not be used at all in the user optimum of the 5link system. For more details on these states the reader is referred to [1].

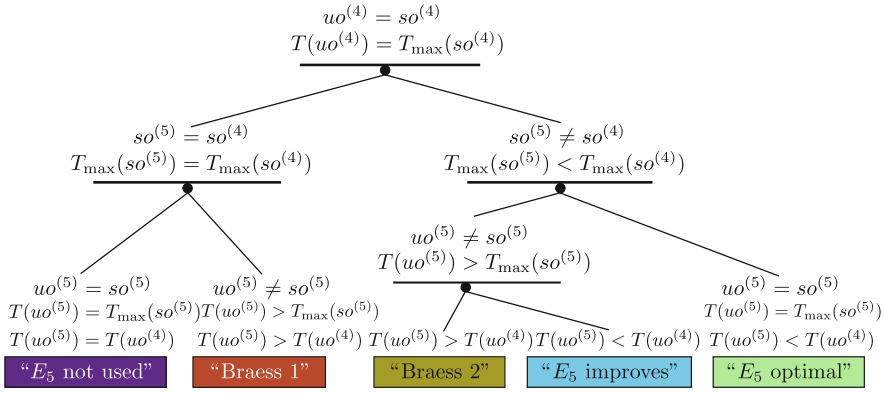

Fig. 3 The possible states which can occur when comparing uo and so states of the 4link and 5link systems with the same M. The tree is derived from the natural starting point $uo^{(4)} = so^{(4)}$ which is true due to the symmetry of the 4link system. Five states can occur: In the two states on the right side ("E_5 improves" and "E_5 optimal") the new road leads to lower traveltimes in the uo. In the "E_5 not used" state, the new road will not be used at all and in the two states "Braess 1/2", the road will lead to higher uo-traveltimes

3 Results

Here we present our results for both versions of the model. The results were obtained through extensive Monte Carlo simulations of the systems. The phase the system is in depends on the global density ρ_{global} which is the total number of particles divided by the total number of cells in the system and the length of the new route compared to the lengths of the two old routes given by the ratio $\hat{L}_{153}/\hat{L}_{14}$.

The phase diagrams of the systems with drivers following fixed strategies and with drivers obeying turning probabilities are shown in Fig. 4a, b. The phases F and V are trivial phases, since at these high 5link global densities, the 4link system is already full and the two systems cannot be compared.

For low global densities $\rho^{(5)}_{\text{global}} \lesssim 0.1$ (phases $A_{1/2}$/phase $I_{a/b}$) the system is in an "E_5 optimal" phase for both route choice mechanisms. Here, the new edge improves the system in the sense that all drivers will have lower traveltimes in the uo due to adding E_5 to the network. The "E_5 optimal" phases are subdivided into two parts. In parts A_1 and I_a in the 5link systems all particles will choose the new route 153. In the other sub-phases A_2 and I_b all routes will be used in the 5link uo. The uo traveltimes of the 5link systems will be lower than the uo traveltimes of the 4link systems.

Proceeding to higher global densities, in both stochasticity levels the "Braess 1" phase (phase B/II) follows. Whereas in the system with fixed driver strategies, it dominates almost the whole phase space up to densities $\rho^{(4)}_{\text{global}} \approx 0.8$ (phase B) followed by a small "Braess 2" phase (phase C), in the more stochastic system it only fills a relatively small part of phase space (phase II) for densities up to $\rho^{(4)}_{\text{global}} \approx 0.3$.

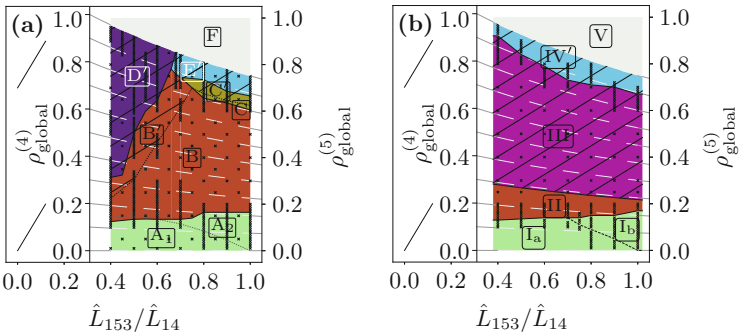

Fig. 4 The phase diagrams of the systems with fixed strategies (part **(a)**) and with turning probabilities (part **(b)**). In both cases results were obtained by simulating systems with $L_1 = L_3 = 100$ and $L_2 = L_4 = 500$. The phases are coloured according to the scheme in Fig. 3. The relevant parameters for the systems are the global density in the 4link/5link systems $\rho^{(4)/(5)}_{\text{global}}$ and the ratio $\hat{L}_{153}/\hat{L}_{14}$ of the lengths of old and new routes. The small 'x's indicate parameters at which Monte Carlo simulations were performed

In the hatched areas of the phase diagrams, no exact *uo* could be found: In the system with turning probabilities a phase (phase III) which is not expected from the straightforward reasoning in Sect. 2.3 follows for the whole density region up to $\rho^{(4)}_{\text{global}} \approx 0.9$. In phase III, fluctuating domain walls dominate the system. They develop since individual TASEPs are in the domain wall state which was briefly mentioned in Sect. 2.1. Here, no stable traveltimes can be measured and thus no *uo* and *so* can be deduced. There is also a phase similar to the "E_5 improves" phase (phase IV') at really high densities.

In the less stochastic system, i.e. for drivers with fixed strategies, the phases in the hatched area are similar to the "Braess 1" and "Braess 2" phases (phases B' and C'), "E_5 not used" phase (phase D') and the "E_5 improves" phase (phase E'). Additionally to the fact that no *uo* can be found in these phases, the system is prone to total gridlocks in all of these phases. The system tends to be in states, where route 153 has lower traveltimes than the others. As more particles switch to this route it suddenly becomes blocked and the whole system is gridlocked.

4 Summary

By simulating the same network that Braess investigated in his original work with two different route choice mechanisms and with TASEPs as edges we could prove that Braess paradox occurs in these networks. Depending on the level of stochasticity, the paradox occurs in a large part of the system's phase space (fixed drivers strategies, low stochasticity) or a smaller part of the system (turning probabilities, higher stochasticity). No fine tuning is needed to achieve the paradox.

Additionally to its occurrence we could show the importance of fluctuations in networks of these stochastic transport models as manifested in the fluctuation dominated phase of the model with turning probabilities. The results are a first step towards understanding the paradox in a more realistic context. In future work, the network will, e.g., be simulated employing the more realistic Nagel–Schreckenberg model [10].

Acknowledgements Financial support by the Deutsche Forschungsgesellschaft (DFG) under grant SCHA 636/8-2 and the Bonn-Cologne Graduate School of Physics and Astronomy (BCGS) is gratefully acknowledged. Monte Carlo simulations were carried out on the CHEOPS (Cologne High Efficiency Operating Platform for Science) cluster of the RRZK (University of Cologne).

References

1. Bittihn, S., Schadschneider, A.: Braess paradox in a network of totally asymmetric exclusion processes. Phys. Rev. E **94**, 062312 (2016)
2. Bittihn, S., Schadschneider, A.: Braess paradox in a network with stochastic dynamics and fixed strategies. Physica A Stat. Mech. Appl. **507**, 133–152 (2018)
3. Blythe, R., Evans, M.: Nonequilibrium steady states of matrix product form: a solver's guide. J. Phys. A **40**, R333 (2007)
4. Braess, D.: Über ein Paradoxon aus der Verkehrsplanung. Unternehmensforschung **12**, 258 (1968)
5. Braess, D., Nagurney, A., Wakolbinger, T.: On a paradox of traffic planning. Transp. Sci. **39**, 446 (2005). *(English translation of Braess, D.: Über ein Paradoxon aus der Verkehrsplanung. Unternehmensforschung **12**, 258 (1968))*
6. Crociani, L., Lämmel, G.: Multidestination pedestrian flows in equilibrium: a cellular automaton-based approach. Comput. Aided Civ. Inf. Eng. **31**(6), 432–448 (2016)
7. Derrida, B., Evans, M., Hakim, V., Pasquier, V.: Exact solution of a 1d asymmetric exclusion model using a matrix formulation. J. Phys. A **26**, 1493 (1993)
8. Kolata, G.: What if they closed 42d Street and nobody noticed? The New York Times (December 1990)
9. MacDonald, C.T., Gibbs, J.H., Pipkin, A.C.: Kinetics of biopolymerization on nucleic acid templates. Biopolymers **6**(1), 1–25 (1968)
10. Nagel, K., Schreckenberg, M.: A cellular automaton model for freeway traffic. J. Phys. I Fr. **2**(12), 2221–2229 (1992)
11. Nagurney, A.: The negation of the Braess paradox as demand increases: the wisdom of crowds in transportation networks. EPL **91**, 48002 (2010)
12. Pas, E., Principio, S.L.: Braess' paradox: some new insights. Transp. Res. Part B Methodol. **31**(3), 265–276 (1997)
13. Penchina, C.M., Penchina, L.J.: The Braess paradox in mechanical, traffic, and other networks. Am. J. Phys. **71(5)**, 479 (2003)
14. Schütz, G., Domany, E.: Phase transitions in an exactly solvable one-dimensional exclusion process. J. Stat. Phys. **72**, 277 (1993)
15. Steinberg, R., Zangwill, W.: The prevalence of Braess' paradox. Transp. Sci. **17**, 301 (1983)
16. Thunig, T., Nagel, K.: Braess's Paradox in an agent-based transport model. Proc. Comput. Sci. **83**, 946–951 (2016)
17. Wardrop, J.G.: Road paper. Some theoretical aspects of road traffic research. Proc. Inst. Civ. Eng. **1**(3), 325–362 (1952)
18. Witthaut, D., Timme, M.: Braess's paradox in oscillator networks, desynchronization and power outage. New J. Phys. **14**(8), 083036 (2012)

Dynamical Universality Class of the Nagel–Schreckenberg and Related Models

Andreas Schadschneider, Johannes Schmidt, Jan de Gier, and Gunter M. Schütz

Abstract Models for vehicular traffic fall into distinct dynamical universality classes of non-equilibrium systems. Such models share model-independent aspects of their dynamics, such as current fluctuations. Up to now the universality class of the Nagel–Schreckenberg (NaSch) model was not known except for the special case $v_{\max} = 1$. In this case the model corresponds to the ASEP (asymmetric simple exclusion process) which belongs to the Kardar–Parisi–Zhang (KPZ) class characterized by the dynamical exponent $z = 3/2$. We have shown that the NaSch model for general $v_{\max}$ also belongs to the KPZ class. Here we demonstrate that the universality class is not changed by extending the model to a two-lane NaSch model with dynamical lane changing rules. As an application we estimate the relaxation time to the (generally unknown) stationary state.

1 Introduction

A central goal of traffic science is the formulation of model paradigms that capture the essential features of road traffic. Dynamical, non-equilibrium systems fall into distinct universality classes that can be modeled by a variety of stochastic, statistical physics simulation models whose properties are similar. It is important therefore to identify such universality classes.

A. Schadschneider (✉) · J. Schmidt
Institut für Theoretische Physik, Universität zu Köln, Köln, Germany
e-mail: as@thp.uni-koeln.de

J. de Gier
ARC Centre of Excellence for Mathematical and Statistical Frontiers (ACEMS), School of Mathematics and Statistics, The University of Melbourne, Melbourne, VIC, Australia
e-mail: jdgier@unimelb.edu.au

G. M. Schütz
Institute of Complex Systems, Forschungszentrum Jülich, Jülich, Germany
e-mail: g.schuetz@fz-juelich.de

S. H. Hamdar (ed.), *Traffic and Granular Flow '17*,
https://doi.org/10.1007/978-3-030-11440-4_7

So far the universality class of the Nagel–Schreckenberg (NaSch) model was not known except for the special case $v_{\max} = 1$ where the model corresponds to the ASEP (asymmetric simple exclusion process) which belongs to the Kardar–Parisi–Zhang (KPZ) class with $z = 3/2$ [5]. Up to now it was unclear whether in the case for general maximum velocities $v_{\max} > 1$ the internal degree of freedom (i.e., the velocity) might lead to a different universality class since previous numerical studies were inconclusive [4, 12].

In [14] we have shown that the NaSch model indeed belongs to the KPZ class and thus shows superdiffusivity, non-Gaussian current fluctuations, and statistics that strongly depends on the initialization of the simulation. Here we demonstrate that the universality class is not changed by extending the model to a two-lane NaSch model with dynamical lane changing rules. As an application we provide an estimate for the relaxation time to the (generally unknown) stationary state.

2 Dynamical Universality Classes

Dynamical universality classes are distinguished by the dynamical exponent z which encodes the asymmetry of space and time in dynamical processes. For example, it relates the relaxation time to the stationary state T and the system size L by

$$T \simeq \lambda L^z \,, \tag{1}$$

where λ is some non-universal constant that depends on the details of the dynamics, e.g., interaction parameters. Systems in the same universality class show for large times of order $1 \ll t \ll L^z$ identical statistical properties such as current fluctuations or relaxation of initial configurations towards the non-equilibrium stationary state. The two most prominent examples are the diffusive class with dynamical exponent $z = 2$ and the superdiffusive Kardar–Parisi–Zhang (KPZ) class with $z = 3/2$.

The dynamical exponent z is not only relevant for relaxation, but also characterizes, e.g., fluctuations in the stationary state where the broadening and amplitude

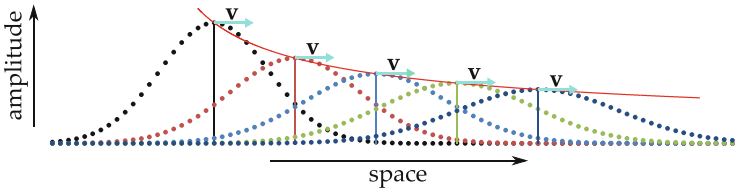

Fig. 1 Dynamics of a (density) fluctuation or perturbation of the stationary state. Different colors indicate snapshots at different times. The perturbation moves with the non-universal collective velocity v. Its broadening and amplitude are controlled by the dynamical exponent z

of a perturbation are controlled by z (Fig. 1). An initial perturbation moves with the non-universal velocity v through the system. This collective velocity can be obtained from the fundamental diagram $J(\rho)$ by $v_{\mathrm{col}} = \partial J/\partial\rho$.

The dynamical exponent can be determined from measurements of the dynamical structure function

$$S_x(t) = \langle n_x(t) n_0(0)\rangle - \rho^2 \simeq \kappa (Et)^{-1/z} f\left((Et)^{-1/z}(x - vt)\right), \tag{2}$$

where $n_x(t)$ is the density at position x at time t and ρ the average density. The generic form of the dynamical structure function can be determined using a hydrodynamic approach called nonlinear fluctuating hydrodynamics (NLFH) [15], i.e., one works in a continuum approximation and looks for asymptotic solutions. It allows for a distinct identification of the universality class via its dynamical exponent z and associated scaling function f. E is a non-universal scaling factor and

$$\kappa = \frac{1}{L}\sum_x S_x(t) \tag{3}$$

the static compressibility which is a time-independent measure of the stationary density fluctuations.

A fluctuation (perturbation) moves with the non-universal collective velocity v. The decay of the amplitude and the broadening are controlled by the dynamical critical exponent. The scaling function f describes the typical shape of the fluctuation. Both z and f are universal, i.e., do not depend on the microscopic details of the dynamics (e.g., interaction constants).

In the following we will briefly present the most important dynamical universality classes of traffic-like systems.

- **Diffusive Class:** The diffusive class is well known. It is characterized by the dynamical exponent $z = 2$ as is evident from the well-known relation

$$\langle x^2\rangle - \langle x\rangle^2 = 2Dt \tag{4}$$

for the mean-quadratic displacement of the diffusing particle where D is the diffusion constant.

A simple realization is a system of diffusing, non-interacting particles (Fig. 2). This system is characterized by the dynamics exponent $z = 2$ and a normalized Gaussian scaling function

$$f(x) = \frac{1}{\sqrt{4\pi Dt}} \exp\left(-\frac{(x - vt)^2}{4Dt}\right) \tag{5}$$

which is known from the exact solution of the diffusion equation (with drift)

$$\frac{\partial f}{\partial t} = -v\frac{\partial f}{\partial x} + D\frac{\partial^2 f}{\partial x^2}, \tag{6}$$

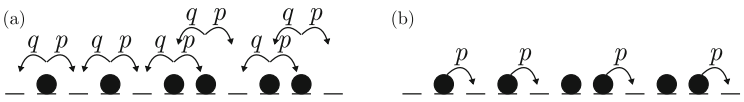

Fig. 2 (**a**) Dynamics of a system of non-interacting diffusing particles. Particles move synchronized with parallel update rule within one time step to right (left) with probability p (q) irrespective of the occupancy of the target site, whereas the probabilities satisfy $p + q \leq 1$. (**b**) The ASEP (asymmetric simple exclusion process) is a simple system of interacting particles. The dynamics is similar to the non-interacting case, but now motion to sites occupied by a particle is not allowed ("exclusion")

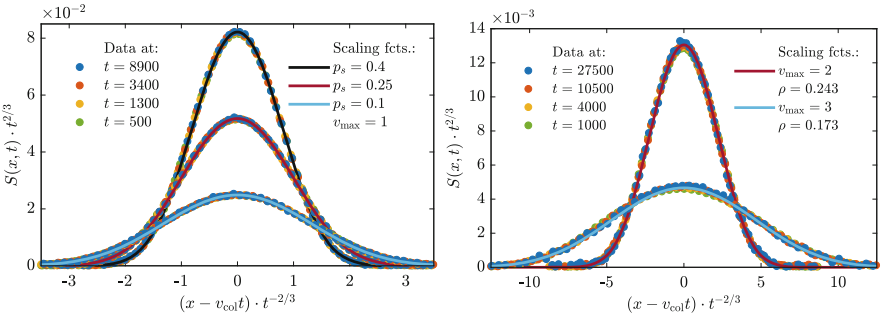

Fig. 3 Left: Data collapse of the structure function for the NaSch model with $v_{\max} = 1$ (ASEP case) and various slow down probabilities p_s for global density $\rho = 1/2$. The system size is $L = 10^7$. Right: The NaSch structure function data collapse for $p_s = 0.25$ and $v_{\max} = 2, 3$ shows a nice agreement to the asymptotic scaling function Eq. (2). The hydrodynamic parameters are for $v_{\max} = 2$ (top) $\kappa = 0.07 \pm 0.001$, $E = 4.94 \pm 0.04$, $v_{\text{col}} = 0.6308 \pm 0.0003$ and for $v_{\max} = 3$ (bottom) $\kappa = 0.0524 \pm 0.0008$, $E = 15.1 \pm 0.1$, $v_{\text{col}} = 1.0513 \pm 0.0002$. The system size is $L = 2 \times 10^5$. For better visibility not all data points are shown. Statistical errors are of the order of the symbol size

with drift velocity $v = p - q$ and diffusion constant $D = (p + q)/2$. The compressibility is given by $\kappa = \rho$, where $\rho \in \mathbf{R}_+$ is the particle density of the system.

- **KPZ Class:** The KPZ class is characterized by the dynamical exponent $z = 3/2$. It first has been discovered in the context of surface growth which is described by a nonlinear stochastic partial differential equation known as Kardar–Parisi–Zhang equation [5]. Figure 3 (left) shows the structure function of the ASEP with parallel update obtained from computer simulations at different times. Time is rescaled with the dynamical exponent $z = 3/2$ to show the data collapse for the structure function that is predicted by Eq. (2). The Prähofer–Spohn scaling function f [11] for this class has not been determined in closed form up to now but is tabulated to very high precision in [10].
- **Fibonacci Class:** Recently it has been shown that the diffusive and KPZ classes are members of an infinite hierarchy of universality classes [8, 9]. There new classes have been found which are realized in models that have more than

one conserved quantity. The diffusive and KPZ class have only one conserved quantity, the particle number. A natural generalization are multispecies models where the particle number of each species is conserved. This includes multilane models where the particle number on each lane is conserved separately while overtaking in the same lane and interactions between particles in different lanes are allowed. These systems are characterized by dynamical exponents of the form $z_\alpha = F_{\alpha+3}/F_{\alpha+2}$ where F_α is the α-th Fibonacci number defined by $F_{\alpha+2} = F_{\alpha+1} + F_\alpha$, i.e., $F_\alpha = 1, 1, 2, 3, 5, 8, \ldots$. Furthermore it includes the golden mean class which corresponds to the limit $z_\infty = \lim_{\alpha\to\infty} z_\alpha = (1+\sqrt{5})/2$. The scaling functions f_α have been determined in [8, 9]. They turn out to be asymmetric Lévy-distributions.

For obvious reasons this hierarchy of universality classes is called Fibonacci class. For $\alpha = 1$ we have $z_0 = F_3/F_2 = 2$, i.e., the diffusive class, for $\alpha = 2$ the KPZ class with $z_1 = F_4/F_3 = 3/2$.

3 Nagel–Schreckenberg Model

The seminal Nagel–Schreckenberg (NaSch) model [7, 13] is *the* minimal cellular automaton model for highway traffic. It can be considered as a generalization of the ASEP with parallel dynamics (synchronous update). Each particle (car) j has now an internal state (the "velocity") v_j that can have integer values $v = 0, 1, \ldots, v_{\max}$ which determines the number of cells that the vehicle moves forward. The velocity of each car is updated in four steps: (1) acceleration: the speed is increased to $v_j = \min(v_j, v_{\max})$; (2) braking: to avoid accidents, the speed is reduced to $v_j = \min(d_j, v_j)$ if necessary, where d_j is the number of empty cells in front of car j; (3) randomization: the velocity is reduced by 1 with probability p_s; (4) motion: the car moves v_j cells forward. All rules are applied to all cars at the same time (parallel update).

Figure 3 shows rescaled structure functions for the NaSch model with $v_{\max} = 1$ and $v_{\max} > 1$. The structure function is rescaled by a $t^{2/3}$ and plotted as a function of the rescaled variable $y = (x - v_{col}t)t^{-2/3}$ where v_{col} is the collective velocity. If the dynamical structure function is of the form (2) with $z = 3/2$ all curves for different times should be identical. This is indeed the case showing that the dynamical exponent is $z = 3/2$.

For the standard ASEP with $v_{\max} = 1$ and random-sequential update this was already known. Figure 3 shows that the use of a parallel update does not change the universality class. For the general case of the NaSch model with $v_{\max} > 1$ previous results were inconclusive due to the limited computational resources which did not allow to relax larger systems sufficiently [4, 12]. The results of [12] could not exclude a density dependent dynamical exponent. However, the results shown in Fig. 3 and [14] provide convincing evidence that the NaSch model belongs to the KPZ class for all values of the maximal velocity $v_{\max}$, the randomization parameter p_s, and all densities.

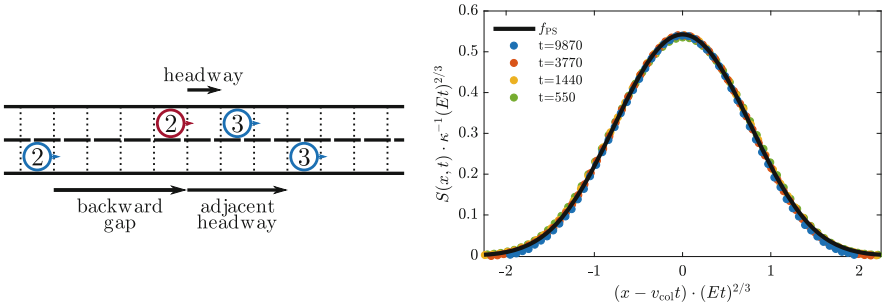

Fig. 4 Left: Definition of the 2-lane NaSch model. Typical configuration showing a vehicle (red) satisfying the *incentive* and *safety* lane changing criteria. Right: Structure function of the 2-lane NaSch model [14]

3.1 Generalizations

In order to determine which properties are essential for a system to be in the KPZ-class we have studied a 2-lane generalization of the NaSch model. The focus here was not on obtaining a realistic behavior, but rather to check whether allowing to change the sequence of particles (i.e., deviations from single-file behavior) will drive the system into a different universality class.

In Fig. 4 the definition of the 2-lane model is shown. As usual the lane changing step is subdivided into an incentive and a safety criterion. If these criteria are fulfilled the lane change is performed with some probability p_c. For details of the rules, we refer to [14]. Figure 4 shows a typical situation where a vehicle changes the lane.

In addition, Fig. 4 shows the (rescaled) structure function of the 2-lane model. It is in very good agreement with the Prähofer–Spohn function [14]. This shows that the possibility of reordering of particles in this model, i.e., deviations from single-file motion, does not lead to a different universality class. In this respect the KPZ class is rather robust.

4 Relaxation of Models

For a stochastic model the relaxation time T is properly defined through the spectral gap g_S of the time evolution operator [13] which depends on the system size as $T \sim 1/g_S \sim L^z$. Here z is the dynamical exponent which was already introduced in Eq. (2). Since the spectral gap is a quantity that is hard to calculate, one can use the structure function to define an equivalent relaxation time. The structure function carries the information about the slow relaxation mode and tells how a perturbation/fluctuation evolves through the system. The amplitude of the structure function will decay exponentially instead of $t^{-1/z}$ after its width has reached the size of the system. The width σ of the structure function spreads as

$\sigma \sim t^{1/z}$. In case of the KPZ universality class one finds for the Prähofer–Spohn scaling function $\int_{-0.5}^{0.5} f_{\mathrm{PS}}(x)\mathrm{d}x = 0.505(7)$. Therefore, the width $(Et)^{2/3}$ covers 50.57% of the structure function and solving $L = (Et)^{2/3}$ for t with λ determined by NLFH-theory will give a lower boundary for a proper relaxation time:

$$T \gtrsim \frac{L^{3/2}}{\sqrt{2\kappa}\,|J''(\rho)|} \tag{7}$$

where $J''(\rho)$ is the second derivative of the (stationary) fundamental diagram and κ the compressibility which is typically of the order 10^{-3} up to 10^{-1}. Note that T can now be estimated from quantities which are easy to access in experiments even for "short" relaxation times.

Although quantities like the fundamental diagram can relax much faster, especially for dynamical quantities one could be lead to erroneous conclusions if the system has not been relaxed sufficiently. For example, in [1] it was concluded from velocity statistics that the NaSch model might undergo a second order phase transition. However, with $T = 10^5$ and $L = 2 \times 10^4$ the criterion (7) is strongly violated which sheds severe doubts on this conclusion.

5 Summary and Conclusions

We have shown that the NaSch model belongs to the KPZ universality class characterized by the dynamical exponent $z = 3/2$ for all densities and independent of the maximal velocity $v_{\max}$ and the randomization parameter p. Somewhat surprisingly, a 2-lane generalization belongs to the same universality class. This raises the question, what actually determines the universality class? It turns out that the number of conservation laws is essential. All the models considered here, the ASEP, the NaSch model, and its 2-lane generalization have only one conserved quantity, the particle number N. In such a case it can be shown that only $z = 2$ (diffusive class) and $z = 3/2$ (KPZ class) are possible [8].

In models with more than one conserved quantity, other universality classes can be realized [8, 9]. A possible realization of such a model is a 2-lane model where lane changes are not allowed, but which includes interactions between cars on different lanes. Such a model has two conservation laws, namely the particle numbers (densities) on each lane.

A next step would be to determine the universality classes of traffic models that are not strictly one dimensional. Recently it has been shown [6] that the two-dimensional variants of the ASEP are marginally superdiffusive, i.e., the 2-point correlation function grows as $t \cdot (\ln t)^{2/3}$. It would also be interesting to determine the universality class for the NetNasch model [16] and the extension of the NaSch model to urban traffic introduced in [2, 3].

Acknowledgements Support by the German Science Foundation (Grant SCHA 636/8-2) and the Bonn-Cologne Graduate School of Physics and Astronomy (BCGS) is gratefully acknowledged. J.S. thanks the Australian Research Council Centre of Excellence for Mathematical and Statistical Frontiers (ACEMS) for funding that allowed him to visit The University of Melbourne where parts of this work were done.

References

1. Bain, N., Emig, T., Ulm, F.J., Schreckenberg, M.: Velocity statistics of the Nagel-Schreckenberg model. Phys. Rev. E **93**, 022305 (2016)
2. Brockfeld, E., Barlovic, R., Schadschneider, A., Schreckenberg, M.: Optimizing traffic lights in a cellular automaton model for city traffic. Phys. Rev. E **64**, 056132 (2001)
3. Chowdhury, D., Schadschneider, A.: Self-organization of traffic jams in cities: effects of stochastic dynamics and signal periods. Phys. Rev. E **59**, R1311 (1999)
4. Csányi, G., Kertész, J.: Scaling behaviour in discrete traffic models. J. Phys. A **28**, L427 (1995). Erratum: 29, 471 (1996)
5. Kardar, M., Parisi, G., Zhang, Y.C.: Dynamic scaling of growing interfaces. Phys. Rev. Lett. **56**, 889 (1986)
6. Krug, J., Neiss, R., Schadschneider, A., Schmidt, J.: Logarithmic superdiffusion in two dimensional driven lattice gases. J. Stat. Phys. **172**, 493 (2018)
7. Nagel, K., Schreckenberg, M.: A cellular automaton model for freeway traffic. J. Phys. I Fr. **2**, 2221 (1992)
8. Popkov, V., Schadschneider, A., Schmidt, J., Schütz, G.M.: Fibonacci family of dynamical universality classes. Proc. Natl. Acad. Sci. U. S. A. **112**, 12645 (2015)
9. Popkov, V., Schadschneider, A., Schmidt, J., Schütz, G.M.: Exact scaling solution of the mode coupling equations for non-linear fluctuating hydrodynamics in one dimension. J. Stat. Mech. 093211 (2016)
10. Prähofer, M., Spohn, H. (2004). http://www.m5.ma.tum.de/kpz
11. Prähofer, M., Spohn, H.: Exact scaling functions for one-dimensional stationary KPZ growth. J. Stat. Phys. **115**, 255 (2004)
12. Sasvári, M., Kertész, J.: On cellular automata models of single lane traffic. Phys. Rev. E **56**, 4104 (1997)
13. Schadschneider, A., Chowdhury, D., Nishinari, K.: Stochastic Transport in Complex Systems: From Molecules to Vehicles. Elsevier, Oxford (2010)
14. Schmidt, J., Schadschneider, A., de Gier, J., Schütz, G.M.: KPZ universality of the Nagel-Schreckenberg model (2019, in preparation)
15. Spohn, H.: Nonlinear fluctuating hydrodynamics for anharmonic chains. J. Stat. Phys. **154**, 1191 (2014)
16. Zhang, L., Garoni, T., de Gier, J.: A comparative study of macroscopic fundamental diagrams of urban road networks governed by different traffic signal systems. Transp. Res. B **49**, 1 (2013)

Prediction of Moving Bottleneck and Associated Traffic Phenomena for Automated Driving

Dominik Wegerle, Boris S. Kerner, Sergey L. Klenov, and Michael Schreckenberg

Abstract A slow driving vehicle within traffic flow is considered as a moving bottleneck (MB). In this paper, we present simulations made with a microscopic stochastic flow model with a moving bottleneck in the framework of the three-phase theory by Kerner. The goal is to predict traffic phenomena that may occur if traffic breakdown is realized at the moving bottleneck. Considered is a traffic flow in which different percentages of probe vehicles are randomly distributed, which send their position and their speed each second (simFCD). We investigate what percentage of probe vehicles is necessary to reliably detect a moving bottleneck and predict its motion.

1 Moving Bottleneck Scenario

A moving bottleneck (MB) had probably been predicted first by Gazis and Herman [1] as well as by Newell [7, 8]. For this paper consider the MB caused by a constant slow driving vehicle on the right lane within traffic flow on a two-lane motorway strip as shown in Fig. 1. Due to the difference in velocities between the moving bottleneck and the other vehicles, these have to brake. Ascending vehicles want to bypass the bottleneck and try to change the lane. Both behaviours cause a disturbance in the traffic flow and may lead to a traffic breakdown. In this case there is an area upstream of the moving bottleneck where synchronized flow patterns can be observed. For safe driving in mixed traffic, automated driving vehicles (AV) should have information about such disturbances in traffic flow, when they are at some distance (2–2.5 km) upstream of the bottleneck. Therefore we analyse if those

D. Wegerle (✉) · B. S. Kerner · M. Schreckenberg
Physics of Transport and Traffic, University of Duisburg-Essen, Duisburg, Germany
e-mail: dominik.wegerle@uni-due.de; boris.kerner@uni-due.de; michael.schreckenberg@uni-due.de

S. L. Klenov
Department of Physics, Moscow Institute of Physics and Technology, Moscow, Russia

S. H. Hamdar (ed.), *Traffic and Granular Flow '17*,
https://doi.org/10.1007/978-3-030-11440-4_8

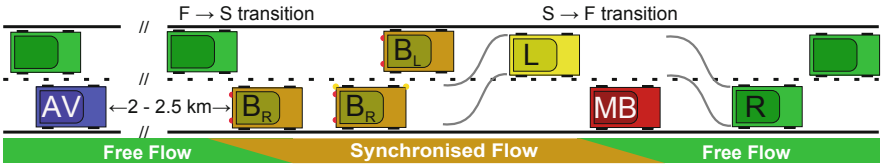

Fig. 1 Simulation scenario: a slow driving car as moving bottleneck (MB) with v_{MB} =28.8 km/h in the right lane on a two-lane motorway strip. Ascending cars with v_{max} =108 km/h have to change the lane behind and in front of the MB (L, R) or need to brake, due to the slow MB (B_R) or lane changing cars (B_L). The vehicle assumed to be automated (AV) should receive information about the downstream traffic situation within a distance of 2–2.5 km

characteristics of traffic breakdown can be found in simulated *floating car data* (simFCD) and if those characteristics enable us to predict the presence of a moving bottleneck. Since it is more or less impossible to study such a traffic scenario with the presence of floating car data in the real world, the traffic scenario as well as the data acquisition will be simulated.

2 Kerner–Klenov Simulation Model

The simulations are based on a microscopic stochastic flow model in the framework of the three-phase theory by Kerner which is described in full detail in [4, Appendix A (Pages 553–623)]. The simulations have been done with the moving bottleneck moving in traffic flow on a two-lane highway section under open boundary conditions. The parameters for the simulation are chosen accordingly to earlier simulations done by Kerner and Klenov [5] and are listed in [5, Table A2]. The speed of the moving bottleneck and the flow rate at the beginning of the simulated road strip are similar to [5, Figure 6(c)]: v_{MB} = 28.8 km/h and q_{in} =1375 $\frac{Veh.}{lane \cdot h}$. Behind the moving bottleneck we assume an area with a length of 300 m, where ascending vehicles try to change the lane by specific lane changing rules [5, Appendix A.2]. The simulation covers a period of 1 h and a road length of 20 km. The generated result is shown in Fig. 2.

3 Identification of Phase Transition Points

The goal is to gain information about the traffic situation from floating car data (FCD) obtained by data transmitting vehicles. We expect the position of the moving bottleneck to be correlated with a front between a synchronized flow phase and the free flow phase denoted as an $S \rightarrow F$ phase transition. There is a model for an approximate detection of phase transition points along a vehicle trajectory, denoted as S_F transition point [6, Chapter 4]. A phase transition is assumed when

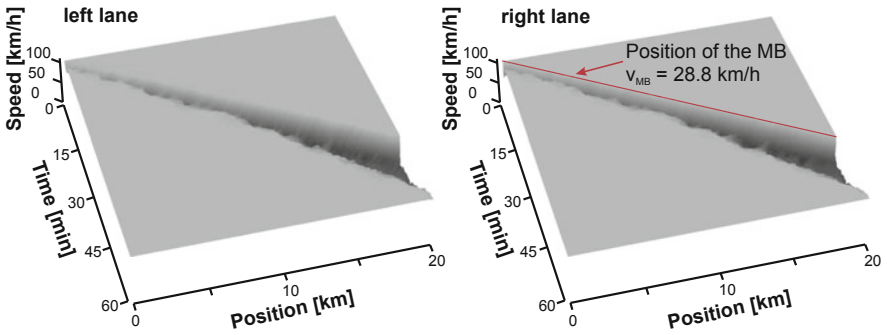

Fig. 2 Simulation result as three dimensional plots of the speed on the left and the right lane. Shades of grey vary from light to dark with decreasing velocity. The red line marks the position of the moving bottleneck (MB) on the right lane in this simulation

Table 1 Parameters for the recognition of phase transition points in vehicle trajectories

Phase transition points	Speed threshold	Time threshold
F_S transition	$v < 85$ km/h	$t > 15$ s
S_F transition	$v > 90$ km/h	$t > 10$ s

Thresholds for speed and time intervals

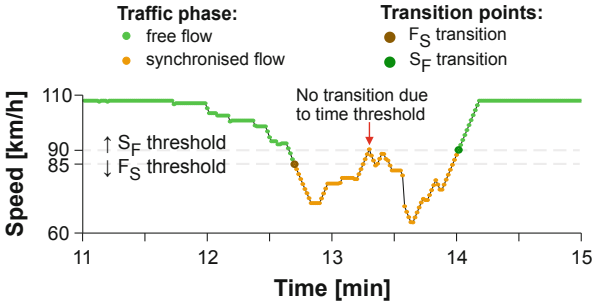

Fig. 3 Identification of phase transition points in a vehicle trajectory: starting at maximum speed within free flow. After a decrease in speed it passes the F_S transition threshold into synchronized flow. The S_F transition occurs in the final acceleration section, in which the vehicle returns to maximum speed

the velocity of the vehicle passes a certain speed threshold and remains in that new phase for a threshold time interval. The chosen parameters used in this study are listed in Table 1. Figure 3 is an example of the recognition of the F_S transition point and the S_F transition point in a vehicle trajectory. In contrast to [6] the speed thresholds for the F_S transition and the S_F transition have been raised for our application by 25 km/h to gain a better sensitivity on smaller speed reductions.

4 Reconstruction of the Moving Bottleneck Velocity

Figure 4 shows that the S_F transition points are situated in the vicinity of the moving bottleneck. But in the first 6 min only a few transition points can be found due to the fact that a breakdown in traffic has not happened until then. As shown in Fig. 5b the occurrence of S_F transitions stabilizes after the 12th minute of the simulation.

As a first test, we examined a 2 min time interval between minute 12.5 and 14.5 to study if it is possible to reconstruct the velocity of the moving bottleneck by a linear regression through the points of the S_F transitions. The slope of that linear regression is then considered the reconstructed velocity ($v_{rec.}$) of the moving

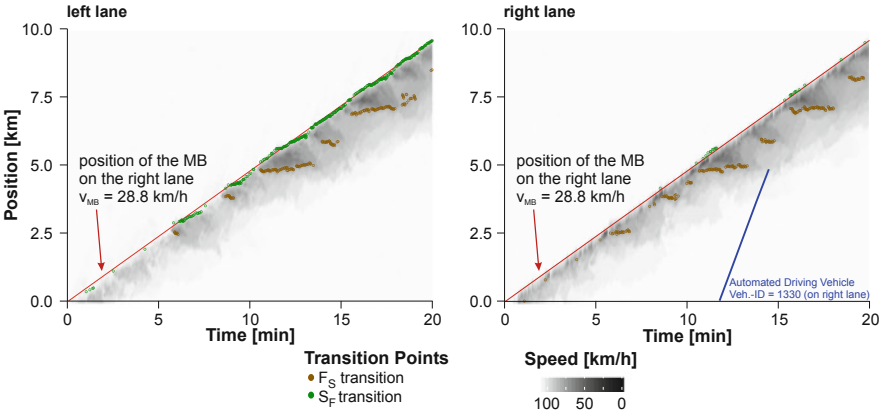

Fig. 4 Spatiotemporal plots of the simulation result for each lane. Shades of grey vary from light to dark with decreasing velocity. The red line is the trajectory of the moving bottleneck (MB) driving on the right lane. The coloured dots mark the transition points recognized in all vehicle trajectories. For our tests we assume the simulated vehicle with ID = 1330 as an automated driving vehicle (AV)

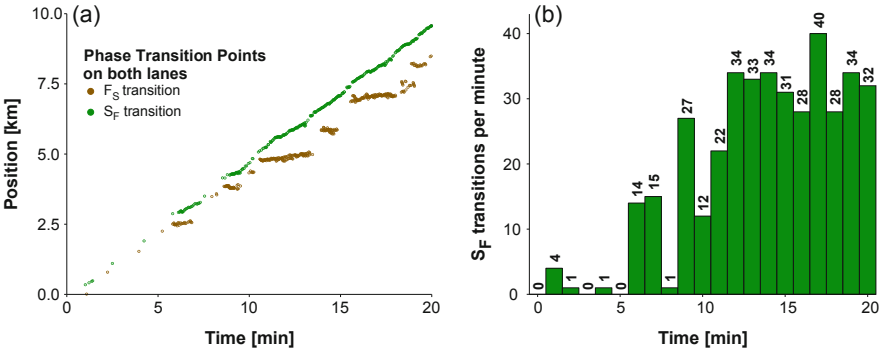

Fig. 5 (**a**) Occurrence of phase transition points on both lanes within the first 20 min of the simulation. (**b**) Counts of the S_F transitions per minute in the first 20 min of the simulation

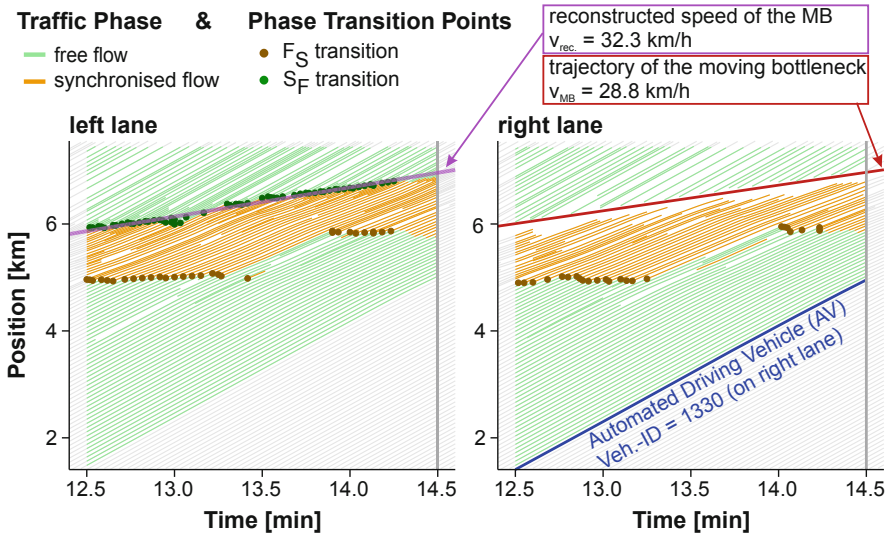

Fig. 6 Full reconstruction from simulation data. Vehicle with ID = 1330, assumed as an automated driving vehicle at minute 14.5 (blue line). Examined period of 2 min with the trajectories of all vehicles up to 2.5 km in front of the automated driving vehicle (AV) at minute 14.5. Contained trajectories coloured according to their traffic phases. Linear regression (purple line) built from S_F transitions (green dots) leads to a reconstructed velocity of 32.3 km/h. The trajectory of the moving bottleneck is drawn in red

bottleneck ($v_{MB} = 28.8$ km/h). In this setup, we consider one of the vehicles as an automated driving vehicle (AV). The vehicle with ID = 1330 in the simulation was chosen arbitrarily. As shown in Fig. 6, there occur 57 S_F transitions on the left lane within this time interval. A linear regression of all transition points leads to a reconstructed velocity $v_{rec.} = 32.3$ km/h. That results in a deviation of about 12% to the real velocity of the moving bottleneck.

5 Statistical Analysis for Different Penetration Rates of Probe Vehicles

In reality until now, it is infeasible to obtain data from each and every vehicle. Only few vehicles or navigational devices are able to collect and send data about their position and speed known as floating car data (FCD). At the moment it can be assumed that the penetration rate of such probe vehicles is in the range of a smaller single-digit percentage. For this reason, such research can only be performed by simulations. To study the effect of the penetration rate on the ability to reconstruct information about a moving bottleneck we did a statistical evaluation for penetration rates between 1% and 30%. We generated 100,000 independent samples with

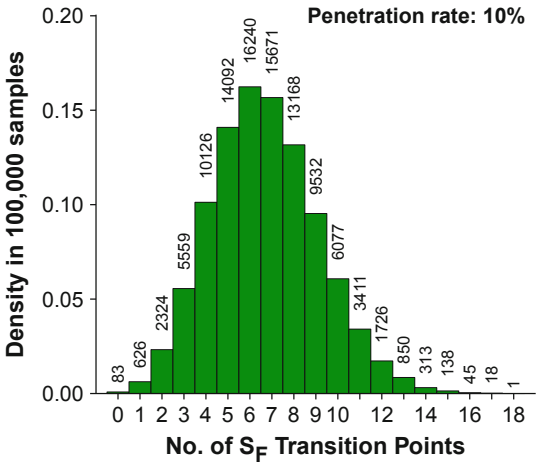

Fig. 7 Density of the occurrence of S_F transition points. Statistical data of 100,000 samples for a penetration rate of 10%. At least two points are needed for a linear regression

randomly assigned vehicles as probes according to each of this penetration rates. As an example Fig. 7 shows the distribution of the number of S_F transitions in the samples for a penetration rate of 10%. From samples with less than two transition points a reconstruction by linear regression is not possible. But that happens in less than 1% of the samples. How such single reconstructions can look like is shown in four examples in Fig. 8. To quantify the results in their quality we define the deviation as

$$deviation\ in\ percent = \left| \frac{v_{rec.} - v_{MB}}{v_{MB}} \right|. \tag{1}$$

The selected time window was evaluated in dependence of the deviation to the velocity of the MB as well as to variable penetration rates of the probe vehicles. The statistical results are presented in Fig. 9. The possibility to identify the moving bottleneck raises with higher percentages of probe vehicles, but the general accuracy is limited. The red curve clearly indicates that with low penetration rates the percentage of samples without enough transition points for a reconstruction is very high. The black curve (g) illustrates that 10% of probe vehicles are sufficient to identify the moving bottleneck in 90% of the samples with an accuracy of the reconstructed velocity with a deviation of less than 20% to the real velocity of the MB.

6 Results and Discussion

The moving bottleneck can only be detected if a significant speed disturbance has occurred, so that there is an amount of vehicles which have transitioned from free flow to synchronized flow and back into the free flow phase. In this simulated and

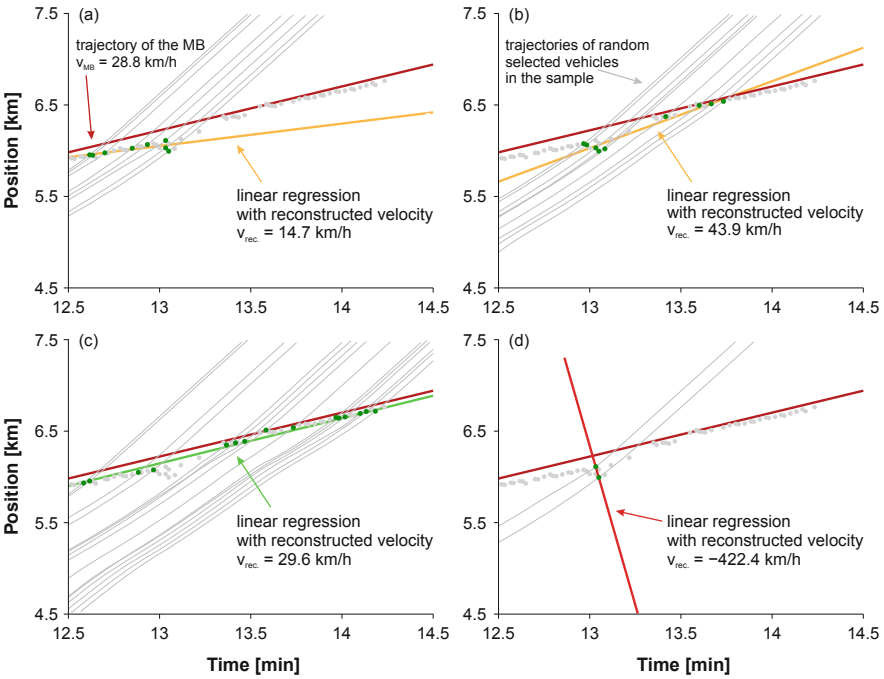

Fig. 8 Four reconstructions of the velocity of the MB. (**a**) Sample 1 shows a reconstructions with a deviation to v_{MB} of 49% out of 8 S_F transition points. (**b**) Sample 2 shows a reconstructions with a deviation to v_{MB} of 52% out of 9 S_F transition points. (**c**) Sample 3 shows a good reconstruction with a deviation to v_{MB} of 3% out of 14 S_F transition points. (**d**) Sample 4 shows a false reconstruction out of only two S_F transition points

studied case, it is possible to detect a moving bottleneck with an identification rate of 90% within a 2 min time interval after a traffic breakdown has happened at a penetration rate of 10% of probe vehicles and with an accuracy of 20% deviation to its real velocity.

7 Outlook

Our first results show that it is possible to gain information about a moving bottleneck within traffic by the method of analysing the transition points in trajectories of probe vehicles. Future work will consider time-increasing periods, where we expect an improved quality of the reconstruction. At the same time smaller penetration rates might be sufficient for a prediction. We consider that the time-dependence of the probability of the MB prediction and the accuracy of the estimation of MB location depend considerably on the occurrence of sequences of Kerner's F→S→F transitions [3] and large speed oscillations in synchronized flow

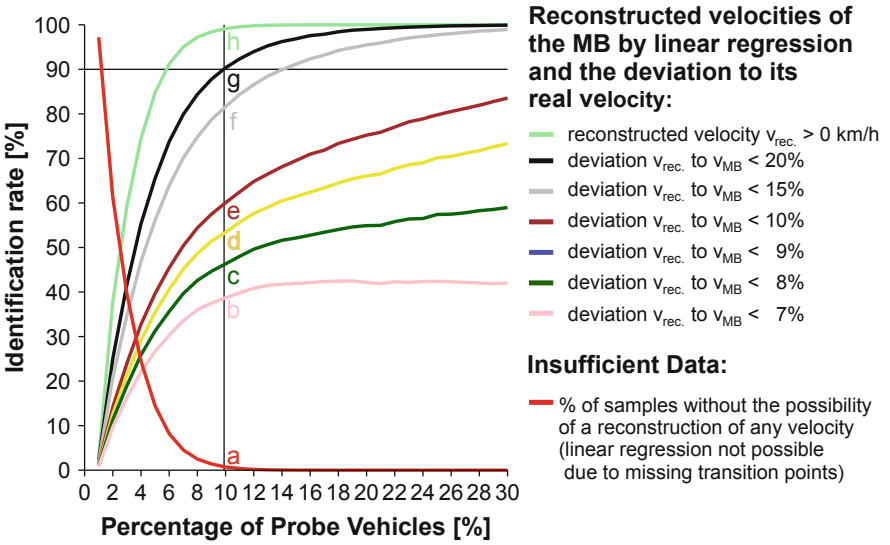

Fig. 9 Result of the statistical analysis on the effect of an increasing penetration rate of probe vehicles. The red curve shows the falling rates of samples with insufficient numbers of transition points. The other curves show the identification rates for different qualities of the reconstructed velocity. The deviation is calculated according to formula (1)

at the MB [2]. However, due to the length limitation of this paper, it is not possible to explain this important point here. We intend to present this methodological issue elsewhere.

Acknowledgements The authors thank the partners for their support within the project "MEC-View—Mobile Edge Computing basierte Objekterkennung für hoch- und vollautomatisiertes Fahren", funded by the German Federal Ministry of Economics and Energy by resolution of the German Federal Parliament.

References

1. Gazis, D., Herman, R.: The Moving and 'Phantom' Bottlenecks. IBM Thomas J. Watson Research Division, New York (1990)
2. Kerner, B.S.: The Physics of Traffic: Empirical Freeway Pattern Features, Engineering Applications, and Theory. Understanding Complex Systems. Springer, Berlin (2004). https://doi.org/10.1007/978-3-540-40986-1
3. Kerner, B.S.: Microscopic theory of traffic-flow instability governing traffic breakdown at highway bottlenecks: growing wave of increase in speed in synchronized flow. Phys. Rev. E Stat. Nonlin. Soft Matter Phys. **92**(6), 062827 (2015). https://doi.org/10.1103/PhysRevE.92.062827
4. Kerner, B.S.: Breakdown in Traffic Networks, Fundamentals of Transportation Science. Springer, Berlin (2017)

5. Kerner, B.S., Klenov, S.L.: A theory of traffic congestion at moving bottlenecks. J. Phys. A Math. Theor. **43**(42), 425101 (2010)
6. Kerner, B.S., Rehborn, H., Schäfer, R.P., Klenov, S.L., Palmer, J., Lorkowski, S., Witte, N.: Traffic dynamics in empirical probe vehicle data studied with three-phase theory: spatiotemporal reconstruction of traffic phases and generation of jam warning messages. Physica A **392**(1), 221–251 (2013)
7. Newell, G.: A moving bottleneck. Technical Report UCB-ITS-RR-93-3. Institute of Transportation Studies, University of California, Berkeley (1993)
8. Newell, G.: A moving bottleneck. Transp. Res. B Methodol. **32**(8), 531–537 (1998)

F → S → F Transitions in Vehicle Probe Data

Sven-Eric Molzahn, Boris S. Kerner, Hubert Rehborn, Sergey L. Klenov, and Micha Koller

Abstract Based on a study of probe vehicle data we have revealed empirical F→S→F transitions before traffic breakdown at the bottleneck theoretically predicted by Kerner. Anonymized probe data from connected vehicles of a large fleet have been collected. The frequency of connected vehicles in our study has been more than ten times larger (on average about 10 s between probe vehicles) than in earlier studies. This data shows that disturbances in free flow evolve in a neighbourhood of the bottleneck leading to small regions of synchronized flow (F→S transition). These regions of synchronized flow dissolve after a random amount of time (traffic recovers to free flow (S→F transition)) before the traffic breakdown occurs. In contrast with the F→S→F transitions, traffic breakdown leads to a long-living congested traffic pattern propagating upstream of the bottleneck. The empirical findings of this paper support some of the theoretical features of the S→F instability.

1 Introduction

The classical traffic flow instability [2, 7, 8, 10] causes the moving jam emergence in traffic flow. In the context of the three-phase traffic theory the classical traffic flow instability is associated with the S→J instability [11].

Recently, a microscopic theory of a so-called S→F instability has been developed [13]. In contrast to the classical traffic flow instability leading to a growing

S.-E. Molzahn (✉) · H. Rehborn · M. Koller
Daimler AG, RD/USN, HPC 059-X901, Sindelfingen, Germany
e-mail: sven-eric.molzahn@daimler.com; hubert.rehborn@daimler.com; micha.koller@daimler.com

B. S. Kerner
Physics of Transport and Traffic, Duisburg, Germany
e-mail: boris.kerner@uni-due.de

S. L. Klenov
Moscow Institute of Physics and Technology, Moscow, Russia

S. H. Hamdar (ed.), *Traffic and Granular Flow '17*,
https://doi.org/10.1007/978-3-030-11440-4_9

wave of local *speed reduction* in traffic flow [2, 7, 8, 10], the S→F instability leads to a growing wave of local *speed increase* in synchronized flow and, consequently, to the transformation of synchronized flow in free flow (S→F transition) [13]. The S→F instability introduced in the three-phase theory should explain the empirical nucleation nature of traffic breakdown as follows [13]: Before traffic breakdown occurs, there should be a sequence of F→S→F transitions that is as follows: The development of an F→S transition is interrupted through the S→F instability leading to an S→F transition. As long as F→S→F transitions are realized, no traffic breakdown occurs at a bottleneck. Thus, F→S→F transitions should play a very important role in the phenomenon of traffic breakdown [13] [14]. However, F→S→F transitions have not been studied in empirical data. One of the main objectives of intelligent transport systems (ITS) is to prevent or decrease traffic congestion in traffic networks.

One of the main problems of the development of ITS, that can improve traffic, is the lack of understanding of real microscopic features of traffic breakdown at a highway bottleneck. To study microscopic features of traffic breakdown, single vehicle data should be measured. In this paper, we study anonymized global positioning system (GPS) data from vehicles driving on the entire road network. The vehicles provide the location data in a 5 or 10 s interval which enables precise microscopic reconstruction and analyses of some microscopic empirical features of traffic breakdown at the bottleneck.

1.1 Motivation to Study Speed Disturbances Before Traffic Breakdown

By means of ITS applications users of traffic and transportation networks would expect that free flow can be maintained in a traffic network. Travel time, fuel consumption, and other travel costs increase significantly as a result of the traffic breakdown and congested traffic in comparison to travel costs in free flow. During the last 30 years significant achievements in a study of empirical features of traffic breakdown and highway capacity have been made, in particular, by Hall and Agyemang-Duah [9], Banks [1] and by Elefteriadou et al. [4] (see other references in a review [6] as well as in a recent book by Elefteriadou [3] and paper [5]). Nevertheless, traffic breakdown has not been sufficiently studied empirically up to now.

1.2 Background: Kerner's F → S Instability and F → S → F Transitions at Highway Bottlenecks

In accordance with the three-phase theory, Kerner's S → F instability should govern traffic breakdown (F → S transition) at freeway bottlenecks [13]. In the theory of the S → F instability it has also been found that before the traffic breakdown (F → S transition) occurs with the resulting congested pattern formation, there can be a series of random F → S transitions that are all followed by S → F transitions caused by the S → F instability. The F → S transition with the subsequent S → F transition has been called a sequence of F → S → F transitions in [13].

From the theory of Kerner's F → S → F transitions [13], it follows that only microscopic empirical studies of single vehicle data can show and confirm the F → S → F transitions that have been found in the three-phase traffic theory. Simulations made in [13] show a random time delay before the breakdown. In accordance with [13], the random time delay of the breakdown is associated with the nucleation features of the S → F instability found in numerical simulations. In particular, it has been found that during the random time period S → F instability can happen and leads to the dissolution of the former F → S transition. At a random time instant an F → S transition occurs that cannot be affected by S → F instability. This F → S transition is traffic breakdown resulting in the formation of a congested traffic pattern at the bottleneck [13]. It is of high interest if these simulated results can be seen in measured traffic data, e.g. by the analyses of vehicle probe data.

The theoretical findings of [13] include the microscopic features of sequence of Kerner's F → S → F transitions at a bottleneck, which are as follows: During the time period a permanent spatiotemporal competition between the speed adaption effect supporting an F → S transition and the over-acceleration effect supporting an S → F instability is observed. These effects result in a permanent average speed decrease in the neighbourhood of the bottleneck that is called "permanent speed disturbance".

1.3 The Objective and Outline of This Paper

Thus, in accordance with the nucleation theory of traffic breakdown of the three-phase theory, F → S → F transitions should determine a random character and random time delay of traffic breakdown [13]. An empirical study of the F → S → F transitions is the main objective of this paper. The paper is organized as follows: In Sect. 2 we discuss empirical environment and how the single vehicle data has been collected. In Sect. 3, microscopic empirical features of F → S → F transitions are presented. Conclusions and future research of F → S → F transitions is the subject of Sect. 4.

2 Floating Car Data and the Problem of Fine Spatiotemporal Analysis

Handheld personal navigation devices (PNDs) and factory-installed navigation devices in vehicles allow microscopic gathering and analysis of GPS data for a big fleet of vehicles. Probably a first analysis of randomly distributed anonymized probe vehicle data that has confirmed the existence of three distinct traffic phases with the traffic breakdown being an $F \rightarrow S$ transition of the three-phase theory [11, 12] has been done in [15]. However, in [15] the share of randomly distributed probe vehicles has been only about or less than $n = 2\%$ (mean time distance between cars has been about 10 min). With $n = 2\%$ it has not been possible to reconstruct the traffic dynamics in space and time with an accuracy that is sufficient to observe $F \rightarrow S \rightarrow F$ transitions. Empirical data available from the NGSIM dataset [17] is not suitable for this particular investigation due to the limited distance covered on the road with this data. Moreover, the transition from free flow to synchronized flow (traffic breakdown) cannot be observed in the compiled NGSIM data for highway traffic [17]. There are two main features of the data used for this work in comparison to known data up to now:

- In contrast to NGSIM data for highway traffic [17], traffic breakdown ($F \rightarrow S$ transition) can be observed in real traffic.
- In contrast to data of [15] in which the mean time distance between cars has been about 10 min, the single vehicle data used in this study has a time distance throughout the examined time span of 25 s on average between cars that have been observed.

With this data we show empirically Kerner's $F \rightarrow S \rightarrow F$ transitions [13] that emerge before the traffic breakdown.

2.1 Features of Empirical Single Vehicle Data Used in the Paper

The data was collected from a large fleet of connected vehicles of more than one million cars in Europe. To find and analyse the $F \rightarrow S \rightarrow F$ transitions in empirical data made in this paper, the German Autobahn A81 south of Stuttgart on a 4 km distance from Herrenberg to Stuttgart (Fig. 2) has been chosen. The data is anonymously gathered by means of a vehicle backend that the fleet vehicles are continuously connected to while driving (see Fig. 1). The vehicles send their locations in a 5 or 10 s (depending on model) interval to the data centre where it is processed to reconstruct the real-world traffic situation for the LiveTraffic service.

The data used in this paper was collected from a fleet of connected vehicles measured on October 25th 2016 during rush hours.

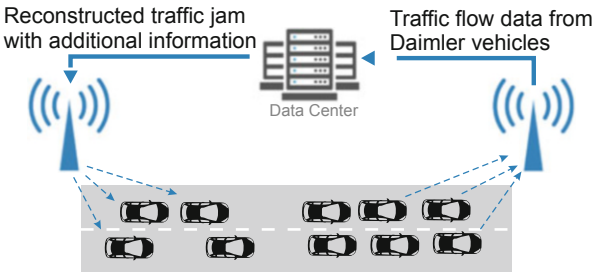

Fig. 1 Illustration of data gathering. Connected vehicles of a large fleet are sending their location to the data centre continuously where the traffic is reconstructed

3 Microscopic Empirical Features of F → S → F Transitions Before Traffic Breakdown

For the empirical studies of the microscopic feature of traffic breakdown, trajectories for the observed freeway section have been extracted and analysed. Figure 2 shows vehicle trajectories from "Herrenberg" to "Stuttgart" on a 4 km span. The time interval in this particular section between two cars is on average 47 s. In the three-phase theory [11, 12], during the time delay of traffic breakdown a permanent spatiotemporal competition between the driver speed adaption effect supporting an F → S transition and the driver over-acceleration effect supporting an S → F instability has been found [13]. In empirical single vehicle data studied in this article we have found the following traffic phenomena: Fig. 3 shows a subset of the trajectories of Fig. 2 with a time interval before the traffic breakdown has occurred. To illustrate speed disturbances before the traffic breakdown has occurred, Fig. 3a shows a distinct F → S → F transition before the traffic breakdown (from 15:55 h to 16:10 h) with the trajectories coloured accordingly to the speed.

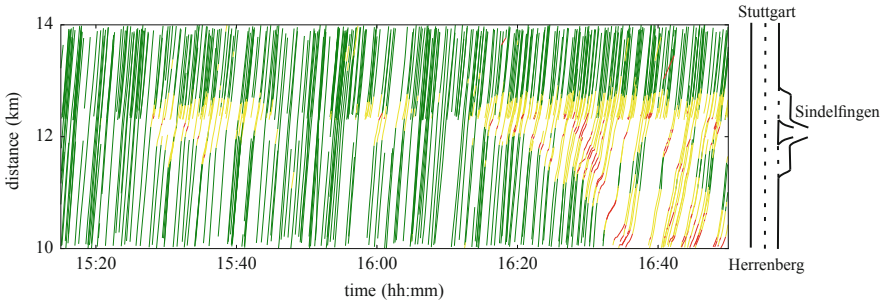

Fig. 2 Examined freeway section with on- and off-ramps. Two-lane highway in the south of Germany (A81) near Stuttgart. The trajectories are coloured as follows: green: above 85 km/h, yellow: between 25 and 85 km/h and red: under 25 km/h

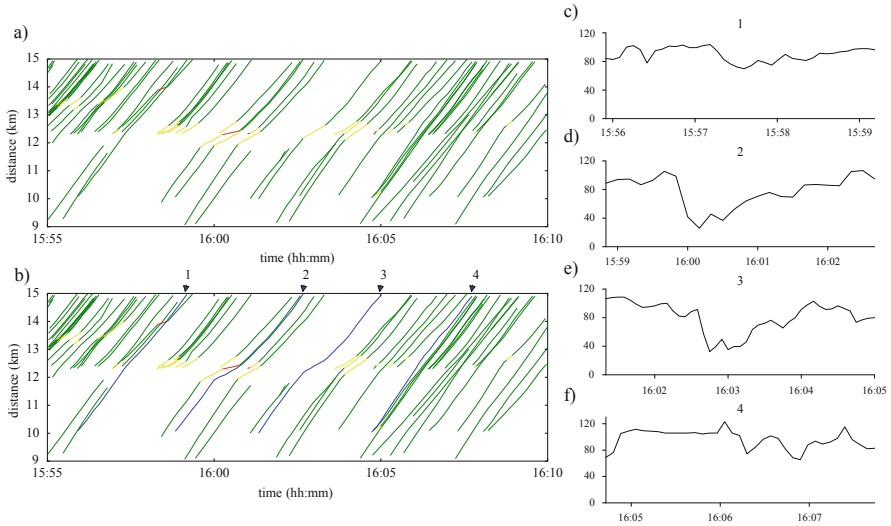

Fig. 3 Detailed view of trajectories as a subset of Fig. 2. Subfigure (**b**) shows single marked trajectories for a more detailed study according to subfigures (**c**–**f**). Single velocity trajectories show F → S transition (**c**) and S → F transition (**f**)

Single vehicle trajectories shown in Fig. 3b have been extracted (Fig. 3c–f) that show the following traffic phenomenon: Vehicle 1 is driving with a constant velocity and passes the bottleneck with no disturbance. As vehicle 2 approaches the effective location of the bottleneck (about 3 min after vehicle 1), the driver has to reduce the speed of the vehicle. The same behaviour can be seen for vehicle 3. Vehicle 4 is driving at a constant velocity. Thus, we observe a sequence of F → S → F transitions. The F → S → F transitions prevent traffic breakdown with subsequent development of a congested traffic pattern at the bottleneck. This is in accordance with the theoretical findings of Kerner [13].

3.1 Benefits for ITS Applications

Modern intelligent transportation systems (ITS) applications rely on data-driven analytics and models that are based on empirical findings from real-world data. One aim of ITS is to suppress local traffic disturbances in traffic flow to retain free flow at a bottleneck. Traffic control and management stakeholders will be able to react to upcoming traffic jams a lot earlier. Automated driving vehicles require to know the traffic situation ahead beyond what the sensors detect to ensure a safe and comfortable driving.

4 Conclusions

Based on an analysis of single vehicle probe data measured on German freeways, we have found empirical F → S → F transitions occurring before traffic breakdown at the bottleneck. Empirical data shows that during a relatively long time interval before traffic breakdown occurs at the bottleneck many local regions of synchronized flow appear (F → S transition) which is followed by an S → F transition (in the example for this study two regions of synchronized flow have been identified). The empirical F → S → F transitions lead to the emergence of local regions of synchronized flow (due to F → S transition) propagating upstream that dissolves over time (due to a subsequent S → F transition). This phenomenon leads to regions of dissolving synchronized flow (see Figs. 2 and 3). The empirical phenomena of the occurrence of F → S → F transitions with the formation of regions of dissolving synchronized flow revealed in this article prove the empirical evidence of Kerner's F → S → F transitions found recently in the three-phase theory [13]. One aim of future ITS-control methods that take into account empirical features of F → S → F transitions could be to suppress local traffic disturbances or even to prevent the development of traffic breakdown at a highway bottleneck. Future empirical works include a study of probabilistic features of the F → S → F transitions in empirical data. To reach this goal, a large amount of datasets for different days and types of bottlenecks are required. The collection of such data and their study will be a very interesting task for further empirical investigations. A more detailed consideration of empirical F → S → F transitions can be found in a recent paper [16].

References

1. Banks, J.H.: Flow processes at a freeway bottleneck. Transp. Res. Rec. **1297**, 20–28 (1990)
2. Chandler, R.E., Herman, R., Montroll, E.W.: Traffic dynamics: studies in car following. Oper. Res. **6**(2), 165–184 (1958)
3. Elefteriadou, L.: An Introduction to Traffic Flow Theory, vol. 84. Springer, New York (2014)
4. Elefteriadou, L., Roess, R.P., McShane, W.R.: Probabilistic nature of breakdown at freeway merge junctions. Transp. Res. Rec. **1484**, 80–89 (1995)
5. Elefteriadou, L., Kondyli, A., Brilon, W., Hall, F.L., Persaud, B., Washburn, S.: Enhancing ramp metering algorithms with the use of probability of breakdown models. J. Transp. Eng. **140**(4), 04014003 (2014)
6. Gartner, N.H., Messer, C.J., Rathi, A.K.: Traffic Flow Theory: A State of the Art Report - Revised Monograph on Traffic Flow Theory. Transportation Research Board, Washington, D.C. (2001)
7. Gazis, D.C., Herman, R., Potts, R.B.: Car-following theory of steady-state traffic flow. Oper. Res. **7**(4), 499–505 (1959)
8. Gazis, D.C., Herman, R., Rothery, R.W.: Nonlinear follow-the-leader models of traffic flow. Oper. Res. **9**(4), 545–567 (1961)
9. Hall, F.L., Agyemang-Duah, K.: Freeway capacity drop and the definition of capacity. Transp. Res. Rec. **1320**, 91–98 (1991)
10. Herman, R., Montroll, E.W., Potts, R.B., Rothery, R.W.: Traffic dynamics: analysis of stability in car following. Oper. Res. **7**(1), 86–106 (1959)

11. Kerner, B.S.: The Physics of Traffic. Springer, Berlin (2004)
12. Kerner, B.S.: Introduction to Modern Traffic Flow Theory and Control: The Long Road to Three-phase Traffic Theory. Springer Science & Business Media, Berlin (2009)
13. Kerner, B.S.: Microscopic theory of traffic-flow instability governing traffic breakdown at highway bottlenecks: growing wave of increase in speed in synchronized flow. Phys. Rev. E **92**(6), 062827 (2015)
14. Kerner, B.S.: Breakdown in Traffic Networks: Fundamentals of Transportation Science. Springer, Berlin (2017)
15. Kerner, B.S., Rehborn, H., Schäfer, R.P., Klenov, S.L., Palmer, J., Lorkowski, S., Witte, N.: Traffic dynamics in empirical probe vehicle data studied with three-phase theory: spatiotemporal reconstruction of traffic phases and generation of jam warning messages. Physica A **392**(1), 221–251 (2013)
16. Molzahn, S.E., Kerner, B.S., Rehborn, H., Klenov, S.L., Koller, M.: Analysis of speed disturbances in empirical single vehicle probe data before traffic breakdown. IET Intell. Transp. Syst. **11**, 604–612 (2017). http://digital-library.theiet.org/content/journals/10.1049/iet-its.2016.0315
17. Next generation simulation programs. http://ops.fhwa.dot.gov/trafficanalysistools/ngsim.htm. Accessed 25 Sept 2016

Microscopic Jam Tail Warning for Automated Driving

Sven-Eric Molzahn, Boris S. Kerner, and Hubert Rehborn

Abstract We perform a spatiotemporal differentiation between two different phases in congested traffic at the upstream front of the congested pattern: (1) the wide moving jam phase (J) and (2) synchronized flow phase (S) as introduced in the three-phase theory by Kerner. With this approach one can derive a conclusion how dangerous certain parts of the congested pattern really are and decide whether oncoming vehicles should be warned with a jam tail warning system. Each of the probe vehicles can distinguish either F→J or F→S transitions through a method for traffic phase identification. With the detailed information about the phase transitions happening at the upstream front of the congested pattern, the automated vehicle can drive safer and more comfortable while maintaining an unobtrusive behavior approaching traffic congestion. In our study made in this paper, empirical data is obtained through the use of probe vehicles with an average frequency of about 10 s. This allows us to reconstruct the F→J or F→S transitions over time at the upstream front of empirical congested patterns with a high quality that is sufficient for microscopic jam warning for automated vehicles.

1 Introduction

Precisely detecting dangerous jams in road networks is one of the main challenges for traffic safety [7, 12]. In previous empirical studies the jam fronts have been reconstructed through the use of connected probe vehicles with a time resolution about 120 s [6]. However, for safety driving in mixed traffic flow, automated driving vehicles require a more accurate and precise jam warning resolution. In this paper we present such a method that should permit to predict the value of speed reduction

S.-E. Molzahn (✉) · H. Rehborn
Daimler AG, RD/USN, HPC 059-X901, Sindelfingen, Germany
e-mail: sven-eric.molzahn@daimler.com; hubert.rehborn@daimler.com

B. S. Kerner
Physics of Transport and Traffic, Duisburg, Germany
e-mail: boris.kerner@uni-due.de

S. H. Hamdar (ed.), *Traffic and Granular Flow '17*,
https://doi.org/10.1007/978-3-030-11440-4_10

at the upstream front of a congested pattern downstream of a vehicle as well as the location and time at which the vehicle should meet the upstream front of this congested pattern as accurate as possible.

It is of highly interest for the general public to improve the safety for road users. One of the most common cases of accidents on highways is to drive into the back of a jam (27% of all recorded accidents in Germany in 2016 [2]) in a lot of cases resulting in a mass coalition. Automotive manufacturers and suppliers introduced solutions for these kinds of situations in the way of using radar, lidar and camera systems. While this improves the safety to a much higher level, it does not cover all the security features one wishes to have. For example, in [1] the authors argue that the radar used in most applications has problems with stationary objects: however, at a jam tail this is often the case as drivers need to slow down and eventually stop to not run into the car in front of them.

1.1 Motivation

To perform a reliable jam tail warning, in this paper we present a spatiotemporal differentiation between two different phases in congested traffic at the upstream front of the congested pattern: (1) the wide moving jam phase (J) and (2) synchronized flow phase (S) as introduced in the three-phase theory. With this approach one can derive a conclusion how dangerous certain parts of the congested pattern really are and decide whether oncoming vehicles should be warned with a jam tail warning system. Reconstructing the different traffic phases has been done by Kerner et al. [6] and recently by Rempe et al. [9, 10].

With this paper, a process to distinguish the different states a jam front can depict with floating car data is proposed. The evaluation data is gathered from a large fleet of continuously connected vehicles and is transferred every 2 min as a collection of timestamped global position system (GPS) data with a short time interval (usually 5 s or 10 s). The data is stored and processed by means of a vehicle backend and is primarily used to reconstruct the traffic on the road network by the traffic service provider. Raw map-matched trajectory data is used for the analysis in this paper.

1.2 Outline of This Paper

This paper is structured as follows: The first section gives a background and overview of the three-phase traffic theory, explaining the phases itself and the differences. The method to identify the states and phases from the microscopic data is shown that concludes the process of identifying jam fronts. Finishing with an example based on measured vehicle probe data and explanation of a jam tail warning system, an explanation and discussion about the different states of a jam front, and the conclusions.

1.3 Three-Phase Traffic Theory

As method to model and explain spatiotemporal traffic patterns the three-phase traffic theory introduced by Kerner [3–5] is used. This theory splits traffic into free flow and congested traffic and furthermore segregates the congested traffic into two distinct phases: synchronized flow and wide moving jam (see Fig. 2). The abbreviations F, S, and J for free flow, synchronized flow, and wide moving jams are used, respectively (Fig. 1).

1.3.1 Free Flow

Free flow (F) is the desired phase for every driver. Free flow describes the characteristics where a driver can freely choose the speed (up to the speed limit on the road), overtaking is possible, and the empirical data shows a positive correlation between the flow rate and vehicle density, meaning that for a higher vehicle density the flow rate increases accordingly up to a certain point.

1.3.2 Synchronized Flow

The empirical characteristics of the synchronized flow have been well examined, evaluated, and documented [3–5]. The downstream jam front is typically localized at a bottleneck, e.g., reduction from three lanes to two lanes on a highway and off/on-ramps, while the upstream jam front moves stream upwards. Drivers cannot freely choose the desired driving speed but can adjust the speed according to the surroundings (hence the name synchronized flow). Vehicles accelerate from a lower

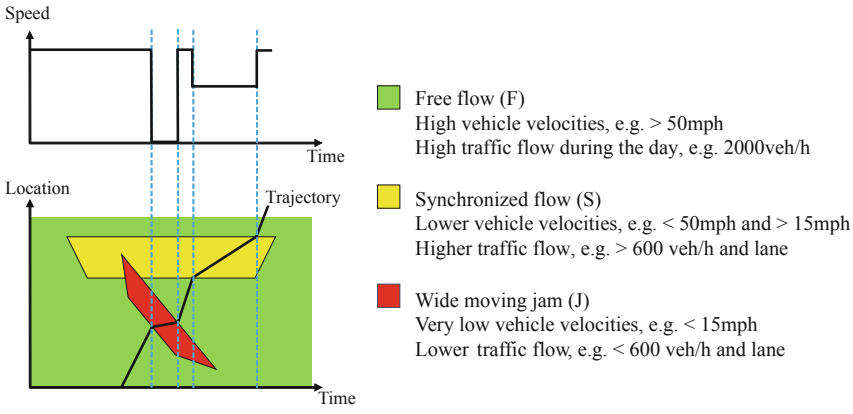

Fig. 1 Illustration of the three-phase traffic theory and the three different phases with some of its characteristics. Traffic values for the related phases are examples only

speed within the synchronized flow to a higher speed passing the bottleneck at the downstream jam front (S → F state transition). Inside the synchronized flow a continuous traffic flow with no significant stoppage is expected.

1.3.3 Wide Moving Jam

Contrary to the synchronized flow the wide moving jam usually propagates through bottlenecks with little to no influence to the characteristics inside of the wide moving jam. The main difference to the synchronized flow is the moving downstream and upstream front, which is continuous throughout the lifespan of the wide moving jam and as stated before does not change due to outside influences like a bottleneck, but keeps the mean velocity of the downstream front.

2 Identifying Traffic States from Empirical Microscopic Data

In order to identify dangerous jam tails, one relies on extracting the upstream jam front for any given congested traffic phase (i.e. synchronized flow and wide moving jams). Particularly the state transitions from F→S, F→J, and S→J that build up one jam front are relevant. These transitions symbolize the change of states from free flow to synchronized flow, from free flow to wide moving jams, and from synchronized flow to wide moving jams. It is a research topic to investigate the state transitions further in terms of frequency, accuracy, and speed delta. In previous works from Kerner et al. [6] a method and algorithm has been developed that identifies the distinctive states of trajectories according to the three-phase traffic theory. Furthermore, probe density in combination with the algorithm has been studied by Kerner et al. [6]. In contrast to these earlier studies, the probe data availability has increased in the meantime to a much higher degree. In our evaluation data an average vehicle interval of about 24 s (depending on highway and date) was present: such probe data is much more precise than loop detector data with 1 min intervals. Rempe et al. [9, 10] showed a method to estimate the traffic flow on highways based on the three-phase traffic theory that shows an improved algorithm to the GASM by Helbing and Treiber [11]. For this work the method from [6] is used and adapted to the needs of a jam tail warning system. The algorithm works based on combining single vehicle trajectories. For each given time and position tuple in a trajectory the traffic state (F, S, and J) is assigned, ensuring a continuous knowledge of every phase the trajectory has been driving and the transitions from one state to another within one trajectory. The assignment is based on a state machine that applies the underlying characteristics of their respective traffic phases. For this analysis the method to assign the traffic states to the time and identify the state transitions from F→S, F→J, and S→J is used (see Refs. [6, 8] for a detailed explanation).

3 Microscopic State Transitions

Jam fronts are identified using the phase transitions F→J and S→J, i.e., coming from a high speed (free flow) or moderately speed (synchronized flow) to a low speed or even full stop (wide moving jam). Even though the state transitions from free flow can generally be considered more relevant, both the transitions from free flow and from synchronized flow to wide moving jam are incorporated. This is done because the algorithm to identify state transitions encapsulates wide moving jams in synchronized flow by design. For this paper, a closer look at different state transitions in an identified jam front is taken. We evaluate the method and algorithm with floating car data (FCD) that is gathered from a large fleet of connected vehicles. The vehicles are continuously connected to a backend and send the GPS location in a 5 or 10 s interval. The backend in return reconstructs the traffic situation and provides the vehicles with the live-traffic data, respectively.

3.1 Evaluation

The following section is dedicated to evaluating the method and algorithm with real probe data. The data was collected from a fleet of connected vehicles on the motorway M4 towards London on April 5th 2016 during evening rush hour. Figure 2 shows the time–space plot of the M4 with the colorized raw trajectory data of the connected vehicles. The choice of color is based on the speed of the vehicles and is defined as follows: 0–25 km/h: red, 26–80 km/h: yellow, and >80 km/h: green. As seen in Fig. 2 the pattern shows characteristics that are typical. At about 16:15 h a small jam emerged at the bottleneck that evolved to a wide moving jam at about 17:15 h. This wide moving jam propagates through multiple bottlenecks upstream and induces small regions at those bottlenecks causing additional jams that evolve to wide moving jams.

Figure 3 illustrates the state transitions that have been identified with the method described in this paper. Generally one can derive from the plot that upstream jam fronts can be recognized qualitatively good. Especially both wide moving jams (see wmj_1 and wmj_2 in Fig. 3) that run through multiple bottlenecks can be identified to a sufficient degree. Surrounding regions of synchronized flow that are induced by these two wide moving jams are identified as such. Looking at the two wide moving jams one can also see that there are changes in the jam front propagating upstream. Indeed, taking a closer look at the two wide moving jams (see Fig. 4) differences in the jam fronts are revealed. Figure 4a shows the first wide moving jam (wmj_1 in Fig. 3), while Fig. 4b shows the second one (wmj_2 in Fig. 3). As seen in Fig. 4a the wide moving jam has two different front states: the first one (1) runs from 17:10 h to 17:25 h with state transitions from free flow to synchronized flow (F→S). The second front state (2) runs from 17:25 h to 18:00 h, where F→S transitions are followed by S→J transitions. This hints to a more dangerous second part of the

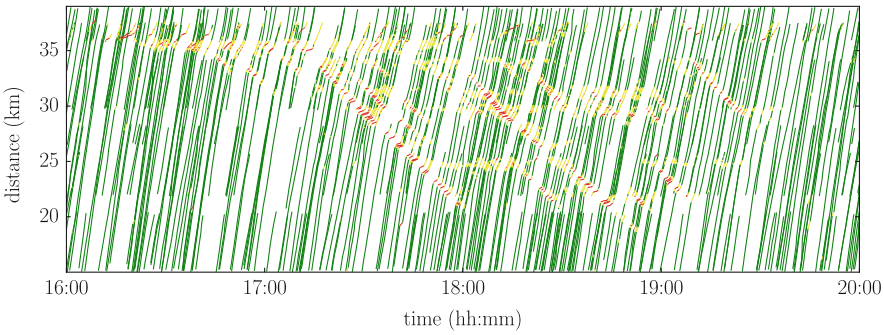

Fig. 2 Plot of connected vehicles colored accordingly to the velocity (0–25 km/h: red, 26–80 km/h: yellow, and >80 km/h: green)

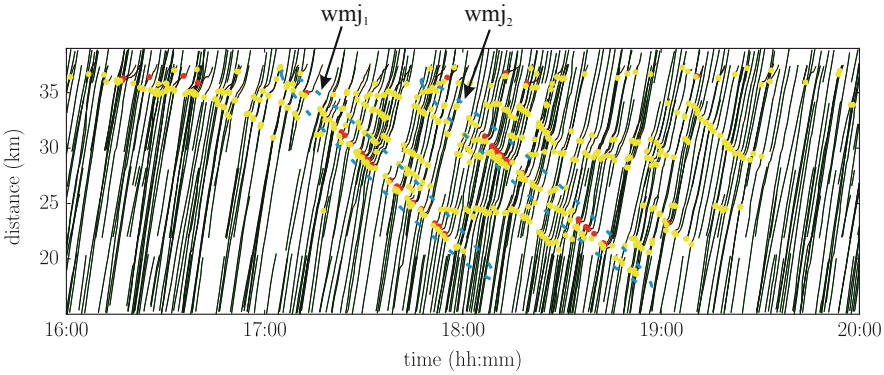

Fig. 3 Identified state transitions. Illustrated are the upstream state transitions. Marked are the two wide moving jams

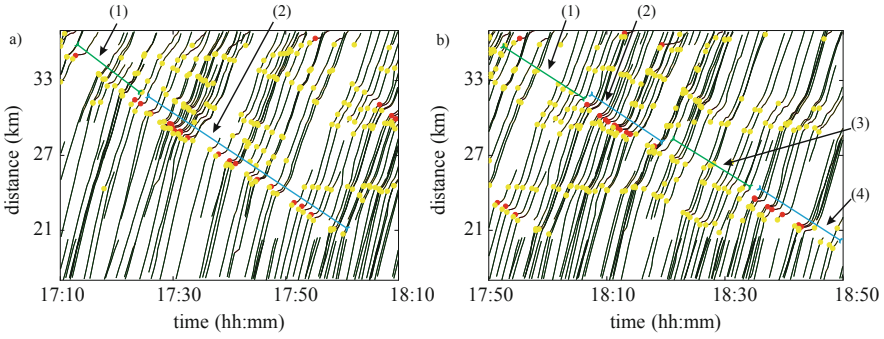

Fig. 4 Zoomed in cutout from Fig. 3 with (**a**) wmj_1 and (**b**) wmj_2. Illustrated with green (S) and blue (J) lines are the different jam front states

jam front. Interestingly the second jam front acts quite differently: while the front starts out as synchronized, after about 15 min it does switch to a dangerous state (Fig. 4b Sect. 2). This state runs for no longer than 10 min and switches states to synchronized again for 15 min. At about 18:30 h the jam front switches to the more dangerous state. This results in four jam front states in one single front.

4 Conclusions and Outlook

In this paper we present a method of identifying potential dangerous jam fronts in congested traffic patterns. Furthermore we showed that jam fronts can have microscopic differences that should make out the dangerousness of the jam front.

The identification is based on the vehicle autonomous state identification, the identification of the tailbacks, and the assignment of state transitions (F→J and S→J). The knowledge of the accurate time–space dimension of the jam fronts (and its propagation) is crucial to a safer and more comfortable automated and autonomous driving as well as useful as assistant system for traditional vehicles. The results show a qualitatively high accuracy of identification of wide moving jams throughout the examined traffic patterns. With this approach and accuracy it is possible to develop a microscopic jam tail warning system.

It is possible to distinguish the different jam front states in one single jam front. It is also crucial to know the propagation of the jam front. As seen in the presented examples jam fronts can show many different jam front state switches and accurately predicting the spatiotemporal development of such jam front is not trivial. Therefore it is needed to investigate jam fronts and front switches in more detail.

Acknowledgements We thank our partners for their support in the project "MEC-View—Object detection for automated driving based on Mobile Edge Computing," funded by the German Federal Ministry of Economic Affairs and Energy.

References

1. Bogenberger, K., Dinkel, A., Totzke, I., Naujoks, F., Mühlbacher, D.: Sicherheitswirkungen von Verkehrsinformationen. Entwicklungen und Evaluation verschiedener Warnkonzepte fuer Stauendewarnungen. Berichte der Bundesanstallt für Straßenwesen. Unterreihe Fahrzeugtechnik (84) (2012)
2. Statistisches Bundesamt: Verkehrsunfälle 2016 (2017)
3. Kerner, B.S.: The Physics of Traffic. Springer, Berlin (2004)
4. Kerner, B.S.: Introduction to Modern Traffic Flow Theory and Control: The Long Road to Three-phase Traffic Theory. Springer Science & Business Media, Berlin (2009)
5. Kerner, B.S.: Breakdown in Traffic Networks: Fundamentals of Transportation Science. Springer, Berlin (2017)
6. Kerner, B.S., Rehborn, H., Schäfer, R.P., Klenov, S.L., Palmer, J., Lorkowski, S., Witte, N.: Traffic dynamics in empirical probe vehicle data studied with three-phase theory: spatiotempo-

ral reconstruction of traffic phases and generation of jam warning messages. Physica A **392**(1), 221–251 (2013)
7. Klunder, G.A., Taale, H., Hoogendoorn, S.P.: The impact of loop detector distance and floating car data penetration rate on queue tail warning. In: 3rd International Conference on Models and Technologies for Intelligent Transport Systems, Dresden, Germany, 2–4 December 2013
8. Molzahn, S.E., Rehborn, H., Koller, M.: Zeitlich-räumliche Erkennung von Stauenden für die assistierte Verzögerung von Fahrzeugen. VDI-Berichte (2016)
9. Rempe, F., Franeck, P., Fastenrath, U., Bogenberger, K.: Online freeway traffic estimation with real floating car data. In: IEEE 19th International Conference on Intelligent Transportation Systems (ITSC), 2016, pp. 1838–1843. IEEE, Piscataway (2016)
10. Rempe, F., Franeck, P., Fastenrath, U., Bogenberger, K.: A phase-based smoothing method for accurate traffic speed estimation with floating car data. Transp. Res. C Emerg. Technol. **85**, 644–663 (2017)
11. Treiber, M., Helbing, D.: An adaptive smoothing method for traffic state identification from incomplete information. In: Interface and Transport Dynamics, pp. 343–360. Springer, Berlin (2003)
12. Wiles, P.B., Cooner, S., Walters, C., Pultorak, E.: Advance warning of stopped traffic on freeways: current practices and field studies of queue propagation speeds. Technical Report (2003)

Study of Vehicle-Following Behavior Under Heterogeneous Traffic Conditions

Narayana Raju, Shriniwas Arkatkar, and Gaurang Joshi

Abstract The research work is attempted in capturing the following behavior of vehicles under Indian traffic conditions. In this context, two access-controlled mid-block sections on multi-lane urban roads were selected in studying the driving behavior. Later with the help of trajectory data from the two study sections, time-space plots are developed for the vehicles' movement in the same lane as well as from adjacent lanes for studying non-lane based movement. Based on close inspection on time-space plot of vehicles, vehicles pairs which are in the tentative following conditions are distinguished along with the vehicles in adjacent lanes, which may affect the tentative leader–follower pairs. From the distinguished leader–follower pairs, vehicle-following behavior is thoroughly investigated. The investigation is carried out by identifying relationship (hysteresis plots) between relative distance versus relative velocity plots among the leader–follower vehicle for the vehicles in the same as well as in adjacent lane that is nearby position. Hysteresis phenomenon (representative of vehicle interaction) for vehicles under following behavior is examined in quantifying the following behavior of vehicles.

1 Background

Since its inception, car-following concept has been used to model the following behavior of vehicles on different road segments under varying flow conditions to assess the capacity and level-of-service of road sections along with safety analysis. Pipes [1] has given his maiden attempt in understanding the following nature and modelled a linear car-following model which is based on safety distance and speed of the following vehicle. With the evaluation of general motors (GM) model, series of models were formulated on the basis that the driver of a following vehicle responds to the stimuli, caused by the motion of the vehicle ahead of it. Response implies mainly acceleration of the following vehicle and this quantity is related to the behavior of that driver. The stimulus could be considered as the relative

N. Raju · S. Arkatkar (✉) · G. Joshi
Sardar Vallabhbhai National Institute of Technology, Surat, India

S. H. Hamdar (ed.), *Traffic and Granular Flow '17*,
https://doi.org/10.1007/978-3-030-11440-4_11

velocity between the following vehicle and vehicle ahead of it. The main drawback of the model is that, it assumes same reaction time for all types of drivers and, moreover, followers can even respond to smaller stimulus also. Further Kerner[2–4] explained physics of traffic break down in driving behavior and come up with three phases of fundamental diagram. Gipps [5] proposed a two-regime model for following, which depends on the desired braking and acceleration rates of following vehicle for maintaining the sufficient safe distance from the leader. Again, safety distance is given as a function of maximum desired braking rates of both leader and following vehicles. Similarly, Bando and Hasebe [6] modelled response of the follower as a function of optimal velocity, which formulate following behavior as process to maintain optimal velocity that depends on vehicle spacing. Gunnay [7] analyzed vehicle interactions based on lateral discomfort among the vehicles, which is considered as a function of frictional clearance among the vehicles. Further, the author has defined maximum escape velocity for following vehicles and tested his model for different leader–follower combinations based on the follower's response in the field conditions. Again, model is verified with Gipps model considering the escape velocity as zero and both models were found to produce similar results. Wiedemann [8] developed a psychophysical following behavior model, which assumes that driving behavior can be of four regimes such as free flow, approaching, following, and braking maneuvers. Based on this, thresholds of following have been specified based on relative distance and relative velocity. From their study, two car-following models, namely Wiedmann74 and Wiedemann99 were developed, in which parameters are defined based on the perception thresholds. All these cars-following models are widely accepted and are used in various studies across the world. Further, researchers realized the importance of calibration of these well-developed car-following models based on field data. In this direction, Menneni [9] has carried out his work in calibrating Wiedemann99 model using micro-level vehicular trajectories data collected from US-101 and I-80 freeways.

But studying vehicle-following behavior under heterogeneous traffic (prevailing in Asian countries including India) is a mammoth task, where vehicle movement is noted as non-lane based along with heterogeneity in traffic. Arkatkar and Arasan [10] analyzed the effect of gradient on the performance on the vehicles and quantified its effect on macro-level characteristics of the road section using simulation technique. Raju et al. [11] modelled the following behavior by means of trajectory data and evaluated the modelled behavior using simulation. Furthermore, some researchers have developed new car-following models for heterogeneous traffic flow conditions considering behavioral difference among the vehicles. From the literature, it can be inferred that very few studies were attempted at detailed calibration of vehicle-following models for vehicular movements under heterogeneous traffic conditions. Further, no appropriate methodology for identification of potential leader–follower pairs for the vehicles involved in following phenomenon is highlighted explicitly. Very few studies (as mentioned above) highlighted the overall simulation methodology of modelling traffic under heterogeneous conditions, but could not provide the sufficient logic lying behind the methodology for capturing vehicle-following parameters. On this basis, the present study had been carried forward.

2 Study Sections

For the present work, two access-controlled midblock road sections were selected, one is on Delhi–Gurgaon road, the video data of which was collected for a duration of 12 h for determining macroscopic traffic flow characteristics like free speed, capacity, and jam density of the roadway section. With the help of video-graphic survey, 20 min of vehicle trajectory data was developed, with the help of traffic data extractor, IIT Bombay. Second study section on an urban arterial road in Chennai, India. For this section, 15 min of vehicular trajectory data is taken from the webpage of Toledo [12]. Due to the absence of macroscopic traffic flow characteristics, data is not available for Chennai road section. In both the study sections, six vehicle categories were observed, namely motorized two-wheeler (2w), car, bus, truck, light commercial vehicle (LCV), and motorized three-wheeler (3w). Similarly, the study section characteristics including lane width, road type, and details of data used in the study are also given in Table 1. By means of trajectory data, time-space plots (longitudinal distance versus time) were developed for the study sections as shown in Fig. 1. From the trajectory dataset, it can be observed that major proportion of cars

Table 1 Roadway characteristics and details of data considered in the study

Study section	Chennai	Delhi
Roadway type	Urban arterial road	Urban multi-lane road
Trap length	250 m	195 m
Width	11.2 m	14 m
Speed limit	60 KMPH	80 KMPH
Duration of trajectory data analysis	15 min	20 min
Duration of macro-level analysis	–	12 h
Vehicles tracked for trajectory data	1506 vehicles	2504 vehicles

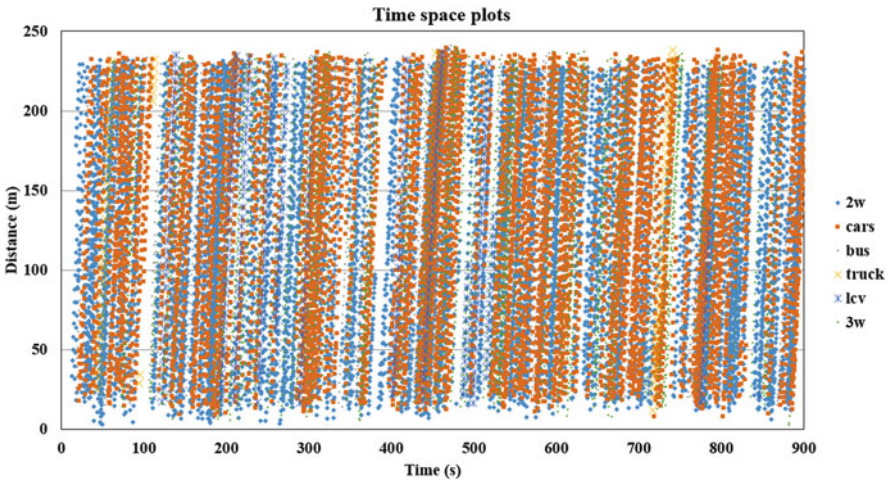

Fig. 1 Time-space plots of vehicles in the Chennai section from trajectory data

were observed in the Delhi section, whereas, in the Chennai section, the dominant vehicular category is motorized two-wheeler.

3 Identification of Following Pairs

Identification of leader–follower vehicular pairs is one of the crucial elements in studying the following behavior of vehicles under non-lane based heterogeneous traffic conditions. In case of homogeneous traffic conditions, it is relatively easy to identify the leader–follower vehicular combination as traffic flow movement is lane based. But, under heterogeneous traffic conditions, traffic flow is highly complex, as it is non-lane based and understanding the following behavior under such scenario is difficult. Even from the available literature, it was found that only few studies have been attempted in understanding the following behavior of vehicles under heterogeneous traffic conditions. In this research work, it is attempted to study the following behavior of vehicles in heterogeneous traffic conditions using vehicular trajectory data. For that purpose, time-space plots are developed for vehicles on a given lane taking lane width as 3.5 m. Based on visual inspection of the vehicular time-space plots (on a given lane) in an exaggerated sense, vehicles which are in the following condition are identified as assumed leader–follower pairs (vehicles in same lane) initially. In a similar way, assumed leader and follower pairs are also identified for individual lanes. From this approach, we can say that leader–follower pairs are selected based on ideal lane-wise following behavior, considering certain lateral staggered behavior (say within 1.5 m from the edge of the leading vehicle) within that lane. But, under heterogeneous traffic conditions, there exists a significant influence of surrounding vehicles from other lanes too. In order to consider this phenomenon, the time-space plots of leader–follower on a given lane are overlaid with time-space plots of vehicles from the adjacent lanes. Based on the overlapped time-space plots, the vehicle trajectories from adjacent lane, which are under the influence of the assumed leader–follower pairs (vehicles in same lane) are identified. In order to check the influence of these kind of vehicles, relative distance versus relative speed (follower vehicle minus leader vehicle) hysteresis graphs are plotted for (1) the assumed leader versus vehicle in adjacent lane and (2) vehicle in adjacent lane with assumed follower. Then, these plots are also compared with (3) assumed leader vs assumed follower (lane wise). The overall methodological framework for identifying leader–follower pairs is clearly explained with the help of a self-explanatory flowchart as shown in Fig. 2a, in different stages.

The process of identifying true leader–follower pairs is explained below with the help of schematic diagram (example), as shown in Fig. 2b, where position of vehicles on the road section at four different time frames is visualized for the subject vehicles (blue-color car, grey-color car, and orange-color bus). Initially, from the lane-wise time-space plots, it can be found that orange bus is following the blue car. Based on the framework, it will be assumed that blue car and orange bus are assumed as leader–follower pairs. But, under heterogeneous traffic conditions, there will be

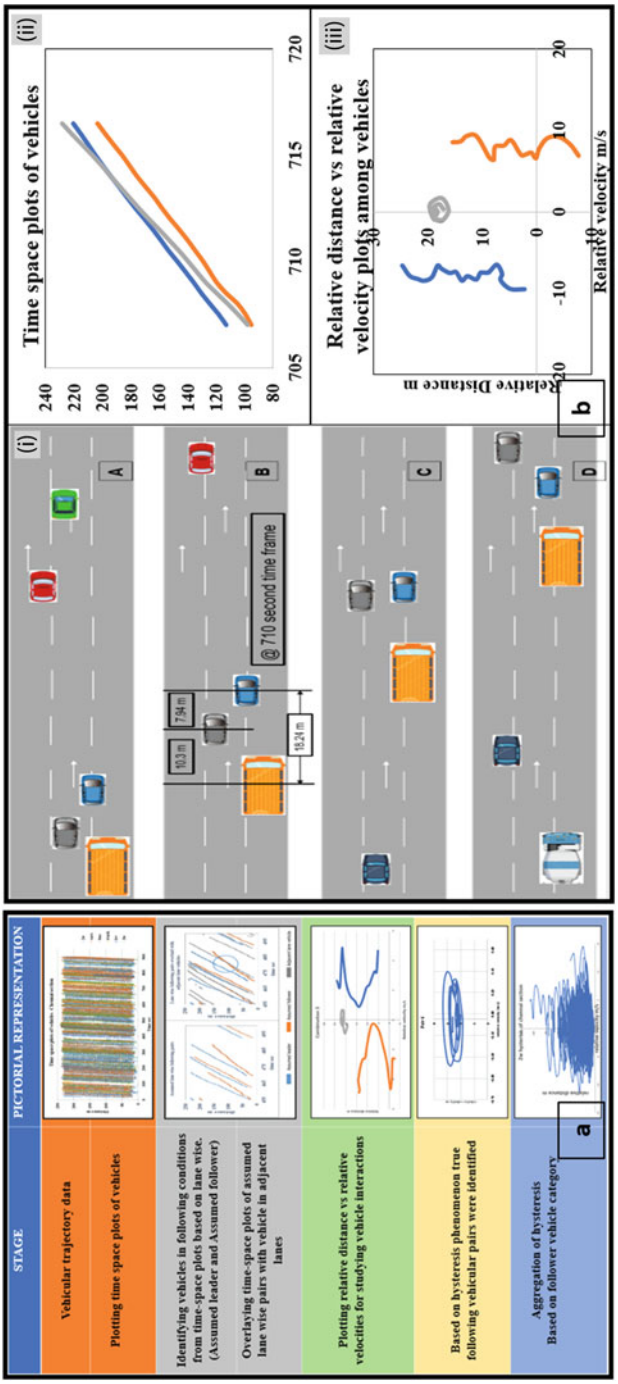

Fig. 2 Methodological framework along with a schematic example for catching following pairs

an influence of vehicle present in adjacent lanes. In the present scenario, grey vehicle is adjacent to the assumed leader–follower pairs, which can be identified, when time-space plots are overlaid. In order to check the interaction among the three vehicles, relative distance vs relative velocity plots are made, for different vehicles, as shown in Fig. 2b(iii), and the data curve had been highlighted with opposite legend color (i.e., if the relative distance vs relative velocity plot is between blue-color car and orange-color bus, it is plotted with other remaining grey color). From Fig. 2b(iii), it can be identified that there is a hysteresis phenomenon (characteristic of vehicle-following interactions) among the blue car and orange bus. Further, this blue car and orange bus were taken as true leader–follower pairs. This methodology is adopted for all the vehicles for each of the lanes across entire available road-space (width) on the two study sections. Using this, the following behavior of vehicles over the study road sections had been captured. Similarly, the vehicle interactions at a time frame of 710 s has been highlighted for a better description in connection with the subject vehicles.

On similar basis, true leader–follower pairs were selected for the two study sections and the number of pairs considering following vehicle category is reported in Table 2. From the relative distance vs relative velocity plots, true leader–follower pairs along with closing and giving-up pairs are identified based on hysteresis phenomenon among different combination of vehicles. Based on the hysteresis frame work, following behavior instincts such as lane based following, staggered following along with closing up and opening up process is investigated in detail. Further six leader-follower pairs are presented as examples in Fig. 3a. Each plot represents the variation of relative distance with respect to relative velocity for identified vehicular pairs. It was found that there exists high intense variation of relative distance with respect to relative speed in pair-1 and pair-2. It can be realized that pair-3, pair-4, and pair-6 shows ideal following behavior as hysteresis is continuous and resembles like concentric circles. Whereas pair-5 represents a moderate following behavior which provides the evidence of existence of aggressive follower with respect to leader. All these pairs exhibiting different following behaviors are considered for further calibration purpose.

Based on the true leader and follower pairs, hysteresis plots developed for a particular category of following vehicle are further aggregated for both Delhi and Chennai sections as shown in Fig. 3b, it was identified that the vehicles (mainly two-

Table 2 Observed true following pairs based on the following vehicle category

Following vehicle category	Chennai	Delhi
Motorized two-wheeler	218	48
Car	190	630
Bus	27	5
Truck	5	3
Light commercial vehicle	14	4
Motorized three-wheeler	59	6
Total number of true following pairs	513 pairs	696 pairs

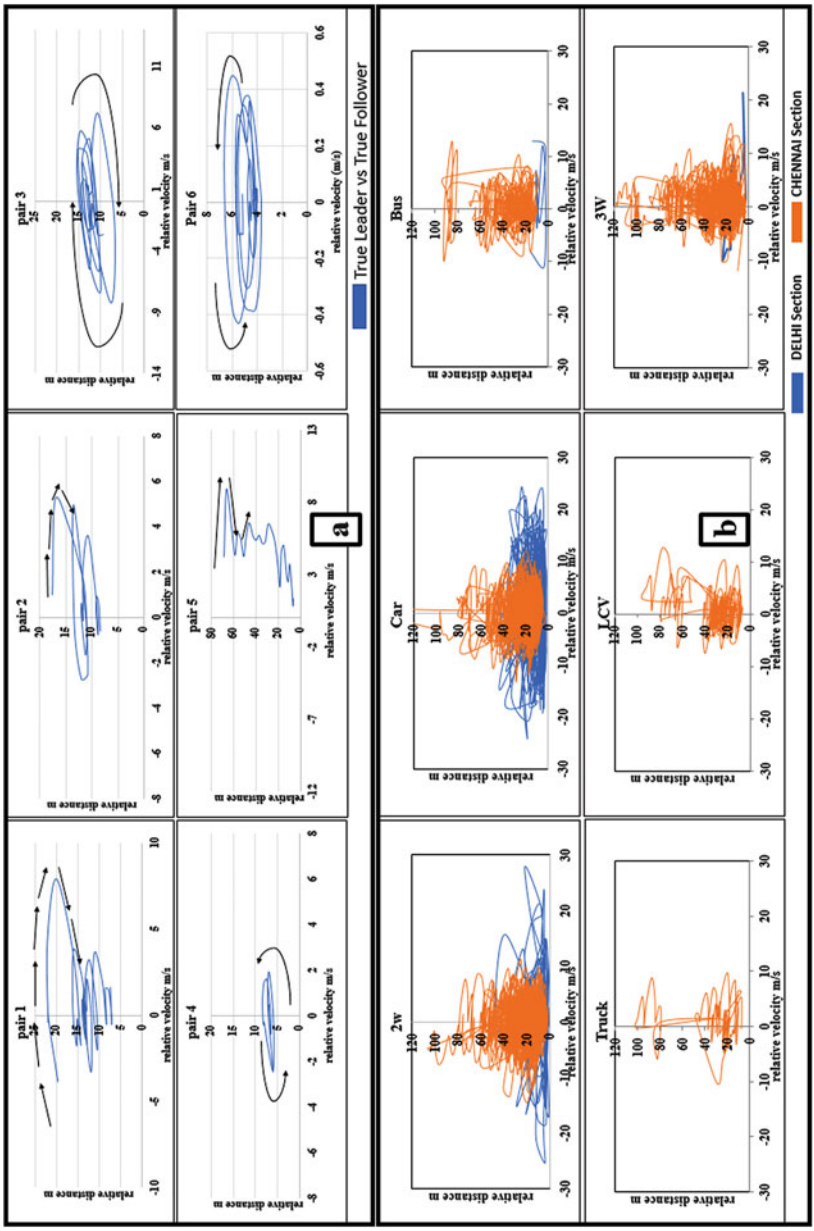

Fig. 3 Observed following pairs showing hysteresis phenomenon

wheelers and cars) in Delhi section are having high relative velocity than Chennai section implies the aggressiveness of the Delhi riders.

4 Conclusions

The following are some of the findings from the study, listed as follows:

- From the literature review, most of the studies used NGSIM data for studying the driving behavior, this research is one of the few studies, where driving behavior has been studied from micro-level aspect through vehicular trajectory data from heterogeneous traffic conditions.
- The frame adopted in the study is helpful in capturing the following behavior of vehicles under non-lane based heterogeneous traffic conditions. Based on studies of these kinds the vehicular following behavior will be captured in much deeper insights and helps in coding driving behavior for autonomous/self-driving vehicles over the road sections under heterogeneous traffic conditions.
- It was observed that even in mixed traffic conditions, there occur significant leader–follower interactions among the vehicles. Based on the relative distance and relative velocity plots among the leader–follower, hysteresis plots are plotted for all the vehicular category combinations of leader–follower. Proper visualization of these plots and hysteresis phenomenon forms core basis in identifying the true leader–follower. Further in heterogeneous traffic conditions, very few studies attempted in understanding the following behavior of vehicles.
- From the hysteresis loops, it was found that there is a variation in driving behavior among the vehicular category for a given roadway segment. It was also observed that there is a significant variation in driving behavior for a given vehicular category combinations of leader–follower pair over different road segments. This highlights the importance of calibration of vehicle-following models for all the vehicular categories under given set of roadway and geometric conditions.

5 Summary

The application of trajectory data and hysteresis phenomenon for the identification of true leader–follower pairs adds novelty to the state of the art in the area of study of vehicle-following behavior. For modelling roadway geometry in simulation, basic inputs like volume, composition, etc. can be derived out with ease, as these can be captured directly from the field. But, driving behavior parameters form crux of any simulation model, which cannot be directly captured from the field. Driving behavior can be better analyzed through the effective use of trajectory data from field and further developing the microscopic simulation models. Also, there is no benchmark for quantifying the driving behavior in heterogeneous and

non-lane based traffic conditions, like in India. It becomes significant to carry out the calibration process for multiple road sections with same roadway conditions located in different parts of the country. This may further lead to the establishment of benchmarking of the unique calibration values for a given set of roadway conditions.

Acknowledgements The authors would like to acknowledge Department of Science and Technology (DST—India) for funding the work which is a part of project titled "Study of traffic flow characteristics on expressways in India (SB/FTP/ETA-421/2012)."

References

1. Pipes, L.: An operational analysis of traffic dynamics. J. Appl. Phys. **24**, 274–281 (1953)
2. Kerner, B.S.: The Physics of Traffic. Springer, Berlin (2004)
3. Kerner, B.S.: Introduction to Modern Traffic Flow Theory and Control. Springer, Heidelberg (2009)
4. Kerner, B.S.: Breakdown in Traffic Networks: Fundamentals of Transportation Science. Springer, Berlin (2017)
5. Gipps, P.G.: A behavioural car-following model for computer simulation. Transp. Res. B Methodol. **15**, 105–111 (1981)
6. Bando, M., Hasebe, K., Nakanishi, K., Nakayama, A.: Analysis of optimal velocity model with explicit delay. Phys. Rev. E **58**, 5429–5435 (1998)
7. Gunay, B.: Car following theory with lateral discomfort. Transp. Res. B Methodol. **41**(7),722–735 (2007)
8. Wiedemann, R.: Schriftenreihe des Instituts für Verkehrswesen der. Universität Karlsruhe Heft 8 (1974)
9. Menneni, S.: Pattern recognition based microsimulation calibration. PhD Thesis, Missouri State University (2008)
10. Arkatkar, S., Arasan, V.: Effect of gradient and its length on performance of vehicles under heterogeneous traffic conditions. J. Transp. Eng. **136**, 1120–1136 (2010)
11. Raju, N., Kumar, P., Chepuri, A., Arkatkar, S., Joshi, G.: Calibration of vehicle following models using trajectory data under heterogeneous traffic conditions. In: 96th Annual Transportation Research Board Meeting, Washington, DC (2017)
12. Toledo, T.: Mixed traffic trajectory data. Available via https://toledo.net.technion.ac.il/mixed-traffic-trajectory-data/ (2014)

Development of a Decision-Making Model for Merging Maneuvers: A Game Theoretical Approach

Kyungwon Kang and Hesham A. Rakha

Abstract The development of advanced vehicle technologies will bring about new transportation system paradigms. In mixed traffic situations, where both connected automated vehicles (CAVs) and human drivers are present, it is important to first have a firm understanding of human driving behavior. Human driving behavior is complicated and will affect how CAVs need to operate. To come to this understanding, a realistic decision-making modeling framework for lane-changing behavior in human-driven vehicles is needed. Earlier, Kang and Rakha proposed a decision-making model for merging maneuvers at freeway on-ramps using a game theoretical approach (Kang and Rakha, Transp Res Rec J Transp Res Board 2623, 2017). To consider efficient integration within a microscopic traffic simulation modeling framework, this paper further develops the previously proposed model. The Next Generation SIMulation (NGSIM) dataset was used for model evaluation purpose. Validation results revealed that the developed model shows better predictability compared to the previous model.

1 Introduction

The development of advanced vehicle technologies such as connected automated vehicles (CAVs) will bring about new transportation paradigms. To harmonize CAVs with human drivers in mixed traffic, an understanding of human driving behavior is essential. In particular, lane-changing behavior should be studied to ensure the safe inter-operation of CAVs with human operated vehicles. Developing a realistic lane-changing model can help in the development of driving and decision-making algorithms for CAVs to address inter-operation factors. Furthermore, the model should be generalizable for incorporation within CAV systems.

K. Kang · H. A. Rakha (✉)
Virginia Polytechnic Institute and State University, The Charles E. Via, Jr. Department of Civil and Environmental Engineering, Blacksburg, VA, USA
e-mail: kwkang@vt.edu; hrakha@vt.edu

S. H. Hamdar (ed.), *Traffic and Granular Flow '17*,
https://doi.org/10.1007/978-3-030-11440-4_12

Various lane-changing models have been developed for traffic simulation software to replicate driver decisions at the microscopic level [1, 4, 5, 8]. However, most lane-changing models, with the exception of game theory models, deal with lane-changing maneuvers from the point of view of the merging vehicle only. The driver of a following vehicle in the target lane, however, must make a decision to react when perceiving a merging vehicle's intention to change lanes. Therefore, a study of the decision-making process between interacting drivers in the lane-changing process is required.

This study uses a game theoretical approach to consider realistic merging decision-making. Kita modeled on-ramp merging behavior using a discrete choice model, and the probability of giving way was estimated based on a game theoretical approach [10, 11]. Liu et al. modeled merging and yielding behavior [12]. The development of advanced vehicle technologies (e.g., vehicle-to-vehicle [V2V] communication and autonomous vehicles) has also led recent research efforts to focus on the interaction between vehicles [9, 13].

The main goal of this study is to further develop Kang and Rakha's merging decision-making model in traditional vehicle systems [6]. In this paper, we first describe the game design, in which the structure of the game is defined by drawing on previous study and proposing simplified payoff functions. Next, we explain how the model was calibrated using datasets extracted from the Next Generation SIMulation (NGSIM) dataset [3]. Finally, model validation is presented before concluding with summary remarks and recommendations for further research.

2 Development of a Decision-Making Lane-Changing Model for Merging

2.1 Game Design

In the model structure (see Table 1), the driver of the subject vehicle (DS), which makes a lane change to merge onto the freeway, and the driver of the lag vehicle (DL), which is the closest following vehicle in the subject vehicle's target lane, are players participating in the game [6]. The DS has three action strategies: change a lane for merging (s_1), wait for the lag vehicle's overtaking maneuver in the acceleration lane (s_2), or overtake the lead vehicle and use a forward gap to merge (s_3). The DL has two action strategies: yield to allow the subject vehicle's lane change maneuver (l_1) or block the subject vehicle's merging maneuver by decreasing the spacing to the subject vehicle (l_2) [6]. Let $S = \{s_1, s_2, s_3\}$ and $L = \{l_1, l_2\}$ denote the set of pure strategies for the DS and DL, respectively. In addition, $a = (s_i, l_j)$ denotes a set of actions ($a \in S \times L$) where i and j indicate the index of action strategies of the DS and DL (i.e., $i = 1, 2, 3$ and $j = 1, 2$). Thus, there are a total of six sets of action strategies in the proposed game.

Table 1 Structure of the merging decision-making game in normal form [6]

Player and action		Driver of lag vehicle (DL)	
		Yield $[l_1(q_1)]$[a]	Block $[l_2(q_2)]$
Driver of subject vehicle (DS)	Change $[s_1(p_1)]$[b]	(P_{11}, Q_{11})[c]	(P_{12}, Q_{12})
	Wait $[s_2(p_2)]$	(P_{21}, Q_{21})	(P_{22}, Q_{22})
	Overtake $[s_3(p_3)]$	(P_{31}, Q_{31})	(P_{32}, Q_{32})

[a] q_j in parentheses denotes the probability assigned to the DL's pure strategy l_j; $\sum_{j=1}^{2} q_j = 1$
[b] p_i in parentheses denotes the probability assigned to the DS's pure strategy s_i; $\sum_{i=1}^{3} p_i = 1$
[c] P and Q denote the payoff for the driver of the subject and lag vehicle, respectively

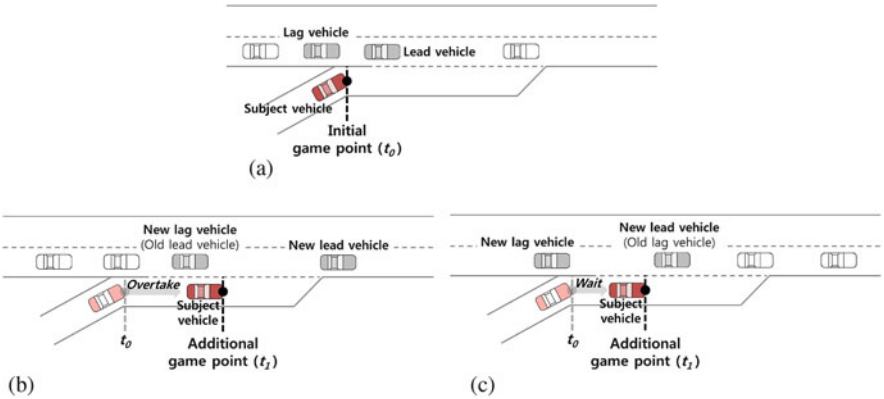

Fig. 1 Definition of decision-making game points. (**a**) Beginning point of an acceleration lane. (**b**) Game point produced by overtaking action. (**c**) Game point produced by waiting action

In the previous study, it was assumed that the DS and DL decide on an individual action only at the moment when the subject, lead, and lag vehicles are identified [6]. This implies that drivers follow their initial decision until a new game is played with a new opposing player. Both the beginning point of an acceleration lane (see Fig. 1a) and additional game points, which are created by overtaking the lead vehicle (see Fig. 1b) or waiting to be overtaken by the lag vehicle (see Fig. 1c), are considered as the decision-making game points.

2.2 Payoff Functions in the Merging Decision-Making Game

Payoff functions in game models reveal a players' outcome (or reward) provided from a base game at a stage t by choosing a specific action strategy set a. Kang and Rakha initially used five decision factors for drivers, which necessitated the use of over 50 parameters [6]. To minimize the number of parameters and avoid correlation between decision factors, this paper uses simplified payoff functions.

2.2.1 Simplified Payoff Functions for the DS

In the payoff functions for the DS, a main decision factor is the *expected lag and lead gap* based on the anticipated acceleration level of the two vehicles in each set of action strategies. The *forced merging factor* is also taken into consideration for the remaining acceleration lane distance as it affects the DS's decision-making, as shown in the third term on the right hand side in Eq. (1). The payoff functions of the DS denoted by P_{ij} are specified as:

$$P_{1j} = \alpha_{1j}^{1} \Delta x_{1j}^{sub,lag}(t + \Delta t) + \alpha_{1j}^{2} \Delta x_{1j}^{lead,sub}(t + \Delta t) + \alpha_{1j}^{3} \exp(x_0 / x_{RD}) + \epsilon_{1j}^{sub} \quad \forall\, j = 1, 2 \tag{1}$$

$$P_{2j} = \alpha_{2j}^{1} \Delta x_{2j}^{sub,lag}(t + \Delta t) + \epsilon_{2j}^{sub} \quad \forall\, j = 1, 2 \tag{2}$$

$$P_{3j} = \alpha_{3j}^{1} \Delta x_{3j}^{lead,sub}(t + \Delta t) + \epsilon_{3j}^{sub} \quad \forall\, j = 1, 2 \tag{3}$$

where

$\Delta x_{ij}^{sub,lag}(t + \Delta t)$: the expected gap between the subject and lag vehicles in the action strategies set $(s_i,\ l_j)$ at time $t + \Delta t$ (in m);
$\Delta x_{ij}^{lead,sub}(t + \Delta t)$: the expected gap between the lead and subject vehicles in the action strategies set $(s_i,\ l_j)$ at time $t + \Delta t$ (in m);
x_0: a distance threshold for forced lane-changing $(= 10 \times x_j)$ (in m);
x_{RD}: a remaining distance in acceleration lane for the subject vehicle (in m);
ϵ_{ij}^{sub}: an error term to capture the unobserved payoffs; and
$\alpha_{11}^{1}, \alpha_{11}^{2}, \alpha_{11}^{3}, \alpha_{12}^{1}, \alpha_{12}^{2}, \alpha_{12}^{3}, \alpha_{21}^{1}, \alpha_{22}^{1}, \alpha_{31}^{1}, \alpha_{32}^{1}$: parameters to be estimated.

2.2.2 Simplified Payoff Functions for the DL

The *expected relative speed* is used for the DL's decision factor in this study. It is assumed that the DL decides an action by comparing the relative speed. The DL's payoff functions denoted by Q_{ij} are specified as:

$$Q_{ij} = \beta_{ij}^{1} \Delta \dot{x}_{ij}^{sub,lag}(t + \Delta t) + \epsilon_{ij}^{lag} \quad \forall\, i = 1, 2, 3,\ \ j = 1, 2 \tag{4}$$

where

$\Delta \dot{x}_{ij}^{sub,lag}(t + \Delta t)$: the expected relative speed between the subject and lag vehicles in the action strategies set $(s_i,\ l_j)$ at time $t + \Delta t$ (in m/s);
ϵ_{ij}^{lag}: an error term to capture the unobserved payoffs; and
β_{ij}^{1}: parameters to be estimated.

3 Model Evaluation

3.1 Data Preparation

The NGSIM data were used for evaluation of the developed merging decision-making model. This study used vehicle trajectory data on a segment of US Highway 101 (Hollywood Freeway) in Los Angeles, California collected between 7:50 a.m. and 8:35 a.m. on June 15, 2005 [3].

To extract observations properly from the field data, all moments of the game were selected in the decision-making period between the beginning point of the acceleration lane and the lane change execution point. Specific observed cases where the initial lag gap at stage t_0 was greater than twice the jam density spacing ($2x_j$) were eliminated from the datasets.

3.2 Classification of Driver's Actions

Reasonable classification of the action strategies chosen by the DS and DL is a critical issue, as it is directly related to the game model's results. Following an approach proposed by Kang and Rakha, for classification of the DS's actions, one of the three following gap types were used: (1) forward gap, (2) original (current) gap, or (3) backward gap [6]. For classification of the DL's actions, the spacing between the subject and lag vehicle was used. Only data that showed a continuously increasing or decreasing of the lag spacing was collected. It was assumed that an increase in lag spacing occurred as a result of a *yielding* action and that lag spacing otherwise decreased by a *blocking* action. To obtain a larger number of observations, instantaneous fluctuations in lag spacing below a certain threshold were considered noise, meaning that that the DL's action did not change. Consequently, only data showing a variation below the noise cancellation range ($\eta = \pm 0.0\,\text{m}$ to $\pm 1.0\,\text{m}$) were collected as observations for the model evaluation.

3.3 Model Evaluation

3.3.1 Model Calibration

In the game model, each player decides on one pure strategy to achieve the goal of the game. The Nash equilibrium was used in this study to find the best set of strategies for both drivers. The Nash equilibrium is a solution where neither player has motivation to change their strategy, as no player can improve their situation by individually switching to another strategy [9]. This study used the MATLAB function NPG developed by Chatterjee to solve a two-player finite non-cooperative

game [2]. Chatterjee's algorithm provides probabilities of choice of pure action strategies for each driver (i.e., p_i and q_j) based on the expected payoffs (i.e., P_{ij} and Q_{ij}) in each observation. The parameters are estimated to minimize the system total deviation of probabilities to choose actual observed actions using the following function:

$$\min \sum_{k=1}^{n} (1 - p_{a^k} \cdot q_{a^k}) \tag{5}$$

where

k is the index of observations;
n is the number of observations;
a^k is the observed action strategies set (s_i^k, l_j^k) in observation k; and
p_{a^k} and q_{a^k} is the probability to choose the observed action in a_k for the DS and the DL, respectively.

The proposed model was calibrated to estimate parameters depending on the noise cancellation range η (between ± 0.0 m and ± 1.0 m). A dataset collected between 7:50 a.m. and 8:20 a.m. was used in model calibration. Table 2 shows the estimated parameters for the payoff functions of the DS and DL.

The mean absolute error (MAE) was calculated using Eq. (6) as follows:

$$\text{MAE} = \frac{1}{n} \sum_{k=1}^{n} |1 - 1(\hat{a}^k - a^k)| \tag{6}$$

where $\hat{a}^k$ denotes model prediction. Note that $1(\hat{a}^k - a^k)$ is equal to one if $\hat{a}^k = a^k$, and is zero otherwise. The model prediction ($\hat{a}^k$) was determined by probabilities. Table 3 reveals the calibration results including the MAE of the calibrated models.

3.3.2 Model Validation

The rest of the data collected between 8:20 a.m. and 8:35 a.m. was used for model validation purposes. Table 3 shows the model evaluation results. The models show prediction accuracy of 85.53–87.44% for each observation dataset. Since the utilized data were collected in the crowded freeway, the developed model shows an ability to represent the merging behaviors in even congested traffic. These results reveal that the developed model shows greater prediction accuracy than the previous model.

Table 2 Estimated parameters for the DS and DL's payoff functions

Payoff functions	Parameters	Calibrated values of the model parameters					
		Model 1 ($\eta = \pm 0.0$)	Model 2 ($\eta = \pm 0.2$)	Model 3 ($\eta = \pm 0.4$)	Model 4 ($\eta = \pm 0.6$)	Model 5 ($\eta = \pm 0.8$)	Model 6 ($\eta = \pm 1.0$)
P_{11}	α_{11}^{1}	2.809	1.990	2.292	2.213	2.993	0.680
	α_{11}^{2}	6.480	14.264	6.154	12.746	7.545	8.050
	α_{11}^{3}	11.354	4.511	5.695	−1.892	10.471	1.470
	ϵ_{11}^{sub}	7.151	2.044	0.979	0.197	−2.028	9.767
P_{12}	α_{12}^{1}	26.001	2.947	6.946	10.238	1.446	8.987
	α_{12}^{2}	4.285	4.083	2.472	1.675	10.532	3.454
	α_{12}^{3}	4.032	6.178	5.167	5.191	6.095	3.499
	ϵ_{12}^{sub}	4.038	15.074	−2.855	0.155	7.330	8.238
P_{21}	α_{21}^{1}	−1.020	−0.227	−0.304	0.444	−1.025	−2.271
	ϵ_{21}^{sub}	0.900	9.046	−10.130	−2.216	−9.644	−14.528
P_{22}	α_{22}^{1}	−4.502	−0.901	−3.205	−4.739	−1.826	−8.698
	ϵ_{22}^{sub}	−3.840	−5.136	−9.868	−5.394	4.469	5.523
P_{31}	α_{31}^{1}	−4.483	−9.749	−7.268	−10.855	−0.622	−5.907
	ϵ_{31}^{sub}	10.508	17.433	−4.399	−0.693	7.665	−0.195
P_{32}	α_{32}^{1}	−5.048	−2.641	−7.838	−5.377	−5.977	−11.330
	ϵ_{32}^{sub}	−5.292	2.053	−6.590	−11.026	8.410	−14.432

(continued)

Table 2 (continued)

Payoff functions	Parameters	Calibrated values of the model parameters					
		Model 1 ($\eta = \pm 0.0$)	Model 2 ($\eta = \pm 0.2$)	Model 3 ($\eta = \pm 0.4$)	Model 4 ($\eta = \pm 0.6$)	Model 5 ($\eta = \pm 0.8$)	Model 6 ($\eta = \pm 1.0$)
Q_{11}	β_{11}^{1}	−0.523	−3.129	−3.836	−6.490	−3.746	−0.261
	ϵ_{11}^{lag}	3.004	18.425	17.042	16.157	4.054	−0.953
Q_{12}	β_{12}^{1}	1.869	6.377	8.366	1.302	1.581	3.146
	ϵ_{12}^{lag}	−3.334	−6.661	−16.305	−4.569	−10.115	−10.082
Q_{21}	β_{21}^{1}	−9.717	−8.224	−4.697	−3.382	−3.250	−13.609
	ϵ_{21}^{lag}	3.045	10.832	10.634	13.289	4.219	18.583
Q_{22}	β_{22}^{1}	4.044	8.419	0.366	6.694	5.779	9.595
	ϵ_{22}^{lag}	1.488	6.590	6.265	−13.679	−1.923	−0.184
Q_{31}	β_{31}^{1}	−2.324	−5.514	−2.898	−3.718	−10.830	−2.049
	ϵ_{31}^{lag}	−4.316	19.527	−1.049	−2.132	0.705	−5.923
Q_{32}	β_{32}^{1}	8.090	12.136	2.506	9.908	6.528	11.649
	ϵ_{32}^{lag}	−12.938	−14.174	0.072	5.102	−1.619	−16.047

Table 3 Model evaluation results

Models	Model 1	Model 2	Model 3	Model 4	Model 5	Model 6
Noise cancellation range (m), η	±0.0	±0.2	±0.4	±0.6	±0.8	±1.0
Number of observations	383	392	397	403	409	413
Calibration result	0.1595[a] (84.05%)[b]	0.1420 (85.80%)	0.1570 (84.30%)	0.1600 (84.00%)	0.1620 (83.80%)	0.1648 (83.52%)
Validation result	0.1273 (87.27%)	0.1256 (87.44%)	0.1422 (85.78%)	0.1447 (85.53%)	0.1304 (86.96%)	0.1429 (85.71%)

[a]The value indicates the MAE
[b]The number in parentheses indicates the prediction accuracy of the calibrated model

4 Conclusions

An understanding of human driving behavior is necessary for harmonization between CAVs and human drivers. As lane-changing is one of the most critical human-driving maneuvers, this study focused on the development of a decision-making model for merging maneuvers. To update the previously proposed model, a simplified payoff function was used. The developed model was evaluated, and was shown to have captured drivers' merging behaviors with a prediction accuracy greater than 85%. The developed model was shown to better predict merging maneuvers than the previous model despite using fewer variables.

Further work is needed to enhance the model by considering a repeated game; considering different traffic conditions, as defined in the three-phase traffic theory [7]; considering both mandatory and discretionary lane-changing; and expanded to consider environments in which vehicles equipped with advanced technologies are in the mix.

Acknowledgements This research was funded partially by the Mid-Atlantic University Transportation Center (MAUTC) and a gift from the Toyota InfoTechnology Center.

References

1. Ahmed, K.I.: Modeling drivers' acceleration and lane-changing behavior. Ph.D. thesis, Department of Civil and Environmental Engineering, Massachusetts Institute of Technology, Cambridge, MA (1999)
2. Chatterjee, B.: An optimization formulation to compute Nash equilibrium in finite games. In: Proceeding of International Conference on Methods and Models in Computer Science 2009. IEEE, Piscataway (2009)
3. FHWA: Next generation simulation: US 101 freeway dataset. http://ops.fhwa.dot.gov/trafficanalysistools/ngsim.htm. Accessed 25 Jan 2016
4. Gipps, P.G.: A model for the structure of lane-changing decisions. Transp. Res. B Methodol. **20**(5), 403–414 (1986)

5. Hunt, J.G., Lyons, G.D.: Modeling dual carriageway lane-changing using neural networks. Transp. Res. C Emerg. Technol. **2**(4), 231–245 (1994)
6. Kang, K., Rakha, H.A.: A game theoretical approach to model decision making for merging maneuvers at freeway on-ramps. Transp. Res. Rec. J. Transp. Res. Board **2623** (2017). https://doi.org/10.3141/2623-03
7. Kerner, B.S.: Introduction to Modern Traffic Flow Theory and Control. Springer, Berlin (2009)
8. Kesting, A., Treiber, M., Helbing, D.: General lane-changing model mobile for car-following models. Transp. Res. Rec. J. Transp. Res. Board **1999**, 86–94 (2007)
9. Kim, C., Langari, R.: Game theory based autonomous vehicles operation. Int. J. Veh. Des. **65**(4), 360–383 (2014)
10. Kita, H.: A merging-giveway interaction model of cars in a merging section: a game theoretic analysis. Transp. Res. A Policy Pract. **33**(3–4), 305–312 (1999)
11. Kita, H., Keishi, T., Fukuyama, K.: A game theoretical analysis of merging-giveway interaction: a joint estimation model. In: Taylor, M.A.P. (ed.) Transportation and Traffic Theory in the 21st Century, Adelaide, pp. 503–518 (2002)
12. Liu, H., Xin, W., Adam, Z.M., Ban, J.X.: A game theoretical approach for modeling merging and yielding behavior at freeway on-ramp section. In: Transportation and Traffic Theory, pp. 197–211. Elsevier, London (2007)
13. Talebpour, A., Mahmassania, H.S., Hamdar, S.H.: Modeling lane-changing behavior in a connected environment: a game theory approach. Transp. Res. C Emerg. Technol. **59**, 216–232 (2015)

Macroscopic Fundamental Diagram Validation for Collision Formation on Freeway Networks

Claire E. Silverstein, Samer H. Hamdar, Seungmo Kang, and Kitae Jang

Abstract Since the introduction of the macroscopic fundamental diagram (MFD), much work has been conducted using field data to estimate MFDs. However, despite some incorporation of collision occurrence into MFD assessment, there have not been any successful attempts to derive/validate the macroscopic fundamental diagram for collision formation. The objective of this research is to validate the MFD for full and partial lane closure due to collision formation. To accomplish such objective, the authors use microscopic collision and loop detector data from the Korea Expressway Corporation (KEC) and account for complete and partial lane closure due to collision in a similar manner to previous research in its incorporation of mixed traffic; collisions are considered moving bottlenecks in the same way as buses are in the previous research. Additionally, a principal component analysis is conducted on the mentioned traffic characteristics as well as lane closure times to investigate the relationships between MFDs and collision lane closures.

1 Introduction

Due to the typical categorization of traffic by the three essential variables of flow, speed, and density, the relationships between these variables are important to understand. When estimated as average values at the link and network levels, flow, speed, and density become macroscopic characteristics and their relationships become the macroscopic fundamental diagram (MFD). Much work has been

C. E. Silverstein (✉) · S. H. Hamdar
George Washington University, Washington, DC, USA
e-mail: csilvs@gwu.edu; csilvs@email.gwu.edu; hamdar@gwu.edu

S. Kang
Korea University, Seoul, South Korea
e-mail: s_kang@korea.ac.kr

K. Jang
Korea Advanced Institute of Science and Technology, Daejeon, South Korea
e-mail: kitae.jang@kaist.ac.kr

S. H. Hamdar (ed.), *Traffic and Granular Flow '17*,
https://doi.org/10.1007/978-3-030-11440-4_13

conducted using field data to estimate MFDs [4, 11, 12]. However, despite some incorporation of collision occurrence into MFD assessment [11], there have not been any successful attempts to derive or validate the macroscopic fundamental diagram for collision formation. Therefore, the objective of this project is to validate the MFD for full and partial lane closure due to collision formation.

To accomplish such objective, the authors analyze the fundamental diagram relationships on both the micro- and macroscopic scales to gain insight into collision formation. Microscopic collision and loop detector data are from the Korea Expressway Corporation (KEC) [2]. To account for complete and partial lane closure due to collisions, the methodology of Xie et al. [12] in their incorporation of mixed traffic is utilized; collisions are considered moving bottlenecks in the same way as buses are in the previous research. In addition, principal component analysis (PCA) is utilized for both full and partial lane closures to identify patterns and relationships between the various traffic characteristics as well as the lane closure times for the collisions. Primary contributions of this paper pertain to validating the MFD for both total and partial lane closures, identifying the impact of changes in the various traffic characteristics on collision lane closures, and setting up the future work on potential collision prediction and mitigation.

The rest of the paper is organized as follows: in the next section, a brief overview of various MFD studies is given. After that, a data description along with the MFD and PCA methodologies will be presented. Empirical and numerical results from the total and partial lane closure collision analyses will follow along with comments on the relationships between the chosen traffic characteristics. Founded on the presented analyses, conclusions and suggestions for future study will be examined.

2 Background

Understanding the relationships between speed, flow, and density is of critical importance in the field of traffic flow theory. Specifically, using average values at the link and network levels allows for these parameters and their relationships to become the macroscopic fundamental diagram (MFD). If estimated correctly, knowing this relationship can give insight into predicting future traffic states based on the various inflow, outflow, accumulation, and production rates. It is of specific interest to attempt to derive MFDs for collision scenarios due to significant impacts of such events on safety and congestion. Substantial difficulty of this task comes from the heterogeneous nature of collisions and the difficulty in predicting their occurrence.

Daganzo [3] presented research supporting the notion that links of a traffic network are interdependent and affect one another throughout the whole network. Specifically, the author showed that under homogeneous traffic conditions, there is a relationship between accumulation and production as well as a correlation between inflow rates, outflow rates, and production for a given network. Further contributions of this work include the implication that future states of traffic can

be predicted based on known network dynamic characteristics and tested initial generalized assumptions. While being able to show that a traffic network under homogeneous conditions exists is significant, realistic traffic is more likely to occur under heterogeneous conditions resulting from disturbances in homogeneous traffic conditions. Two main causes of disturbances discussed in the literature include junctions (with and without traffic signals) and incident occurrence. A more recent study [12] focused on the estimation of MFDs for mixed traffic on a signalized arterial using a variety of methods. One method endogenously incorporates temporal and local reductions in capacity along the arterial to account for buses, making the introduction of buses being represented by the moving bottleneck theory. Results show that this method appears to be the preferred estimation technique. While the microscopic movement of buses is not accurately modeled in any of the presented methods, this research presented a good base for the assessment of traffic dynamics of a signalized arterial.

Since this study considers collisions and MFDs, a more extensive background is presented on incident studies. It was shown that there exist robust relationships between traffic flow conditions and likelihood of crashes by crash type [6]. Using traffic flow data measured using single inductive loop detectors, the authors found that mean volume and median speed along with temporal variations in volume and speed are the most impactful traffic flow elements on safety. Another study investigated incident affect on freeways in terms of capacity reduction using videos of traffic flow around two incidents recorded from a helicopter [10]. Performing traffic counts at the precise location of an incident allowed for the estimation of the capacity at the bottleneck per lane and for more accurate truck counts to be incorporated. While the use of high definition video data appears to be a very accurate method to obtain traffic data, there is a trade-off for the time it requires to parse through the videos and the applicability to a real-time application.

Looking further into traffic disturbances caused by incidents requires a better assessment of the traffic states surrounding such occurrences. A 2011 study examined real data from Minnesota freeways to determine if well-defined macroscopic relationships are apparent for freeway networks [5]. Results show that the MFDs have high scatter and exhibit hysteresis phenomena and have path dependence. The intrinsic characteristics of the hysteresis phenomena at the network level are shown to be different from these phenomena at the micro- and mesoscopic levels. This study also shows the importance of data type and collection as well as the level of aggregation when estimating MFDs; MFDs should not be automatically anticipated. In 2015, researchers studied the correlation of crashes and traffic flow [1]. Changes in speed and density were found to have more impact on safety than changes in flow. Results from the model provide evidence of the real-time link between traffic characteristics and safety at the macroscopic level. Another study investigated a generalized MFD (g-MFD) that relates the network traffic density and the spatial variation of density [7]. Using average and standard deviation of density, the authors could estimate clear g-MFDs for networks containing both homogeneous and non-homogeneous traffic. The authors believe that the resilience of a network can be evaluated by comparing service levels before and after an incident using

such indicators as production or mean speed. Extending the investigation into the resiliency of a traffic network, another study explored the link between mobility and safety through MFD estimation and structural equation models (SEM) for different traffic scenarios corresponding to various levels of traffic disruptions [11]. The authors used microscopic loop detector data and collision data for thousands of km of South Korean highways. MFDs for subnetworks reinforced results from the full network that collisions caused the biggest MFD disruptions and lowest maximum flow rates compared to weather conditions and holiday demand. Areas of needed research addressed by the authors include the formulation for a generalized MFD estimation methodology that can accurately account for heterogeneity regardless of the network characteristics.

As it can be seen in the literature, much research has been conducted on MFD estimation to account for various heterogeneities in traffic flow. While there are estimation techniques and safety assessment tools that allow for relatively accurate modeling, challenges still exist. When analyzing the impacts of collisions on traffic flow characteristics, a generalized MFD estimation technique could contribute to a better understanding and prediction capabilities. To accomplish this, the authors believe that a microscopic perspective is necessary to incorporate the individual vehicle movement on individual network links leading up to and during a collision to better estimate traffic flow parameters at the macroscopic level.

3 Data

Microscopic-level collision and loop detector data from the KEC [2] are aggregated and utilized for this research. Almost 4000 km of high-speed motorways in South Korea have tolls operated by the KEC [2]. Between the years 2011 and 2013, the KEC recorded almost 30,000 discrete collisions, with 14,286 of these being viable for analysis with inclusive information records. More data filtering has been conducted to identify specific links on which collisions have occurred within the network. Links were determined by detector locations for both eastbound and southbound roadways. A total of 7893 links were formed with link lengths no greater than 4 km. Detector data (speed and volume) was recorded for every 5 min, leading to 288 time steps per day per link. A linear relationship between speed, flow, and density is assumed. Seven days' worth of data (February 4, September 14, September 19, September 29, October 8, November 27, and December 14 of 2013) were used from the KEC dataset to potentially compare the results to that of the previously mentioned study [11]. Collision data extracted from the KEC dataset include day, time, and lane closure time (partial and full). After filtering out incomplete collision records, 8 total lane closure collisions and 50 partial lane closure collisions were analyzed.

4 MFD Estimation and PCA Formulation

In addition to the use of the flow, speed, and density values used for analysis at the link level, MFD estimation is conducted for various subnetworks upstream and downstream of the collision links. The chosen weighted average method for MFD estimation is used for calculating average flow and average density for a specific time. These values are calculated as [4]:

$$q_{avg,t} = \frac{\sum q_{i,t} L_i}{\sum L_i}, \tag{1}$$

$$k_{avg,t} = \frac{\sum k_{i,t} L_i}{\sum L_i}, \tag{2}$$

where $q_a vg, t$ is the weighted average flow, q_i is the flow rate of each segment of the road, L_i is the length of each segment of the road, $k_a vg, t$ is the weighted average density, and k_i is the density of each segment of the road.

From the averaged values, the extended method of cuts is used as outlined in [12]. This extension is originally used to include various traffic signal timings and to represent buses as moving obstacles (bottlenecks). In this work, instead of using buses and signal timings, the authors use collisions and lane closure times. Additionally, to assess the accuracy of the construction of the MFD for heterogeneous traffic conditions, the flow vs. density graph at the link level is compared to the MFD for different subnetworks of the link plus 2, 5, and 10 upstream links are compared. As in [12], capacities are compared for the MFDs of the subnetworks. However, further practical cuts are made to only look at the free-flow (positive slope) section of the reconstructed MFDs from the time of collision through the lane closure time.

Due to the multicollinearity of the variables of interest, PCA is applied to reduce dimensionality of the correlated and possibly redundant data [8]. The variables of interest include lane closure (full and partial) time, flow, and density for the collision link at the time of collision, flow, and density for the collision link 5, 10, and 15 min before the collision, difference between the flow and density for 5, 10, and 15 min before the collision. Additional variables include the described collision link variables for the collision link plus 2, 5, and 10 upstream links (weighted averaged values). This analysis orthogonally transforms correlated measures into uncorrelated principal components (PCs). PCs are linear combinations of the observed metrics that have been optimally weighted. The first PC has the largest variance and explains the highest percentage of the data variability. Each successive PC has the next highest variance and preserves orthogonality with the previous PCs.

5 Results

First, results for the construction of the MFDs for both partial and total lane closure collisions are presented. Scatter plots of the original data using [4] and then the reconstruction MFDs using the method of cuts [12] are presented for selected collisions. These collisions are chosen based on their representation of distinctions that were empirically observed from the datasets; for both total and partial lane closure collisions, collisions occurred in the free-flow, transition, or congested regimes of the fundamental diagram as defined by [9]. Figure 1 columns 1 and 2 show that for total lane closure collisions, compared to the flow vs. density plots for the collision link, for all three collision regimes, the MFDs show significant dissipation/reduction in scattering. It is interesting to note that for the transition and congested regime collisions (rows 2 and 3 of Fig. 1), there is a bigger drop in capacity (both flow and density) compared to the free-flow regime collision (row 1). This result aligns with previous results [10] regarding capacity reductions due to incidents. By taking the step further to investigate the traffic flow regime, further insights can be gained. Contrary to the results from the total lane blocked collisions, Fig. 1 columns 3 and 4 show differences for partially blocked lane collisions. Despite similar results in terms of scatter decreases, the capacity reductions are reversed; the free-flow regime collision (row 1 of Fig. 1) shows a bigger capacity reduction than the transition and congestion regime collisions (rows 2 and 3 and Fig. 1). Such results could be due to the different internal dynamics associated with the different regimes of the fundamental diagram and that the process of lane-changing to avoid the closed lanes due to a collision impacts free-flow traffic more.

Figure 2 presents the results of the MFD reconstruction for collisions with total (left column) and partial (right column) lane blockage. It is observed that for the free-flow collisions (row 1), the collision link has the highest capacity, while the averaged values of the link plus 5 and 10 upstream links have the lowest capacities. This supports the previous findings that when collisions occur during the free-flow regime, there is a higher impact on the upstream network, especially for collisions with only partial lane blockage. For the collisions occurring during the transition traffic regime (row 2) it appears that for the reconstructed MFDs, the capacity increases with inclusion of more upstream links. The congested regime collisions (row 3) have mixed results with an increase in capacity with 10 and 2 links upstream for totally and partially blocked lane collisions, respectively. Clearly differences can be seen for the different traffic regime collisions for both total and partial lane blockages. This could give insight into changes in MFD values and likelihood of the formation of the different types of collisions. To explore further into this idea, the PCA modeling results are discussed next.

Separate total and partial lane blockage collision PCA analysis was conducted 57 dimensions. After standardizing each dataset, eigen-decomposition allowed for the selection of ten principal components. For the total and partial lane blockage collisions, the ten PCs describe 99.3% and 96.9% of the explained variance, respectively. The highest lane closure time correlation occurs for PC6 (0.6609) for

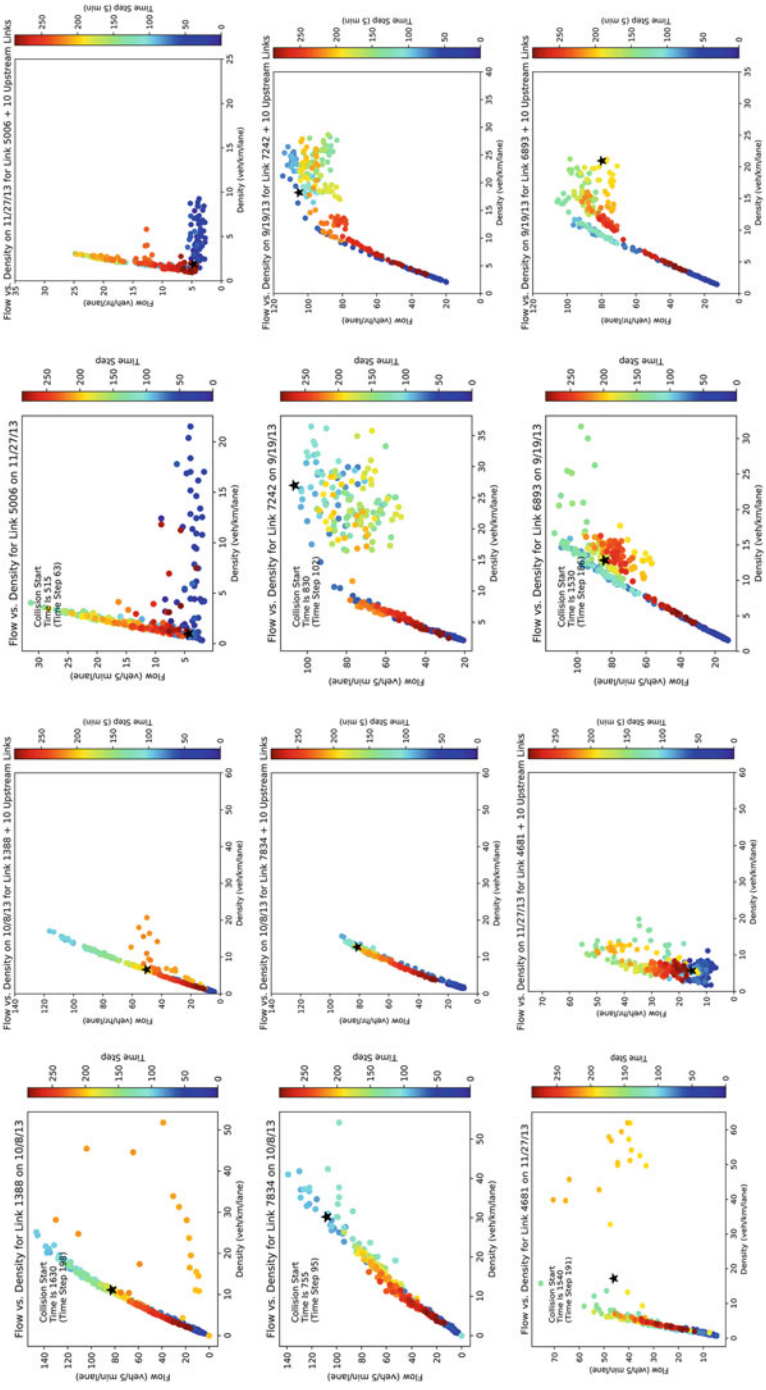

Fig. 1 Total lane closure (columns 1 and 2) and partial lane closure (columns 3 and 4) collision flow vs. density and MFDs for the collision link plus 10 upstream links for collisions occurring in the free-flow, transition, and congestion regimes

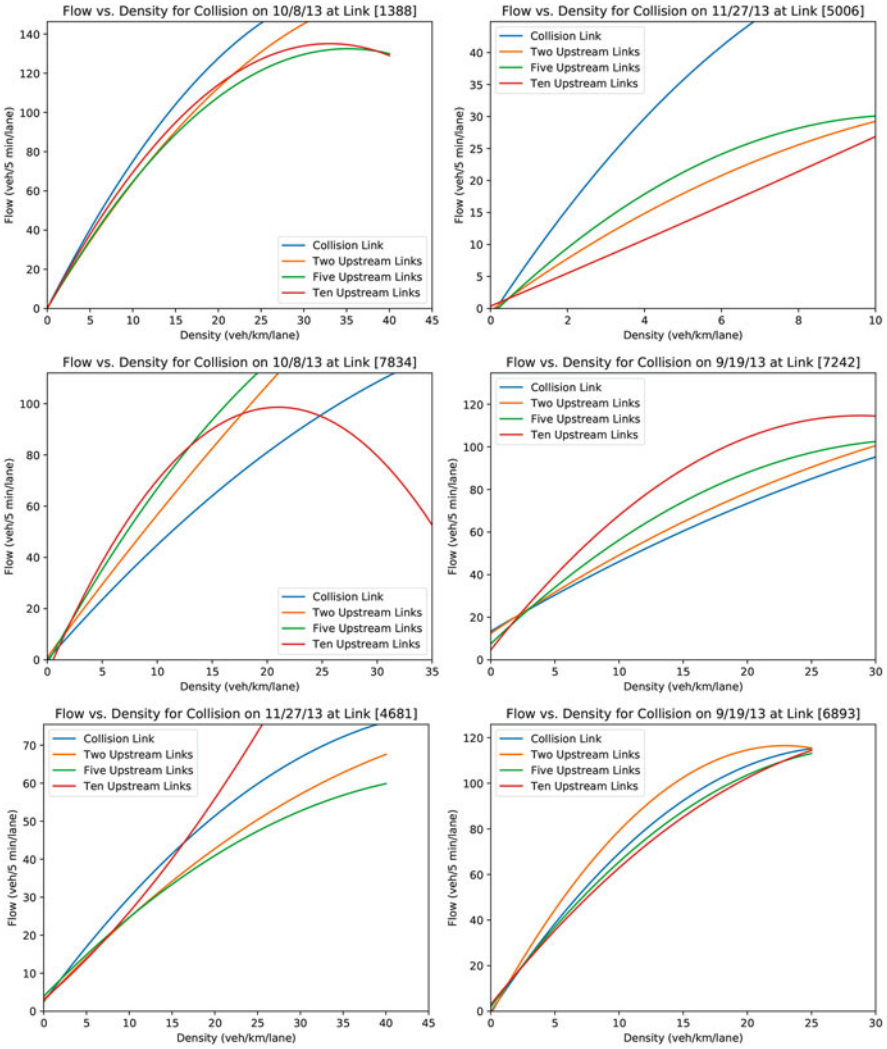

Fig. 2 Total (left column) and partial (right column) lane closure collision method of cut flow vs. density and MFDs for the collision link plus 2, 5, and 10 upstream links for collisions occurring in the free-flow, transition, and congestion regimes

total lane blocked collisions and for PC9 (0.7412) for partial lane blocked collisions. The highest traffic characteristic weights for PC6 for the total lane blocked collisions are observed with the 10 min difference in density for the collision link (0.2827), the 5- and 10 min differences in density for 2 links upstream (0.1751 and 0.1721), the 10 min difference in flow for 5 links upstream (−0.2863), and the 10 min difference

for 10 links upstream (−0.2712). Regarding the partially blocked lane collisions, the highest traffic characteristic weights for PC9 are observed with the 5- and 10 min differences in density for the collision link (0.2256 and −0.3692), the 10-min difference in flow for 2 links upstream (−0.1358), the 10- and 15-min differences in flow for 10 links upstream (0.1396 and −0.2136), and the 10- and 15-min differences in density for 10 links upstream (0.1376 and −0.1456). It is interesting to note that for both types of collisions, the PCs associated with the highest lane closure times do not have significant weights for any of the flow or density values at the collision link or the averaged upstream links. While there is some overlap in the significant difference values, the weights and their signs differ. These differences and unique relationships between closure times and the type of collision can be used for control/monitoring purposes in identifying potentially dangerous collision-forming traffic conditions.

6 Conclusions

In this research, collisions with both partially and totally blocked lanes are analyzed on both a microscopic link flow vs. density scale and the macroscopic subnetwork of aggregated upstream links MFD scale. The authors constructed the MFDs for various traffic state regime collisions for the chosen collision types with subnetworks including 2, 5, and 10 upstream links of the collision link. Results show that partial lane closure collisions may prevent the moving bottleneck phenomenon depending on the traffic regime in which the collision occurs. Furthermore, PCA results help further evaluate the collision MFDs for both temporal and spatial variations and show that closure times appear to play significant role. Differences in the flow and density values of the collision link as well as aggregated upstream links at the 5-, 10-, and 15-min time scales appear to have significant relationships with closure time for both partial and total lane closure collisions. Such results could help with collision prediction/mitigation for varying lengths of lane closure times. Additional research will build on these findings by attempting to derive a general MFD formulation that can accurately identify/predict the discussed collision types and possibly be used for real-time traffic management of various subnetworks. Specifically, the authors wish to target areas where collision-prone links are present. The authors also want to look at how specific numbers of closed lanes, link/network size, and bigger datasets affect the achieved results and if thresholds exist for the presented results to hold true. The MFD, while allowing practitioners to look at averaged/diluted traffic characteristics for an entire network, does not give a full picture of the traffic dynamics that take place before, during, and after a collision occurs.

References

1. Alsalhi, R., Dixit, V.: The relationship between traffic safety and macroscopic fundamental diagram (MFD). In: 37th Australasian Transport Research Forum (ATRF), 2015, Sydney, New South Wales (2015)
2. Corporation, K.E.: Expressway construction (2015). http://www.ex.co.kr/site/com/pageProcess.do/http://www.808multimedia.com/winnt/kernel.htm
3. Daganzo, C.F.: Urban gridlock: macroscopic modeling and mitigation approaches. Transp. Res. B Methodol. **41**(1), 49–62 (2007)
4. Daganzo, C.F., Geroliminis, N.: An analytical approximation for the macroscopic fundamental diagram of urban traffic. Transp. Res. B Methodol. **42**(9), 771–781 (2008)
5. Geroliminis, N., Sun, J.: Hysteresis phenomena of a macroscopic fundamental diagram in freeway networks. Transp. Res. A Policy Pract. **45**(9), 966–979 (2011)
6. Golob, T.F., Recker, W.W., Alvarez, V.M.: Freeway safety as a function of traffic flow. Accid. Anal. Prev. **36**(6), 933–946 (2004)
7. Hoogendoorn, S.P., Knoop, V.L., van Lint, H., Vu, H.L.: Applications of the generalized macroscopic fundamental diagram. In: Traffic and Granular Flow'13, pp. 577–583. Springer, Berlin (2015)
8. Jolliffe, I.T.: Principal component analysis and factor analysis. In: Principal Component Analysis, pp. 150–166. Springer, Berlin (2002)
9. Kerner, B.S.: Three-phase traffic theory and highway capacity. Physica A **333**, 379–440 (2004)
10. Knoop, V., Hoogendoorn, S., van Zuylen, H.: Capacity reduction at incidents: empirical data collected from a helicopter. Transp. Res. Rec. J. Transp. Res. Board **2071**, 19–25 (2008)
11. Schorr, J.P., Hamdar, S.H., Kang, S., Jang, K., Kachouch, H.: From structural equation modeling to macroscopic fundamental diagrams: investigating the impact of road segments safety on network level efficiency. In: 17th International Conference Road Safety on Five Continents (RS5C 2016), Rio de Janeiro, 17–19 May 2016, pp. 1–17. Statens väg-och transportforskningsinstitut (2016)
12. Xie, X., Chiabaut, N., Leclercq, L.: Macroscopic fundamental diagram for urban streets and mixed traffic: cross comparison of estimation methods. Transp. Res. Rec. J. Transp. Res. Board **2390**, 1–10 (2013)

Towards a More Stable Traffic Flow Performance: Applying and Calibrating the Intelligent Driver Model

Dong Pan, Samer H. Hamder, and Antonio J. Caamaño

Abstract The surrounding conditions (e.g., weather condition) under which a roadway segment operates may affect its performance, impairing its capacity level and consequently resulting into the formulation and propagation of congestion. In this study, we translated the traffic data from continuous count station (CCS, administrated by Virginia Department of Transportation—VDOT) in Northern Virginia into fundamental diagrams (FDs). By overlapping such data with weather data (available on Weather Channel), two travel condition types were defined, namely normal commute condition and inclement weather condition. The conditional FDs indicate a significant decrease in capacity under inclement weather condition compared to normal commute condition. To reveal the underlying factors leading to such capacity decrease, we obtained the parameters from intelligent driver model (IDM, as the car-following algorithm) and minimizing overall braking induced by lane changes (MOBIL, as the lane-changing algorithm), trained with real traffic data to simulate multilane behavior and weather conditions, adjusted to match the characteristics in the capacity breakdown situations. It is found that reaction time will affect the capacity level at a location of roadway and thus the congestion formulation while the lane-changing will influence the traveling of shock waves over a length of roadway and thus the congestion propagation.

D. Pan (✉)
Department of Civil and Environmental Engineering, George Washington University, Washington, DC, USA
e-mail: pandong@gwu.edu

S. H. Hamder
George Washington University, Washington, DC, USA
e-mail: hamdar@gwu.edu

A. J. Caamaño
Rey Juan Carlos University, Móstoles, Spain
e-mail: antonio.caamano@urjc.es

S. H. Hamdar (ed.), *Traffic and Granular Flow '17*,
https://doi.org/10.1007/978-3-030-11440-4_14

1 Introduction

The formulation of roadway congestion depends on the roadway characteristics (e.g., horizontal and vertical curves, number of lanes, lane width, shoulder width and median type), vehicular flow compositions (e.g., percentage of heavy trucks versus passenger cars) as well as the drivers' behaviors (e.g., reaction time, politeness, and patience). While the former two exogenous factors have been well investigated, the role of drivers' behaviors (the endogenous factor) in congestion formulation remains largely unexplored. In line with such limitation, this study developed a multilane car-following simulation program incorporating reaction time. The simulations enable the analysis of vehicles' trajectories and the traffic flow fundamental diagrams and by training the simulations with the real traffic data under different travel conditions, the underlying human factors (interpreted by the model parameters in the simulations) that influence congestion formulation and propagation were investigated.

2 Literature Review

To describe the longitudinal interactions between vehicles on the roadway (i.e., how individual vehicles efficiently and safely follow their preceding vehicles in a traffic stream), numerous car-following models were developed during the past decades. These models can be classified into the following categories: Gazis–Herman–Rothery (GHR) model and its extensions, safety distance models, desired measures (or stimulus) models, optimal velocity (OV) model, and cellular automata (CA) models [1]. The former three categories have been extensively used and examined and the remainder of this section gives the sample models under these categories.

Gazis et al. proposed the non-linear GHR model in 1961 [2] as shown in Eq. (1), where $v_n(t)$ is the velocity of subject vehicle n at time t, $\Delta v_n(t-\tau)$ and $\Delta x_n(t-\tau)$ are the differences in velocity and distance between the subject vehicle and the preceding vehicle at time $t-\tau$ given τ is the reaction time, and α, β, and γ are the parameters to be calibrated. Though the model is simple and the parameters can be easily estimated, the high sensitivity to speed difference overestimates drivers' ability to perceive such difference in nature. Vehicles may also maintain unrealistic small space headway at high speed level when speed difference is zero.

$$\dot{v_n}(t) = \alpha v_n(t)^{\beta} \frac{\Delta v_n(t-\tau)}{\Delta x_n(t-\tau)^{\gamma}} \tag{1}$$

Newell proposed a non-linear safety distance model in 1961 [3] assuming that the speed of the subject vehicle is a function of the spacing to the preceding vehicle as shown in Eq. (2), where V_n, λ_n, and d_n are the parameters to be calibrated. However, the direct dependency on spacing may result in unrealistic high acceleration and

deceleration upon the sudden change in traffic flow status.

$$v_n(t) = V_n - V_n \exp\left\{-\lambda_n V_n^{-1}\left(\Delta x_n(t-\tau) - d_n\right)\right\} \tag{2}$$

Gipps proposed the most popular safety distance model in 1981 [4] considering the driving behavior under two regimes: free-flow regime and car-following regime. The velocity of a vehicle will be determined by either the free-flow term (the upper) or car-following term (the lower) whichever is smaller, as shown in Eq. (3), where parameters V_n, a_n, and b_n are the desired velocity, acceleration, and deceleration of vehicle n, s_{n-1} is the effective size of the preceding vehicle, and $\widehat{b}$ is the estimate of its deceleration. Though the model may take account of both the free-flow regime and car-following regime, the model parameters are difficult to be estimated given the discontinuity at their transition.

$$v_n(t+\tau) = \min \begin{cases} v_n(t) + 2.5 a_n \tau (1 - v_n(t)/V_n)(0.025 + v_n(t)/V_n)^{1/2} \\ b_n \tau + \sqrt{b_n^2 \tau^2 - b_n \left[2\left[x_{n-1}(t) - s_{n-1} - x_n(t)\right] - v_n(t)\tau - v_{n-1}(t)^2/\widehat{b}\right]} \end{cases} \tag{3}$$

Addressing the limitations of the above model (the pure dependency on either difference in velocity or spacing of the GHR model and the Newell's model, and the discontinuity of the Gipps' model), Treiber et al. proposed the intelligent driver model (IDM) in 2000 as a desired measures model [5]. Such car-following model and the coherent lane-changing model, minimizing overall braking induced by lane changes (MOBIL, proposed by Kesting et al. in 2007) [6], also enable better association with human factors. Therefore, this study adopted these two models for simulating multilane vehicular flow. Their introductions are included in the following Sect. 3.

3 Methodology

To simulate the microscopic traffic flow dynamics, IDM and MOBIL were adopted in this study to explain the car-following and lane-changing behaviors of vehicles (as the two main degrees of freedom when simulating vehicular flow on a roadway). According to IDM (Eqs. (4) and (5), see Table 1 for the definitions of model variables and parameters), the first-order derivative of vehicle speed (i.e., the acceleration/deceleration) is a function of two ratios, the ratio of current speed to desired speed and the ratio of desired headway to current headway. IDM presumes a collision-free traffic condition that at low speed level, the derivative of vehicle speed is dominated by the first ratio, that is, the lower the ratio of current speed to desired speed, the higher the acceleration; at high speed level, the derivative of vehicle speed is dominated by the second ratio, that is, the higher the ratio of desired

Table 1 IDM variable and parameter definitions

Variable	*Definition*	*Variable*	*Definition*
v_a	Current speed	s_a	Current space headway
Δv_a	Difference in speed compared to the preceding vehicle		
Parameter	*Definition*	*Parameter*	*Definition*
v_0	Desired speed	T	Safe time headway
a	Maximum acceleration	b	Comfortable deceleration
δ	Acceleration exponent	s_0	Minimum distance

Table 2 MOBIL variable and parameter definitions

Variable	*Definition*	*Variable*	*Definition*
$\widetilde{a_c}$	Acceleration of driver's vehicle after lane change	a_c	Acceleration of driver's vehicle before lane change
$\widetilde{a_n}$	Acceleration of new follower after lane change	a_n	Acceleration of new follower before lane change
$\widetilde{a_o}$	Acceleration of old follower after lane change	a_o	Acceleration of old follower before lane change
Parameter	*Definition*	*Parameter*	*Definition*
p	Politeness factor	Δa_{th}	Switching threshold

headway to current headway, the higher the deceleration.

$$\dot{v_a} = a\left(1 - \left(\frac{v_a}{v_0}\right)^{\delta} - \left(\frac{s^*(v_a, \Delta v_a)}{s_a}\right)^2\right) \tag{4}$$

$$\text{where } s^*(v_a, \Delta v_a) = \max(0, s_0 + v_a T + \frac{v_a \Delta v_a}{2\sqrt{ab}}) \tag{5}$$

MOBIL is established on the basis of IDM (as it also uses the first-order derivative of vehicle speed to evaluate and estimate lane change) and it defines that a lane change is worthwhile when the total improvement of accelerations (or decelerations in case the derivative of speed is negative) of the local vehicles is greater than the given threshold (Eq. (6), see Table 2 for the definitions of model variables and parameters). The local vehicles include the vehicle initiating a lane change, its following vehicle before the lane change (i.e., the old follower) and its following vehicle after the lane change (i.e., the new follower).

$$\widetilde{a_c} - a_c + p\,(\widetilde{a_n} - a_n + \widetilde{a_o} - a_o) > \Delta a_{th} \tag{6}$$

To emphasize the role of drivers in congestion formulation, reaction time, the time lag between a person's exposure to a stimulus and his/her action in response to such stimulus, was also taken into account. In this study, reaction time refers to the delay of drivers' acceleration/breaking when facing the changes of the surrounding traffic flow conditions.

The simulation program was coded and run on MATLAB. To simplify the program and enhance its efficiency, the vehicle trajectories were estimated based on a quarter-second time step, that is, vehicle speed is assumed to be linear (i.e., the derivative of vehicle speed remains unchanged) within each time step.

To train the simulations for better representing the real traffic conditions, traffic data collected by continuous count stations (CCS, maintained by Virginia Department of Transportation) in Northern Virginia was mined for calibration purpose. Such data was further associated with historical weather record (available on Weather Channel) to be classified into two travel conditions: normal commute condition (with clear weather) and inclement weather condition (typically, heavy rain condition).

4 Results

In this study, there was a focus on simulating the uninterrupted flow on two typical freeway segments in Northern Virginia: 4-lane Interstate 66 segment (I-66) and 10-lane Interstate 495 segment (I-495). By training the model to minimize the overall percentage errors in terms of free-flow speed and capacity, the model parameters of simulating traffic flow in I-66 and I-495 under different weather conditions are shown in Table 3. Note that in the training exercises, the maximum acceleration, comfortable deceleration, acceleration exponent, politeness factor, and switching threshold were not examined and their suggested values were adopted and remained unchanged, where $a = 1.4\,\mathrm{m/s^2}$, $b = 2.0\,\mathrm{m/s^2}$, $p = 1$, and $\Delta a_{th} = 1$ [7].

The corresponding fundamental diagrams (FDs) of I-66 and I-495 under different weather conditions (as a result of the simulations) are presented in Fig. 1. The FDs here were computed using point method, that is, for a given time interval of observation, flow is to the total number of vehicles passing through a given cross section (i.e., the observation point), space mean speed is approximated by the harmonic mean of the speeds of the passing vehicles, and consequently according to the fundamental equation of traffic flow, density equals to flow over space mean speed.

It seems that inclement weather does not directly impact the desired speed, safe time headway, and minimum distance; on the other hand, it is the increase of reaction time that leads to the transition of FDs from the clear weather scenario to the

Table 3 Parameter values after training

Parameter	Tick	I-66 (NC)	I-66 (IW)	I-495 (NC)	I-495 (IW)
v_0	5 mi/h	60 mi/h	60 mi/h	65 mi/h	65 mi/h
T	0.5 s	1.0 s	1.0 s	1.0 s	1.0 s
s_0	0.5 m	2.0 m	2.0 m	1.0 m	1.0 m
t_0	0.25 s	0.75 s	1.0 s	0.75 s	1.0 s

NC normal commute condition, *IW* inclement weather condition

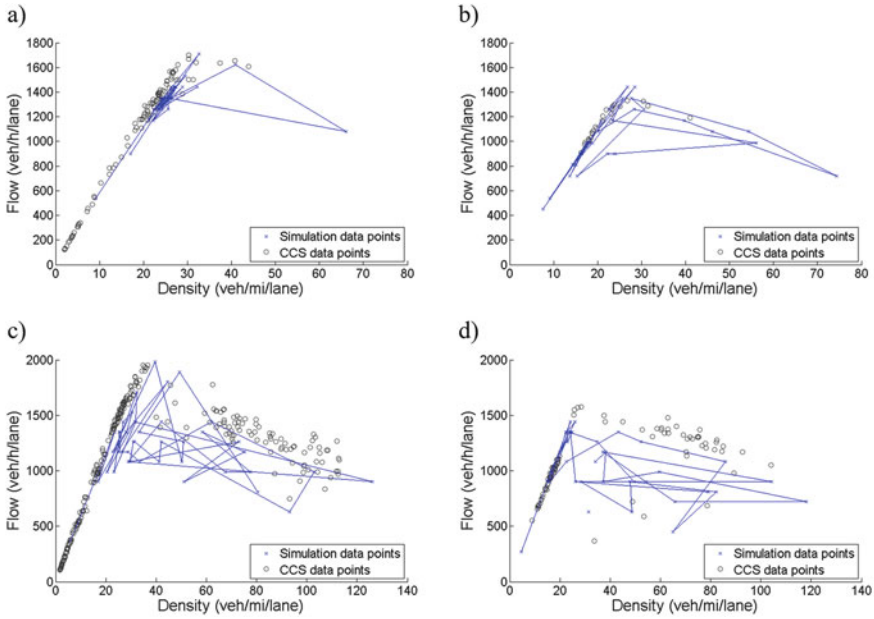

Fig. 1 FDs of I-66 and I-495 under different weather conditions. (**a**) FD of I-66 under clear weather. (**b**) FD of I-66 under inclement weather. (**c**) FD of I-495 under clear weather. (**d**) FD of I-495 under inclement weather

inclement weather scenario. Such outcome can be associated with the catastrophe theory that a small change in certain parameter can lead to a sudden change of the behavior of the corresponding (non-linear) system [8].

To further understand the influence of lane-changing behavior, the MOBIL parameters (i.e., politeness factor p and switch threshold Δa_{th}) were adjusted while controlling the IDM parameters. Based on the comparison of the trajectories in Fig. 2, it is found that when drivers are more selfish in lane-changing (i.e., politeness factor change from 1 to 0; see the comparison of Fig. 2a and c), the shock waves travel backward faster and longer; on the other hand, when drivers are more sensitive in lane-changing (i.e., switch threshold change from 1 to 0; see the comparison of Fig. 2a and e), there are more local perturbations at the bottleneck.

The trajectories are accompanied with FDs for better illustration. Note that to allow the understanding of traffic flow dynamics over a section of roadway, the FDs in Fig. 2 were computed using section method; that is, for a given timestamp, density is the number of vehicles over the length of the roadway section at the point of time, space mean speed is the average speed of the vehicles within the section, and consequently according to the fundamental equation of traffic flow, flow equals to the multiplication of density and space mean speed. It is obvious that the slopes between data points in the congestion regime in Fig. 2d are steeper than those in Fig. 2b, and Fig. 2f has wider span of data points in the congestion regime than in Fig. 2b, which are in line with the aforementioned findings, respectively.

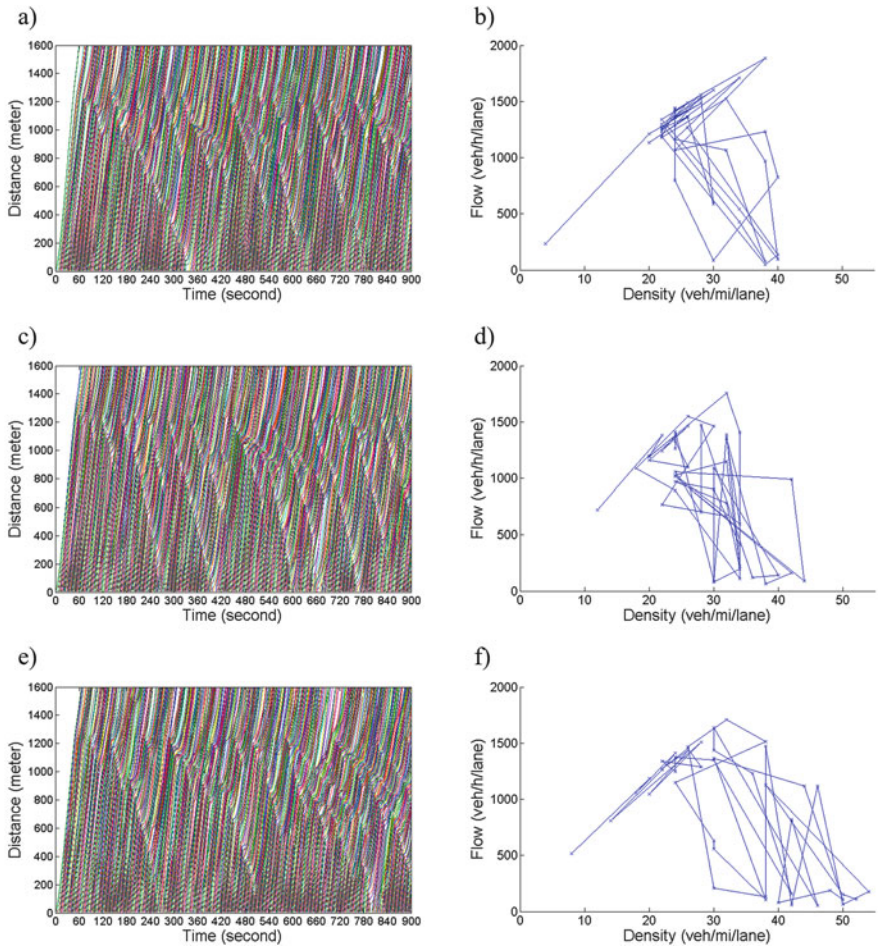

Fig. 2 Trajectories and FDs of I-495 with different lane-changing parameters. (**a**) Trajectory with $p = 1$, $\Delta a_{th} = 1$. (**b**) FD with $p = 1$, $\Delta a_{th} = 1$. (**c**) Trajectory with $p = 0$, $\Delta a_{th} = 1$. (**d**) FD with $p = 0$, $\Delta a_{th} = 1$. (**e**) Trajectory with $p = 1$, $\Delta a_{th} = 0$. (**f**) FD with $p = 1$, $\Delta a_{th} = 0$

5 Conclusions

In this study, a traffic flow simulation platform was built cooperating IDM (as the car-following algorithm) and MOBIL (as the lane-changing algorithm) with reaction time. Traffic data and weather data were mined to train the simulations in order to reproduce the traffic flow dynamics under different scenarios (i.e., with and without inclement weather). The model parameters of the simulations help revealing the underlying factors leading the congestions and the propagation of congestions. It is found that reaction time will affect the capacity level at a location of roadway and

thus the congestion formulation while the lane-changing will influence the traveling of shock waves over a length of roadway and thus the congestion propagation.

For future research, vehicle trajectory data is needed to calibrate the model parameters regarding lane-changing under different travel conditions; there is also a need of adjacent detector stations with shorter-time-interval records to further validate the congestion propagation over a length of roadway segment.

References

1. Saifuzzaman, M., Zheng, Z.: Incorporating human-factors in car-following models: a review of recent developments and research needs. Transp. Res. C Emerg. Technol. **48**, 379–403 (2014)
2. Gazis, D.C., Herman, R., Rothery, R.W.: Nonlinear follow-the-leader models of traffic flow. Oper. Res. **9**(4), 545–567 (1961)
3. Newell, G.F.: Nonlinear effects in the dynamics of car following. Oper. Res. **9**(2), 209–229 (1961)
4. Gipps, P.G.: A behavioural car-following model for computer simulation. Transp. Res. B Methodol. **15**(2), 105–111 (1981)
5. Treiber, M., Hennecke, A., Helbing, D.: Congested traffic states in empirical observations and microscopic simulations. Phys. Rev. E **62**(2), 1805 (2000)
6. Kesting, A., Treiber, M., Helbing, D.: General lane-changing model MOBIL for car-following models. Transp. Res. Rec. J. Transp. Res. Board **1999**, 86–94 (2007)
7. Kesting, A., Treiber, M., Helbing, D.: Enhanced intelligent driver model to access the impact of driving strategies on traffic capacity. Philos. Trans. R. Soc. Lond. A Math. Phys. Eng. Sci. **368**(1928), 4585–4605 (2010)
8. Persaud, B.N., Hall, F.L.: Catastrophe theory and patterns in 30-second freeway traffic data—implications for incident detection. Transp. Res. A Gen. **23**(2), 103–113 (1989)

Numerical Comparison Between Traffic Flow Models with and Without Adaptation Behavior

Alma Rosa Méndez, Rosa María Velasco, and Wilson Marques Jr.

Abstract When over-acceleration and adaptation effects are present in traffic situations which involve a mixture of vehicle classes, microscopic effects translate in the appearance of interesting traffic patterns, including the synchronized flow phase. The establishment of this situation has been studied in the literature. The aim of the present work is to compare numerically two different kinetic based models for a two-class system of aggressive drivers. Model I considers the adaptation effect whereas Model II does not allow its presence. As far as a numerical comparison concerns, it is only in Model I where traffic breakdown appears.

1 Introduction

The macroscopic approach to the study of traffic flow has provided us with several models to deal with the empirical characteristics shown in real traffic. Those models are based on different hypotheses which go from the analogies with compressible fluid mechanics [6], kinetic theory [1, 2, 12] up to discrete descriptions written in their continuum limit [3, 11] . In this work, we revisit a pair of models for a binary mixture of aggressive drivers in the highway based on the kinetic theory approach and work out the numerical comparison between them. Both models consider two drivers classes and they start with similar hypotheses about the drivers behavior. However in the first model (Model I), which has been reported in the literature [8, 9]

A. R. Méndez (✉)
Departamento de Matemáticas Aplicadas y Sistemas, Universidad Autónoma Metropolitana, Cuajimalpa, Mexico
e-mail: amendez@correo.cua.uam.mx

R. M. Velasco
Departamento de Física, Universidad Autónoma Metropolitana, Iztapalapa, Mexico
e-mail: rmvb@xanum.uam.mx

W. Marques Jr.
Departamento de Física, Universidade Federal do Paraná, Curitiba, Brazil
e-mail: marques@fisica.ufpr.br

S. H. Hamdar (ed.), *Traffic and Granular Flow '17*,
https://doi.org/10.1007/978-3-030-11440-4_15

it is shown that both, the adaptation and the over-acceleration effects give place to congested phases. The adaptation is observed when the more numerous class is the leading one and it is the only one that survives for long time. In contrast, the second model (Model II) does not have the adaptation terms, meaning that the drivers do not adapt to the traffic conditions [7]. Consequently the number of vehicles in each class is preserved.

2 The Macroscopic Traffic Models

The dynamic equations to be compared correspond to two different models which have been obtained from the Paveri-Fontana kinetic equation. The first model (Model I) is given in a detailed way in Refs. [8, 10] where it is shown how the synchronized phase of traffic can be found. The densities evolution equations for the two-class model read,

$$\frac{\partial \rho_i}{\partial t} + \frac{\partial \left(\rho_i v_i\right)}{\partial x} = (1-p)\rho\rho_i(v - v_i), \quad i = a, b \tag{1}$$

where ρ_i, v_i are the density and average speed of $i-$class, respectively, $\rho = \rho_a + \rho_b$ is the total density, $v = \left(\rho_a v_a + \rho_b v_b\right)/\rho$ is the barycentric velocity of the mixture, and p is the probability of overtaking, which is modeled as $(1-p) = \rho/\rho_0$ for both classes. The average speed satisfies the following equation:

$$\frac{\partial v_i}{\partial t} + v_i \frac{\partial v_i}{\partial x} + \frac{1}{\rho_i}\frac{\partial \left(\rho_i \theta_i\right)}{\partial x} = \frac{(\omega_i - 1)}{\tau_i} v_i - (1-p)\rho\theta_i, \quad i = a, b \tag{2}$$

where the speed variance reads

$$\rho_i \theta_i = \frac{\rho_i v_i^2}{\alpha_i}\left[1 - \frac{2(\alpha_i + 1)}{\sigma_i \alpha_i}\frac{\partial v_i}{\partial x}\right], \quad i = a, b. \tag{3}$$

Here $\alpha_i = \tau_i(1-p)\rho_e v_e/(\omega_i - 1)$ is a parameter which depends on the model characteristics given by the reaction time τ_i and the aggressivity ω_i, and σ_i is a collective relaxation time introduced to find an approximate solution for a collective distribution function. The steady and homogeneous state is denoted by the "e" subindex.

The numerical solution shown in Refs. [8, 10] corresponds to a simplified model obtained by an iterative procedure assuming a deviation from the fundamental diagram $v_i^{(0)}(x,t) = V_e\left(\rho_i(x,t)\right)$, $\hat{v}_i = v_i - v_i^{(0)}$, so we get

$$\hat{v}_i = -\frac{\rho v_i^{(0)2} \Gamma_i}{\left[\rho_e v_e - 2\rho v_i^{(0)}\right]}\frac{\partial v_i^{(0)}}{\partial x}, \tag{4}$$

when the average velocities v_i are written in terms of the partial densities ρ_i the result is a first order model for each class.

On the other hand, the second model (Model II) was introduced in Ref. [7]. The dynamical equations for the partial densities and average speeds read as

$$\frac{\partial \rho_i}{\partial t} + \frac{\partial (\rho_i v_i)}{\partial x} = 0, \quad i = a, b \tag{5}$$

$$\frac{\partial v_i}{\partial t} + v_i \frac{\partial v_i}{\partial x} + \frac{1}{\rho_i} \frac{\partial (\rho_i \theta_i)}{\partial x} = \frac{v_i^* - v_i}{\tau_i}, \quad i = a, b \tag{6}$$

where we have defined v_i^* as follows:

$$\begin{aligned} v_a^* &= \omega v_a - \tau_a (1 - p_a) \frac{\rho_a v_a^2}{\alpha}, \\ v_b^* &= \omega v_b - \tau_b (1 - p_b) \frac{\rho_b v_b^2}{\alpha} - \tau_b (1 - p_b) \rho_a (v_b - v_a)^2. \end{aligned} \tag{7}$$

In order to close the system (5)–(6) the traffic pressure is proposed

$$\rho_i \theta_i = \frac{\rho_i v_i^2}{\alpha} - \mu_i \frac{\partial v_i}{\partial x}, \quad i = a, b, \tag{8}$$

where μ_i is a constant. In this model it is assumed that $v_b > v_a$, which is a very hard constraint and difficult to achieve and preserve.

3 Comparison of the Models

It should be noticed that both models are constituted by nonlinear EDPs, all of them coupled through the relevant variables which are considered (ρ_a, ρ_b, V_a, V_b) but certainly they have inherent differences that difficult the comparison. The remarkable difference between those models is contained in the densities Eqs. (1) and (5). In the first model the density balance contains a source term, see Eq. (1), which allows the adaptation between classes, no matter that the total density is conserved. On the other hand, in the second model, the density for each class satisfies a conservation equation meaning that adaptation is not allowed, see Eq. (5). The momentum balance equations (2) and (6) have essentially the same structure for both models, but they are not exactly equal. Should be noted the differences between those equations in the diffusion coefficient (see Eqs. (3) and (8)) and the asymmetry of the quantities v_i^* in Eq. (7).

The overtaking probability p is usually modeled as $(1 - p) = \rho_{eff}$ where $\rho_{eff} = \rho/\rho_{max}$ and, as stated in [4] for the slow class-a, $\rho_{eff} = \rho_a/\rho_{max}$ while for the fast class-b, $\rho_{eff} = \rho/\rho_{max}$. In consequence, in Model I we suppose that ρ_{eff} is

proportional to the total density for both classes while in Model II we use the partial density for the slow class a and the total density for the fast class b. Additionally, should be noted the differences between Eqs. (3) and (8), in Eq. (8) the diffusion coefficient depends on the partial density while in Eq. (3) this coefficient depends on (ρ_i, v_i).

4 Numerical Results and Concluding Remarks

The onset of congestion is numerically observed in very special conditions. In Ref. [8] the authors find that over-acceleration is important in order to traffic breakdown appears [5]. Model I is a binary-class model where drivers can change their class, so the question is whether this mechanism is necessary for traffic breakdown happens. The numerical solution of Model I is obtained from the first order model obtained through (1–2) and (4) in Ref. [8]. The out of phase initial partial densities are shown in Fig. 1 (left), and the model parameters used for this simulation are shown in Table 1. The presence of synchronized traffic is shown in Fig. 1 (right) where the initial state is amplified and a fixed cluster appears around km 11.

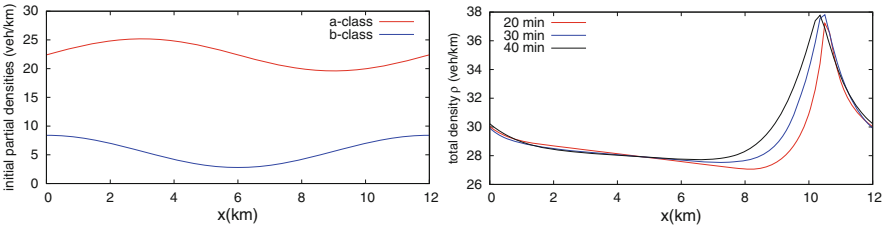

Fig. 1 The initial state for Model I (left) and the cluster fixed at km 11 (right)

Table 1 The set of parameters used in Model I and Model II where $\rho_0 = 140$ veh/km, $v_0 = 120$ km/h, and $\tau = 30$ s

Parameters	Model I	Model II
τ_a	τ	$10\,\tau$
τ_b	τ	τ
ω_a	–	1.02
ω_b	–	1.02
α_a	120	125
α_b	100	125
σ_a	0.0001τ	–
σ_b	0.0005τ	–
μ_a	–	v_0
μ_b	–	$5v_0$
ρ_e	$0.2\rho_0$	$0.4\rho_0$

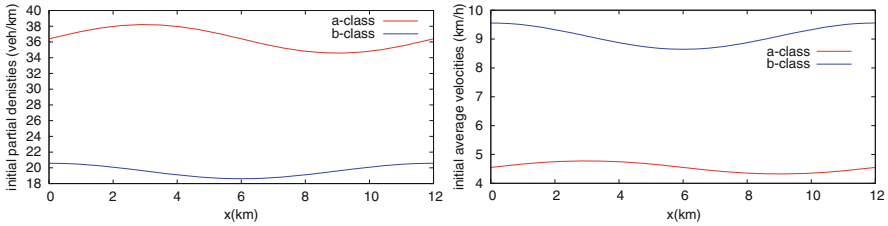

Fig. 2 The initial state for Model II: partial densities (left) and average velocities (right)

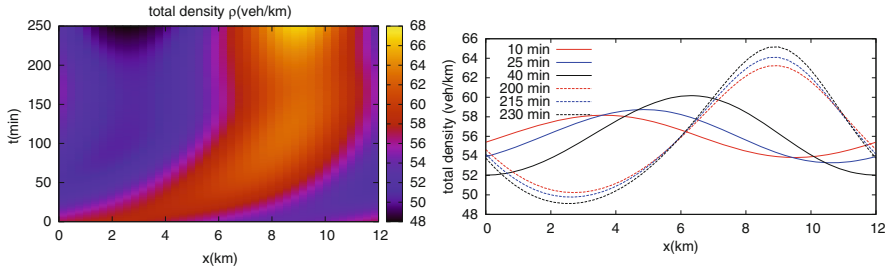

Fig. 3 The density evolution in Model II

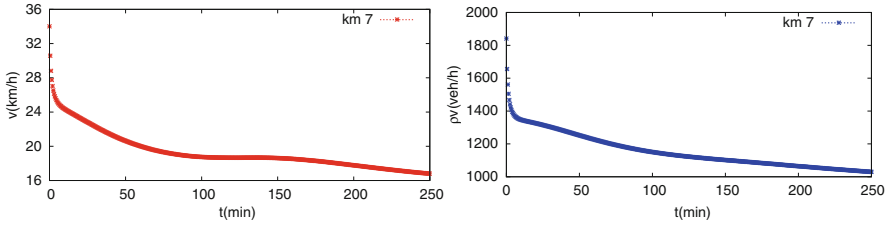

Fig. 4 The barycentric velocity and total flux as functions of time around km 7 (Model II)

On the other hand, Model II in Eqs. (5)–(6) was solved using a Lax–Wendroff scheme considering the initial condition shown in Fig. 2. Note that the initial state in Fig. 2 is slightly different from that in Fig. 1 (left) because Model II is a second order model, the initial state is out of phase also. The initial state $(\rho_a(x,0), \rho_b(x,0), v_a(x,0), v_b(x,0))$ is perturbed. One can elect the values $v_a(x,0)$ and $v_b(x,0)$ accordingly with the equilibrium state imposed by Eq. (7), in such a case Model II is strongly restricted by this fact and by the relation $v_a < v_b$. A number of parameters and initial states were variated searching for traffic breakdown. The numerical results shown in Fig. 3 correspond with the parameters in Table 1, in that case we observe the initial perturbation amplifies and travels downstream, after approximately 50 min a fixed structure appears around km 9 (see Fig. 3). In Fig. 4 we show the temporal evolution of the barycentric velocity and the total flow, we could not observe traffic breakdown in any position before the fixed structure appears.

The combination of over-acceleration and adaptation to traffic situation in Model I starts the development of synchronized traffic. Model II was probed with several sets of parameters and initial conditions and the results seem to be the same always, we have not been able to observe the emergence of the synchronized phase. In fact, the initial perturbation amplifies and a cluster appears traveling downstream, after a while there appears a localized structure around km 9 but traffic breakdown is not observed in this case (see Fig. 4). The characteristics of this pattern corresponds with free flow, so we may conclude that both adaptation and over-acceleration are necessary conditions to produce traffic breakdown.

Acknowledgement The authors acknowledge support from CONACyT through grant number CB2015/251273.

References

1. Bellomo, N., Delitala, M.: On the mathematical theory of vehicular traffic flow. I. Fluid dynamic and kinetic modelling. Math. Models Methods App. Sci. **12**(12), 1801–1843 (2002)
2. Bellomo, N., Marasco, A., Romano, A.: From the modelling of driver's behavior to hydrodynamic models and problems of traffic flow. Nonlinear Anal. Real World Appl. **3**, 339–363 (2002)
3. Berg, P., Mason, A., Woods, A.: Continuum approach to car-following models. Phys. Rev. E **61**(2), 1056–1066 (2000)
4. Hoogendoorn, S., Bovy, P.: Modeling multiple user-class traffic. Transp. Res. Rec. J. Transp. Res. Board **1644**, 57–69 (1998)
5. Kerner, B.S., Klenov, L.: Phase transitions in traffic flow on multilane roads. Phys. Rev. E **80**, 056101 (2009)
6. Kerner, B.S., Konhauser, P.: Cluster effect in initially homogeneous traffic flow. Phys. Rev. E **48**(4), R2335–R2338 (1993)
7. Marques, J.W., Velasco, R.M., Méndez, A.R.: A multi-class vehicular flow model for aggressive drivers. In: Knoop, V.L., Daamen, W. (eds.) Traffic and Granular Flow'15, pp. 475–482. Springer, Berlin (2016). https://doi.org/10.1007/978-3-319-33482-060
8. Méndez, A.R., Velasco, R.M.: Kerner's free-synchronized phase transition in a macroscopic traffic flow model with two classes of drivers. J. Phys. A Math. Theor. **46**, 462001 (2013). https://doi.org/10.1088/1751-8113/46/4/462001
9. Méndez, A.R., Velasco, R.M.: The stability analysis of a macroscopic traffic flow model with two-classes of drivers. In: Chraibi, M. et al. (ed.) Traffic and Granular Flow'13, pp. 525–531. Springer, Berlin (2015). https://doi.org/10.1007/978-3-10629-858
10. Méndez, A.R., Velasco, R.M.: The onset of traffic phases in highways: a two vehicle-class macroscopic model. Int. J. Pure Appl. Math. **112**(3), 531–556 (2017). https://doi.org/10.12732/ijpam.v112i3.7
11. van Wageningen-Kessels, F., van Lint, H., Vuik, K., Hoogendoorn, S.: Genealogy of traffic flow models. EURO J. Transp. Logist. **4**(4), 445–473 (2015)
12. Velasco, R.M., Marques Jr., W.: Navier-Stokes-like equations for traffic flow. Phys. Rev. E **72**, 046102 (2005). https://doi.org/10.1103/PhysRevE.72.046102

A Game-Theoretic Approach for Minimizing Delays in Autonomous Intersections

Robert P. Adkins, David M. Mount, and Alice A. Zhang

Abstract Traffic management systems of the near future will be able to exploit communication between vehicles and autonomous traffic control systems to significantly improve the utilization of road networks. In this work, a novel game-theoretic model for the traffic management of vehicles in intersections is introduced. A core concept from game theory that captures the important interplay between independent decision making and centralized control is the notion of a correlated equilibrium. We characterize the correlated equilibria under this model, yielding interesting connections to maximum-weight independent sets in graphs and maximal matchings in bipartite outerplanar graphs. We develop efficient algorithms for computing optimal correlated equilibria and demonstrate through simulations the effectiveness of our algorithms for improving traffic throughput.

1 Introduction

In this paper, we describe a model for intersection management using game-theoretic principles. The core of our model rests on the idea of a *correlated equilibrium* (CE). Here, the actions of agents are entrusted to an external entity, whose decisions—which may be probabilistic—satisfy the property that it is not in the interest of any agent to unilaterally deviate from the recommendations of this entity. In the context of traffic, drivers entrust their decisions to the traffic signals. It therefore makes intuitive sense that an intelligent traffic manager should use a CE as the basis for deciding how to best direct traffic. Other game-theoretic metrics exist, but are not used in this paper (see the work of Blum et al. [3]).

R. P. Adkins (✉) · D. M. Mount
Department of Computer Science, University of Maryland, College Park, MD, USA
e-mail: radkins2@umd.edu; mount@umd.edu

A. A. Zhang
Montgomery Blair High School, Silver Spring, MD, USA

S. H. Hamdar (ed.), *Traffic and Granular Flow '17*,
https://doi.org/10.1007/978-3-030-11440-4_16

Our model incorporates a vehicle-to-infrastructure (V2I) communication protocol (see [9] for more on V2I technology). We assume a V2I system that allows (a) vehicles to communicate their intended paths (e.g., turn left, go straight, turn right) and request permission; and (b) the infrastructure to perform computations and send permission approval. The Autonomous Intersection Management (AIM) project has demonstrated how an intersection management system can be designed in the case of fully autonomous vehicles [5]. We compare our algorithms for connected vehicles against AIM's reservation-based algorithm for autonomous vehicles in Sect. 6. The AIM group as well as Talebpour et al. show the advantages of game theory in modeling driver incentives and defining metrics for analysis (see [4] and [11]). Even so, Carlino et al. create a surrogate incentive (a currency used by vehicles) to support their game-theoretic model, whereas our approach models driver incentives directly through a function of delay the driver has suffered. The work by Papadimitriou and Roughgarden in designing time-efficient algorithms for computing CE in games that yield space-efficient representations served as early theoretical reassurance that CE as a solution concept could be a computationally viable choice [8].

2 Definitions

The full version of the paper gives more complete definitions [1] (or see, e.g., [7] for further information). The *Nash equilibrium* is the traditional standard for analyzing the choices of rational players in game theory. A generalization of the Nash equilibrium, which more accurately reflects situations where a centralized controller (in our case, the traffic system) can recommend strategy choices, is the *correlated equilibrium*. This is defined to be a probability distribution characterized by the random vector $X = (X_1, \ldots, X_n)$ describing the strategy choice of each player such that for every player i and for every pair of strategy choices $s_i, s_i' \in S_i$,

$$\sum_{s_{-i} \in S_{-i}} \left(u_i(s_{-i}, s_i) - u_i(s_{-i}, s_i')\right) \Pr\left[X = (s_{-i}, s_i)\right] \geq 0,$$

where s_{-i} is $s \in S_1 \times \cdots \times S_n$ without s_i and u_i is player i's utility. That is, no player can increase its expected utility by unilaterally deviating from X's value. In contrast to the Nash equilibrium, which requires exponential time to compute in the worst case, a CE can be computed in polynomial time [8]. Given a global utility function u, a CE maximizing u in expectation is called an *optimal correlated equilibrium*.

A useful concept for expressing games succinctly is a *graphical game*. Each player's utility depends only upon a subset of the other players, and these dependencies are represented as a graph in which an edge (u, v) exists when the utilities of players u and v depend upon each other. This property, which will hold for our formulations, reduces the complexity of a game's description, and hence decreases the time needed to compute CE. A treatment of CE in graphical games is given in [6].

3 Overview of Our Traffic Model

Each vehicle has an intended path through a single intersection. If two paths intersect, these vehicles should avoid entering the intersection at the same time (see Fig. 1a). We model each path as a node in a *conflict graph*, where two intersecting paths are connected by an edge (see Fig. 1b).

The paths serve as convenient surrogates for representing the vehicles' incentives. Therefore, the paths are the players in the game for this model. At any time, a path can either be "on" or "off," corresponding to whether vehicles traveling along the path are permitted through the intersection. It is the job of a system called the *intersection manager* to decide from one time interval to the next which paths are to be switched on and which are switched off. With an appropriate discretization of time, the intersection manager can alter its recommendation at periodic intervals.

Given paths $p_1, \ldots, p_n$ through an intersection, each path has the strategy set $\{0, 1\}$, where 0 corresponds to "off" (or "stop") and 1 to "on" (or "proceed"). Hence, the strategy space for this model is simply $\{0, 1\}^n$. Let $\delta(p_i)$ be a positive number representing the sum of delays for vehicles traveling along p_i. Define p_i's utility $u_i : \{0, 1\}^n \to \mathbb{R}$ as

$$u_i(s) = \begin{cases} 0 & \text{if } s_i = 0 \\ \delta(p_i) & \text{if } s_i = 1 \text{ and no other "on" path intersects } p_i \\ -f(p_i) & \text{otherwise,} \end{cases}$$

where s is a strategy profile as in Sect. 2 and f is some appropriate positively valued function. A collision is an undesirable event, justifying the negative utility for crossing paths. (Traffic management systems like AIM [5] may allow vehicles with intersecting trajectories to enter the intersection at the same time, but it assumes complete control of vehicle motions, thus preventing collisions from occurring.) With the intention to provide a balance between fairness and delay minimization, it seems natural to have the intersection manager calculate an optimal CE with respect to the global utility $u = \sum_i u_i$ then sample from this distribution for permitting vehicles through the intersection.

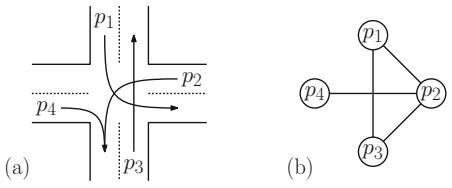

Fig. 1 (**a**) Configuration of paths and (**b**) conflict graph

4 Correlated Equilibria in Independent Set Games

An *independent set* in a graph is any subset of vertices that share no edge in common. Given the goal of avoiding collisions, it is natural that the strategies suggested by an intersection manager should correspond to independent sets in the conflict graph. Based on this principle, we introduce the concept of an *independent set game*. The possible profile vectors $s = (s_1, \ldots, s_n) \in \{0, 1\}^n$ are in one-to-one correspondence with subsets of vertices of the conflict graph G, where vertex i is included in the subset if and only if $s_i = 1$. We can assert $s \in IS(G)$, where $IS(G)$ denotes the collection of independent sets in G. We will denote vertex i's neighborhood as $N_i = \{j \mid (i, j) \text{ is an edge in } G\}$. Finally, we will write $N_i(s) = \sum_{j \in N_i} s_j$ to mean the sum of vertex i's neighbors in s. Note that $N_i(s) = 0 \Leftrightarrow \forall_{j \in N_i}\ s_j = 0$ and $N_i(s) > 0 \Leftrightarrow \exists_{j \in N_i}\ s_j = 1$. Vertex i's utility can therefore be expressed as

$$u_i(s) = \begin{cases} 0 & \text{if } s_i = 0 \\ a_i & \text{if } s_i = 1 \text{ and } N_i(s) = 0 \\ -b_i & \text{if } s_i = 1 \text{ and } N_i(s) >, \end{cases}$$

where $a_i, b_i > 0$.

We consider two types of independent set games. The first type, a *finite independent set game*, applies when $b_i < \infty$. The second type, an *infinite independent set game*, is the limiting case $b_i \to \infty$ as an extension of the finite case. Formally, given any positive sequence $b_i(n)$ for $n \geq 1$ such that $\lim_{n \to \infty} b_i(n) = \infty$, we require that there exists an N such that the CE constraints hold for all $b_i(n)$ where $n \geq N$. For the traffic application, this is a natural condition where a collision between two vehicles is assigned an infinitely high cost.

We first consider the finite case. By the definition of a CE we have the following.

Lemma 1 *A random vector X is a correlated equilibrium of a finite independent set game if and only if X satisfies*

$$\Pr[X_i = 1, N_i(X) = 0] \geq \frac{b_i}{a_i} \cdot \Pr[X_i = 1, N_i(X) > 0]$$

$$\Pr[X_i = 0, N_i(X) = 0] \leq \frac{b_i}{a_i} \cdot \Pr[X_i = 0, N_i(X) > 0].$$

(Due to space limitations, the proof of this and other results have been omitted from this version of the paper. They appear in the full version of the paper.)

Given that b_i denotes the penalty incurred by allowing the possibility of a collision, it is natural to ask whether there is some sufficiently large finite value of b_i that guarantees that X only evaluates to independent sets? Does an answer to this question require non-trivial restrictions on G? The answer is, surprisingly, contrary. (Again, the proof appears in the full version.)

Theorem 1 *If a finite independent set game with graph G has at least one edge, then there exists a correlated equilibrium X for which* $\Pr[X = s] > 0$ *for some* $s \notin IS(G)$.

We now consider the infinite case. Our analysis of this case will make use of a property of collections of independent sets. A collection of independent sets $\{V_1, \ldots, V_n\}$ is said to be *mutually maximal* if, for all V_i and vertices v, it holds that $v \notin V_i$ implies there is some V_j such that $V_j \cup \{v\}$ is not independent. Note that $\{V_1\}$ is mutually maximal if and only if V_1 is a maximal independent set.

Given this concept, we can characterize the distributions that are CE.

Theorem 2 *A random vector X is a correlated equilibrium of an infinite independent set game if and only if X evaluates to mutually maximal independent sets in the game graph.*

After exploring the nature of equilibria in independent set games, one may wonder how the optimal CE behaves. We will set the global utility function as $u = \sum_i u_i$ and weight each vertex i in the graph by a_i. The ensuing result is quite interesting and holds for both finite and infinite independent set games.

Theorem 3 *A random vector X is an optimal correlated equilibrium of an independent set game with respect to the global utility $u = \sum_i u_i$ if and only if X evaluates to maximum-weight independent sets in the weighted game graph.*

5 Independent Sets and Non-crossing Matchings

In this section we consider how to compute maximum-weight independent sets in the conflict graph. In general, computing maximum independent sets is known to be hard, even to approximate (see, e.g., [2]). But here, n is practically bounded by the size of intersections, and we can exploit special properties of these graphs to obtain efficient solutions. We present two algorithms. The first is a simple and efficient greedy heuristic, which does not necessarily generate an optimal solution. The second, which is based on dynamic programming, guarantees an optimal solution, but it has higher computational complexity.

A single intersection is given, which is modeled as a central resource that is surrounded by a circular collection of lanes, radiating outwards from the intersection. Each lane is directed either into the intersection (*in-lane*) or out from the intersection (*out-lane*). For example, in Fig. 2a, the lanes with odd indices are in-lanes and the lanes with even indices are out-lanes. A graph G is given, each of whose edges represents a path along which vehicles wish to travel. Its nodes are the lanes and each edge p consists of one in-lane and one out-lane (see Fig. 2b). A *matching* M is a subset of edges of G, such that each node of G is an endpoint of at most one edge of M. A matching is *non-crossing* if the path associated with the edges of the matching do not conflict with each other (see Fig. 2c). The *weight* of a matching is $u(M)$. Given G and the δ values for its paths, it is easy to see

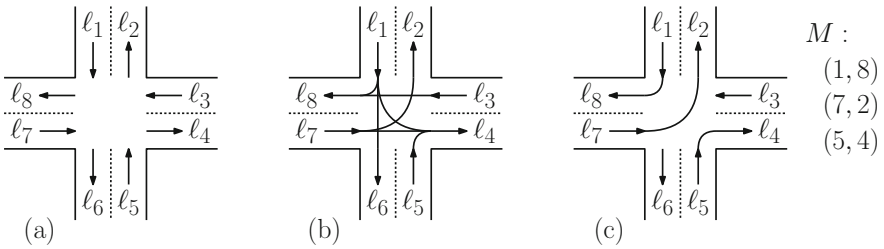

Fig. 2 An intersection and a non-crossing matching

Algorithm 1: Greedy heuristic for a maximum-weight independent set

```
1 Greedy(P[n])
2     M ← ∅;
3     P′ ← sort P by delay;
4     foreach (p ∈ P′) do
5         if doesNotCross(p, M) then
6             M ← M ∪ {p};
```

that an independent set of maximum weight in the conflict graph is equivalent to a non-crossing matching M that maximizes $u(M)$ in the intersection graph.

We first present a simple greedy heuristic to determine which paths to admit (see Algorithm 1). Let P be the set of all paths through the intersection (of the form (i, j) as in Fig. 2). Recall that for each path $p \in P$, $\delta(p)$ denotes the summed delays of vehicles traveling along p. A simple greedy heuristic is to sort P in the decreasing order of $\delta(p)$, and include a path p in the non-crossing matching if it does not cross any previously selected path.

We next present a more sophisticated dynamic-programming algorithm. While our dynamic-programming algorithm is slower than the greedy heuristic, it is guaranteed to compute an independent set of maximum weight. The intersection is modeled as a graph whose vertices correspond to the entry–exit points of the lanes, and edges correspond to paths. Define $G_{i,j}$ to be the induced subgraph consisting of the vertices from i to j in clockwise order about the intersection. Define $W[i, j]$ to be the weight of the maximum non-crossing matching on this subgraph. The dynamic-programming presented in Algorithm 2 computes $W[i, j]$ by considering all possible ways of connecting i to another vertex k in the $[i, j]$ interval, and then recursively solving the two subproblems, from $[i + 1, k - 1]$ and $[k + 1, j]$.

Algorithm 2: DP algorithm for a maximum-weight non-crossing matching

```
1  ComputeWeight(δ[n, n])
2      for (d ← 1 to n − 1) do                    // length of the vertex interval
3          for (i ← 0 to n − d − 1) do             // first vertex of the interval
4              j ← i + d;                           // last vertex of the interval
5              wt ← W[i + 1, j];
6              G′ ← induced(G, i, j);                  // induced subgraph on [i, j]
7              foreach (k adjacent to i in G′) do              // try path (i, k)
8                  curr ← δ[i, k] + W[i + 1, k − 1] + W[k + 1, j];
9                  wt ← max(wt, curr);
10             W[i, j] ← wt;
```

6 Experimental Results

We wrote an intersection simulator that implements the greedy and DP algorithms from the previous section, and we compare the queueing behavior in our system versus other systems. Define $Q_{T,L}$ as the number of vehicles with zero velocity in lane L after simulator time step T. Then, let $Q_T = \max_L Q_{T,L}$. We define the *average max queue length* as $\bar{Q}_T = (1/T) \sum_{t \leq T} Q_t$.

Figure 3 shows the effect of traffic flow on $\bar{Q}_{100,000}$ corresponding to 33 min of simulated physical time. Note that the $\bar{Q}_{100,000}$ values approach an asymptote due to the lane capacity in the simulations. We confirm the common knowledge that stop signs are more effective than traffic lights for low traffic flows, but traffic lights are more effective for higher traffic flows. However, our greedy algorithm outperforms both of these systems, and is able to handle much higher traffic flows without filling the lane capacities. While the AIM reservation-based protocol from UT Austin [5] can handle higher traffic flows, our system supports the weaker assumption of connected vehicles as opposed to the fully autonomous vehicles of AIM. Finally, the optimal CE minimizes delay while simultaneously ensuring a certain degree of fairness. Smith and Gali [10] support the notion that it is often desirable to constrain delay minimization in traffic networks by some notion of fairness.

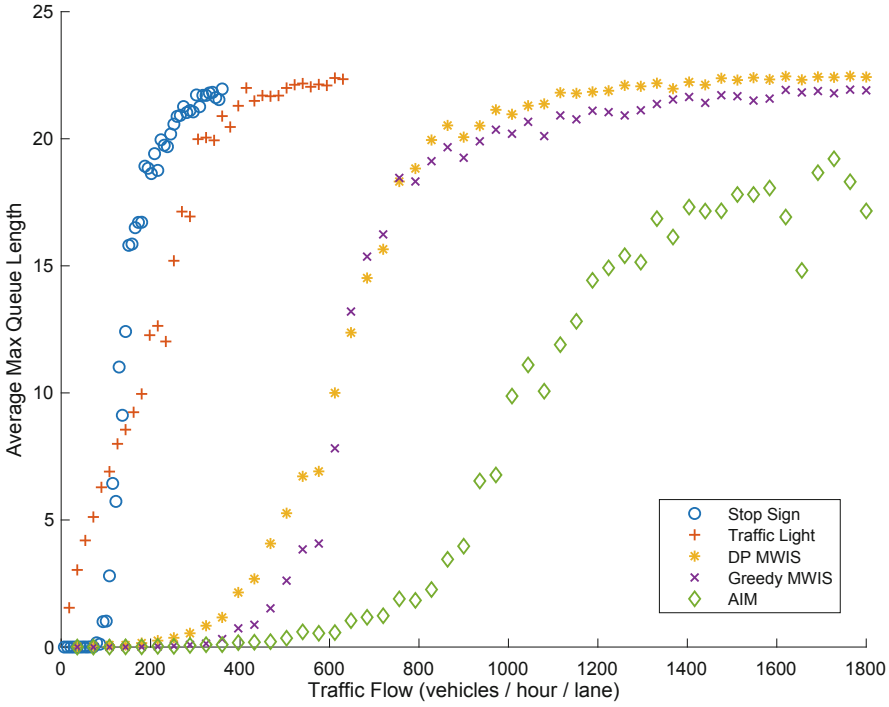

Fig. 3 Effect of traffic flow on average max queue length

7 Conclusion

We showed that our game-theoretic traffic model based on delay and safety reduces to an independent set game. Theorems 1 and 2 show that if one wants to prohibit the possibility that vehicles could accept an accident with small probability, then the model needs to assign an infinite cost to an accident. Theorem 3 shows that regardless of the choice of cost, a coordinating agent can select a maximum-weight independent set and guarantee an optimal CE. Our experimental simulations show that our approach for connected vehicles allows more throughput than standard control mechanisms yet less throughput than AIM's reservation-based protocol for fully autonomous vehicles. Therefore, our approach provides practical improvement over current methods while vehicles on the road are not yet fully autonomous.

Acknowledgement Research supported by NSF grant CCF-1618866.

References

1. Adkins, R., Mount, D., Zhang, A.: A game-theoretic approach for minimizing delays in autonomous intersections (2017). http://www.cs.umd.edu/~mount/pubs.html#tgf2017
2. Berman, P., Schnitger, G.: On the complexity of approximating the independent set problem. Inf. Comput. **96**(1), 77–94 (1992)
3. Blum, A., Hajiaghayi, M., Ligett, K., Roth, A.: Regret minimization and the price of total anarchy. In: Proceedings of the Fortieth Annual ACM Symposium on Theory of Computing, pp. 373–382. ACM, New York (2008)
4. Carlino, D., Boyles, S.D., Stone, P.: Auction-based autonomous intersection management. In: Proceedings of IEEE Conference on Intelligent Transportation Systems (ITSC), pp. 529–534 (2013)
5. Dresner, K., Stone, P.: Multiagent traffic management: a reservation-based intersection control mechanism. In: Proceedings of 3rd International Joint Conference on Autonomous Agents and Multiagent Systems, pp. 530–537 (2004)
6. Kakade, S., Kearns, M., Langford, J., Ortiz, L.: Correlated equilibria in graphical games. In: Proceedings of the 4th ACM Conference on Electronic Commerce, EC'03, pp. 42–47. ACM, New York (2003)
7. Nisan, N., Roughgarden, T., Tardos, E., Vazirani, V.: Algorithmic Game Theory. Cambridge University Press, New York (2007)
8. Papadimitriou, C.H., Roughgarden, T.: Computing correlated equilibria in multi-player games. J. Assoc. Comput. Mach. **55**, 14:1–14:29 (2008)
9. Priemer, C., Friedrich, B.: A decentralized adaptive traffic signal control using v2i communication data. In: 2009 12th International IEEE Conference on Intelligent Transportation Systems, pp. 1–6 (2009)
10. Smith, M.J., Ghali, M.: The dynamics of traffic assignment and traffic control: a theoretical study. Transp. Res. B **24B**, 409–422 (1990)
11. Talebpour, A., Mahmassani, H.S., Hamdar, S.H.: Modeling lane-changing behavior in a connected environment: a game theory approach. Transp. Res. Proc. **7**, 420–440 (2015). 21st International Symposium on Transportation and Traffic Theory Kobe, 5–7 August, 2015

Part II
Pedestrian Traffic: Analytical and Empirical Studies

Empirical Evaluation of Crowds Using Automated Methods

Muhammad Baqui, Michelle Isenhour, and Rainald Löhner

Abstract This work presents a novel framework for automated monitoring of high density crowds from closed circuit television (CCTV) image data. The framework obtains pedestrian velocities from particle image velocimetry (PIV) technique and densities from a boosted ferns machine learning model. A pinhole camera based perspective correction scheme is employed to convert the 2D pixel coordinates into 3D metric coordinates. The framework is trained with and tested against real-world event data from the Hajj.

1 Introduction

Video and image data have played a major role in revealing the dynamics and movement of crowds. There has been a variety of works done with video image data that contribute in exploring various aspects of pedestrian dynamics. Schadschneider et al. [13] used video data from experiments to describe the dynamics of pedestrian crowd behavior. Damien [3] used it to optimize parameters for the SimPed simulation tool. Hoogendoorn et al. [8] also used video data to obtain pedestrian flow properties. Although there have been numerous studies of pedestrian movement in controlled settings, the number of studies in high density crowds is quite limited. Individual safety is the prime reason: as the pedestrian density increases and a crowd forms, individual safety becomes a major concern. An alternative to experiments with high density crowds could be studying video data of large crowd events such as the Hajj, the World Youth Day, or the Chinese New Year celebration. An automated approach for extracting flow properties (pedestrian speed, density) from video could provide valuable insights into high density crowds. In this context,

M. Baqui (✉) · R. Löhner
George Mason University, Fairfax, VA, USA
e-mail: mbaqui@gmu.edu; rlohner@gmu.edu

M. Isenhour
Naval Post Graduate School, Monterey, CA, USA
e-mail: mlisenho@nps.edu

S. H. Hamdar (ed.), *Traffic and Granular Flow '17*,
https://doi.org/10.1007/978-3-030-11440-4_17

the current work proposes an automated framework to extract flow properties of high density crowds. The framework obtains crowd velocities from a PIV technique and densities from a boosted ferns machine learning model on crowd images. Once the pedestrian flow properties are obtained, a pinhole based perspective correction scheme is incorporated to convert the image data into real-world metric coordinates.

The paper is organized in the following manner, Sect. 2 demonstrates how the methods for extracting flow properties were applied to empirical data from the Hajj and Sect. 3 provides the results from a temporal study of the event.

2 Empirical Evaluation of the Hajj

This section will outline the pedestrian velocity and density extraction techniques and demonstrate how those techniques were tested using high-resolution images of the Hajj. Two types of image datasets from the Hajj were studied. A set of 50 time-lapse photos (5760 × 3840 pixels) captured at 3 fps and a 6 min video (1920 × 1080 pixels) captured at 25 fps. These images were obtained from surveillance cameras mounted inside the Grand Mosque. The video data was converted into 150 time-lapse photos for processing.

2.1 Velocity Extraction

Particle image velocimetry [1, 11] or PIV technique is widely used to obtain instantaneous velocity measurements of fluid flows. We adapted the PIV algorithm to evaluate velocities from successive images of a high density moving crowd. To use the technique, we divided each image into equally spaced blocks, commonly referred to as spot sizes. For our high-resolution test images (5760 × 3840 pixels), an interrogation spot size of 150 × 150 pixels was used, which is approximately equivalent to the width of one person in the image. For each block, the PIV technique obtains pixel displacements by performing cross correlation from one block on an image frame to the next. Given relative displacements and frame frequency, pedestrian instantaneous velocities are computed. More information on our adaption of the PIV extraction technique can be found in [2].

An example image from the Hajj and the corresponding PIV extracted velocity vectors are shown in Fig. 1. It can be seen that the vectors accurately denote the circular nature of the flow of the pedestrians. To have a clearer look at the motion pattern, two magnified views with velocity vectors are shown in Fig. 1. More results on velocities obtained from the adapted PIV technique can be found in [2].

Fig. 1 Input image and vectors of first dataset. Magnified views accurately show the direction of crowd movement

2.2 Density Extraction

In order to obtain crowd density from the Hajj images, we needed a method to automatically count the number of individuals occupying each unit area of the image. We obtained this count using a set of training images, a histogram of oriented gradients (HOG) feature extraction algorithm [4] provided by Dollar [6], and a boosted ferns regression machine learning model (see Algorithm 1). The machine learning model was trained with manually annotated counts (ground truths).

The HOG technique obtains localized occurrences of image gradients for a given image frame. An example image block from the Hajj and the corresponding HOG descriptor is shown in Fig. 2.

The pedestrian counts for each of the training images were manually annotated and their corresponding ground truth locations were provided in the form $(x_1, y_1), (x_2, y_2), \ldots, (x_n, y_n)$ where n is the number of training images (100 in this case). The goal of Algorithm 1 is to formulate an approximate function $F : x \rightarrow y$ that minimizes dissimilarity between the ground truth and the model prediction via a step-wise loss function. A squared loss function is considered in the form

Algorithm 1: Boosted regression

Input: training set $(x_i, y_i)_{i=1}^{n}$, a differentiable loss function L(y,F(x)), number of iteration M.
Algorithm:
1. Initialize the model with training data.
2. compute F_0
$F_0 = \text{argmin} \sum_{i=1}^{n} L(y_i, w)$
3. For m=1 to M:
(a) Compute residual
$r_{im} = \frac{\partial L(y_i, F)}{\partial F}$, i=1, . . .,n.
(b) Fit decision tree h_m to residual, i.e., train it with the training set $(x_i, r_{im})_{i=1}^{n}$
(c) Compute weights w_m by solving the following line search problem
$w_m = \arg\min_w \sum_{i=1}^{n} L(y_i, F_{m-1} + w\, h_m)$
(d) update the model
$F_m = F_{m-1} + w_m h_m$
4. Output F_M

Fig. 2 Input image **(a)** and corresponding HOG histogram plot **(b)**. HOG features are used to train the machine learning model

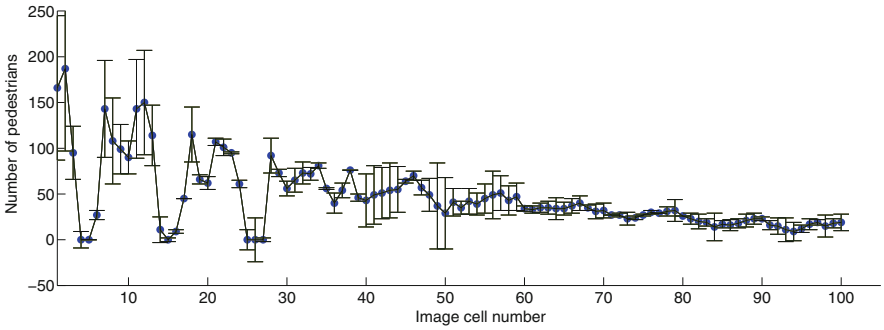

Fig. 3 Ground truth pedestrian counts per block with prediction error as error bars

of $(y' - y)^2$, where y' is the model prediction and y is the corresponding ground truth (known values). More details on the boosted regression algorithm can be found in [7].

Each individual input image (5760×3840 pixels) was divided into 100 individual subimages (blocks) of 576×384 pixels. In Fig. 3, the individual block numbers are presented along the x axis. These blocks are numbered sequentially from top left to the bottom right of the test image. The circular dots represent blockwise head counts from the machine learning model. The error bars, on the other hand, represent the difference between the machine learning and ground truth count. As one can see, in some blocks the model overestimates and in some it underestimates the head counts. However, the cumulative count from all these blocks is found to be close to the ground truth.

The crowd density of a particular block is obtained by dividing the count (obtained from regression model) by the area of the block. In order to compute the area, the four corners of the blocks are first converted to the metric (world) coordinates following the method outlined in the next Sect. 2.3.

Table 1 Comparison of actual location vs projected location

World x (m)	World y (m)	World z (m)	Projected x (m)	Projected y (m)	Projected z (m)	Error (person width)
1.77	15.35	0.0	2.54	14.65	0.0008	2.08
−1.84	15.40	0.0	−0.183	15.39	0.0008	2.02
5.85	−6.52	0.0	4.09	−6.31	0.0008	3.54
−4.27	5.52	0.0	−4.87	5.18	0.0008	1.37

2.3 Perspective Correction

Both pedestrian densities and velocities need to be transformed to metric coordinates. Since the images have known landmarks, we were able to use these locations as reference points to approximate the intrinsic and extrinsic camera parameters and therefore convert all of the pixel coordinates to real-world coordinates. A more detailed description of the projective geometry and pinhole camera model used to correct the perspective can be found in [2].

In Table 1 the accuracy of the perspective correction process can be seen for four landmark points visible in the Hajj images. The error is defined as the ratio of difference of projection and actual points to the width of a person. The width of a person is taken from [12]. The error column indicates the number of people that can be accommodated in the difference of the projected and actual points. It can be seen that the maximum amount of error incorporated during the projection is 3.54. Which means the actual location of pedestrian may be off by a maximum of 4 body width.

3 Temporal Study of the Hajj

The turbulent and ever changing nature of high density pedestrian traffic has been reported in a number of studies done before [5, 9]. In this section, the temporal evolution of high density crowds is explored with the tools outlined in this paper.

Density: Fig. 4 shows two crowd density plots created using the machine learning model on two of the high-resolution images taken 4 s apart. One can see the areas where density changes are substantial between t = 0 s and t = 4 s. The two plots depict the highly evolving nature of crowd turbulence and the need for efficient tools capable of instantaneously monitoring crowd density.

Vorticity and Streamlines: Turbulence has been reported repeatedly for high density crowds [9, 10]. Vorticity and streamlines are two very common metrics that can be used to report instantaneous properties of the flow [turbulence]. Vorticity values represent the amount of spinning motion experienced in a local flow. Streamlines, on the other hand, are a collection of curves that are instantaneously

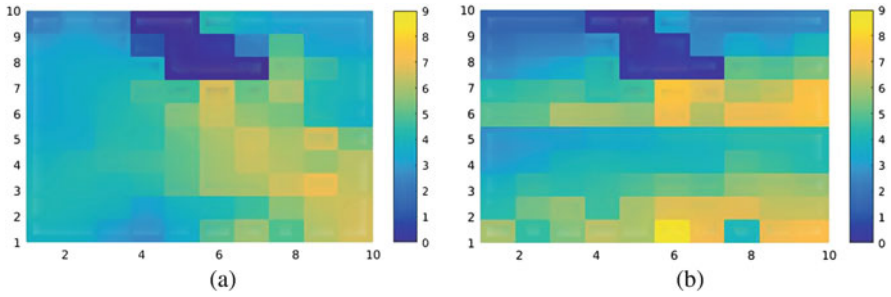

Fig. 4 Dynamic nature of crowd density **(a)** density at t = 0 s, **(b)** density at t = 4 s. Areas of high density change is rapid within 4 s

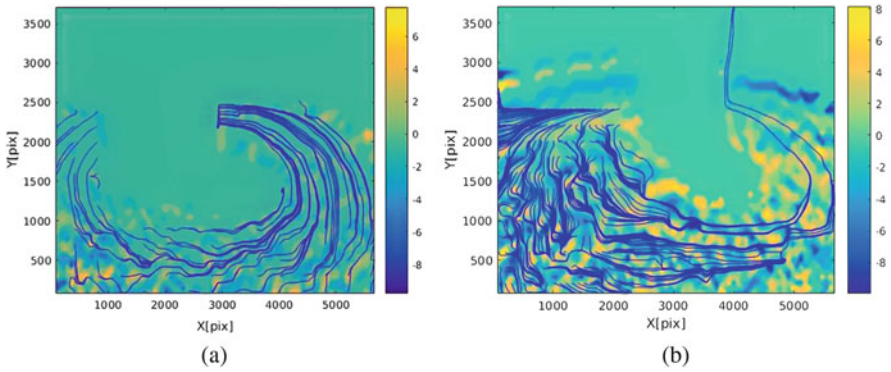

Fig. 5 Change in vorticity and streamlines at **(a)** low density crowd, **(b)** high density crowd. Streamlines appear unsteady at high density. More areas with higher amount of vorticity is visible

tangent to the direction of the flow. Streamlines can instantaneously capture the unsteady nature of the flow.

In Fig. 5 the crowd velocity streamlines superimposed on the vorticities can be seen for both low and high crowd densities of the same image. In the low density situation the flow experiences less unsteadiness so only few unstable areas are seen. The high density image has more areas of higher vorticity and the streamlines appear to vacillate fairly significantly.

The temporal change of streamlines of high density flows is captured in the plots shown in Fig. 6. The snapshots are taken at evenly spaced intervals (100 s). A closer look of the streamlines at t = 0 s and t = 253 s reveals a chaotic transformation of the streamlines along the temporal dimension. The vorticity and streamlines plots in this way can provide supplemental flow information at any given time.

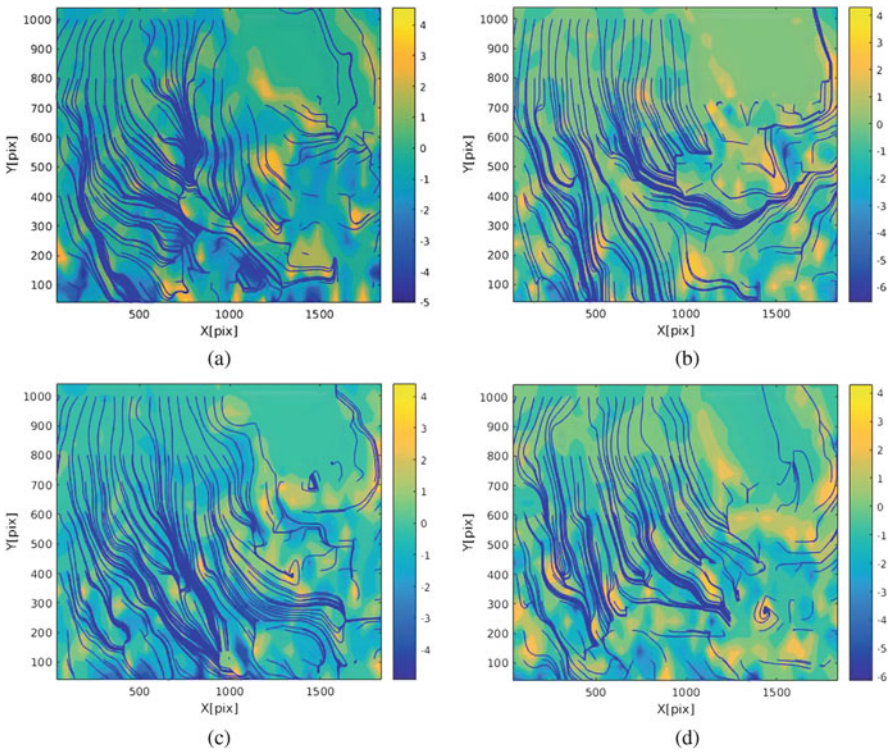

Fig. 6 Dynamic nature of high density crowd captured through vorticity–streamlines plot: **(a)** t = 0 s, **(b)** t = 80 s, **(c)** t = 180 s, **(d)** t = 250 s. Unsteady and erratic streamlines are often seen with crowds of high density

Additionally, the vorticity and streamline plots may be useful when the CCTV image resolution is poor (i.e., not in 5760 × 3840 level) and areas for which no training data is available to train the regression based machine learning model.

4 Conclusions

A framework was presented to automatically extract crowd fundamental properties from image data. For velocity, the PIV technique was used; for density, a machine learning model was constructed with boosted ferns regression. A pinhole camera based projective transformation was applied to convert the results from pixel to real-world coordinates. Accuracy of the individual components of the model was tested against empirical data from the Hajj. The results conform to the earlier studies of similar type crowd events.

References

1. Adrian, R.: Particle-imaging techniques for experimental fluid-mechanics. Annu. Rev. Fluid Mech. **23**, 260–304 (1991)
2. Baqui, M., Löhner, R.: Real-time crowd safety and comfort management from CCTV images. pp. 10223–10223–14 (2017). http://dx.doi.org/10.1117/12.2262319
3. Daamen, W.: Modelling passenger flows in public transport facilities. DUP Science Deflt, Delft (2004)
4. Dalal, N., Triggs, B.: Histograms of oriented gradients for human detection. In: IEEE Computer Society Conference on Computer Vision and Pattern Recognition, 2005 (CVPR 2005), vol. 1, pp. 886–893. IEEE, San Diego (2005)
5. Dambalmath, P., Muhammad, B., Haug, E., Löhner, R.: Fundamental diagrams for specific very high density crowds. In: Proc. Pedestrian and Evacuation Dynamics, pp. 6–11. University of Science and Technology Press, Hefei (2016)
6. Dollár, P.: Piotrs image and video matlab toolbox (PMT). https://pdollar.github.io/toolbox/ (2013)
7. Elith, J., Leathwick, J.R., Hastie, T.: A working guide to boosted regression trees. J. Anim. Ecol. **77**(4), 802–813 (2008)
8. Hoogendoorn, S.P., Daamen, W., Bovy, P.H.: Extracting microscopic pedestrian characteristics from video data. In: Transportation Research Board Annual Meeting, Washington, pp. 1–15 (2003)
9. Johansson, A., Helbing, D., Al-Abideen, H.Z., Al-Bosta, S.: From crowd dynamics to crowd safety: a video-based analysis. Adv. Complex Syst. **11**(04), 497–527 (2008)
10. Johansson, A., Batty, M., Hayashi, K., Al Bar, O., Marcozzi, D., Memish, Z.A.: Crowd and environmental management during mass gatherings. Lancet Infect. Dis. **12**(2), 150–156 (2012)
11. Keane, R., Adrian, R.: Optimization of particle image velocimeters. Part I. Double pulsed systems. Meas. Sci. Technol. **11**(1), 1202–1215 (1990)
12. Predtechenskii, V., Milinskii, A.: Planning for foot traffic flow in buildings. National Bureau of Standards, US Department of Commerce, and the National Science Foundation, Washington, DC (1978)
13. Schadschneider, A., Klingsch, W., Klüpfel, H., Seyfried, A.: Evacuation dynamics: empirical results, modeling and applications. Encycl. Complexity Syst. Sci. 3142–3176 (2008). https://doi.org/10.1007/978-1-4419-7695-6

Micro and Macro Pedestrian Dynamics in Counterflow: The Impact of Social Groups

Luca Crociani, Andrea Gorrini, Claudio Feliciani, Giuseppe Vizzari, Katsuhiro Nishinari, and Stefania Bandini

Abstract Although it is widely recognised that the presence of groups influences microscopic and aggregated pedestrian dynamics, a precise characterisation of the phenomenon still calls for evidences and insights. The present paper describes micro- and macro-level original analyses on data characterising pedestrian behaviour in the presence of counterflows and grouping, in particular dyads, acquired through controlled experiments. Results suggest that the presence of dyads and their tendency to walk in a line-abreast formation influences the formation of lanes and, in turn, aggregated observables, such as overall specific flow.

1 Introduction

Research on pedestrian dynamics has systematically analysed the influence of group behaviour only in the last years (see, e.g., [2, 8, 10]): although observations and experiments agree on some aggregated and microscopic effects of the presence of groups (e.g. group members walk slower than individuals), there is still need for additional insights, for instance, on the spatial patterns assumed by groups in their movement and in general on the interaction among different factors influencing overall pedestrian dynamics (e.g. do obstacles still make egress from a room smoother in the presence of groups?). Models incorporating mechanisms

L. Crociani (✉) · A. Gorrini · G. Vizzari
CSAI Research Center, University of Milano-Bicocca, Milan, Italy
e-mail: Luca.Crociani@disco.unimib.it; Andrea.Gorrini@disco.unimib.it; Giuseppe.Vizzari@disco.unimib.it

C. Feliciani · K. Nishinari
The University of Tokyo, Tokyo, Japan
e-mail: feliciani@jamology.rcast.u-tokyo.ac.jp; tknishi@mail.ecc.u-tokyo.ac.jp

S. Bandini
CSAI Research Center, University of Milano-Bicocca, Milan, Italy

The University of Tokyo, Tokyo, Japan
e-mail: stefania.bandini@disco.unimib.it

S. H. Hamdar (ed.), *Traffic and Granular Flow '17*,
https://doi.org/10.1007/978-3-030-11440-4_18

reproducing the cohesion of group members, in fact, are just partially able to reproduce overall phenomena related to the presence of groups in the simulated population of pedestrians (see, e.g., [1] in which groups preserve their cohesion and they move slower than individuals) and they would benefit from additional insights on how members manage their movements balancing (for instance) goal orientation, tendency to stay close to other members, opportunities offered by the presence of lanes.

In this framework, the present work discusses results of experiments carried out to investigate the potentially combined impact of counterflow situations [13] and grouping [11]. Experiment 1 [5] tested the impact of four different configurations of counterflow in a corridor setting (from uni-directional to fully balanced bi-directional flow). Experiment 2 [7] replicated the same procedures and about half of participants were paired to compose dyads (the simplest and most frequent type of group), asking them to walk close to their companion. In the following, both the experimental procedures and the achieved results will be presented in detail.

2 Description of Experiments

The two experiments have been performed on June 13, 2015 at the Research Center for Advanced Science and Technology of the University of Tokyo (Tokyo, Japan). Experiments have been executed in a corridor-like setting composed as in Fig. 1. The central area of 10×3 m^2 was recorded for the tracking of participants and it was surrounded by two start areas of 12×3 m^2 and two buffer zones of 2 m length that allowed participants to reach a stable speed at the measurement area. Participants were asked to wear coloured caps so that trajectories could be automatically recorded with the software *PeTrack*[3].

Each experiment was composed of four procedures, to which 54 male students participated. To achieve a more consistent dataset, every procedure was iterated four times. The aim of the whole investigation has been to test the following hypotheses: (Hp1) the increase of flow ratio negatively impacts the speed of pedestrians; (Hp2)

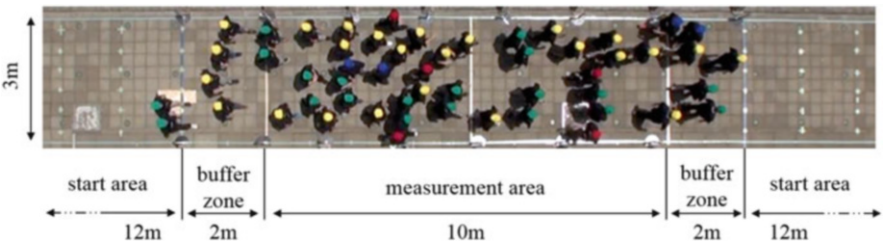

Fig. 1 A screenshot from the video of the experiments and a schematic representation of the setting

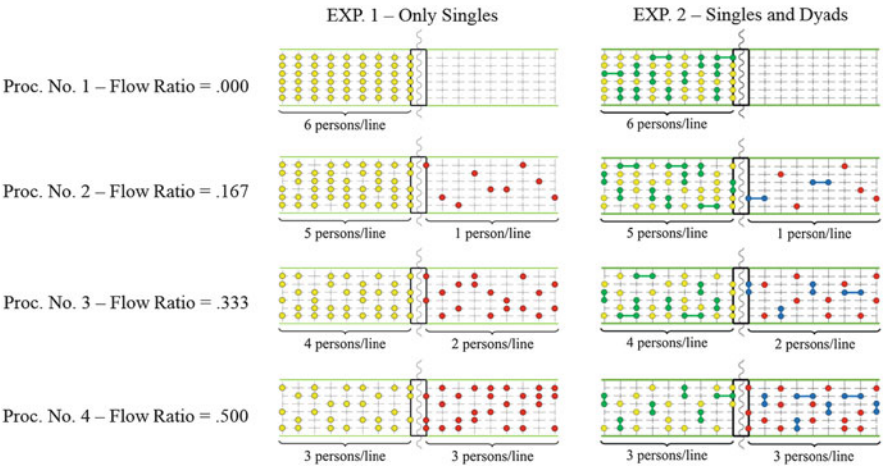

Fig. 2 Experiments and procedure tested in this investigation

the cohesion of dyad members affects their speed; (Hp3) the cohesion of dyads leads to a lower pedestrian flow at a macroscopic level.

With *flow ratio* we denote the rate between the *minor flow* and the *total flow* in bi-directional scenarios. Flow ratio was managed as independent variable among four experimental procedures, as graphically exemplified in Fig. 2.

At the beginning of each iteration and according to the tested flow ratio, pedestrians were placed in the marked positions of the start areas. Figure 2 exemplifies the arrangement in all experimental procedures. In case of Exp. 2, roughly 44% of the participants (24 out of the 54 total) was configured as dyads. These were formed by coupling two random members and asking them to possibly walk close to the other companion during the iteration. As shown in Fig. 2, dyads could be initially disposed either in *line abreast* or *river-like* pattern, except in Proc. 2 where only the latter was possible for dyads belonging to the minor flow. In the other cases the choice was purely random.

3 Data Analysis

Individual data analysis on each of the two experiments has been already described in [5] and [7]. As expected, both facing a counterflow and being part of a group were found to influence the walking speed of pedestrians. In addition, there is a difference between the behaviour found in balanced and un-balanced configurations of counterflow in terms of lanes' formation and amount of lateral motion required to avoid conflicts with participants from the opposite direction [5, 6]. In this paper we will compare the results of the two experiments, with the aim of verifying whether their spatial patterns and different speeds affect the dynamics at a more macroscopic level.

3.1 Microscopic Analysis on Dyads

A comparison of speeds among dyads and individuals in Exp. 2 shows that dyads are slower in procedures characterised by a counterflow situation. In the presence of a uni-directional flow essentially exempt from collisions (Proc. 1), on the other hand, the difference is rather small (see Fig. 3a). This suggests that the bi-directional flow affects more the spatial pattern of the dyad members that more frequently switch from the desired *line-abreast* pattern to a *river-like* one. Moreover, it is also observed that group members have perceived a sensibly higher density during the procedures with counterflow: Fig. 3b shows the distributions of local densities for all procedures of Exp. 2, calculated using the *Voronoi* method [9] (density values used here are instantaneous and collected from the time the first participant enters the measurement area to the time the last one leaves it). While average density is almost equal in Proc. 1, the difference becomes already noticeable in the second one. Later on we will show that this is due to the fact that dyad members tend to walk close to each other compared to the other individual pedestrians that instead take more frequently the opportunities offered by unoccupied gaps in front of them.

A first analysis on the distributions of relative positions of dyads, with respect to their centroid, has shown a decrease of distance between them with the increase of counterflow conditions [7]. Moreover, it is observed that conflicts arising from the bi-directional flow frequently lead dyad members to assume a river-like pattern, which is barely visible in the first procedure. As with the analysis on speed and local density distribution, no significant difference arises between Proc. 3 and 4 of the second experiment. The relation between density, speed and relative positions is shown in Fig. 4a, b. While a dependency between density and angular arrangement

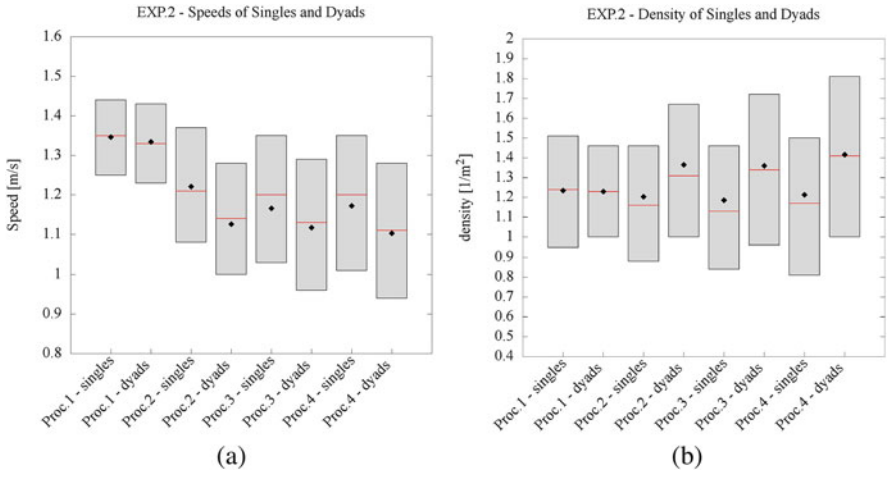

Fig. 3 Distribution of pedestrian speeds **(a)** and local densities **(b)** among procedures of Exp. 2. Black dots indicate the mean, red lines the median and the box size defines the standard deviation

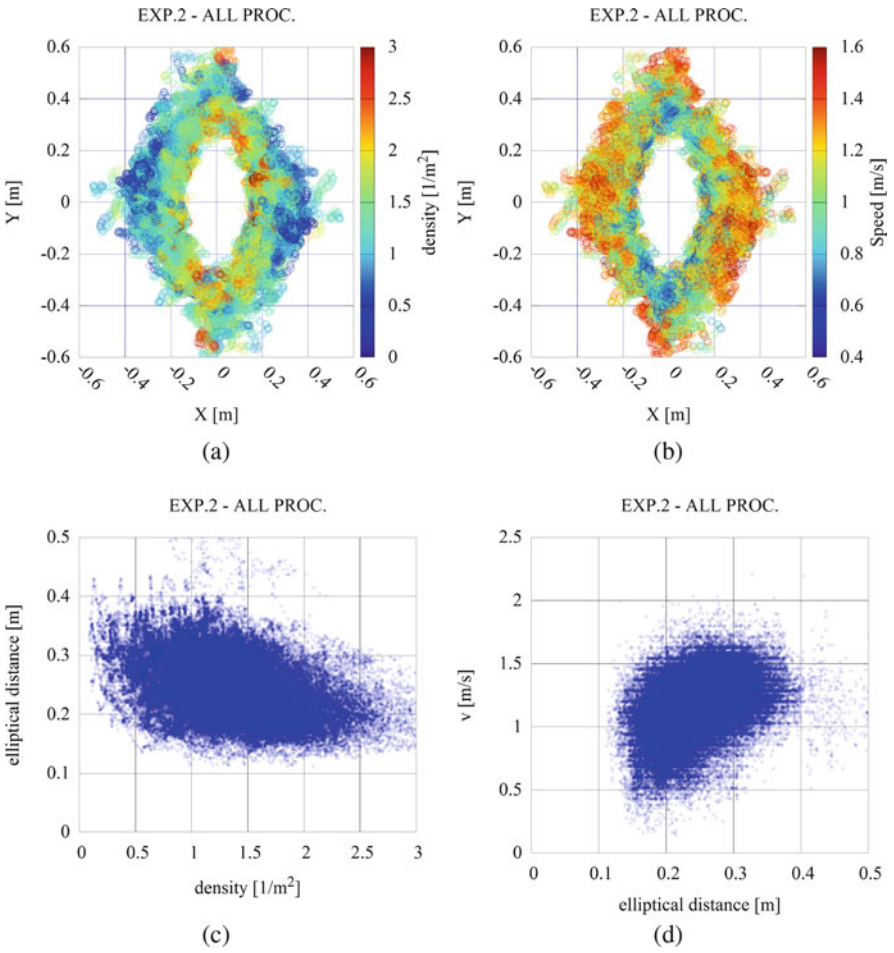

Fig. 4 **(a, b)** Relative position of dyads according to their centroid. Positions are rotated so that the movement direction is up. Colours indicate the information of local density **(a)** or instantaneous speed **(b)**. **(c, d)** Relations between density, distance and speed of dyads

(i.e. spatial pattern) of dyads was not found to be significant, it is apparent how points of high densities are mostly close to the centre (the few outliers are probably due to a transient stretched river-like pattern) and they describe a pattern with an elliptical shape, whose long side is associated with the walking direction. The same regularity is also visible with the data about the speed: points associated with higher speeds are located in the outer part of the dataset, while close to the centre speeds are lower, about 0.6 m/s.

The elliptical appearance of diagrams in Fig. 4a, b is not surprising and it reflects the physics of pedestrian movement already considered with former works on the modelling side (e.g. [4]). According to these data, it is possible to define a distance metric that applies distortion on the y-axis and helps to analyse the relation between density, speed and *elliptical distance*:

$$f(x, y) = \sqrt{x^2 + \left(\frac{y}{2}\right)^2}$$

The outcome of this analysis is shown in Fig. 4c, d. It is fair to state that the defined elliptical distance between dyad members acts as a mediator between the fundamental characteristics of the dynamics (more logically the local density leads group members to walk closer and not vice versa). On the other hand, this analysis suggests that there is a positive effect of the density on the cohesion of dyad members that consequently affects their instantaneous speed. However, the relation between walking speed and elliptical distance is less clear and points in Fig. 4d appear to be in a rather large area which is difficult to describe using a linear function. Considering these observations, we can say that models of dyads should be able to reproduce a growing trend between elliptical distance and speed.

An additional analysis carried out on microscopic data about the instantaneous position of pedestrians is focused on evaluating the position of the other nearby pedestrians: this kind of analysis, shown in Fig. 5, highlights a different kind of behaviour between members of dyads and individuals with regard to the lane formation phenomenon. We focus in particular on Proc. 4 since it is the most interesting one in terms of macroscopic results. It must be said that lane formation is a rather fuzzy concept and several methods are proposed in the literature as attempt for its quantification: [5], for example, analyse the *rotation* of the pedestrian

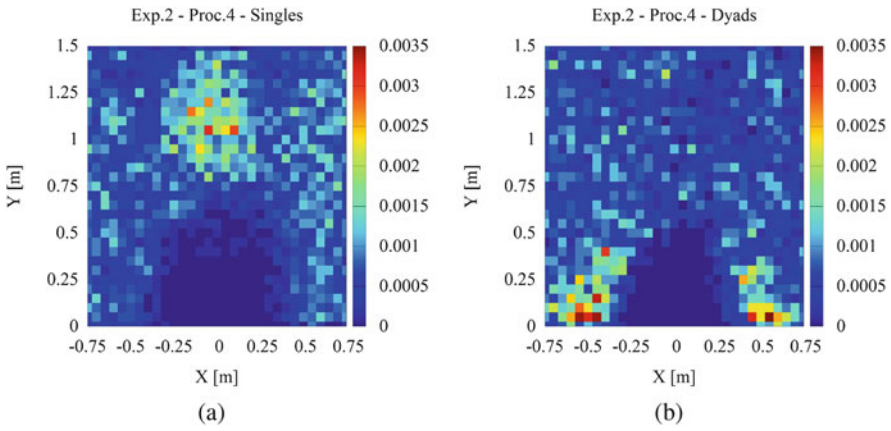

Fig. 5 Distribution of relative positions of neighbour pedestrians, according to the position of each individual **(a)** or dyad member **(b)**

directions to achieve a numerical value describing the stability of lanes. We also do not try to provide a definition of lane, but the data describing the proxemic behaviour of individuals and dyads, respectively, shown in Fig. 5a, b, show that, on the one hand, there is a clear following behaviour for the individuals, where the most frequent position of neighbouring pedestrians is in a spot about 1 m ahead. On the other hand, members of dyads mostly try to keep a line-abreast pattern: the most frequent positions for neighbours are in fact on the side instead that ahead the considered pedestrian. In other words, lanes composed of dyad members tended to be wider and this led to a less efficient utilisation of the space available on average.

3.2 Effects of Dyads at a Macroscopic Scale

Previous results highlighted the effects of density and counterflow situations on the behaviour of dyads at a very detailed scale whereas we present here the aggregated effect of these microscopic observations on the overall pedestrian flow at different levels of density.

The presence of groups in Proc. 1 did not bring to significant differences, since only a simple free-flow situation emerged from it. In counterflow situations, instead, differences become apparent and the most interesting result is represented by the scenario with a perfectly balanced counterflow, whose data are reported in Fig. 6. The diagram shows very little difference at low densities, but starting from 0.5 peds/m^2 the specific pedestrian flow observed in the experiment with dyads grows at a slower rate, compared to Exp. 1. The range of observed densities does not reach a critical density for any of the experiments, but the trend of the diagrams supports the conjecture that the situation of Exp. 2 would lead to a lower maximum flow.

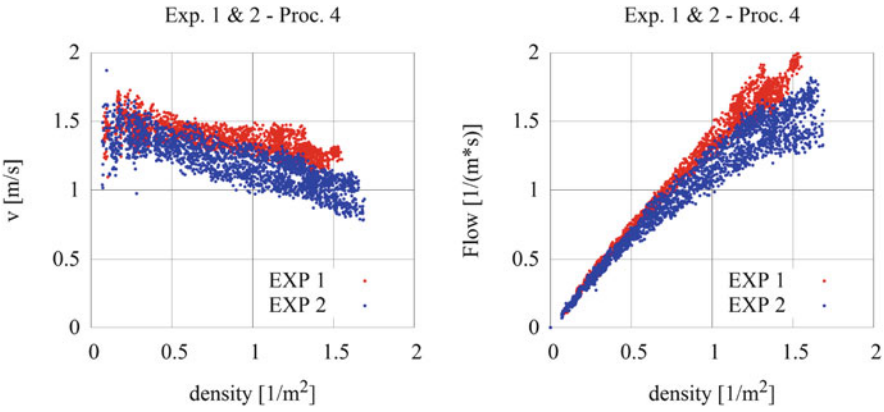

Fig. 6 Comparison of fundamental diagrams in the form density–speed (left) and density–flow (right) of Exp. 1 and 2—Proc. 4

4 Conclusions and Future Works

The paper has presented original results of analyses of pedestrian dynamics achieved through an experimental observation aimed at characterising the influence of dyads, both at micro and macroscopic level. Micro-level results underline that different counterflow situations affect local density, and that groups walk slower compared to singletons, depending also on their spatial patterns at variable density situations. The introduction of dyads in the pedestrian demand leads to a higher level of measurable density in analogous initial conditions and a more chaotic macro-level dynamics characterised by fragmented lanes, inducing a lower observed specific flow.

Future works are aimed, on the one hand, to transfer the achieved results to the modelling activities in the presence of groups (preliminary results are discussed in another paper in this volume [12]), but additional observations and experiments would be needed to further investigate whether previously observed aggregated phenomena are still observed in the presence of groups.

References

1. Bandini, S., Crociani, L., Gorrini, A., Vizzari, G.: An agent-based model of pedestrian dynamics considering groups: a real world case study. In: 17th International IEEE Conference on Intelligent Transportation Systems (ITSC), pp. 572–577. IEEE, Qingdao (2014)
2. Bandini, S., Gorrini, A., Vizzari, G.: Towards an integrated approach to crowd analysis and crowd synthesis: a case study and first results. Pattern Recogn. Lett. **44**, 16–29 (2014)
3. Boltes, M., Seyfried, A.: Collecting pedestrian trajectories. Neurocomputing **100**, 127–133 (2013)
4. Chraibi, M., Seyfried, A., Schadschneider, A.: Generalized centrifugal-force model for pedestrian dynamics. Phys. Rev. E **82**(4), 46111 (2010)
5. Feliciani, C., Nishinari, K.: Empirical analysis of the lane formation process in bidirectional pedestrian flow. Phys. Rev. E **94**(3), 032304 (2016)
6. Feliciani, C., Nishinari, K.: Estimation of pedestrian crowds' properties using commercial tablets and smartphones. Transportmetrica B **7**(1), 865–896 (2019)
7. Gorrini, A., Crociani, L., Feliciani, C., Zhao, P., Nishinari, K., Bandini, S.: Social groups and pedestrian crowds: experiment on dyads in a counter flow scenario (2016). Preprint. arXiv:1610.08325
8. Moussaïd, M., Perozo, N., Garnier, S., Helbing, D., Theraulaz, G.: The walking behaviour of pedestrian social groups and its impact on crowd dynamics. PLoS One **5**(4), e10047 (2010)
9. Tordeux, A., Zhang, J., Steffen, B., Seyfried, A.: Quantitative comparison of estimations for the density within pedestrian streams. J. Stat. Mech: Theory Exp. **2015**(6), P06030 (2015)
10. von Krüchten, C., Schadschneider, A.: Empirical study on social groups in pedestrian evacuation dynamics. Phys. A: Stat. Mech. Appl. **475**, 129–141 (2017)
11. Zanlungo, F., Ikeda, T., Kanda, T.: Potential for the dynamics of pedestrians in a socially interacting group. Phys. Rev. E **89**(1), 012811 (2014)
12. Zeng, Y., Crociani, L., Gorrini, A., Vizzari, G., Song, W.: Investigating the effect of social groups in uni-directional pedestrian flow. In: Hamdar, S.H. (ed.) Traffic and Granular Flow '17, Springer, Cham (2019). https://doi.org/10.1007/978-3-030-11440-4
13. Zhang, J., Klingsch, W., Schadschneider, A., Seyfried, A.: Ordering in bidirectional pedestrian flows and its influence on the fundamental diagram. J. Stat. Mech. (02), 9 (2012)

Pedestrian Flow Through Complex Infrastructure, Experiments, and Mass-Transport Processes

Pavel Hrabák, Marek Bukáček, Peter M. Kielar, and André Borrmann

Abstract Simple mass-transport model is used to describe the phenomenon of decreasing bottleneck flow during egress of pedestrians through complex infrastructure. The considered mass-transport model combines the macroscopic hydrodynamics approach with concept of queuing processes (thus belongs to the class of hand-calculation models). The realization of such process can be described by means of temporal evolution of the flow through individual bottlenecks and number of pedestrians in front of given bottleneck. These two state variables are used to compare the model prediction with experimental data from two original experiments. The commonly used approach of constant width-related bottleneck capacity cannot capture the observed decrease of flow caused by the loss of motivation while the room is getting empty. Therefore, the dynamical part of the bottleneck capacity derived from the slope of the temporal evolution of the crowd size has been introduced, in order to capture the phenomenon.

1 Introduction

Main goal of the pedestrian and fire safety engineering is to estimate the evacuation time, i.e., how long it takes before all people in the premises manage to leave it, a review of the concepts how to estimate the evacuation time, see, e.g., in [2]. One of the simplest ways how to calculate the evacuation time is to use the hydrodynamic approach and look at the crowd as it is a fluid. Such macroscopic methods are often referred to as "hand-calculation" methods since they are not based on simulations.

P. Hrabák (✉) · M. Bukáček
Faculty of Information Technology, Czech Technical University in Prague, Prague 6, Czech Republic
e-mail: pavel.hrabak@fit.cvut.cz; hrabapav@fit.cvut.cz; marek.bukacek@fjfi.cvut.cz

P. M. Kielar · A. Borrmann
Technische Universität München, Munich, Germany
e-mail: peter.kielar@tum.de; andre.borrmann@tum.de

S. H. Hamdar (ed.), *Traffic and Granular Flow '17*,
https://doi.org/10.1007/978-3-030-11440-4_19

For the applicability of such methods in evacuation time prediction we refer the reader to [5] or [6] and the references therein.

The hydrodynamics can be reduced to simple mass-transport model on the graph with vertices representing rooms (or rather exits) and edges representing possible routes between the vertices. Mass-transport process is based on the rules (usually probabilistic) of the transportation of part of the mass from one node to another. Theoretical description is summarized in [7, Chapter Three] and the references therein.

In order to use the hand-calculation method for evacuation time prediction, it is necessary to assign crucial parameters to individual elements of the network: the maximal flow intensity through the bottleneck, flow density relation (fundamental diagram) in the corridor, initial distribution of pedestrians, and others. A lot of experimental studies and their evaluation have been performed in order to capture such aspects, for review, see e.g., [6–8]. The study presented here leans mainly on the observation that the pedestrian flow through the bottleneck depends mainly on the bottleneck width, and hence rather smoothly due to the zipper effect. Since the experimental layout did not contain any corridor movement, the flow reduction due to the increasing density (the fundamental diagram) has not been considered.

In [8] the author suggested that the dependence of flow J on the bottleneck width w is linear and hence

$$J = 1.9 \cdot w\,. \tag{1}$$

The used mass-transport model, in more detail presented already in [4], is partially based on this assumption; however, we found out that the average flow through the bottlenecks was significantly lower in the second experiment than the first one (which was quite in agreement with Eq. (1)). Therefore, the characteristic flow C through the bottleneck was determined by means of the average flow through the bottleneck. Nevertheless, to exclude other external influence, it is reasonable to measure the characteristic flow in a steady state, determined by the levelling of crucial quantities as density, velocity, and flow [3].

It has been observed, see, e.g., [1], that the actual flow through the bottleneck is not given by the characteristic flow C only, but is influenced by the clogging size in front of the bottleneck as well. More precisely, while the crowd size is increasing, the flow is greater than C (maybe because more aggressive pedestrians are pushing forward), and while the crowd size is decreasing, especially in the last phase of the egress, the flow is lower than C (maybe because the loss of motivation or the less aggressive nature of the crowd). In such a case it is necessary to measure the actual flow in more smooth way than just counting pedestrians per time unit. The study on how to smoother the flow is presented in [9].

2 Experiments

Two original experiments, denoted as E5 and E6, were conducted at the Faculty of Nuclear Sciences and Physical Engineering of the Czech Technical University in Prague, namely in the lecture room T-201 and adjacent hallway. The pedestrian crowd consisting of second year students was rather homogeneous; however, differences in motivation to leave the premisses were observed.

The layout of the experiment is schematically depicted in Fig. 1. At the beginning of each trial, students were gathered in four groups at four staircases in the lecture room (level 3). After the given signal, students started to leave the lecture room. The pedestrian streams merged in front of the two exits (level 2). Both exits lead to one common vestibule with one main exit (level 1), through which the premises was left.

The experiments were recorded by several synchronized cameras, the main focus was given to the precise determination of the passing times through all seven involved exits denoted as $v_1, v_2, \ldots, v_7$, see Fig. 1. Here we note that the exits v_1-v_4 were associated with the last step of the staircase and there was no bottleneck in front of them. Furthermore, the flow through these "leaves" of the tree was partially controlled by the experimenters (slowed down or speeded up) and differed trial after trial. The used hand-calculation model was then considered in the data-driven sense, i.e., the measured flow through the leaves was input to the estimation, for details see [4].

The number of pedestrians in front of the bottleneck and flow through given bottleneck were the main measured quantities used for analysis. It is worth noting that the experiments were not equivalent, slight differences were present. In experiment E5, pedestrians were already standing on the staircases during the initiation, contrarily in experiment E6, pedestrians were gathered under the staircases and had to climb the stairs up. This was reflected in the average flow and free-flow velocity of the pedestrians. For details see overview in Table 1.

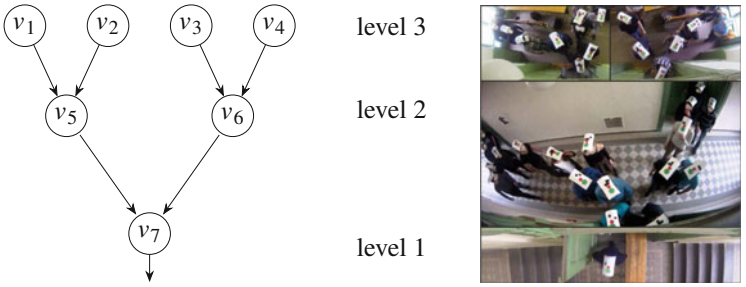

Fig. 1 Schematic illustration of the experimental layout. Students were leaving the lecture room via a tree-like structure of consecutive bottlenecks. The experiment was recorded by four cameras placed above the exits v_5 to v_7

Table 1 Experiment details

	Date	#part.	#trials	$\bar{T}_{evac}$	$\bar{V}_0$	$\bar{J}_7$	Note
E5:	07.03.16	54 ped	8 trials	43.2 s	1.7 m/s	1.45 ped/s	On staircases
E6:	20.12.16	53 ped	4 trials	49.7 s	1.4 m/s	1.25 ped/s	Below staircases

#part stands for number of participants, #trials for number of trials, $\bar{T}_{evac}$ for average evacuation time, $\bar{V}_0$ for average free-flow velocity, $\bar{J}_7$ for average characteristic outflow through the main exit

3 Estimation Method

The mass-transport process used to describe observed phenomena was developed under three main assumptions fulfilled by the experiment:

1. The capacity of individual rooms is never reached, i.e., the outflow from one room is not affected by the state in the consecutive room.
2. None part of the layout could be considered as narrow corridor, i.e., the flow intensity drop due to high density is not observed.
3. Pedestrians build a compact clogging in front of the exit.

Such assumptions enable to build a simple deterministic mass-transport process based on explicit/forward difference equations (the state in time t is calculated from the state in time $t-1$). The process is defined on the graph consisting in nodes $V = \{v_1, \ldots, v_7\}$ representing exits and edges $E = \{e_{15}, e_{25}, e_{36}, e_{46}, e_{57}, e_{67}, \}$ representing paths from one exit to another. The observable quantities are the actual flow $J_i(t)$ through the exit v_i and number of pedestrians $m_i(t)$ in the clogging in front of exit v_i. The model consists in coupled difference equations

$$J_i(t) = \min(m_i(t), J_i^c)\,, \tag{2}$$

$$m_i(t+1) = m_i(t) - J_i(t) + \sum_{\{j|e_{ji}\in E\}} J_j(t - t_{ji})\,, \tag{3}$$

where J_i^c is the capacity of the bottleneck, i.e., maximal possible flow through the exit v_i, depending mainly on the bottleneck width and shape; t_{ji} is the estimated time of a pedestrian to walk from exit v_j to the clogging in front of the exit v_i. The basic time step used in the difference equation was chosen as one second; however, the method can be used equivalently for arbitrary time interval: the longer the interval is, the smoother flow is observed; the shorter the interval is, the more sensitive is the prediction to fluctuations.

As the term capacity suggests, the maximal flow J_i^c has been considered constant in time accordingly to [4], i.e.,

$$J_i^c \equiv C_i\,. \tag{4}$$

Table 2 Calibrated values for vertices V

Exit	w [m]	$1.9 \cdot w$ [ped/s]	E5 C_i [ped/s]	E6 C_i [ped/s]
v_5	0.70	1.33	1.40	1.20
v_6	0.70	1.33	1.40	1.20
v_7	0.75	1.43	1.45	1.25

Table 3 Calibrated values for edges E

Edge	l [m]	E5 t_{ji} [s]	E6 t_{ji} [s]
e_{15}	3.3	2	2
e_{25}	1.7	1	1
e_{36}	1.7	1	1
e_{46}	3.3	2	2
e_{57}	5.7	3	4
e_{67}	4.1	2	3

As will be shown further, this assumption was not fulfilled by the experiment and dependence on other conditions is to be introduced. Furthermore, the experiments have shown that the capacity J_i^c cannot be considered as the geometric property of the bottleneck only (suggested by (1)), but reflects the crowd properties/motivation as well. Therefore, the values of C_i have been calibrated based on the average flow through given bottleneck over the time the bottleneck was saturated, i.e., there was a clogging of significant size in front of the bottleneck to maintain steady flow. The calibrated values used for prediction are given in Table 2. The value expected according to [6] is given for comparison as well.

Here we note that due to the list of assumptions given above the value of t_{ji} can be considered as fixed and the outflow from v_j as independent from the state of the target exit v_i. The value of t_{ji} has been estimated as

$$t_{ji} = \text{dist}(v_j, v_i)/V_0\,, \tag{5}$$

where the distance dist is the length of the shortest path between exits and V_0 is the expected desired free-flow velocity of pedestrians estimated from the data. As can be seen in Table 1, the average velocity has differed significantly among experiments, probably due to the different initial conditions (climbing up the staircase or not). The calibrated values of t_{ji} are given in Table 3. The value of t_{ji} has been rounded to the closer integer in order to fit to the difference equations without necessity of interpolation.

The comparison of the estimation model and the experiment was performed in the "data-driven" sense, i.e., the flow through the leaves $v_1, \ldots, v_4$ (level 1) was considered to be known (e.g. measured by kinects as suggested in [4]) and the measured flow served as the input to the mass-transport model. In order to do so, the input flow needs to be discretized, i.e., the mass of pedestrian flowing per each second to be expressed. Counting the number of passing pedestrian during each second is highly imprecise and "jumpy". Therefore we used an interpolation

approach for the flow estimation. More precisely, the cumulative flow function CFF has been defined as linear interpolation of the pairs (time of passing, number of pedestrians passed through given bottleneck). Then the flow $J_i(t)$ is given as $J_i(t) = CFF(t) - CFF(t-1)$. Such approach gives smoother flow and better sensitivity of the estimator to initial flow fluctuations.

It is worth noting that the values C_i and t_{ji} have been rather tuned to fit the experimental data. Of course, it would be beneficial to calibrate the estimation model to be applicable even in the case that only the geometric layout of the premisses is available, i.e., without the measurement of the characteristic flow and desired velocity. Such auto-calibration concept based on other information from the flow through the leaves may be subject to further investigation.

4 Observations

The goal of the estimation tool was to predict the observable quantities flow and occupancy at the main exit v_7. In Fig. 2 the time evolution of measured and predicted flow and occupancy is plotted. From the graph it can be observed that the overall

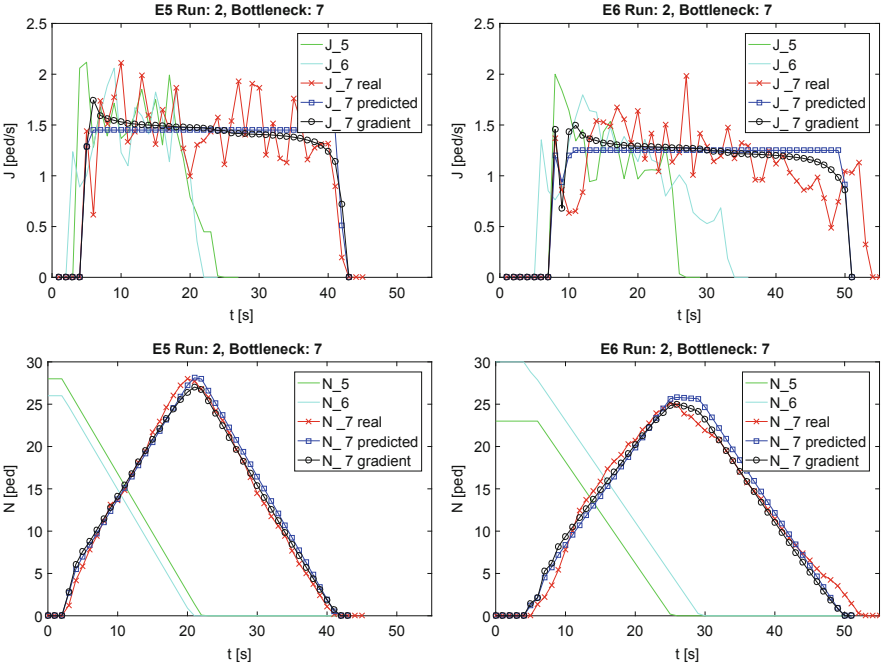

Fig. 2 Comparison of the actual flow (upper row) and actual occupancy (lower row) of the main exit v_7. The measured data (red crosses) compared with the constant flow prediction (blue squares) and the modified flow prediction (black circles)

flow and evacuation time are in a good agreement for both experiments. However, the estimation tool is not able to capture the increased flow at the beginning of the evacuation and the decreasing flow at the end of the evacuation.

That motivated us to introduce the dependence of J_i^c on the gradient of the mass $m_i(t)$, since it is observed that during the emptying of the room the motivation of pedestrians to leave is decreasing and therefore even the flow is decreasing. The suggested dependence is

$$J_i^c(t) = C_i + \frac{\mathrm{d}m_i(t)}{\mathrm{d}t} / m_i(t)\,. \tag{6}$$

The idea behind this equation is as follows. While the size of the clogging is increasing, pedestrians are more motivated to leave the room (or alternatively, more motivated pedestrians reach the door room faster than the less motivated) and therefore the flow through the door is higher. Contrarily, while the clogging size is decreasing and the room is getting empty, the pedestrians are less motivated to leave the room (or alternatively, more motivated pedestrians already left the room and less motivated pedestrians are leaving) and therefore the flow is lower. The slow-to-start effect plays an important role as well. Further, the flow through the bottleneck is less affected when the clogging size is high since the propagation of the information about the increasing or decreasing number of pedestrians is dampened by the crowd.

The constant C_i can be then characterized as the steady-state flow through given bottleneck. In the case of mentioned experiments, the steady-state like behaviour can be observed at the time between the increase and decrease of pedestrian mass $m_i(t)$. In the case of this study, the values of C_i for both approaches (4) and (6) can be chosen identical, since the estimation techniques give similar values of C_i.

The results are plotted in Fig. 2. The lower graph represents the number of pedestrians in the room, i.e., waiting in the clogging plus walking towards the clogging. The reason is that the actual size of the clogging cannot be derived exactly from the experiment records.

5 Summary and Conclusions

Main goal of this study was to describe some bottleneck flow phenomena using a simple "hand-calculation" method for evacuation time estimation. Contrarily to common approach, not only the evacuation time was examined, but even the temporal evolution of observable quantities as actual flow and number of pedestrians in the clogging in front of given bottleneck.

A simple mass-transport model based on difference equations has been used as the estimation tool. It has been shown that the estimated quantities are in quite good agreement with the experimentally measured data; however, some aspects cannot be captured by the classical concept of constant capacity of the bottleneck.

The presented experiments as well as earlier works evince significant decrease of the bottleneck flow at the end of the evacuation when the space in front of the bottleneck is getting empty. This phenomenon can be explained by the loss of motivation of the evacuees. On the other hand, the performed experiments have shown that the flow at the beginning of the experiment is higher that the steady-state flow causes probably by the fact that the more motivated pedestrians reach the bottleneck earlier than the less motivated.

To capture such phenomenon, the dependency of the capacity on the gradient of the clogging size has been introduced as given by Eq. (6). The comparison of the measured and predicted quantities given in Fig. 2 shows that such modification makes the estimation more accurate with respect to the temporal evolution of the quantities preserving the evacuation time and overall flow.

Acknowledgements This work was supported by the Czech Science Foundation under grant GA15-15049S and by the internal grant SGS15/214/OHK4/3T/14 of the Czech Technical University in Prague.

References

1. Bukáček, M., Hrabák, P., Krbálek, M.: Experimental study of phase transition in pedestrian flow. In: Daamen, W., Duives, D.C., Hoogendoorn, S.P. (eds.) Pedestrian and Evacuation Dynamics 2014, Transportation Research Procedia, vol. 2, pp. 105–113. Elsevier Science B.V., Amsterdam (2014). https://doi.org/10.1016/j.trpro.2014.09.014
2. Candy, M.N., Chow, W.: A brief review on the time line concept in evacuation. Int. J. Archit. Sci. **7**(1), 1–13 (2006)
3. Liao, W., Tordeux, A., Seyfried, A., Chraibi, M., Drzycimski, K., Zheng, X., Zhao, Y.: Measuring the steady state of pedestrian flow in bottleneck experiments. Phys. A Stat. Mech. Appl. **461**, 248–261 (2016). https://doi.org/10.1016/j.physa.2016.05.051
4. Porzycki, J., Hrabák, P., Bukáček, M., Was, J., Lubaś, R.: Data driven method of pedestrian flow estimation for evacuation scenario using queuing model. In: 23rd International Workshop of the European Group for Intelligent Computing in Engineering, EG-ICE 2016 (2016)
5. Rogsch, C., Weigel, H., Klingsch, W.: Hand-Calculation Methods for Evacuation Calculation–Last Chance for an Old-Fashioned Approach or a Real Alternative to Microscopic Simulation Tools? pp. 523–528. Springer, Berlin (2010). https://doi.org/10.1007/978-3-642-04504-2_45
6. Schadschneider, A., Klingsch, W., Klüpfel, H., Kretz, T., Rogsch, C., Seyfried, A.: Evacuation Dynamics: Empirical Results, Modeling and Applications, pp. 3142–3176. Springer, New York (2009). https://doi.org/10.1007/978-0-387-30440-3_187
7. Schadschneider, A., Chowdhury, D., Nishinari, K.: Stochastic Transport in Complex Systems: From Molecules to Vehicles. Elsevier Science B. V., Amsterdam (2010). https://doi.org/10.1016/B978-0-444-52853-7.00016-6
8. Seyfried, A., Passon, O., Steffen, B., Boltes, M., Rupprecht, T., Klingsch, W.: New insights into pedestrian flow through bottlenecks. Transp. Sci. **43**(3), 395–406 (2009). https://doi.org/10.1287/trsc.1090.0263
9. Steffen, B., Seyfried, A.: Methods for measuring pedestrian density, flow, speed and direction with minimal scatter. Phys. A Stat. Mech. Appl. **389**(9), 1902–1910 (2010). https://doi.org/10.1016/j.physa.2009.12.015

Mining the Social Media Data for a Bottom-Up Evaluation of Walkability

Christian Berzi, Andrea Gorrini, and Giuseppe Vizzari

Abstract Urbanization represents a huge opportunity for computer applications enabling cities to be managed more efficiently while, at the same time, improving the life quality of their citizens. One of the potential applications of this kind of systems is a bottom-up evaluation of the level of walkability of the city (namely, the level of usefulness, comfort, safety and attractiveness of an urban area for walking). This is based on the usage of data from social media for the computation of structured indicators describing the actual usage of areas by pedestrians. This paper will present an experimentation of analysis of data about the city of Milano (Italy) acquired from Flickr and Foursquare. Over 500 thousand points, which represent the photos and the POIs collected from the above-mentioned social media, were clustered through an iterative approach based on the DBSCAN algorithm, in order to achieve homogeneous areas defined by the actual activity of inhabitants and tourists rather than by a top-down administrative procedure and to supply useful indications on the level of walkability of the city of Milan.

1 Introduction

Urbanization is one of the most significant trends of the twenty-first century. Today over half of the world's population lives in urban areas and all the regions of the world are expected to urbanize further over the coming decades: by 2050 66% of the world's population will reside in cities [15]. This demographic trend requires institutions to more effectively design and plan the cities and to improve the quality of life of the inhabitants, considering the rising demand of services and infrastructures. One of the most essential elements of new development agendas for future cities is based on the need to adopt sustainable mobility strategies, based,

C. Berzi · A. Gorrini · G. Vizzari (✉)
CSAI-Complex Systems and Artificial Intelligence Research Centre, Department of Informatics, Systems and Communications, University of Milano-Bicocca, Milan, Italy
e-mail: Christian.Berzi@disco.unimib.it; Andrea.Gorrini@disco.unimib.it; Giuseppe.Vizzari@disco.unimib.it

S. H. Hamdar (ed.), *Traffic and Granular Flow '17*,
https://doi.org/10.1007/978-3-030-11440-4_20

for example, on increasing public transport services in order to decongest vehicular traffic volumes and reduce the level of environmental pollution. Facing this trend, advanced urban planning activities [17] are shifting toward a focus on pedestrian mobility and walkability [1], namely how friendly the urban environment is for walking.

In general, the term walkability [7] refers to those infrastructural-design elements which guarantee the comfort, safety and accessibility of the urban settings for walking, considering also the specific needs of those people with limited mobility. More in detail, Jeff Speck [14] has recently proposed a *general theory of walkability*, which defines the four essential criteria for the assessment of the walkability level of urban environments:

- *Usefulness*: the urban territory should be designed and planned in order to guarantee the presence of diverse public services, commercial activities and green areas within a walkable distance of 150 m;
- *Comfort*: side-walks should be designed according to a series of standard criteria of quality and accessibility (e.g. adequate width of the pavement, ramps for people with impaired mobility, legible road sign for way-finding);
- *Safety*: streets should be designed in order to guarantee the safety of pedestrians (e.g. bumpers in proximity of the zebra, sufficient illumination systems, adequate horizontal and vertical signage);
- *Attractiveness*: the city should be designed to have a polycentric structure, with several and distinctive areas of attraction for both the citizens and the visitors; this is based on the presence of points of interest and events, the quality of the architectural streetscape and the vitality of the social context.

According to the multi-faceted definition of walkability depicted by Speck, the assessment of the pedestrian friendliness of a determined urban area should comprise the evaluation of: (1) *structured indicators* related to the topographical and spatial elements of the area (e.g. the presence of public services, quality of road infrastructures) and to the census of the socio-demographic characteristics of its inhabitants; (2) *behavioural indicators* related to how the spatial features of the area influence the actual behaviours of people while walking (e.g. problematic level of services, pedestrian exposure to risks); (3) *subjective indicators* focused on the evaluation of the city users about the level of walkability of the area (e.g. perceived comfort and safety). Within a multi-disciplinary approach (e.g. urban studies, architecture, urban sociology, environmental psychology, computer science), a wide range of methods and techniques have been developed and applied to empirically measure the level of walkability of the urban environments: field observations [4]; questionnaires [16]; GIS-analyses [2]; web-based applications [5] (see Table 1 for a schematic summary).

In this framework, the most novel and promising approach for walkability assessment is the one proposed by *urban informatics* [8], a relatively new term invented to define a category of computer-based applications somehow gravitating around urban studies, and incorporating different types of knowledge and skills ranging from computer science, architecture and social science. Urban informat-

Table 1 A schematic summary of the methods developed for walkability assessment, according to different criteria and indicators

Methods	Assessment criteria	Assessment indicators
Field observations [4]	Comfort and safety	Behavioural
Questionnaires [16]	Comfort and safety	Subjective
GIS-analyses [2]	Usefulness	Structured
Web applications [5]	Comfort and safety	Subjective
Social media data [11, 12]	Comfort and attractiveness	Structured and subjective

ics approach is based on the recent developments of advanced information and communication technologies (ICTs) and on the possibility to gather and analyse large-scale heterogeneous data (e.g. institutional, user generated social media data). This scenario enables the use of geo-referred social media data for a bottom-up evaluation of walkability, directly based on user's experience of the urban environment (without requiring ad-hoc infrastructures, surveys or observations). In particular, the contributions proposed by Daniele Quercia [11, 12] provide a characterization of the urban areas in terms of comfort and pleasantness for walking path recommendation employing user generated contents.

In this vein, we propose a method to automatically identify and characterize the attractive entities within the city of Milan (Italy), by using some data gathered from Flickr and Foursquare. The rational of the approach is based on two pillars: (1) the usage of social media data for identifying and characterizing with a bottom-up perspective particular areas within the city (not unlike in [3]) considering the popularity factor (also associated with different times of day, and days of week, potentially correlated to special events) motivating the choice of taking a picture and uploading it on Flickr; (2) the possibility of interpreting this kind of proxy for attractiveness of the area within the above overall walkability assessment framework. The bottom-up nature of this approach provides results that represent an interesting integration to existing, top-down and more traditional techniques for walkability assessment and already available institutional data and previous urban plans.

The enabling data which set the current work are presented in Sect. 2. Sections 3 and 4, respectively, present the identification and the characterization processes of the identified entities of the city. The paper concludes with remarks about the achieved results and their future use for a bottom-up evaluation of walkability through social media data.

2 Enabling Data

Thanks to the increasing popularity of social media web sites and the parallel diffusion of smart devices embedded with camera, high speed Internet connection and GPS, massive social media sources of geo-referenced data about user behaviours

have recently become available. This work considers two particular social media sources, Flickr and Foursquare. A preliminary analysis revealed that within a reasonable bounding box including the city of Milano and relevant surroundings (e.g. including Milano Fiera—Rho, adjacent to the area that hosted Expo 2015 and regularly hosting additional fairs) about 450 thousand Flickr photos, and related metadata, are present. Additionally, approximately 50 thousand Foursquare points of interest (POI) are also present in the relevant area. The metadata derived from the two datasets are complementary: in fact Flickr tags are a free form, bottom-up type of description of the photo content (and potentially also describing the place/context in which the photo was taken) whereas Foursquare POIs are associated with a centrally defined taxonomy, representing a more authoritative form of description. The main motivation behind this choice is that potentially interesting urban areas/events should attract people who take photos and upload them on a social media like Flickr or they should contain points of interest (e.g. gardens, monuments, events) accessible on a social media like Foursquare.

3 City Entities Identification

We chose to use the term *entity* instead of (urban) area of interest[10] since it may refer to any type of element within the city such as a square, an avenue, a building, a monument, but also an event (associated with a place, but a distinct concept). The approach employed to identify the entities within the city, analogously as the above cited[10], is based on the application of a clustering technique on the above-mentioned social media data. The proposed characterization of the identified entities is based on a set of features (e.g. temporal features, textual features) extracted from the elements (social media data) that are associated with those identified entities.

DBSCAN (density-based spatial clustering of applications with noise [6]) is a density-based clustering algorithm which is suited to this specific situation (e.g. good efficiency on large databases, often employed for analysis of spatial data, discovery of clusters with arbitrary shape, no need to specify a priori the number of clusters to identify). Therefore, this algorithm was chosen to identify the entities within the city: it allows to identify and delineate regions of high density (i.e. city areas where there are many photos or POIs) that are separated by regions of lower density. The intuition is that around areas of interest there are regions separating them from potentially nearby other areas, so a sort of border can be identified around the area.

The heterogeneous density that characterizes Milano toward the centre of the city does not allow to apply a one-shot algorithm that covers the entire city. Indeed, a first run of DBSCAN allows to achieve a satisfactory result outside the city centre, by identifying some peripheral entities such as Expo 2015, Milano Fiera, San Siro Stadium and Milano Bovisa. On the other hand, the whole centre of Milano is represented by a single cluster (i.e. a single entity) that can be considered an unsatisfactory result. Of course, it is possible to tune the sensitivity of DBSCAN according to the density of the centre of Milano but, in this case, the algorithm would

produce the opposite situation, by achieving an unsatisfactory result outside the centre of the city and a satisfactory result within the centre of the city. Consequently, with the purpose to produce a satisfactory result in the whole city, the proposed solution is to employ an iterative approach, by re-applying DBSCAN on the clusters for which an unsatisfactory result is achieved by the previous iteration, adjusting each time the sensitivity of the algorithm according to the density of the currently considered area. At the end of the entire process, each identified cluster refers to a potentially interesting entity within the city of Milano (see Fig. 1).

A quantitative evaluation approach has been proposed to identify potentially interesting entities within the city of Milano. A validity index (i.e. silhouette coefficient) is calculated to measure the quality of the clustering process through the different iterations that are conducted. The silhouette coefficient is a composite index that reflects both the compactness (i.e. how closely related are objects in a cluster) and the separation (i.e. how distinct or well separated a cluster is from other clusters) of clusters (i.e. the entities within the city) [9].

4 City Entities Characterization

The identified entities in the city have been characterized with a set of features extracted from the elements (Flickr photos and Foursquare POIs) that are contained within those entities (see Fig. 2, as an example of the characterization process of a single cluster—the Navigli area). In particular, for each identified entity, the following features are computed:

- Flickr temporal features: they are extracted by using the timestamp of when photos are taken. In particular, the following two temporal features are considered: (1) number of photos taken during the different days of the week (e.g. Monday, Tuesday, Wednesday); (2) number of photos taken during the different hours of the day, 24 h format.
- Flickr photo tags: the most frequent tags that are used to tag the photos on Flickr. With the purpose to consider the most significant tags, a stop-words-removing phase is included to remove the tags that are not considered significant, such as the language stop words (i.e. function words) and the considered domain stop words. The second one refers to a manually created list of words which must not be considered, since they do not refer to the city entities but they are automatically added by some Flickr extensions of other social media, for instance, tags such as: $instagram\_id = \langle ID \rangle$, $Foursquare\_id = \langle ID \rangle$, $Facebook\_id = \langle ID \rangle$, *Flickr_mobile*, *geotagged*.
  Furthermore, an algebraic model for representing unstructured data (vector space model [13]) is used since it allows to calculate how important a tag is for a specific entity of the city, by using the tf-idf (i.e. term frequency inverse document frequency) weighting.

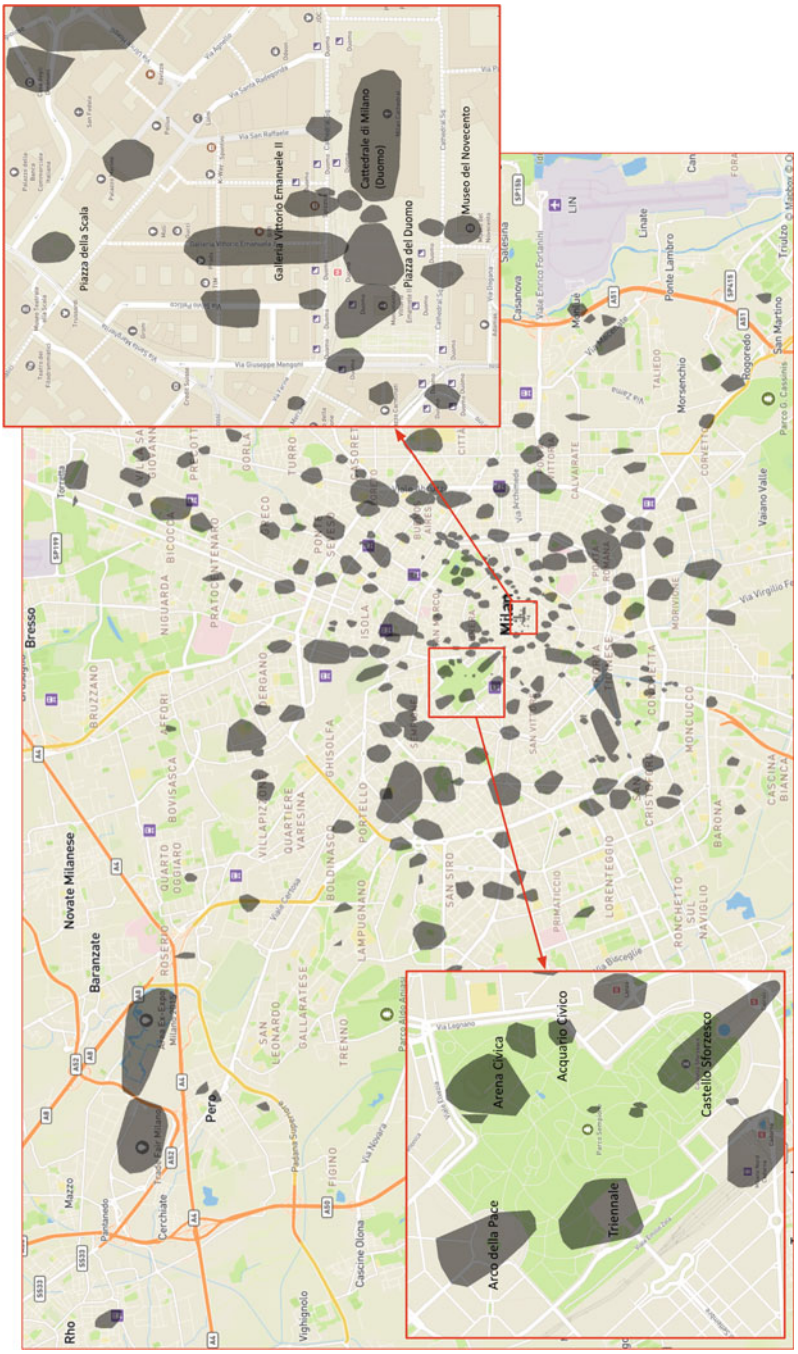

Fig. 1 The clusters identified within the whole city (notice the Rho Fiera area in the North Western part of the map) and two examples of clusters in the city centre (i.e. the Sforzesco Castle—on the left, and the Cathedral area—on the right)

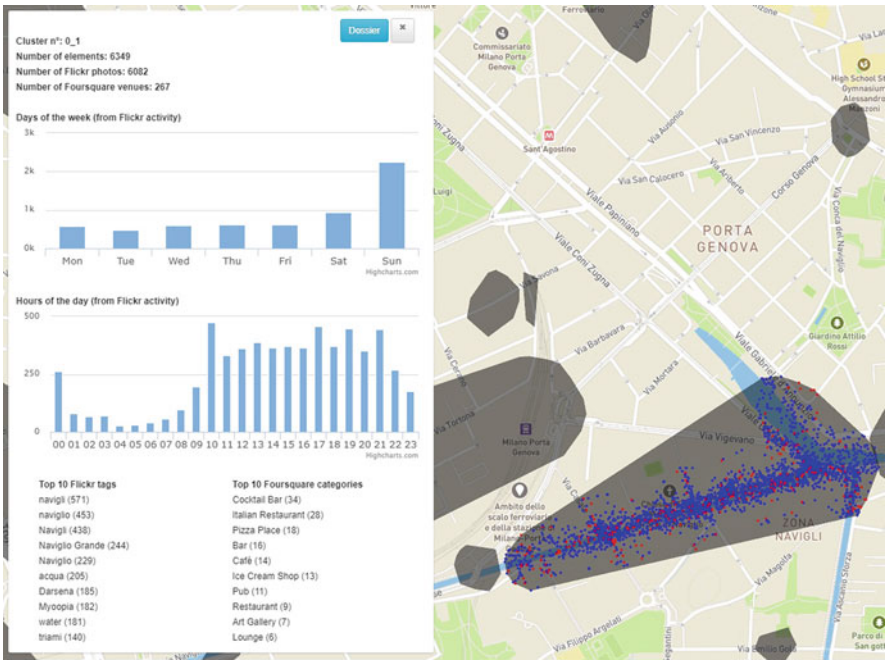

Fig. 2 The detailed description of a single cluster (i.e. the Navigli area), with indication on the day of week and the time of day in which Flickr photos were taken, and the top ten Flickr tags and Foursquare POI categories

- Foursquare POI categories: the number of points of interest which are associated with each of the 10 main Foursquare categories that are *Arts and Entertainment, College and University, Event, Food, Night-life Spot, Outdoors and Recreation, Professional and Other Places, Residence, Shop and Service, Travel and Transport*.
- The number of photos that are taken over time (i.e. in the course of the years), in relation with the most frequent tags. Figure 2 shows a graphic representation of this feature for the cluster associated with the *Navigli area*.

5 Conclusions and Future Works

Within the urban informatics approach, the present work is based on the analysis of social media data (Flickr and Foursquare data) for a bottom-up assessment of the level of walkability of the city of Milano. This is focused on studying the attractiveness of the city for inhabitants and visitors (thanks to the presence of points of interest, the organization of events and the vitality of the social context) to evaluate its overall pedestrian friendliness. The bottom-up nature of this approach

provides results that represent an interesting integration to existing, top-down and more traditional techniques for walkability assessment and already available institutional data and previous urban plans (e.g. institutional data about the presence of public services within a walkable distance of 150 metres, the topographical features of the spatial setting, the localization of pedestrian-car accidents). The proposed multi-layer approach for walkability assessment could be then translated into practice by designers, who would create people-centred optimal environments.

An interesting future work might be the implementation of the labelling process of the identified entities within the city. Through a manual inspection of most of the identified entities, it is apparent that many entities can be labelled simply by using the most frequent tag used in that entity or, in some cases, a tag within the first 10 most frequent tags. On the other hand, it is not always the case that the most frequent tag is the best one and, moreover, some of the identified entities are related to events that frequently take place in an area of the city rather than actual places so, in these cases, tags would not really be descriptive of the environment. Thus, the most frequent tags list can certainly be a good starting point for the labelling task, even though this task requires a more structured process rather than simply use the most frequent tag as the label of the entity. For instance, this process might include some NLP (natural language processing) techniques (e.g. entity linking) and some external linguistic resources (e.g. thesaurus, ontologies) to support the choice of a particular tag (or a combination of tags) as the label of the entity.

References

1. Abley, S.: Walkability scoping paper. Charted Traffic Transp. Eng. **4**, 2011 (2005)
2. Agampatian, R.: Using GIS to Measure Walkability: A Case study in New York City (April), pp. 1–65. Royal Institute of Technology (KTH), Stockholm (2014)
3. Brindley, P., Goulding, J., Wilson, M.L.: Generating vague neighbourhoods through data mining of passive web data. Int. J. Geogr. Inf. Sci. 1–26 (2017)
4. Day, K., Boarnet, M., Alfonzo, M., Forsyth, A.: Irvine Minnesota Inventory, pp. 1–6. (2005)
5. Duncan, D.T.: Whats your walk score®? Am. J. Prev. Med. **45**(2), 244–245 (2013)
6. Ester, M., Kriegel, H.P., Sander, J., Xu, X., et al.: A density-based algorithm for discovering clusters in large spatial databases with noise. In: KDD, vol. 96, pp. 226–231. AAAI Press, Portland (1996)
7. Ewing, R., Handy, S.: Measuring the unmeasurable: urban design qualities related to walkability. J. Urban Des. **14**(1), 65–84 (2009)
8. Foth, M., Choi, J.H.J., Satchell, C.: Urban informatics. In: Proceedings of the ACM 2011 Conference on Computer Supported Cooperative Work, pp. 1–8. ACM, New York (2011)
9. Han, J., Pei, J., Kamber, M.: Data mining: concepts and techniques. Elsevier, Amsterdam (2011)
10. Hu, Y., Gao, S., Janowicz, K., Yu, B., Li, W., Prasad, S.: Extracting and understanding urban areas of interest using geotagged photos. Comput. Environ. Urban. Syst. **54**(Supplement C), 240–254 (2015)
11. Quercia, D., Aiello, L.M., Schifanella, R., Davies, A.: The digital life of walkable streets. In: Proceedings of the 24th International Conference on World Wide Web, WWW '15, pp. 875–884. International World Wide Web Conferences Steering Committee, Republic and Canton of Geneva, Geneva (2015)

12. Quercia, D., Schifanella, R., Aiello, L.M.: The shortest path to happiness: recommending beautiful, quiet, and happy routes in the city. In: Proceedings of the 25th ACM Conference on Hypertext and Social Media, HT '14, pp. 116–125. ACM, New York (2014)
13. Salton, G., Wong, A., Yang, C.S.: A vector space model for automatic indexing. Commun. ACM **18**(11), 613–620 (1975)
14. Speck, J.: Walkable city: how downtown can save America, one step at a time. Farrar, Straus and Giroux (2012)
15. United Nations: World Urbanization Prospects: The 2014 Revision. United Nations, Department of Economic and Social Affairs, Population Division (2014)
16. Walkable America: Walkability checklist: How walkable is your community? (2013). https://www.nhtsa.gov/sites/nhtsa.dot.gov/files/walkingchecklist.pdf
17. Wefering, F., Rupprecht, S., Bührmann, S., Böhler-Baedeker, S.: Guidelines. Developing and implementing a sustainable urban mobility plan. In: Workshop, March, p. 117 (2013)

Experimental Investigation of Pedestrian Queuing Behaviour

Jiahua Zhang, Miho Iryo-Asano, and Charitha Dias

Abstract One key aspect of pedestrian dynamics is the pedestrian queuing behaviour particularly in front of bottlenecks. As previous studies have highlighted, features of pedestrian queues in front of different types of bottlenecks are considerably dissimilar. Insights into similarities and differences of pedestrian queuing behaviour for typical bottlenecks can be important for the planning and design of public walking space. However, no sufficient empirical studies have been carried out so far to examine the diversity of pedestrian queuing behaviour. In this study, a series of experiments were performed to explore the characteristics of pedestrian queue formations under different conditions.

As the results suggest, pedestrians tend to form organized queues before bottlenecks with a clear pass control (e.g., service counters where only one person can be served once). Wider bottlenecks, capacity reductions and low service rates were found to motivate pedestrians to merge or overtake in the upstream of the bottleneck.

1 Introduction

Studies on pedestrian dynamics are receiving growing interest as understanding pedestrian behaviour is essential in the planning and design of public spaces such as railway stations and shopping malls. Unlike traffic jams on the roadways, pedestrian congestion in public spaces is not only an issue of time waste, it may

J. Zhang (✉)
Graduate School of Engineering, The University of Tokyo, Tokyo, Japan
e-mail: zhangjh@iis.u-tokyo.ac.jp

M. Iryo-Asano
Department of Environmental Engineering and Architecture, Nagoya University, Nagoya, Japan
e-mail: iryo@nagoya-u.jp

C. Dias
Institute of Industrial Science, The University of Tokyo, Tokyo, Japan
e-mail: cdias@iis.u-tokyo.ac.jp

S. H. Hamdar (ed.), *Traffic and Granular Flow '17*,
https://doi.org/10.1007/978-3-030-11440-4_21

also develop into stampedes when the density is extremely high. Balancing the efficiency of the facility and comfort of the pedestrians is a challenging task not only during emergencies but also during day-to-day activities. Microscopic pedestrian walking behaviour as well as macroscopic flow characteristics could be considerably different depending on the situation and bottleneck type. Thus, it is important to understand pedestrian walking behaviour corresponding to bottlenecks with different characteristics (i.e., geometrical settings and bottleneck capacity) before planning and designing pedestrian facilities. As highlighted in the previous studies, pedestrian walking behaviours in front of different types of bottlenecks (e.g., ticket counters, exits, stairways, and elevators) are non-identical[6, 8]. That is, in general people do not always arrange themselves into mushroom- or semicircular-shaped queues in front of bottlenecks that are produced by most of the available simulation models[4, 8].

In the context of understanding pedestrian queuing behaviour, several studies can be found in the literature. Kim et al. [5] developed a micro-simulation model to replicate queuing behaviour at a ticket booth system based on social force model. Yasufuku [12] introduced a multi-agent simulation system based on the social force model to represent pedestrian queuing behaviour by adding ellipse-based collision detection and following mechanisms. These studies have basically investigated queuing behaviour as a one-dimensional transition process that is applicable for strictly one-by-one queues with FIFO principle. However, for more chaotic queue formations, it is difficult to construct mathematical models to represent the complicated queuing phenomenon. Köster and Zönnchen [7] proposed a dynamic floor field to simulate pedestrian queuing behaviour and successfully represented a loose and more realistic pedestrian queue. However, as also highlighted by them, empirical studies are necessary to understand when, where and how to switch between behaviour patterns. Zheng et al. [14] incorporated new rules into the social force model and replicated behaviours such as selecting a queue, entering to a queue and waiting under a uncongested condition. However, the author only considered queue length as the influencing factor. All these studies are either outcomes of simulations or confined to a few types of pedestrian queues. Thus, the existing studies cover a limited range of cases, and therefore characteristics of pedestrian queues under different situations have not been completely understood.

This study aims to explore the characteristics of pedestrian queuing behaviour in the upstream of bottlenecks based on experimental investigation. Three features of bottlenecks are considered as the main factors.

- Bottleneck width
- Bottleneck type
- Unit width capacity (service rate) of bottleneck.

In order to explore the relationship between these factors and characteristics of pedestrian queues, the experiment was designed by changing the properties of bottlenecks from two aspects: (a) directly changing the width of bottleneck, and (b) controlling the service rate of the bottleneck. The detailed settings are discussed in the following section.

2 Experiment

The experiment was performed in an open space at the University of Tokyo with 60 participants (29 males and 31 females) whose ages ranged from 20 to 60. Bottleneck scenarios were prepared with three kinds of widths (0.8 m, 1.0 m and 1.2 m) and under the following four conditions:

(a) Free flow (uncontrolled)
(b) Departure control slow
(c) Departure control fast
(d) Stairway.

In condition (a), participants walked through bottlenecks freely, and it represented a typical narrow corridor. Conditions (b) and (c) were realized by passing a plastic ball to each participant approaching the entrance of the bottleneck with a certain frequency (one ball every 2 s and one ball every 1.3 s to replicate slow and fast service rates, respectively). The passing frequency was accurately controlled using a metronome software application. This condition was designed to simulate service counters that are common at transfer stations. Note that in conditions (b) and (c), only one person passed the ball to the participants for 0.8 m cases, and two people were arranged at both sides for the 1.2 m cases. The aim of condition (d) was to observe queuing behaviour at stairways, and it was imitated by installing two pairs of polystyrene blocks within the bottleneck. The height and separation between these polystyrene blocks were carefully adjusted to obtain a flow rate similar to the flow rate through an actual staircase. Further discussions on comparison of these flow rates are provided in Sect. 3. For simplicity, we abbreviate these conditions as FF (free flow), DS (departure control slow), DF (departure control fast) and SW (stairway) hereinafter.

The bottleneck was arranged with four lightweight wooden boards (Fig. 1). Prior to each experiment run, participants were asked to stand in six lines inside a 5×6 m rectangular holding area (Fig. 1a) so that the same start pattern was guaranteed. Ten experiment scenarios were designed with three repetitions for each scenario as shown in Table 1. The entire experiment was video recorded with two overhead video cameras. The configuration of the experiment site and a snapshot are shown in Fig. 1. After the experiment, trajectories of the pedestrians were extracted using a video image-processing system, called *Traffic Analyzer*[11]. Trajectory data were recorded every 0.2 s. The coordinate was built as shown in Fig. 1a. The bottleneck located from $Y = 10.85$ m to $Y = 12.85$ m with a centre line at $X = 4.0$ m. The estimated average location error of the coordinate conversion in the tracking system was 0.023 m.

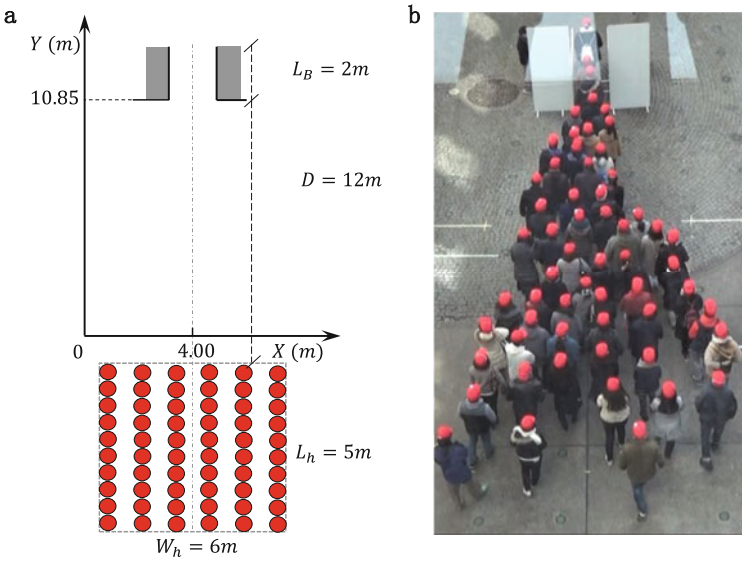

Fig. 1 (**a**) Experiment configuration. (**b**) Snapshot from 0.8 m DS scenario

Table 1 Average bottleneck capacity (ped/s)

Condition		FF	SW	DS	DF
Width (m)	0.8	1.05	0.65	0.50	0.75
	1.0	1.80	1.25		
	1.2	2.01	1.36	1.00	1.41

3 Analysis Results

By analysing the walking trajectories, three issues (i.e., bottleneck capacity, lateral distribution of the queue and spatial distribution of walking speed) are focused on to explore the characteristics of pedestrian queuing behaviour.

3.1 Bottleneck Capacity

The bottleneck capacity J was measured using the mean value of the time headway $(t_{i+1} - t_i)$ of two pedestrians, with one following the other when they crossed the departure line specified at the exist of bottleneck as explained in Eq. (1). The

Table 2 Maximum flow rate comparison on stairways (ped/s/m)

Type	Chen [1]	Cheung [2]	Daly [3]	Shaha [10]	Ye [13]	This study		
						0.8 m	1.0 m	1.2 m
Ascend	1.22	1.17	1.03	–	1.01	0.81	1.25	1.13
Descend	1.13	1.33	1.14	–	1.24			
Mixed	1.05	–	–	0.83	–			

calculation results of the average bottleneck capacities for 10 scenarios are shown in Table 1.

$$\langle \Delta t_i \rangle = \frac{1}{N-1} \sum_{i=1}^{N-1} t_{i+1} - t_i, \quad \text{and} \quad J = \frac{\Delta N}{\Delta t} = \frac{1}{\langle \Delta t_i \rangle} \tag{1}$$

The bottleneck capacities in FF conditions were found to be consistent with past results when a comparison was made with data summarized by Seyfried et al. [9]. The capacities in SW conditions and unit width maximum flow observed on real stairways were also compared as shown in Table 2. Although it was difficult to consider SW conditions exactly as ascending or descending stairways, flow rates still lay in the range of previous data. Thus, it can be stated that the flow conditions of stairways are adequately replicated with the set-up used in this study.

3.2 Lateral Distribution of Pedestrian Queue

Unlike queues in vehicular traffic, pedestrian queues are two dimensional, i.e., pedestrian queues spread in lateral directions as well. In order to compare the lateral distribution of pedestrian queues in each scenario, several horizontal lines $Y = A$ (perpendicular to the approaching direction of the pedestrians) were selected, and cross points coordinates of trajectories with horizontal lines were recorded. By comparing the distribution of the X-coordinates of the cross points, differences in pedestrian queuing behaviour between scenarios were expected to be revealed. In this study, $S = 0.24$ m is used as a bin and the probability of finding one pedestrian in 13 bins that symmetrically lay at both sides of the centre line was calculated. The calculation results of the 0.8 m and 1.2 m cases are shown in Fig. 2.

By comparing Fig. 2 vertically, it can be found that only one peak exists for the 0.8 m bottleneck and two peaks for the 1.2 m cases, and they grow steeper when pedestrians approach the bottleneck, as lanes that can be accommodated within the bottleneck are formed gradually when pedestrians are approaching it. On the other hand, if we compare the probability of each condition, especially in (b) and (c), higher peaks for two departure control cases are confirmed, which can be regarded as a stronger tendency of pedestrians to form a one-by-one queue.

Further, a statistical analysis was performed to quantitatively examine the similarities and differences in pedestrian queues' lateral distribution between

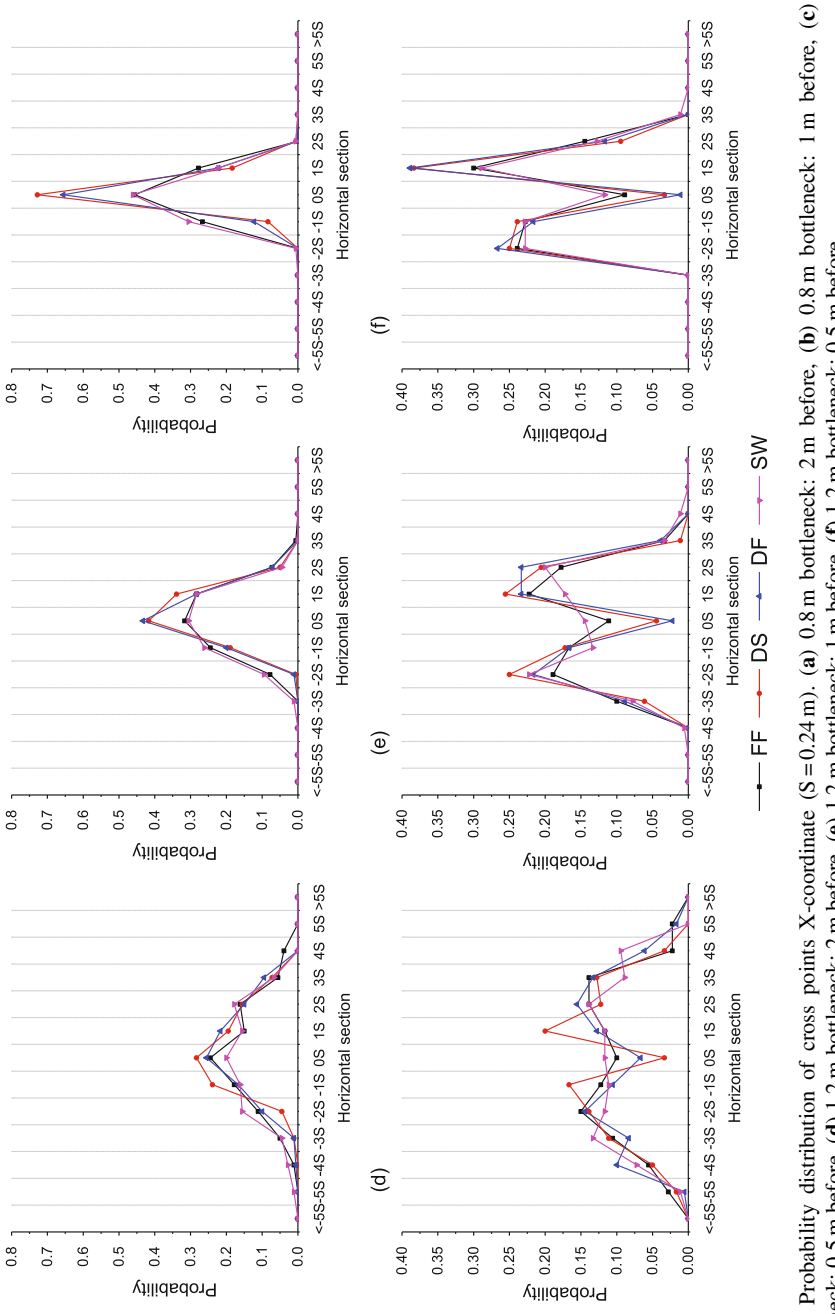

Fig. 2 Probability distribution of cross points X-coordinate (S = 0.24 m). (**a**) 0.8 m bottleneck: 2 m before, (**b**) 0.8 m bottleneck: 1 m before, (**c**) 0.8 m bottleneck: 0.5 m before, (**d**) 1.2 m bottleneck: 2 m before, (**e**) 1.2 m bottleneck: 1 m before, (**f**) 1.2 m bottleneck: 0.5 m before

scenarios. The standard deviation of the cross points X-coordinate in DS and DF (i.e., 1 m before: 0.185 m and 0.206 m, respectively; 0.5 m before: 0.111 m and 0.121 m, respectively) was remarkably smaller than those of FF and SW (i.e., 1 m before: 0.251 m and 0.258 m, respectively, 0.5 m before: 0.155 m and 0.157 m, respectively), which indicates a higher concentration of the queue in the centre for departure control cases. Moreover, the K-S test was applied to examine whether the probability distributions differed under a significance level of 0.05. The test results show that probability distributions between FF and DS were significantly different from 1 m before the bottleneck (Asymp. Sig. (2-tailed) = 0.001 (0.5 m before) < 0.019 (1 m before) < 0.05). Similarly, significant differences could be confirmed 0.5 m before the bottleneck between FF and DF (0.010 (0.5 m before) < 0.05 < 0.106 (1 m before)). Moreover, given the smaller standard deviations in DS and DF conditions, it can be concluded that, at least for 0.8 m bottleneck, which can only allow one person to comfortably pass once, pedestrians have a tendency to form a one-by-one queue in departure control conditions.

3.3 Spatial Distribution of Walking Speed

One approach to investigate the characteristics of pedestrian queuing behaviour is to analyse the walking speed spatio-temporally. While walking speed transition over time (e.g., stop-and-go duration) is mainly dominated by bottleneck capacity, spatial distribution of walking speed may provide an instructive point of view on overtaking and merging behaviour during the queuing process. In this section, an analysis of area-based average speed is conducted, and several findings are obtained from the comparison between scenarios. Here, area-based average walking speed is defined as shown in Eq. (2).

$$\overline{v_s} = \frac{\sum_{i=1}^{n} s_i}{\sum_{i=1}^{n} t_{i,in} - t_{i,out}} \tag{2}$$

where $\overline{v_s}$ is the average speed of an area; n is the time aggregated number of pedestrians within this area; s_i is the distance travelled by pedestrian i in the area; $t_{i,in}$ is the time when pedestrian i enters the area and $t_{i,out}$ is the time when pedestrian i leaves the area. Using the definition in Eq. (2), the average walking speed in different zones was compared. In this study, three vertical zones were divided with the same length of 7 m (queue is formed in this range for all scenarios). The centre zone had the same width as bottleneck, while two side zones lay at two sides of the centre zone with an infinite width. Owing to the symmetry, the two side zones were handled as a whole. The calculation results are shown in Table 3.

Table 3 Average walking speed (m/s) in vertical zones

Bottleneck width		0.8 m	1.0 m	1.2 m
FF	Centre zone	0.447	0.640	0.591
	Side zone	0.412	0.697	0.684
	Difference (%)	−8	9	16
SW	Centre zone	0.287	0.466	0.444
	Side zone	0.331	0.572	0.612
	Difference (%)	15	23	38
DS	Centre zone	0.242		0.346
	Side zone	0.296		0.543
	Difference (%)	22		57
DF	Centre zone	0.348		0.445
	Side zone	0.326		0.554
	Difference (%)	−6		24

In Table 3, the centre zone is considered to be the benchmark so that if speed in the side zone is higher than that in the centre zone, the difference will be a positive value; otherwise it is negative. If a comparison is made under the same condition for different widths, it can be found that the difference increases with bottleneck width. This is because pedestrians tend to walk faster from two sides in order to merge or overtake in front of a wider bottleneck. On the other hand, larger differences can be observed in SW compared to FF for the same width, and similarly with DS and DF. Therefore, it can be inferred that capacity reduction (stairway) or low service rate will lead to a stronger preference to quickly merge or overtake from two sides of walking groups.

4 Conclusion

This study experimentally investigated the queuing behaviour of pedestrians in the upstream of different types of bottlenecks. By comparing the bottleneck capacities with previous experiments, the feasibility of using controlled passing rules to simulate different types of bottlenecks was confirmed. Based on the extracted trajectory data two characteristics of queuing behaviour, i.e., lateral distribution of the queue and spatial distribution of walking speed, were investigated. On the one hand, it was found that pedestrians tend to form organized queues before bottlenecks with a clear pass order, especially for 0.8 m wide bottlenecks, which can only allow one person to comfortably pass. On the other hand, it is concluded that wider bottlenecks, capacity reductions and low service rates would motivate pedestrians to walk faster from two sides of walking groups to merge or overtake.

In the future work, traffic waves of queue propagation will be compared between these scenarios. Further, the effect of pedestrian queues on macroscopic characteristics of pedestrian flow should also be confirmed.

Acknowledgements The authors are thankful to the Research Center for Advanced Science and Technology, the University of Tokyo, for providing the experimental spaces.

References

1. Chen, X., Ye, J., Jian, N.: Relationships and characteristics of pedestrian traffic flow in confined passageways. J. Transp. Res. Board **2198**, 32–40 (2010)
2. Cheung, C., Lam, W.H.: Pedestrian route choices between escalator and stairway in MTR stations. J. Transp. Eng. **124**(3), 277–285 (1998)
3. Daly, P., McGrath, F., Annesley, T.: Pedestrian speed/flow relationships for underground stations. Traffic Eng. Control **32**(2), 75–78 (1991)
4. Helbing, D., Farkas, I., Vicsek, T.: Simulating dynamical features of escape panic. Nature **407**(6803), 487–490 (2000)
5. Kim, I., Galiza, R., Ferreira, L.: Modeling pedestrian queuing using micro-simulation. Transp. Res. A Policy Pract. **49**, 232–240 (2013)
6. Kneidl, A.: How do people queue? A study of different queuing models. In: Traffic and Granular Flow'15, pp. 201–208. Springer, Cham (2016)
7. Köster, G., Zönnchen, B.: Queuing at bottlenecks using a dynamic floor field for navigation. Transp. Res. Proc. **2**, 344–352 (2014)
8. Okazaki, S., Matsushita, S.: A study of simulation model for pedestrian movement with evacuation and queuing. In: International Conference on Engineering for Crowd Safety, vol. 271 (1993)
9. Seyfried, A., Passon, O., Steffen, B., Boltes, M., Rupprecht, T., Klingsch, W.: New insights into pedestrian flow through bottlenecks. Transp. Sci. **43**(3), 395–406 (2009)
10. Shaha, J., Joshi, G., Parida, P.: Behavioral characteristics of pedestrian flow on stairway at railway station. Proc. Soc. Behav. Sci. **104**, 688–697 (2013)
11. Suzuki, K., Nakamura, H.: Trafficanalyzer-the integrated video image processing system for traffic flow analysis. In: Proceedings of the 13th Its World Congress, London, 8–12 October 2006 (2006)
12. Yasufuku, K.: Reproduction of pedestrian movement in queue by using multi-agent system and analysis of crowd flow affected by following behavior. J. Archit. Plann. **81**(722), 821–829 (2016)
13. Ye, J., Chen, X., Yang, C., Wu, J.: Walking behavior and pedestrian flow characteristics for different types of walking facilities. J. Transp. Res. Board **2048**, 43–51 (2008)
14. Zheng, X., Li, H.Y., Meng, L.Y., Xu, X.Y., Yang, Y.H.: Simulating queuing behaviour of pedestrians in subway stations. In: Proceedings of the Institution of Civil Engineers-Transport, pp. 1–8. Thomas Telford Ltd., London (2017)

Safety Training Through Educational Online Computer Games on Crowd Evacuations?

Nikolai W. F. Bode

Abstract Research into pedestrian evacuation dynamics has many direct applications in building design, facility management and event planning. It is therefore crucial that research findings and the need for further work are communicated to researchers, policy makers, planners, practitioners and, ultimately, the public. Experiments in virtual environments are a popular research tool, as they allow users an immersive experience of crowd evacuations. Online computer games derived from such experiments could thus be a useful tool for communicating pedestrian dynamics research. This paper is part of a project that aims to raise awareness for research into crowd evacuations by using online computer games. Here, I explore the suitability of evacuation games as educational tools by conducting a pilot study into user learning outcomes and engagement levels. I find that games achieve learning and engagement in less time than text-based information, but not as comprehensively. This preliminary study is intended as a starting point for developing the games further.

1 Introduction

Experiments in virtual environments are a popular tool to investigate human behaviour in crowd evacuations [3, 8, 9]. They facilitate the safe, controlled and cheap assessment of behaviour and provide an interactive and immersive experience [8]. These properties make virtual crowd evacuations useful beyond immediate use in research.

Research into pedestrian evacuation dynamics has many direct applications. It is therefore crucial that research findings and the need for further work are communicated to a broad audience of researchers, policy makers, planners, practitioners and, ultimately, the public. Computer games that simulate virtual environments could be

N. W. F. Bode (✉)
Department of Engineering Mathematics, University of Bristol, Bristol, UK
e-mail: nikolai.bode@bristol.ac.uk

S. H. Hamdar (ed.), *Traffic and Granular Flow '17*,
https://doi.org/10.1007/978-3-030-11440-4_22

a useful tool in this important task, as they can be more engaging and achieve a better retention of knowledge than text-, video- or audio-based techniques [4, 5, 10, 12].

A range of studies has explored educational uses of computer games, often called 'serious games', in evacuation or pedestrian contexts [4, 10, 11]. Some game-based education is aimed at professional first responders, such as firefighters [12]. Here, I am interested in users who have no specialist training and experience crowd evacuations only by accident. In this context, previous studies have investigated the use of virtual environments to increase the retention of safety instructions for passengers in aviation [4, 5], for example.

Assessing the suitability of games as educational tools is paramount [5, 10]. The main purposes of educational computer games are first to engage users, second to impart knowledge, third to challenge existing views and fourth to allow users to develop and test their own theories. Unfortunately, the causes and dynamics of crowd evacuations depend heavily on the context, which makes a generally valid and detailed training program unattainable. For example, training people for specific scenarios could be counter-productive by reducing their flexibility in responding to changing situations. In response, some educational games include a mixture of general and specific training goals, such as responding quickly to alarms and familiarising building occupants with building egress routes, respectively [6].

Instead of focussing on specific training goals, I design educational online computer games on crowd evacuations that are aimed at raising awareness for the complexity of decision-making and interactions during crowd evacuations, to ensure that people can reflect in an informed way on the progress and limitations in planning for emergencies. Importantly, findings from previous research (e.g. [1–3]) make it possible to provide evidence-based feedback to individual users on how their behaviour compares to what people do on average. In this contribution, I present findings from a preliminary study into user learning outcomes and engagement levels that compares my games to text-based information dissemination (as previously suggested [4, 5]).

2 Methods

In my study, I asked participants to either play a simple computer game that was based on a previously published virtual environment experiment [1] or to read a short report on the same experiment. Screenshots of the computer game and the start of the text can be seen in Figs. 1 and 2, respectively. The main difference between the computer game and the original experiment [1] was that participants could play the game as many times as they wanted and that they were given feedback comparing their behaviour to what participants did on average in the original experiment. For example, participants were informed that they had avoided a longer queue and what percentage of participants in the experiment had done the same. In this way, participants could explore the four different experimental conditions (reported in [1]) and thus important factors for decision-making in crowd evacuations. The text

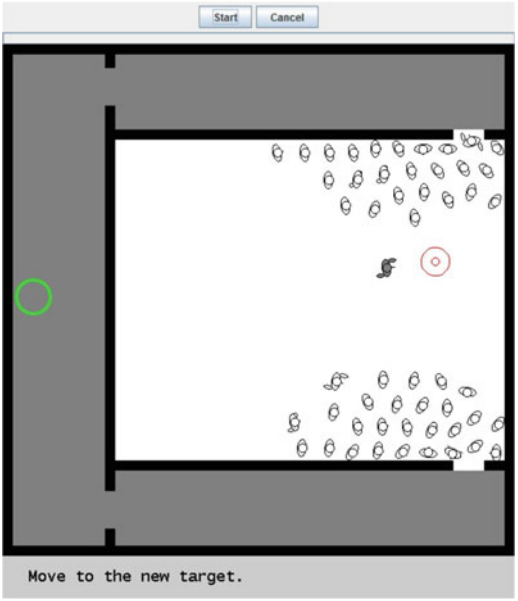

Fig. 1 Still image of computer game. After an evacuation is initiated, players (indicated in grey) have to exit a simple room layout by reaching a target (green circle). Computer-simulated evacuees can be seen to queue at the exits. Players have to decide between two evacuation routes. In the original experiment, changing experimental conditions were used to investigate determinants of human route choice. In the game, players can explore these different scenarios obtaining feedback on how their behaviour compares to the average

was just over 1100 words long and described the background, methodology and findings of the original experiment.

To assess how participants learned from and engaged with the game and the text, I invited them to answer questions testing learning and engagement. In the learning assessment, I asked participants the same questions before and after they had played the game or read the text. Changes in participants' answers were indicative of self-reported learning. Participants provided their answers by adjusting a slider between values of 0 and 100. The default value of the slider was 50 when the questions were asked first and when the questions were asked for the second time, the sliders were positioned where participants had moved them when first answering the questions. The learning questions are listed below. Information in brackets indicated the interpretation of the slider position to participants.

1. How confident are you about knowing what a 'crowd evacuation' is? (LEFT: very unsure; RIGHT: very confident)
2. How confident are you in your understanding of current research on crowd evacuations? (LEFT: very unsure; RIGHT: very confident)
3. To what extent do you think can researchers predict the behaviour of individuals in crowd evacuations? (LEFT: not at all; RIGHT: completely)
4. In crowd evacuations, we have to make decisions that may carry a risk (e.g. which exit to use? Is it the shortest?). How many such risks do you feel you can identify? (LEFT: 0; RIGHT: 100)

Questions about engagement in the study were asked only once, after participants had answered the learning questions for the second time. Participants provided

Fig. 2 Screenshot of text about evacuation computer game experiment provided in the study

answers to engagement questions in the same way as for learning questions and the default value, representing indifference, was also set to 50. Positive or negative deviations from this default value were interpreted as increased or decreased self-reported engagement with the study. The engagement questions were as follows:

1. How much did you enjoy the activity? (LEFT: not at all; RIGHT: a lot)
2. How likely is it that you would do something like this again? (LEFT: never again; RIGHT: keen to do this again)
3. How likely is it that you would talk to others about this activity? (LEFT: not at all; RIGHT: definitely tell others)
4. How interested are you to find out more about research on crowd evacuations? (LEFT: not at all; RIGHT: very keen)

In addition to answering these questions to indicate their engagement, participants could also write free-text comments or feedback.

My analysis was based on the difference in answer score for learning (subtracting the score of the first from the second answer) and the answer score for engagement questions. I performed two types of tests on these summary statistics. First, I used bootstrap tests with $n = 10{,}000$ samples to assess if the learning and engagement score were different to 0 and 50, respectively. Second, I used permutation tests ($n = 10{,}000$ permutations) to determine whether the difference in scores between

participants who played the game and ones who read the text was larger than expected by chance.

Ethical approval for my study was granted by the Faculty of Engineering Ethics Committee of the University of Bristol and I obtained informed consent from all participants. I recruited a total of 20 participants (10 each for game and text). Most of them were doctoral students, 8 were female, 11 male and 1 did not report gender. The median age was 26.5 years with a range from 21 to 33 years.

3 Results

Participants spent less time playing the game than reading the text (117 s versus 287 s, $W = 97$, $p = 7.58 \times 10^{-5}$, Wilcoxon rank-sum test). With the exception of one question, question 2, self-reported learning did not differ between participants who read the text and ones who played the game (Fig. 3). Participants who read the

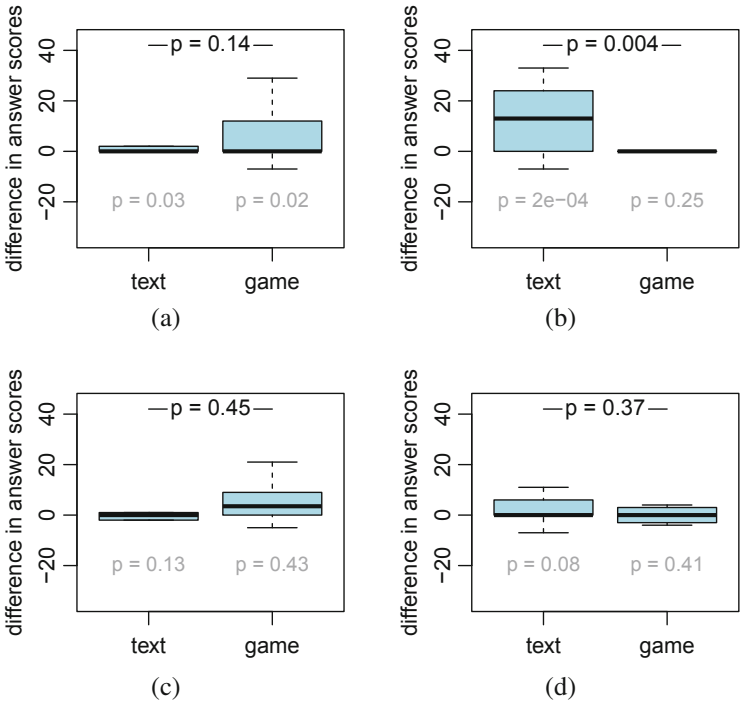

Fig. 3 Box-and-whisker plots of changes in answer scores for learning questions 1–4 in panels (**a**)–(**d**), respectively. Boxes indicate the upper and lower quartile. The line inside boxes indicates the median, whiskers indicate 1.5 times the interquartile range or the maximal/minimal values if they are within this range. *P*-values are from tests for differences between participants who read the text and ones who played the game (black) and from tests on mean answer score changes being different to zero (grey)

text reported on average significantly positive changes in answer scores indicating an increase in self-reported knowledge (with the exception of question 3, Fig. 3). In contrast, changes in answer scores for participants who played the game were only significantly positive for question 1 (Fig. 3a). These results suggest that on average, learning effects were stronger for participants who read the text, but that there was not a consistently large difference in score changes caused by the text compared to the game.

There was no difference in self-reported engagement between game and text (Fig. 4). On average, answer scores for all questions, both for participants playing the game and for ones reading the text, were significantly higher than 50, the score indicating indifference (Fig. 4). This suggests that text and game positively engaged participants in equal measure.

In addition to the quantitative measures reported above, four participants, all of whom read the text, provided free-text comments. Two out of these comments indicated a desire to play the games.

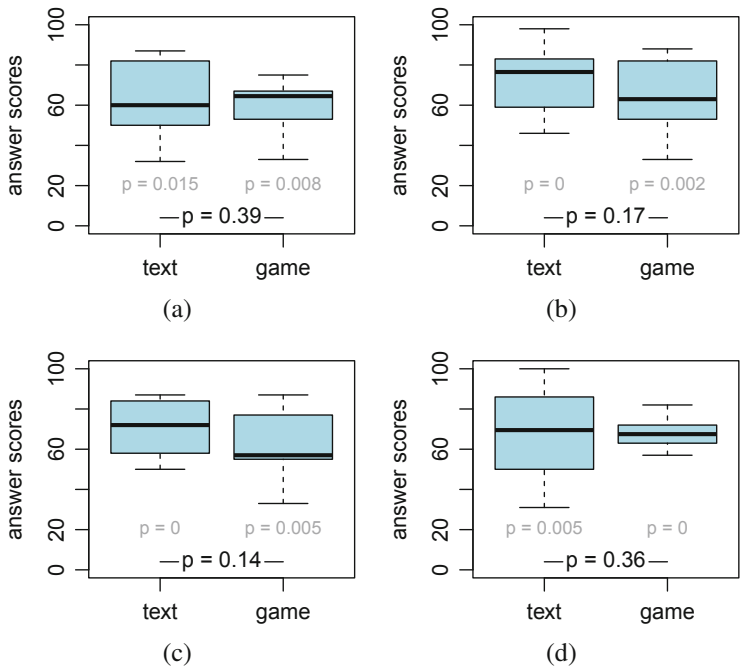

Fig. 4 Box-and-whisker plots of answer scores for engagement questions 1–4 in panels (**a**)–(**d**), respectively. *P*-values are from tests for differences between participants who read the text and ones who played the game (black) and from tests on mean answer score changes being different to the default of 50 (grey)

4 Discussion and Outlook

In summary, the results of my pilot study suggest that my games achieve learning and engagement in less time than text, but do not impart information as comprehensively. However, these findings have to be viewed in light of the preliminary nature of my study. The low number of participants included in the study means that effects have to be interpreted carefully. All participants read the text or played the game in the presence of the experimenter. It is likely that this affected the extent to which they engaged with the study. For example, if text and game were placed online, participants may be less motivated to read the entire text or play the game multiple times. Furthermore, the evaluation of engagement and learning effects could be improved. Physiological measures, such as heart rate or electrodermal activity could be used to assess engagement more objectively than the self-reported measures approach I used here [5].

The display and controls of my computer games are deliberately simple. The display is in two dimensions, providing participants with a top-down view of a building, and controls are based on simple mouse clicks (for details, see [1]). It has previously been discussed controversially if high-fidelity, i.e. highly realistic, virtual environments aid the goals of educational computer games [10]. For example, on the one hand, users may have expectations on game displays from playing entertainment games, but on the other hand, rich displays and more complex controls associated with them may distract from the educational content [10]. Overall, it has been suggested that increases in fidelity are not directly linked with increases in knowledge transfer [7]. I suggest that considering the target audience is useful for deciding on the required realism of the display. When preparing firefighters for what smoke-filled rooms look like [12], high-fidelity simulations may be appropriate. However, when the goal is to raise awareness for research, as I intend to do with my games, simple displays and controls could facilitate addressing a broad audience.

To conclude, in my view the present study is a useful starting point. While only indicative, the findings presented here will be useful for developing crowd evacuation games for online deployment. In particular, feedback from participants indicated that a narrative contextualising the game is desirable. This suggestion is corroborated by the previous research [10]. Anecdotally, from talking to participants in game-based studies (e.g. the present study or [1–3]), individuals are keen to receive specific advice on how to behave in crowd evacuations. My view is that while very general recommendations may be possible (e.g. ‘respond quickly to alarms’, ‘listen to safety personnel’, etc.), detailed advice is not. Therefore, my aim is to convey the complexity of crowd evacuations and the differences between individuals to players. As such, future developments of my games seek to engage and make people think, rather than offering advice.

Acknowledgements N.W.F.B. was supported by a Leverhulme Early Career Fellowship and the AXA Research Fund. The author thanks all participants in the study.

References

1. Bode, N., Codling, E.: Human exit route choice in virtual crowd evacuations. Anim. Behav. **86**(2), 347–358 (2013)
2. Bode, N., Kemloh Wagoum, A., Codling, E.: Human responses to multiple sources of directional information in virtual crowd evacuations. J. R. Soc. Interface **11**(91), 20130904 (2014)
3. Bode, N., Miller, J., O'Gorman, R., Codling, E.: Increased costs reduce reciprocal helping behaviour of humans in a virtual evacuation experiment. Sci. Rep. **5**, 15,896–15,896 (2015)
4. Chittaro, L.: Designing serious games for safety education: learn to brace versus traditional pictorials for aircraft passengers. IEEE Trans. Vis. Comput. Graph. **22**(5), 1527–1539 (2016)
5. Chittaro, L., Buttussi, F.: Assessing knowledge retention of an immersive serious game vs. a traditional education method in aviation safety. IEEE Trans. Vis. Comput. Graph. **21**(4), 529–538 (2015)
6. Chittaro, L., Ranon, R.: Serious games for training occupants of a building in personal fire safety skills. In: Conference in Games and Virtual Worlds for Serious Applications, 2009. VS-GAMES'09, pp. 76–83. IEEE, Piscataway (2009)
7. Feinstein, A.H., Cannon, H.M.: Constructs of simulation evaluation. Simul. Gaming **33**(4), 425–440 (2002)
8. Kinateder, M., Ronchi, E., Nilsson, D., Kobes, M., Müller, M., Pauli, P., Mühlberger, A.: Virtual reality for fire evacuation research. In: 2014 Federated Conference on Computer Science and Information Systems (FedCSIS), pp. 313–321. IEEE, Piscataway (2014)
9. Moussaïd, M., Kapadia, M., Thrash, T., Sumner, R., Gross, M., Helbing, D., Hölscher, C.: Crowd behaviour during high-stress evacuations in an immersive virtual environment. J. R. Soc. Interface **13**(122), 20160414 (2016)
10. Ravyse, W.S., Blignaut, A.S., Leendertz, V., Woolner, A.: Success factors for serious games to enhance learning: a systematic review. Virtual Real. **21**(1), 31–58 (2017)
11. Schwebel, D.C., Gaines, J., Severson, J.: Validation of virtual reality as a tool to understand and prevent child pedestrian injury. Accid. Anal. Prev. **40**(4), 1394–1400 (2008)
12. Williams-Bell, F.M., Kapralos, B., Hogue, A., Murphy, B., Weckman, E.: Using serious games and virtual simulation for training in the fire service: a review. Fire Technol. **51**(3), 553–584 (2015)

Hybrid Tracking System for Pedestrians in Dense Crowds

Jette Schumann, Maik Boltes, and Armin Seyfried

Abstract For a proper understanding and modeling of pedestrian dynamics reliable empirical data are needed. Often the level of heterogeneity of pedestrians in laboratory experiments does not correspond with the level in the field. New studies have been carried out to examine one factor of heterogeneity by considering people with physical, mental, and age-related disabilities. In these studies a novel hybrid tracking system consisting of a camera system and inertial measurement units (IMUs) was used for the first time. The use of IMUs solves the critical issue of occlusion caused by the perspective view of the camera system and different body heights expected for participating wheelchair users in dense crowds. The IMUs act as an extension of the camera system to enable a complete data extraction of the participants' trajectories and gathering of additional movement data. This paper focuses on the hybrid tracking system and proposes a tracking procedure for wheelchair users participating in these studies.

1 Introduction

The understanding of the nature of pedestrian streams is a fundamental step towards a safe and comfortable design of public buildings and facilities. To get new insights laboratory pedestrian experiments are conducted with varying factors influencing the movement of the pedestrians such as the width of a bottleneck or the motivation of the participants. For analyzing the movement in detail a complex tracking system is needed which provides data of each participant with a high temporal and spatial resolution [4]. Based on the extracted information important measures for transport characteristics such as flow, velocity, and density can be determined describing, e.g., the level of comfort or safety.

J. Schumann (✉) · M. Boltes · A. Seyfried
Institute for Advanced Simulation, Forschungszentrum Jülich, Jülich, Germany
e-mail: j.schumann@fz-juelich.de; m.boltes@fz-juelich.de; a.seyfried@fz-juelich.de

S. H. Hamdar (ed.), *Traffic and Granular Flow '17*,
https://doi.org/10.1007/978-3-030-11440-4_23

In our past experiments [5, 8, 9] the heterogeneous composition of pedestrian streams was not considered, even though interactions between the different groups of people might affect the dynamics of the whole crowd. To gather data for a deeper analysis of the influence of the heterogeneity of a crowd on its movement new experiments have been carried out involving people with and without disabilities. Those experiments have been conducted within the scope of the research project SiME [2] with the aim of improving the safety for people with physical, mental, and age-related disabilities.

Consisting of several cameras on the ceiling, the basic tracking system is not capable of detecting small people, especially wheelchair users, in a crowd. Because of the perspective view small people might not be visible to the cameras when they are surrounded by taller people temporarily. For a comprehensive analysis of pedestrian streams incomplete trajectories should be prevented. To tackle this problem an extended tracking system is needed. Usually the pedestrian experiments are performed indoor for stable and homogeneous light conditions and therefore the tracking system must be applicable in buildings as well.

Due to the arising needs of location-based services in areas like medical technology, advertising, tourism, sports, or rescue many indoor localization technologies have been developed over the past years and can be classified into [16]:

- Wireless-communication-based localization technologies such as WiFi, Bluetooth, ultra-wideband, ultrasound, and radio frequency,
- Dead reckoning techniques using motion sensors and odometers, and
- Video scene analysis using methods for tag detection, scene matching, or tracking moving objects (which is partly implemented by the camera tracking system).

A major advantage of dead reckoning techniques is that no additional infrastructure is needed in contrast to other systems. For pedestrian dead reckoning (PDR) inertial measurement units (IMUs) are widely used. Wearable IMUs are available as micro-electro-mechanical systems (MEMS), which can be attached to the persons' body without restricting their movement. They are cost-efficient, light-weighted, and consist of only few moving parts which makes them durable [7, 18]. IMUs are self-contained so that no time is required for the preparation of the tracking area. The use of IMUs keeps the extension of the camera system simple, but requires methods for calibration, fusion, and restriction of the drift (see Sect. 2). Besides it is possible to track movement processes inside the crowd which are not perceptible by cameras such as the bobbing movement of steps and even full body tracking [1, 13, 14].

The focus of this paper is the tracking of wheelchair users with IMUs. Due to noisy IMU signals it is necessary to constrain the movement of the wheelchair users with data from the camera system resulting in a hybrid tracking algorithm fusing IMU and camera data.

2 Hybrid Tracking System

For the SiME studies the movement of the test persons has been recorded with a camera detection system (see Fig. 1). The cameras were aligned in a grid on the ceiling so that the complete coverage of the area was ensured. For a more precise detection the participants were wearing markers in form of caps which color encodes their height. In addition IMUs were worn by wheelchair users that might get covered due to their small height. To distinguish the wheelchair users (and the IMUs they have worn) labels were attached to their shoulders. The IMUs have a size of just a few centimeters and were attached with clamps or tape to the wheelchairs. As the camera tracking system is described in [3] this section focuses on the IMU tracking algorithms and the fusion of camera and IMU data.

2.1 IMU Tracking

The used IMUs from SabelLabs [11] consist of an accelerometer, a gyroscope, and a magnetometer which provide measurements along three axis, respectively. With those inertial sensors it is possible to keep track of movement changes by measuring the acceleration, rotation rate, and magnetic field. For the tracking of the homogeneous movement of a wheelchair algorithms of inertial navigation systems (INS) [17] can be applied which are also used for tracking mobile robots as in [6, 10]. Starting from an initial position the next absolute position is calculated using the measured sensor signals. The basic approach of an INS algorithm can be described as follows:

1. The current orientation of the device is calculated based on several sensor data. For this purpose the orientation filter of Madgwick [12] is used as described in [15]. The filter provides an orientation represented as a quaternion by a fusion of accelerometer, gyroscope, and magnetometer data.

Fig. 1 Perpendicular view of the central camera for studies with wheelchair users in two different geometries is shown. Participants are wearing colored caps for automatic trajectory extraction. (**a**) Bottleneck, (**b**) Corridor

2. This is followed by a rotation of the acceleration data from the local frame of reference (IMU coordinate system) to the global frame of reference (world coordinate system where the z-axis points down) by a multiplication with the calculated quaternion.
3. By subtracting the earth gravity from the z-axis and double integrating the global acceleration the position can be calculated.

Those steps are repeated for each time step which comes along with an accumulation of errors and therefore a drift in position. Methods for constraining the drift are needed (see Sect. 2.2.2).

2.2 Fusion of Camera and IMU Data

For the tracking of pedestrians with two different tracking systems the datasets need to be synchronized and aligned at first. After that it is possible to improve the IMU tracking quality by fusing the IMU data with input of the camera system.

2.2.1 Merging the Datasets

To receive a consistent dataset of camera and IMU data a synchronization in time is needed. With a dedicated IMU hub device it is possible to send a signal to each IMU so that they are synchronized among each other and to emit a LED signal which is visible by the camera system. By pairing the corresponding frame in the camera data and the record in the IMU data the datasets are synchronized.

When extracting trajectories from the camera data a coordinate system needs to be chosen which is often aligned to the geometry setup. The global IMU coordinate system needs to be aligned with this camera coordinate system. For this purpose the initial velocity vector of the wheelchair (calculated from IMU data) is aligned with the velocity vector of the wheelchair calculated from the camera data (see [15]).

2.2.2 Constraining the Drift

As described in [18] the tracking of a person with general purpose inertial navigation algorithms is not possible because of the rapid accumulation of error. To limit the drift of the wheelchair trajectory additional data of the surrounding people extracted by the camera system can be used. In case of an occlusion characteristics of the enclosing group are applicable for the occluded person as well.

Based on this idea the velocity of the wheelchair user is corrected by the velocity of the pushing person as a first approach. It is assumed that the velocity of the wheelchair user, v_{imu}, calculated from IMU data (at step i) is close to the velocity of the pushing person, v_{pusher}, calculated from the trajectory extracted with the

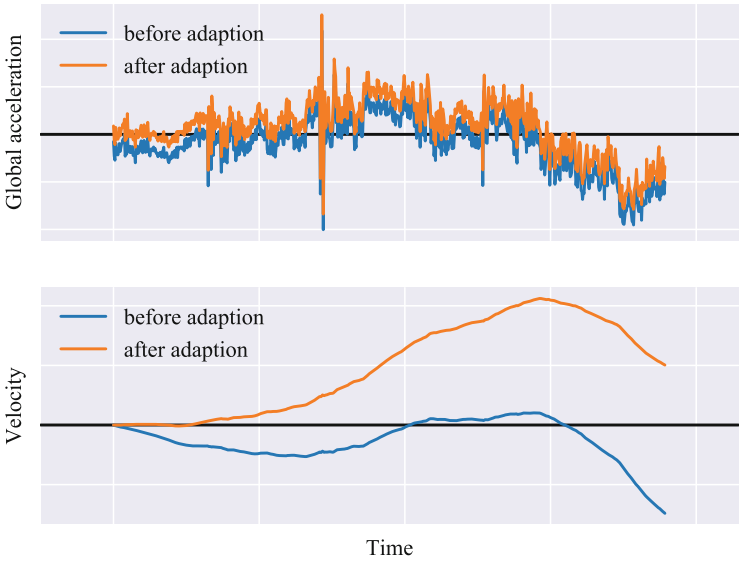

Fig. 2 Qualitative example for retroactive adaption of the acceleration and velocity: The black line represents the zero axis. It is assumed that a noisy acceleration (blue, upper figure) leads to a wrong velocity at the end (blue, lower figure). To reach a given velocity (given by a reference value) the acceleration is adapted (orange, upper figure). In this way the adapted velocity (orange, lower figure) reaches the reference value. For this example the velocity was underestimated at first and reaches a higher reference value after the adaption

camera system. If the difference v_{diff} defined as in (1) exceeds a predefined range v_{range} as in (2) at step k the noisy velocity of the wheelchair v_{imu} is corrected by adapting the global acceleration acc_{global} for the previous (since last correction) and future time period. The basic idea for the adaption is to estimate the difference in acceleration acc_{diff} that caused the difference in velocity v_{diff} as in (3) with Δt defining the time since the last correction from step k_{prior} to k. The global acceleration is corrected by adding acc_{diff} as in (4) for previous time steps starting after the last adaption k_{prior}. After each adaption v_{imu} is calculated again based on the corrected global acceleration. Following adaption takes place at the earliest at $i > k$.

Due to the homogeneous movement of the wheelchair without up and down movements (and since only two-dimensional trajectories are extracted with the camera system) the velocity along the z-axis is neglected and set to zero. An example dataset for one adaption step is shown in Fig. 2.

$$v_{diff,i} = |v_{imu,i} - v_{pusher,i}| \quad \forall i \in \{1, \ldots, n\} \tag{1}$$

$$v_{diff,k} > v_{range} \tag{2}$$

$$acc_{diff,k} = v_{diff,k}/\Delta t \tag{3}$$

$$acc_{global,j} = acc_{global,j} + acc_{diff,k} \quad \forall j \in \{k_{prior}+1, \ldots, n\} \tag{4}$$

3 Results

To evaluate the tracking procedure it was tested on a SiME dataset of a wheelchair user who was visible for the whole time so that the ground truth (camera data) is available. The sensor was attached to the backrest of the wheelchair. The analysis of the velocity of the pusher and wheelchair user (based on the positions extracted with the camera data) showed that the absolute maximum difference of their norms does not exceed 0.3 m/s which value was taken as a reference for v_{range}. The highest difference in velocities appears when the direction of the trajectory changes significantly because the direction (and velocity) of the wheelchair user changes not at the same moment but some milliseconds before.

The lower v_{range}, the more information of the pushing person is used for calculating the IMU trajectory. A balance between v_{range} and the number of adaptions needs to be found. For analyzing this relation the number of adaptions, the maximum error of the IMU trajectory (compared to the trajectory extracted with the camera system), and the time periods between consecutive adaptions were investigated. In addition the same analysis was done with the velocity of the ground truth as reference value. So instead of v_{pusher} the velocity of the wheelchair extracted with the camera system was used for calculating v_{diff} and the subsequent adaption. On this basis the influence of the referenced velocity (used for adaption) on the tracking quality can be investigated. The results are shown in Table 1.

For this example a v_{range} of 0.3 m/s seems to be suitable to adapt the velocity in a proper way with only 9 adaptions in intervals of nearly 1–4 s. The analysis has shown that a more accurate reference value (ground truth) decreased the maximum error by almost the half. Based on this the calculation of the referenced velocity

Table 1 Overview of analysis results for a total tracking time of 15 s for the adaption with the velocity of the pusher and ground truth as reference value

v_{range} (m/s)	Reference velocity from	Number of adaptions	Maximum error (m)	Longest period between adaptions (ms)	Shortest period between adaptions (ms)
0.1	Pusher	34	0.32	114	15
0.1	Ground truth	16	0.29	199	34
0.3	Pusher	9	0.49	363	84
0.3	Ground truth	8	0.25	252	100
0.5	Pusher	5	0.97	310	195
0.5	Ground truth	4	0.58	374	227

should be improved in future steps, e.g., by taking the velocity of other surrounding people into account.

A selection of resulting trajectories can be seen in Figs. 3, 4, and 5. The figures show the trajectories of the wheelchair user (blue) and the pushing person (orange) extracted with the camera system and the IMU trajectory of the wheelchair (green) moving through a bottleneck. The trajectory of the pusher is fluctuating due to the swaying of the person while walking and the tracking of the head by the camera.

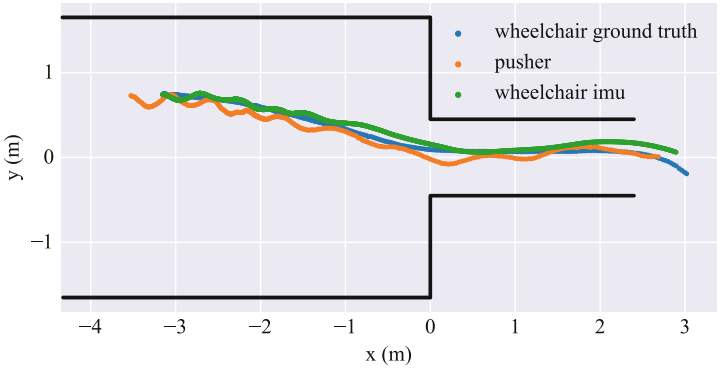

Fig. 3 Trajectories for $v_{range} = 0.1\,\mathrm{m/s}$ and v_{pusher} as reference value for correction. Due to the low v_{range} the swaying of the pusher is also visible in the IMU trajectory

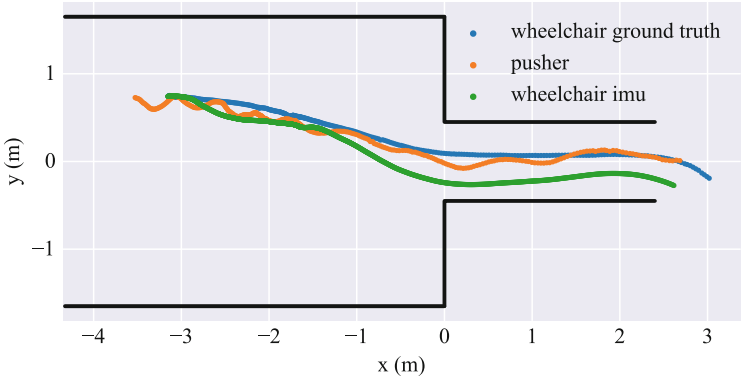

Fig. 4 Trajectories for $v_{range} = 0.3\,\mathrm{m/s}$ and v_{pusher} as reference value for correction. The swaying of the pusher is not visible in the IMU trajectory anymore. Nevertheless it is not as smooth as the ground truth due to the correction with a roughly similar reference velocity

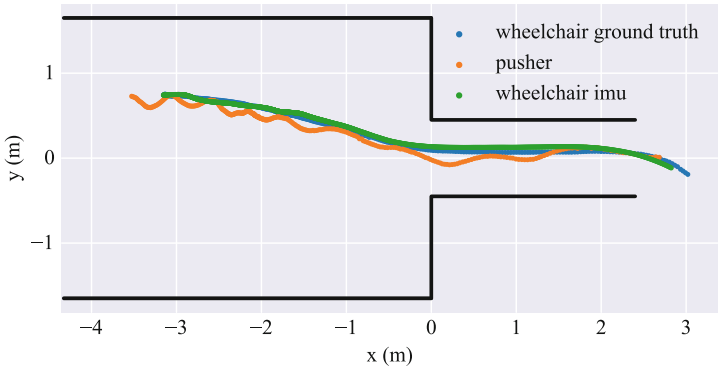

Fig. 5 Trajectories for $v_{range} = 0.3\,\mathrm{m/s}$ and v_{ground_truth} as reference value for correction. By correcting with a more accurate velocity the tracking gets much better

4 Conclusion and Outlook

A hybrid tracking system consisting of cameras and IMUs was developed and tested for tracking wheelchair users in dense crowds. By including the velocity of the pushing person (extracted with a camera system) it is possible to limit the drift of the wheelchair user (calculated with IMU data) resulting in a trajectory with a maximum error of a half meter over a period of 15 s. The fusion of IMU data with a more accurate velocity is promising and would result in a higher tracking quality.

In future work additional restrictions of the IMU trajectory will be implemented. It is possible to limit the drift by taking the velocity and position of surrounding people (not just the pusher) and walls into account. Wheelchairs were actually equipped with several IMUs so that the fusion of IMU data of multiple sensors attached to one wheelchair will be examined. Besides IMU tracking algorithms will be extended by approaches to track walking people (e.g., step detection) and human motion processes (e.g., orientation of shoulders) as well.

Acknowledgements Thanks to the funding provided by the Federal Ministry of Education and Research of Germany (BMBF, FKZ 13N13946) the SiME experiments could have been conducted and the novel hybrid tracking system could be realized.

References

1. Attal, F., Mohammed, S., Dedabrishvili, M., Chamroukhi, F., Oukhellou, L., Amirat, Y.: Physical human activity recognition using wearable sensors. Sensors **15**(12), 31,314–31,338 (2015)
2. Boltes, M., Holl, S.: SiME–improved safety for disabled people. inSiDE **14**(1), 75 (2016)
3. Boltes, M., Seyfried, A., Steffen, B., Schadschneider, A.: Automatic extraction of pedestrian trajectories from video recordings. In: Klingsch, W.W.F., Rogsch, C., Schadschneider, A.,

Schreckenberg, M. (eds.) Pedestrian and Evacuation Dynamics 2008, pp. 43–54. Springer, Berlin (2010). https://doi.org/10.1007/978-3-642-04504-2-3
4. Boltes, M., Schumann, J., Salden, D.: Gathering of data under laboratory conditions for the deep analysis of pedestrian dynamics in crowds. In: 2017 14th IEEE International Conference on Advanced Video and Signal Based Surveillance (AVSS), pp. 1–6. IEEE, Piscataway (2017). https://doi.org/10.1109/AVSS.2017.8078471
5. Cao, S., Seyfried, A., Zhang, J., Holl, S., Song, W.: Fundamental diagrams for multidirectional pedestrian flows. J. Stat. Mech: Theory Exp. **2017**(3), 033404 (2017). http://stacks.iop.org/1742-5468/2017/i=3/a=033404
6. Cho, B.S., Sung Moon, W., Seo, W.J., Baek, K.R.: A dead reckoning localization system for mobile robots using inertial sensors and wheel revolution encoding. J. Mech. Sci. Technol. **25**(11), 2907–2917 (2011). https://doi.org/10.1007/s12206-011-0805-1
7. Hoflinger, F., Zhang, R., Reindl, L.M.: Indoor-localization system using a micro-inertial measurement unit (imu). In: European Frequency and Time Forum (EFTF), 2012, pp. 443–447. IEEE, Piscataway (2012). https://doi.org/10.1109/EFTF.2012.6502421
8. Holl, S., Seyfried, A.: Hermes–an evacuation assistant for mass events. inSiDE **7**(1), 60–61 (2009)
9. Holl, S., Seyfried, A.: Laboratory experiments on crowd dynamics. inSiDE **11**(2), 102–103 (2013)
10. Koch, J., Hillenbrand, C., Berns, K.: Inertial navigation for wheeled robots in outdoor terrain. In: Proceedings of the Fifth International Workshop on Robot Motion and Control, 2005. RoMoCo05. IEEE, Piscataway (2005). https://doi.org/10.1109/romoco.2005.201419
11. Labs, S.: Sabel sense (2017). https://sabellabs.com/sense/
12. Madgwick, S.O.H., Harrison, A.J.L., Vaidyanathan, R.: Estimation of IMU and MARG orientation using a gradient descent algorithm. In: 2011 IEEE International Conference on Rehabilitation Robotics, pp. 1–7. IEEE, Piscataway (2011). https://doi.org/10.1109/icorr.2011.5975346
13. Pons-Moll, G., Baak, A., Helten, T., Müller, M., Seidel, H.P., Rosenhahn, B.: Multisensor-fusion for 3D full-body human motion capture. In: CVPR, pp. 663–670. IEEE, Piscataway (2010)
14. Roetenberg, D., Luinge, H., Slycke, P.: Xsens MVN: full 6DOF human motion tracking using miniature inertial sensors. Xsens Motion Technologies BV, Tech. Rep (2009)
15. Schumann, J., Boltes, M.: Tracking of wheelchair users in dense crowds. In: 2017 International Conference on Indoor Positioning and Indoor Navigation (IPIN) (2017)
16. Stojanović, D., Stojanović, N.: Indoor localization and tracking: methods, technologies and research challenges. Facta Univ. Ser. Mech. Automat. Control Robot. **13**(1), 57–72 (2014)
17. Woodman, O.J.: An introduction to inertial navigation. University of Cambridge, Computer Laboratory, Tech. Rep. UCAMCL-TR-696 **14**, 15 (2007)
18. Woodman, O.J.: Pedestrian localisation for indoor environments. Dissertation, University of Cambridge (2010)

Investigating the Effect of Social Groups in Uni-directional Pedestrian Flow

Luca Crociani, Yiping Zeng, Andrea Gorrini, Giuseppe Vizzari, and Weiguo Song

Abstract The influence of cohesion among members of dyads is investigated in scenarios characterized by uni-directional flow by means of a discrete model: a corridor and the egress from a room with a bottleneck of varying width are simulated. The model manages the dynamics of simulated group members with an adaptive mechanism, balancing the probability of movement according to the dispersion of the group; the cohesion mechanism is calibrated through the parameters κ_c and δ. All scenarios are simulated with two procedures: (Proc. 1) population composed of individual pedestrians, in order to validate the simulation model and to provide baseline data; (Proc. 2) population including dyads (50% of the simulated pedestrians), in order to verify their impact. In the corridor scenario, the presence of dyads causes a reduction of the velocities and specific flow at medium-high densities. Egress from a square room with a unique central exit produces results in line with recent studies in the literature, but also shows that the dyads negatively affect the dynamics, leading generally to a slower walking speed and a lower pedestrian flow. Ignoring the presence of dyads would lead to an overestimation of egress flows.

1 Introduction

Recently, the topic of social groups has gathered a growing interest from researchers studying the dynamics of pedestrians. One the one side, field observations (e.g. [4]) have highlighted that a crowd of pedestrians is mostly composed of groups of up

L. Crociani · A. Gorrini · G. Vizzari
CSAI Research Center, University of Milano-Bicocca, Milano, Italy
e-mail: luca.crociani@disco.unimib.it; andrea.gorrini@disco.unimib.it; giuseppe.vizzari@disco.unimib.it

Y. Zeng (✉) · W. Song
State Key Laboratory of Fire Science, University of Science and Technology of China, Hefei, China
e-mail: ypzeng@mail.ustc.edu.cn; y.zeng2@campus.unimib.it; wgsong@ustc.edu.cn

S. H. Hamdar (ed.), *Traffic and Granular Flow '17*,
https://doi.org/10.1007/978-3-030-11440-4_24

to 4 members (dyads are typically the most frequent) and that people walking in a group are generally slower than individuals. Controlled experiments involving groups have been designed to investigate their aggregated effect, and a relevant impact is observed in a corridor setting with bi-directional flow (see, e.g., [2, 3]) and a bottleneck scenario (see, e.g., [8]). On the modelling side, many works are being proposed for the simulation of group behaviour: for example, the work in [9] proposes a continuous model for the behaviour of groups of 2 or 3 members based on field observations, while [6] design leader–follower structure of dyads using dynamic floor fields. In this paper, we present a discrete model considering groups, based on the work in [1], which is extended and calibrated to fit the data from a controlled experiment [3]. The calibrated model is then used to investigate the aggregated effect of dyads in uni-directional pedestrian flows at high densities (Sect. 4) and passing through a bottleneck (Sect. 5).

2 A Model for Group Cohesion

The simulation model here presented is designed to achieve a more realistic simulation of pedestrian and group dynamics, with particular attention to the shape of the group. The model is discrete in space and time, and at each time-step of the simulation agents evaluate cells c of the Moore neighbourhood with the utility function $U(c)$. This aggregates the components associated with the reproduction of a particular behaviour by means of a weighted sum:

$$U(c) = \frac{\kappa_g G(c) + \kappa_{ob} Ob(c) + \kappa_s S(c) + \kappa_c C(c) + \kappa_d D(c) + \kappa_{ov} Ov(c)}{d} \tag{1}$$

Individual functions model, respectively: (1) goal attraction; (2) obstacle repulsion; (3) keeping distance from other pedestrians; (4) cohesion with other group members; (5) direction inertia; (6) overlapping to avoid gridlock in counterflow situations. The first three elements are modelled with the usage of the well-known *floor-field* approach to model the base behaviour of pedestrians: movement towards a target, obstacle avoidance, proxemics with other pedestrians in a repulsive sense.

The function $C(c)$ is introduced to manage the cohesion among group members and its strength is mainly adjustable by the parameter κ_c. The function calculates the level of attractiveness of each neighbour cell, according to the position and velocity of the other agents of the group. These information are used to estimate their next positions and then evaluate the attractiveness of each cell according to the cohesion, as the following:

$$C(c) = \left[\left(\eta \cdot \sum_{\hat{a} \in G \setminus \{a\}} \frac{\|\mathbf{x}_a - \mathbf{x}^{\bullet}_{\hat{a}}\| - \|\mathbf{x}_c - \mathbf{x}^{\bullet}_{\hat{a}}\|}{|G| - 1} \right) \cdot 2 \right] - 1 \tag{2}$$

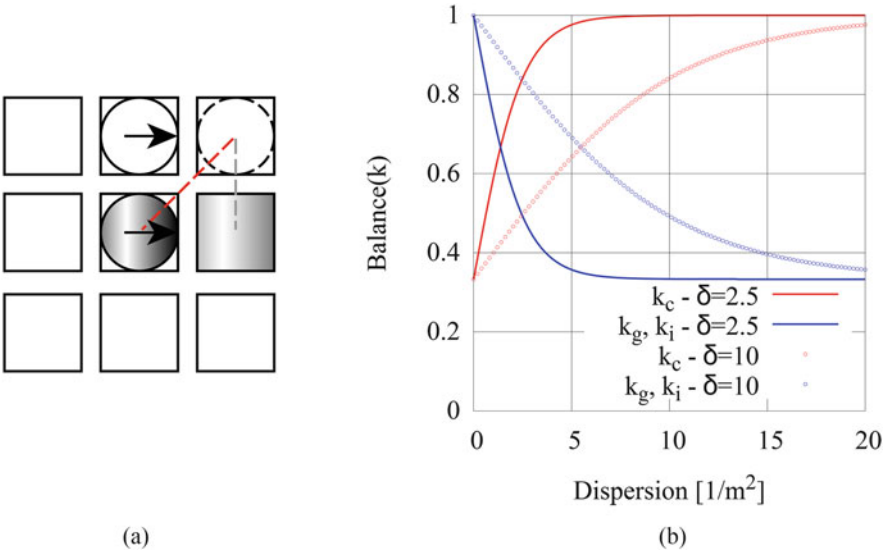

Fig. 1 (**a**) Example of calculation of $C(c)$ for a 2-member group. Cells ahead both pedestrians will be the most desirable according to the function. (**b**) Example of values of the function *Balance* for the different calibration weights, configuring different values of δ

where η is a normalization factor that, along with numerical values, allows to translate the cohesion value into the range $[-1, 1]$. $|G|$ defines the size of the group and $\|\mathbf{x}\|$ denotes the 2-norm of a vector $\mathbf{x}$. $\mathbf{x}^{\bullet}_{\hat{a}}$ describes a prediction of the next position of the agent $\hat{a}$ and it represents a small advancement to the model that allowed to improve the plausibility of the simulated behaviour. The estimation is calculated using the velocity vector $\mathbf{v}_{\hat{a}}$: $\mathbf{x}^{\bullet}_{\hat{a}} = \mathbf{x}_{\hat{a}} + \mathbf{v}_{\hat{a}}$. The functioning of the function is exemplified in Fig. 1a.

By acting on the parameters of $U(c)$ during the simulation it is possible to describe different states of the same pedestrian in different moments of a single simulated scenario. This strategy is applied to allow group members to adapt their behaviour in dense situations or in the presence of obstacles. According to this method, weights $\kappa_g, \kappa_c, \kappa_i$ are varied and possibly inhibited according to an index that describes the instantaneous *dispersion* of the group, as shown in Fig. 1b. This *adaptation* of the behaviour of group members can be calibrated according to the parameter δ that, together with κ_c, will be investigated for the calibration of the model in the next section.

After the utility evaluation for all the cells of the neighbourhood, the choice of action is decided by the probability to move in each cell c as (N is the normalization factor): $P(c) = N \cdot e^{U(c)}$.

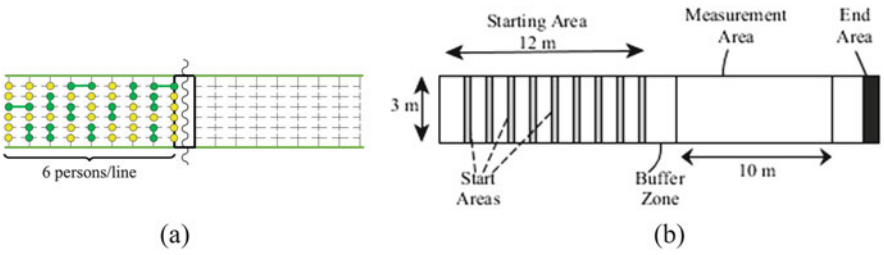

Fig. 2 Example configuration of the first procedure of the controlled experiment in [3] (**a**) and its realization with the simulation model (**b**)

3 Calibration of the Group Behaviour

In order to calibrate the model and reproduce plausible movement of pedestrians and groups, data from the first procedure of a controlled experiment studying the movement of dyads [3] have been used. In the experimental procedure, a uni-directional pedestrian flow composed of 30 individuals and 24 dyad members[1] crossed a corridor-like setting of 3 m width. Trajectories were automatically extracted in a measurement area of 10 m length located at the centre of the corridor, after a buffer zone of 2 m that allowed participants to reach a stable speed.

As shown in Fig. 2, a corridor-like setting similar to the experiment has been designed with the simulation model, with an analogous initial configuration of the pedestrian flow: starting positions are given by 9 start areas which generates 6 pedestrians each. Members of dyads are generated close to each other to avoid bias given by the initial configuration. Moreover, only information about pedestrians inside the measurement area are analysed. Given that all participants were young male student, we configured a *desired speed* of simulated pedestrians of 1.6 m/s.

The aim of the simulation campaign was to calibrate parameters δ and κ_c, managing the group behaviour, to fit the results about average speeds of all participants and the distribution of relative positions of dyads, which describes their spatial behaviour during the experimental iteration. To gather stable results, a set of 100 simulation iterations is configured for each configuration of the two parameters that, as pure assumption, is explored in the range $[0 : 30]$ with an increase rate of 1.

The calibration phase led to the optimal configuration of parameters $(\delta, \kappa_c) = (7, 12)$, which generates average speeds of singles, dyads and of the overall population as shown in Table 1. Results are in line with the observation. By looking at the distribution of relative positions (Fig. 3a, b), the difference is a bit more marked than with the speed, but overall the results are close and they highlight that also in the simulations the most frequent pattern was the line-abreast one.

[1]Dyads were artificially and randomly formed at the beginning of the iteration by asking participants to try to walk close to their companion as they were friends.

Table 1 Comparison of average speeds [m/s] of pedestrians in the experiment and in the simulations

	Individual	Dyads	Population
Experiment	1.32	1.30	1.31
Simulations	1.308	1.305	1.3067

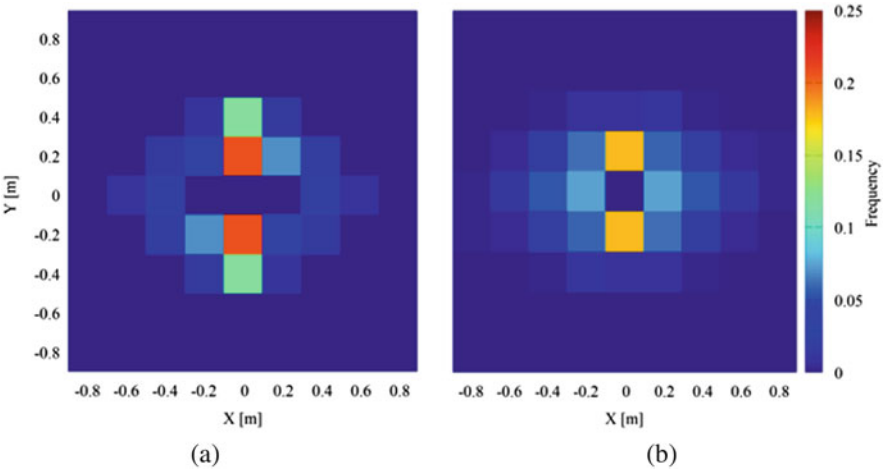

Fig. 3 Distribution of relative positions of dyads (direction of movement towards right) of the experiment (**a**) and simulation (**b**). The same colour-scale is applied in both pictures

4 Validation at Basic Movement

In this section, we will study the effects of the presence of dyads on the specific flow in a corridor environment with uni-directional movement. A graphic description of the setting is shown in Fig. 4. Two case studies have been configured: a baseline with only singles and one with 50% presence of dyads. To compute the fundamental diagram, simulation campaigns of 10 iterations of 5000 steps each have been run per each investigated average density of pedestrians in the whole environment. The environment was configured as toroidal, so that the number of pedestrians is constant during each iteration. To gain precision with the analysis, data are generated within a *measurement area* of 8 m length, where entrance/exit events are recorded for each agent. This allowed to compute the number and the average speed of pedestrian inside the measurement area for a given time window and to achieve larger datasets with every simulation. Finally, at each run we considered only data generated from step 2000, where a steady state was generally reached.

Results in the form density–speed and density–flow are shown in Fig. 5. Both datasets are in agreement with empirical guidelines and datasets from the literature. At the same time, the specific flow of dyads is smaller than that of individuals for densities higher than 1.5 p/m^2. On the one hand, dyads walk slower than individuals in low density situations, but the difference is quite limited with a similar configuration of their desired speed. The increase of density, on the other hand, has

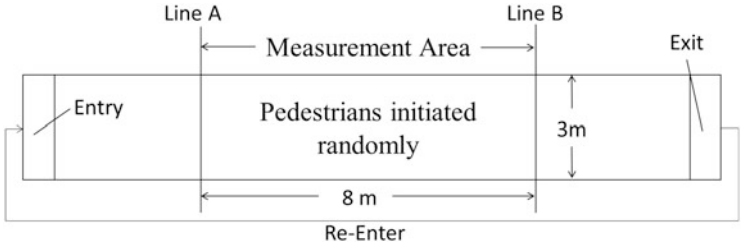

Fig. 4 The corridor environment used for the test of the fundamental diagram

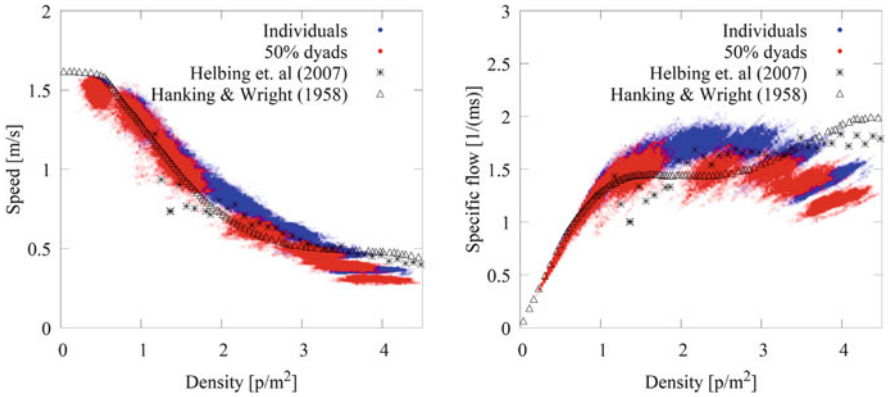

Fig. 5 Results of the fundamental diagram in the form density–speed (left) and density–flow (right)

stronger effects on the average speed of the population with the presence of dyads, emphasizing that dyads had a negative effect on the observed dynamics. This is due to the cohesion mechanism configured for the walking behaviour of dyads, which makes them to keep short distances to each other and to slow down while congested situation leads to a fragmentation of the group. While this behaviour is assumed for this model and it could be considered rather strong compared to the reality, a similar difference among fundamental diagrams observed with only individuals and with about 40% of dyads was observed in an experiment also presented in this book [2].

5 Analysis of Group Influence on a Bottleneck Scenario

Up to now, the model is calibrated to reproduce a plausible behaviour of dyads and it is validated for the simulation of uni-directional flow in a corridor. In this section the model will be used to study the effect of two-member groups in a periodical scenario representing a room with a bottleneck, as in Fig. 6a. Again, we configure two simulation campaigns to study the phenomena: (a) a scenario with only individuals

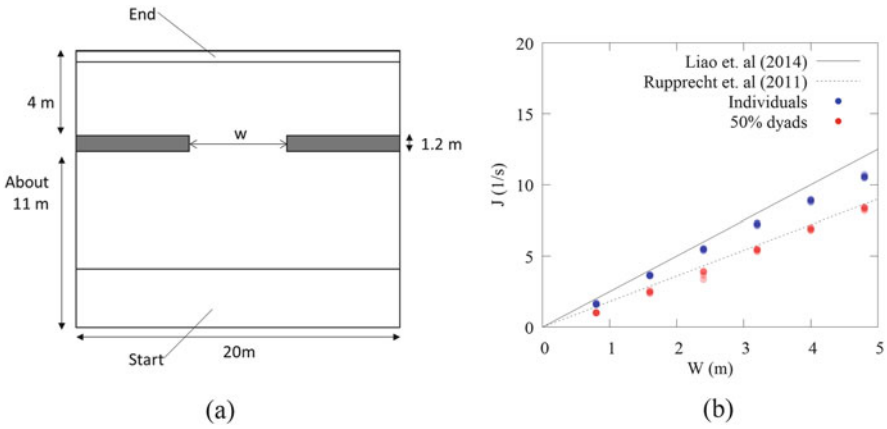

Fig. 6 (**a**) Simulated scenario to test the outflow from the bottleneck. (**b**) Total flow achieved in the two case studies and two empirical datasets from the literature [5, 7] for comparison

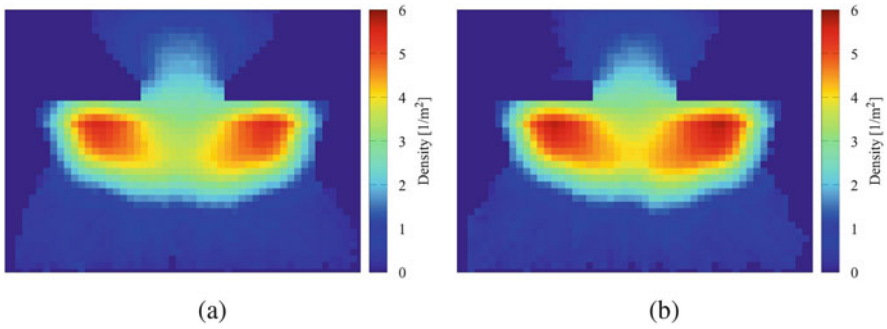

Fig. 7 Cumulative mean density at a steady state for the scenario with only individuals (**a**) and the one with 50% presence of dyads (**b**)

and (b) one with 50% presence of dyads. 400 simulated pedestrians are generated in the scenario for each configuration of the bottleneck width and 5 iterations of 5000 steps are run to get a sufficient dataset. Again, output data are gathered only in a steady state of the system (time-step from 2000 to 5000). Figure 7 exemplifies two density maps for one iteration with bottleneck width of 4.0 m and highlights a slightly higher congestion in the scenario with dyads. This provides an explanation of the results describing the outflow of pedestrians from the bottleneck, which is calculated as $J = \frac{N}{t}$. The corresponding results are shown in Fig. 6b. While the baseline scenario generates a specific flow at the bottleneck of about 2.1 ped/m*s, the scenario with dyads provides a sensibly lower result following the trend of about 1.8 ped/m*s observed in the dataset from Rupprecht et al. [7].

6 Conclusions

The influence of cohesion among members of dyads and its aggregated effect in scenarios characterized by uni-directional flow has been investigated by applying a discrete model to two benchmark scenarios: a one way corridor and the egress from a room with a central bottleneck. The simulation model represents the dynamics of simulated group members with an adaptive mechanism, balancing the probability of movement according to the dispersion of the group; the cohesion mechanism is calibrated through two parameters κ_c and δ, acting on the utility of a movement, and according to data coming from a controlled experiments involving dyads.

The investigated scenarios are simulated with two procedures, configuring a population composed of only individual pedestrians and one half composed of dyad members. In accordance with recent studies in the literature, simulated results show that the dyads negatively affect the dynamics, leading generally to a lower velocity and a lower pedestrian flow. The difference in the fundamental diagram observed in the scenario of the corridor is sensible and for the range of densities lower than 1.5 ped/m^2 is similar with the empirical data from the experiment used for the calibration (see [2] in this book). Results coming from the simulation of the bottleneck show again a negative effect of the presence of dyads, which in this case is even more apparent. The achieved trend and the difference between the two simulation scenarios are in line with other studies from the literature and, overall, suggest further research to investigate the microscopic behaviour of pedestrian groups and its aggregated effects on pedestrian dynamics.

Acknowledgements This research has been supported by the Key Research and Development Program (2016YFC0802508), the Program of Shanghai Science and Technology Committee (16DZ1200106), the Specialized Research Fund for the Doctoral Program of Higher Education of China (20133402110009), the China Scholarship Council (CSC) and Fundamental Research Funds for the Central Universities (WK2320000035).

References

1. Bandini, S., Crociani, L., Vizzari, G.: An approach for managing heterogeneous speed profiles in cellular automata pedestrian models. J. Cell. Autom. **12**(5), 401–421 (2017)
2. Crociani, L., Gorrini, A., Feliciani, C., Vizzari, G., Nishinari, K., Bandini, S.: Micro and macro pedestrian dynamics in counterflow: the impact of social groups. This volume (2018)
3. Gorrini, A., Crociani, L., Feliciani, C., Zhao, P., Nishinari, K., Bandini, S.: Social groups and pedestrian crowds: experiment on dyads in a counter flow scenario. In: Proceedings of the 8th International Conference on Pedestrian and Evacuation Dynamics–PED2016, Hefei, China, October 17–21, 2016, pp. 179–184 (2016)
4. Gorrini, A., Vizzari, G., Bandini, S.: Age and group-driven pedestrian behaviour: from observations to simulations. Collectiv. Dyn. **1**, 1–16 (2016)
5. Liao, W., Seyfried, A., Zhang, J., Boltes, M., Zheng, X., Zhao, Y.: Experimental study on pedestrian flow through wide bottleneck. Transp. Res. Proc. **2**(Supplement C), 26–33 (2014). The Conference on Pedestrian and Evacuation Dynamics 2014 (PED 2014)

6. Müller, F., Schadschneider, A.: Evacuation dynamics of asymmetrically coupled pedestrian pairs. In: Traffic and Granular Flow'15, pp. 265–272. Springer, Cham (2016)
7. Rupprecht, T., Klingsch, W., Seyfried, A.: Influence of Geometry Parameters on Pedestrian Flow Through Bottleneck, pp. 71–80. Springer, Boston (2011)
8. von Krüchten, C., Schadschneider, A.: Empirical study on social groups in pedestrian evacuation dynamics. Physica A Stat. Mech. Appl. **475**, 129–141 (2017)
9. Zanlungo, F., Ikeda, T., Kanda, T.: Potential for the dynamics of pedestrians in a socially interacting group. Phys. Rev. E **89**, 012811 (2014)

Towards Microscopic Calibration of Pedestrian Simulation Models Using Open Trajectory Datasets: The Case Study of the Edinburgh Informatics Forum

Ruggiero Lovreglio, Charitha Dias, Xiang Song, and Lucia Ballerini

Abstract The investigation of crowd behaviours in normal and emergency situations has been greatly facilitated by various agent-based pedestrian models. Those models are built upon different assumptions in order to represent or mimic reality. One of the key challenges in pedestrian modelling is the verification of those assumptions or the best model specification by using existing datasets and suitable calibration approaches.

This paper illustrates a case study where we calibrate different pedestrian model specifications with an open pedestrian trajectory dataset from Edinburgh Informatics Forum and select the best model according to various model selection criteria. Two floor field cellular automaton models with Euclidean and modified Euclidean distance metrics are presented for the static floor field. Our study shows that the modified Euclidean distance metrics can provide better fitting for the navigation environments without obstacles.

R. Lovreglio (✉)
School of Built Environment, Massey University, Auckland, New Zealand
e-mail: r.lovreglio@massey.ac.nz

C. Dias
Institute of Industrial Science, University of Tokyo, Tokyo, Japan
e-mail: cdias@iis.u-tokyo.ac.jp

X. Song
Department of Civil and Environmental Engineering, Massachusetts Institute of Technology, Cambridge, MA, USA
e-mail: bensong@mit.edu

L. Ballerini
Department of Neuroimaging Sciences, University of Edinburgh, Edinburgh, UK
e-mail: Lucia.ballerini@ed.ac.uk

S. H. Hamdar (ed.), *Traffic and Granular Flow '17*,
https://doi.org/10.1007/978-3-030-11440-4_25

1 Introduction

The last decades witnessed an enormous growth of evacuation and pedestrian models aimed at investigating crowd behaviours in normal and emergency situations [13]. Despite such growth and the improvements in modelling techniques, the calibration of navigation models for agent-based pedestrian simulation is an issue to which a definitive standard solution has yet to be defined [14, 15].

The existing calibration approaches can be divided into macroscopic and microscopic approaches [17]. Although microscopic approach is more reliable, it requires sophisticated fitting procedures [17]. Thus, a critical limitation for the use of microscopic calibrations is the lack of empirical data. The creation of open dataset can 'catalyse' the growth of new calibration studies and can allow the comparison of prediction capabilities of different models [15].

The objective of this paper is to highlight how existing open datasets can be useful to gain insight on pedestrian dynamics. This is achieved by an open pedestrian trajectory dataset collected at the Informatics Forum of the University Edinburgh in 2010 [16]. This dataset includes 299,082 trajectories of pedestrians who navigate through an open space in normal situations. Therefore, this dataset differs from most of existing datasets, including results from laboratory experiments, in terms of behavioural ecological validity (i.e. pedestrians are not aware to be observed) and in terms of sample size (i.e. this dataset is one of the biggest open datasets) [14]. In this work, we filtered those trajectories and create a new MATLAB dataset. We used the individual trajectories (i.e. each pedestrian does not interact with any other pedestrian) of the dataset and a microscopic calibration procedure for floor field cellular automation models described in [15] to compare two floor field specifications: the classical Euclidean metric and the modified Euclidean metric proposed in [15].

2 Related Works

In the calibration process, model parameters are adjusted by comparing a predefined output (i.e. either a macroscopic property like fundamental diagram or a microscopic property like a trajectory) of the model with the same output observed from empirical data [7, 9]. Accordingly, the calibration approaches can mainly be categorized as macroscopic and microscopic approaches. The choice of calibration approaches may depend on the purpose of the model as well. For instance, if the main purpose of a model is the analysis of pedestrian flows, then macroscopic approaches may be adequate. On the other hand, if the main purpose of a model is to understand behaviours such as interactions between individuals, then microscopic approaches become more suitable. Thus, both methods are extensively being adopted to calibrate microscopic pedestrian tools. Table 1 summarizes several

Table 1 Previous studies which used microscopic calibration methods

Reference	Calibrated model	Calibration approach and remarks
[1]	Discrete choice model	Biogeme package that uses maximum likelihood estimation (MLE) method
[10]	Social force model	Evolutionary method comparing the relative error between empirical and simulated trajectories using least squares estimation (LSE)
[8]	Nomad model	Comparison of modelled and observed acceleration using MLE
[6]	Discrete choice model	Comparison of deviation angles and step velocities using LSE
[3]	Nomad model	Comparison of pedestrian state using MLE. Used hybrid optimization algorithm based on genetic algorithm and simplex methods
[12]	Social force-based model	Comparison of velocities (both magnitude and direction) of individual pedestrians using MLE
[4]	Social force-based model	Comparison of simulated and empirical trajectories and speed profiles using LSE
[18]	Social force model	Comparing mean Euclidean distance between empirical and simulated trajectories using evolutionary algorithm. Objective function uses LSE
[15]	CA model	Likelihood function optimization to match with observed trajectories using MLE method
[5]	Social force model	Minimizing location error using an evolutionary algorithm based on cross entropy method. Objective function uses LSE

studies based on well-known microscopic models which adopted microscopic calibration methods.

Details of the calibration method used in this study, the dataset and results are discussed in the following sections.

3 Methodology

The following methodology is applied to the existing floor field cellular automaton models [2, 11]. The general main assumption of those models is that the walkable space is divided into squared cells which can either be empty or occupied by exactly one pedestrian. Further, it is assumed that a pedestrian can move to any of the eight cells surrounding the cells he or she is occupying (C_{ij}) as illustrated in Fig. 1a. The movements for the pedestrian q are based on probabilities (p_{ij}) which are functions of two floor fields, namely static (S_{ij}^{q}) and dynamic (D_{ij}^{q}). The static floor field is generally used to define the pedestrians' goals while the dynamic floor field is a virtual trace left by the pedestrians through dynamic formulations defining its diffusion and decay [7, 11]. Thus, the static and dynamic floor fields can be used to

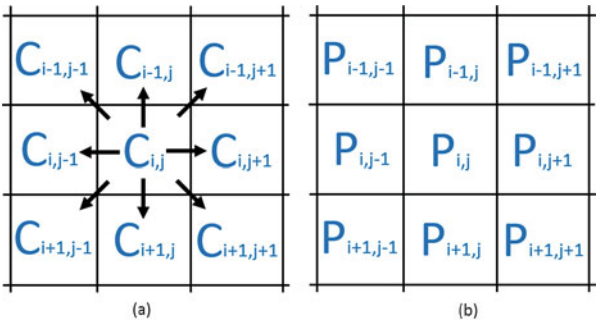

Fig. 1 (**a**) Allowed movements for a pedestrian and (**b**) their probabilities

define utility that pedestrian q associates with the C_{rs} (where, $r = i-1, i+1, s = j-1, j+1$) cell:

$$U_{r,s}^{q} = k_s S_{r,s}^{q} + k_D D_{r,s}^{q} + \epsilon \tag{1}$$

where ϵ is the error term associated with those utilities.

Assuming that ϵ follows generalized extreme value distribution type-I, the probability of pedestrian q choosing the C_{rs} cell is defined by a multinomial logit formulation.

Given the probabilistic nature of those pedestrian models, it is possible to define a likelihood function to estimate the unknown parameters using observed trajectories [15]. Let $T^q = \{C_1^q, \ldots, C_t^q, \ldots, C_n^q\}$ be the n-vector including all the observed cells occupied by the pedestrian q for each consecutive time step ($t = 1, \ldots, n$). The probability of pedestrian passing from C_i^q to C_{i+1}^qcan be defined by

$$P(C_i^q \rightarrow C_{i+1}^q) = p^q(C_i^q, C_{i+1}^q | k_s, k_D) \tag{2}$$

Thus, the probability of pedestrian q having the T^q trajectory can be formulated as

$$P(T^q) = \prod_{i=1}^{n-1} P(C_i^q \rightarrow C_{i+1}^q) \tag{3}$$

The likelihood function associated with the Q observed pedestrians can be written as

$$L(k_s, k_D) = \prod_{q=1}^{Q} P(T^q) \tag{4}$$

4 Case Study

This paper presents a microscopic calibration study by using the open pedestrian trajectory dataset collected at the Informatics Forum of the University Edinburgh [16]. This dataset includes 299,082 trajectories of pedestrians who navigate through Informatics Forum in normal situations (Fig. 2). These trajectories were collected through a camera (resolution: 640 × 480) fixed approximately 23 m above the floor with a capture rate of nine frames per second over a period of 117 days. The data of these trajectories, originally available in 117 text files, are now available on a single mat file (download link: *will be available after publication*).

4.1 Selected Trajectories and Final Dataset

For this calibration study, we selected the trajectories of pedestrians navigating individually (i.e. each pedestrian does not interact with any other pedestrian) as the goal of this study is to investigate different static floor fields. Among those individual trajectories, we selected all the trajectories of pedestrians that used the door on bottom right to exit from the atrium, which is a visible target in the recorded scenes. Thus, the final dataset included 2204 trajectories (Fig. 2b).

Two-dimensional square cells were employed to subdivide the Informatics Forum. The size of each cell is $0.1 \times 0.1\,m^2$ as 0.05 m (i.e. 0.1 m/2) represents the 2.5% quantiles of the distance travelled by the 2204 pedestrians in each time step. In other words, the probability of a pedestrian to change a cell each time step is 97.5%.

The cells occupied by each pedestrian at each time step were analysed. Therefore, it was possible to build up a dataset detecting all the choices made by each pedestrian

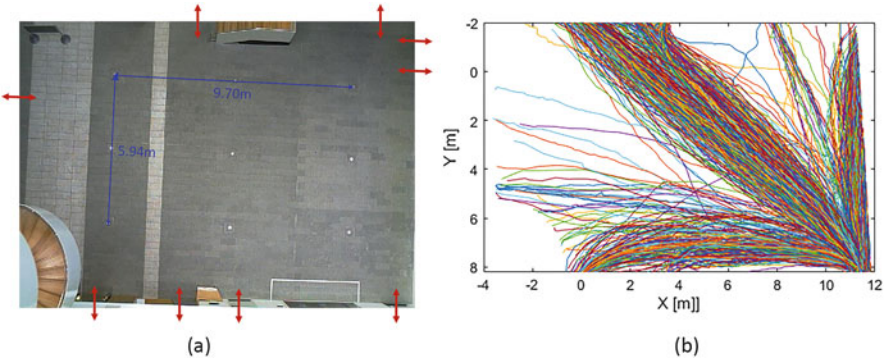

Fig. 2 (**a**) Top view of Informatics Forum of the University Edinburgh. The read markets indicate the entry/exit points; (**b**) subset of trajectories used in the calibration study

at each time step. Each participant is assumed to occupy one cell (starting cell) and then move to a new cell at next time step. The new position is one of the nine possible cells (to move to one of the eight neighbouring cells or to remain in the starting cell) as illustrated in Fig. 1. It is, therefore, possible to define the choices made by pedestrians by detecting their starting and final positions at each time step. A total of 137,841 choices were collected and used to calibrate and compare two floor field cellular automaton models as described in [15].

4.2 Model Specification and Calibration

The final dataset allows the comparison of different static floor fields as the selected pedestrian navigates individually in the Informatics Forum. In this paper, we used the following formulation as the static floor field:

$$S_{i,j}^{q} = \sqrt{(x_{i,j} - x_G)^2 + z(y_{i,j} - y_G)^2} \tag{5}$$

where x_G and y_G represent the coordinate of the pedestrians' goal (i.e. the door on bottom right to exit from the atrium in Fig. 2). Equation (5) is a generalization of the widely used Euclidean metric (i.e. radial floor field) where z is the distortion parameter [15].

As a cellular automaton model, we used this multinomial logit formulation to specify the probabilities to select a cell:

$$p_{r,s}^{q} = \frac{e^{(k_s S_{r,s}^{q})}}{\sum_{(r,s)} e^{(k_s S_{r,s}^{q})}} \tag{6}$$

Then, a log-likelihood function can be calculated for the proposed case study by using the information concerning the cells occupied by each participant in each time step. In this paper, we estimate two nested models by assuming z in Eq. (5) equals to one and a positive constant value, respectively.

The quasi-Newton method called Broyden–Fletcher–Goldfarb–Shanno (BFGS) implemented in MATLAB R2015b was used to find the values of the parameters maximizing the log-likelihood function. This method allows the estimation of the Hessian for the optimal solution. Thus, it is possible to verify whether the estimated parameters are statistically different from zero by using the t-test.

The estimated values for k_s and z and fitting measurements for the two models are illustrated in Table 2. The value of the log-likelihood (LL) for a model in which all parameters are null (see Model 0) is also given in Table 2. In this case, a pedestrian randomly selects the next cell. This value has been estimated in order to calculate the adjusted McFadden R-squared (AdjR^2). The AdjR^2 value suggests the level of improvement over the intercept model (i.e. Model 0) offered by Models 1 and 2. Since the estimated models are nested, it is possible to use the likelihood ratio

Table 2 Estimated parameters

Model	k_s	p-Value	z	p-Value	LL	AdjR^2	LRT*
0	0.000	Fixed	0.000	Fixed	-3.028×10^5	0.000	–
1	−31.437	0.000	1.000	Fixed	-1.304×10^5	0.570	0.000
2	−35.161	0.000	0.691	0.000	-1.282×10^5	0.577	0.000

* p-Values of likelihood ratio tests (LRT)

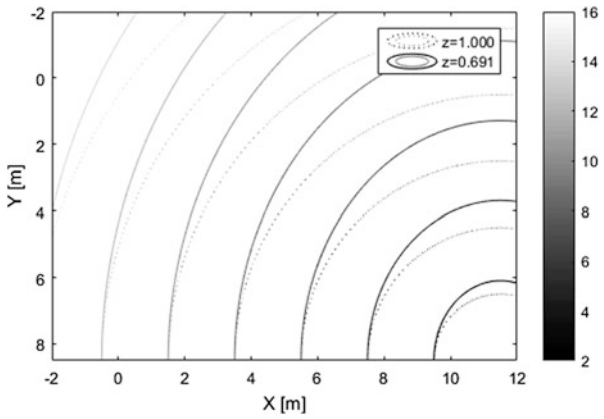

Fig. 3 Static floor field for Model 1 (z = 1.000) and Model 2 (z = 0.691)

test (LRT) to compare the fit of those models. Each model was compared with the previous one in order to verify whether the increased degree of complexity fits significantly better the data.

4.3 Results

Table 2 shows that Model 1 (i.e. radial floor field) results in the lower fitting of the data having an AdjR^2 equal to 0.570. In contrast, Model 2 demonstrates that there is a better agreement when the z parameter has a value lower than 1. In other words, results show that a modified Euclidean metric ($z \neq 1$) performs better than the classical Euclidean metric ($z = 1$) when there are no obstacles in the navigation space. The likelihood ratio test is used to compare the estimated nested models. The results of this test show that Models 1 and 2 improve the fitting of the data if compared with the previous case (p-value <0.05). Figure 3 shows the contour lines for Models 1 and 2. The contour lines of Model 2 show that pedestrians do not move following a radial path (i.e. following a linear path) but they prefer to walk increasing their steering while approaching the exit.

5 Discussion and Conclusion

This paper illustrates how existing open pedestrian trajectory datasets can be useful to gain insight on pedestrian dynamics. The trajectories of the dataset collected at the Informatics Forum of the University Edinburgh in 2010 [16] were filtered to create a new MATLAB dataset. This data allows the comparison of different pedestrian model specifications by using different statistical optimization methods.

The created dataset was used to compare two model specifications (i.e. modified Euclidean metric and the classical Euclidean metric) as a static floor filed for cellular automaton models. The microscopic calibration approach proposed in [15] was used for that purpose. The strength of this approach is that it allows the comparison of different model specifications by using different statistical tests (e.g. likelihood ratio test, Akaike's information criterion, Bayesian information criterion). Calibration results, based on the analysis of 2204 individual trajectories, show that a modified Euclidean metric performs better than the classical Euclidean metric when there are no obstacles in the navigation space. The pedestrians did not move in the environment following a radial path (i.e. following a linear path) but they preferred to walk increasing their steering with the decrease of the longitudinal distance (i.e. X) from the exit following a curved path. Such behaviour, already observed in [15] in a virtual experiment, does exist also in real environments as well. The results of this work suggest that modified Euclidean metric needs to be preferred over the classical Euclidean metric to model pedestrian dynamics in environments without obstacles.

References

1. Antonini, G., Bierlaire, M., Weber, M.: Discrete choice models of pedestrian walking behavior. Transp. Res. B **40**(8), 667–687 (2006)
2. Burstedde, C., Klauck, K., Schadschneider, A., Zittartz, J.: Simulation of pedestrian dynamics using a two-dimensional cellular automaton. Physica A **295**(3), 507–525 (2001)
3. Campanella, M.C., Daamen, W., Hoogendoorn, S.P.: A methodology to calibrate pedestrian walker models using multiple objectives. In: Pedestrian and Evacuation Dynamics, pp. 755–759. Springer, Boston (2011)
4. Dias, C., Ejtemai, O., Sarvi, M., Burd, M.: Exploring pedestrian walking through angled corridors. Transp. Res. Procedia **2**, 19–25 (2014)
5. Dias, C., Iryo-Asano, M., Shimono, K., Nakano, K.: Calibration of a social force-based shared space model for personal mobility vehicle and pedestrian mixed traffic. In: 96th TRB Annual Meeting (2017)
6. Guo, R.Y., Wong, S.C., Huang, H.J., Zhang, P., Lam, W.H.: A microscopic pedestrian-simulation model and its application to intersecting flows. Physica A **389**(3), 515–526 (2010)
7. Guo, R.Y., Huang, H.J., Wong, S.C.: Route choice in pedestrian evacuation under conditions of good and zero visibility: experimental and simulation results. Transp. Res. B **46**(6), 669–686 (2012)
8. Hoogendoorn, S.P., Daamen, W.: Microscopic calibration and validation of pedestrian models: cross-comparison of models using experimental data. In: Traffic and Granular Flow'05, pp. 329–340. Springer, Berlin (2007)

9. Hoogendoorn, S.P., Daamen, W.: A novel calibration approach of microscopic pedestrian models. In: Pedestrian Behavior: Models, Data Collection and Applications, pp. 195–214. Emerald Group Publishing Limited, Bingley (2009)
10. Johansson, A., Helbing, D., Shukla, P.K.: Specification of a microscopic pedestrian model by evolutionary adjustment to video tracking data. Adv. Complex Syst. **10**(02), 271–288 (2007)
11. Kirchner, A., Schadschneider, A.: Simulation of evacuation processes using a bionics-inspired cellular automaton model for pedestrian dynamics. Physica A **312**(1), 260–276 (2005)
12. Ko, M., Kim, T., Sohn, K.: Calibrating a social-force-based pedestrian walking model based on maximum likelihood estimation. Transportation **1**(40), 91–107 (2013)
13. Kuligowski, E.D., Peacock, R.D., Hoskins, B.L.: A Review of Building Evacuation Models, 2nd Edition-(NIST TN). Tech. Rep., US Department of Commerce, National Institute of Standards and Technology, Gaithersburg, MD (2010)
14. Lovreglio, R.: Modelling decision-making in fire evacuation using the random utility theory. Ph.D. thesis, Politecnico of Bari, Milan and Turin (2016)
15. Lovreglio, R., Ronchi, E., Nilsson, D.: Calibrating floor field cellular automaton models for pedestrian dynamics by using likelihood function optimization. Physica A **438**, 308–320 (2015)
16. Majecka, B.: Statistical models of pedestrian behaviour in the forum. Master's thesis, School of Informatics, University of Edinburgh (2009)
17. Schadschneider, A., Eilhardt, C., Nowak, S., Will, R.: Towards a calibration of the floor field cellular automaton. In: Peacock, R.D. (ed.) Pedestrian and Evacuation Dynamics, pp. 557–566. Springer, Boston (2001)
18. Seer, S., Brandle, N., Ratti, C.: Kinects and human kinetics: a new approach for studying pedestrian behavior. Transp. Res. C **48**, 212–228 (2014)

Influence of Gender on the Fundamental Diagram and Gait Characteristics

Jiayue Wang, Maik Boltes, Armin Seyfried, Antoine Tordeux, Jun Zhang, Verena Ziemer, and Wenguo Weng

Abstract The crowd structures in different public places or mass events are diverse. Areas with a large fraction of children, elderly pedestrians, or women, who are always referred to as vulnerable groups, will require higher standard for facility design and emergency evacuation. The fundamental diagram and gait characteristics, the basic properties for pedestrian traffic flow and human stepping locomotion, respectively, are essential for facility design and emergency evacuation. Therefore to investigate the influence of gender on the fundamental diagram and gait characteristics is one step to improve facility design and public safety. In this paper, results from experiments on single-file movements involving male and female youngsters are introduced. The fundamental diagram and gait characteristic parameters such as free-flow speed, stop space (minimal required distance to the

J. Wang (✉)
Institute of Public Safety Research, Department of Engineering Physics, Tsinghua University, Beijing, China

Center for Capital Social Safety, People's Public Security University of China, Beijing, China

Juelich Supercomputing Centre, Juelich Research Centre, Juelich, Germany

M. Boltes · A. Tordeux
Juelich Supercomputing Centre, Juelich Research Centre, Juelich, Germany
e-mail: m.boltes@fz-juelich.de; a.tordeux@fz-juelich.de

A. Seyfried · V. Ziemer
Juelich Supercomputing Centre, Juelich Research Centre, Juelich, Germany

Faculty of Architecture and Civil Engineering, University of Wuppertal, Wuppertal, Germany
e-mail: a.seyfried@fz-juelich.de; v.ziemer@fz-juelich.de

J. Zhang
State Key Laboratory of Fire Science, University of Science and Technology of China, Hefei, China
e-mail: junz@ustc.edu.cn

W. Weng
Institute of Public Safety Research, Department of Engineering Physics, Tsinghua University, Beijing, China
e-mail: wgweng@tsinghua.edu.cn

S. H. Hamdar (ed.), *Traffic and Granular Flow '17*,
https://doi.org/10.1007/978-3-030-11440-4_26

preceding person), and free-flow space (minimal required distance to walk at free-flow speed) are analyzed considering the impacts of gender. It is found that males have significantly larger stop space and smaller free-flow space than females even if these differences are small. Besides, the gait characteristics between males and females are compared.

1 Introduction

A pedestrian keeps a certain distance to the preceding person at a certain speed. This relation is called fundamental diagram and is one benchmark for facility design and safety evaluation. However, it was found that the fundamental diagrams reported in different studies have significant differences [19, 30, 31]. Several external and individual factors may explain the deviations, including pedestrian facility types, trip purpose, measurement method, age, gender, and so on. Therefore, to investigate the influence of gender on the fundamental diagram is one step to understand the differences.

One parameter of the fundamental diagram is walking speed. It was reported that gender may affect the walking speed of pedestrians [4, 7, 15, 16, 27]. Results have been reported in several statistical forms such as mean speed, specific percentile values, and the variation. On the averaged value of free-flow speeds, males walked faster than females on sidewalks [18, 21, 22, 28] and off-road conditions [8, 24]. Huo et al. [13] found that gender had larger influences on pedestrian speeds under no grouping than grouping. By comparing the variations in speed, males had higher value than females [28]. However, it was found that the effect of gender on walking speed changed with age. There were two different results. One was that in the entire age interval, there was no statistically significant difference in the mean speeds of males and females. But when the data was segregated into various age groups, noticeable differences were discovered [29]. Fitzpatrick et al. [7] found statistical difference in gender for the median speed of the young group. For the young pedestrians, males walked faster than females [29]. Another result was contrary to the first one. The gender of the subject was a significant factor in the walking speed over the entire age range from 19 to 102. However, for the separated age groups, the influence of gender disappeared [1, 11].

Gender also affects gait characteristics (step lengths, step frequencies, and swaying amplitudes) of pedestrians. Compared with females, males have larger step length but smaller step frequency at a speed larger than 1.2 m/s [10]. Versluis [24] analyzed the difference in gait characteristics of males and females in unhindered walking at two different motion paces, such as normal and hurry. It was shown that on average men had larger step length and swaying amplitude, but smaller step frequency than women, especially at the normal motion pace. Males increased their speed of walking by mainly increasing their step length, while females increased their step length and step frequency [11]. Differences in the step length and frequency between males and females become smaller with increasing age [11].

The results about the influence of gender are sometimes contradictory. So this study is performed to investigate the influence in a less complex situation, where pedestrians walk in single file and lateral interactions can be ignored. In the second part, the single-file movement experiments, methods to measure headway, speed, and gait characteristics, and methods to obtain pseudo-independent observations are introduced. In the third part, some results and discussions about the influence of gender on the fundamental diagram and gait characteristics are presented, followed by the conclusions.

2 Experiments and Methods

To study the influence of gender on pedestrian movement, single-file experiments were conducted in a 0.8 m wide oval path in Dusseldorf, Germany (see Fig. 1). It is comprised of two straight parts ($l = 2.5$ m) and two semi-circle parts (the radius of the outer line $r = 2.25$ m). 34 male youngsters and 19 female youngsters aged 16 participated in the experiments. Eleven runs were performed with different numbers of participants ranging from 6 to 25 (see Table 1). The participants in each run were selected randomly. They were instructed not to overtake each other.

Human walks with right and left feet alternately. They sway perpendicular to the walking direction with each step [12, 14, 24]. This consequence from pedestrian locomotor system appears in the oscillation of trajectories determined by tracking the movement of the head. So based on the trajectories extracted by PeTrack [2, 3], human stepping locomotion can be detected [25, 26]. Then the headway, speed, and gait characteristics (step length, step frequency, and swaying amplitude) could be measured based on the projected coordinate system considering the influence of the projection line with different radii. Detailed information about these two methods is provided in [25, 26].

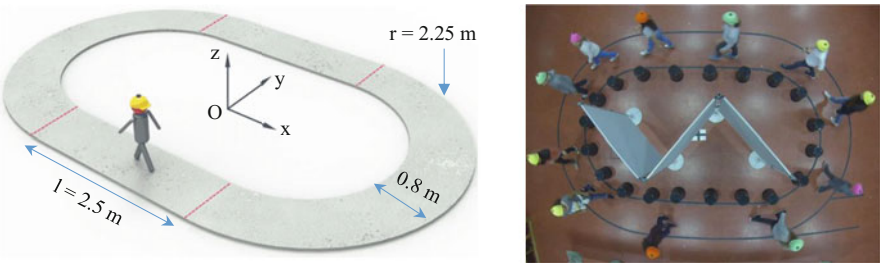

Fig. 1 Experimental setup. The path composed of two straight parts ($l = 2.5$ m) and two semi-circle parts (the radius of the outer line $r = 2.25$ m) is 0.8 m wide. The red dotted lines indicate the border between the straight part and the semi-circle part

Table 1 Experiments of youngsters aged 16

Number of pedestrians	Global density[a] (ped/m)	Runs of clockwise movement	Runs of anti-clockwise movement
6	0.36		1
10	0.60	1	
12	0.72	1	1
15	0.90	1	
16	0.96	1	1
17	1.02	1	
24	1.44	2	
25	1.50		1

[a]The global densities are calculated based on the circumference of the middle line, 16.62 m

3 Results and Discussions

With increasing headway, pedestrians' available space gets larger and the speed increases. When the headway is large enough, pedestrians walk in unhindered situation and the speed is denoted as the free-flow speed. Thus there are two states [5, 23]: one is the congested state and the other is the free-flow state. The relation between headway and speed can be fitted with a piecewise linear function, including an oblique line and a horizontal line:

$$v = \begin{cases} a(h - h_0) & h_0 \le h \le h_e \\ v_0 & h > h_e \end{cases} \tag{1}$$

where the x-intercept h_0 of the oblique line indicates the headway when $v = 0$. It indicates pedestrians' least required distance from the preceding person, named stop space in this study. When the available distance is less than the stop space, pedestrians stop walking. h_e is the headway when the oblique line and horizontal line intersect and indicates the space where the speed is no longer influenced by the preceding pedestrian. When the available distance reaches h_e, pedestrian movement is not limited by the available space anymore and pedestrians walk at free-flow speed v_0. Therefore, h_e is the least required distance for pedestrians to walk at free-flow speed, named free-flow space in this study.

To investigate whether gender and age have significant influence on headway–speed relation, the observations should be independent. 872 and 385 statistically independent observations are obtained, respectively, from males and females based on the autocorrelation, marked by blue and red points in Fig. 2. By using these pseudo-independent observations, the headway–speed relations of different genders are fitted with Eq. (1), see Fig. 2 and Table 2. The one-tailed t-test is adopted for comparison of the parameter estimates to check whether gender has significant influence or not. If the P-value of one-tailed t-test is smaller than 0.05, significant difference is found between the two comparison objects at a significance level of

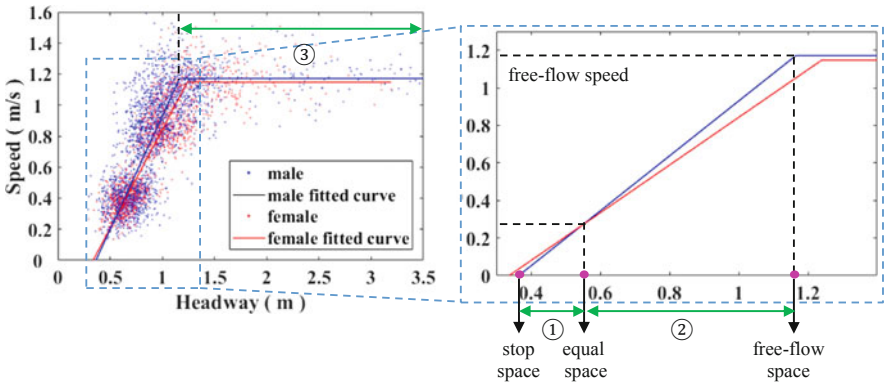

Fig. 2 The relation between headway and speed. The relation is fitted by a piecewise linear function. The statistically independent data and fitting results from males and females are marked with blue and red colors. In the right, a cropped and enlarged sketch from the area marked by a rectangle is shown to illustrate the two important points for personal space (named stop space and free-flow space) and the condition where males and females have equal headway

0.05. The comparison results of the parameter estimates between different genders are shown in Table 2.

Figure 2 and Table 2 show the influence of gender. The stop space of males is larger than that of females. This is mainly because males have larger body size and they require more space to stand still. But compared with males, females have larger free-flow space mainly due to their strong desire to keep distance from others. Besides, there is a situation where the headway of females is the same as the headway of males, referred to as equal space. So according to the stop space, free-flow space, and equal space, there are three stages for the influence of gender on the headway. In the first stage, between the stop space and equal space, males have larger space than females at the same speed mainly due to the physical factors like body size. The second stage is between the equal space and free-flow space. Females remain larger distance from the preceding person than males at the same speed because in this stage psychological factors play the main role. For the third stage, the available space is larger than the free-flow space. Gender has no influence on personal space. In conclusion, personal space is influenced by not only physical factors like body size, but also psychological factors [6, 9, 17]. As the headway becomes larger, the influence of physical factors decreases, while the impacts of psychological factors increase. With regard to the free-flow speed, males have a larger value than females. This maybe because males have larger body height than females.

The natural process of human locomotion is stepwise [20]. The choice of the walking speed is a function of the step length and the step frequency [11]. Thus the study on the gait characteristics helps to understand how pedestrians walk. Figure 3 shows the distributions of gait characteristics of males and females using 2463 and 1251 pseudo-independent observations, respectively. The K-S (Kolmogorov–

Table 2 The fitting results of headway–speed relation and comparison between different genders

Gender	Mean(95% confidence interval)				Comparison result			
	Slope a	Stop space h_0 (m)	Free-flow space h_e (m)	Free-flow speed v_0 (m/s)	a	h_0	h_e	v_0
Male	1.464 (1.463, 1.465)	0.365 (0.364, 0.366)	1.165 (1.153, 1.177)	1.171 (1.152, 1.190)	$P < 0.01$ $M > F$	$P < 0.01$ $M > F$	$P < 0.01$ $M < F$	$P = 0.04$ $M > F$
Female	1.271 (1.270, 1.272)	0.337 (0.336, 0.338)	1.24 (1.226, 1.254)	1.147 (1.127, 1.167)				

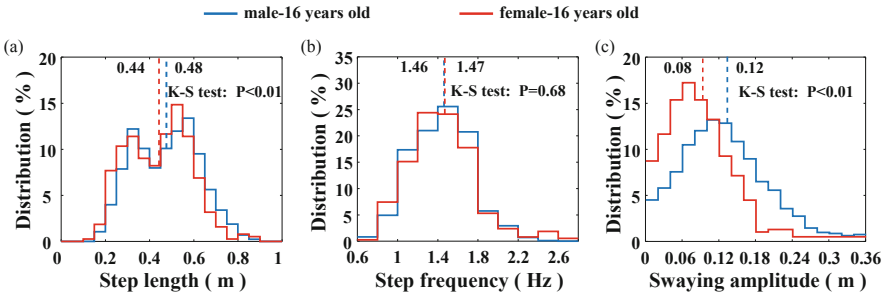

Fig. 3 The distributions of (**a**) step lengths, (**b**) step frequencies, and (**c**) swaying amplitudes. In each picture the distributions from males and females are marked with blue and red color, respectively. The mean value is illustrated by the dashed line using the corresponding color with the distribution. The P-value of the K-S (Kolmogorov–Smirnov) test comparing the difference in distribution between males and females is shown in the corresponding picture

Smirnov) test is adopted to check whether the two comparison distributions are from the same distribution or not. The t-test is adopted to compare the mean value of gait characteristics of the two comparison objects. The comparison results between males and females of these two tests are shown in Table 3. The results of K-S test show that gender has significant influence on step length and swaying amplitude. But whether gender has significant impact on step frequency or not is not clear here because of the large P-value. Males have significantly larger mean values of step length and swaying amplitude than females.

4 Conclusions

To investigate the impacts of gender on human traffic flow, experimental study on single-file movements involving male and female youngsters aged 16 is conducted. The headway, speed, and gait characteristics (step length, step frequency, and swaying amplitude) are measured based on the projected coordinate system considering the influence of the projection line with different radii. Based on statistically independent observations, gender differences in the fundamental diagram and characteristic parameters such as free-flow speed, stop space, and free-flow space are analyzed by statistical test. Due to the connection of walking speed and gait characteristics, the gait characteristics of different genders are compared to understand the difference in the fundamental diagram in more detail. It is found that males always have larger stop space and smaller free-flow space than females. The free-flow speed of males is larger than that of females. We want to emphasize that these differences are small even if they are statistically significant. For gait characteristics, males have significantly larger mean values of step length and swaying amplitude than females.

Table 3 The comparison of gait characteristics of different gender

Gender	Count	Mean (standard deviation)			K-S test P-value			T-test P-value		
		Step length s (m)	Step frequency f (Hz)	Swaying amplitude w (m)	s	f	w	s	f	w
Male	852	0.476 (0.147)	1.463 (0.297)	0.123 (0.064)	$P < 0.01$	$P = 0.68$	$P < 0.01$	$P < 0.01$	$P = 0.71$	$P < 0.01$
Female	377	0.443 (0.144)	1.471 (0.334)	0.083 (0.046)						

Acknowledgements This study was supported by the German Research Foundation (Grant. No. SE 1789/4-1), the National Science Fund for Distinguished Young Scholars of China (Grant No. 71725006), National Natural Science Foundation of China (Grant No. 71473147), the Joint Funds of Beijing Natural Science Foundation and Beijing Academy of Science and Technology (Grant No. L150010), and the China Scholarship Council (CSC). We are in particular grateful to Daniel Salden, Mohcine Chraibi, Bernhard Steffen, and Yang Zhou.

References

1. Bassey, E.J., Macdonald, I.A., Patrick, J.M.: Factors affecting the heart rate during self-paced walking. Eur. J. Appl. Physiol. Occup. Physiol. **48**(1), 105–115 (1982). https://doi.org/10.1007/BF00421170
2. Boltes, M., Seyfried, A., Steffen, B., Schadschneider, A.: Automatic Extraction of Pedestrian Trajectories from Video Recordings. Springer, Berlin (2010). https://doi.org/10.1007/978-3-642-04504-2
3. Boltes, M., Holl, S., Tordeux, A., Seyfried, A., Schadschneider, A., Lang, U., Tordeux, A., Lang, U., Holl, S., Seyfried, A.: Influences of Extraction Techniques on the Quality of Measured Quantities of Pedestrian Characteristics Collective Dynamics **1**, 1–618 (2016)
4. Bosina, E., Weidmann, U.: Generic description of the pedestrian fundamental diagram. In: Proceeding of Pedestrian and Evacuation Dynamics 2016, pp. 548–555. 8th International Conference on Pedestrian and Evacuation Dynamics (2016)
5. Cao, S., Zhang, J., Salden, D., Ma, J., Shi, C., Zhang, R.: Pedestrian dynamics in single-file movement of crowd with different age compositions. Phys. Rev. E Stat. Nonlinear Soft Matter Phys. **94**(1), 1–10 (2016). https://doi.org/10.1103/PhysRevE.94.012312
6. Curtis, S., Manocha, D.: Pedestrian simulation using geometric reasoning in velocity space. In: Pedestrian and Evacuation Dynamics 2012, pp. 875–890. Springer, Cham (2014)
7. Fitzpatrick, K., Turner, S., Brewer, M., Carlson, P., Ullman, B., Trout, N., Park, E.S., Whitacre, J., Lalani, N., Lord, D.: Improving Pedestrian Safety at Unsignalized Crossings, vol. 47. Transportation Research Board, Washington (2006). https://doi.org/10.17226/13962
8. Fruin, J.J.: Pedestrian planning and design. Tech. Rep. (1971)
9. Hall, E.T.: The Hidden Dimension. Doubleday & Co, New York (1966)
10. Hediyeh, H.: Investigation of microscopic pedestrian walking behavior. Ph.D. thesis, University of British Columbia (2012). https://doi.org/10.14288/1.0050873
11. Himann, J.E., Cunningham, D.A., Rechnitzer, P.A., Paterson, D.H.: Age-related changes in speed of walking. Med. Sci. Sports Exerc. **20**(2), 161–166 (1988)
12. Hoogendoorn, S.P., Daamen, W.: Pedestrian Behavior at Bottlenecks. Transp. Sci. **39**(2), 147–159 (2005). https://doi.org/10.1287/trsc.1040.0102
13. Huo, F., Lv, W., Song, Y.: Experimental study on pedestrian stair descent walking behaviours in building stairs. In: Proceeding of Pedestrian and Evacuation Dynamics 2016, pp. 49–56. Springer, Hefei (2016)
14. Inman, V.T., Ralston, H.J., Todd, F.: Human Walking. Williams & Wilkins, Baltimore (1981)
15. Ishaque, M.M., Noland, R.B.: Behavioural issues in pedestrian speed choice and street crossing behaviour: a review. Transp. Rev. **28**(1), 61–85 (2008). https://doi.org/10.1080/01441640701365239
16. Li, S., Sayed, T., Zaki, M., Mori, G., Stefanus, F., Khanloo, B., Saunier, N.: Automated collection of pedestrian data through computer vision techniques. Transp. Res. Rec. J. Transp. Res. Board **2299**, 121–127 (2012). https://doi.org/10.3141/2299-13
17. Narang, S., Best, A., Curtis, S., Manocha, D.: Generating pedestrian trajectories consistent with the fundamental diagram based on physiological and psychological factors. PLos One **10**(4), e0117856 (2015). https://doi.org/10.1371/journal.pone.0117856

18. O'Flaherty, C.A., Parkinson, M.H.: Movement on a city centre footway. Traffic Eng. Control **13**(10), 434–438 (1972)
19. Schadschneider, A., Klingsch, W., Klüpfel, H., Kretz, T., Rogsch, C., Seyfried, A.: Evacuation dynamics: empirical results, modeling and applications. In: Extreme Environmental Events, vol. 50, pp. 517–550. Springer, New York (2011)
20. Seitz, M.J., Köster, G.: Natural discretization of pedestrian movement in continuous space. Phys. Rev. E **86**(4), 046108 (2012). https://doi.org/10.1103/PhysRevE.86.046108
21. Tanaboriboon, Y., Guyano, J.A.: Analysis of pedestrian movements in Bangkok. Transp. Res. Rec. **1294**, 52–56 (1991)
22. Tanaboriboon, Y., Hwa, S.S., Chor, C.H.: Pedestrian characteristics study in Singapore. J. Transp. Eng. **112**(3), 229–235 (1986). https://doi.org/10.1061/(ASCE)0733-947X(1986)112:3(229)
23. Tordeux, A., Schadschneider, A.: White and relaxed noises in optimal velocity models for pedestrian flow with stop-and-go waves. J. Phys. A Math. Theor. **49**(18), 185101 (2016). https://doi.org/10.1088/1751-8113/49/18/185101
24. Versluis, D.: Microscopic interaction behavior between individual pedestrians. Ph.D. thesis, Delft University of Technology (2010). https://doi.org/10.1007/978-3-319-02447-9
25. Wang, J., Boltes, M., Seyfried, A., Zhang, J., Ziemer, V., Weng, W.: Linking pedestrian flow characteristics with stepping locomotion. Phys. A **500**, 106–120 (2018). https://doi.org/10.1016/j.physa.2018.02.021
26. Wang, J., Weng, W., Boltes, M., Zhang, J., Tordeux, A., Ziemer, V.: Step styles of pedestrians at different density. *J. Stat. Mech. Theor. Exp.* **2018**(2), 023406 (2018). https://doi.org/10.1088/1742-5468/aaac57
27. Weidmann, U.: Transporttechnik der Fussgänger. Transporttechnische Eigenschaften des Fussgängerverkehrs, Literaturauswertung. Tech. Rep. (1992). https://doi.org/10.3929/ethz-a-000687810
28. Willis, A., Gjersoe, N., Havard, C., Kerridge, J., Kukla, R.: Human movement behaviour in urban spaces: implications for the design and modelling of effective pedestrian environments. Environ. Plan. B Plan. Des. **31**(6), 805–828 (2004). https://doi.org/10.1068/b3060
29. Wilson, D.G., Grayson, G.B.: Age-related differences in the road crossing behaviour of adult pedestrians. Tech. Rep. (1980)
30. Zhang, J.: Pedestrian Fundamental Diagrams: Comparative Analysis of Experiments in Different Geometries, vol. 14. Forschungszentrum Jülich, Jülich (2012)
31. Zhang, X., Weng, W., Yuan, H., Chen, J.: Empirical study of a unidirectional dense crowd during a real mass event. Physica A **392**(12), 2781–2791 (2013). https://doi.org/10.1016/j.physa.2013.02.019

Evaluation of Pedestrian Density Distribution with Respect to the Velocity Response

Marek Bukáček and Jana Vacková

Abstract There are many approaches to evaluate density within pedestrian scenarios including point approximation, Voronoi cells or more sophisticated methods. In this project we focus on the individual density, where each pedestrian is considered as a source of density distribution. A cone can be used as a reasonable shape with its diameter as a blur parameter. Naturally, pedestrians adapt their velocity and path selection with respect to the conditions around them in given range. The correlation of density and velocity was evaluated on laboratory experiment data for all acceptable blur–range combinations. Because of the fact that negative correlation corresponds to a more significant response of velocity to the density, the correlations seem to be a perfect tool to estimate density parameters. Surprisingly, the expected negative correlation was observed only for one segment of pedestrian's trajectory, observations were much more complex.

1 Introduction

The pedestrian movement, including egress situations, walking in corridors or in cross-section areas, has been widely studied in the last 20 years [7, 9]. This period seems long enough to bring the answer to such fundamental question as "how pedestrians react to their surrounding", but so far, there are only qualitative studies [1] or macroscopic approximations describing behaviour in front of the bottleneck [6, 8, 10, 12] or incorporating heterogeneity [4, 5]. Moreover, the definitions of fundamental quantities are not unified [11] and the only criteria to use some method is to show desired phenomena.

The reaction measured by velocity changes is considered to be induced by the trend of density. There are many ways to evaluate density and even the reaction range should be parametrized, thus the pedestrian behaviour in front of the exit is

M. Bukáček (✉) · J. Vacková
Czech Technical University, Prague, Czech Republic
e-mail: marek.bukacek@fjfi.cvut.cz; marek.bukacek@seznam.cz; janca.vackova@fjfi.cvut.cz

S. H. Hamdar (ed.), *Traffic and Granular Flow '17*,
https://doi.org/10.1007/978-3-030-11440-4_27

analysed on a parametric grid with respect to multiple defined densities (defined below). This parametric grid is generally based on two features

- blur, e.g. the size of area affected by one pedestrian,
- range, e.g. the size of area affecting one pedestrian.

Generally, pedestrian's reaction covers even trajectory changes with constant velocity, but in this paper, we focus only on velocity and density.

At the end, Pearson correlation coefficient

$$\mathscr{R}\left(\rho_{\omega_\alpha}, v_\alpha\right) = \frac{\mathrm{Cov}\left(\rho_{\omega_\alpha}, v_\alpha\right)}{\sqrt{\mathrm{Var}\left(\rho_{\omega_\alpha}\right)\ \mathrm{Var}\left(v_\alpha\right)}} \tag{1}$$

is used as a metric to select the density with the best fit to pedestrian reactions. Time development of correlation coefficient is provided by rolling correlation with window (memory time $\tau = 1.56$ s), i.e. $\mathscr{R}_t\left(\rho_{\omega_\alpha}, v_\alpha\right) = \mathscr{R}\left(\rho_{\omega_\alpha}(t-\tau, t), v_\alpha(t-\tau, t)\right)$.

Numerical study is based on an egress experiment organized in the study hall of FNSPE CTU in Prague in 2014, see [2] or [3] for details.

2 Definitions

As mentioned above, the analysis is provided on pedestrian trajectory data. The velocity $v_\alpha(t)$ of pedestrian α is defined as usual using central differences of space coordinates.

The density is the only flexible variable in this study. The value is integrated over the distribution generated individually by each pedestrian α, as seen in Fig. 1:

$$\rho = \frac{N}{|A|} = \frac{\int_A p(\mathbf{x})\,\mathrm{d}\mathbf{x}}{|A|} = \frac{\int_A \sum_{\alpha=1}^{N} p_\alpha(\mathbf{x})\,\mathrm{d}\mathbf{x}}{|A|} = \sum_{\alpha=1}^{N} \frac{\int_A p_\alpha(\mathbf{x})\,\mathrm{d}\mathbf{x}}{|A|}. \tag{2}$$

The range (r) of pedestrian reaction circle $A = \pi r^2$ is one of the examined parameters.

There are several methods to define the individual density distribution function (kernel) $p_\alpha(\mathbf{x})$:

- Point approximation

$$p_\alpha(\mathbf{x}) = \delta_{\mathbf{x},\mathbf{x}_\alpha},$$

where $\int_A \delta_{\mathbf{x},\mathbf{x}_\alpha}\,\mathrm{d}\mathbf{x} = \begin{cases} 1 & \text{if} \quad \mathbf{x}_\alpha \in A, \\ 0 & \text{otherwise.} \end{cases}$

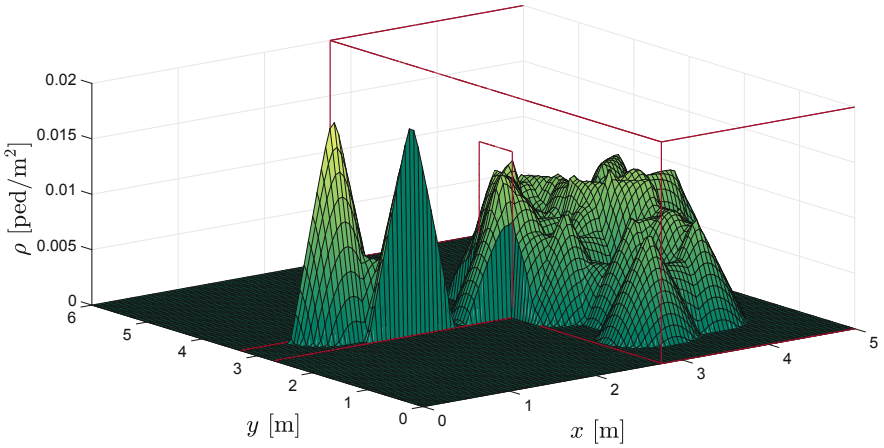

Fig. 1 Example of density distribution near the exit for blur equal to 0.5 m—every cone corresponds to one pedestrian. The cones right next to the walls have reduced bases not to expand from the room (without damaging the normalization)

- Stepwise function

$$p_\alpha(\mathbf{x}) = \begin{cases} \frac{1}{|A_\alpha|} & \text{if} \quad \mathbf{x} \in A_\alpha, \\ 0 & \text{otherwise}, \end{cases}$$

  where $A = \pi R^2$ for cylindrical distribution with blur (R) or $A = A_\alpha$ in case of distribution based on Voronoi cells. In this case, pedestrians are "blurred" dynamically, based on the distance to their neighbours. The whole area is divided into cells according to a simple rule: each point $\mathbf{x}$ is assigned to the nearest pedestrian, see [11] for details.
- Linear (conic) distribution

$$p_\alpha(\mathbf{x}, R) = \begin{cases} \frac{3}{R^3\pi}(R - \|\mathbf{x} - \mathbf{x}_\alpha\|) & \text{if} \quad \|\mathbf{x} - \mathbf{x}_\alpha\| < R, \\ 0 & \text{otherwise}. \end{cases}$$

In this paper, linear (conic) distribution was used due to its decreasing trend with increasing distance, limited support and independence of one pedestrian to others.

3 Analysis

Basic overview is provided by the velocity–density relation of all trajectories. For each blur and range parametric set, Pearson correlation coefficient was evaluated over the whole trajectory, and then averaged over all trajectories of the experiment, see Fig. 2.

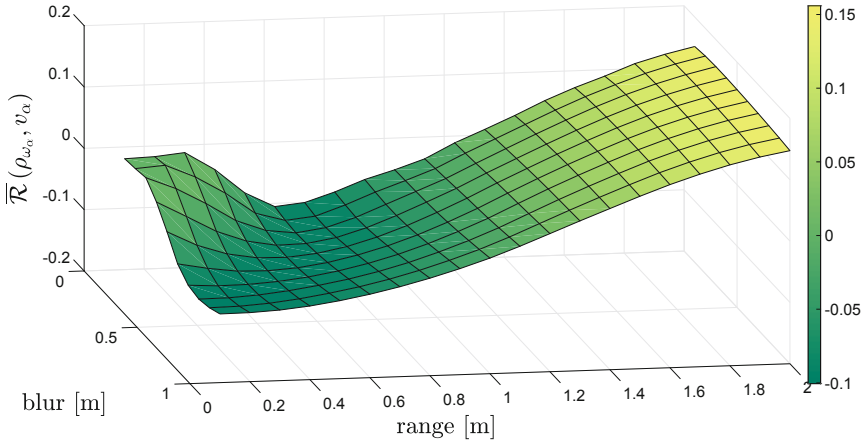

Fig. 2 Pearson correlation coefficient over the whole trajectory. Mean is calculated in every point in parametric space over all trajectories from the experimental data

We can see zero correlation for zero range point approximation as well as natural negative velocity correlation for short range narrow approximation as expected. On the other hand, positive velocity correlation for any long-range approximation was not expected at all. Moreover, the absolute value of correlation is rather small, which indicates weak dependency of density and pedestrian reaction.

To see the source of positive or negative correlation, it is necessary to study individual level and check rolling correlation for segments of each trajectory. For purposes of this case study, we selected one representative illustrated in Fig. 3. This path is interesting due to the long slowing down interval caused by overtaking the crowd, see measured quantities in Fig. 4 and related correlations in Fig. 5.

There is strong positive correlation of velocity and long-range density in free flow area, which can be explained by competitiveness between pedestrians. When another pedestrian approaches one's personal area, it increases the motivation to get to the exit faster, not to be overtook.

Strong negative correlation of velocity and all densities in avoiding/joining the cluster area corresponds to adjusting velocity to higher density. The decrease of velocity fits the increasing trend of long-term densities better, because participants decelerate few seconds before the contact with the crowd. Only long-range densities cover such distance (1.5 m in this paper).

The correlation peak near $t = 248$ s illustrates the differences between different parametric sets. As shown in Fig. 4, short range densities are affected by temporary increased distance to another pedestrian.[1] From long-range perspective, the density was decreased only slightly, the effect is more significant for low blur models.

[1]Link and QR code in Acknowledgements refers to website with animations illustrating the situation.

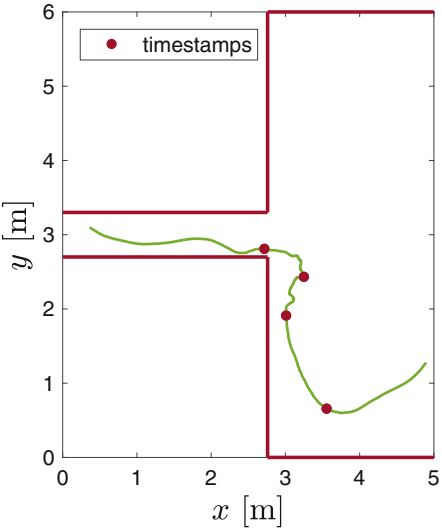

Fig. 3 Path 1240 from a high density period. Pedestrian overtakes the crowd (first spot), joins it at the wall area (second spot), enters the most dense area in front of the door (third spot) and meets the exit (fourth spot)

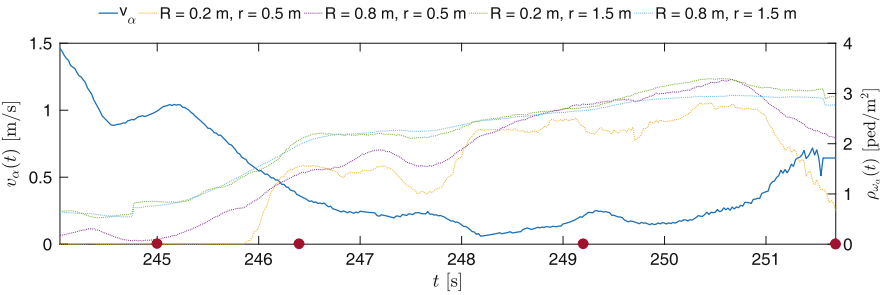

Fig. 4 Velocity and four densities with different blur R and range r parameters. First drop of velocity (1.5–1 m/s) at the beginning of avoiding the crowd is followed by continuous decrease of velocity (1–0.2 m/s) while joining the crowd, meanwhile the density increases from 0.5 ped/m^2 up to 3 ped/m^2 based on parameters. Timestamps are placed at the positions corresponding to the spots of the chosen path in Fig. 3

In this case, the pedestrian did not react to this disturbance by velocity change, the deceleration caused by joining to cluster area prevails. Such stability of long-range high blur density models is very useful to bridge insignificant deviations of pedestrian paths.

Positive correlation of velocity and all densities in the cluster area is caused by the flow conservation law. Closer to the exit, a lower number of participants carry the flow, therefore the velocity near the exit is much higher than inside the crowd, as well as the density might be higher.

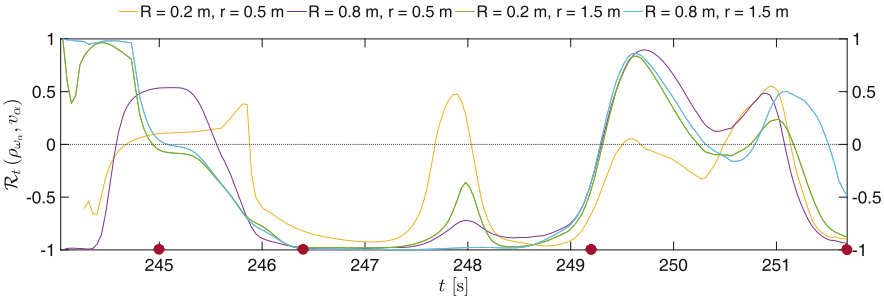

Fig. 5 Pearson correlation coefficient of densities for four blur R and range r combinations and velocity (memory time $\tau = 1.56$ s). Timestamps are placed at the positions corresponding to the spots of the chosen path in Fig. 3

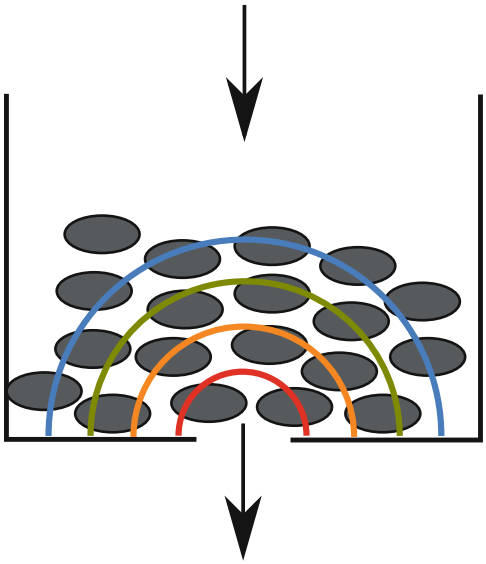

Fig. 6 Illustration of the flow conservation law. The absolute flow must be the same across all curves separating the exit and entry area

This observation may be derived directly from hydrodynamic approximation assuming linear flow

$$J = \frac{N}{t} = \frac{N}{A}\frac{s \cdot d}{t} = \rho v d, \tag{3}$$

where d represents the width of a cross-section. Each participant crosses every separating curve (see Fig. 6) just once, therefore flow through all these cross-sections (indexes $1, 2, \ldots$) must be the same

$$J = \rho_1 v_1 d_1 = \rho_2 v_2 d_2. \tag{4}$$

In the cluster area, the density is almost constant (slightly increasing closer the exit), therefore the relation of velocities is given mainly by the cross-section length, i.e. the distance to the exit

$$\frac{v_1}{v_2} = \frac{d_2}{d_1}\frac{\rho_2}{\rho_1} \approx \frac{d_2}{d_1}. \tag{5}$$

At the end, just in the exit area, density drops due to the empty space in adjacent corridor. Pedestrians start to walk faster, in agreement with the expected negative correlation.

4 Conclusions

Correlation between velocity and density is not as clear as it can be expected at the first sight. Assumed decrease of velocity implied by increasing density is observed only in the transition phase between free flow and congested areas. Conversely in both free flow and congested state, an increase of density is followed by increasing velocity. We do not think that there is such inverse causality, in both cases the velocity does not actually react to the density.

In free flow, pedestrians walk their desired velocity and when there is another pedestrian nearby, they may increase their velocity in order to overtake them. The presence of another pedestrian increases local density as well, but it is just coincidence, not causality.

In cluster area, the pedestrians are more likely to stay in the queue than to walk, their velocity is limited by the velocity of pedestrians in front of them. Due to the semicircular geometry of the clusters, the number of waiting lines decreases with the decreasing distance and each joining of queues slow down the motion. This process is well described by flow conservation law. Concurrently, the density inside the cluster is higher, the peak value is observed approximately 1 m in front of the exit. Again, this is just coincidence, the velocity deep in the crowd is not higher because the density is higher, but it is higher due to the lower number of queues sharing the flow.

In general, individual pedestrian density reflects phase transition changes very well, as can be seen in Fig. 7. For each phase, parametric set maximizing negative correlation was picked to describe conditions in pedestrian reaction area. As expected, reaction range decreases with decreasing velocity and pedestrian blur is more significant in more dense areas.

The value of correlation of velocity and one specific density is variable in time and differs with personal preferences and individually selected strategy. The analysis of such complexity is a subject of further research. We hope that deep decomposition and clustering of trajectories will reveal more fundamental facts that will increase our ability to predict the pedestrian reactions.

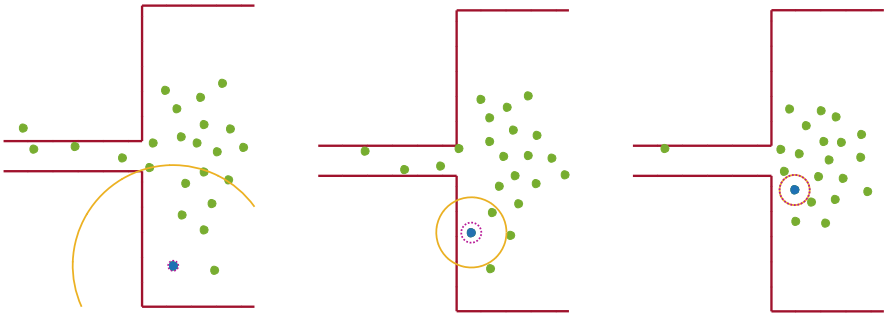

Fig. 7 Changes of blur (pink dotted neighbourhood) and range (yellow neighbourhood) parameters according to the phase transitions during movement of the chosen pedestrian in the experiment

Fig. 8 Link to the animated results as a QR code

Go to www.youtube.com/playlist?list=PLf1k-N3Jifrr3slVBLXnJciIMD9S608cl to see animated results or use QR code in Fig. 8.

Acknowledgements This work was supported by the Czech Science Foundation under the grant GA15-15049S and by Czech Technical University under the grant SGS15/214/OHK4/3T/14. We would like to thank GAMS team members, namely Pavel Hrabák and Matěj Kotrba, for significant help with organizing the experiment. All experiment participants approve for the experimental data to be stored, used and published for academic purposes.

References

1. Bode, N.W.F., Codling, E.A.: Statistical models for pedestrian behaviour in front of bottlenecks. In: TGF'15, pp. 81–88. Springer, Cham (2016)
2. Bukáček, M., Hrabák, P., Krbálek, M.: Experimental study of phase transition in pedestrian flow. Transp. Res. Procedia **2**, 105–113 (2014). In: PED'14
3. Bukáček, M., Hrabák, P., Krbálek, M.: Individual microscopic results of bottleneck experiments. In: TGF'15, pp. 105–112. Springer, Cham (2016)

4. Bukáček, M., Hrabák, P., Krbálek, M.: Microscopic travel time analysis of bottleneck experiments. Transportmetrica A: Transp. Sci. **14**, 1–20 (2018)
5. Campanella, M., Hoogendoorn, S.P., Daamen, W.: Effects of heterogeneity on self-organized pedestrian flows. Transp. Res. Rec. **2124**, 148–156 (2009)
6. Duives, D., Winnie, D., Hoogendoorn, S.P.: Anticipation behavior upstream of a bottleneck. Transp. Res. Procedia **2**, 43–50 (2014). In: PED'14
7. Kretz, T., Grunebohm, A., Schreckenberg, M.: Experimental study of pedestrian flow through a bottleneck. J. Stat. Mech: Theory Exp. **10**, 1–20 (2006)
8. Liao, W., Tordeux, A., Seyfried, A., et al.: Measuring the steady state of pedestrian flow in bottleneck experiments. Physica A **461**, 248–261 (2016)
9. Schadschneider, A., Chowdhury, D., Nishinari, K.: Stochastic Transport in Complex Systems. Elsevier, Amsterdam (2010)
10. Seyfried, A., Passon, O., Steffen, B., et al.: New insights into pedestrian flow through bottlenecks. Transp. Sci. **43**(3), 395–406 (2009)
11. Steffen, B., Seyfried, A.: Methods for measuring pedestrian density, flow, speed and direction with minimal scatter. Physica A **389**(9), 1902–1910 (2010)
12. Zhang, J., Seyfried, A.: Quantification of bottleneck effects for different types of facilities. Transp. Res. Procedia **2**, 51–59 (2014). In PED'14

Using Raspberry Pi for Measuring Pedestrian Visiting Patterns via WiFi-Signals in Uncontrolled Field Studies

Peter M. Kielar, Pavel Hrabák, Marek Bukáček, and André Borrmann

Abstract Research on pedestrian behavior requires empirical field studies. A number of methods for data acquisition are available. However, a low-budget approach that can be applied to measure pedestrian destination choice in large-scale uncontrolled field studies is still missing. The measurement of destination choice patterns is important for validating strategic models, which describe in which order pedestrians visit locations to perform activities. We propose a *Raspberry Pi* setup for *WiFi*-based tracking of pedestrians by their handhelds in an anonymized manner. The method is useful for recording the microscopic and macroscopic crowd dynamics of large-scale uncontrolled field studies, e.g., public events. Furthermore, we provide a concept for strategic model validation that is based on the measurements.

1 Introduction

In pedestrian dynamics research, empirical data is used to validate computational models of pedestrian behavior. Validation is a process that evaluates whether a computational model can forecast or simulate specific features of the real world with certain accuracy.

Models that describe strategic pedestrian behavior [10] are used for simulating destination choices of pedestrians in complex environments (e.g., transport hubs or public events). Hence, strategic models describe how pedestrians repetitively find destinations to visit. The resulting visiting patterns are the spatial choice sequences in which people perform activities [8]. In order to validate models that simulate the

P. M. Kielar (✉) · A. Borrmann
Technische Universität München, Munich, Germany
e-mail: peter.kielar@tum.de; andre.borrmann@tum.de

P. Hrabák · M. Bukáček
Faculty of Information Technology, Czech Technical University in Prague, Prague 6, Czech Republic
e-mail: pavel.hrabak@fit.cvut.cz; hrabapav@fit.cvut.cz; marek.bukacek@fjfi.cvut.cz

S. H. Hamdar (ed.), *Traffic and Granular Flow '17*,
https://doi.org/10.1007/978-3-030-11440-4_28

strategic decision making in complex environments, data of a large spatiotemporal coverage is mandatory.

The method of choice to acquire raw data for strategic model validation purposes is to measure the *WiFi*-signatures of the mobile devices of pedestrians in large-scale studies [3, 5]. The analysis of the signatures provides the localization and unique identification of the devices. Furthermore, the method can measure the duration the devices stayed at a location. In contemporary research, *WiFi*-signature is measured by exploiting the local network infrastructure [5] or utilizing commercial devices [3]. Unfortunately, applying such methods in uncontrolled field studies is seldom possible. Many environments do not provide a network infrastructure (e.g., open air festivals) or the existing infrastructures may not be accessed due to security reasons. Furthermore, the application of commercial *WiFi*-measuring devices in large-scale field studies can generate high costs. To overcome these issues, we provide a solution for *WiFi*-signature measuring based on *Raspberry Pi* computers. The approach enables researchers to set up a low-budget measuring infrastructure in large-scale uncontrolled field studies to capture *WiFi*-signature of people with active *WiFi*-devices. The *WiFi*-signatures enable to analyze the pedestrian visiting patterns for validating strategic models of pedestrian dynamics.

2 Related Work

Modeling pedestrian behavior is typically approached in a behavior concept comprising a strategic, a tactical, and an operational behavioral layer [10]. Each layer can comprise different models that describe pedestrian behavior and each model needs to be validated to proof its practical applicability and correctness.

Operational behavior models address the movement of pedestrians. The validation criteria of operational models are typically based on the fundamental diagram [2] and observable crowd-behavior phenomena [9].

Tactical behavior models typically address directed wayfinding behavior [11]. Wayfinding models are validated based on data that captures the route choices of pedestrians from GPS-based studies [1] or laboratory experiments [6].

Strategic behavior describes how pedestrians solve the destination choices problem [8, 10, 12]. This means that a pedestrian repetitively selects a location to visit. After a destination choice, the pedestrian walks to the location and performs the activity at the destination. Typical activities are buying a coffee, waiting for the bus, or enjoying a street performance. However, strategic pedestrian behavior is complex in the sense that multiple personal and environmental factors influence and guide the destination choice process of pedestrians [8, 12].

The process of validating strategic models needs large data sets of visiting patterns. Such data can be acquired by large-scale uncontrolled field studies, e.g., public events. Furthermore, laboratory experiments that use virtual worlds are not suited for strategic data acquisition because the interaction of a large number

of pedestrians in a complex environment demands an extremely high number of interacting participants over multiple hours.

The challenge in measuring data for strategic model validation purposes is to reach a high level of data coverage and data accuracy. In contemporary research, the analysis of *WiFi*-signatures of pedestrians' mobile devices is a method to approach this challenge [4, 5]. *WiFi*-signatures are especially suited for validating strategic models because they can provide information about the localization and identification of individual *WiFi*-devices over a long time period.

A *WiFi*-signature comprises the unique MAC-address (media-access-control-address) of the mobile devices and the RSSI (received signal strength indicator) of the signal [15]. The RSSI is a relative parameter of a signal for which large values indicate a better signal strength. The *free-space path loss* function [7] can estimate the distance between a *WiFi*-sender and a receiver by means of the RSSI. Unfortunately, all obstacles introduce damping and decrease the RSSI values. This damping leads to a bad noise to signal ratio, which distorts distance estimations.

3 Methodology

In this section, we provide the methodological aspects of setting up a *WiFi*-signature measuring network for validating strategic models of pedestrian behavior based on *Raspberry Pi* computers. Figure 1 shows the general approach of the methodology. We explain each aspect of the method in the following subsections.

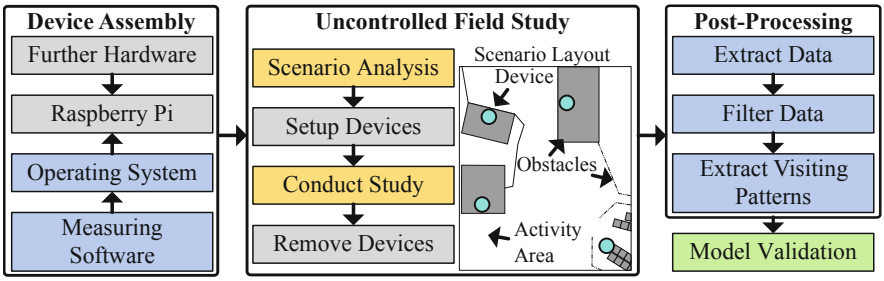

Fig. 1 This schema shows the core aspects of the paper's approach. Initially, the hardware and software are assembled. The assembly has to be set up for multiple devices. In a field study, the devices are placed at the activity locations of the scenario. Therefore, the scenario has to be analyzed first. After the study, the measured data is post-processed. The validation of a pedestrian behavior simulation with focus on strategic behavior can be done with the processed data

3.1 Device Assembly

Here, we provide information for the software and hardware assembly of the measuring devices.

A goal of this research is to use a set of low-cost hardware devices that read *WiFi*-signals from pedestrians' mobile devices in field studies. Typically, all locations of a scenario where pedestrians can perform activities are points of interest and need to be equipped with at least a single measurement device. Furthermore, all measuring devices have to operate power-independent because it is not guaranteed that every point of interest provides a stable power supply.

Our solution to the aforementioned requirement is to use a *Raspberry Pi* hardware, a portable USB-based power bank with $\geq$10,400 mA h, and a *microSD*-card with a Linux operating system. Each device reads *WiFi*-signals via a low-cost USB-*WiFi*-dongle that is able to operate in the so-called monitor mode. This mode changes the operative behavior of the dongle to listening. Thus, the dongle will capture all incoming signals. The availability of the monitor mode is hardware and driver dependent. Any USB-*WiFi*-dongle that supports monitor mode can be used. However, every dongle-type provides different physical *WiFi*-properties. Finally, most large-scale field studies are conducted in open-air conditions. Therefore, we used waterproof boxes to protect the hardware. Figure 2 shows the hardware setup.

The basis of the software is the *Arch Linux* operation system. Furthermore, we utilize the *scapy* and the *hashlib* Python libraries. The *scapy* library provides code to access received *WiFi*-signals. Each signal comprises the RSSI and the MAC address of an incoming signal. We encrypt received MAC addresses by computing a *SHA-256* hash before storing data in a file. In large-scale field studies, multiple measuring devices are used. Hence, all devices use the identical private-key for hashing. This provides the identical hash value for the same MAC address.

The time at which the signal was received is the device's system time and is also stored in the data file. The used *Raspberry Pi* computers do not provide an internal

Fig. 2 This figure shows hardware in a waterproof box. The setup comprises a power bank, a USB-power-connector, a *WiFi*-dongle, a *microSD*-card, and a *Raspberry Pi*

real-time clock. Thus, we applied a time-server concept so that the devices read the current time if connected a setup computer. Another solution is to set the internal time of the devices by the command line. The clock on all used devices needs to be synchronized for good analysis results.

3.2 Use in Uncontrolled Field Studies

The setup of a measuring network in uncontrolled field studies starts with analyzing the scenario. In this process, we used maps, layouts, and general information provided by the organizer and operator of the area of the study. The analysis focuses on identifying locations where pedestrians can perform activities. These are, for example, shops, restrooms, dedicated entrances, or leisure areas. All spatially clearly distinguishable locations should be equipped with measuring devices.

We tested the *WiFi*-measuring method in two open-air case studies: a music festival and a Christmas market. Figure 3 shows the layouts and test positions of the measuring devices for the music festival. Details of the Christmas market study are given in [14].

The power supply enables to run the devices approximately 12 h. Therefore, we activated all devices and started the measuring procedure via Ethernet connection before mounting the devices at available spaces at the locations. It is recommended to find elevated mounting positions with a minimum of obstacles between device

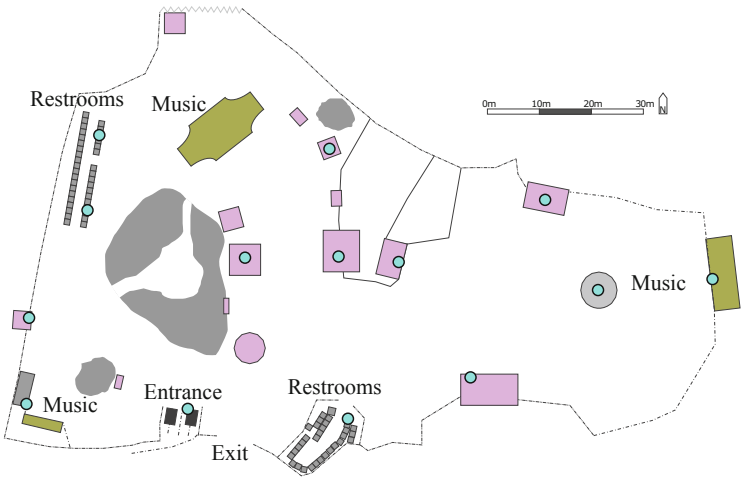

Fig. 3 The figure shows the layout of the music festival field study based on data from VABEG Event Safety Limited. The positions of the measuring devices are indicated as blue circles. Stationary obstacles are given as gray lines and polygons. Visitors can interact with areas (e.g., buy food) which are shown in dark pink. Other areas are explicitly named

and area where the crowd will perform activities. We also marked the different locations on a map and via GPS.

3.3 Post-processing

The measured *WiFi*-data comprises the encrypted MAC address, the date and time of measuring, the RSSI, and the number of the *Raspberry Pi* device, which did the measurement. The post-processing of the data includes the following operations:

1. Extract the data of all devices and merge all data files into a single file.
2. Remove duplicate data entries by deleting data entries with a worse RSSI value if all other data elements of the signal are identical.
3. Sort the data based on the encrypted MAC address, the date, and the time.
4. Compute the *free-space path loss* for all RSSI values for the data. This provides the estimated distance for each measurement.
5. Remove all data entries that exceed a maximal estimated distance threshold d. This provides an estimated maximal distance to the measuring devices.
6. Remove all data entries that exceed a minimal estimated distance threshold k and cover a time-span of s. This deletes data of staff members near the devices.
7. Remove all data entries if the number of entries for a single MAC address is smaller than a threshold z. This reduces data from passers-by.
8. Aggregate the data for each device and each encrypted MAC address.

Typical study dependent parameters we applied in the field studies are: $d_1 = 10\,\text{m}$, $d_1 = 5\,\text{m}$, $k = 2\,\text{m}$, $s = 120\,\text{min}$, and $z = 10$.

3.4 Strategic Model Validation

The post-processing of the *WiFi*-measurements provides a data set for each *Raspberry Pi* device and each encrypted MAC address. Both data sets are sorted regarding the time and date of each signal. Figure 4 provides data samples of the music festival field study. Such data is used for validation of strategic pedestrian behavior simulation output.

Strategic models that are implemented in microscopic pedestrian simulations determine the sequence in which each pedestrian visits locations. Therefore, the microscopic decisions of pedestrians lead to macroscopic properties of the crowd. These properties describe the number of pedestrians at any destination over time.

The first validation approach addresses the macroscopic properties of strategic models and uses the device-based data of the *WiFi*-measurements. If the strategic model predicts the destination choice dynamics of a crowd correctly, the number of pedestrians at destinations over time will correspond to the measured data. We propose a comparison metric for the data that is based on grouping the data into the

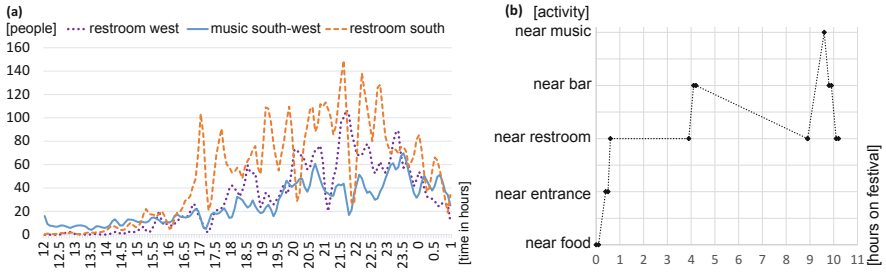

Fig. 4 The figure provides example data of the music festival study. (**a**) It shows the number of *WiFi*-devices with an estimated maximal distance of 10 m from the measuring devices over time in hours. We applied a discrete 1D-Gaussian filter of size 5 for smoothing. (**b**) It shows the visiting sequence of a pedestrian with an estimated maximal distance of 5 m to the measuring devices. Leisure areas are close to restrooms. Diagonal lines indicate inaccuracies due to missing data

operational phases of a field study, e.g., rush-hour, music performance, or entry. The method compares the mean and variance of the number of pedestrian in the study and of the simulation in each phase at each destination.

The second validation focuses on the microscopic visiting patterns of simulated pedestrians and uses the encrypted MAC address data. The data provides an estimator for the destination visiting sequences of pedestrians. The validation evaluates whether the visiting sequences of individual people of the study and the simulation correspond. The comparisons should use categories of destination, e.g., group shops with the same goods. Thereafter, the procedural conformity of the simulated and measured activity-sequences can be compared.

4 Accuracy Discussion

The *WiFi*-method to acquire data of the pedestrian dynamics of a large-scale scenario provides a method to validate strategic models of pedestrian behavior. However, we have to be aware of important inaccuracies in measuring *WiFi*-signals:

- The percentage of people $p\%$ that have a handheld with active *WiFi* is unknown. We applied the value $p = 81.43\%$ based on the Christmas market field study [14].
- The mobile devices check for *WiFi*-networks in intervals. The duration between two checks is dependent on the devices' hardware and the operating system.
- The estimated distance is computed via the *free-space path loss* function. In field studies, this function provides a quite inaccurate estimator for the real distance between a mobile device and a measuring device [15]. The research field on *WiFi*-localization [13] provides improvements for the distance estimations.

- Each *WiFi*-receiver and -sender does have different wave propagation and signal strength properties. In order to improve the accuracy of the measurement, the properties of the devices have to be identified accurately. We conducted a laboratory experiment with different mobile devices to evaluate the wave propagation properties of the applied USB-*WiFi*-dongles and measuring device positioning.

5 Conclusion

In this paper, we presented a *WiFi*-based method to acquire pedestrian visiting patterns in large-scale uncontrolled field studies for strategic model validation. The method is based on *Raspberry Pi* computers and is a low-cost approach that does not require a *WiFi*-infrastructure. The measured data is anonymized via encryption and provides the number of pedestrians with an active *WiFi*-device in proximity to measurement devices and the location visiting sequences of pedestrians.

Strategic models describe the destination choices of pedestrians. Hence, these models provide an approach to simulate the pedestrian dynamics of complex large-scale environments. We explained a microscopic and a macroscopic validation approach for validating strategic models based on post-processed *WiFi*-data.

The proposed method needs to be improved regarding the accuracy of the measurements. Still, it provides a unique approach for validating strategic models by data of large-scale uncontrolled field studies.

Acknowledgements We like to thank Antonin Danalet for discussions. Furthermore, the authors like to thank Daniel H. Biedermann and Micheal Rosteck for conducting the Christmas market field study. This work was partially supported by the Federal Ministry for Education and Research (BMBF) under the grant FKZ 13N12823, by the Czech Science Foundation under the grant GA15-15049S, and by Czech Technical University under the grant SGS15/214/ OHK4/3T/14.

References

1. Biedermann, D.H., Kielar, P.M., Riedl, A.M., Borrmann, A.: Oppilatio+ - a data and cognitive science based approach to analyze pedestrian flows in networks. Collective Dynamics **1**(0), 1–30 (2016)
2. Chattaraj, U., Seyfried, A., Chakroborty, P.: Comparison of pedestrian fundamental diagram across cultures. Adv. Complex Syst. **12**(3), 393–405 (2009)
3. Daamen, W., Yuan, Y., Duives, D., Hoogendoorn, S.P.: Comparing three types of real-time data collection techniques: counting cameras, Wi-Fi sensors and GPS trackers. In: Conference on Pedestrian and Evacuation Dynamics, pp. 568–574 (2016)
4. Danalet, A., Farooq, B., Bierlaire, M.: A Bayesian approach to detect pedestrian destination-sequences from WiFi signatures. Transp. Res. C Emerg. Technol. **44**, 146–170 (2014)
5. Danalet, A., Tinguely, L., de Lapparent, M., Bierlaire, M.: Location choice with longitudinal WiFi data. J. Choice Model. **18**, 1–17 (2016)

6. Dijkstra, J., Vries, B.D., Jessurun, J.: Wayfinding search strategies and matching familiarity in the built environment through virtual navigation. Transp. Res. Procedia **2**, 141–148 (2014)
7. Friis, H.T.: A note on a simple transmission formula. Proc. IRE **34**(5), 254–256 (1946)
8. Gärling, T.: Human information processing in sequential spatial choice. Wayfinding Behavior: Cognitive Mapping and other Spatial Processes pp. 81–98. Johns Hopkins University Press, Baltimore (1999)
9. Helbing, D., Buzna, L., Johansson, A., Werner, T.: Self-organized pedestrian crowd dynamics: experiments, simulations, and design solutions. Transp. Sci. **39**(1), 1–24 (2005)
10. Hoogendoorn, S.P., Bovy, P.H.L.: Pedestrian route-choice and activity scheduling theory and models. Transp. Res. B Methodol. **38**(2), 169–190 (2004)
11. Kielar, P.M., Borrmann, A.: Coupling spatial task solving models to simulate complex pedestrian behavior patterns. In: Conference on Pedestrian and Evacuation Dynamics (2016)
12. Kielar, P.M., Borrmann, A.: Modeling pedestrians' interest in locations: a concept to improve simulations of pedestrian destination choice. Simul. Model. Pract. Theory **61**, 47–62 (2016)
13. Liu, C., Wu, K., He, T.: Sensor localization with ring overlapping based on comparison of received signal strength indicator. In: IEEE International Conference on Mobile Ad-hoc and Sensor Systems, 2004, pp. 516–518. IEEE, Piscataway (2004)
14. Rostek, M.: Evaluierung von messgeräten zur detektion von fußgängerströmen. Bachelor's thesis, Technische Universität München (2017)
15. Wireless LAN Medium Access Control (MAC) and Physical Layer (PHY) Specifications. IEEE Std. 802.11 (2016)

Group Parameters for Social Groups in Evacuation Scenarios

Cornelia von Krüchten and Andreas Schadschneider

Abstract Social groups are often an essential part of pedestrian crowds and influence their behaviour. In order to describe not only the influence of social groups in evacuations on entire pedestrian crowds, but also the dynamics of the groups themselves, we introduce a new set of quantitative group parameters. This set includes (1) the centre of mass of social groups with its velocity and orientation and (2) the shape of the groups. They are approximated as an ellipse of minimal area while containing all social group members. The main properties of this ellipse give some indication about the dynamics of the members, whereas the centre of mass quantities describe the dynamics of an entire social group. By combining both aspects it is possible to determine whether the members order along the group's direction of movement. Additionally, the orientation of the social groups is determined via a gyration tensor approach. All quantities are determined from data of an experimental study on the influence of social groups on pedestrian evacuation dynamics. This study investigated several evacuation scenarios with groups and was performed in schools. Young adults performed evacuation runs including social groups of different sizes.

1 Introduction

Since social groups are known to dominate in pedestrian traffic [1, 11, 12, 15], their behaviour and the impact on the crowd dynamics are an area of interest for some time. For social groups in evacuation scenarios the experimental data basis is

C. von Krüchten (✉)
Institut für Theoretische Physik, Universität zu Köln, Cologne, Germany
e-mail: cvk@thp.uni-koeln.de

A. Schadschneider
Institut für Theoretische Physik, Universität zu Köln, Cologne, Germany

Institut für Physikdidaktik, Universität zu Köln, Cologne, Germany
e-mail: as@thp.uni-koeln.de

S. H. Hamdar (ed.), *Traffic and Granular Flow '17*,
https://doi.org/10.1007/978-3-030-11440-4_29

diverse. Whereas in [4, 11, 13] the authors observed a negative influence of social groups in terms of the evacuation time, this impact can also depend on the initial conditions [7], the order of the experiments [3] or other, yet unknown factors [14]. However, a positive impact of grouping was observed in [6].

In order to investigate the influence of social groups on evacuations laboratory experiments were performed with pupils who went through several evacuation runs of crowds with social groups of different sizes. Based on these data quantities were introduced to describe the behaviour of single social groups and their members. These "group parameters" were directly determined by the configuration and dynamics of the group members and considered the centre of mass of the groups, their shape and orientation. They can give five first indications how groups may behave during evacuation scenarios.

2 The Group Parameters

The choice of the group parameters aimed at the analysis of the behaviour and the configuration of social groups during the evacuation process. They are microscopic parameters that allow to describe the dynamics quantitatively.

2.1 Centre of Mass

Using the centre of mass and its dynamics helps at describing the dynamics of a single group as a whole. This approach was used for the investigation of starling flocks [2] and is here adapted for the two-dimensional space.

The position of the centre of mass at a time t $\mathbf{R}_{CoM}(t)$ of a social group is calculated as the average position of its members,

$$\mathbf{R}_{CoM}(t) = \frac{1}{N_m} \sum_{i=1}^{N_m} \mathbf{r}_i(t) \tag{1}$$

where N_m is the number of the group members, and $\mathbf{r}_i(t)$ their respective position at time t. The velocity of the centre of mass at time t $\mathbf{v}_{CoM}(t)$ is then calculated by

$$\mathbf{v}_{CoM}(t) = \frac{\mathbf{R}_{CoM}(t) - \mathbf{R}_{CoM}(t - \Delta t)}{\Delta t}. \tag{2}$$

This velocity can be used to describe the general movement of the social group.

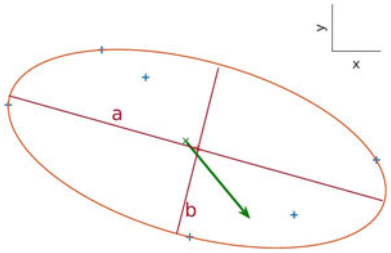

Fig. 1 Typical minimal area ellipse: the blue crosses are the positions of the group members, the green "x" and arrow represent the position and orientation of the group's centre of mass. *a* and *b* are the major and minor axis of the ellipse

2.2 Shape of a Social Group

The second group parameter represents the dynamics and the configuration of the pedestrians within a group. The group is approximated as a minimal area ellipse that contains all group members while having the minimal possible area at the same time [9, 10]. Its shape, that contains the aspect ratio and the area of the ellipse, directly depends on the positioning of the group members, see Fig. 1. It therefore helps to analyse the spatial group cohesion and configuration.

2.3 Orientation of a Social Group

There are three different approaches to determine the orientation of the social groups. The orientation of the centre of mass is given by the angle between its velocity and an axis of reference, e.g. the room axis. It describes the orientation of the general movement of the group.

The orientation of the configuration of the group members can be described by the ellipse. It is given by the angle between the ellipse's major axis and the axis of reference. This can be used to analyse in which way the pedestrians order within the group.

A third approach is to determine the orientation of the group as a complex construct by calculating the gyration tensor [8]

$$G_{ij}(t) = \frac{1}{N_m} \sum_{k=1}^{N_m} \left(x_{k,i}(t) - x_{CoM,i}(t)\right)\left(x_{k,j}(t) - x_{CoM,j}(t)\right) \tag{3}$$

where $x_{k,l}$ are the coordinates of the group member k, $x_{CoM,l}$ the coordinates of the group's centre of mass and N_m the total number of group members. This orientation can be used to estimate how good the approximation of a group as the minimal area ellipse works.

3 Empirical Study

The data that are used to probe the group parameters stem from a experimental study carried out by teams of the universities of Wuppertal and Cologne and the Forschungszentrum Jülich. The experiments were performed in two schools with pupils of different ages. To analyse the influence of larger groups on evacuation scenarios youths were asked to perform evacuation runs in social groups of different sizes. There were evacuation in pairs, groups of four, six and eight as well as individual runs. In addition, there was a single run with groups of six where the students were told to particularly concentrate on their group members and to try to stay together even more. This run is referred to as "cooperative behaviour".

The experimental set-up included an artificial square room with a door of 1.2 m width. The students stood together in their social groups at the beginning. Then they should leave the room as fast as possible without running and scrambling. All experiments were filmed from a camera system at the ceiling and processed using the PeTrack software [5]. For further information on the experiments we refer to [14].

The group parameters were applied to the experimental data in both schools. In this contribution we restrict exemplarily to the first dataset.

3.1 Mean Velocity of the Centre of Mass

The velocity of the centre of mass was calculated for each group and then averaged over the number of groups. As shown in Fig. 2, the mean velocity of groups increases almost linearly at the beginning of the evacuation for every group size. After a few seconds the velocities reach a rather constant level. The curves for the runs with groups of four, six and eight flatten down at around 0.7 m/s, whereas the run with groups of six and cooperative behaviour has a velocity of 0.5 m/s. Therefore, the social groups accelerated in the first seconds of the evacuation and then reached a constant velocity. Very cooperative groups moved slower, due to the stronger group cohesion.

3.2 Mean Aspect Ratio of the Minimal Area Ellipse

The aspect ratio of the minimal area ellipse is the ratio between its major and minor axis. Figure 3 shows the mean aspect ratio averaged over the number of social groups. It is always greater than 1, so the groups form prolate ellipses that are elongated towards the door. It increases a bit in time with a small decrease at the end. Whereas the groups of six and eight have a similar mean aspect ratio, it later is significantly larger in the case of groups of four and smaller for cooperative

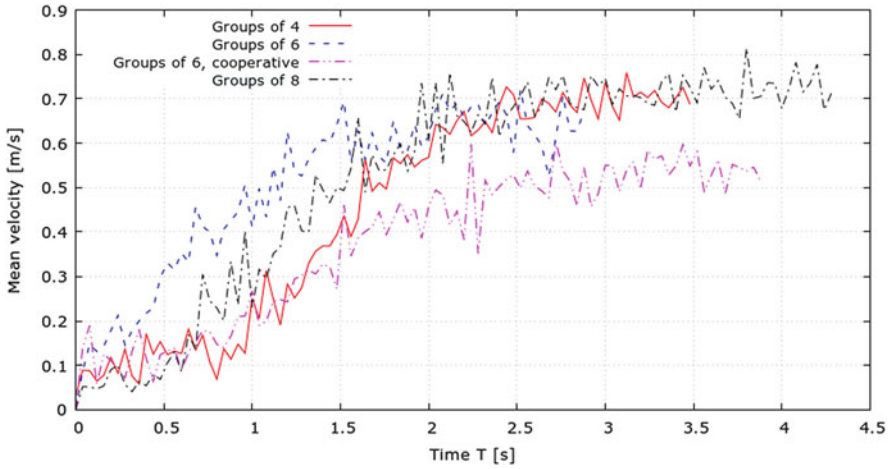

Fig. 2 Averaged velocity of the centre of mass using the data of the first school. The groups accelerate but reach a constant velocity level soon for all group sizes

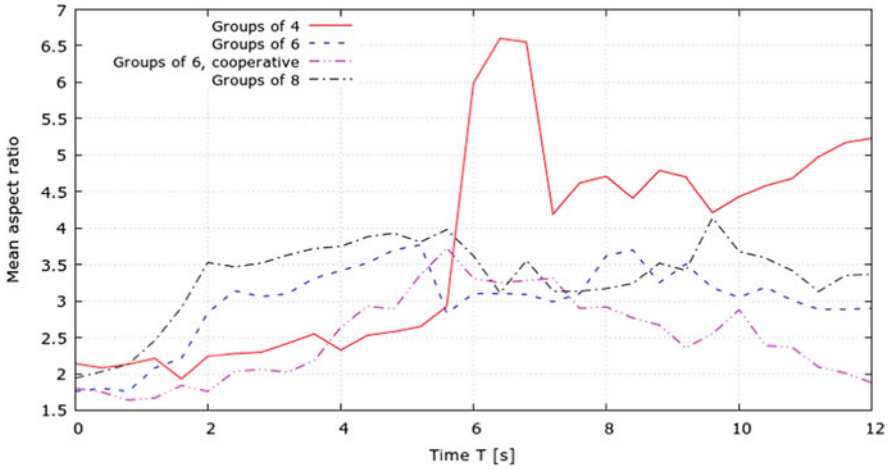

Fig. 3 The mean aspect ratio of the minimal area ellipses for the first dataset shows that in general the groups are elongated during the evacuation towards the exit

groups. So, cooperative behaviour leads to a more rotund configuration compared to normal behaviour. The run with four participants per group shows a sharp increase in between. Here, the groups lost some of their group members.

3.3 Mean Normalized Area of the Minimal Area Ellipse

The area of the minimal area ellipses was averaged and normalized with respect to the number of group members in order to get the averaged space requirement per person. In Fig. 4, the mean normalized area increases over time, so the group members fanned out during the evacuation. The groups of four and six only have a small difference in the normalized area; however, the space requirement per person in the groups of eight is significantly higher. This indicates that group members need more space in larger groups. Comparing the groups of six with normal behaviour to these with cooperative behaviour, the latter show a smaller aspect ratio. The group members of the cooperative groups stand closer together due to the stronger cohesion.

3.4 Orientation

The orientation of the centre of mass was averaged over the number of groups (Fig. 5): in the first seconds of the evacuation the angle of the mean orientation decreases fast and flattens out at a constant level between 0° and 40° for all groups. Therefore, the groups move in a narrow cone around the room axis independently of the group size.

The results for the minimal area ellipse cannot reasonably be averaged due to large differences between single group results for groups of four. However, the ellipse orientation can be compared to the orientation of the centre of mass and the gyration tensor result for single groups. A good match between the ellipse and the

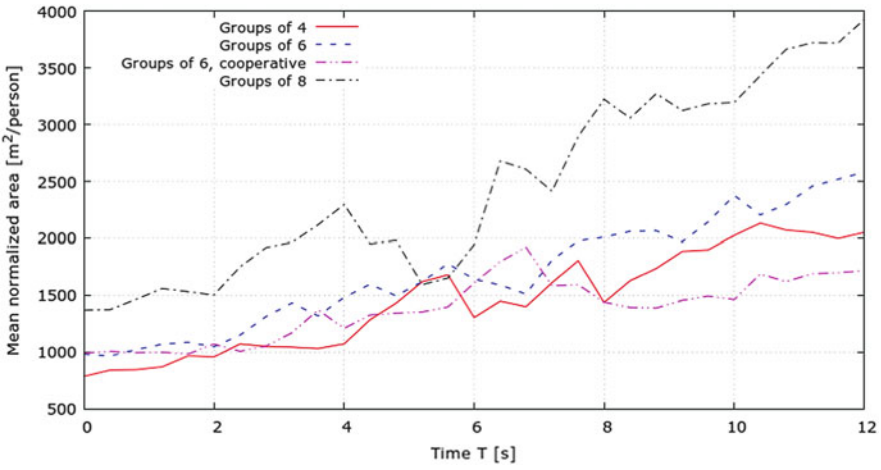

Fig. 4 The mean normalized area indicates a higher space requirement per person for large groups with eight participants

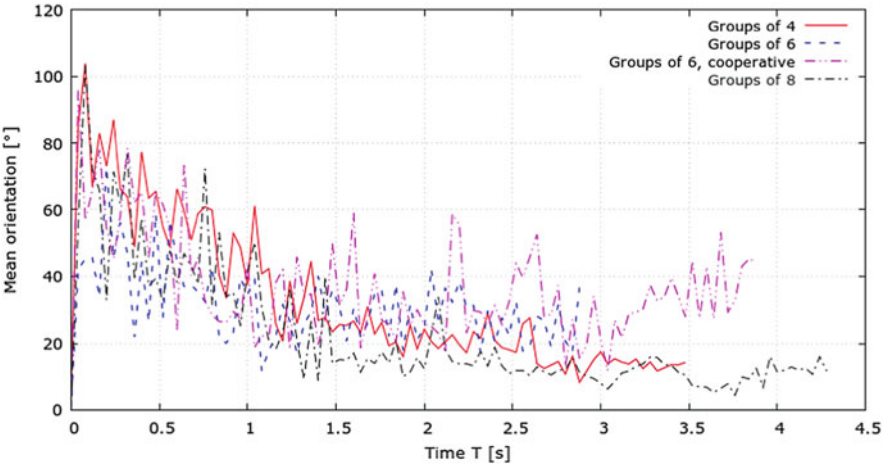

Fig. 5 The mean orientation of the centre of mass decreases fast, so the social groups move in a narrow cone of maximum 40° around the room axis

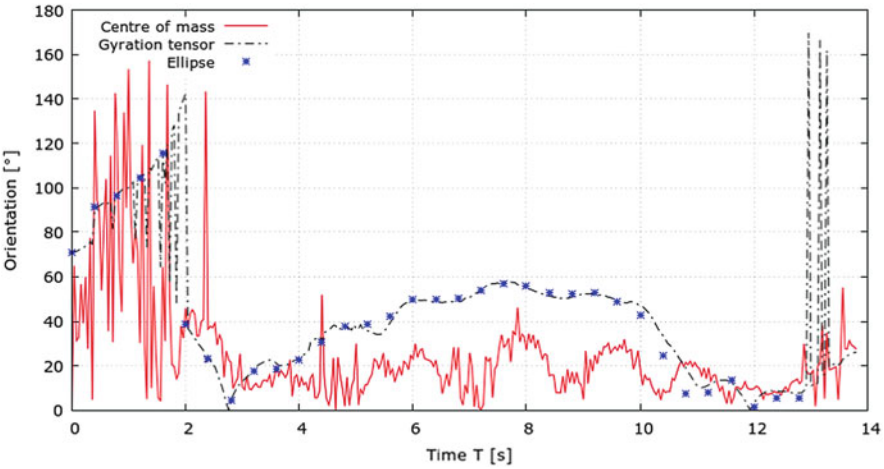

Fig. 6 Comparison of the orientations of a single social group. The results of the gyration tensor and the ellipse match very well and the orientations of the centre of mass and the ellipse look similar

gyration tensor orientation shows that the approximation of the groups as ellipses works well. The comparison of the orientations of the ellipse and the centre of mass shows the relation between the general direction of movement and ordering of the group members. If both orientations look similar, the pedestrians stand behind each other in the direction of the general movement.

In Fig. 6 a typical result is shown. The orientation of the centre of mass and the minimal area ellipse match at least temporarily. That means that the group

members mainly order along their direction of movement. In addition, the results of the gyration tensor calculation fit the ellipse data very well. So the social groups can be approximated as ellipses.

4 Conclusion

We introduced quantitative group parameters to describe and investigate the behaviour and dynamics of social groups during an evacuation. The general dynamics of a group is characterized by the motion of the centre of mass. Approximating the groups as minimal ellipses that contain all members allows to determine their shape and internal dynamics. The gyration tensor was used to calculate the orientation of the group. A comparison of the orientations of the centre of mass, the ellipse and the tensor helps to investigate the relation between the general movement and the individual behaviour and to assess how good social groups can be approximated as ellipses.

All parameters were applied to data of an experimental study with pupils. The young adults performed evacuation runs in different crowd compositions. The results show that all groups accelerated at the beginning of the evacuation but reached a constant velocity soon. They moved within a small cone around the room axis and were elongated towards the exit. In many cases, the orientation of a group calculated by the centre of mass and the ellipse agreed well, so the group members order along their general direction of motion during the evacuation. Larger groups seem to have a higher space requirement per person. Cooperative group members stand closer and more rotund and moved slower. Using the gyration tensor we could show that groups can be well described by ellipses.

Acknowledgements We thank the teams of Forschungszentrum Jülich and University Wuppertal and the pupils and teachers of the participating schools. Financial support by the Deutsche Forschungsgesellschaft (DFG) under grant SCHA 636/9-1 and Bonn-Cologne Graduate School of Physics and Astronomy (BCGS) is gratefully acknowledged.

References

1. Aveni, A.F.: The not-so-lonely crowd: friendship groups on collective behavior. Sociometry **40**(1), 96–99 (1977)
2. Ballerini, M., Cabibbo, N., Candelier, R., Cavagna, A., Cisbani, E., Giardina, I., Orlandi, A., Parisi, G., Procaccini, A., Viale, M., Zdravkovic, V.: Empirical investigation of starling flocks: a benchmark study in collective animal behavior. Anim. Behav. **76**, 201–215 (2008)
3. Bode, N.W.F.: The effect of social groups and gender on pedestrian behaviour immediately in front of bottlenecks. In: 8th International Conference on Pedestrian and Evacuation Dynamics, pp. 92–99. University of Science and Technology of China Press, Hefei (2016)
4. Bode, N.W.F., Holl, S., Mehner, W., Seyfried, A.: Disentangling the impact of social groups on response times and movement dynamics in evacuations. PLoS One **10**, e0121227 (2015)

5. Boltes, M., Seyfried, A., Steffen, B., Schadschneider, A.: Automatic extraction of pedestrian trajectories from video recordings. In: Pedestrian and Evacuation Dynamics 2008, pp. 43–54. Springer, Berlin (2010)
6. Guo, N., Jiang, R., Hu, M.B., Ding, J.X., Ding, Z.J.: Escaping in couples facilitates evacuation: experimental study and modeling. arXiv:1512.05120 (2015)
7. Köster, G., Seitz, M.J., Treml, F., Hartmann, D., Klein, W.: On modelling the influence of group formations in a crowd. Contemp. Soc. Sci. **6**, 397–414 (2011)
8. Mauer, J.: Shapes and dynamics of blood cells in Poiseuille and shear flows. Ph.D. thesis, Universität zu Köln (2016)
9. Moshtag, N.: MATLAB File Exchange (2006). http://www.mathworks.com/matlabcentral/fileexchange/9542-minimum-volume-enclosing-ellipsoid/content/MinVolEllipse.m
10. Moshtag, N.: MATLAB File Exchange (2007). http://www.mathworks.com/matlabcentral/fileexchange/13844-plot-an-ellipse-in--center-form-
11. Moussaïd, M., Perozo, N., Garnier, S., Helbing, D., Theraulaz, G.: The walking behavior of pedestrian social groups and its impact on crowd dynamics. PLoS One **5**, e10047 (2010)
12. Oberhagemann, D., Könnecke, R., Schneider, V.: Effect of social groups on crowd dynamics: empirical findings and numerical simulations. In: Pedestrian and Evacuation Dynamics 2012, pp. 1251–1258. Springer, Berlin (2013)
13. Reuter, V., Berger, B.S., Köster, G., Seitz, M.J., Hartmann, D.: On modeling groups in crowds: empirical evidence and simulation results including large groups. In: Pedestrian and Evacuation Dynamics 2012, pp. 835–845. Springer, Berlin (2014)
14. von Krüchten, C., Schadschneider, A.: Empirical study on social groups in pedestrian evacuation dynamics. Phys. A **475**, 129–141 (2017)
15. Xu, S., Duh, H.B.L.: A simulation of bonding effects and their impacts on pedestrian dynamics. IEEE Trans. Intell. Transp. Syst. **11**, 153–161 (2010)

Simulating Assisted Evacuation Using Unity3D

Anass Rahouti, Ruggiero Lovreglio, Charitha Dias, and Sélim Datoussaïd

Abstract Past studies on emergency events have revealed that occupants' behaviours and capabilities, procedural aspects and environmental constraints affect the evacuation performance of different types of buildings including healthcare facilities. Healthcare facility management needs to consider the occupants' capabilities as well as the unique floor layouts of such environments to design occupant-centric evacuation systems. Occupants at a healthcare facility can be divided into three groups as *independent* (whose mobility is not impaired in any way), *dependent* (except those defined as independent or highly-dependent) and *highly-dependent* (whose clinical condition creates a high-dependency on other people). Dependent and highly-dependent occupants should be assisted by others during the evacuation process. Therefore, assisted evacuation sub-model can be considered as a fundamental feature of an evacuation modelling tool when simulating healthcare facility evacuation to estimate total evacuation times. Currently, there exist over 60 evacuation models, however, few can simulate assisted evacuation. This paper demonstrates that game engines, such as Unity3D, could be useful tools to develop assisted evacuation sub-models based on the artificial intelligence of autonomous agents.

A. Rahouti (✉) · S. Datoussaïd
Department of Civil Engineering and Structural Mechanics, Risks Institute, University of Mons, Mons, Belgium
e-mail: anass.rahouti@umons.ac.be; selim.datoussaid@umons.ac.be

R. Lovreglio
Department of Civil and Environmental Engineering, University of Auckland, Auckland, New Zealand

C. Dias
Institute of Industrial Science, University of Tokyo, Tokyo, Japan
e-mail: cdias@iis.u-tokyo.ac.jp

S. H. Hamdar (ed.), *Traffic and Granular Flow '17*,
https://doi.org/10.1007/978-3-030-11440-4_30

1 Introduction

Disaster planning is crucial for the mitigation of both mortality and injury associated with disasters. However, in complex buildings like hospitals, planning for a safe, efficient and timely evacuation is particularly challenging. Indeed, in such environments, the performance of the evacuation is closely related to the physical and mental abilities of evacuees as well as to their response to such an event [7]. Internationally, structures are designed by adhering to prescriptive codes or following guidance in support of performance-based regulations [2]. Many developed countries adopt performance-based alternatives (i.e., fire safety engineering approach) involving engineering calculations to increase design flexibility [7]. Numerical simulation can support this fire safety engineering approach and can be used to design new safer healthcare buildings and improve fire safety and emergency preparedness in existing ones [7, 13]. To date, there are over 60 evacuation models [14]. However, most of them are unsuitable to simulate evacuations of healthcare facilities due to the limitations in those models [7, 14]. Many models have attempted to include vulnerable occupants by simply reducing their walking speeds. However, to accurately simulate the evacuation of healthcare occupants with many presenting with mobility and mental impairments (dependent and highly-dependent patients), assisted evacuation feature is fundamental in evacuation modelling tools. Recently, buildingEXODUS [6] and Pathfinder2017 [5] have incorporated specific features that allow analysis of evacuation in healthcare environments considering assisted evacuation. In this paper, we propose a novel approach using Unity3D [18] game engine as a tool to simulate assisted evacuation. As part of a performance-based design, this sub-model can be used by designers to quantify the evacuation time in healthcare environments. As thus, it can also be used to quantify the effectiveness of different evacuation strategies to ensure the safety for all building occupants. Another possibility could be the usage of this sub-model in the development of training tools for enhancing the safety and triage skills of healthcare facility staff members in case of an emergency.

2 Background

In this section, an overview of existing evacuation models which attempted to incorporate features to simulate the evacuation of people with disabilities and to simulate assisted evacuation is presented (Sect. 2.1). Further, relevant studies which implicitly simulated assisted evacuation are also presented (Sect. 2.2).

2.1 Evacuation Models

In recent decades, many evacuation models have been developed to evaluate the effectiveness of a design, and to assist the evacuation planning of new and existing buildings. However, when considering scenarios that involve assisted individuals, it might be difficult or inappropriate to apply most of the existing evacuation models. Some models attempted to include vulnerable people by reducing their speeds, based on engineering data on the literature. For instance, FDS+Evac [10] simulates elderly agents evacuating at a lower speed than adult agents. Such features might be useful to simulate the reduced speed of patients depending on their physical and mental conditions. However, the larger footprint of the transportation devices and the medical equipment associated with patients could not be represented and subsequently nor their effect on the evacuation process (e.g., occurrence of bottlenecks in narrow corridors or in the stairs). EXITT [11] includes two categories of occupants, the able-bodied agents and those in need of assistance to leave the building. The BUMMPEE [4] can simulate the evacuation of people with disabilities, and their interaction with the built environment. This model includes seven categories of individual disabilities and includes both motorized and manual wheelchair users. Disabilities are represented by a reduction in speeds, and the size of these larger devices is considered in the model. However, from the existing literature, it is not clear whether this model can simulate assisted evacuation. Exitus [12] is another model based on BUMMPEE, that can represent disabilities, and assisted evacuation, but not the presence of vertical stair transportation devices. SimWalk [16] can represent many disabilities and accessories such as backpacks, canes, crutches, handcarts, shopping bags, suitcases and wheelchairs. However, no stair devices or beds are defined, and it is not clear from published literature whether the physical sizes of the additional accessories are represented explicitly. ASERI [15] depicts wheelchair users as circular objects with a maximum speed of 0.9 m/s horizontally and 0.3 m/s vertically assisted. Pushed wheelchairs are represented by two circles, and the assistance on the stairs is represented by three circles, unlike the human shaped representation of other agents. The model demonstrates the ability to model a wheelchair being carried down the stairs, modelled as a series of three circles. While a circular representation of a device may reasonably occupy the space required for a wheelchair, the circular shape specification significantly restricts the ability to represent different devices. For example, a wheelchair and an evacuation chair may have a similar width but a different depth and therefore their comparative size may not be well represented by a collection of circular shapes. Furthermore, large devices such as beds or stretchers have an elongated shape. A circular shape may therefore take up the required area, but the rectangular shape itself is not fully represented. STEPS [20] has a 3D representation of a wheelchair, people with backpacks and trolleys, etc. However, this large space and shape is not represented within the model beyond a reduction in speeds. Furthermore, there are two models that specialize in the evacuation of hospitals: G-HES [9] and the assisted evacuation simulation system [17]. Both have been developed to simulate assisted evacuations.

However, they are not publicly available. In the G-HES, beds and wheelchairs are explicitly represented, although it is not clear how any conflict resolution occurs in multiple evacuation of the same path, nor whether the results are validated against data. Further, no vertical evacuation of vulnerable people was explored in this study. Since 2016, buildingEXODUS includes an explicit theoretical model comprising algorithms derived to represent the use of patient transportation devices during the evacuation process. Finally, Pathfinder2017 includes an explicit assisted evacuation sub-model. However, both models do not provide the flexibility to modify the existing algorithms and investigate other ranges of evacuation procedures.

2.2 Assisted Evacuation Modelling

Only a limited number of studies have examined the assisted evacuation. This might be associated with the lack of explicit assisted evacuation sub-models in most of current evacuation models. Another alternative is the use of existing evacuation models (e.g., FDS+Evac, STEPS, etc.) that are not explicitly designed to simulate assisted evacuation but they are flexible enough to achieve this goal implicitly. In fact, some of them include specific features such as checkpoints and delays, which can be used to represent the preparation time associated with people in need of assistance. This approach was used to simulate prescript assisted evacuation procedures implicitly by Hunt et al. [8], Alonso et al. [1], Ursetta et al. [19] and Rahouti et al. [14]. However, this approach does not consider the staff-transportation devices interactions and the blockage effect of the transportation devices on the evacuation process [7].

3 Methodology

Figure 1 shows the development pipeline implemented to simulate agents evacuation from the simulated hospital structure (in practice, it can be any type of building). The 3D model of the simulated building was developed by using building information modelling (BIM) tools. The main data was pre-existing 2D CAD DWG files which were used within Autodesk Revit to create the 3D geometry. The 3D model of the building was then imported in Unity3D in FBX format. The third step consisted of making final adjustments of the virtual world within Unity3D by importing hospital furniture (e.g., Beds, wheelchairs, etc.) form the Asset Store of Unity3D and fixing textures. The 3D models of agents were created in Adobe Fuse CC, which is a software for creating 3D human models as well as other non-player characters (e.g., Monsters, etc.). Then, the models were uploaded to Adobe Mixamo for skeleton rigging and animating. Mixamo is a 3D character cloud-based animation software that contains several animations and avatars in its library, allowing rapid character and animation development. After rigging and animating,

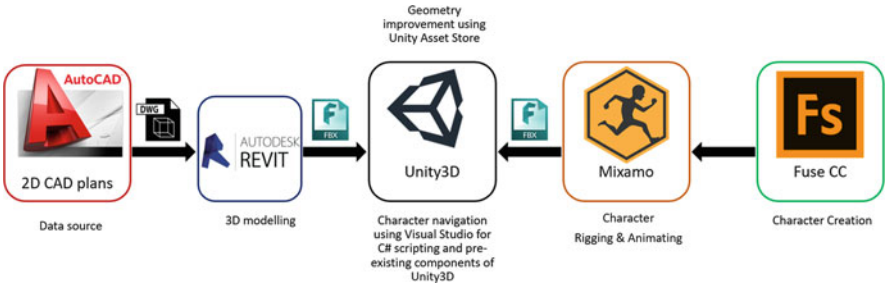

Fig. 1 Development pipeline for simulating agents evacuation from a virtual environment within Unity3D

the characters were exported in FBX format and then imported in Unity3D. To make the agents navigate towards a place of safety and to dictate their pre-evacuation and evacuation behaviour in the virtual world, several pre-existing components of Unity3D (e.g., colliders, rigid bodies, navigation mesh agents, navigation mesh obstacles, animation controllers) and new components (C# scripts) were attached to the 3D model of each agent within Unity3D. The following section gives more details on the explicit assisted evacuation sub-model development.

4 Explicit Assisted Evacuation Sub-model

4.1 Agents Type

In healthcare facilities, occupants with varying dependency levels can be expected. To accurately simulate the evacuation process in such environments, two groups of agents should be introduced: ambulant (e.g., independent patients, staff members or visitors) and non-ambulant (e.g., dependent and highly-dependent patients). The behaviour of an ambulant agent can be simply modelled by reducing its speed and assigning her/him a place of safety or multiple places of safety (typically, emergency exits or areas of refuge) as known targets. Then, the agent can decide either randomly or using the shortest path as a criteria of target selection through an embedded C# script. Also, in this study, we focus on explicitly representing the assisted evacuation of dependent (i.e., can be moved using a wheelchair) and highly-dependent (i.e., bed-ridden) agents considering an appropriate mode of transportation device (i.e., a wheelchair or a bed) and the available day and night shift personnel.

4.2 Transportation Devices

Usually, transport tasks can be carried out by using one- or two-person manual carry techniques (e.g., a hand-carried chair, etc.) or, if available, by using one of several different types of transportation devices (e.g., a wheelchair, a bed, a stretcher, an evacuation chair, a rescue sheet, etc.) [2, 7]. In this study, we are considering only the use of transportation devices such as wheelchairs and beds, while the simulation of other devices will be investigated in a future study. A key requirement in simulating healthcare facilities evacuation is the explicit representation of these devices. Figure 2 shows the 3D representation of the transportation devices used in the assisted evacuation sub-model, their dimensions [21], their shape (represented using Unity3D colliders and navigation mesh obstacles), as well as the handler(s) positioning when assisting a patient.

4.3 Assisted Evacuation Algorithms

Figure 3 shows a detailed flow chart of the developed assisted evacuation sub-model. Initially, the user defines a list of emergency groups constituted of one or two assistants because the transportation devices used in this study required one or two handler(s) for transporting the patients. Then, each emergency group would have a predefined priority list of patients who need to be assisted. If the priority list of the emergency group is empty, each handler leaves the fire compartment by seeking a place of safety. Otherwise, the group assists the first unassisted patient, tagged as "P_u", in its priority list. The sub-component "assist action" consists of four phases (i.e., gathering, attachment, preparation and movement). In the gathering phase, each assistant of the emergency group seeks the associated attachment point until she/he reaches it. When a member of an emergency group reaches an unassisted patient, the patient's tag becomes "P_h", which means "helped patient". This step is necessary to prevent that another emergency group seeks the same patient. Each time an assistant reaches their associated attachment point, she/he starts rotating until she/he faces the same direction as the helped patient. In the attachment phase, each assistant of the emergency group attaches to their associated attachment point. In the preparation phase, the assistants wait until the preparation time elapses. From a simulation point of view, we do not need animations to show the preparation of the patient (i.e., get the patient dressed, take patient's belongings or take the associated medical equipment, etc.). In the movement phase, the patient drives the movement and the knowledge of the group is embedded in the vehicle agent. The group moves at the patient walking speed value "WS_{P_h}".

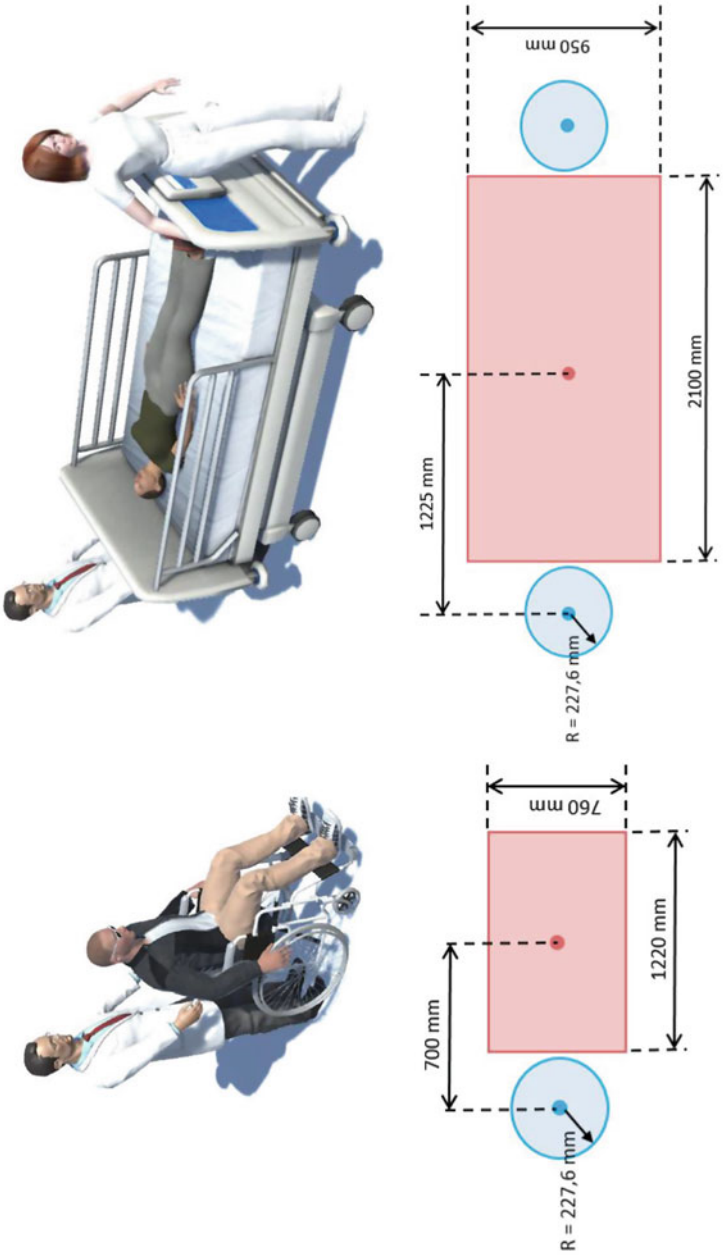

Fig. 2 Transportation devices 3D representation, their dimensions, their shape and the handler(s) positioning when assisting a patient

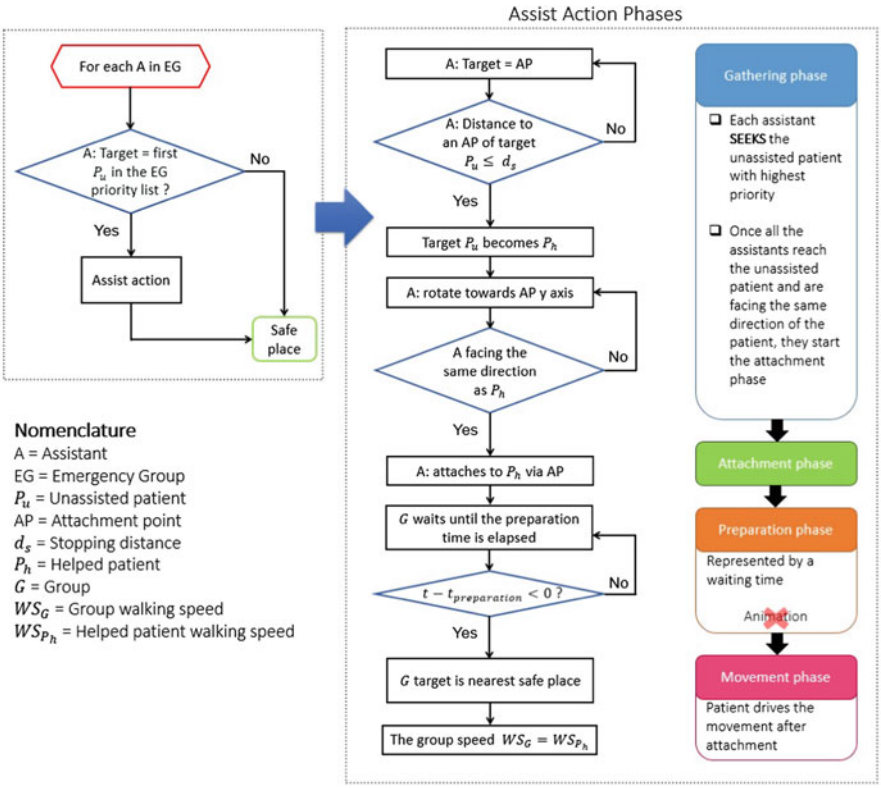

Fig. 3 Flow chart of the assisted evacuation sub-model

5 Case Study

We simulated the evacuation of the left ward of the 6th floor of a Belgian hospital considering the barriers (fire doors), which divide the floor into three compartments. This floor is one of the most critical floors of this hospital in terms of fire safety [14]. The fire is supposed to break out in the storage premise of the evacuated ward. The occupancy level and the occupants' characteristics are given in Table 1.

Table 1 Characteristics of the assistants and patients [3, 7, 8, 19]

Type of the agent	Number of agents	Walking speed (m/s)	Preparation time (s)
Assistants	7	1.20–1.55	0
Independent patients	13	0.70–1.55	0
Dependent patients	11	1.10–1.30	0–35
Highly-dependent patients	1	0.90–1.10	20–90

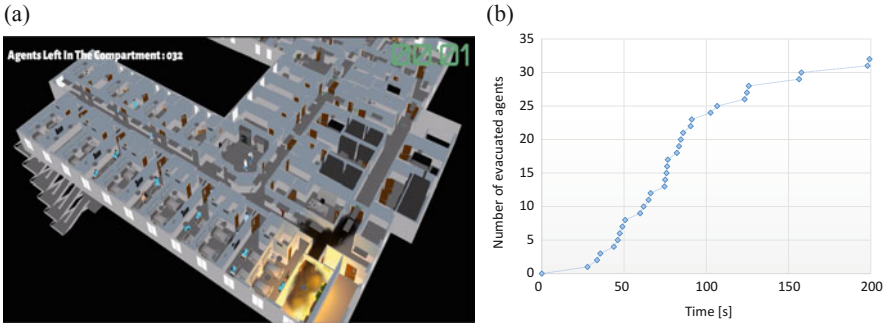

Fig. 4 Qualitative and quantitative outputs. (**a**) Visualization of the situation at $t = 1$ s. (**b**) Evacuation curve

6 Results

Figure 4a shows an example of the initial stage of the evacuation. In this example, the patients are positioned in their rooms and the staff members (assistants) are positioned in a patient room or in a nursing station. However, the position of the agents can be modified by the user to run several simulations and study the impact of this parameter on the performance of the evacuation. Locations of jams can be identified through visualization of the simulation. By recording the time at which each agent leaves, it is possible to plot the associated evacuation curve (see Fig. 4b).

7 Conclusions and Outlooks

In this paper, we described an algorithmic formulation of a new assisted evacuation sub-model, which took into account the shape of transportation devices used to evacuate dependent and highly-dependent patients. We also simulated explicitly all the phases of an assisted evacuation; i.e., gathering, attachment, preparation and movement phases. We embedded our algorithm into Unity3D, which is a widely used game engine. We applied this model to a real ward of a Belgian hospital. Qualitative and quantitative outputs of such modelling approach could be useful for designers to evaluate designs of healthcare facilities. This model can also be applied to other buildings or used by game developers to simulate assisted evacuation to design evacuation training tools for educating healthcare facilities personnel.

Quantitative validation of the developed sub-model against real data, such as trajectories of evacuees or evacuation times, is still open. Future studies should use real data to calibrate the model. Moreover, in this research study, only two types of transportation devices were simulated. Future work would consider the simulation of other types of transportation devices such as evacuation chairs, stretchers and

rescue sheets. Future research could also focus on improving the decision making of the agents. For example, a communication model between the assistants could be useful to exchange information in real time. Finally, future versions of the model could consider the effect of exhaustion on the performance of the assistants after repeated collection of patients.

References

1. Alonso-Guttierrez, V., Cuesta, A., Alvear, D., Lazaro, M.: The impact of a change on the size of the smoke compartment in the evacuation of health care facilities. Fire Technol. **54**(1), 335–354 (2018). https://doi.org/10.1007/s10694-017-0686-7
2. Boyce, K.E.: Safe evacuation for all—fact or fantasy? Past experiences, current understanding and future challenges. Fire Saf. J. **91**, 28–40 (2017)
3. Boyce, K.E., Shields, T.J., Silcock, G.W.H.: Toward the characterization of building occupancies for fire safety engineering: capabilities of disabled people moving horizontally and on an incline. Fire Technol. **35**, 51–67 (1999)
4. Christensen, K., Sasaki, Y.: Agent-based emergency evacuation simulation with individuals with disabilities in the population. J. Artif. Soc. Soc. Simul. **11**(3), 9–21 (2008)
5. Engineering, T.: Pathfinder 2017, technical reference guide. Tech. Rep. (2017)
6. Gwynne, S., Galea, E.R., Owen, M., Lawrence, P., Filippidis, L.: A comparison of predictions from the buildingexodus evacuation model with experimental data. In: Shields, J. (ed.) Pedestrian Behavior: Models, Data Collection and Applications, pp. 711–721. University of Ulster, Coleraine (1998)
7. Hunt, A.: Simulating hospital evacuation. Ph.D. thesis (2016)
8. Hunt, A., Galea, E.R., Lawrence, P.: An analysis and numerical simulation of the performance of trained hospital staff using movement assist devices to evacuate people with reduced mobility. Fire Mater. (2013). https://doi.org/10.1002/fam.2215
9. Johnson, C.W.: Using computer simulations to support a risk-based approach for hospital evacuation. Tech. Rep., University of Glasgow (2005)
10. Korhonen, T., Hostikka, S.: Fire dynamics simulator with evacuation—FDS+evac, version 2.5.0—technical reference and user's guide. Tech. Rep., VTT Technical Research Center of Finland, Helsinki (2009)
11. Levin, B.M.: EXITT: a simulation model of occupant decisions and actions in residential fires (Rep. No. NBSIR 88-3753). Tech. Rep., NIST (1988)
12. Manley, M.T.: Exitus: an agent-based evacuation simulation model for heterogeneous populations. Ph.D. thesis, Utah State University (2012)
13. Rahouti, A., Datoussaïd, S.: Prédiction du risque incendie en milieu hospitalier. In: Proceedings of la 8éme Conférence Francophone en Gestion et Ingénierie des Systémes Hospitaliers GISEH16 (2016)
14. Rahouti, A., Datoussaïd, S., Lovreglio, R.: A sensitivity analysis of a hospital evacuation in case of fire: the impact of the percentage of people with reduced mobility and the staff to occupant's ratio. In: Proceedings of Fire and Evacuation Modeling Technical Conference 2016 (FEMTC2016) (2016)
15. Schneider, V.: Modelling of human response and behaviour in complex surroundings. In: 3rd International Symposium on Human Behaviour in Fire (2004)
16. Steiner, A., Philipp, M., Schmid, A.: Parameter estimation for a pedestrian simulation model. In: 7th Swiss Transport Research Conference (2007)
17. Uehara, S., Tomomatsu, K.: Evacuation simulation system considering evacuee profiles and spatial characteristics. In: Proceedings of the 7th international symposium on Fire Safety Science, pp. 963–974 (2003)

18. Unity Technologies, unity 5 game engine (2017). https://unity3d.com/fr/unity
19. Ursetta, D., D'Orazio, A., Grossi, L., Carbotti, G., Casentini, S., Poggi, L.: Egress from a hospital ward: a case study. In: Proceedings of Fire and Evacuation Modeling Technical Conference 2014(FEMTC2014) (2014)
20. Wall, J., Waterson, N.: Predicting evacuation times—a comparison of the STEPS simulation approach with NFPA 130. Fire Command Stud. **1**(1), 151–171 (2002)
21. Wheelchair Measurements Standard (2017). http://suntran.com/pop_access_measurements.htm

An Application of New Pedestrian Tracking Sensors for Evaluating Platform Safety Risks at Swiss and Dutch Train Stations

Jeroen van den Heuvel, Jasmin Thurau, Martin Mendelin, Rik Schakenbos, Marcel van Ofwegen, and Serge P. Hoogendoorn

Abstract Due to rapid rail passenger growth in the last years, crowding challenges have risen at several stations in Switzerland and The Netherlands. Particularly at platforms, safety risks can increase when a station is operated near or at pedestrian capacity. Therefore, Swiss and Dutch station managers started several initiatives to measure crowding-related safety risks. Recently, pedestrian measurement technology has improved substantially. New technology is capable of anonymously tracking individual pedestrians within a predefined area under high intensity conditions. This technology has not been implemented at train stations before. Therefore the Swiss and Dutch station managers have developed and applied a methodology to determine the validity of the data which are generated by the newest generation of pedestrian measurement systems at the stations of Bern (CH), Amsterdam Zuid, and Utrecht Centraal (NL). This paper presents the results of the tests in both countries and their (first) implications for science and practice.

J. van den Heuvel (✉)
Department of Transport and Planning, Faculty of Civil Engineering and Geosciences, Delft University of Technology, Delft, The Netherlands
e-mail: j.p.a.vandenheuvel@tudelft.nl
NS Stations, Netherlands Railways (NS), Utrecht, The Netherlands

J. Thurau · M. Mendelin
Swiss Federal Railways AG (SBB), Bern, Switzerland
e-mail: jasmin.thurau@sbb.ch

R. Schakenbos
NS Stations, Netherlands Railways (NS), Utrecht, The Netherlands
e-mail: rik.schakenbos@nsstations.nl

M. van Ofwegen
ProRail, Utrecht, The Netherlands
e-mail: marcel.vanofwegen@prorail.nl

S. P. Hoogendoorn
Delft University of Technology, Delft, The Netherlands
e-mail: s.p.hoogendoorn@tudelft.nl

S. H. Hamdar (ed.), *Traffic and Granular Flow '17*,
https://doi.org/10.1007/978-3-030-11440-4_31

1 Introduction

Due to rapid rail passenger growth in the last years, crowding challenges have risen at several stations in Switzerland and The Netherlands. Particularly at platforms, safety risks can increase when a station is operated near or at pedestrian capacity.

The safety line is the line at the platform between the circulation/waiting zone and the platform edge near the tracks [5]. Passengers are observed to cross this safety line at busy platforms more often than at less busy or more spacious platforms. Platform enlargement projects take years to implement and are extremely costly. In most cases risks cannot be reduced sufficiently by a rearrangement of platform objects. Risk-targeted, operational interventions are limited by a lack of insight into passenger behavior at platforms, which in turn are limited by a lack of empirical data.

Until recently, pedestrian measuring systems at Swiss and Dutch train stations have been used only for counting the number of pedestrians at a predefined area (occupancy) or passing a counting line (flow rate). Advanced systems have not been sufficiently accurate as well due to challenging semi-outdoor environment with high flow rates at a train station (see Fig. 1).

During the last years, pedestrian counting technology has improved substantially. New technology of the Swiss company ASE—hardware and software—is capable of anonymously tracking individual pedestrians within a predefined area under high intensity conditions. This has created the potential of measuring pedestrians' paths through an area (trajectories) and to assess walking speeds and densities under different traffic conditions. As this technology has not been applied at train stations before, Swiss and Dutch station managers have tested the newest generation of pedestrian measurement systems in practice to assess the quality of the data.

Fig. 1 Crowding at train station platforms. Left: Bern SBB, track 3/4, 8 March 2016, 7.03 h; Right: Utrecht Centraal, track 5, 7 December 2015, 8.01 h. These pictures are representative for peak hours at regular work days

This paper is structured as follows: in the next Sect. 2, sensor data quality is defined. Validity definitions are based on a review of literature and an assessment methodology is proposed. Section 3 covers the experiments, and Sect. 4 the results. This paper is concluded in the fifth and final section with conclusions and recommendations for science and practice.

2 Path Data Quality Definition

The sensor data describes the paths of pedestrians who have used the measurement area for walking or waiting, in existing research also referred to as "trajectories." The data for each path consists of an anonymous ID and its spatial coordinates (x and y) at each moment in time (t). The sensors register these data ten times per second for each path ID. With this level of detail, the data resolution is extremely high. High resolution, however, is not an indicator of data quality, which in this context is defined as validity: the extent to which the paths in the data accurately describe the real location of the corresponding pedestrian at each recorded timestamp.

To assess the quality of the path data from the sensors, a definition has been developed based on the previous research. The PhD research by Daamen [3] has been one of the first publications with a detailed description of a validation procedure of microscopic pedestrian model output. In their validation of automatically extracted pedestrian trajectory data from video recordings, Boltes et al. [1] have identified occlusion caused by height differences between pedestrians as a source of measurement error. Occlusion occurs when a relatively small person is standing in the "shadow" of a taller person in areas relatively far away from the sensor. These errors are caused by the situation in which the sensors are deployed, not by the sensors themselves. In their state-of-the-art overview on measurement techniques for slow mode travel behavior, Daamen et al. [4] describe detection, location, and identification as the fundamental characteristics of Bluetooth and WiFi measurements of travel behavior. Detection is about capturing correctly if a pedestrian is present in the measurement area. Location is about the correct representation of the position of each pedestrian in the measurement area. Identification refers to attributing the correct identification to each measurement of each unique pedestrian.

Based on the existing research, the data quality levels have been defined for this study, in order of increasing complexity:

1. **Correct count**: the degree to which the number of pedestrians in the data who have passed a line during timeframe Δt (flow) or who have been present in a specific area (density) at time t is according to reality;
2. **Correct position**: the degree to which the x- and y-coordinates of all pedestrians in the measurement area during a timeframe t is according to reality;

3. **Stable identification**: the degree to which the x- and y-coordinates of a unique pedestrian have been linked to the same ID in the sensor data during the total time the person has been in the measurement area;
4. **Path continuity**: the degree to which a sequence of x- and y-coordinates with the same ID during total time describes the real path of a unique pedestrian.

For this study, we have used level 4 (path continuity) as data quality indicator. Firstly, because from a research perspective, this study imposed no limits on which technical capabilities of the sensors could be tested. Secondly, because from a practical perspective, individual behavior in some cases is an important factor in assessing safety risks.

3 Experiment Setup

The unavailability of any ground-truth data with a similar level of aggregation as the sensor data has been a validation challenge to overcome by the research methodology. Another challenge has been the combination of an extremely dynamic character of pedestrian behavior at train platforms, combined with large numbers of pedestrians present at the same time (particularly at peak hours). This combination makes it extremely time consuming to make a structured comparison of the data from the sensors and empirical observations of the same situation from another source (i.e., CCTV-footage or outdoor observations) in an uncontrolled environment. Performing experiments in a controlled environment (similar to [3] and [1]) would have been inconsistent with the research objective, as the objective has been linked to the practical use of the sensors in real-life train station environments. Moreover, a significant number of sensors already had been installed at the stations of Bern (CH), Amsterdam Zuid (NL), and Utrecht Centraal (NL). This offered the unique opportunity to perform experiments without the need to purchase and install sensors for research purpose only. So for this study, we have chosen for controlled experiments at the three stations where the sensors already had been installed.

The experiments have been performed in the context of our research on the use of the danger zone at train platforms (see [5]). The validation of the correct position of pedestrians at the platform before train arrival(s) in the sensor data has been the main objective of this experiment. As indicated in Fig. 2, a pedestrian is in the danger zone when standing or walking with at least one foot at the track side of the safety line at the platform. Both feet at the safety line or at the non-track side of the safety line are considered as safe. The objective is to assess if measurements are according to reality, with a small margin of measurement error. For this experiment, we have chosen to set the margin of error at ± 10 cm or approximately a foot width. In practice, there is no need for a higher accuracy.

For the implementation of the experiments, a group railway and research staff has been recruited; as test person or for assistance in performing the experiment; all have been wearing safety vests and have been instructed on safety risks and procedures.

Fig. 2 Safety line at platform of Bern (CH); red arrow is "in danger zone"—indicator

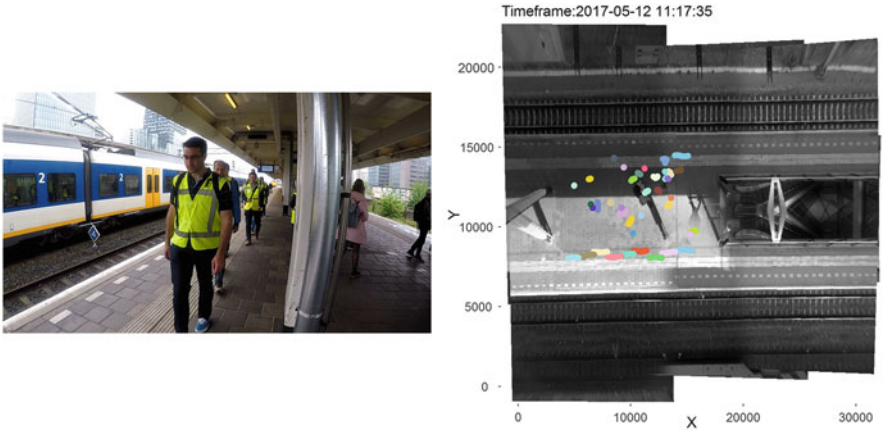

Fig. 3 Left: impression of experiment "at of beyond the line" at track 3 of Amsterdam Zuid (NL); Right: graphical representation of data collected during the same experiment

To minimize safety risks for the railway staff and inconvenience of train passengers, each run was performed directly after departure of a train during off-peak hours only. In Switzerland the experiments have also been used to identify the safety line in the data. There, the experiments were conducted at the boarder between safety and danger zone. To get sufficient data for validation, four runs per track have been performed with three positions simultaneously, each representing a degree between safe and unsafe: 1. next to the line, 2. with one foot at the line, and 3. with both feet at the line. For Amsterdam Zuid, the experiments have been performed for two tracks (3 and 4). This resulted in 2 tracks $\times$ 4 runs $\times$ 3 positions $\times$ 3 test persons per position = 72 experiments. The left part of Fig. 3 gives a visual impression of the experiments performed at Amsterdam Zuid. Similar runs have been performed at Utrecht Centraal (NL; 36 experiments) and Bern SBB (CH).

During the experiments, the sensors have measured the location of each pedestrian in the measurement area with an interval of 10 times per second. The right part of Fig. 3 gives a graphical representation of this data at track 3/4 of Amsterdam Zuid for the indicated timeframe. Note that this figure shows data of 10 observations during 1 s. The small dots represent passengers who were standing, while the larger shapes represent pedestrians who were walking. From the figure, the formation of 9 test persons at three positions can be recognized.

For evaluation, the non-parametric k-nearest-neighbor-based regression method LOESS has been used [2]. With LOESS, the Y-positions (along the platform width) for a smoothly fitted line for each run have been determined for all X-positions (along platform length) of each ID in their order of occurrence in timeframe Δt. Sensor data quality has been assessed by a relative comparison of the Y-position of all data points for each individual test person (see Fig. 3) against the LOESS-line, which has been derived from all data points per position in the formation of test persons in the same run.

4 Results

Figure 4 shows the regression analysis on the data of a well-assessed run at track 3 of Amsterdam Zuid (NL). The three test persons have walked at the second position (with one foot at the safety line) in the formation of nine test persons. The line in the graph indicates the LOESS-line of the measurements of the three test persons. The gray area refers to the allowed measurement error (± 10 cm). The up/downward movement in individual measurements clearly shows the swaying which is typical for pedestrian movement. The red dots outside the gray area show that one test person (Hans) deviated from his path during a short segment of his path. This observation in the data has been confirmed by the video recordings made during the experiments. All 36 experiments at track 3 of Amsterdam Zuid have resulted in similar outcomes. Moreover, during the experiments at Bern SBB (CH), the divergent behavior of test persons and support staff could be easily distinguished in the datasets.

Figure 5 shows the results of a badly assessed run at track 4 at the same platform, for the same position, and the same test persons. In this graph, it is clearly visible that the ID of the second test person (Marcel) is lost after approximately 13 m. Further inspection of the data revealed that the path ID got lost. The path continued with a new ID, which has been caused by an unsuccessful transfer of the ID between two sensors. All 36 experiments at track 4 of Amsterdam Zuid have resulted in similar outcomes.

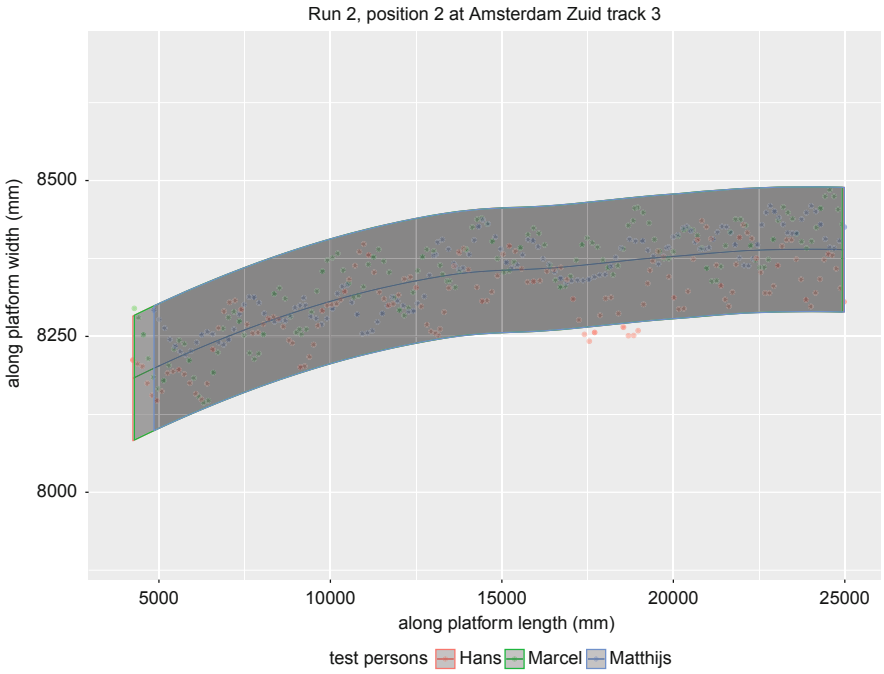

Fig. 4 LOESS analysis of run 2 and position 2 at track 3 of Amsterdam Zuid (NL)

Most probable cause is a slightly different position of one sensor at the track 4 side of the platform, compared with the same set of sensors at the track 3 side, where this issue did not occur. The 36 experiments at Utrecht Central station (track 5) have revealed that the issue of discontinued ID's also can occur due to objects which are located between the sensors and the measurement area at the platform. For example, train information screens, lighting, signing, and columns can cause "object shadows" in the measurement area.

In addition to the sensor technology, ASE has developed a post-process path stitching algorithm at its data server. This algorithm can be used to reassign the correct ID to paths for which the ID has been replaced by a new ID, while in reality both path sections are generated by the same pedestrian. Figure 6 shows the results of the same experiment. The only difference is the application of the path stitching algorithm on the data. The continuation of the path of test person 2 (Marcel) shows that the stitching has been successful.

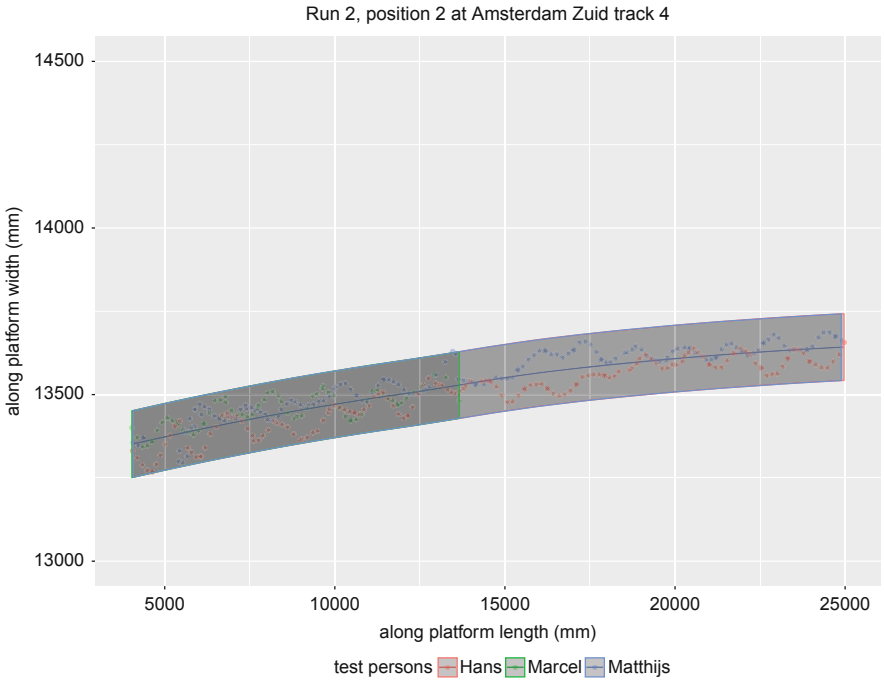

Fig. 5 LOESS analysis of run 2 and position 2 at track 4 of Amsterdam Zuid (NL)

5 Conclusions

The experiments at stations of Bern (CH), Amsterdam Zuid (NL), and Utrecht Centraal (NL) have shown that the pedestrian measurement technology of ASE is capable of delivering a high degree of accuracy of pedestrian measurements at train stations, even at the highest level of complexity (path continuity) that has been defined for this study. These data open up the possibility to research patterns in individual and collective passenger behavior and safety risks at platforms. This conclusion is supported by an extensive data analysis, combined with visual comparisons between data of individual paths and video recordings made during the experiments. The natural swaying of pedestrians, inconsistencies in test person behavior and even the divergent behavior of pilot stewarts and test persons can be detected in the data and linked to visual observations during the experiment.

The experiments have also revealed the importance of a well-designed and installed sensor installation. The experiments at track 4 of Amsterdam Zuid (NL) have revealed that a minor misalignment in the sensor positions can cause significant issues with handing over path IDs between sensors. The experiments at track 5 of Utrecht Centraal (NL) and Bern SBB (CH) have revealed a similar issue due to object shadows on the platform. These challenges can be overcome by increasing

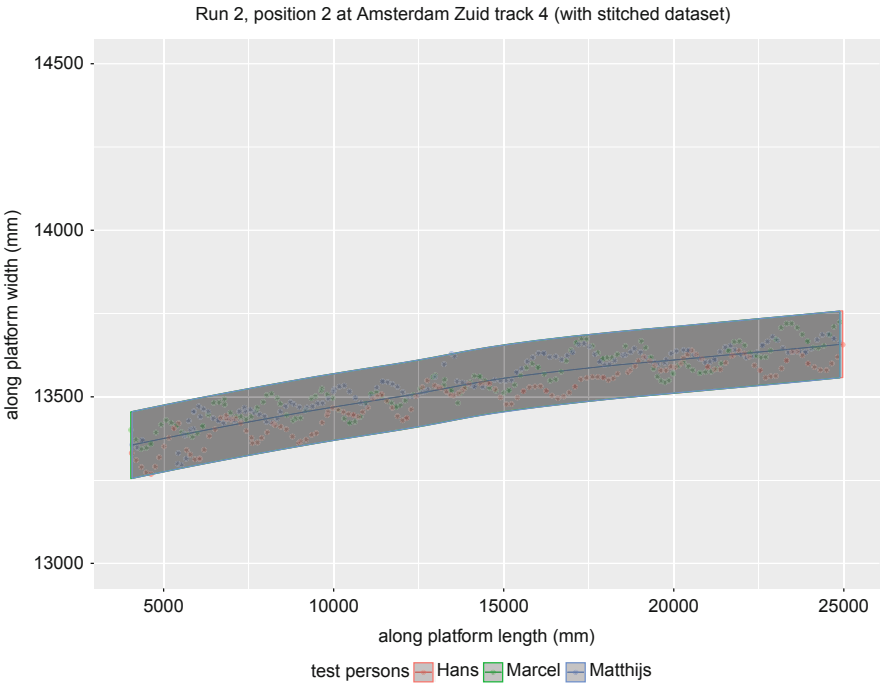

Fig. 6 LOESS analysis on stitched dataset of Fig. 5

the number of sensors, at the price of increased investments and operating costs. Before this is considered, there should be a clear need for data with an accuracy at the highest level of complexity. If the data user is only interested in correct counts and/or positioning of pedestrians in a measurement area without the need of stable IDs, a lower number of sensors can be sufficient.

Alternatively, post-measurement stitching of paths can be considered. Our study has shown that this can solve ID-inconsistencies in the data. However, the conditions for successful or unsuccessful stitching are a topic for further research. The same applies to the evaluation of data quality when high densities occur (i.e., peak hours) and/or when passengers travel with large objects (i.e., luggage or bikes). During the experiments of this study, several tests have been performed with measurements at high densities. The data of these experiments has to be analyzed to assess data quality under more challenging pedestrian traffic conditions.

Acknowledgements For this study, ASE has applied its self-developed stitching algorithm to a subset of the Amsterdam Zuid (NL) data. The authors express their gratitude for this support. At the same time, they explicitly state that ASE has not been involved in any way in the design and execution of the experiments and the data quality assessment.

References

1. Boltes, M., Seyfried, A., Steffen, B., Schadschneider, A.: Automatic extraction of pedestrian trajectories from video recordings. Pedestrian Evacuation Dyn. 2008 pp. 43–54 (2010)
2. Chambers, J., Hastie, T.: Statistical Models in S. Taylor & Francis, Boca Raton (1991)
3. Daamen, W.: Modelling passenger flows in public transport facilities. Ph.D. thesis, TRAIL Research School The Netherlands (2004)
4. Daamen, W., van den Heuvel, J., Ton, D., Hoogendoorn, S.: Using Bluetooth and WiFi to unravel real-world slow mode activity travel behaviour. In: Fourteenth International Conference on Travel Behaviour Research (2015)
5. Thurau, J., van den Heuvel, J., van Ofwegen, M., Keusen, N., Hoogendoorn, S.: Influence of pedestrian density on the use of the danger zone at platforms of train stations. In: Traffic and Granular Flow 2017, Washington DC (2017)

Influence of Pedestrian Density on the Use of the Danger Zone at Platforms of Train Stations

Jasmin Thurau, Jeroen van den Heuvel, Nicolas Keusen, Marcel van Ofwegen, and Serge P. Hoogendoorn

Abstract Due to rapid rail passenger growth in the last years, crowding challenges have risen at several stations in Switzerland and The Netherlands. Particularly at platforms, safety risks can increase when a station is operated near or at pedestrian capacity during peak times. Passengers are observed to cross the safety line at busy platforms when a train is due to arrive. From our daily practice, we expect high densities to be one of the main factors driving use of the danger zone at platforms of train stations. Some previous academic research has also addressed pedestrian densities at the platforms to be one of the factors driving the involuntary use of the danger zone. By using stereo sensors to track persons on a platform in Bern (Switzerland) as well as in Utrecht Centraal (The Netherlands) we were able to show that the use of the danger zone is related to the pedestrian density but also to other factors like obstacles on the platform. An additional survey conducted in Switzerland showed that the persons interviewed were not always aware of their use of the danger zone. Risks are not always clear.

J. Thurau
Swiss Federal Railways AG (SBB), Bern, Switzerland
e-mail: jasmin.thurau@sbb.ch

J. van den Heuvel (✉)
NS Stations, Netherlands Railways (NS), Utrecht, The Netherlands
e-mail: jeroen.vandenheuvel@nsstations.nl; j.p.a.vandenheuvel@tudelft.nl

N. Keusen
Bundesamt fuer Verkehr BAV, Ittigen, Switzerland
e-mail: nicolas.keusen@bav.admin.ch

M. van Ofwegen
ProRail, Utrecht, The Netherlands
e-mail: marcel.vanofwegen@prorail.nl

S. P. Hoogendoorn
Delft University of Technology, Delft, The Netherlands
e-mail: s.p.hoogendoorn@tudelft.nl

S. H. Hamdar (ed.), *Traffic and Granular Flow '17*,
https://doi.org/10.1007/978-3-030-11440-4_32

1 Introduction

1.1 Background and Importance

During the last years general mobility of people and thus the number of passengers frequenting train stations grew significantly in Switzerland and The Netherlands. Because of limited space on train platforms at several train stations they are getting overcrowded, particularly during peak hours. Train stations and their platforms cannot be expanded easily to meet the increasing demand, not only due to limited space available in and around stations, but also for economic reasons. Short term solutions are not appropriate. Therefore, it is necessary to use existing capacity as efficiently as feasible.

In the Swiss and Dutch practice of the design and operations of train stations, the limits for capacity of platforms are directly related to the safety of passengers who use the platform. The Swiss Federal Office of Transport states that pedestrians should not use the marked zone at the platform edge, referred to as "danger zone" [1]. This requirement has been operationalised by maximum pedestrian densities at platforms for a number of typical situations [1, 13]. Typical situations refer to situations before train arrival, during boarding and alighting, and during train departure. In The Netherlands a similar zone near the platform edge is required as part of the current standard and design guidelines of train stations [8, 9].

From a scientific perspective, research aspects of pedestrian flows at train platforms are very different from the cases commonly studied. Common studies focus at generic pedestrian processes or facilities, like corridors, flows at high densities and evacuation situations. Scientific research regarding train platforms is limited. In the 1970s, Fruin has developed a generic level of service concept for pedestrian facilities [4]. Regarding train platforms, he states that the interval between train arrivals should exceed platform clearance time to prevent overcrowding. In the 1990s, Weidmann has developed models to estimate dwell times of rail vehicles in train stations based on the characteristics of the passenger exchange process [14]. Clustering of departing passengers at the platform is found to be an important factor, because this phenomenon results in an uneven distribution of passengers over the available platform space. At the beginning of this century, Heinz has extended Weidmann's work by a large-scale empirical research in Sweden [6]. Srikukenthiran [11] confirms the issue of clustering found by Weidmann and Heinz. Hoogendoorn and Daamen show by the case of Delft station that platform densities can be well reproduced by a well-calibrated pedestrian model with valid input data [2]. Recently, Haenseler has developed a model which can generate valid input data for "train-induced pedestrian flows" in train stations [5]. Although existing research refers to relevant processes at train platforms, no research has been found on the influence of pedestrian density on the use of the danger zone near the platform edge when no train is present at the platform.

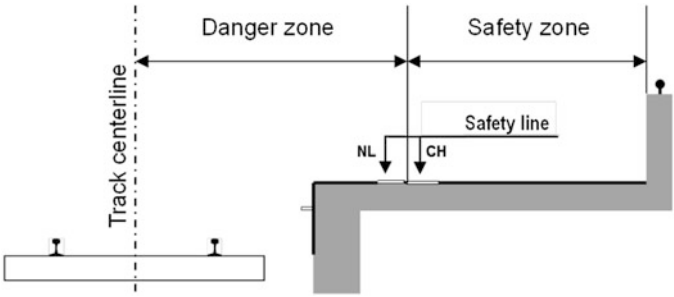

Fig. 1 Definition of safety line and areas on the train platform

1.2 Assumptions

In the Netherlands and in Switzerland different definitions and terms for safe and unsafe areas on platforms are in place. Figure 1 illustrates the different definitions of the safety line. In the Netherlands the safety line is already within the danger zone. In Switzerland it is fully inside the safety zone, as it is also used as a guideline for blind people. In this paper the Swiss definition of the safety line, the safety and the danger zones is used.

After defining the different relevant zones on platforms it is possible to define safety on platforms, as it will be used in this paper: "A person is safe, within the safety zone and remains safe, as long as he or she is not forced to use the danger zone". While a train is standing at the platform, the danger zone is considered as safe. The voluntary use of the danger zone is not considered safe, but the possible influence on this misbehaviour of passengers is low. Therefore this paper will identify the circumstances for an involuntary use of the danger zone.

1.3 Hypotheses

To develop limits describing the maximum allowed occupancy of platforms two connected hypotheses, observed in stations, are presented. Firstly, it is expected that the number of uses of the danger zone rises with higher pedestrian densities on the platform. We base this hypothesis on the thought that on a platform with more persons present, the probability of persons stepping voluntarily into the danger zone increases. (H1): The number of persons using the danger zone rises with higher pedestrian densities on the platform.

Because we consider the nearer surroundings on the platform as relevant, this analysis will be conducted separately for different areas on platforms. Secondly, we expect obstacles to influence the use of the danger zone. The smaller the area next to an obstacle, the harder it becomes to overtake without stepping into the danger zone. (H2): The ratio of persons using the danger zone rises near obstacles.

In addition we expect the majority of the persons on train platforms not to realise the use of the danger zone. (H3): More than 50% of the passengers on train platforms, who used the danger zone, do not state they did if being asked.

2 Methodology

2.1 Description of Datasets

Data from stereo sensors installed at a platform in Switzerland (Bern, track 3 and 4) and a platform in the Netherlands (Utrecht Centraal, track 5) is used. In addition to the sensor based data collection, a survey was conducted at several Swiss stations.

Highly accurate sensors were installed to track people on platforms. Accuracy was tested at the point of interest [12]. For the analysis conducted in this paper, data of 1 month (24 April 2017 to 19 May 2017) was used for both Switzerland and The Netherlands. We focused on a time without holidays in Switzerland. The analysis concentrated on weekdays and peak hours to analyse the most crowded situations.

To determine people's knowledge about the safety line, a survey was conducted in Switzerland. The survey was given to the passengers due to a link or QR-Code on a biscuit-packaging which lead to an invitation to fill out an online questionnaire. The main question of the questionnaire was: *have you been in situations in which you have overstepped the safety line (except when entering or leaving the train)?* Observants who handed out the biscuits differentiated between people who used the danger zone ($n = 32$) and those who did not ($n = 307$). Passengers did not know they were given different links, and the questionnaires behind the two links were identical. The biscuits were distributed during morning and afternoon peak, which means that we mainly reached commuters.

For the survey big and medium stations were chosen. The stations included were Bern, Zurich Hardbruecke, Lenzburg, Visp and Schlieren. Lenzburg is a station with a lot of drive-through trains, as well as high pedestrian densities. Zurich Hardbruecke is known for a high train frequency and also high pedestrian densities. Visp is a tourist station and Schlieren has a high number of customer reclamations concerning platform safety although calculations do not indicate too narrow platforms. Bern was chosen because sensors are installed at this station and it has many different types of obstacles.

2.2 Description of Data Analysis

For being able to differentiate between areas especially with and without obstacles (H2), the platforms were divided into 5 (Bern) 8 (Utrecht Centraal) zones, respectively. For each zone the average number of uses of the danger zone per

metre platform length and second is calculated. These results are compared against each pedestrian density within the zone. The pedestrian density is calculated as the number of persons within the zone for each second divided by the surface available for passengers in the safety zone. The use of the danger zone is analysed when no train is present on the tracks of the analysed platforms. In Utrecht Centraal only one platform side is covered with sensors, therefore only the presence of a train at that certain platform side is considered.

Survey data was analysed regarding people who used the danger zone but didn't realise doing so (H3). It was researched whether people identify the safety line correctly as a safety line as well as the guide line for blind people. Additionally the safety feeling on platforms was researched. The full results of the survey will be part of a different publication [10].

3 Results

3.1 Sensor Data

A general rise of people stepping into the danger zone with also rising pedestrian densities can be observed (Fig. 2). This is what we call the voluntary use of the danger zone: the probability of a person using the danger zone rises with the number of persons present (H1). The number of overstepping persons per metre safety line and second is reaching a higher level at Utrecht Centraal (orange) compared to Bern (blue). The higher maximum number of overstepping persons can be explained by higher pedestrian densities occurring.

By looking more detail at the results for each zone (Fig. 3) it can be found that some zones seem to reach a point when the number of overstepping persons starts rising exponentially (blue). Other zones don't reach this point (red). This leads to the conclusion that additional factors influence the use of the danger zone.

The zones in which we observe the seemingly exponential rise of the use of the danger zone are zone 5 in Bern and zones 3–8 in Utrecht Centraal. The zones in Utrecht are the ones with a narrow safety zone. Zone 5 in Bern has only few small obstacles but is known for a lot of circulation. Because of the lack of free waiting space and the high number of movements from the platform entrances to the preferred waiting positions these circulations might also occur in Utrecht. Berne's zones with bigger obstacles have a wider safety zone and lower pedestrian densities than detected in Utrecht. This is why we think that the effect of a seemingly exponential rise of the number of persons using the danger zone does not happen in zones with obstacles in Bern. In zone 5 in Bern, the high number of pedestrians seems to operate as obstacles towards other pedestrians. Further research is needed to describe all factors influencing the involuntary use of the danger zone in detail.

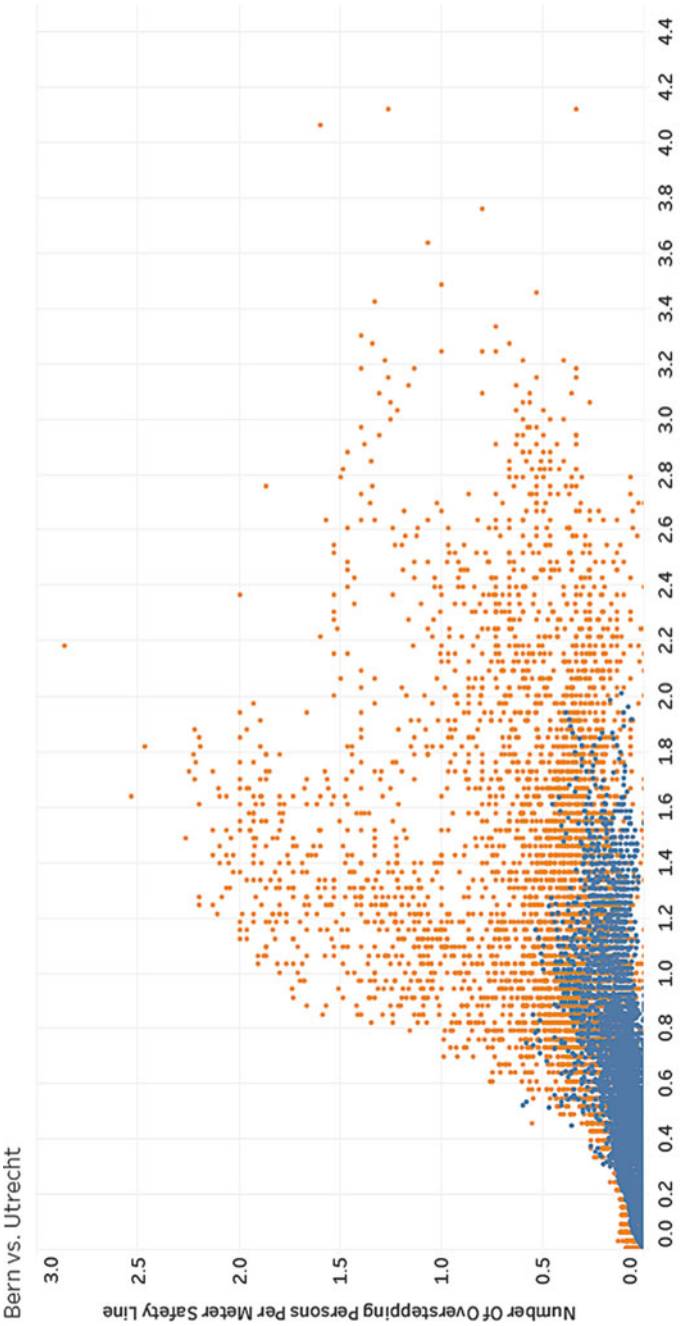

Fig. 2 Number of overstepping persons per metre safety line compared to the pedestrian density (in persons/m^2)—a comparison between Bern and Utrecht Centraal

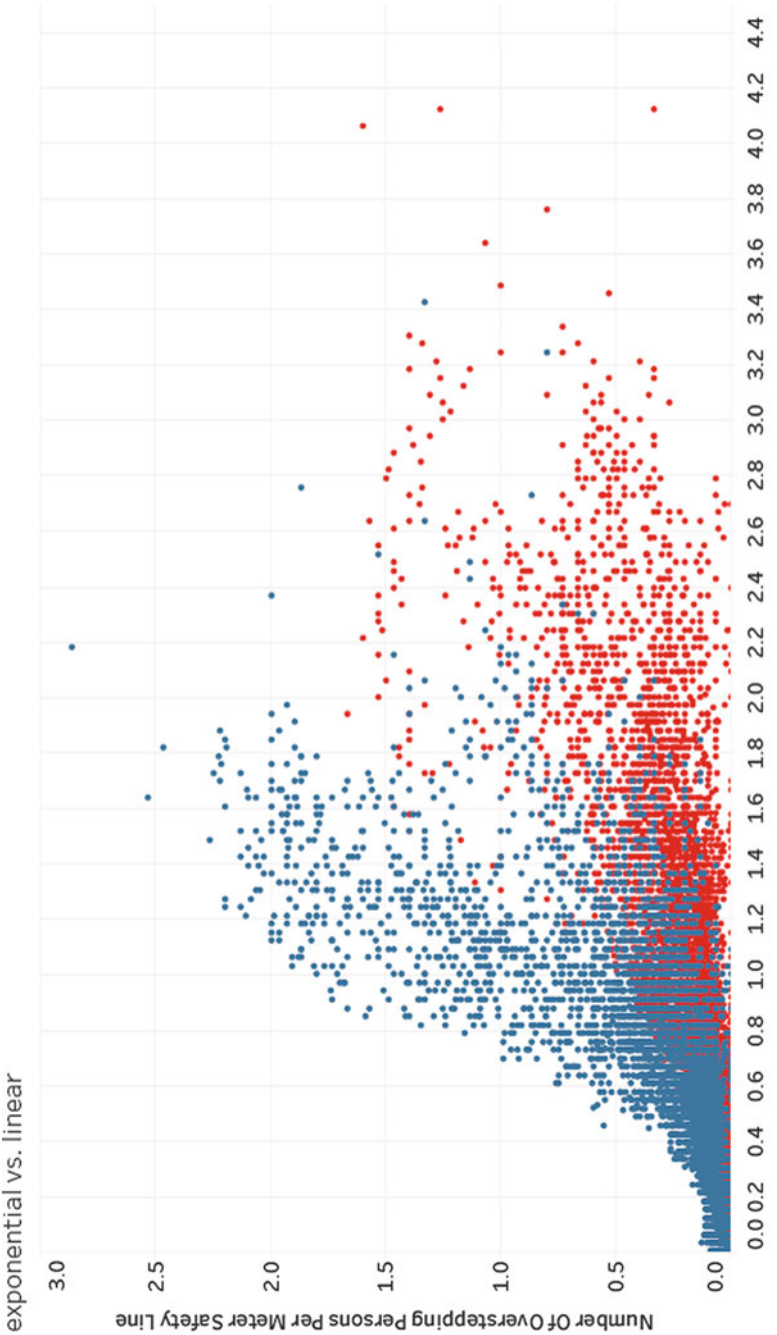

Fig. 3 Number of overstepping persons per metre safety line compared to the pedestrian density (in persons/m^2)—a comparison between different rates of growth

3.2 Survey

After distributing 6000 biscuits with links to the survey, we received 429 qualified answers on the questionnaire. The group of respondents is, as expected due to the time of distribution, composed of 72% commuters. Most of the answers were received from Bern, Lenzburg and Zurich Hardbruecke. 80% of the respondents identified the safety line correctly as well as they knew it is a guideline for blind people. In contrary, only one third of the people using the danger zone stated that they ever used it. When comparing the feeling of safety on platforms, we clearly see that people in Lenzburg feel less safe than in Bern or Zurich Hardbruecke. Lenzburg shows higher pedestrian densities than Bern and more or less the same densities as Zurich Hardbruecke but it has by far the highest number of drive-through trains. Reasons given for feeling unsafe underlined this. More than 50% of the respondents named high pedestrian densities and drive-through trains as reasons for feeling unsafe.

4 Conclusion

Concluding the analysis of the sensor data we were able to show that the number of persons using the danger zone rises with higher person densities (H1). The use of the danger zone is related to the number of persons being present at the platform. We also found that the use of the danger zone varies between zones, but also between days. This leads to the conclusion that other factors than the pedestrian density as well influence the use of the danger zone. One reason can be obstacles or the safety zone remaining next to obstacles (H2). Further research is needed to describe all factors influencing the use of the danger zone.

Concluding the results of the survey, we were able to show that, despite knowing the safety line, more than 60% of the respondents do not respect it (H3). They prefer to overtake or to have more space, over remaining in the safety zone on the platform. Additionally, we found that the feeling of safety is manly influenced by crowded platforms and drive-through trains.

5 Discussion

5.1 Practical Use for Station Planning

As a result of the survey, we clearly identify the necessity of a campaign explaining the possible risks of the use of the danger zone. First steps were done by distributing flyers and explaining the risks to children. The next step could be a media campaign similar to railway companies in Austria (OEBB) [7] and Germany (DB) [3].

In general, platforms with the least amount of obstacles should be planned. As this number is already reduced to the minimum, the number of waiting people next to long obstacles at narrow platforms should be minimised. The area next to staircases or ramps is a favoured waiting area because of the possibility of leaning against it.

The sensor data analysis showed the influence of densities, obstacles and other factors on the use of the danger zone. By further analysis and equipping other stations the key influence factors of the use of the danger zone are going to be quantified. To determine the moment when the risk of the involuntary use of the danger zone gets too high, a safety level shall be introduced. As a result station safety can be determined with higher reliability and additionally a more efficient distribution of financial resources can be achieved. Moreover the necessity and form of crowd management concepts can be identified.

5.2 Further Research

The presented hypotheses should be analysed further for different dates and shorter time intervals as well as obstacles of different length. Additionally the presented hypotheses have to be analysed regarding the time of use of the danger zone to find out whether, e.g., longer obstacles have an influence on this. Moreover personal spaces can be analysed as an influencing factor for the use of the danger zone.

To overcome the high number of persons waiting in narrow areas on Swiss train platforms, because of the possibility to lean against something other similar possibilities could be provided at wider parts of the platform. To support this, narrow areas can be made less comfortable to wait in, for example, by using an “uneven” floor. SBB will test the effect of both at different narrow platform areas in Switzerland. In The Netherlands, stations operator ProRail and NS have already installed leaning bars at less used areas of a platform of Amsterdam Airport Schiphol train station to induce more efficient waiting behaviour.

References

1. Bundesamt fuer Verkehr BAV: Abstaende auf perrons. gefahrenbereich - sicherer bereich. Tech. rep., Bundesamt fuer Verkehr BAV (2011)
2. Daamen, W., Hoogendoorn, S.: Pedestrian traffic flow operations on a platform: observations and comparison with simulation tool SimPed. In: Computers in Railways IX, pp. 125–134 (2004)
3. DB: “Wir wollen, dass Du sicher ankommst”. http://www.deutschebahn.com/de/nachhaltigkeit/verantwortung-gesellschaft/unfallpraevention/kurzfilme.html (2017). Accessed 31 Oct 2017
4. Fruin, J.J.: Pedestrian Planning and Design, rev edn. Elevator World, Inc., Mobile (1987)

5. Haenseler, F.: Modeling and estimation of pedestrian flows in train stations. Ph.D. thesis, Ecole Polytechnique Federale de Lausanne (2016)
6. Heinz, W.: Passenger service times on trains. Ph.D. thesis, Royal Institute of Technology, Stockholm (2003)
7. OEBB: The railway isn't a playground. http://infrastruktur.oebb.at/en/company/safety-is-our-agenda/education-and-campaigns/be-safe (2017). Accessed 31 Oct 2017
8. ProRail: Ontwerprichtlijnen, Beheerrichtlijnen en Afkeurnormen voor de transferkwaliteit van treinstations in Nederland (RLN00286 V002) (2010)
9. ProRail: Ontwerpvoorschrift Perrons (OVS00067) (2012)
10. Schneider, A., Thurau, J., Ehrat, F., Vollenwyder, B., Krueger, E.: Using multi-method approaches to investigate passenger's safety perception in train station environments. In: 6th International Human Factors Rail Conference, London, 6–9 Nov 2017 (2017)
11. Srikukenthiran, S.: Integrated microsimulation modelling of crowd and subway network dynamics for disruption management support. Ph.D. thesis, University of Toronto (2016)
12. van den Heuvel, J., Thurau, J., Schakenbos, R., van Ofwegen, M., Hoogendoorn, S.: An application of new pedestrian tracking sensors for evaluating platform safety risks at Swiss and Dutch train stations. In: Traffic and Granular Flow 2017, Washington DC (2017)
13. Verband oeffentlicher Verkehr (VoeV): Planungshilfe Publikumsanlagen (2017)
14. Weidmann, U.: Transporttechnik der Fussgaenger. Transporttechnische Eigenschaften des Fussgaengerverkehrs (Literaturauswerting). ETH Zuerich (1993)

Detecting Competitive Behaviors in Conflicts

Daichi Yanagisawa and Keisuke Yamazaki

Abstract We developed a method for detecting aggressive agents in egress simulations with a cellular-automata model. There are two types of agents, which are normal agents and aggressive agents. Aggressive agents tend to push out others in conflicts and try to move to their target cell aggressively. We considered all the possible combinations of agent types, labeled them, and computed the joint probabilities of the labels from the conflict data obtained from the egress simulations. The label which achieved the maximum joint probability was regarded as the expected label. The accuracy of our method achieved larger than 95% when a few very aggressive agents exist in a group of normal agents. On the other hand, the accuracy decreases when the aggressiveness of aggressive agents decreases or the fraction of the aggressive agents increases.

1 Introduction

Previous researches have shown that non-competitive (non-aggressive) behaviors reduce total egress time through the narrow exit [5]. Thus, to achieve smooth egress, we should discourage evacuees from aggressive behaviors. Here we bump into a problem. How should we distinguish non-aggressive (normal) and aggressive behaviors? Walking speed is sometimes regarded as aggressiveness; however, evacuees usually walk fast in a low-density area. Therefore, we focused on conflicts during egress processes. Then, we regarded the frequency of giving way to others as

D. Yanagisawa (✉)
Research Center for Advanced Science and Technology, The University of Tokyo, Meguro-ku, Tokyo, Japan
e-mail: tDaichi@mail.ecc.u-tokyo.ac.jp

K. Yamazaki
The Artificial Intelligence Research Center, National Institute of Advanced Industrial Science and Technology, Koto-ku, Tokyo, Japan
e-mail: k.yamazaki@aist.go.jp

S. H. Hamdar (ed.), *Traffic and Granular Flow '17*,
https://doi.org/10.1007/978-3-030-11440-4_33

non-aggressiveness, in other words, aggressive evacuees do not give way to others but try to proceed aggressively.

We employed the cellular-automata (CA) floor-field (FF) model [1] for egress simulations since conflicts are easily defined in CA models. The FF model succeeded to reproduce the phenomenon described in the beginning of this paper, i.e., achievement of small egress time by non-aggressive behaviors, by introducing the friction parameter [4]. The friction parameter was extended to the friction function, which enabled us to explain an unexpected obstacle effect, that is, an obstacle set near the exit shorten the total egress time, in [7]. From these facts, we considered that the FF models can perform realistic simulations in spite of its simplicity and discrete space.

We obtained conflict data, which represent the consequences of conflicts, i.e., which evacuees succeed to move and which evacuees remain in their present cell, through FF simulations. Then, we calculated joint probabilities of all the possible combinations of evacuees' types by using the conflict data and predicted which evacuees are aggressive ones.

The remainder of the paper is organized as follows. In the next section, we introduce the FF model used in this paper. In Sect. 3, we conduct simulations and see how the aggressive behaviors affected on the total evacuation time. In Sects. 4 and 5, we explain our detecting method and investigate the accuracy of it. Finally, Sect. 6 is devoted to summary of this paper.

2 Cellular-Automata Floor-Field Model with Normal and Aggressive Agents

2.1 Static Floor Field and Update Rule

We consider a room divided with cells as in Fig. 1a. The length of the horizontal side and the vertical side of the room are $L(\in \mathbb{N})$. The exit is at the center of the bottom side. In the beginning of the simulation, evacuees, who are called agents in the following, are randomly distributed in the room. Each cell can contain only one agent at most, so that the exclusion-volume effect of the agents is included.

Time is discrete, and the position of the agents is updated in parallel in every time step. Static floor field (SFF), which is L_1 norm distance from the exit cell, is given to each cell. The agents can refer to the SFF and try to move to a vacant Neumann neighboring cell with smaller SFF than the present cell in the next time step. If agents find more than one cell with smaller SFF than the present cell, they choose their target cell randomly with the equal probability. Target cell of the agents is determined stochastically in the original FF model [1]. We simplified the rule because we would like to consider the situation where every agent knows the position of the exit well and move there directly in order to focus on conflicts.

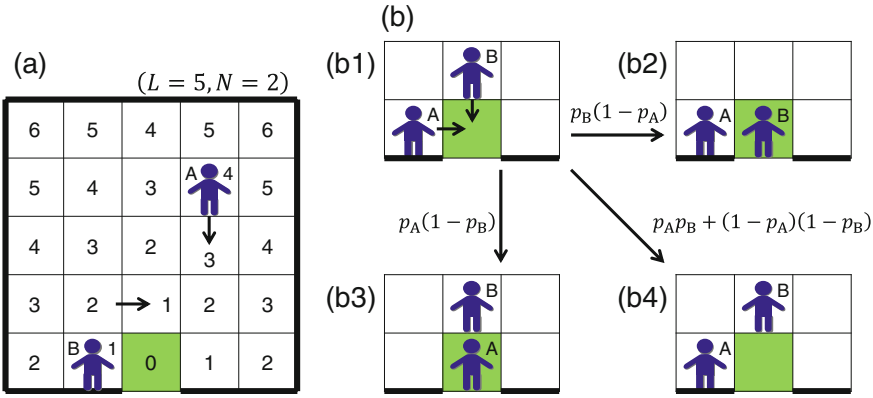

Fig. 1 (**a**) Schematic view of the simulation for $L = 5$ and $N = 2$. The green cell is the exit cell and the number described at each cell represents SFF. Two agents are trying to move to their Neumann neighboring cell with smaller SFF than their present cell. Since there are two Neumann neighboring cells with smaller SFF for agent A, agent A randomly chose the lower cell in the figure. (**b**) Schematic view of a conflict at the exit cell in the simulation. (**b1**) In the conflict between two agents, there are three consequences: (**b2**) agent B moves, (**b3**) agent A moves, and (**b4**) neither of them move, which occur with the probabilities $p_B(1 - p_A)$, $p_A(1 - p_B)$, and $p_A p_B + (1 - p_A)(1 - p_B)$, respectively

2.2 *Conflict*

Due to the parallel-update rule, more than one agent may choose the same cell as their target cell in the same time step as in Fig. 1b1. In the FF model, such situation is regarded as conflict. Conflicts were solved by introducing the friction parameter [4] or the fiction function [7] in the previous models. The friction parameter and the friction function are global parameters, so that they cannot represent the difference of aggressiveness among agents. Thus, we newly introduced persisting probability p, which represents aggressiveness of each agent in conflict. When $n(\geq 2)$ agents choose the same cell as their target cell and conflict occurs, they do not change their target cell with the probability p_i $(i \in [1, n])$, while they change their mind and decide to stay their present cell with the probability $1 - p_i$. Thus, the conflict is solved, i.e., one of the n agents succeed to move their original target cell and $n - 1$ agents stay their present cell with the resolution probability

$$P_{\mathrm{sol}} = \sum_{i=1}^{n} p_i \prod_{j \neq i} (1 - p_j) \tag{1}$$

as in Fig. 1b2, b3. On the other hand, all the agents are forced to stay at their present cell with the probability $1 - P_{\mathrm{sol}}$ as in Fig. 1b4.

2.3 Normal Agents and Aggressive Agents

We consider two types of agents, which are normal agents and aggressive agents, in this paper. The persisting probability p is different between them. Note that implementation of the heterogeneity of agents (normal agents and aggressive agent) considered in [3] is different from ours.

Normal agents give consideration to others and try to maximize the resolution probability P_{sol}. Consider the situation where agents involving in a conflict are all normal agent. When all of them try to move to the target cell (give way to others) similarly, that is, $p_i = p_{\mathrm{nor}}$ for $i = 1, 2, \ldots, n$, we can maximize the resolution probability P_{sol} by setting

$$p_{\mathrm{nor}}(n) = \frac{1}{n}. \tag{2}$$

Therefore, the persisting probability $p = 1/2$ and $1/3$ in conflicts among two and three agents as in Fig. 2a, b, respectively.

On the other hand, aggressive agents try to reach the exit cell as fast as they can and do not give consideration to others. We represent this aggressive behavior by setting large persisting probability $p = p_{\mathrm{agg}}(\geq 0.5)$. Thus, unlike normal agents, aggressive agents always try to move in a conflict with the same probability p_{agg} as in Fig. 2c, d irrespective to the number of agents involving in the conflict. Generally, $p_{\mathrm{agg}} \geq p_{\mathrm{nor}}$ because p_{nor} achieves the maximum value 0.5 at $n = 2$.

We introduced fraction of aggressive agents $r_{\mathrm{agg}} \in [0, 1]$, and simulated egress process with $(1 - r_{\mathrm{agg}})N$ normal agents and $r_{\mathrm{agg}}N$ aggressive agents in the next section.

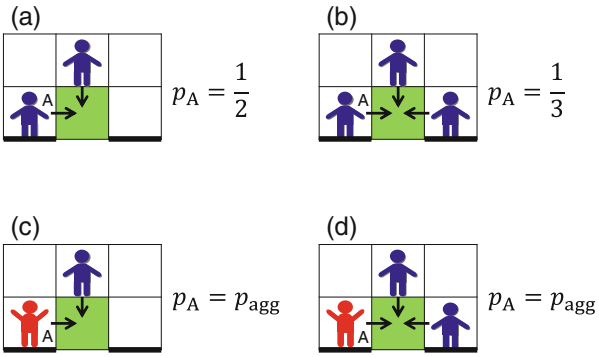

Fig. 2 Schematic view of the persisting probability p. (**a**) Normal agent for $n = 2$. (**b**) Normal agent for $n = 3$. (**c**) Aggressive agent for $n = 2$. (**d**) Aggressive agent for $n = 3$. Blue persons and red persons raising their hands represent normal agents and aggressive agents, respectively. The persisting probability of normal agents is $p_{\mathrm{nor}} = 1/n$, so that $p_{\mathrm{A}} = 1/2$ and $1/3$ in (**a**) and (**b**), respectively. The persisting probability of aggressive agents is $p_{\mathrm{agg}} = \mathrm{const.}(\geq 0.5)$ irrespective to the number of agents involved in the conflict

3 Total Egress Time and Egress Time Ratio

In this section, we conducted egress simulations and investigated how the aggressive behavior affects the total egress time T_{total}. Figure 3a shows T_{total} as a function of the ratio of aggressive agents r_{agg} for various p_{agg}. We see that T_{total} increases as r_{agg} increases, and the slope of the curves increases as p_{agg} increases. Large r_{agg} indicates large fraction of aggressive agents, so that many conflicts among aggressive agents, which require more time for resolution than those among normal agents, occur. When p_{agg} becomes large, the duration of conflicts increases because of strong persistent to the target cells of aggressive agents. Therefore, both r_{agg} and p_{agg} contribute to increase of T_{total}.

In order to investigate how much aggressive agents benefit from their behaviors, we calculated the mean total egress time of normal agents T_{nor} and that of aggressive agents T_{agg}, respectively. Then, we plotted the ratio of them, i.e., $T_{\text{agg}}/T_{\text{nor}}$, as a function of p_{agg} for various r_{agg} as in Fig. 3b. We observed no significant difference among different r_{agg}, so that we used the same makers for same p_{agg} in the figure. We see that $T_{\text{agg}}/T_{\text{nor}}$ decreases as p_{agg} increases, that is, aggressive agents egress faster than normal agents as their aggressiveness p_{agg} increases.

Figure 3a, b indicates the problems of aggressive agents in egress processes as follows. From Fig. 3a, we find that many (large r_{agg}) strong (large p_{agg}) aggressive agents greatly increase T_{total}. Therefore, we should prevent the agents from such aggressive behavior to achieve small T_{total}. From Fig. 3b, we observe that aggressive agents attain smaller egress time than normal agents by their aggressive behavior. Actually, when r_{agg} is small, T_{total} does not greatly increase as in Fig. 3a at

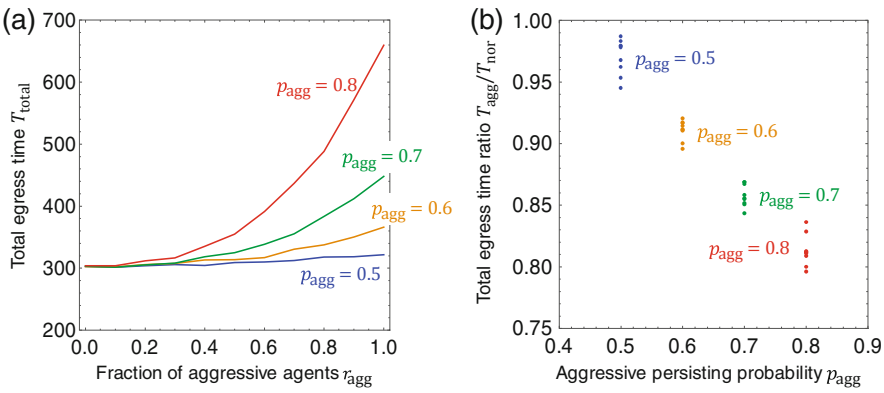

Fig. 3 (**a**) Total egress time T_{total} as a function of fraction of aggressive agents r_{agg} for aggressive persisting probability $p_{\text{agg}} = 0.5, 0.6, 0.7$, and 0.8. (**b**) Total egress time ratio between aggressive agents and normal agents $T_{\text{agg}}/T_{\text{nor}}$ as a function of aggressive persisting probability p_{agg} for fraction of aggressive agents $r_{\text{agg}} = 0.1, 0.2, \ldots, 0.9$. We observed no significant difference among different r_{agg}, so that we used the same makers for same p_{agg}. Both figures are the average results of 100 simulations with $L = 11$ and $N = 100$

$r_{\mathrm{agg}} = 0.1$ and 0.2. Thus, one may think that small number of aggressive agents are acceptable. However, such situation is not desirable because normal agents may become aggressive agents to decrease their T_{total} if we introduce the dynamics of changing agent types, which is considered in [2, 6]. (Note that the numbers of normal and aggressive agents are constant in this paper.)

Therefore, we should encourage agents not to behave aggressively in conflicts. In order to tell such advice to aggressive agents, we need to know who are the aggressive ones. Therefore, we developed a method for detecting aggressive agents, which are explained in detail in the next section.

4 Method for Detecting Aggressive Agents

Aggressive agents are more likely to succeed to move to their target cell in conflicts than normal agents. Thus, we consider that the agents who succeeded to move more than the other agents are aggressive agents.

To be more precise, we considered all the 2^N combinations (labels) of N agents, i.e., {nor, nor, . . . , nor, nor}, {nor, nor, . . . , nor, agg}, . . . , {agg, agg, . . . , agg, agg} and computed the joint probability

$$P_{\mathrm{joint}}(\boldsymbol{\theta}) = \prod_{\text{conflict data}} \left[\prod_{i=1}^{N} p_{\theta_i}(n)^{a_i} (1 - p_{\theta_i}(n))^{b_i} \right], \tag{3}$$

where $\boldsymbol{\theta}$ is one of the 2^N labels, θ_i is the ith element of $\boldsymbol{\theta}$, and n is the number of agents involved in the conflict. $a_i = 1$ if agent i succeeded to move in the conflict and $a_i = 0$ otherwise. $b_i = 1$ if agent i stayed in their cell in the conflict and $b_i = 0$ otherwise. The label $\boldsymbol{\theta}$ which achieves the maximum joint probability P_{joint} is the expected label and the type of each agent is determined from the corresponding element in the expected label.

Conflict data were obtained as $\mathbf{d}^1 = \{1*, 2, 3\}$, which represents that a conflict occurred among agent 1, 2, and 3, and agent 1 succeeded to move, whereas the others stayed at their cell. We only used the conflict data including a moving agent, i.e., one $*$ is putted on one agent number, for calculating the joint probability of the labels in this paper. Note that the number of conflict data obtained in one egress simulation is not determined and depends on stochastic nature of the initial condition and the resolution of conflicts.

We would like to show an example of calculating P_{joint}. Consider the situation where there are four agents ($N = 4$) with two conflict data $\mathbf{d}^1 = \{1*, 2, 3\}$ and

$\mathbf{d}^2 = \{1, 4*\}$. Then, the joint probability of $\boldsymbol{\theta}_{\text{example}} = \{\text{nor, agg, nor, agg}\}$ is

$$P_{\text{joint}}(\boldsymbol{\theta}_{\text{example}}) = \prod_{\mathbf{d}^1,\mathbf{d}^2} \left[\prod_{i=1}^{N=4} p_{\theta_i}(n)^{a_i} (1 - p_{\theta_i})(n)^{b_i} \right]$$
$$= \left[p_{\text{nor}}(3)(1 - p_{\text{agg}})(1 - p_{\text{nor}}(3)) \right] \left[(1 - p_{\text{nor}}(2)) p_{\text{agg}} \right]. \quad (4)$$

The accuracy of the detecting method is represented by the fraction of similarity between the true label and the expected label which achieve the maximum joint probability. For instance, when the true label and the expected label are {nor, agg, nor, nor} and {nor, agg, nor, agg}, respectively, the accuracy is 75%.

5 Evolution of Accuracy of the Detecting Method

We plotted the accuracy of our detecting method as a function of the number of observations on egress simulations M for $(p_{\text{agg}}, r_{\text{agg}}) = (0.8, 0.1)$, $(0.8, 0.3)$, and $(0.6, 0.1)$ as in Fig. 4. Number of conflict data increases approximately linearly as increase of M, so that the accuracy increases as M increases. We see that the accuracy increases and approximately achieves 97% at $M = 8$ for $(p_{\text{agg}}, r_{\text{agg}}) = (0.8, 0.1)$. This result indicates that we can distinguish normal agents and aggressive agents very accurately when a few very aggressive agents exist in a group of normal agents. Moreover, $M = 8$ is not very large from the view point of real observation. Thus, there is a possibility of applying our method to the real world if conflict data are obtained continuously. The accuracy of the two other cases saturates around

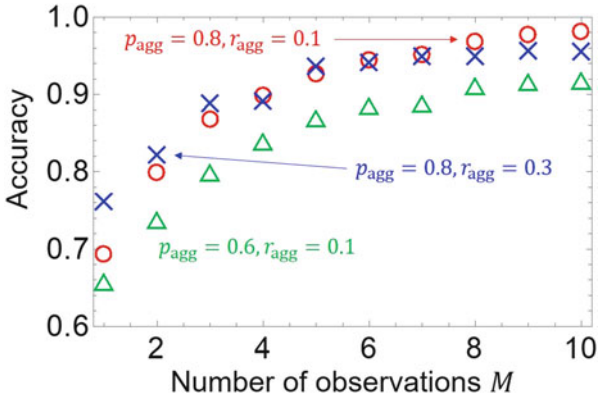

Fig. 4 Accuracy as a function of the number of observations of egress simulations M. Red circles, blue crosses, and green triangles represent the results of $(p_{\text{agg}}, r_{\text{agg}}) = (0.8, 0.1)$, $(0.8, 0.3)$, and $(0.6, 0.1)$, respectively. All the plots are the average results of 100 simulations with $L = 5$ and $N = 10$

95% and 92%, which are smaller than that of $(p_{\mathrm{agg}}, r_{\mathrm{agg}}) = (0.8, 0.1)$. This result implies that it becomes difficult to distinguish normal agents and aggressive agents when the aggressiveness of the aggressive agents becomes weak and the fraction of aggressive agents increases. Hence, we need to improve our method to increase the accuracy in such cases. One option is using conflict data where no agents succeed to move, for example, {1, 2, 3}, for calculating the joint probability of the labels.

6 Summary

In this paper, we developed a method for detecting aggressive agents in egress simulations. First, we conducted egress simulations with two types of agents, which are normal agents and aggressive agents. Then, we obtained the conflict data from the simulations and computed the joint probability of the labels, which represent the combination of the type of each agent. Finally, we obtained the label which achieves the maximum joint probability as the expected label.

We computed the accuracy of distinguishing normal agents and aggressive agents. When a few very aggressive agents exist in a group of normal agents, the accuracy achieved larger than 95% with eight times observations of egress processes, which is not very large from the view point of real observation. On the other hand, when the aggressiveness of aggressive agents becomes weak and the fraction of aggressive agents increases, the accuracy decreases. Improvement of accuracy in such cases is a remained work, which should be solved in the near future.

Although research in this paper is completely based on simulations without any experimental or observational results, we have shown that distinguishing normal agents and aggressive agents is possible if we obtain conflict data, i.e., which agents succeeded to move in conflicts. Therefore, we believe that our result will lead to the development of detecting aggressive behaviors in the real world in the future.

References

1. Burstedde, C., Klauck, K., Schadschneider, A., Zittartz, J.: Simulation of pedestrian dynamics using a two-dimensional cellular automaton. Phys. A Stat. Mech. Appl. **295**(3–4), 507–525 (2001)
2. Heliövaara, S., Ehtamo, H., Helbing, D., Korhonen, T.: Patient and impatient pedestrians in a spatial game for egress congestion. Phys. Rev. E **87**(1), 012802 (2013)
3. Hrabák, P., Bukáček, M.: Influence of agents heterogeneity in cellular model of evacuation. J. Comput. Sci. **21**, 486–493 (2017)
4. Kirchner, A., Klüpfel, H., Nishinari, K., Schadschneider, A., Schreckenberg, M.: Simulation of competitive egress behavior: comparison with aircraft evacuation data. Phys. A Stat. Mech. Appl. **324**(3–4), 689–697 (2003)
5. Muir, H.C., Bottomley, D.M., Marrison, C.: Effects of motivation and cabin configuration on emergency aircraft evacuation behavior and rates of egress. Int. J. Aviat. Psychol. **6**(1), 57–77 (1996)

6. Von Schantz, A., Ehtamo, H.: Spatial game in cellular automaton evacuation model. Phys. Rev. E **92**(October), 1–13 (2015)
7. Yanagisawa, D., Kimura, A., Tomoeda, A., Nishi, R., Suma, Y., Ohtsuka, K., Nishinari, K.: Introduction of frictional and turning function for pedestrian outflow with an obstacle. Phys. Rev. E **80**(3), 036110 (2009)

Towards Faster Navigation Algorithms on Floor Fields

Benedikt Zönnchen, Matthias Laubinger, and Gerta Köster

Abstract Many microscopic models for crowd dynamics use floor fields to navigate agents through geometries. Recently, dynamic floor fields were introduced which adapt to changes in geometry and the density of crowds. They significantly increase the realism of floor field-based simulations. However, the computation of floor fields is time consuming. In case of multiple or dynamic floor fields, which require frequent recomputations, the total simulation run time is dominated by their computation. We present an algorithm to construct floor fields for continuous space models that uses unstructured meshes. Due to the geometrical flexibility of unstructured meshes, our method reduces the computational complexity by using fewer but well-positioned mesh points.

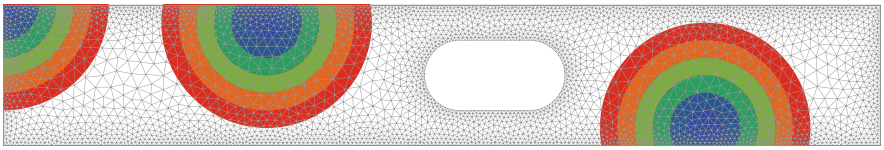

1 Introduction

Floor fields assign each position a certain use depending, e.g., on the distance to the target while skirting obstacles. They are a well-established method to implement static and dynamic medium scale navigation in continuous and discrete microscopic

B. Zönnchen (✉)
Munich University of Applied Sciences, Munich, Germany

Technical University of Munich, Garching, Germany
e-mail: zoennchen.benedikt@hm.edu

M. Laubinger · G. Köster
Munich University of Applied Sciences, Munich, Germany
e-mail: mlaubing@hm.edu; gerta.koester@hm.edu

S. H. Hamdar (ed.), *Traffic and Granular Flow '17*,
https://doi.org/10.1007/978-3-030-11440-4_34

models such as [3, 8, 11]. Dynamic floor fields can be used to model navigation around large crowds or queuing [3, 6].

The major drawback of floor fields is their computational complexity in time and space, especially in case of continuous space models. Let $\Omega \subset \mathbb{R}^2$ be the scenario domain and $\Gamma \subset \Omega$ its destination area then, in the continuous case, floor fields are the solution of the eikonal equation

$$||\nabla T(x)|| \cdot V(x) = 1, \text{ and } T(x) = 0, \text{ if } x \in \Gamma, \tag{1}$$

where T is the traveling time of a propagating wave which starts at Γ and moves with the traveling speed V. To solve the eikonal equation, one has to apply a numerical solver like the fast sweeping method [13], the fast iterative method [4], or the fast marching method [9]. The most common approach is to discretize Ω by a rectangular orthogonal mesh using an edge length r which leads to $n = r^{-2} \cdot w \cdot h$ points, where w is the width and h is the height of a bounding box containing Ω. In case of the fast marching method, this results in a complexity of $\mathcal{O}(n \log(n))$ in time and $\mathcal{O}(n)$ in space.

The question is: How can we reduce the number of discretization points and preserve accuracy?

In this contribution we introduce unstructured high-quality meshes for the space discretization. Compared to rectangular meshes, unstructured meshes offer far greater geometrical flexibility such as variable and adaptive spatial resolution which lead to a significant smaller point size [10]. For solving Eq. (1) accurately, a high resolution is required where the change in V is large, e.g., at the boundary of obstacles or, in case of dynamic floor fields, at areas with high pedestrian density differences (see [3, 6]). In this first investigation we developed an adapted version of DistMesh for mesh generation. We choose DistMesh because of its accessibility and its high-quality results. The algorithm is easy to understand, and therefore easy to adapt and to integrate into existing projects.

In the first section we explain the original DistMesh algorithm and the changes we implemented. In the second section, we describe the computation of T in the fast marching method for unstructured meshes. In the third section we compare the exact solution of the eikonal equation with its approximation on unstructured and rectangular meshes. We conclude this work by a short discussion.

2 An Efficient Implementation of DistMesh

We want to stress that there are other meshing techniques for unstructured meshes like the advancing front method, grid overlay techniques, and Delaunay-based approaches. However, in this first contribution we only focus on the force-based smoothing procedure DistMesh. We first give some insights into DistMesh's principles. Then our changes to it.

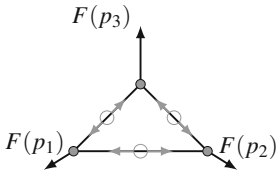

Fig. 1 Repulsive forces acting at the midpoint of each edge (gray) added up to forces acting on mesh points (black)

DistMesh is an iterative mesh generator which utilizes the Delaunay criterion. It is based on the physical analogy between a mesh and a truss structure [7]. Let $\Omega_S \subset \Omega$ be the obstacle domain including the scenario boundary. Let P_k be the set of points of iteration k and E_k the set of edges of its Delaunay triangulation defining the mesh connectivity. As an analogy, imagine a truss structure where each node represents a mesh point $p \in P$ and each bar represents an edge $e \in E$ of the mesh. Furthermore, imagine an external force $F_{ext}(P)$ acting on the truss boundary pulling each boundary mesh point towards the boundary of Ω_S. In addition, internal forces $F_{int}(P)$ acting between internal mesh points (see Fig. 1). In an equilibrium forces cancel each other out, that is

$$F(P) = 0 \tag{2}$$

holds, where $F(P) = F_{ext}(P) + F_{int}(P)$. To solve Eq. (2), an artificial time-dependence is introduced

$$\frac{dP}{dt} = F(P), \ t \geq 0, \tag{3}$$

which is solved by using the forward Euler method, i.e., $P_{k+1} = P_k + \Delta t \cdot F(P_k)$. Two functions, which can be chosen by the user, influence the result. The distance function $d : \Omega \to \mathbb{R}$ gives the signed distance to the boundary of Ω_S, i.e., $d(x) < 0$ if $x \in \Omega \setminus \Omega_S$ and $d(x) \geq 0$ if $x \in \Omega_S$. The second function $l_0 : \Omega \to \mathbb{R}^+$ gives the relative edge length in an equilibrium. An internal force between two mesh points p, q depends on the difference between the current edge length l of $e = (p, q)$ and its relative edge length in an equilibrium $l_0(x_e)$, where x_e is the midpoint of e. These forces are always repulsive. By choosing

$$l_0(x) := 1.0 + \min\{-d(x), 0\} \tag{4}$$

DistMesh generates an adaptive unstructured mesh, which is coarse in open space and fine near the boundary and obstacles (see Fig. 2). We changed the initial mesh generation and the recomputation of the mesh connectivity, which reduces the number of performed re-triangulation.

The original DistMesh constructs a uniform triangulation and deletes some points based on a distribution function [7]. We adapt the initialization by the following technique: We start with a regular super triangle which contains the whole scenario

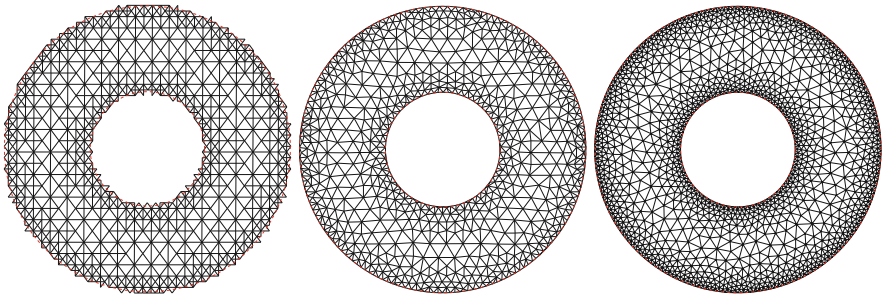

Fig. 2 Meshes generated by our implementation of DistMesh with 805 mesh points. Unstructured mesh after 0 (left), 20 (middle), and 200 (right) iterations. After 200 iterations 3 re-triangulations were performed

domain Ω. We recursively construct two (or four) sub-triangles by splitting edges of all triangles if the following two conditions hold: The edge e is too long with respect to l_0 and at least one neighboring triangle of e is not completely contained in Ω_S. Finally, we clean up useless triangles, i.e., triangles inside Ω_S by removing them from the mesh, if their centroid is in Ω_S (see Fig. 2). This procedure reduces the construction of useless triangles and produces a high-quality initial mesh which is close to a good solution of Eq. (2). We use the quality measure defined in [7], i.e., the ratio between the radius of the largest inscribed circle r_{in} (times two) and the smallest circumscribed circle r_{out}

$$q = 2 \cdot r_{in}/r_{out} \tag{5}$$

To save computation time, we adapt the recomputation of the mesh connectivity. During the run of DistMesh, the amount of changes in connectivity decreases drastically with the time. This is no surprise since the force $||F||$ decreases, and therefore the overall movement of mesh points. The original DistMesh algorithm computes the mesh connectivity by computing the Delaunay triangulation of the whole point set if some large displacement was performed [7]. The need for a re-triangulation is clearly connected to the amount of movement of mesh points on average. However, a large displacement does not always destroy the mesh connectivity. Furthermore, all the information of the previous mesh connectivity are discarded. Since the computation of the Delaunay triangulation is the most computational expensive part of DistMesh, we propose a non-recursive flip algorithm which flips all non-Delaunay edges in parallel. This requires $\mathcal{O}(|E|)$ instead of $\mathcal{O}(|P|\log(|P|))$ time. However, if a mesh point crosses an edge, due to its displacement, we fall back to the re-triangulation, since the mesh connectivity becomes illegal (see Fig. 3). Note that we do not guarantee that our mesh is fully Delaunay, since a flip could invalidate neighboring triangles. However, we still increase the quality with the same rate and most of the triangles still satisfy the criterion. After we compute the Delaunay triangulation using the Delaunay hierarchy [1], we delete low quality triangles

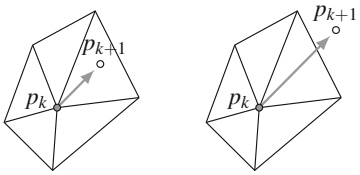

Fig. 3 Legal (left) and illegal (right) displacement from p_k to p_{k+1}

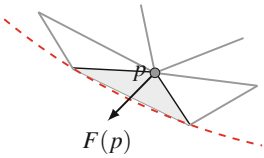

Fig. 4 Sketch of a bad triangle (gray) at the boundary (red, dashed). F eventually pushes p towards the boundary

(Eq. (5)) with large angles neighboring the boundary (see Fig. 4) and move their points towards the boundary. Such low quality triangles will disappear eventually, since $F(p)$ acts towards the boundary. We observed that these triangles cause a lot of illegal displacements, and therefore re-triangulations. We integrated our Java-based implementation into the open-source crowd simulation software VADERE [12].

3 The Fast Marching Method on Unstructured Meshes

We implemented the algorithm described by Kimmel and Sethian [5], using the half-edge data structure. The only difference, using an unstructured instead of a rectangular mesh, is the computation of $T(p)$ for a given mesh point p. Let's first assume that all triangles incident to p are non-obscure. In this case we compute $T(p)$ with respect to each incident triangle and take the minimum [5]. If we consider an obscure triangle, we can no longer guarantee that any front entering the side of a triangle has two points to provide values before the third is computed. We use the construction described by Kimmel and Sethian [5] to build numerical supports. Searching the splitting mesh point inside the extended section is done by using the straight walk algorithm discussed by Devillers et al. [2]. In Fig. 5, the extended section is a cone containing all points q, such that the angles p_3qp_4, p_2qp_4 are non-obscure. The time complexity of the fast marching method on unstructured meshes is $\mathcal{O}(n \log(n))$ [5].

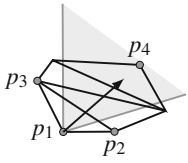

Fig. 5 Straight walk towards a numerical support p_4 inside the shaded extended section. $T(p_1)$ is computed using the triangle $p_3p_1p_4$ and $p_2p_1p_4$

4 Performance

To measure the performance of the introduced method we use a curved scenario defined by the distance function $d(x) := \text{abs}(6 - ||x||) - 4$ (see Fig. 6). In this contribution we focus on static floor fields, and therefore we choose V to be constant. More precisely: $\forall x \in (\Omega \setminus \Omega_S) : V(x) = 1$ and $\forall x \in \Omega_S : V(x) = 0$. We test three different equilibrium edge length functions:

$$l_0^{uni}(x) := 1.0,$$
$$l_0^{dist}(x) := 1.0 - 0.5 \cdot d(x) \text{ and}$$
$$l_0^{travel}(x) := 1.0 + 0.5 \cdot \min\{-d(x), \text{abs}(||x|| - 6)\}.$$

Furthermore, we define two different destination domains $\Gamma_1 := \{x : ||x|| \geq 2\}$ (the inner disc) and $\Gamma_2 = \Omega_S = \{x : d(x) \geq 0\}$ (the boundary domain). An unstructured mesh with only 842 equidistant mesh points, i.e., $l_0 = l_0^{uni}$, can represent the scenario domain more precisely than a rectangular orthogonal mesh with the same amount of points (see Fig. 7a, b). In all test cases the maximum distance between any boundary mesh point and the boundary is less than 1.0^{-9} for unstructured and r for rectangular meshes. If we compare errors of the solution of Eq. (1) on an almost uniform and well-aligned unstructured mesh (see Table 1) with the solution on a rectangular mesh (see Table 2) the errors are in the same range but smaller for unstructured meshes. We can also observe that the number of iterations and re-triangulations does not depend on n. In these test cases, our implementation of DistMesh requires ≈ 550 iterations and ≈ 8 re-triangulations to achieve an average mesh quality of 0.96. In case of $\Gamma = \Gamma_1$, errors are greater since the propagating wave travels two times longer. Furthermore, we can slightly improve accuracy, without increasing n, by using l_0^{adapt} instead of l_0^{uni} (see Table 1). To achieve the

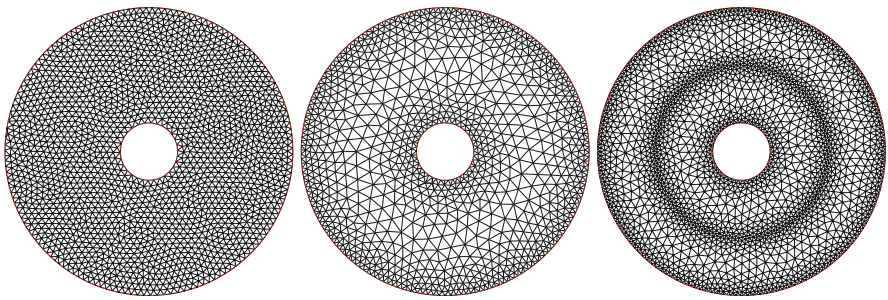

(a) (b) (c)

Fig. 6 Resulting mesh of scenario defined by $d(x) := |6 - ||x|| | - 4$ using different equilibrium edge lengths l_0. Boundary points are almost perfectly aligned. (**a**) l_0^{uni}. (**b**) l_0^{adapt}. (**c**) l_0^{travel}

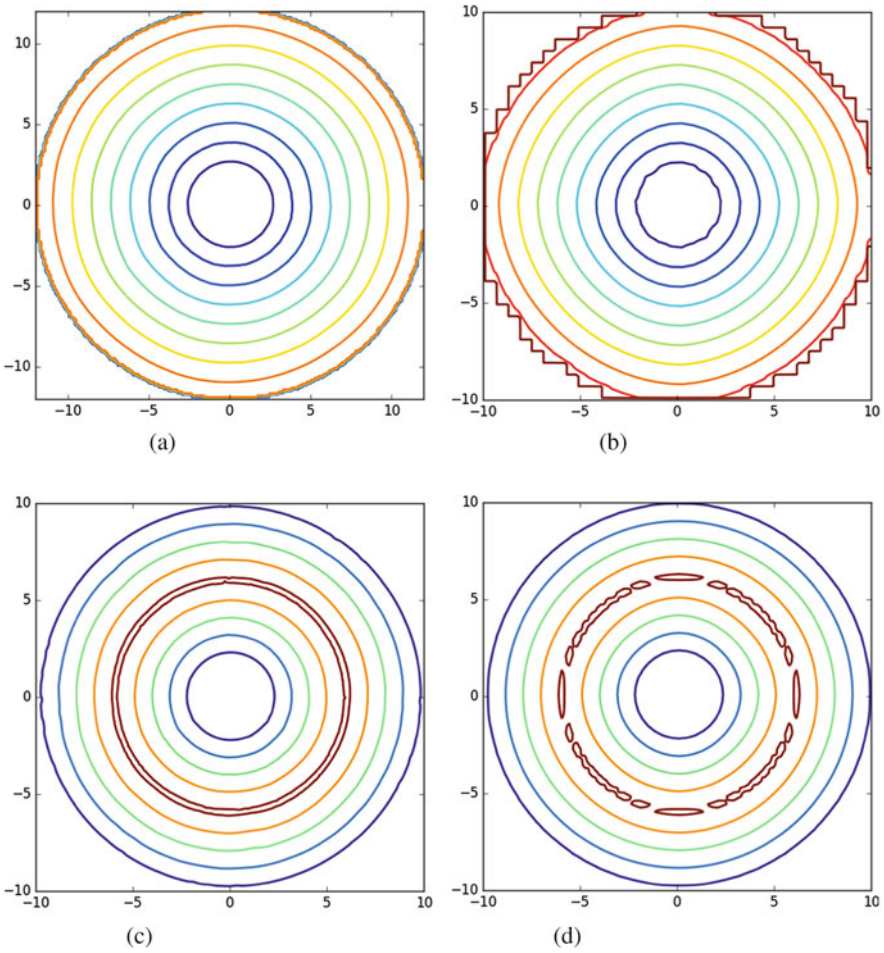

Fig. 7 Solutions of T for different meshes and grids. We use $l_0 = l_0^{uni}$ (**a**) and $l_0 = l_0^{travel}$ (**c**). (**a**) Mesh, $n \approx 800$. (**b**) Grid, $n \approx 800$. (**c**) Mesh, $n \approx 2000$. (**d**) Grid, $n \approx 2000$

same improvement for Γ_2, we rely on l_0^{travel} (see Table 1 and Fig. 7c, d), since the wave front changes its traveling direction at the center of the ring.

5 Conclusion and Future Work

We presented a Java implementation of DistMesh which requires less re-triangulations than the original version. We showed that using unstructured meshes, they can reduce the number of mesh points significantly. In our test cases, L_2 and

Table 1 Listing of errors with respect to Γ_1 and Γ_2, minimal and maximal edge lengths l_{min}, l_{max} and required iteration and re-triangulation to achieve an average quality of 0.96 (Eq. (5)) for different edge length function l_0^i

l_0	#triangulations	#iterations	n	l_{min}	l_{max}	L_2 error	L_∞ error	Γ
$l_0^{uni}(x)$	7	599	842	0.380	0.944	0.071	0.142	Γ_1
	7	514	1676	0.327	0.691	0.045	0.093	
	7	630	2474	0.110	0.561	0.043	0.073	
	6	501	6481	0.110	0.338	0.025	0.061	
	9	515	38,315	0.062	0.155	0.010	0.016	
	11	610	101,646	0.037	0.100	0.006	0.002	
$l_0^{adapt}(x)$	8	610	850	0.248	1.276	0.068	0.104	Γ_1
$l_0^{uni}(x)$	5	601	843	0.511	0.922	0.047	0.341	Γ_2
	6	420	1656	0.311	0.831	0.029	0.228	
	6	560	2463	0.273	0.582	0.022	0.195	
	5	503	6569	0.151	0.351	0.013	0.109	
	11	515	38,233	0.071	0.161	0.005	0.048	
	10	610	101,456	0.042	0.101	0.003	0.031	
$l_0^{adapt}(x)$	7	530	1081	0.254	1.294	0.075	0.549	Γ_2
$l_0^{travel}(x)$	7	610	1100	0.25	0.870	0.028	0.171	Γ_2

Table 2 Listing of errors with respect to Γ_1, Γ_2 and different grid resolutions r

		Γ_1		Γ_2	
r	n	L_2 error	L_∞ error	L_2 error	L_∞ error
0.6	870	0.155	0.409	0.078	0.520
0.4	1900	0.111	0.230	0.044	0.177
0.2	7800	0.057	0.178	0.021	0.091
0.1	31,000	0.029	0.056	0.012	0.030

L_∞ errors still increase with roughly the same rate with the decrease in the number of points. However, unstructured meshes align perfectly with the geometry using only a few mesh points. Considering pedestrian dynamics, this property improves the approximation of T in Eq. (1) at the most crucial areas, that is near obstacles. Therefore, we belief that this property results in equal navigation behavior using few discretization points. This belief has to be challenged by further investigations comparing simulation results using different meshes. We also have to study how our implementation of DistMesh behaves for different geometries, which are relevant in pedestrian dynamics. Furthermore, we have to incorporate dynamic floor fields by using an equilibrium edge lengths function l_0 which depends on the pedestrian density.

References

1. Devillers, O.: The Delaunay hierarchy. Int. J. Found. Comput. Sci. **13**(02), 163–180 (2002)
2. Devillers, O., Pion, S., Teillaud, M.: Walking in a triangulation. In: 17th Annual ACM Symposium on Computational Geometry (SCG), Boston, June 2001, pp. 106–114 (2001)
3. Hartmann, D., Mille, J., Pfaffinger, A., Royer, C.: Dynamic medium scale navigation using dynamic floor fields. In: Weidmann, U., Kirsch, U., Schreckenberg, M. (eds.) Pedestrian and Evacuation Dynamics 2012, pp. 1237–1249. Springer, Cham (2014)
4. Jeong, W.-K., Whitaker, R.T.: A fast iterative method for eikonal equations. SIAM J. Sci. Comput. **30**(5), 2512–2534 (2008)
5. Kimmel, R., Sethian, J.A.: Computing geodesic paths on manifolds. In: Proceedings of the National Academy of Sciences of the United States of America, vol. 95, pp. 8431–8435. National Academy of Sciences, Washington (1998)
6. Köster, G., Zönnchen, B.: Queuing at bottlenecks using a dynamic floor field for navigation. In: The Conference in Pedestrian and Evacuation Dynamics 2014, Delft. Transportation Research Procedia, pp. 344–352, (2014)
7. Persson, P.-O., Strang, G.: A simple mesh generator in matlab. SIAM Rev. **46**(2), 329–345 (2004)
8. Seitz, M.J., Köster, G.: Natural discretization of pedestrian movement in continuous space. Phys. Rev. E **86**(4), 046108 (2012)
9. Sethian, J.A.: A fast marching level set method for monotonically advancing fronts. Proc. Natl. Acad. Sci. **93**(4), 1591–1595 (1996)
10. Thompson, J.F., Soni, B.K., Weatherill, N.P.: Handbook of Grid Generation. CRC-Press, Boca Raton (1999)
11. Treuille, A., Cooper, S., Popović, Z.: Continuum crowds. ACM Trans. Graph. (SIGGRAPH 2006) **25**(3), 1160–1168 (2006)
12. VADERE-team: VADERE simulation framework (2016). www.vadere.org
13. Zhao, H.: A fast sweeping method for eikonal equations. Math. Comput. **74**(250), 603–627 (2005)

Automated Quality Assessment of Space-Continuous Models for Pedestrian Dynamics

Valentina Kurtc, Mohcine Chraibi, and Antoine Tordeux

Abstract In this work we propose a methodology for assessment of pedestrian models continuous in space. With respect to the Kolmogorov–Smirnov distance between two data-clouds, representing, for instance, simulated and the corresponding empirical data, we calculate an evaluation factor between zero and one. Based on the value of the herein developed factor, we make a statement about the goodness of the model under evaluation. Moreover this process can be repeated in an automatic way in order to maximize the above-mentioned factor and hence determine the optimal set of model parameters.

1 Introduction

Mathematical models have been developed to describe and simulate the dynamics of complex systems. For pedestrian dynamics several kinds of models have been built with different intentions. For an overview of the existing models the reader is referred to [20]. In order to develop and use mathematical models for pedestrian dynamics with high fidelity level, the verification and validation process should be considered as key part in the development cycle.

According to conventional terminology [19] **verification** is the process of assuring if the computer programming and implementation of a mathematical model is correct. The verification process does not assess the quality of mathematical models nor does it allow to make any conclusions related to its realism. In the literature

V. Kurtc (✉)
Peter the Great St. Petersburg Polytechnic University, St. Petersburg, Russia

M. Chraibi
Forschungszentrum Jülich, Jülich, Germany
e-mail: m.chraibi@fz-juelich.de

A. Tordeux
University of Wuppertal, Wuppertal, Germany
e-mail: tordeux@uni-wuppertal.de

S. H. Hamdar (ed.), *Traffic and Granular Flow '17*,
https://doi.org/10.1007/978-3-030-11440-4_35

some verification-driven works regarding the goodness of fit of a pedestrian model have been published. In [16] several verification tests were recommended to assess the quality of simulations of ships. In the RiMEA project [17] verification tests were proposed to evaluate the quality of pedestrian simulations. Based on the above-mentioned works Ronchi et al. [18] suggested some modified and new verification tests with the aim to additionally consider the movement of pedestrians in case of fire.

Having verified the numerical implementation of the given model, the question that should be of concern is "does the implemented model show sufficient accuracy in emulating the targeted system?" In order to answer this question reliably, an iterative **validation** process is required, that is, comparing the model/simulation results with empirical findings and evaluating their discrepancies to enhance the behavior of the model. Repeating this process leads to a better description of the targeted system (pedestrian dynamics). The process of validation in pedestrian dynamics can benefit from the tremendous development of empirical research. Several experiments were conducted to investigate crowd performances and to build a well-documented database. Empirical research does not only contain data of controlled experiments [1, 2, 5, 7–9, 12–15], but also data issued from field studies [3, 4, 21]. These empirical works capture relevant properties of the crowd in *normal* situations and for basic geometries. Examples are uni-directional flows (fundamental diagram), bottleneck (jam formation), counter-flow (lane formation), and intersection (e.g., T-junction).

The goal of this paper is to develop an automatic assessment of the predictive capability of pedestrian models. We introduce new quantities, in order to quantify the degree of success (or failure) of a model/simulation with respect to a given set of empirical data. The introduced "validity factor" is a measure for the verification *and* the validation process of a given implementation of a model. In the first stage of the model's assessment (verification) we use tests mostly based on the RiMEA guideline [17]. While in the second stage (validation) we compare the model with experimental data issued from six different experiments: uni-directional flow (1D and 2D), bi-directional flow, corners, bottlenecks, and T-junctions. Comparing the model results with empirical findings and automatically evaluating their discrepancies is important for the validation process as well as for making a precise estimation of its goodness.

2 Verification and Validation Tests

We implement two different kinds of tests: verification and validation tests. In the first stage of the pedestrian model assessment, the verification step, we use tests based on the RiMEA guideline [17]. During the validation process we propose to compare the simulation results with experimental data issued from six different experiments: uni-directional flow (1D and 2D), bi-directional flow, corners, bottlenecks, and T-junctions (Fig. 1). The proposed geometries are different in order

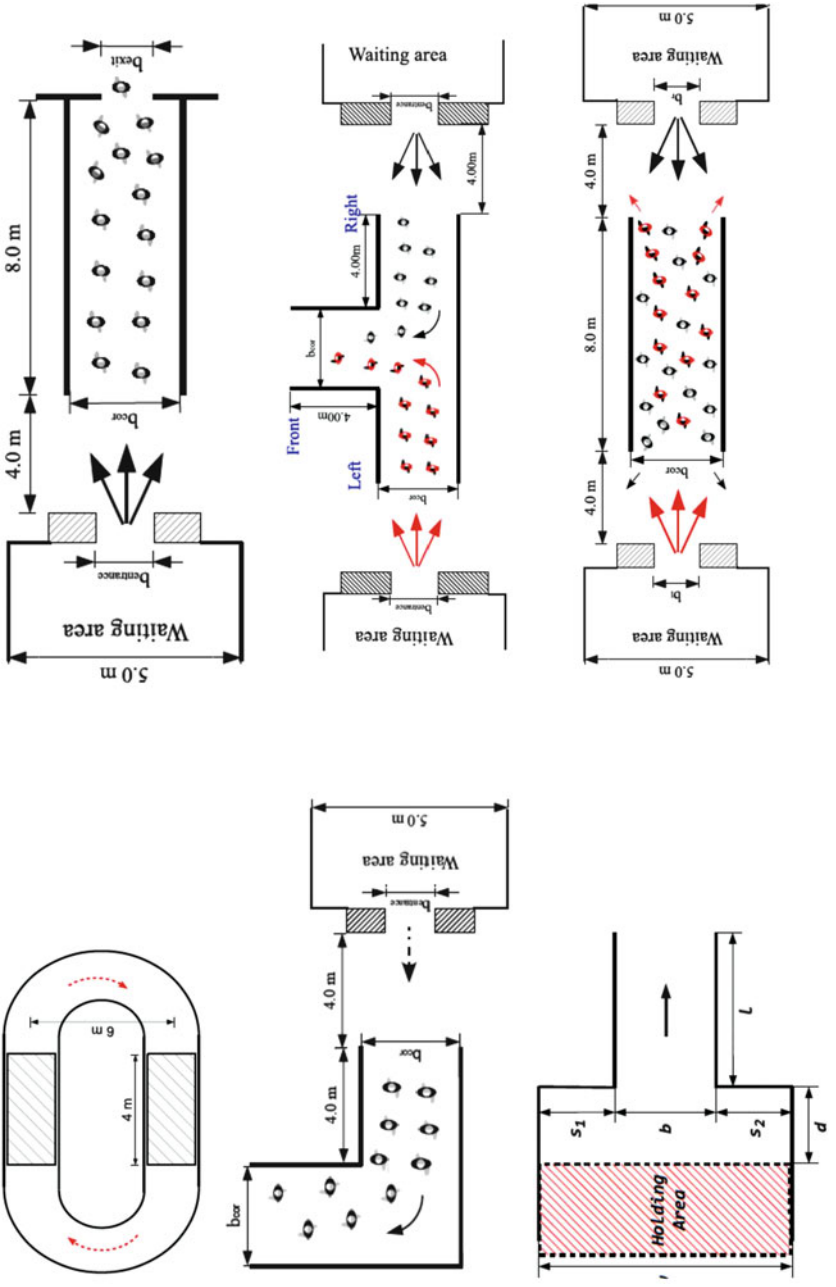

Fig. 1 Validation tests: six different experimental setups suggested to validate a model

to cover various dynamics of pedestrians and hence, the validation results may show more significance with respect to empirical findings.

Considering the pedestrian model and specifying area geometry and initial conditions, which are speed and position of pedestrians, one can compute trajectories of all pedestrians. The simulations are performed with JuPedSim [10, 11], using models [22, 23].

Afterwards, both for simulated and empirical trajectories the fundamental diagram is calculated using one of the measurement methods implemented in the JPSreport module of JuPedSim. For an accurate comparison it is important to use the same measurement method for both the experimental and the simulation data.

3 Methodology

This section presents the methodology for quantitative comparison of results obtained from experiments and simulations on basis of the verification and validation tests introduced earlier. Firstly, we suggest the approach for similarity assessment of two fundamental diagrams (speed–density relations), which are the main outcome of the validation tests. This approach exploits the data-binning and cumulative distribution functions calculation. Secondly, the quantitative quality assessment metric is formulated, which aggregates the comparison results of experiments and simulations both for verification and validation tests.

3.1 Comparison of Two Data-Clouds

Assessment of validation results is made by means of comparison of two fundamental diagrams (FD), i.e., the speed–density relation. Given observation points of speed and density from experiments $\{[\rho_i^{\text{data}}, v_i^{\text{data}}]\}$ and simulations $\{[\rho_i^{\text{model}}, v_i^{\text{model}}]\}$, our goal is to quantify the degree of similarity among these two point clouds. Therefore, we create a partitioning of the data points by filtering them according to N equally spaced density intervals (Fig. 2),

$$V_j^{\text{src}} = \{v_i^{\text{src}} : \rho_i^{\text{src}} \in [\rho_j, \rho_{j+1}], i = 1, \ldots, N^{\text{src}}\}, \tag{1}$$

where $j = 1, \ldots, N$, src $= \{\text{data, model}\}$ and N^{src} is the number of observations. The key idea here is to interpret V_j^{src} as a one-dimensional random variable. Now we calculate the cumulative distribution functions (CDFs) both for the experiment, $F_{V_j^{\text{data}}}(x)$, and for the simulations, $F_{V_j^{\text{model}}}(x)$, and calculate the Kolmogorov–Smirnov distance

$$D_j = \sup_x |F_{V_j^{\text{data}}}(x) - F_{V_j^{\text{model}}}(x)|, \; j = 1, \ldots, N. \tag{2}$$

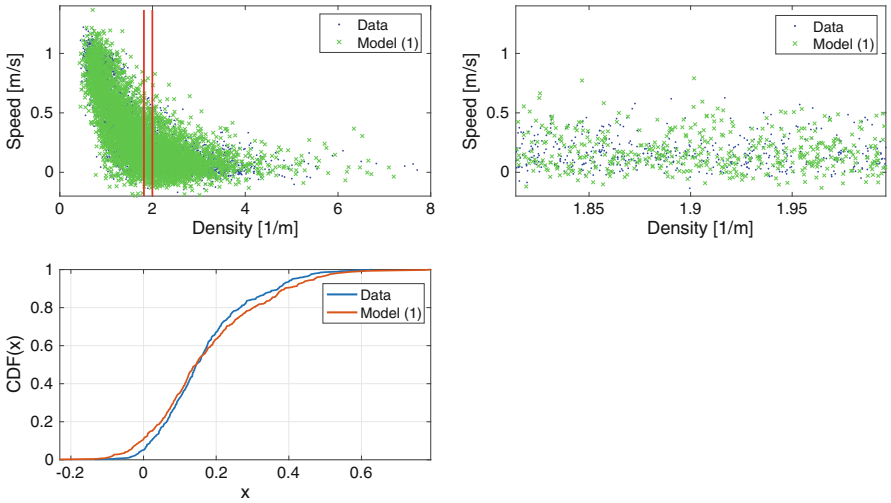

Fig. 2 Comparison of simulated (green) and empirical (blue) speed–density relations with data-binning method (upper plots). Cumulative distribution functions for specific bin (bottom plot)

Finally, the weighted arithmetic mean of distances D_j is used as a quantitative metric estimating the similarity of two data-clouds

$$D^* = \frac{\sum_{j=1}^{N} (N_j^{\text{data}} + N_j^{\text{model}}) D_j}{N^{\text{data}} + N^{\text{model}}}, \tag{3}$$

where N_j^{data} and N_j^{model} are the number of observations in the jth bin for data and model, respectively. In other words, metric D^* quantifies the degree of success (or failure) of the validation process.

3.2 Validity Factor

Verification tests are considered to be relatively simple and are expected to be fulfilled. For each verification test there are only two possible outputs which are 0 (failure) and 1 (success). The quantitative metric for N_{ver} verification tests is

$$\delta_{\text{ver}} = \prod_{k=1}^{N_{\text{ver}}} v_k^{\text{ver}}, \tag{4}$$

where v_k^{ver} is the outcome of the kth verification test.

We quantify the degree of success of the considered pedestrian model for the k-th validation test with $v_k^{\text{val}} \in [0, 1]$. 0 and 1 correspond to complete failure and absolute

success, respectively. The value v_k^{val} is computed according to the methodology described in Sect. 3.1, that is, $v_k^{\text{val}} = 1 - D^*$. To quantify the degree of success for N_{val} validation tests we write

$$\delta_{\text{val}} = \frac{\sum_{k=1}^{N_{\text{val}}} w_k \cdot v_k^{\text{val}}}{N_{\text{val}}}, \tag{5}$$

with a weight w_k equal to 1.

However, in general the parameter values of the model are obtained after a calibration process involving several scenarios simultaneously [6]. In this case we calculate w_k as follows:

$$w_k = \frac{N_{\text{cal}}}{N_{\text{val}}}, \tag{6}$$

where $N_{\text{cal}} \in [0, N_{\text{val}}]$ is a number of scenarios used simultaneously in the calibration procedure. Equation (6) expresses the following assumption: it is less beneficial to get the value v_k^{val} by calibration obtained on the basis of one scenario, that is, $w_k = \frac{1}{N_{\text{val}}}$, than if we get the same value v_k^{val} with the parameter set from calibration with all scenarios simultaneously ($w_k = 1$).

Finally the success estimator of the considered model on the basis of verification and validation tests is as follows:

$$\delta = \delta_{\text{ver}} \times \delta_{\text{val}}. \tag{7}$$

4 Results

We tested this methodology on two continuous pedestrian speed models based on optimal velocity function and specific stochastic additive noises. The noise is white for the first model (Model (1)) [23], while it is determined by the inertial Ornstein–Uhlenbeck process for the second model (Model (2)) [22]. In this section we show only results of one of the validation tests—uni-directional 1D flow. In other validation test (except bottleneck scenario) the fundamental diagram is produced by the measurement module (Jpsreport) using Voronoi diagrams (method D). Figure 3 shows the results. The first row represents speed–density relations calculated on the basis of real trajectories and obtained from simulations of Model (1) and Model (2).

We consider 20 bins for the density partitioning of the validation test and limit the observations for densities not higher than $4\,\text{m}^{-2}$. For both models and each density bin the Kolmogorov–Smirnov distance is calculated (lower-left subplot of Fig. 3), the mean value of which (Eq. (3)) is equal to 0.13 and 0.11 for Model (1) and Model (2), respectively.

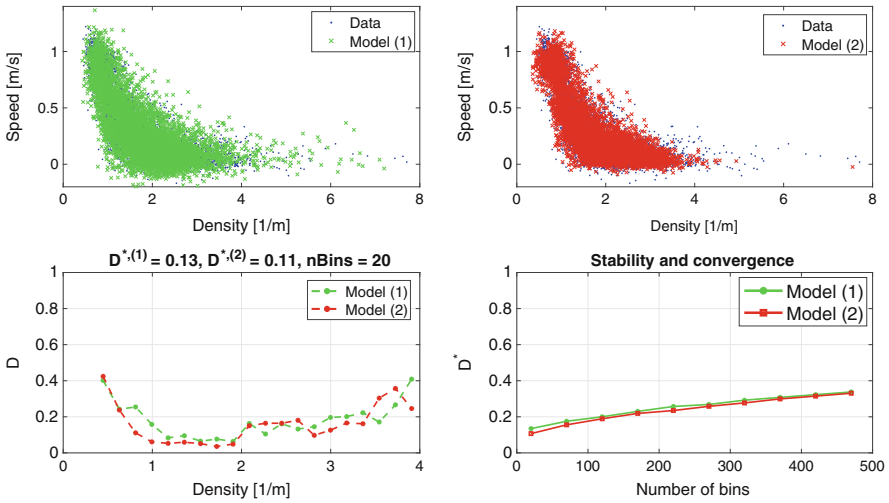

Fig. 3 Uni-directional 1D flow. Fundamental diagrams calculated on the basis of real trajectories and trajectories produced with Model (1) (upper-left) and Model (2) (upper-right). The Kolmogorov–Smirnov distance (2) for each density bin (lower-left). The dependence of the value D^* (3) on the number of density bins N

Moreover, we investigated how the number of density bins N influences the final value D^*. Considering values of N from 20 to 470 we calculated corresponding values of D^* (bottom-right subplot of Fig. 3). Firstly, one can conclude that Model (2) is always better than Model (1), which confirms with the results in [22]. Secondly, for both models the value of D^* is increasing when the number of bins N is increasing. This can be explained by the fact that, with increasing number of bins, the number of points each bin contains becomes more scarce. For example, if a bin contains only two points from each compared data set it is obvious that the Kolmogorov–Smirnov distance (Eq. (2)) will be large.

5 Discussion and Conclusions

In this paper we present a methodology for quantitative assessment of pedestrian models exploiting results of verification and validation tests. However, this procedure can be applied to any space-continuous model describing pedestrian dynamics. Two stochastic pedestrian models were compared using the results of 1D uni-directional flow test. We investigated stability properties of the proposed metric (3) by considering different number of bins for density partitioning. According to the results, the metric for quantitative assessment shows a monotonic increasing behavior.

More generally, the method of quantitative comparison of two data-clouds (here, two fundamental diagrams) using an averaged Kolmogorov–Smirnov distance D^* (Sect. 4) can be interpreted as a separate result. In other words, this method can be used for comparison of two data-clouds of any nature.

The approach for comparison of two data-clouds allows a detailed analysis for different density ranges (lower densities, higher densities) by means of Kolmogorov–Smirnov distances per density interval D_j, $j = 1, \ldots, N$. Analyzing values of D_j, it is possible to determine for which density ranges the underlying model performs better wrt. to experimental data.

Finally, the proposed metric (3) can be used in the calibration procedure as the minimized objective function. We suggest to use the introduced quantity D^* (3) as a goodness of fit function in the calibration procedure.

References

1. Asja, J., Appert-Rolland, C., Lemercier, S., Pettré, J.: Properties of pedestrians walking in line: fundamental diagrams. Phys. Rev. E **85**(85), 9 (2012). https://doi.org/10.1103/PhysRevE.85.036111. http://pre.aps.org/abstract/PRE/v85/i3/e036111
2. Boltes, M., Zhang, J., Seyfried, A., Steffen, B.: T-junction: experiments, trajectory collection, and analysis. In: IEEE Workshop on Modeling, Simulation and Visual Analysis of Large Crowds, vol. 13. International Conference on Computer Vision (ICCV) (2011)
3. Burghardt, S.: Dynamik von personenströmen in sportstadien. Dissertation, Bergische Universität Wuppertal (2013)
4. Burghardt, S., Seyfried, A., Klingsch, W.: Improving egress design through measurement and correct interpretation of the fundamental diagram for stairs. In: Panda, M., Chattaraj, U. (eds.) Developments in Road Transportation, pp. 181–187. Macmillan Publishers India Ltd, Noida (2010)
5. Burghardt, S., Seyfried, A., Klingsch, W.: Fundamental diagram of stairs: Critical review and topographical measurements. In: Weidmann, U., Kirsch, U., Schreckenberg, M. (eds.) Pedestrian and Evacuation Dynamics 2012, pp. 329–344. Springer International Publishing, Cham (2014) https://doi.org/10.1007/978-3-319-02447-9_27
6. Campanella, M., Hoogendoorn, S., Daamen, W.: Quantitative and Qualitative Validation Procedure for General Use of Pedestrian Models, pp. 891–905. Springer International Publishing, Cham (2014). https://doi.org/10.1007/978-3-319-02447-9_74
7. Chattaraj, U., Seyfried, A., Chakroborty, P.: Comparison of pedestrian fundamental diagram across cultures. Adv. Complex Syst. **12**(3), 393–405 (2009). https://doi.org/10.1142/S0219525909002209
8. Holl, S., Seyfried, A.: Laboratory experiments on crowd dynamics. inSiDE **11**(2), 102–103 (2013)
9. Hoogendoorn, S.P., Daamen, W.: Pedestrian behavior at bottlenecks. Transport. Sci. **39**(2), 147–159 (2005). https://doi.org/10.1287/trsc.1040.0102
10. Kemloh, U., Chraibi, M., Zhang, J.: Jupedsim: Jülich pedestrian simulator. https://doi.org/10.5281/zenodo.592209. http://jupedsim.org
11. Kemloh Wagoum, A.U., Chraibi, M., Zhang, J.: Jupedsim: an open framework for simulating and analyzing the dynamics of pedestrians. In: 3rd Conference of Transportation Research Group of India (2015)
12. Kretz, T., Grünebohm, A., Kaufman, M., Mazur, F., Schreckenberg, M.: Experimental study of pedestrian counterflow in a corridor. J. Stat. Mech. **10**, P10001 (2006). https://doi.org/10.1088/1742-5468/2006/10/P10001

13. Kretz, T., Grünebohm, A., Schreckenberg, M.: Experimental study of pedestrian flow through a bottleneck. J. Stat. Mech Theory Exp. **10**, 10014 (2006). https://doi.org/10.1088/1742-5468/2006/10/P10014
14. Liu, X., Song, W., Zhang, J.: Extraction and quantitative analysis of microscopic evacuation characteristics based on digital image processing. Physica A **388**(13), 2717–2726 (2009). https://doi.org/10.1016/j.physa.2009.03.017
15. Moussaid, M., Garnier, S., Theraulaz, G., Helbing, D.: Collective information processing and pattern formation in swarms, flocks and crowds. Top. Cogn. Sci. **1**(3), 469–497 (2009)
16. MSC.1-Circ.1238: Guidelines for evacuation analysis for new and existing passenger ships. Technical report, International Maritime Organization, Marine Safety Committee, London, June 6, 2008. MSC/Circ. 1033
17. Rimea-richtlinie für mikroskopische entfluchtungs-analysen (2007). www.rimea.de
18. Ronchi, E., KuKuligowski, E.D., Reneck, P.A., Peacock, R.D., Nilsson, D.: The process of verification and validation of building fire evacuation models. Technical Report, National Institute of Standards and Technology (2013)
19. Sargent, R.G.: Verification and validation of simulation models. J. Simul. **7**(1), 12–24 (2013). https://doi.org/10.1057/jos.2012.20
20. Schadschneider, A., Klingsch, W., Kluepfel, H., Kretz, T., Rogsch, C., Seyfried, A.: Evacuation dynamics: empirical results, modeling and applications. In: Meyers, R.A. (ed.) Encyclopedia of Complexity and System Science, vol. 5, pp. 3142–3176. Springer, Berlin (2009)
21. Seer, S., Rudloff, C., Matyus, T., Brändle, N.: Validating social force based models with comprehensive real world motion data. Transp. Res. Procedia **2**(0), 724–732 (2014). https://doi.org/10.1016/j.trpro.2014.09.080. http://www.sciencedirect.com/science/article/pii/S2352146514001161. The Conference on Pedestrian and Evacuation Dynamics 2014 (PED 2014), 22–24 October 2014, Delft, The Netherlands
22. Tordeux, A., Schadschneider, A.: White and relaxed noises in optimal velocity models for pedestrian flow with stop-and-go waves. J. Phys. A Math. Theor. (2016). https://doi.org/10.1088/1751-8113/49/18/185101
23. Tordeux, A., Chraibi, M., Seyfried, A.: Collision-Free Speed Model for Pedestrian Dynamics, pp. 225–232. Springer International Publishing, Cham (2016). https://doi.org/10.1007/978-3-319-33482-0_29.

Prediction of Pedestrian Speed with Artificial Neural Networks

Antoine Tordeux, Mohcine Chraibi, Armin Seyfried, and Andreas Schadschneider

Abstract Pedestrian behaviours tend to depend on the type of facility. Accurate predictions of pedestrian movement in complex geometries (including corridor, bottleneck or intersection) are difficult to achieve for models with few parameters. Artificial neural networks have multiple parameters and are able to identify various types of patterns. They could be a suitable alternative for forecasts. We aim in this paper to present first steps testing this approach. We compare estimations of pedestrian speed with a classical model and a neural network for combinations of corridor and bottleneck experiments. The results show that the neural network is able to differentiate the two geometries and to improve the estimation of pedestrian speeds.

1 Introduction

Microscopic pedestrian models are frequently used in traffic engineering to predict crowd dynamics. Classical operational approaches are in general decision-based, velocity-based or force-based models (see [24] and the references therein). Such models consider physical as well as social or psychological factors. They are basic rules or generic functions depending locally on the environment. Few parameters having generally physical interpretations allow to adjust the model.

A. Tordeux (✉) · A. Seyfried
Forschungszentrum Jülich, Jülich, Germany
e-mail: a.tordeux@fz-juelich.de; tordeux@uni-wuppertal.de; a.seyfried@fz-juelich.de
University of Wuppertal, Wuppertal, Germany

M. Chraibi
Forschungszentrum Jülich, Jülich, Germany
e-mail: m.chraibi@fz-juelich.de

A. Schadschneider
University of Cologne, Cologne, Germany
e-mail: as@thp.uni-koeln.de

S. H. Hamdar (ed.), *Traffic and Granular Flow '17*,
https://doi.org/10.1007/978-3-030-11440-4_36

Before applying simulations to make predictions, the model parameters have to be calibrated and the models have to be validated, experimentally or statistically by using real data. The validation can be carried out by checking whether the models are able to describe the dynamics accurately for configurations different from the ones used for the calibration (cross-validation) [28]. A good model should provide realistic dynamics in different conditions (i.e. different geometries, initial or boundary conditions) for the same setting of the parameters.

The parameter for the convection part of the models (for instance, desired speed or time gap) can be referred to the fundamental diagram (FD), a phenomenological relation between speed and surrounding distance spacing to the neighbours and obstacles [25]. This relation can be explicitly used to model the speed of the pedestrian and is then related to *optimal velocity*, a concept borrowed from traffic modelling [2], see, e.g., [15, 18, 19]. It is also used as an implicit relation (see, e.g., [3, 10, 11]) that is determined by considering uni-dimensional flows [4]. By neglecting anisotropic effects in the models (such as the vision-based effect), microscopic models can be characterised at an aggregated level by fundamental diagrams determining a speed to a local density given by the mean distance spacing to the closest neighbours [6]. In the following we refer a model simply based on a fundamental diagram as *FD-based model*.

Despite of their simplicity, microscopic models can describe realistic pedestrian flows, as well as self-organisation phenomena such as lane formation or alternation of flow at a bottleneck in bi-directional streams [12, 24]. However, the prediction of pedestrian movement in complex spatial structures (e.g. buildings like stadia or stations) remains problematic. Observations show that pedestrians tend to adapt their behaviour according to the facilities [5]. For instance, the flow tends to locally increase at bottlenecks [20, 26, 30]. This leads to geometry-dependent characteristics and makes aggregated models based on a single fundamental diagram unable to accurately describe transitions between different types of facilities (such as corridor, T-junction, crossing or bottleneck), as well as from platforms to stairs.

An alternative data-driven approach for the prediction of pedestrian dynamics in complex geometries could be provided by using artificial neural networks (ANN). Neural networks have already proven their efficiency for motion planning in robotic or autonomous vehicles [13, 23], and start to be used for pedestrian dynamics as well [1, 6, 8, 16]. Such approach is data based and, by opposition to classical models, has artificially a very large number of parameters with no explicit physical meaning (see Fig. 1). ANN can reproduce complex patterns that FD-based models, describing dynamics at an aggregated level, cannot.

The aim of this work is to evaluate whether ANN could accurately describe pedestrian behaviour for different types of geometries. A feed-forward neural network is compared to a FD-based model with data gained by experiments at bottleneck and corridor with closed boundary conditions (in the following 'bottleneck' and 'ring' experiments) [7, 27]. The performances (i.e. the fundamental diagram) significantly differ according to the spatial structure. Training and testing (cross-validation) are carried out for different combinations of bottleneck and ring experiments. The results show that the neural network is able to identify the spatial

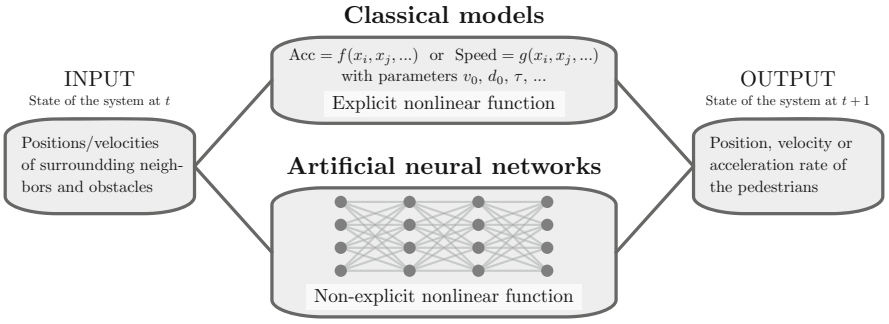

Fig. 1 Minimalistic illustrative scheme for the distinction between FD-based models, which are explicit non-linear functions calibrated by few meaningful parameters, and neural networks, for which the non-linear function is data based and has deliberately a large number of parameters

structure of the facility and improve the prediction in case of mixed structures. The data and the models used are presented in Sects. 2 and 3. The fitting of the neural network is proposed in Sect. 4 while the comparison to the FD-based model over combinations of bottleneck and ring experiments is given in Sect. 5. Conclusions are presented in Sect. 6.

2 Models

The pedestrian modelling approaches are continuous speed models based on the $K = 10$ closest neighbours. We denote in the following (x, y) as the position of the considered agent, v as its speed and $\big((x_i, y_i), i = 1, \ldots, K\big)$ as the positions of the K closest neighbours.

The first modelling approach is the Weidmann model for the fundamental diagram [29] for which the speed is a function of the mean spacing (i.e. the local density)

$$v = \mathrm{FD}(\bar{s}_K, v_0, T, \ell) = v_0\Big(1 - e^{\frac{\ell - \bar{s}_K}{v_0 T}}\Big). \tag{1}$$

Here $\bar{s}_K = \frac{1}{K}\sum_{i=1}^{K}\sqrt{(x - x_i)^2 + (y - y_i)^2}$ is the mean spacing with the $K = 10$ closest neighbours while the time gap T, the pedestrian size ℓ and the desired speed v_0 are the parameters of the model.

The second modelling approach is a feed-forward artificial neural network with hidden layers H

$$v = \mathrm{NN}\big(H, \bar{s}_K, (x_i - x, y_i - y, 1 \le i \le K)\big). \tag{2}$$

The network has $2K + 1$ inputs: the mean spacing and the K relative positions. The number of parameters in the network depends on the number of nodes in the hidden layers.

3 Data

Two datasets obtained in laboratory conditions are used to compare the FD-based and ANN modelling approaches. The data are available on the internet (see [27]). They are part of the online database of pedestrian experiments [7]. The first dataset, denoted R and called the ring experiment, comes from an experiment done on a closed geometry of length 30 m and width 1.8 m for different density levels (ranging from 0.25 to 2 ped/m^2—the participant number ranges from 15 to 230). The second dataset, denoted B, is an experiment for a bottleneck geometry. The width of the system in front of the bottleneck is 1.8 m while the width of the bottleneck varies (from 0.70, 0.95, 1.20 to 1.80 m—150 participants by experiment). See [27] for details on the data. The flow and density are measured every 10 s to deal with pseudo-independent measurements. Each sample contains around $N = 2000$ observations.

The two datasets describe two different interaction behaviours (see Fig. 2). The speed for a given mean spacing tends to be higher in the bottleneck than on the ring when the system is congested. Consequently the estimation of the time gap significantly differs according to the geometry (see Table 1).

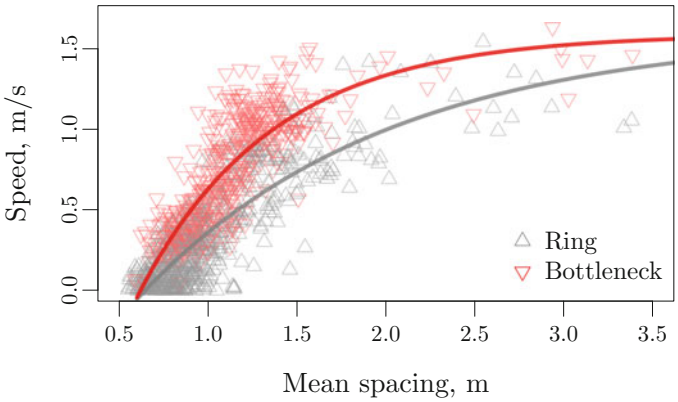

Fig. 2 Observations of the pedestrian speeds as function of the mean spacing with the ten closest neighbours for the ring and bottleneck experiments. Two distinct relationships can be identified

Table 1 Fitting of the time gap T, the pedestrian size ℓ and the desired speed v_0 parameters of the Weidmann model on the ring and bottleneck experiment

Experiment	R	B
ℓ (m)	0.64	0.61
T (s)	0.86	0.48
V_0 (m/s)	1.60	1.58

The time gap significantly differs according to the geometry

4 Fitting the Neural Network

The neural network is fitted with cross-validation and bootstrap [14, 17] over 50 subsamples. The training is performed using half of the data while the network is tested on the remaining. The training is carried out with the back-propagation method [22] on the normalised data, by minimising from the top to the bottom of the network the mean square error

$$\text{MSE} = \frac{1}{N} \sum_i \left(v_i - \tilde{v}_i\right)^2, \tag{3}$$

with v_i the observed speed, $\tilde{v}_i$ the predicted speed and N the number of observations. The computation is done with the statistical software R [21] and the package `neuralnet` [9].

The different hidden layers (1), (2), (3), (4,2), (5,2), (5,3), (6,3), (10,4) and (12,5) are tested (see Fig. 3). As expected, the training error tends to decrease as the complexity of the network increases, while the testing error shows a minimum before overfitting. Such a minimum is reached for the single hidden layer $H = (3)$ with three nodes. Note that here the calibration is done on a combination of the ring and bottleneck experiment datasets. Yet similar results are obtained when calibrating separately on the ring and on the bottleneck datasets.

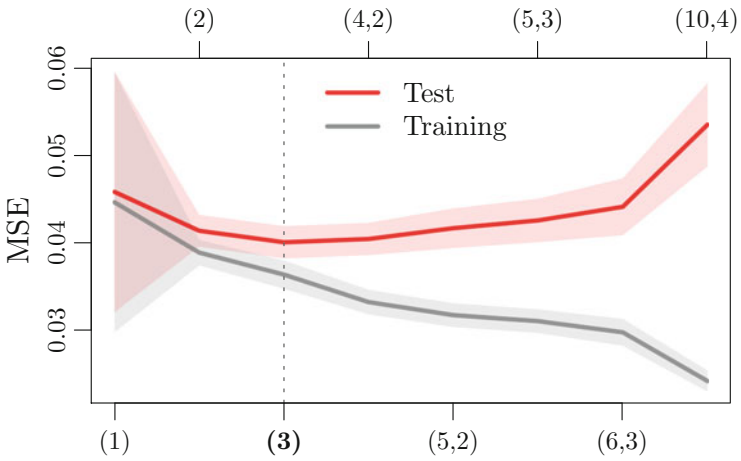

Fig. 3 Training and testing errors according to different hidden layer in the network. The curves correspond to the average of 50-bootstrap estimates while the bands describe the standard deviation. The training error systematically decreases as network complexity increases while the testing error admits a minimum for hidden $H = (3)$

5 Model Comparison

The calibrated FD-model and the trained neural network with $H = 3$ are compared to different combinations of data of the ring R and bottleneck B experiments. Here the first argument in the notation '$./.$' corresponds to the training phase, while the second argument corresponds to the testing phase. The testing errors are presented in Fig. 4. The modelling approaches are firstly analysed on the identical sets R/R and B/B. Here the network is slightly better than the FD-model. For the ring experiment, the performances are relatively homogeneous and the MSE is only approximately 5% smaller by using the network. While for the bottleneck, the performances fluctuate more and the improvement is more significant (around 15%). The improvement is also significant when the approaches deal with unobserved situations, i.e. for the datasets R/B and B/R (around 15%). The best results are obtained when training the models on the combination of ring and bottleneck experiments, i.e. the scenarios R/R+B, B/R+B and R+B/R+B. As shown in Fig. 5 and Table 2, the network is able in such situation to partially differentiate the two geometries and to improve the speed estimation by a factor of approximately 20%. The orders of improvement are similar to the ones obtained in [1] with the social LSTM neural network and the social force pedestrian model [11].

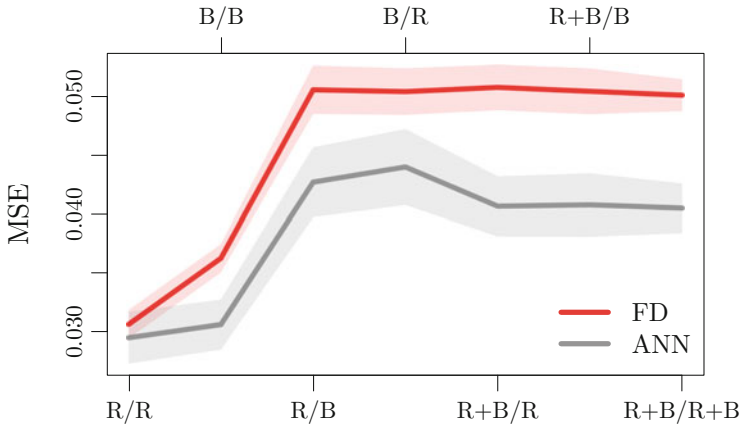

Fig. 4 Testing error of the FD-model and the neural network according to combinations of the ring R and bottleneck B experiments. The curves correspond to the average of 50-bootstrap estimates while the bands describe the standard deviation. The improvement of the speed is significant by using the network when the experiments are mixed (i.e. R+B)

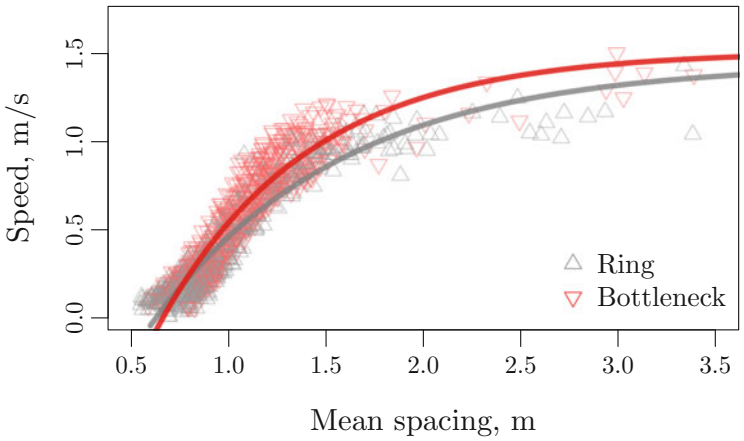

Fig. 5 Prediction by the neural network of the pedestrian speed for the R+B/R+B training and testing datasets. The network is able to, at least partially, identify the two geometries. As observed in the real data, the speed for a given mean spacing is in average in the bottleneck higher than the flow in the corridor for congested situations

Table 2 Fitting of the time gap T, the pedestrian size ℓ and the desired speed v_0 parameters for the data predicted by the neural network

Experiment	R	B
ℓ (m)	0.63	0.66
T (s)	0.68	0.50
V_0 (m/s)	1.44	1.51

6 Conclusion

The data-driven approach using an artificial neural network is able to distinguish pedestrian performances in ring and bottleneck experiments from the relative positions of the $K = 10$ closest neighbours and the mean spacing. Consequently, we observe that the speed prediction for mixed data can be improved by a factor up to 20% by using a network compared to an aggregated model based on fundamental diagrams.

The results are first steps suggesting that neural networks could be suitable tools for the prediction of pedestrian dynamics in complex geometries. Yet, the simulation of the networks remains to be carried out over full trajectories and compared to the performances obtained with existing models and notably anisotropic models. Furthermore, other inputs, hidden layers and training on different geometries have to be investigated. Especially, one remains to test the complexity necessary to the network for accurate precisions regarding to the size and heterogeneity of the datasets.

Acknowledgements Financial supports by the German Science Foundation (DFG) under grants SCHA 636/9-1 and SE 1789/4-1 are gratefully acknowledged.

References

1. Alahi, A., Goel, K., Ramanathan, V., Robicquet, A., Fei-Fei, L., Savarese, S.: Social LSTM: human trajectory prediction in crowded spaces. In: IEEE ICCV Conference, pp. 961–971 (2016)
2. Bando, M., Hasebe, K., Nakayama, A., Shibata, A., Sugiyama, Y.: Dynamical model of traffic congestion and numerical simulation. Phys. Rev. E **51**(2), 1035–1042 (1995)
3. Chraibi, M., Seyfried, A., Schadschneider, A.: Generalized centrifugal-force model for pedestrian dynamics. Phys. Rev. E **82**(4), 046111 (2010)
4. Chraibi, M., Ezaki, T., Tordeux, A., Nishinari, K., Schadschneider, A., Seyfried, A.: Jamming transitions in force-based models for pedestrian dynamics. Phys. Rev. E **92**, 042809 (2015)
5. Daamen, W.: Modelling passenger flows in public transport facilities. Dissertation, TU Delft (2004)
6. Das, P., Parida, M., Katiyar, V.K.: Analysis of interrelationship between pedestrian flow parameters using artificial neural network. J. Mod. Transport. **23**(4), 298–309 (2015)
7. Forschungszentrum Jülich: Dataset of experiments with pedestrians. http://ped.fz-juelich.de/database
8. Fragkiadaki, K., Levine, S., Felsen, P., Malik, J.: Recurrent network models for human dynamics. In: IEEE ICCV Conference, pp. 4346–4354 (2015)
9. Fritsch, S., Guenther, F., Suling, M.: neuralnet: training of neural networks. http://CRAN.R-project.org/package=neuralnet (2012)
10. Guo, R., Wong, S., Huang, H., Zhang, P., Lam, W.: A microscopic pedestrian-simulation model and its application to intersecting flows. Physica A **389**(3), 515–526 (2010)
11. Helbing, D., Molnár, P.: Social force model for pedestrian dynamics. Phys. Rev. E **51**(5), 4282–4286 (1995)
12. Helbing, D., Buzna, L., Johansson, A., Werner, T.: Self-organized pedestrian crowd dynamics: experiments, simulations, and design solutions. Transport. Sci. **39**(1), 1–24 (2005)
13. Jackel, L., Hackett, D., Krotkov, E., Perschbacher, M., Pippine, J., Sullivan, C.: How DARPA structures its robotics programs to improve locomotion and navigation. Commun. ACM **50**(11), 55–59 (2007)
14. Kohavi, R.: A study of cross-validation and bootstrap for accuracy estimation and model selection. In: IJCAI'95 Conference, pp. 1137–1143. Morgan Kaufmann, San Francisco (1995)
15. Lv, W., Song, W.G., Ma, J., Fang, Z.M.: A two-dimensional optimal velocity model for unidirectional pedestrian flow based on pedestrian's visual hindrance field. IEEE Trans. Intell. Transp. Syst. **14**(4), 1753–1763 (2013)
16. Ma, Y., Lee, E.W.M., Yuen, R.K.K.: An artificial intelligence-based approach for simulating pedestrian movement. IEEE Trans. Intell. Transp. Syst. **17**(11), 3159–3170 (2016)
17. Mooney, C., Duval, R.: Bootstrapping: A Nonparametric Approach to Statistical Inference. 94–95. Sage Publications, Thousand Oaks (1993)
18. Moussaïd, M., Guillot, E., Moreau, M., Fehrenbach, J., Chabiron, O., Lemercier, S., Pettré, J., Appert-Rolland, C., Degond, P., Theraulaz, G.: Traffic instabilities in self-organized pedestrian crowds. PLOS Comput. Biol. **8**(3), 1–10 (2012)
19. Nakayama, A., Hasebe, K., Sugiyama, Y.: Instability of pedestrian flow and phase structure in a two-dimensional optimal velocity model. Phys. Rev. E **71**, 036121 (2005)
20. Parisi, D., Patterson, G.: Influence of bottleneck lengths and position on simulated pedestrian egress. Pap. Phys. **9**, 090001 (2017)
21. R Core Team: R: A Language and Environment for Statistical Computing. R Foundation for Statistical Computing (2014). http://www.R-project.org/

22. Rumelhart, D., Hinton, G., Williams, R.: Learning representations by back-propagating errors. Nature **323**, 533–536 (1986)
23. Sadati, N., Taheri, J.: Solving robot motion planning problem using Hopfield neural network in a fuzzified environment. In: IEEE FS Conference, vol. 2, pp. 1144–1149 (2002)
24. Schadschneider, A., Klingsch, W., Klüpfel, H., Kretz, T., Rogsch, C., Seyfried, A.: Evacuation dynamics: empirical results, modeling and applications. In: Encyclopedia of Complexity and Systems Science, pp. 3142–3176. Springer, New York (2009)
25. Seyfried, A., Steffen, B., Klingsch, W., Boltes, M.: The fundamental diagram of pedestrian movement revisited. J. Stat. Mech. Theory Exp. **2005**(10), P10002 (2005)
26. Seyfried, A., Passon, O., Steffen, B., Boltes, M., Rupprecht, T., Klingsch, W.: New insights into pedestrian flow through bottlenecks. Transport. Sci. **43**(3), 395–406 (2009)
27. Tordeux, A., Chraibi, M., Seyfried, A., Schadschneider, A.: Data from: Prediction of pedestrian speed with artificial neural networks (2017). https://doi.org/10.5281/zenodo.1054017
28. Treiber, M., Kesting, A.: Traffic Flow Dynamics. Springer, Berlin (2013)
29. Weidmann, U.: Transporttechnik der Fußgänger. Technical Report, Schriftenreihe des IVT Nr. 90 (ETH Zürich) (1994)
30. Zhang, J., Seyfried, A.: Experimental studies of pedestrian flows under different boundary conditions. In: ITSC IEEE Conference, pp. 542–547 (2014)

Noise-Induced Stop-and-Go Dynamics

Antoine Tordeux, Andreas Schadschneider, and Sylvain Lassarre

Abstract Stop-and-go waves are commonly observed in traffic and pedestrian flows. In traffic theory, they are described by phase transitions of metastable models. The self-organisation phenomenon occurs due to inertia mechanisms but requires fine tuning of the parameters. Here, a novel explanation for stop-and-go waves based on stochastic effects is presented for pedestrian dynamics. We show that the introduction of specific coloured noises in a stable microscopic model allows to describe realistic pedestrian stop-and-go behaviour without requirement of metastability and phase transition. We compare simulation results of the stochastic model to real pedestrian trajectories and discuss plausible values for the model's parameters.

1 Introduction

Stop-and-go waves in traffic flow is a fascinating collective phenomenon that attracted the attention of scientists for several decades [15, 19, 25] (see [7, 18] for reviews). Curiously, congested flows self-organise in waves of slow and fast traffic (stop-and-go) instead of streaming homogeneously. Stop-and-go dynamics are observed in road traffic, bicycle and pedestrian movements [39] in reality as well as during experiments, where the disturbance due to the infrastructure cannot explain

A. Tordeux (✉)
Forschungszentrum Jülich, Jülich, Germany
e-mail: a.tordeux@fz-juelich.de; tordeux@uni-wuppertal.de
University of Wuppertal, Wuppertal, Germany

A. Schadschneider
University of Cologne, Cologne, Germany
e-mail: as@thp.uni-koeln.de

S. Lassarre
IFSTTAR COSYS GRETTIA, Marne la Vallée Cedex 2, France
e-mail: sylvain.lassarre@ifsttar.fr

S. H. Hamdar (ed.), *Traffic and Granular Flow '17*,
https://doi.org/10.1007/978-3-030-11440-4_37

their presence [28]. Besides its scientific interest, such self-organisation phenomena impact transportation networks in terms of safety, economy and comfort.

Stop-and-go behaviours are often analysed with microscopic, mesoscopic (kinetic) and macroscopic models based on non-linear differential systems (see, for instance, [2, 8, 13]), but also with discrete models like cellular automata. The models based on systems of differential equations have homogeneous equilibrium solutions that can be unstable for certain values of the parameters. Periodic or quasi-periodic solutions in unstable cases describe non-homogeneous dynamics, with potentially stop-and-go waves for fine tuning of the parameters, while the stable cases describe homogeneous dynamics.

Phase transition and metastability in self-driven dynamical systems far from the equilibrium are commonly observed in physics, theoretical biology or social science [3–5, 16, 35]. In traffic, typical continuous models are inertial second order systems based on relaxation processes. Stop-and-go and matching to Korteweg–de Vries (KdV) and modified KdV soliton equations occur when the inertia of the vehicles exceeds critical values [2, 24, 30]. Empirical evidence for phase transitions in traffic, like hysteresis or capacity drop, has been observed in real data as well as during experiments [19, 28]. Yet the number of phases and their characteristics remain actively debated [34].

Some studies describe pedestrian stop-and-go dynamics by means of, as traffic models, instability and phase transitions [20, 21, 23, 26]. However, to the best of our knowledge, empirical evidence for phase transitions and metastability has not been observed for pedestrian flow. Pedestrian dynamics shows no pronounced inertia effect since human capacity nearly allows any speed variation at any time. Furthermore, pedestrian motion does not show mechanical delays. Nevertheless, stop-and-go behaviour is observed at congested density levels [27, 39].

In this work, we propose a novel explanation of stop-and-go phenomena in pedestrian flows as a consequence of stochastic effects. We first present statistical evidence for the existence of Brownian noise in pedestrian speed time series. Then a microscopic model composed of a minimal deterministic part for the convection and a relaxation process for the noise is proposed and analysed. Simulation results show that the stochastic approach allows to describe realistic pedestrian stop-and-go dynamics without metastability for large tuning of the parameters.

2 Definition of the Stochastic Model

Stochastic effects can have various roles in the dynamics of self-driven systems [11]. Generally speaking, the introduction of white noise in models tends to increase the disorder in the system [35] or to prevent self-organisation [14], while coloured noises can affect the dynamics and generated complex patterns [1, 6]. Coloured noise has been observed in human response [9, 38]. Pedestrian as well as driver behaviours result from complex human cognition. They are intrinsically stochastic in the sense that the deterministic modelling of the driving, i.e. the modelling of the

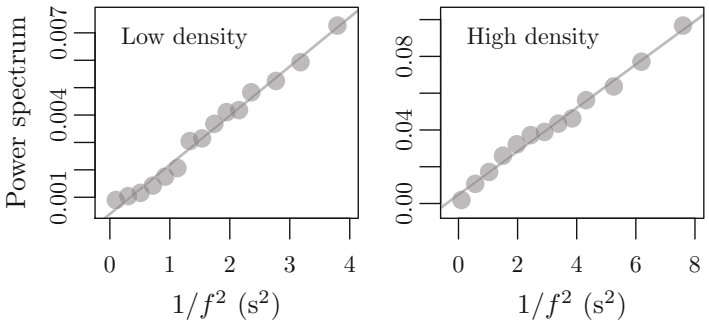

Fig. 1 Periodogram power spectrum estimate for the speed time series of pedestrians at low and high density levels. The power spectrum is roughly proportional to the inverse of square frequency $1/f^2$. This is a typical characteristic of a Brownian noise

human cognition composed of up to 10^{11} neurons [37], is not possible. Furthermore the behaviour of a pedestrian, as well as a driver, may be influenced by multiple factors, e.g. experience, culture, environment, psychology, etc. Stochastic effects and notion of noise are the main emphasis of many pedestrian or road traffic modelling approaches (see, e.g., white noises [12, 30], pink-noise [29], action-point [36], or again inaccuracies or risk-taking behaviour [10, 33]).

Figure 1 presents statistical evidences for the existence of a Brownian noise in time series of pedestrian speeds. Such a noise has power spectral density (PSD) proportional to the inverse of the square noise frequency $1/f^2$. A characteristic linear tendency is observed independent of the density (see [31] for details on the data). Such a noise with exponentially decreasing time-correlation function can be described by using the Ornstein–Uhlenbeck process (see, e.g. [22]).

We denote in the following $x_k(t)$ the curvilinear position of the pedestrian k at time t. The pedestrian $k+1$ is the predecessor of k. The model is the Langevin equation

$$\begin{cases} \mathrm{d}x_k(t) = V\big(x_{k+1}(t) - x_k(t)\big)\,\mathrm{d}t + \varepsilon_k(t)\,\mathrm{d}t, \\ \mathrm{d}\varepsilon_k(t) = -\frac{1}{\beta}\varepsilon_k(t)\,\mathrm{d}t + \alpha\,\mathrm{d}W_k(t). \end{cases} \tag{1}$$

Here $V : s \mapsto V(s)$ is a differentiable and non-decreasing *optimal velocity* (OV) function for the convection [2], while $\varepsilon_k(t)$ is a noise described by the Ornstein–Uhlenbeck stochastic process. In the following, an affine function $V(s) = \frac{1}{T}(s - \ell)$ is used with T the time gap between the agents and ℓ their size. The quantities (α, β) are positive parameters related to the noise. α is the volatility, while β is the noise relaxation time. $W_k(t)$ is a Wiener process. Note that alternatively, the model can be defined as the special stochastic form of the full velocity difference model [17] $\ddot{x}_k = \big[V(x_{k+1} - x_k) - \dot{x}_k\big]/\beta + V'(x_{k+1} - x_k)(\dot{x}_{k+1} - \dot{x}_k) + \alpha\xi_k$, where ξ_k is a white noise.

Considering a line of n agents with periodic boundary conditions, the system is

$$\begin{cases} \mathrm{d}\eta(t) = (A\eta(t) + a)\,\mathrm{d}t + b\,\mathrm{d}w(t) \\ \text{with} \quad \eta(t) = {}^{\mathrm{T}}\big(x_1(t), \varepsilon_1(t), \ldots, x_n(t), \varepsilon_n(t)\big) \in \mathbb{R}^{2n} \\ A = \begin{bmatrix} R & S & \\ & \ddots & \\ S & & R \end{bmatrix} \in \mathbb{R}^{2n\times 2n} \text{ with } R = \begin{bmatrix} -1/T & 1 \\ 0 & -1/\beta \end{bmatrix} \text{ and } S = \begin{bmatrix} 1/T & 0 \\ 0 & 0 \end{bmatrix} \\ a = -\frac{\ell}{T}\,{}^{\mathrm{T}}(1, 0, \ldots, 1, 0) \in \mathbb{R}^{2n} \text{ and } b = \alpha\,{}^{\mathrm{T}}(0, 1, \ldots, 0, 1) \in \mathbb{R}^{2n}. \end{cases} \tag{2}$$

Here $w(t)$ is a $2n$-vector of independent Wiener processes. Such a linear stochastic process is Markovian. It has a normal distribution with expectation $m(t)$ and variance/covariance matrix $C(t)$ such that, by using the Fokker–Planck equation,

$$\dot{m}(t) = Am(t) + a \qquad \text{and} \qquad \dot{C}(t) = AC(t) + (C(t))^{\mathrm{T}}A + \mathrm{diag}(b) \tag{3}$$

with $m(0) = \eta_0$ and $C(0) = 0$. The expected value $m(t)$ is asymptotically the homogeneous solution for which $x_{k+1}(t) - x_k(t) = L/n$ and $\varepsilon_k(t) = 0$ for all k and t, L being the length of the system. The roots (λ_1, λ_2) of the characteristic equation for the homogeneous configuration

$$\big[\lambda + \tfrac{1}{T}\big(1 - e^{i\theta}\big)\big]\big[\lambda + 1/\beta\big] = 0 \tag{4}$$

have strictly negative real parts for any $\theta \in (0, 2\pi)$. Therefore the homogeneous solution is stable for the system (2) for any values of the parameters. Note that the more unstable configuration is the one with maximal period for which $\theta \to 0$.

3 Numerical Experiments

The system (2) is simulated using an explicit Euler–Maruyama numerical scheme with time step $\delta t = 0.01\,\mathrm{s}$. The parameter values are $T = 1\,\mathrm{s}$, $\ell = 0.3\,\mathrm{m}$, $\alpha = 0.1\,\mathrm{ms}^{-3/2}$ and $\beta = 5\,\mathrm{s}$. Such values are close to the statistical estimates for pedestrian flow presented in [31]. The length of the system is $L = 25\,\mathrm{m}$, corresponding to the experimental situation, and the boundary conditions are periodic.

Simulations are carried out for systems with $n = 25$, 50 and 75 agents with the stochastic model Eq. (2) and the unstable deterministic optimal velocity model introduced in [32] from jam initial condition. The mean time-correlation functions for the distance spacing in stationary state (i.e. for large simulation time) are presented in Fig. 2. The peaks of the time-correlations match for both stochastic and deterministic models, i.e. the frequency of the stop-and-go waves are the same. A wave propagate backward in the system at a speed $c = -\ell/T$, while vehicles travel in average at the speed $v = (L/n - \ell)/T$. In adequacy with the first order LWR theory, the wave period is $L/(v - c) = nT$.

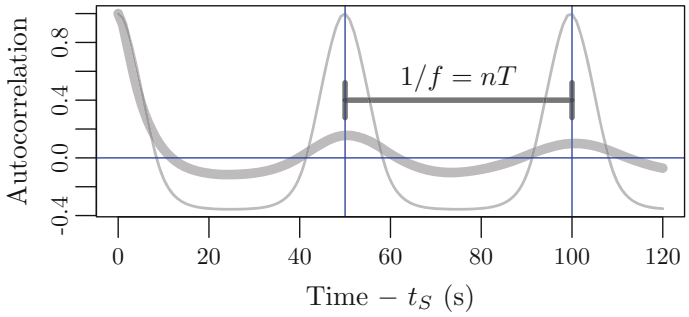

Fig. 2 Mean time-correlation function of the distance spacing for the stochastic and deterministic models in stationary state. The same period $1/f = nT$ for the stop-and-go waves is observed. The simulation time to consider the system stationary is $t_S = 2{\cdot}10^5$ s

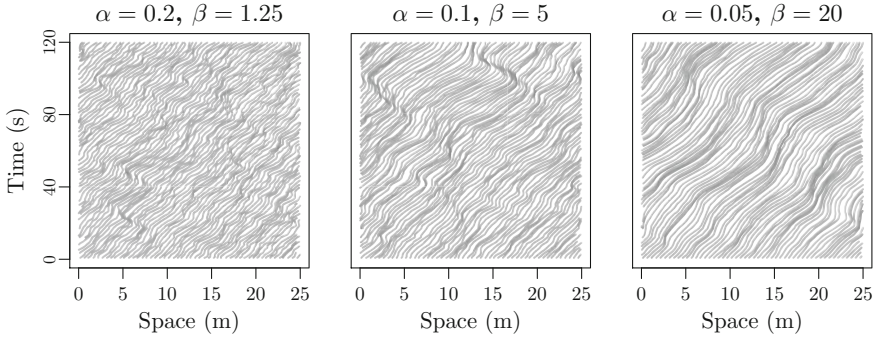

Fig. 3 Simulated trajectories for different values of the noise parameters (units: α in $\mathrm{ms}^{-3/2}$, β in s). The initial configuration is homogeneous. Here $n = 50$ agents are considered

Some experiments are carried out for different values of the noise parameters α and β. In Fig. 3, the trajectories of 50 agents are presented for $\alpha = 0.05$, 0.1 and 0.2 $\mathrm{ms}^{-3/2}$, while $\beta = 1.25$, 5 and 20 s (the values are set in order to keep the amplitude of the noise $\sigma = \alpha\sqrt{\beta/2}$ constant). The noise tends to be white when β is low, while the noise autocorrelation is high for large relaxation times β. Unstable waves emerge locally and disappear when β is small (i.e. for a white noise, see Fig. 3, left panel), while stable waves with large amplitude occur for high β (Fig. 3, right panel). The parameters of the noise influence the amplitude of the time-correlation function, but not the frequency that only depends on the parameters n and T, see Fig. 4.

Figure 5 presents the real trajectories for experiments with 28, 45 and 62 participants (see [31]) and simulations with the stochastic model. The simulations are in good agreement with the data. Stop-and-go waves appear for semi-congested ($n = 45$) and congested ($n = 62$) states, while free states ($n = 28$) seem homogeneous in both empirical data and simulation.

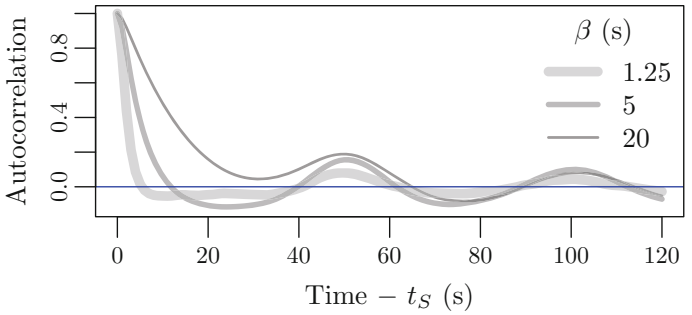

Fig. 4 Mean time-correlation function of the distance spacing in the stationary state for different values of the noise parameters. The noise parameters do not influence the frequency of the waves (that only depends on n and T). The simulation delay time is $t_S = 2{\cdot}10^5$ s

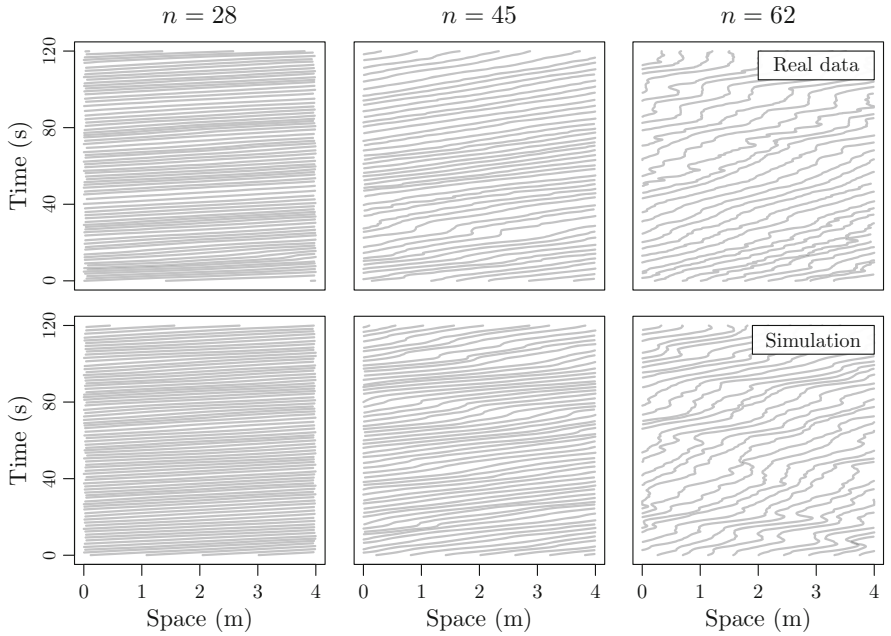

Fig. 5 Real (top panels) and simulated (bottom panels) trajectories for different densities. The initial configuration is homogeneous in both real experiments and the simulation

4 Discussion

We have proposed an original explanation for stop-and-go phenomena in pedestrian flows as the consequence of a coloured noise in the dynamics of the speed. In this stochastic approach, oscillations in the system are due to the perturbations provided by the noise. Such a mechanism qualitatively describes stop-and-go

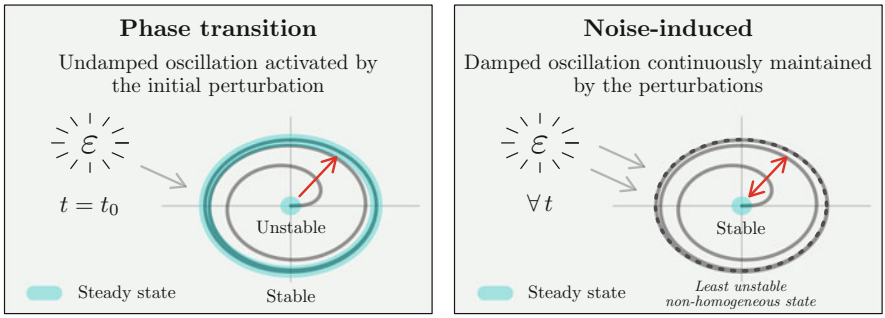

Fig. 6 Illustrative scheme for the modelling of stop-and-go dynamics with phase transition in the periodic solution (left panel) and the noise-induced oscillating behaviour (right panel)

waves, especially when the system is poorly damped. The approach differs from classical deterministic traffic models with inertia for which stop-and-go occurs due to metastability and phase transitions to periodical dynamics (see Fig. 6).

Two mechanisms based on relaxation processes are identified for the description of stop-and-go waves. In the novel stochastic approach, the relaxation time is related to the noise and is estimated to approximately 5 s [31]. The parameter corresponds to the mean time period of the stochastic deviations from the phenomenological equilibrium state. Such a time can be high, especially when the deviations are small and the spacings are high. In the classical inertial approaches, the relaxation time is interpreted as the driver/pedestrian reaction time and is estimated by around 0.5–1 s.

Acknowledgements The authors thank Prof. Michel Roussignol for his help in the formulation of the model. Financial support by the German Science Foundation under grant SCHA 636/9-1 is gratefully acknowledged.

References

1. Arnold, L., Horsthemke, W., Lefever, R.: White and coloured external noise and transition phenomena in nonlinear systems. Z. Phys. B Condens. Matter **29**(4), 367–373 (1978)
2. Bando, M., Hasebe, K., Nakayama, A., Shibata, A., Sugiyama, Y.: Dynamical model of traffic congestion and numerical simulation. Phys. Rev. E **51**(2), 1035–1042 (1995)
3. Ben-Jacob, E., Schochet, O., Tenenbaum, A., Cohen, I., Czirok, A., Vicsek, T.: Generic modelling of cooperative growth patterns in bacterial colonies. Nature **368**, 46–49 (1994)
4. Buhl, J., Sumpter, D.J.T., Couzin, I.D., Hale, J.J., Despland, E., Miller, E.R., Simpson, S.J.: From disorder to order in marching locusts. Science **312**(5778), 1402–1406 (2006)
5. Bussemaker, H., Deutsch, A., Geigant, E.: Mean-field analysis of a dynamical phase transition in a cellular automaton model for collective motion. Phys. Rev. Lett. **78**, 5018–5021 (1997)
6. Castro, F., Sánchez, A.D., Wio, H.S.: Reentrance phenomena in noise induced transitions. Phys. Rev. Lett. **75**, 1691–1694 (1995)
7. Chowdhury, D., Santen, L., Schadschneider, A.: Statistical physics of vehicular traffic and some related systems. Phys. Rep. **329**(4–6), 199–329 (2000)

8. Colombo, R.: Hyperbolic phase transitions in traffic flow. SIAM J. Appl. Math. **63**(2), 708–721 (2003)
9. Gilden, D., Thornton, T., Mallon, M.: $1/f$ noise in human cognition. Science **267**(5205), 1837–1839 (1995)
10. Hamdar, S., Mahmassani, H., Treiber, M.: From behavioral psychology to acceleration modeling: calibration, validation, and exploration of drivers' cognitive and safety parameters in a risk-taking environment. Transp. Res. B Methodol. **78**, 32–53 (2015)
11. Hänggi, P., Jung, P.: Colored Noise in Dynamical Systems, pp. 239–326. Wiley, New York (2007)
12. Helbing, D., Molnár, P.: Social force model for pedestrian dynamics. Phys. Rev. E **51**(5), 4282–4286 (1995)
13. Helbing, D., Treiber, M.: Gas-kinetic-based traffic model explaining observed hysteretic phase transition. Phys. Rev. Lett. **81**, 3042–3045 (1998)
14. Helbing, D., Farkas, I., Vicsek, T.: Freezing by heating in a driven mesoscopic system. Phys. Rev. Lett. **84**(6), 1240–1243 (2000)
15. Herman, R., Montroll, E., Potts, R., Rothery, R.: Traffic dynamics: analysis of stability in car following. Oper. Res. **7**(1), 86–106 (1959)
16. Hermann, G., Touboul, J.: Heterogeneous connections induce oscillations in large-scale networks. Phys. Rev. Lett. **109**, 018702 (2012)
17. Jiang, R., Wu, Q., Zhu, Z.: Full velocity difference model for a car-following theory. Phys. Rev. E **64**, 017101 (2001)
18. Kerner, B.: The Physics of Traffic. Springer, Berlin (2004)
19. Kerner, B.S., Rehborn, H.: Experimental properties of phase transitions in traffic flow. Phys. Rev. Lett. **79**, 4030–4033 (1997)
20. Kuang, H., Fan, Y., Li, X., Kong, L.: Asymmetric effect and stop-and-go waves on single-file pedestrian dynamics. Procedia Eng. **31**, 1060–1065 (2012)
21. Lemercier, S., Jelic, A., Kulpa, R., Hua, J., Fehrenbach, J., Degond, P., Appert-Rolland, C., Donikian, S., Pettré, J.: Realistic following behaviors for crowd simulation. Comput. Graph. Forum **31**(2pt2), 489–498 (2012)
22. Lindgren, G., Rootzen, H., Sandsten, M.: Stationary Stochastic Processes for Scientists and Engineers. Taylor & Francis, Boca Raton (2013)
23. Moussaïd, M., Helbing, D., Theraulaz, G.: How simple rules determine pedestrian behavior and crowd disasters. Proc. Nat. Acad. Sci. **108**(17), 6884–6888 (2011)
24. Muramatsu, M., Nagatani, T.: Soliton and kink jams in traffic flow with open boundaries. Phys. Rev. E **60**, 180–187 (1999)
25. Orosz, G., Wilson, R.E., Szalai, R., Stépán, G.: Exciting traffic jams: nonlinear phenomena behind traffic jam formation on highways. Phys. Rev. E **80**(4), 046205 (2009)
26. Portz, A., Seyfried, A.: Modeling stop-and-go waves in pedestrian dynamics. In: International Conference on Parallel Processing and Applied Mathematics, pp. 561–568 (2010)
27. Seyfried, A., Portz, A., Schadschneider, A.: Phase coexistence in congested states of pedestrian dynamics. Lecture Notes in Computer Science, vol. 6350, pp. 496–505 (2010)
28. Sugiyama, Y., Fukui, M., Kikushi, M., Hasebe, K., Nakayama, A., Nishinari, K., Tadaki, S.: Traffic jams without bottlenecks. Experimental evidence for the physical mechanism of the formation of a jam. New J. Phys. **10**(3), 033001 (2008)
29. Takayasu, M., Takayasu, H.: 1/f noise in a traffic model. Fractals **01**(04), 860–866 (1993)
30. Tomer, E., Safonov, L., Havlin, S.: Presence of many stable nonhomogeneous states in an inertial car-following model. Phys. Rev. Lett. **84**, 382–385 (2000)
31. Tordeux, A., Schadschneider, A.: White and relaxed noises in optimal velocity models for pedestrian flow with stop-and-go waves. J. Phys. A **49**(18), 185101 (2016)
32. Tordeux, A., Seyfried, A.: Collision-free nonuniform dynamics within continuous optimal velocity models. Phys. Rev. E **90**, 042812 (2014)
33. Treiber, M., Kesting, A., Helbing, D.: Delays, inaccuracies and anticipation in microscopic traffic models. Physica A **360**(1), 71–88 (2006)

34. Treiber, M., Kesting, A., Helbing, D.: Three-phase traffic theory and two-phase models with a fundamental diagram in the light of empirical stylized facts. Transp. Res. B Methodol. **44**(8–9), 983–1000 (2010)
35. Vicsek, T., Czirók, A., Ben-Jacob, E., Cohen, I., Shochet, O.: Novel type of phase transition in a system of self-driven particles. Phys. Rev. Lett. **75**, 1226–1229 (1995)
36. Wagner, P.: How human drivers control their vehicle. Eur. Phys. J. B Condens. Matter **52**(3), 427–431 (2006)
37. Williams, R., Herrup, K.: The control of neuron number. Annu. Rev. Neurosci. **11**(1), 423–453 (1988)
38. Zgonnikov, A., Lubashevsky, I., Kanemoto, S., Miyazawa, T., Suzuki, T.: To react or not to react? Intrinsic stochasticity of human control in virtual stick balancing. J. R. Soc. Interface **11**(99), 20140636 (2014)
39. Zhang, J., Mehner, W., Holl, S., Boltes, M., Andresen, E., Schadschneider, A., Seyfried, A.: Universal flow-density relation of single-file bicycle, pedestrian and car motion. Phys. Lett. A **378**(44), 3274–3277 (2014)

Evacuation Simulation and Experiment Without Exit Information

Yusuke Miyoshi, Daichi Yanagisawa, and Katsuhiro Nishinari

Abstract The configuration of a room and the evacuee information are important factors that determine evacuation performance. While several studies have investigated the impact of these factors on evacuation behavior, little research has been done on the evacuation of a room with blocked exits and uninformed evacuees who are unaware about the position of open exit. In this paper, we propose an extended floor field model that accounts for these types of conditions and is validated by experiments. The simulation results of our model show that optimal total evacuation time is achieved when more than 40% of evacuees are informed evacuees (IEs) who know the position of the open exit if their initial positions are uniformly distributed in the crowd. Our model indicates that total evacuation time is reduced when IEs are near an open exit. In addition, our model indicates that the ratio of IEs to total evacuees, required for achieving optimal evacuation time, changes with the change in the initial position of IEs.

1 Introduction

The characterization of evacuation performance in emergency situations importantly informs the design of buildings. Thus, many research studies have been done on evacuation under various conditions [1, 2, 4, 7, 9]. For example, studies have been conducted involving a simple evacuation from a square room with one exit [1, 9]. More recent studies investigated evacuation from a room with multiple exits [1, 2, 4] or evacuation with assistants [7]. However, there is little research on more realistic evacuation situations such as a room with blocked exits and evacuees who are

Y. Miyoshi (✉)
Department of Aeronautics and Astronautics, School of Engineering, The University of Tokyo, Bunkyo-ku, Tokyo, Japan

D. Yanagisawa · K. Nishinari
Research Center for Advanced Science and Technology, The University of Tokyo, Meguro-ku, Tokyo, Japan
e-mail: tdaichi@mail.ecc.u-tokyo.ac.jp; tknishi@mail.ecc.u-tokyo.ac.jp

S. H. Hamdar (ed.), *Traffic and Granular Flow '17*,
https://doi.org/10.1007/978-3-030-11440-4_38

unaware about the position of open exit. Our research attempts to address these types of situations by proposing an extended floor field model [6] that introduces a judgment mark concept into the model to better account for blocked exits and uninformed evacuees in evacuation scenarios. The judgment mark is similar to dynamic floor field and includes two pieces of information concisely: an evacuee's inference of open and blocked exits and the trajectories of other evacuees.

2 Model

2.1 Basic Floor Field Model

The floor field model is a cellular automaton [8] based model in which time and space are discretized and exits, obstacles, people, etc. are placed at each cell. A cell can have no more than one evacuee and is characterized by a quantity of state, named "floor field," which controls the transition probability, $p_{i,j}$.

Floor field typically includes a static floor field S and a dynamic floor field D. S represents the distance from the evacuee cell to the evacuee target destination such as an exit. For intricately configured rooms, the distance is often calculated using Dijkstra's algorithm [5]. D is the virtual trace left by the evacuee with its characteristic dynamics of diffusion and decay [3]. These two floor fields are used to calculate the transition probability $p_{i,j}$, which is given in Eqs. (1) and (2)

$$p_{i,j} = \begin{cases} N\xi_{i,j} f_{i,j} & (i,j) \neq (0,0), \\ N\xi_{i,j} \left(\dfrac{\Delta x}{v\tau} - 1 \right) \displaystyle\sum_{(i,j)\neq(0,0)} f_{i,j} & (i,j) = (0,0), \end{cases} \tag{1}$$

$$f_{i,j} = \exp(-k_{\mathrm{S}} S_{i,j} + k_{\mathrm{D}} D_{i,j}), \tag{2}$$

where

$p_{i,j}$: probability of moving to cell (i, j),
N : normalization term to ensure that $\sum p_{i,j} = 1$,
$\xi_{i,j}$: obstacle value that returns 0 for forbidden transitions such as to walls, obstacles, or occupied cell and 1 for others,
$f_{i,j}$: weight of probability of moving to cell (i, j),
Δx : length of one side of a cell,
v : average velocity of evacuees,
τ : time length of a time step,
k_{S} : strength of the static floor field,
$S_{i,j}$: static floor field as the distance from the cell (i, j) to evacuee's destination,
k_{D} : strength of the dynamic floor field, and
$D_{i,j}$: dynamic floor field dropped at cell (i, j).

2.2 Informed Evacuees (IEs) and Uninformed Evacuees (UEs)

In real evacuations, in particular, that follow a disaster, exits that are normally opened may be blocked and evacuees may not know the position of the open exits. Therefore, the exit information is often different depending on the evacuees. In this study, we divided evacuees into two groups: informed evacuees (IEs) who know the position of the open exits and uninformed evacuees (UEs) who do not know the position of the open exit. During an evacuation, UEs search for open exits by observing the behavior of other evacuees and by walking around the room. We introduced judgment mark J, into the floor field model to describe this type of UE search behavior.

2.3 Judgment Mark

To be able to describe evacuation scenarios that involve a room with blocked exits, we introduced judgment mark J into the floor field model for our evacuation simulations. In general, J contains two pieces of information: the position of open and blocked exits that an evacuee infers and the trajectories of other evacuees. J is dropped by all evacuees and diffuses and decays in the same dynamics as that of D. However, there are two differences between J and D. First, the varieties of J are not one, namely the varieties of J are equal to the number of exits, including the blocked ones. Second, the amount of J dropped by the evacuees changes according to the evacuees' location and information. We explain J further by focusing on these two differences.

2.3.1 Varieties of J Dropped by Evacuees

As mentioned above, the varieties of J are equal to the number of exits, including the blocked exits. For example, when J is applied to the evacuation simulation from a room with four exits, four types of J are dropped by evacuees: J_1, J_2, J_3, and J_4. In addition, evacuees can drop multiple types of J (e.g., J_1 and J_3) at the same time step.

2.3.2 Amount of J Dropped by Evacuees

In this section, we explain the amount of J dropped by evacuees at one time step, which changes depending on evacuee location and exit information. Hereinafter, we characterize evacuation as the evacuation of a room with n exits that include open exit l.

First, we explain the amount of J dropped by IEs. The IEs' target exit is always the open exit l. Therefore, if IEs are around blocked exits, they move away from them. When UEs observe this behavior, UEs tend to infer that an exit is blocked. Given this set of behaviors, we set J dropped by IEs as follows:

1. If from their present cells IEs move to neighboring cells in the next time step,
   IEs always drop $J_l = 1$ at the present cell.
   IEs drop $J_m = -E$ ($E \in (1, \infty]$) at the present cell if blocked exit m ($m \neq l$) is visible from the position of the IEs.
2. If IEs remain in the same cell in the next time step,
   IEs always drop $J_l = c$ ($c \in (0, 1)$) at the present cell.
   IEs drop $J_m = -cE$ at the present cell if blocked exit m ($m \neq l$) is visible from the position of the IEs.

Second, we explain the amount of J dropped by UEs. We defined the quantity of J dropped by UEs as follows:

1. If from their present cells UEs move to neighboring cells in the next time step,
   UEs, whose target exit is exit m, always drop $J_m = 1$ at the present cell.
   UEs, whose infer exit m is blocked, drop $J_m = -E$ at the present cell if exit m is visible from the UEs.
2. If UEs remain in the same cell in the next time step,
   UEs, whose target is exit m, always drop $J_m = c$ at the present cell.
   UEs, whose infer exit m is blocked, drop $J_m = -cE$ at the present cell if exit m is visible from the position of the UEs.

2.3.3 Target Exit and the Inference of Blocked Exits

During evacuation of a room with blocked exits, all evacuees have their target exit and UEs must infer the position of the blocked exits. Since IEs know the position of open exits, their target is always toward the open exit; however, UEs' target exit and their inference about blocked exits are subject to change because they do not know the position of the open exits. In our model, UEs choose their target exit and infer blocked exits in every time step by referencing J at their present cell. For instance, in an evacuation simulation of a room with n exits, n varieties of J exist in every cell. Each UE refers these n varieties of J dropped at his/her cell. Each UE decides to aim at exit m, when J_m is the largest one among all J dropped at his/her cell, and infer exit m is blocked when $J_m < 0$. This constitutes the dynamics of UE's behavior in targeting exit and inferring blocked exits.

2.4 Extended Floor Field Model

By incorporating J into the floor field model, we are able to account for the evacuation of a room with n exits, including the open exit l. The transition probability, $p_{i,j}$, is given in Eqs. (1) and (3)

$$f_{i,j} = \exp\left\{\left(\sum_{m=1}^{n} -k_{\mathrm{S}}^{m} S_{i,j}^{m}\right) + k_{\mathrm{D}} D_{i,j}\right\}, \tag{3}$$

where

k_{S}^{m} : strength of the static floor field to exit m, and
$S_{i,j}^{m}$: static floor field as the distance from cell (i, j) to exit m.

2.4.1 k_{S}^{m} and k_{D} of Informed Evacuees (IEs)

The target exit of IEs is exit l. IEs do not follow other evacuee during an evacuation because they know exit l is open. Therefore, we set k_{S}^{m} and k_{D} of IEs as follows: $k_{\mathrm{S}}^{m} = 0$ when $1 \leq m \leq n, m \neq l$ and $k_{\mathrm{S}}^{m} = 10$ when $m = l$ and $k_{\mathrm{D}} = 0$.

2.4.2 k_{S}^{m} and k_{D} of Uninformed Evacuees (UEs)

UEs may occasionally follow others and change their target exit because they do not know which exit is open. In real evacuations, UEs tend to stop and observe others, in particular, during the initial stage of evacuation. Therefore, when $t \leq T_{\mathrm{delay}}$, $k_{\mathrm{S}}^{m} = 10$ and $k_{\mathrm{D}} = 1.4$ if $\forall m'$ $(1 \leq m' \leq n, m' \neq m)$ satisfy $J_m \geq J_{m'} + J_{\mathrm{th}}$, and $k_{\mathrm{S}}^{m} = k_{\mathrm{D}} = 0$ otherwise. When $t > T_{\mathrm{delay}}$, $k_{\mathrm{S}}^{m} = 10$ when exit m is the target exit of the evacuee and set $k_{\mathrm{S}}^{m} = 0$ otherwise. $k_{\mathrm{D}} = 1.4$ when $t > T_{\mathrm{delay}}$. T_{delay} is the time delay of UEs' initial movement and J_{th} is the threshold of judgment mark.

3 Evacuation Simulation Using Extended Floor Field Model and Experiment to Validate the Model

Using our extended floor field model, we conducted simulations of evacuation from an intricately configured virtual room as shown in Fig. 1, where the exits, one opened and three blocked, were invisible from the initial position of the evacuees, and 25 virtual evacuees were initially located at the center of the room. In these simulations, we changed r (ratio of IEs to total evacuees) and the initial position of IEs.

Furthermore, to validate our model, we conducted evacuation experiments that essentially duplicated simulation conditions. The experiments were performed in

Fig. 1 Schematic view of a simulation field divided into 15×15 cells. The colored cells represent both open and blocked exits. Gray arrows are IEs and the other colored arrows are UEs. UEs' color indicates their nearest exit. The parameter set adopted in our simulation is as follows: $\Delta x = 0.5$, $v = 0.95$, $\tau = 0.1$, $c = \frac{1}{38}$, $E = 100$, $J_{\text{th}} = 7.6$, and $T_{\text{delay}} = 4.0$

the dark (the illumination less than 0.01 lux) because we additionally wanted to investigate the effect of visibility on the evacuation performance. The geometry of the room included one open and three blocked exits; the exits were invisible from the initial position of the evacuees, 25 evacuee subjects were initially positioned at the center of the room. As in the simulations, we changed r and the initial position of IEs.

4 Results

4.1 When Informed Evacuees (IEs) Are Uniformly Distributed

Figure 2 shows the relation between r and the total evacuation time. The solid (simulation) and broken (experiment) lines trend closely as shown in Fig. 2. Our model reproduced the experimental results when IEs are distributed uniformly in the crowd. The optimal evacuation time occurred when $r \geq 0.4$. Furthermore, r does not affect the total evacuation time if $r \geq 0.4$. This is because UEs rarely fail to move toward the open exit since they can find their neighboring IEs when $r \geq 0.4$.

4.2 When Informed Evacuees (IEs) Are NOT Uniformly Distributed

We conducted evacuation simulations and experiments where IEs are initially near the open exit and IEs are initially far from the open exit. Our simulation results indicate that total evacuation time is lower when IEs are near an open exit as shown in Fig. 3 because IEs head to the open exit immediately when they are near the open exit, and UEs are able to identify the open exit by observing the behavior of IEs

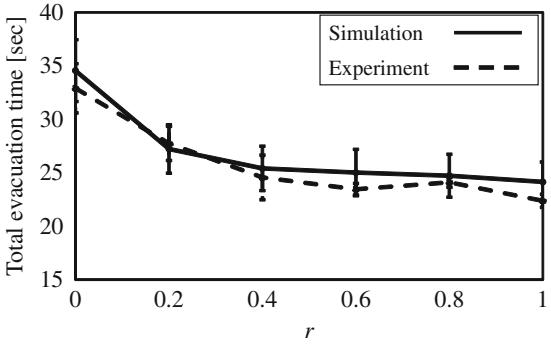

Fig. 2 Simulation and experimental results of total evacuation time as a function of r in an evacuation where the initial position of IEs is uniformly distributed. The r ratio acquired six different values: 0, 0.2, 0.4, 0.6, 0.8, and 1.0 in simulations and experiments. Error bars represent the standard deviation in every condition. The number of simulation repetitions was 1000 for every condition compared with the two or three experiments conducted for every condition

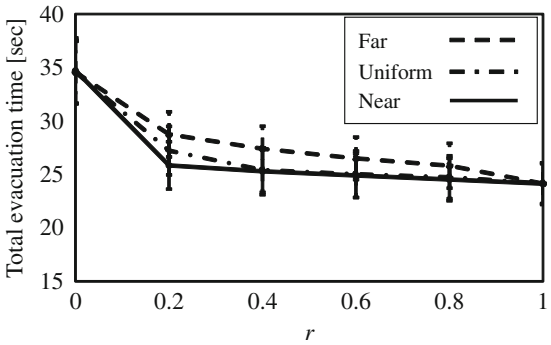

Fig. 3 Simulation results of total evacuation time as a function of r for three different initial position of IEs. The r ratio acquired six different values: 0, 0.2, 0.4, 0.6, 0.8, and 1.0. Error bars represent the standard deviation in every condition. The number of simulation repetitions was 1000 for every condition

or other UEs, who already identified the open exit. However, if IEs are far from an open exit, they are slower to get to the open exit because IEs are blocked by UEs who halt to observe the others at the beginning of an evacuation. Hence, the total evacuation time is greater when IEs are far from an open exit as shown in Fig. 3. We have obtained the similar tendency in the evacuation experiment as shown in Fig. 4. Moreover, our simulation results show that optimal total evacuation time is achieved when $r \geq 0.2$, when IEs are near an open exit, and when $r > 0.8$, when IEs are far from an open exit.

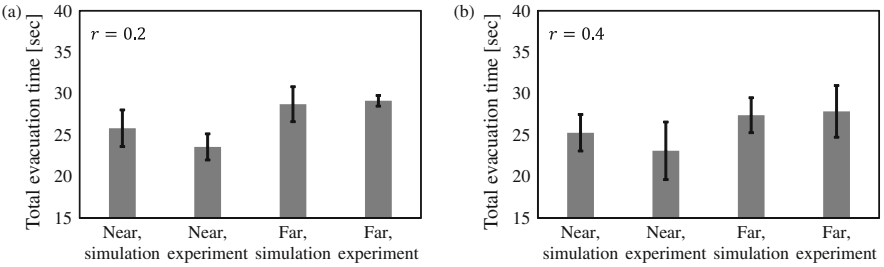

Fig. 4 A comparison of simulation and experimental results when IEs are near an open exit and when IEs are far from an open exit in terms of total evacuation time in the case (**a**) $r = 0.2$ and (**b**) $r = 0.4$. Error bars represent the standard deviation in every condition

5 Conclusion

We proposed an extended floor field model by introducing judgment mark J. Our model functioned in evacuation simulations of a room with blocked exits and was validated by using experiments. Our findings indicate that when IEs are uniformly distributed in a crowd, $r \geq 0.4$ is required to achieve optimal total evacuation time. In addition, we found that the initial position of IEs affects the total evacuation time. The nearer the IEs are to an open exit, the lower is the total evacuation time. Finally, our model indicates that a different r value is required for achieving optimal evacuation when IEs are near an open exit, far from an open exit, or are uniformly distributed in a crowd.

Acknowledgement This work was supported by JSPS KAKENHI Grant Numbers 25287026 and 15K17583.

References

1. Helbing, D., Farkas, I., Vicsek, T.: Simulating dynamical features of escape panic. Nature **794**, 487–490 (2000)
2. Huang, H.J., Guo, R.Y.: Static floor field and exit choice for pedestrian evacuation in rooms with internal obstacles and multiple exits. Phys. Rev. E Stat. Nonlinear Soft. Matter. Phys. **78**(2), 1–6 (2008). https://doi.org/10.1103/PhysRevE.78.021131
3. Kirchner, A., Schadschneider, A.: Simulation of evacuation processes using a bionics-inspired cellular automaton model for pedestrian dynamics. Phys. A Stat. Mech. Appl. **312**(1–2), 260–276 (2002). https://doi.org/10.1016/S0378-4371(02)00857-9
4. Liu, S., Yang, L., Fang, T., Li, J.: Evacuation from a classroom considering the occupant density around exits. Phys. A Stat. Mech. Appl. **388**(9), 1921–1928 (2009). http://dx.doi.org/10.1016/j.physa.2009.01.008
5. Nishinari, K., Kirchner, A., Namazi, A., Schadschneider, A.: Extended floor field CA model for evacuation dynamics. Preprint: arXiv:cond-mat/0306262 (2008)

6. Peng, Y.C., Chou, C.I.: Simulation of pedestrian flow through a "T" intersection: a multi-floor field cellular automata approach. Comput. Phys. Commun. **182**(1), 205–208 (2011). http://dx.doi.org/10.1016/j.cpc.2010.07.035
7. Wang, X., Zheng, X., Cheng, Y.: Evacuation assistants: an extended model for determining effective locations and optimal numbers. Phys. A Stat. Mech. Appl. **391**(6), 2245–2260 (2012). http://dx.doi.org/10.1016/j.physa.2011.11.051
8. Wolfram, S.: Theory and applications of cellular automata: including selected papers 1983–1986. Advanced Series in Complex System. World Scientific, Singapore (1986). http://cds.cern.ch/record/108435
9. Yanagisawa, D., Nishinari, K., Floor, A.: Mean-field theory for pedestrian outflow through an exit. Phys. Rev. E **76**, 061117 (2007). http://dx.doi.org/10.1103/PhysRevE.76.061117

Fluctuations in Pedestrian Evacuation Times: Going One Step Beyond the Exit Capacity Paradigm for Bottlenecks

Alexandre Nicolas

Abstract For safety reasons, it is important that the designs of buildings and public facilities comply with the guidelines compiled in building codes. The latter are often premised on the concept of exit capacity, i.e., the mean pedestrian flow rate through a bottleneck (at congestion). Here, we argue that one should duly take into account the evacuation time fluctuations when devising these guidelines. This is particularly true when the narrowing is abrupt and the crowd may behave competitively. We suggest a simple way to assess the extent of (part of) these fluctuations on the basis of the statistics of time gaps between successive escapes through the considered bottleneck, which in practice could be garnered by analysing recordings of future real evacuations or, perhaps, realistic drills (in the limits of what is ethically possible). We briefly present a test of the proposed strategy using a cellular automaton model and confirm its validity under some conditions, but also disclose some of its limitations. In particular, it may severely underestimate fluctuations in the presence of strong correlations in the pedestrians' behaviours (while still performing better than only the mean capacity).

1 Introduction

In emergency situations (whether it be a fire outbreak, an earthquake, a terrorist attack, etc.), buildings and public facilities usually need to be evacuated quickly and safely. Building architectures should be designed accordingly. In particular, corridors and doorways on the egress pathway must be wide enough to allow the occupants to egress without excessive delay and to reduce the risk of clogging at the bottlenecks. How can this plain condition translate into a practical guideline? Building codes answer this question either by prescribing minimal requirements in

A. Nicolas (✉)
LPTMS, CNRS, Université Paris-Sud, Université Paris-Saclay, Orsay, France
e-mail: alexandre.nicolas@polytechnique.edu

S. H. Hamdar (ed.), *Traffic and Granular Flow '17*,
https://doi.org/10.1007/978-3-030-11440-4_39

terms of bottleneck widths or by setting the minimal standards (performances) that should be met with respect to the evacuation time.

To take a few examples, building codes in the United States (for instance, in Florida [2]) prescribe a minimal clear width $w = \max\{813,\ 5.1\,N\}$ mm for doorways, where N is the occupant load. Note that w is lowered to $\max\{813,\ 3.8\,N\}$ mm in suitably equipped low-risk buildings. In France, emergency exit doorways and corridors in public buildings must typically be larger than $\left(1 + \left\lceil \frac{N}{100} \right\rceil\right) \times 0.6\,\mathrm{m}$ if $200 < N \leqslant 500$, where $\lceil x \rceil \in \mathbb{N}$ is the ceiling of x, or $\left\lceil \frac{N}{100} \right\rceil \times 0.6\,\mathrm{m}$ if $N > 500$ [1]. French railway stations must be designed in such a way that they can be evacuated in less than 10 min. To evaluate the evacuation time, a walking velocity $v = 1.4\,\mathrm{m\,s^{-1}}$ is assumed, along with a specific capacity $J_s = 1.67\,\mathrm{m^{-1}\,s^{-1}}$, i.e., a maximal flow rate of 1.67 people per second per metre of corridor width. These figures are reduced to $v = 1.0\,\mathrm{m\,s^{-1}}$ and $J_s = 1.0\,\mathrm{m^{-1}\,s^{-1}}$ if it is a regional or national station [1]. Finally, in the UK, the maximal evacuation time for sports stadiums is set to a value between 2.5 and 8 min, depending on the risks, and a specific capacity $J_s = 1.37\,\mathrm{m^{-1}\,s^{-1}}$ is assumed for level walkways [3].

These guidelines are thus premised on the concept of exit capacity, or in other words mean flow rate in saturated conditions. Not surprisingly, the values indicated in the above building codes are slightly lower, but comparable to the values measured in controlled experiments where participants were asked to walk through a bottleneck in normal conditions (for instance, $J_s = 1.85\,\mathrm{m^{-1}\,s^{-1}}$ was reported in [7]). On the other hand, they are considerably lower than the values measured in controlled competitive conditions through narrow doors: in [14], Zuriguel et al. measured $J_s \approx 3.7\,\mathrm{m^{-1}\,s^{-1}}$. Varying the participants' (prescribed) eagerness to escape, my colleagues and I observed the whole range of values $1.4 \leqslant J_s \leqslant 3.3$ (in $\mathrm{m^{-1}\,s^{-1}}$) [12]. The underestimates provided in building codes can be interpreted as safety margins, intended to absorb unforeseen delay. But is this enough to ensure that the evacuation time will always be within the chosen bounds?

Here, we show that the presence of significant fluctuations, of diverse origins, undermines this reasoning based on mean values (Sect. 2). We then propose a simple method to assess these fluctuations in Sect. 3 and test it in Sect. 4.

2 Beyond the Mean Exit Capacity: Fluctuations

2.1 Importance of Fluctuations

Since the dynamics of evacuations depend on many details that are out of control, significant fluctuations should be foreseen. They undermine any reasoning based exclusively on mean values. Indeed, in the presence of strong fluctuations, knowing that evacuations are quick enough *on average* does not tell you how often they will be excessively lengthy. Even if we focus only on the delays expected at bottlenecks (doorways, relatively narrow corridors, etc.), experiments involving mice that were forced to flee through a narrow orifice showed that realisations

conducted in virtually identical conditions exhibit a significant dispersion, with standard deviations (std) that typically amount to 6–14% of the total evacuation times of about 90 mice, for a variety of settings [8, 9] (the figure is closer to the upper bound when there are many realisations). Similar figures are reported for the entrance of 85 sheep into a barn through a narrow gate, with a std-over-mean ratio of around 15% for the total time [4], and the importance of the dispersion of the evacuation times was underscored by the authors. Considering a crowd of about 90 participants walking through a narrow (69 cm wide) door in a controlled experiment, the ratio is found to be around 7%, with moderately competitive participants as well as with highly competitive ones [5]. (Note that the given std-over-mean ratios are the results of my own calculations using the data of the cited papers.) Importantly, even though intermittence in the dynamics is favoured by the presence of abrupt narrowings, the fluctuations do not vanish when the constriction gets wider and they may be very considerable if the crowd behaves frantically. A striking example is the huge clog that occurred in the running of the bulls during the 2013 San Fermín in Pamplona, when the crowd running in front of the bulls pushed so hard on the human clog formed at the entrance of the arena that, despite its being a few metres wide, not even a handful of people could enter per second. This very large deviation from the mean flow rate is a sign of anomalously broad statistics.

As a consequence, it is of paramount interest to have an idea of the distribution of evacuation times, beyond its mean value. This distribution corresponds to an ensemble of realisations, for a fixed number of occupants N and a fixed geometry. Unfortunately, it is unrealistic to expect the collection of such statistics for any N and any geometry. In the following, we will propose a strategy to bypass this need. To this end, we will first disentangle the origins of the fluctuations.

2.2 Origins of the Fluctuations

Statistical Fluctuations As any complex system, pedestrian crowds feature an amount of disorder: the pedestrian's morphologies and their preferential velocities are different, their initial positions at the beginning of the evacuation are more or less random, etc. For these reasons, successive realisations (even conducted with identical crowds and in seemingly identical conditions) will not display exactly the same dynamics. The observed differences are statistical fluctuations due to the stochasticity of uncontrolled parameters and are also present in the flow of purely mechanical systems, such as grains discharging from a silo [10].

Extrinsic Variations Besides these statistical fluctuations, extrinsic variations are also expected in real evacuations. In particular, the composition of the crowd that might need to evacuate the building is not the same from day to day nor will their eagerness or competitiveness to egress be the same. Turning up the last parameter, for instance, was shown to produce more intermittent (bursty) evacuation dynamics [12, 14].

3 A Practical Method to Assess Statistical Fluctuations

Having disentangled the origins of the fluctuations, we now propose a practical way to predict the statistical fluctuations of the global evacuation time.

3.1 Distribution of Time Gaps Between Successive Egresses

Consider a given escape zone. Let t_i be the time of the i-th escape (out of N) in a realisation of the evacuation and let Δt_i be the time gap $t_i - t_{i-1}$, where we have set $t_0 = 0$, as illustrated in Fig. 1. The premise of our approach is that it is possible to collect enough statistics about these time gaps to get a decent approximation of their distribution $p(\Delta t)$ for a typical crowd composition. This requires the observation of a reasonable number of real evacuations, which may be achieved in the near future, owing to the increased monitoring of public facilities. Alternatively, one may choose to perform evacuation drills in conditions as realistic as is ethically possible.

3.2 Micro-Macro Relation

To proceed, we remark that the total evacuation time of the N occupants (i.e., here, the delay at the bottleneck) reads

$$T_{\mathrm{esc}}(N) = \sum_{i=1}^{N} \Delta t_i \,.$$

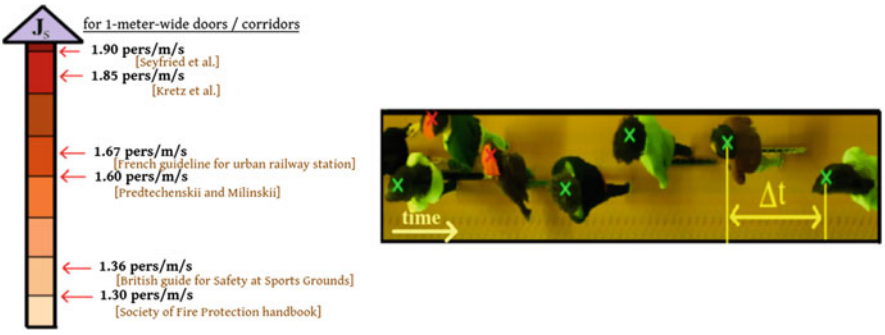

Fig. 1 (*Left*) Some guidelines or measurements for the specific capacity of doors and corridors (i.e., the flow rate per metre of cross section). (*Right*) Timeline of a controlled evacuation [12] obtained by stitching pixel lines corresponding to the doorway in successive frames; the definition of the time gap Δt is illustrated

It can thus be regarded as a sum of N random variables drawn from the distribution $p(\Delta t)$. If we overlook possible correlations between successive time gaps, the distribution of $T_{\rm esc}(N)$ is given by the following *micro-macro relation*, based on a convolution product $(*)$,

$$P_N\left(T_{\rm esc}\right) = p^{*N}\left(T_{\rm esc}\right). \tag{1}$$

In particular, provided that the 'microscopic' distribution $p(\Delta t)$ has a finite mean $\overline{\Delta t}$ and a finite standard deviation σ, the central limit theorem implies that, in the limit of large attendance $N \gg 1$, $P_N\left(T_{\rm esc}\right)$ follows a normal law of mean $N\overline{\Delta t}$ and of variance $N\sigma^2$. Thus, we have managed to assess the global distribution $P_N\left(T_{\rm esc}\right)$, whose direct assessment would require a hopelessly large amount of data because of its dependence on N, on the basis of the more accessible $p(\Delta t)$ [11].

3.3 Caveats and Possible Issues

Already at this stage, we ought to mention some caveats with respect to the *micro-macro relation*. First, one may think that $p(\Delta t)$ actually depends on N. But we believe that, granted that N is large enough (typically $N > 100$ for a narrow door [5]), this dependency can be overlooked (unless huge pressure builds up at the door, in which case pressure itself will cause a tragedy, regardless of the delay at the door). Indeed, in the controlled experiments we performed (see [12] for details), the flow rate was not found to vary substantially when there were fewer people left in the room. Second, contrary to the assumption of uncorrelated time gaps, we recently demonstrated that an alternation between short time gaps and longer ones is generally expected in bottleneck flows [13]. Nevertheless, these are short-time (anti)correlations and they should not very substantially affect the results (where long clogs play an important role). In any case, the problem can be remedied easily, by reasoning on the distribution of time lapses for a handful of successive escapes (e.g., $\sum_{p=0}^{3} \Delta t_{i+p}$), instead of considering the individual time gap Δt_i.

4 Validity and Limits of the Micro-Macro Relation

In this section, we outline a validation test for the *micro-macro relation* relying on model pedestrian dynamics. More precisely, the model under consideration is a cellular automaton that we designed to reproduce the dynamics of competitive escape through a narrow door observed experimentally by Zuriguel et al. [14], in particular the heavy-tailed, power-law-like distribution of time gaps, viz., $p(\Delta t) \sim \Delta t^{-\alpha}$ for large Δt, with $\alpha > 0$.

4.1 Succinct Description of the Model

In the model, space is discretised into a regular rectangular grid, in which each cell hosts at most one agent. At each time step, all pedestrians start by selecting the site that they target among the adjacent cells (denoted k and including the present one). A move from site i to site j has probability $p_{i\to j} \equiv e^{\frac{A_j - A_i}{x}} / \sum_{\langle i,k\rangle} e^{\frac{A_k - A_i}{x}}$, where A_k is the attractiveness of the site (how close it is to the exit) and the noise intensity $x = 1$ has been introduced to avoid the artefacts caused by strictly deterministic moves. If the target site is occupied or if other people have selected it as target site and are therefore competing for it, the agent simply waits. Otherwise, (s)he moves to the target site. Following this round of motion, some sites have been vacated. This allows other agents to move to their target cell. The round is iterated until all possibilities of motion have been exhausted. The limit of strong friction considered in the model is noteworthy: as soon as two or more agents are competing for a site, the conflict is sterile and nobody can move. Further details can be found in [11].

Simulations showed that this model is able to capture the exponential distributions of burst sizes (i.e., egresses in rapid succession). But adding one last ingredient was crucial in order to replicate the heavy tails in $p(\Delta t)$. Indeed, some amount of disorder was required. This was achieved by introducing behaviours: each agent (i) is endowed with a propensity to cooperate $\Pi_i \in]0, 1[$. At each time step, this propensity determines whether agent i cooperates (which occurs with probability Π_i) or not. Nothing changes if the agent behaves cooperatively. In the opposite case, the agent is impatient to move to another site, so (s)he undervalues the attractiveness of the current site, viz., $A(x_i, y_i) \longrightarrow A(x_i, y_i) + \frac{1}{2} \ln \Pi_i$. With this additional ingredient, the model succeeded in describing a 'faster-is-slower' effect [6] when the crowd becomes more impatient, but also in yielding power-law tails in $p(\Delta t)$ for impatient crowds and narrow doors [11].

4.2 Validation of the Micro-Macro Relation

For each distribution of behaviours Π_i and each door width, a large number of evacuation realisations were simulated for an arbitrary number of occupants N. The resulting histogram of total evacuation times is plotted as cyan bars in the right box of Fig. 2. In parallel, the distribution of time gaps $p(\Delta t)$ was computed from the simulation of an evacuation involving a very large crowd. On this basis, the global distribution of evacuation times predicted using the *micro-macro relation* is shown in the same figure. Clearly, there is excellent agreement between the prediction line and the histogram, which gives credence to the validity of the *micro-macro relation*.

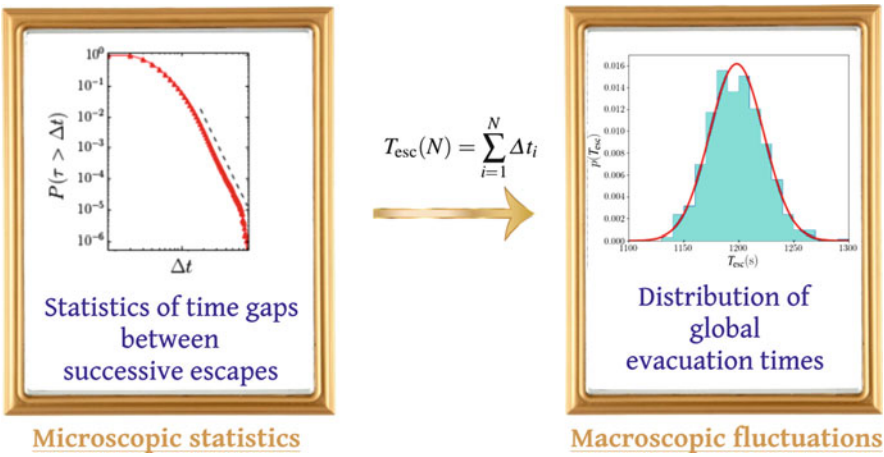

Fig. 2 Illustration of the *micro-macro relation*, which takes as input the 'microscopic' statistics of time gaps Δt at the door and predicts the global distribution of evacuation times T_{esc} for the N occupants

4.3 Limits to the Validity

However, the proposed relation was found to fail in some conditions, and sometimes severely so. This notably happened when a process of social contagion was incorporated into the model, whereby the neighbours of an impatient agent tended to behave more selfishly. At high contagion strengths, system-spanning correlations emerged and the crowd sometimes ended up being extremely impatient (thus evacuating more slowly in the model), whereas it remained in its initial, patient state during other realisations, thus evacuating faster. Such scenario splitting completely undermined the *micro-macro relation*.

More generally, we also expect extrinsic fluctuations, as defined in Sect. 2.2, to lead to a broader distribution of global evacuation times than the micro-macro prediction. Despite these limitations, by accounting for statistical fluctuations, the latter prediction is more informative regarding the probability of dangerously long evacuations than just the exit capacity.

4.4 Conclusion

In this contribution we have argued that estimates for the time spent at doors, gates or in corridors during an evacuation should not be based exclusively on the mean flow rate at the bottleneck under study, i.e., its capacity. Indeed, these times may fluctuate considerably, especially when the relative narrowness of the bottleneck and the competitiveness of the crowd favour highly intermittent dynamics. We have

suggested a simple way to assess the extent of these fluctuations (more precisely, their statistical component) on the basis of the 'microscopic' statistics of time gaps between successive escapes, which could be collected in practice. Putting the proposed relation to the test with a cellular automaton model [11] has confirmed its validity under some conditions, but also pointed to its limitations: fluctuations are underestimated when there are strong correlations in the pedestrians' behaviours.

References

1. Arrêté du 25 juin 1980 portant approbation des dispositions générales du règlement de sécurité contre les risques d'incendie et de panique dans les établissements recevant du public (ERP)—section 9, co 36. Journal Officiel (1980-06-25–last modified 2017-07-01). https://www.legifrance.gouv.fr/affichTexte.do?cidTexte=JORFTEXT000000290033
2. Florida Building Commission, et al.: Florida building code. Florida Building Commission, Tallahassee (2010)
3. Football League Authority: Guide to Safety at Sports Grounds, 5th edn. Department for Culture, Media and Sports, Norwich (2008)
4. Garcimartín, A., Pastor, J., Ferrer, L.M., Ramos, J., Martín-Gómez, C., Zuriguel, I.: Flow and clogging of a sheep herd passing through a bottleneck. Phys. Rev. E **91**(2), 022808 (2015)
5. Garcimartín, A., Parisi, D., Pastor, J., Martín-Gómez, C., Zuriguel, I.: Flow of pedestrians through narrow doors with different competitiveness. J. Stat. Mech. Theory Exp. **2016**(4), 043402 (2016)
6. Helbing, D., Farkas, I., Vicsek, T.: Simulating dynamical features of escape panic. Nature **407**(6803), 487–490 (2000)
7. Kretz, T., Grünebohm, A., Schreckenberg, M.: Experimental study of pedestrian flow through a bottleneck. J. Stat. Mech. Theory Exp. **2006**(10), P10014 (2006)
8. Lin, P., Ma, J., Liu, T., Ran, T., Si, Y., Li, T.: An experimental study of the 'faster-is-slower' effect using mice under panic. Phys. A Stat. Mech. Appl. **452**, 157–166 (2016)
9. Lin, P., Ma, J., Liu, T.Y., Ran, T., Si, Y.L., Wu, F.Y., Wang, G.Y.: An experimental study of the impact of an obstacle on the escape efficiency by using mice under high competition. Phys. A Stat. Mech. Appl. **482**, 228–242 (2017)
10. Lozano, C., Janda, A., Garcimartín, A., Maza, D., Zuriguel, I.: Flow and clogging in a silo with an obstacle above the orifice. Phys. Rev. E **86**(3), 031306 (2012)
11. Nicolas, A., Bouzat, S., Kuperman, M.N.: Statistical fluctuations in pedestrian evacuation times and the effect of social contagion. Phys. Rev. E **94**, 022313 (2016)
12. Nicolas, A., Bouzat, S., Kuperman, M.N.: Pedestrian flows through a narrow doorway: Effect of individual behaviours on the global flow and microscopic dynamics. Transp. Res. Part B Methodol. **99**, 30–43 (2017)
13. Nicolas, A., Touloupas, I.: Origin of the correlations between exit times in pedestrian flows through a bottleneck. J. Stat. Mech. Theory Exp. **2018**, 013402 (2018)
14. Pastor, J.M., Garcimartín, A., Gago, P.A., Peralta, J.P., Martín-Gómez, C., Ferrer, L.M., Maza, D., Parisi, D.R., Pugnaloni, L.A., Zuriguel, I.: Experimental proof of faster-is-slower in systems of frictional particles flowing through constrictions. Phys. Rev. E **92**(6), 062817 (2015)

Macroscopic Fundamental Diagram for Train Platforms

Winnie Daamen, Jeroen van den Heuvel, Victor L. Knoop, and Serge P. Hoogendoorn

Abstract The macroscopic fundamental diagram (MFD) relates the flow, density and speed of an entire network. So far, the MFD has been mostly applied to cases where pedestrians and vehicles were aiming to reach their destinations as fast as possible. However, pedestrian facilities involve different behaviours. Especially in train stations, travellers spend more time waiting than walking. Moreover, complex passenger flows (i.e. flows in different directions moving to stairs and escalators distributed over the platform) may occur on the platform, due to passengers. In this paper we show that passenger flows on platforms can be described by an MFD.

1 Introduction

For vehicular traffic, the concept of the MFD (at the time not by that name) has been introduced by Daganzo [4]. For locations with a single bottleneck, the exit rate equals the capacity of the bottleneck and queuing processes can be described with queuing theory. However, for other situations, there are internal bottlenecks, caused by the traffic load. This can be the case for pedestrian networks as well. Essential in this phenomenon is that different pedestrians have different (intermediate) destinations. Without different destinations, all pedestrians will queue for the bottleneck. However, if some pedestrians want to go into one direction, and others into another direction, one flow may block the other.

W. Daamen (✉) · V. L. Knoop · S. P. Hoogendoorn
Delft University of Technology, Delft, The Netherlands
e-mail: w.daamen@tudelft.nl; v.l.knoop@tudelft.nl; s.p.hoogendoorn@tudelft.nl

J. van den Heuvel
Delft University of Technology, Delft, The Netherlands

NS Stations (Netherlands Railways), Utrecht, The Netherlands
e-mail: jeroen.vandenheuvel@nsstations.nl

S. H. Hamdar (ed.), *Traffic and Granular Flow '17*,
https://doi.org/10.1007/978-3-030-11440-4_40

The outflow of traffic out of a network, called *performance*, is—under the assumption of a constant trip length—proportional to the internal flow of a network, called *production*. A reduction of speed of pedestrians due to queuing in the system will lead to a lower outflow. Moreover, this lower outflow will lead to higher number of pedestrians in the system, which increases queuing, which reduces outflow. This effect hence strengthens itself.

Apart from the total number of pedestrians in a network, their distribution also plays an important role. Suppose that the pedestrians are equally spread over the network and all have just sufficient space to walk towards their destination at their desired speed. An alternative distribution would be that the same number of pedestrians would be clustered, i.e. some are in a more dense area and some are in a less dense area. Then, the ones in a less dense area still walk at their free speed, but the ones in a more dense area have to slow down. Consequently, the average speed reduces, and with that the production. The same reasoning as for the total networks also holds for parts of the network. Once congestion occurs, outflow of that part decreases, hence increasing congestion. This effect is also called "nucleation of congestion", see [12].

This principle holds in particular for platforms in train stations. Pedestrians waiting on the platform to board the train will hinder alighting pedestrians moving towards the platform exits (i.e. stairs or escalators). Although the existence of an MFD for pedestrians has been shown in other papers [3, 5, 10, 11], in this paper we will check the relation between density and flows, and explore the effect of spatial inhomogeneity of density. We thus will find whether an MFD is capable of reproducing the pedestrian dynamics on the platform. This way, the MFD might be used in the design and assessment of the performance of a platform.

This paper starts with a description of the experimental design and the data used to derive the MDF (Sect. 2), followed by an overview of the methodology (Sect. 3). In Sect. 4 the results are shown. The paper ends with conclusions and discussion in Sect. 5.

2 Experimental Design

The first choice to be made in the experimental design is whether to use simulation data or empirical data. The advantage of simulation data is that the conditions to be simulated can be fully controlled. That implies that the full range of densities can be covered, as well as different flow shares. Therefore, we have chosen to derive our MFDs from simulation data. To simulate, we have applied our microscopic pedestrian simulation model Nomad [1, 8], which has been extensively calibrated [2] and previously applied in transfer stations [9].

The investigated situation covers only the part of the platform where passengers enter and exit (see Fig. 1). The situation is as follows: a train has stopped alongside the platform, passengers alight from four doors (bottom part of the figure) and move to two stairs on the platform (top part of the figure). In order to create hindrance,

Fig. 1 Screenshot of the Nomad simulation. Different colours indicate different origins (train door) and destinations (stairs)

Table 1 Overview of the scenarios

[pes/s]	Low	Medium	High
Doors left	0.2	1.2	1.2
Doors right	0.2	1.2	1.0

passengers alighting at the left two doors move to the right exit, while passengers alighting at the two doors on the right-hand side walk towards the exit on the left. The demand is triangular, increasing during 90 s, and then reduced to 0. We distinguish three demand scenarios, see Table 1.

3 Methodology

The individual spacing for a pedestrian i (s_i) can be found by the personal space this person has. Literature shows many alternatives to calculate this individual spacing, see [6] for an overview. Here, we have chosen to use a combination of the Voronoi space [13], and an upper boundary of a circular personal space with a range of 1.5 m [7]. Figure 2 shows three examples of the resulting individual spacing.

This individual spacing can be transformed into a local density k_i:

$$k_i = 1/s_i \tag{1}$$

Locally, the average density is now the average of the local densities:

$$k_{\mathrm{lc}} = 1/N \sum_{i=1}^{N} k_i \tag{2}$$

A global definition for the density would be the number of pedestrians per space occupied by these pedestrians. This would be proportional to the accumulation in

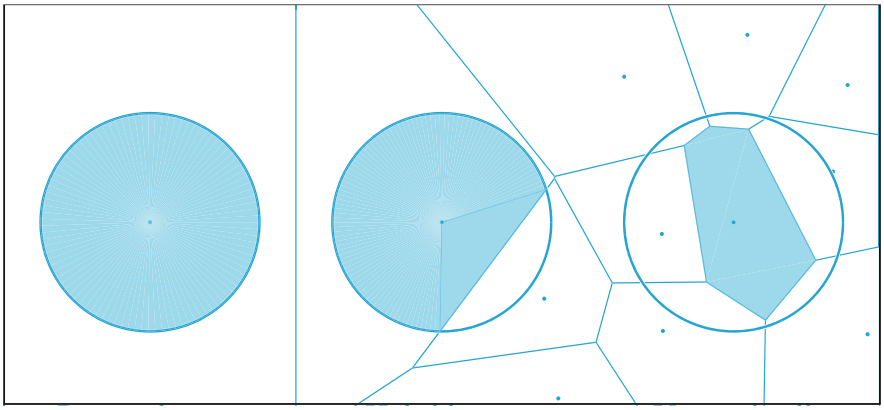

Fig. 2 Example to calculate the individual spacing for a pedestrian using the Voronoi diagram and a personal space. The most left circle shows a pedestrian whose circular personal space is within the Voronoi personal space, so the circle is taken as individual spacing. The most right situation shows a pedestrian whose Voronoi personal space is within the circular personal space, so the Voronoi space is taken as individual spacing. For the pedestrian in the middle, the circular personal space overlaps the Voronoi personal space, so the individual spacing is the intersection of both personal spaces

terms of the MFD. In equations, we derive

$$k_{\text{gb}} = \frac{\text{Number of pedestrians}}{\text{Occupied space}} = \frac{\sum_{i=1}^{N} 1}{\sum_{i=1}^{N} s_i} = N \frac{1}{\sum_{i=1}^{N} s_i} = 1 \Bigg/ \left(\frac{1}{N} \sum_{i=1}^{N} s_i \right) \tag{3}$$

This shows that the global average density is the inverse of the mean spacing per pedestrian.

Note that this is equivalent to the *weighted* mean density, with weights w equal to the size of the area of one pedestrian.

$$k_{\text{gb}} = \frac{\sum w_i k_i}{\sum w_i} = \frac{\sum s_i k_i}{\sum s_i} \tag{4}$$

This derivation illustrates that the global density is the average density in which each part of *space* gets an equal value, rather than each pedestrian.

The (instantaneous) inhomogeneity of the pedestrians is defined by the standard deviation of the local densities:

$$\gamma_{\text{lc}} = \sqrt{1/N \sum_{i=1}^{N} (k_i - k_{\text{lc}})^2} \tag{5}$$

Table 2 Different measures to describe the MFD

Perspective	Local (from user)	Global (system)
Density	$k_{\mathrm{lc}} = \frac{1}{N}\sum_{i=1}^{N} k_i$	$k_{\mathrm{gb}} = N\frac{1}{\sum_{i=1}^{N} s_i}$
Inhomogeneity	$\gamma_{\mathrm{lc}} = \sqrt{1/N\sum_{i=1}^{N}(k_i - k_{\mathrm{lc}})^2}$	$\gamma_{\mathrm{gb}} = \sqrt{\frac{1}{\sum_{i=1}^{N} s_i}\sum_{i=1}^{N} s_i\left(k_i - k_{\mathrm{gb}}\right)^2}$

Equivalent to density, we can also define a measure of inhomogeneity weighted for the area

$$\gamma_{\mathrm{gb}} = \sqrt{\frac{1}{\sum_{i=1}^{N} s_i}\sum_{i=1}^{N} s_i\left(k_i - k_{\mathrm{gb}}\right)^2} \tag{6}$$

Table 2 shows an overview of the measures defined above.

For the analysis, we check for the relationships between the quantities mentioned above. We are interested how the global and local densities relate. To check whether an MFD approach is feasible, we check the relationship between local density and speed, and between local density and internal flow. Finally, check whether there is a relation between density and inhomogeneity.

4 Results

Figures 3, 4, 5, and 6 show the results. For readability, we only included medium (in grey) and high (in blue) demand in the figures. Moreover, we have removed the small local densities which correspond to the circular personal spaces (indicated by the dotted line in the left-hand side of the figure). In all figures, we clearly see the scenarios, covering different density ranges and different severity of the gridlock.

Figure 3 shows the relation between global density and local density. We see that these densities differ more when densities increase, where the local density is higher than the global density. This is according to our expectations. In the following, we will therefore focus on the local density.

Secondly, we look at the relation between speed and local density in Fig. 4. We see the well-known shape of the fundamental diagram. However, for the medium demand, we see a second, "horizontal line". This horizontal "line" is the result of gridlock situations due to the internal bottleneck caused by the crossing flows: due to lower demands, pedestrians keep moving slowly and one by one the pedestrians exit the platform.

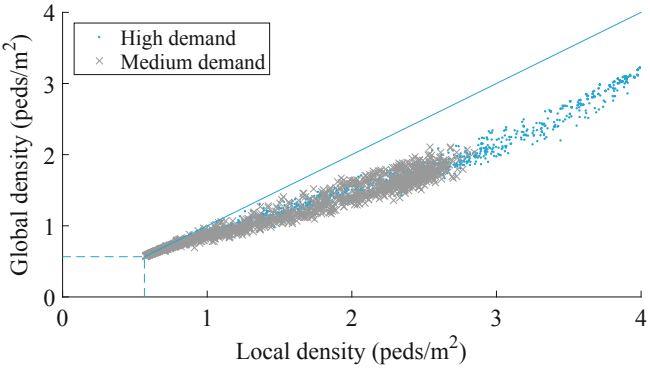

Fig. 3 Relation between the global density and the local density

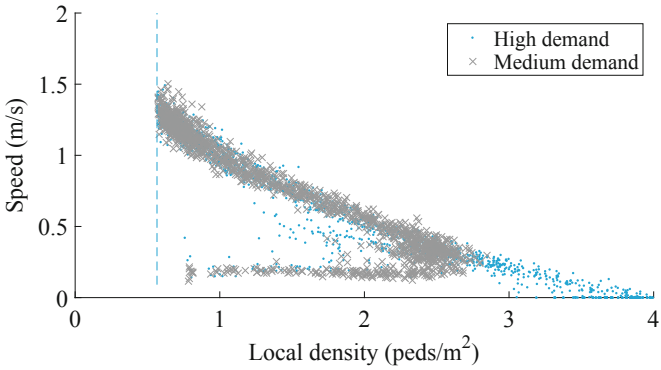

Fig. 4 Relation between speed and local density

The MFD is shown as the relation between the local density and the internal flow (calculated as speed times local density) in Fig. 5. Just like for the speed–density relation, we see the gridlock situation where the internal flow is reduced to almost zero for high local densities. For the medium demand, this gridlock does not occur. Only temporary deadlocks occur, which decrease the outflow, but the passengers do not come to a complete standstill.

Finally, we show the relation between local inhomogeneity and local density in Fig. 6. Starting from the minimum local density, we see that the local inhomogeneity gradually increases. This increase is not linear, though, as it reduces when local densities get higher. It looks like a limit exists for the local inhomogeneity, which is probably due to the limited space and the fact that parts of this space are not used by passengers, as they are heading towards the exits.

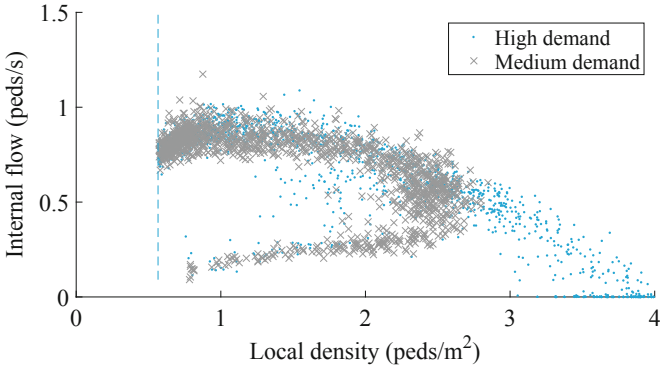

Fig. 5 Relation between internal flow and local density

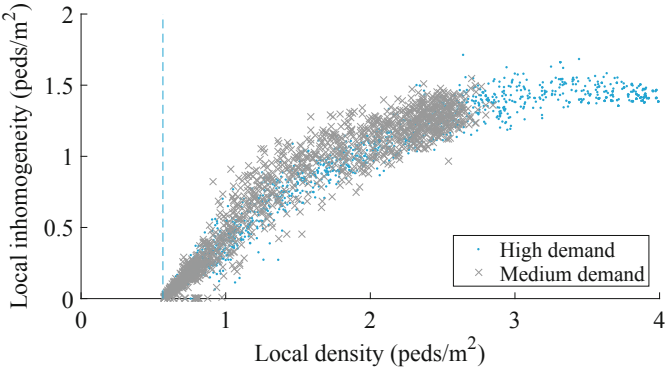

Fig. 6 Relation between inhomogeneity and local density

5 Conclusions

We have calculated the macroscopic fundamental diagram (MFD) describing passenger flows on a platform using simulation data. Local densities have been calculated based on the joint surface of Voronoi cells and circles surrounding passengers describing their personal space. A clear relation between outflow (production) and local density has been found. This shows that speed reduction on a platform is not due to the limited capacity of the exits, but due to internal bottlenecks (hindrance due to crossing flows). The pedestrian dynamics cause a reduction of the outflow. This proves the importance of using MFDs to predict passenger flow operations on platforms.

Whereas inhomogeneity in density on the platform might be of influence, we found it to link directly to local density, so it might be redundant to use two variables to describe flow, and local density could suffice as independent variable.

In future work, we will investigate the shape of the MFD using empirical data, and see how we can use the MFD in the design and assessment of passenger flows on platforms.

Acknowledgements This research was supported by the ALLEGRO project, which is funded by the European Research Council (Grant Agreement No. 669792) and the Amsterdam Institute for Advanced Metropolitan Solutions.

References

1. Campanella, M.C.: Microscopic modelling of walking behaviour. Ph.D. thesis, Delft University of Technology (2016)
2. Campanella, M., Hoogendoorn, S., Daamen, W.: A methodology to calibrate pedestrian walker models using multiple-objectives. In: Pedestrian and Evacuation Dynamics, pp. 755–759. Springer, Boston (2011)
3. Daamen, W., Knoop, V.L., Hoogendoorn, S.P.: Generalized macroscopic fundamental diagram for pedestrian flows. In: Traffic and Granular Flow'13, pp. 41–46. Springer, Cham (2015)
4. Daganzo, C.: Urban gridlock: macroscopic modeling and mitigation approaches. Transp. Res. B Methodol. **41**(1), 49–62 (2007)
5. Daganzo, C.F., Knoop, V.L.: Traffic flow on pedestrianized streets. Transp. Res. B Methodol. **86**, 211–222 (2016)
6. Duives, D.C., Daamen, W., Hoogendoorn, S.P.: Quantification of the level of crowdedness for pedestrian movements. Phys. A Stat. Mech. Appl. **427**, 162–180 (2015)
7. Hall, E.T.: The Hidden Dimension, vol. 1990. Anchor Books, New York (1969)
8. Hoogendoorn, S.P.: Normative pedestrian flow behavior theory and applications. LVV rapport, VK 2001.002 (2001)
9. Hoogendoorn, S., Daamen, W.: Design assessment of Lisbon transfer stations using microscopic pedestrian simulation. WIT Trans. Built Environ. **74**, 135–147 (2004)
10. Hoogendoorn, S.P., Campanella, M., Daamen, W.: Macroscopic fundamental diagrams for pedestrian networks. In: 89th Annual Meeting of the Transportation Research Board, Washington, DC (2010)
11. Hoogendoorn, S.P., Daamen, W., Knoop, V.L., Steenbakkers, J., Sarvi, M.: Macroscopic fundamental diagram for pedestrian networks: theory and applications. Transp. Res. Procedia **23**, 480–496 (2017)
12. Knoop, V.L., van Lint, H., Hoogendoorn, S.P.: Traffic dynamics: its impact on the macroscopic fundamental diagram. Phys. A Stat. Mech. Appl. **438**, 236–250 (2015)
13. Steffen, B., Seyfried, A.: Methods for measuring pedestrian density, flow, speed and direction with minimal scatter. Phys. A Stat. Mech. Appl. **389**(9), 1902–1910 (2010)

Towards Safer Pedestrian Traffic: Investigation of the Impact of Social Field Characteristic on Crowd Dynamics

Jingwan Fu, Boxiao Cao, Samer H. Hamdar, and Tianshu Li

Abstract The objective of this paper is to investigate pedestrian safety on vehicle-free platforms. Towards realizing such objective, a microscopic pedestrian movement model is expanded to analyze the implications of different pedestrian behavioral characteristics on pedestrian movement under different density levels. This microscopic modeling approach is flexible and may be efficiently implemented while accounting for different traffic dynamics caused by complex geometric and operational features, such as those observed in transit stations, football stadiums, and rallies. The integrated modeling framework is built based on the Social Field method (i.e., the social force model): the surrounding stimulus is considered, while adding a stopping/vibration module and a tangential force module to the basic Social Field method to account for additional behavioral dimensions based on atomistic interactions between particles. C++ was used to build a simulator to obtain the trajectory of pedestrians in the system. The research has been already translated to two simulated scenarios: the bottleneck scenario and the bi-direction flow scenario. Realistic flow patterns have been produced with a triangular fundamental diagram (flow-density curve) as observed in real-life conditions. When the density goes up, the flow will go up then go down to meet the capacity of the system. The expanded social force model provided improved (lower) error levels once the simulated pedestrian trajectories are compared to the observed pedestrian trajectories. Results show the expanded model produces high-density congestion dynamics that are not captured by the traditional social force model. The dynamics represented the higher clustering of flow-density data points at low flow and high pedestrian levels represent these dynamics.

J. Fu (✉)
School of Engineering and Applied Science, Department of Civil and Environmental Engineering, The George Washington University, Washington, DC, USA
e-mail: fujingwan77@gwmail.gwu.edu

B. Cao · S. H. Hamdar · T. Li
The George Washington University, Washington, DC, USA
e-mail: cbx@gwu.edu; hamdar@gwu.edu; tsli@gwu.edu

S. H. Hamdar (ed.), *Traffic and Granular Flow '17*,
https://doi.org/10.1007/978-3-030-11440-4_41

1 Introduction

In the recent decades, pedestrian safety has become a significant problem in metropolitan areas both on roadways (mainly due to pedestrian-vehicle collisions) and on pedestrian platforms (mainly due to overcrowding and lack of supply with respect to demand: as is the case crowded metro stations, stadiums, concert halls ..., etc.). Using Washington, D.C. as an example, there were 2624 collisions from 01/01/2013 to 01/01/2015.[1] The report of National Highway Traffic Safety Administration (NHTSA) may indicate that increased volumes for all types of traffic (bicycles, pedestrian, motor vehicles, etc.) create an increase in exposure to risky conflict conditions and the safety of all users requires examination [4].

Towards performing such investigation, the authors explore an integrated modeling approach that captures pedestrian walking behavior in congested and uncongested conditions. The modeling approach is flexible and may be efficiently implemented in order to account for different traffic dynamics caused by complex geometric and operational characteristics, such as those observed in transit stations, football stadiums, and rallies. The integrated modeling framework is built using concepts from the social force model [6, 10, 11, 13], behavioral heuristics [5, 12], and material science [14, 15]. Daamen and Hoogendoorm have done some of the experiments to capture the behavior of pedestrian [2, 3, 8]. C++ was used to build a simulator to obtain the trajectory [1, 9] of pedestrians in the system. From these trajectories, flow-density fundamental [7, 16, 17] diagrams can be derived and analyzed.

2 Methodology

The two behavior modules that are added to Helbing's social force model [6] in order to capture the movement behavior at different density levels are: the tangential force module and the stopping module. The details of the social force model, the tangential force module, and the stopping module are presented next.

2.1 The Basic Social Force Model

According to the social force model [6], we can calculate this directional acceleration or movement. Since the social force model is physics based model, the acceleration is determined through a force vector. The sum of all social force vectors determines the movement of pedestrians.

[1] http://dc.ms2soft.com/tcds/tsearch.asp?loc=dc&mod=tmc.

When a pedestrian wants to reach a destination, the desired direction is determined by

$$\mathbf{e} = \frac{\mathbf{x_i^0} - \mathbf{x_i}}{\|\mathbf{x_i^0} - \mathbf{x_i}\|} \tag{1}$$

where $\mathbf{e_i} \equiv$ desired direction, $\mathbf{x_i^0} \equiv$ the original location of pedestrian i, $\mathbf{x_i} \equiv$ the destination of pedestrian i.

The comfortable velocity and the desired velocity are defined as following:

$$\mathbf{v_i^0} = v_i^0 \mathbf{e_i^0} \tag{2}$$

where $\mathbf{e_i^0} \equiv$ desired direction of pedestrian, i $v_i^0 \equiv$ the value of desired velocity, $\mathbf{v_i^0} \equiv$ desired velocity.

The social force is proportional to the difference between the desired velocity and current velocity and is scaled by a relaxation time

$$\mathbf{f_i} = \frac{1}{\tau_i}(\mathbf{v_i^0} - \mathbf{v_i}) \tag{3}$$

where $\mathbf{f_i} \equiv$ social force, $\tau_i \equiv$ relaxation time, $\mathbf{v_i^0} \equiv$ desired speed of pedestrian i, $\mathbf{v_i} \equiv$ current speed of pedestrian i.

Moreover, a pedestrian prefers to keep a distance away from other pedestrians through a repulsion potential. The direction of repulsion force is defined by

$$\mathbf{e_{ij}} = \frac{\mathbf{x_i} - \mathbf{x_j}}{\|\mathbf{x_i} - \mathbf{x_j}\|} \tag{4}$$

$$\mathbf{f_{ij}} = \mathbf{e_{ij}} \frac{\partial v}{\partial r} \|\mathbf{x_i} - \mathbf{x_j}\| \tag{5}$$

where $\mathbf{U_{ij}} \equiv$ repulsion potential between i and j, $\frac{\partial v}{\partial r} \equiv V$ is a monotonic decreasing function of r, $\mathbf{x_i} \equiv$ current location of pedestrian i, $\mathbf{x_j} \equiv$ current location of pedestrian j, $r \equiv$ euclidean distance between pedestrian i and j, $\mathbf{f_{ij}} \equiv$ repulsion force.

In our research, we considered the surrounding stimulus, then added a tangential force module and a stopping module to the basic social force model to account for additional behavioral dimensions.

2.2 Tangential Force Module

The previous social force model considered repulsion force, but did not consider the collision avoidance. Pedestrians would keep distance away from others while moving towards a destination. When we detected the direction of pedestrian i is different of the direction of pedestrian j, we will force pedestrian i to "detour"

$$\mathbf{e_i} \cdot \mathbf{e_{ij}} < 0 \tag{6}$$

where $\mathbf{e_i} \equiv$ desire direction of i, $\mathbf{e_{ij}} \equiv$ desire direction of j with respect to i.

In order to bypass pedestrian j, the force on pedestrian i should be perpendicular to $\mathbf{e_i j}$, in the direction of

$$\frac{\mathbf{f_i}}{\|\mathbf{f_i}\|} = \mathbf{e_{ij}} \times (\mathbf{e_i} \times \mathbf{e_{ij}}) \tag{7}$$

where $\mathbf{f_i} \equiv$ social force for pedestrian$i$, $\mathbf{e_i} \equiv$ desire direction of i, $\mathbf{e_{ij}} \equiv$ desire direction of j with respect to i.

2.3 Stopping Module

The stopping module is introduced to account for the difference between the human behavior during every-day congested regimes (waiting in lines, stopping with no contact) and particle movements. Particles oscillate at equilibrium position while pedestrians have zero velocity/acceleration at equilibrium position. The velocity at time t is $\mathbf{v}(t)$ and the velocity at the subsequent time step dt becomes $\mathbf{v}(t + dt)$. When $\mathbf{v}(t)$ and $\mathbf{v}(t + dt)$ have different directions

$$\mathbf{v}(t) \cdot \mathbf{v}(t + dt) \leq 0 \tag{8}$$

where $\mathbf{v}(t) \equiv$ velocity at time t, $\mathbf{v}(t + dt) \equiv$ velocity at the subsequent time step dt.

In such situation, the pedestrian is forced to make "full stop".

To move again, a pedestrian's movement is governed by a gap acceptance function that can be described as

$$\| \int_0^\infty \mathbf{f}(t - \xi) g(\xi) \| \geq F_0 \int_0^\infty g(\xi) d\xi \tag{9}$$

where $F_0 \equiv$ pre-set starting force magnitude for a pedestrian, $\xi \equiv$ infinitesimally small time period/duration.

3 Results

The fundamental diagrams for the different narrow bottleneck scenario for the different models adopted were extracted from trajectory data and plotted through the use of MATLAB.

Different fundamental diagram under the bottleneck scenario was produced depending on the type of walking model adopted and the measurement area. The original size of the playground is 25 × 25 m and with 5 m-width bottleneck. As a first study area (Area1 shows in Fig. 1): the focus was on the coordinates from $x = 3$ m to $x = 23$ m and from $y = 20.5$ m to $y = 4.5$ m (area width = 20 m and arealength = 16 m).

To reach higher congestion levels, Area2 (shows in Fig. 2) is considered: the point of consideration has the coordinates from $x = 5$ m to $x = 10$ m and from $y = 20$ m to $y = 15$ m.

As mentioned earlier, two types of models were tested: the Modified SF models [13] and the basic social force model [6]. In the Modified SF model-1 (i.e., without the tangential force and the stopping modules), two assumptions were made: the first assumption considered that the movement of each pedestrian was impacted by the forces resulting from the nearest three pedestrians who are within a subject's sight-distance; the second assumption considered the nearest three pedestrians irrespectively of the sight-distance. In the Modified SF model-2, all the surrounding forces within a given sight-distance to a target pedestrian were accounted for. Moreover, the stopping module and the tangential force module were incorporated into the basic social force model.

In order to compare the differences between the fundamental diagrams for all the SF model versions, we plot the plow/density fundamental diagrams of these three models on the same graph in Fig. 3.

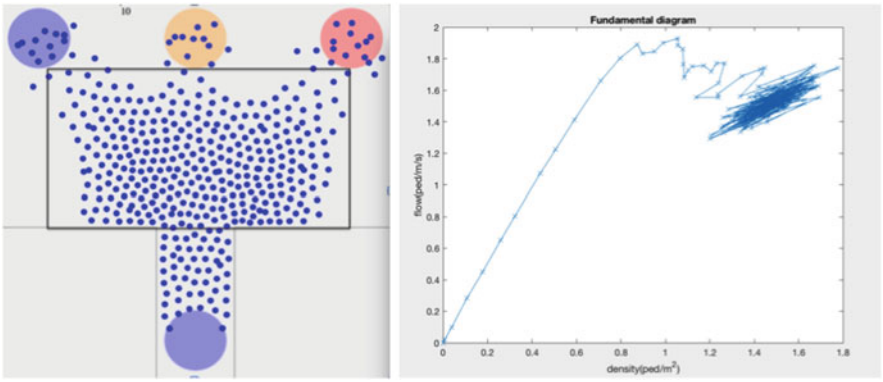

Fig. 1 Area 1: the expanded model fundamental diagram/flow/density relationship under the narrow bottleneck scenario

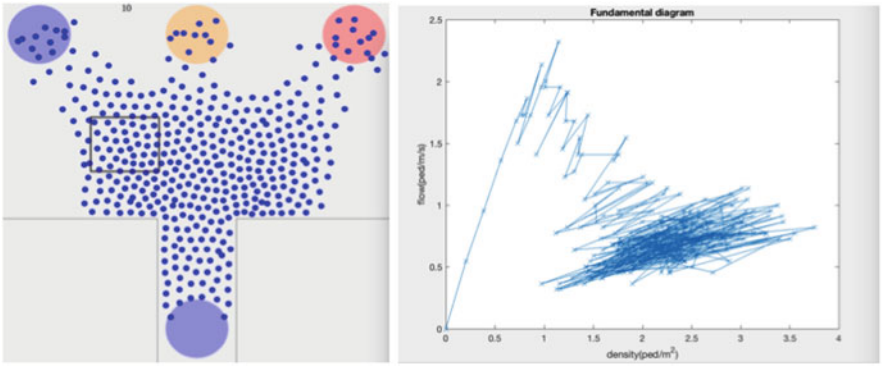

Fig. 2 Area 2: the expanded model fundamental diagram/flow/density relationship under the narrow bottleneck scenario

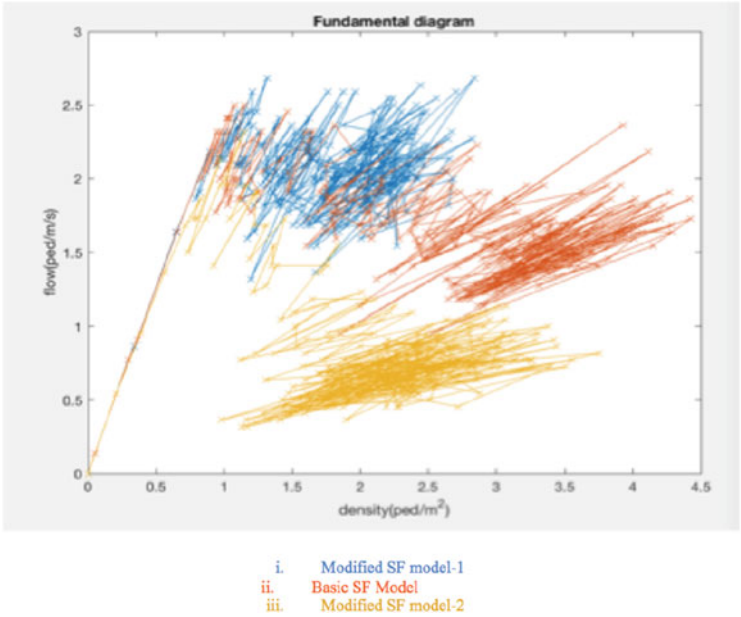

Fig. 3 Comparative illustration of different SF model versions studied in this thesis

The resulting Fig. 3 shows that only the Modified SF model-2 allows the formation of a complete triangular fundamental diagram.

For added insights, the trajectory data for some pedestrians were extracted from both the experimental TU Delft data and the simulation tool in Fig. 4. The X axis represents the time step while the Y axis represents the horizontal directional displacement. A clear shock wave phenomenon (consistent decrease in the slope of the space-time/x-y function) is seen in the first figure of Fig. 4. The only model that

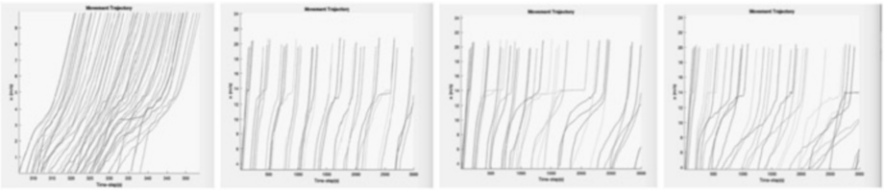

Fig. 4 Trajectory data extracted from the experimental data, the Basic SF model, the Modified SF model-1, and the Modified SF model-2

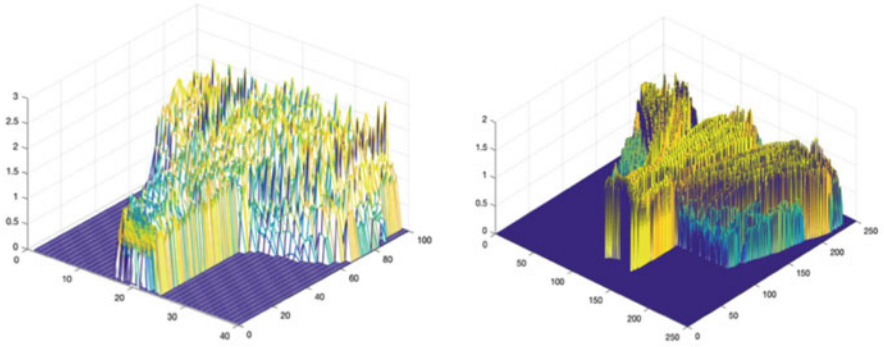

Fig. 5 3D diagrams for the experimental trajectories and the SF model-2 simulated trajectories

captures similar shockwave phenomena is the Modified SF model-2 (the last figure of Fig. 4).

In order to observe the distribution of the average speed in the bottleneck scenario, the 3-Dimensional trajectory figures (with speed represented by the z-axis) are offered in Fig. 5. The 3D diagrams record the average speed for each time step (0.1 s) for both the experimental data and the simulated data generated by the Modified social force model-2. It can be observed that the average speeds are similar in both diagrams.

4 Conclusion

Two modules have been added to expand on the basic social force model while incorporating perception related constraints associated with the cognitive and physiological capabilities of pedestrians (i.e., number of pedestrians considered and sight-distances). The modules added are a tangential force module to allow avoidance maneuvers and a stopping module allowing waiting and gap acceptance maneuvers in crowded situations. Different versions of the SF model (along with the proposed expanded SF model) are implemented and simulated. From the simulation exercise, by comparing the expanded SF model with the remaining versions of the

SF model, it was deduced that the formulation suggested in this thesis leads to more realistic pedestrian trajectories and thus behavior. The fundamental flow/density diagram resulting from the expanded SF model captured jamming and shockwave conditions observed in real-word crowded conditions. In other words, the model suggested in this thesis can efficiently be implemented while accounting for different crowd dynamics caused by complex geometric and operational features. In the future works, we will concentrate on the model calibration via genetic algorithm and combine the pedestrian traffic with bicycle and vehicle traffic.

Acknowledgements The research team would like to thank the Delft University of Technology Transportation Research Team, especially Dr. Winnie Daamen, for providing the trajectory data needed to test the proposed modeling framework.

References

1. Antonini, G., Bierlaire, M., Weber, M.: Discrete choice models of pedestrian behavior. Tech. rep. (2004)
2. Campanella, M., Hoogendoorn, S., Daamen, W.: Calibrating walker models: variations of parameter due to traffic regimes. In: European Conference on Mathematical and Theoretical Biology, Kraków, Poland, June 28–July 2 (2011)
3. Daamen, W., Hoogendoorn, S.: Experimental research of pedestrian walking behavior. Transp. Res. Rec. J. Transp. Res. Board **1828**, 20–30 (2003)
4. Ewing, R., Dumbaugh, E.: The built environment and traffic safety: a review of empirical evidence. CPL Bibliogr. **23**(4), 347–367 (2009)
5. Hamdar, S.H., Mahmassani, H.S., Chen, R.B.: Aggressiveness propensity index for driving behavior at signalized intersections. Accid. Anal. Prev. **40**(1), 315–326 (2008)
6. Helbing, D., Molnar, P.: Social force model for pedestrian dynamics. Phys. Rev. E **51**(5), 4282 (1995)
7. Hoogendoorn, S.P., Daamen, W.: Pedestrian behavior at bottlenecks. Transp. Sci. **39**(2), 147–159 (2005)
8. Hoogendoorn, S., Daamen, W.: Microscopic calibration and validation of pedestrian models: cross-comparison of models using experimental data. In: Traffic and Granular Flow '05, pp. 329–340 (2007)
9. Johansson, A., Helbing, D., Shukla, P.K.: Specification of the social force pedestrian model by evolutionary adjustment to video tracking data. Adv. Complex Syst. **10** (Suppl. 02), 271–288 (2007)
10. Kuhn, M.H.: Lewin, kurt. field theory of social science: selected theoretical papers. In: Cartwright, D. (ed.), pp. xx, 346. New York: Harper & Brothers (1951). $5.00. Ann. Am. Acad. Pol. Soc. Sci. **276**(1), 146–147 (1951)
11. Lakoba, T.I., Kaup, D.J., Finkelstein, N.M.: Modifications of the Helbing-Molnar-Farkas-Vicsek social force model for pedestrian evolution. Simulation **81**(5), 339–352 (2005)
12. Moussaïd, M., Helbing, D., Theraulaz, G.: How simple rules determine pedestrian behavior and crowd disasters. Proc. Natl. Acad. Sci. **108**(17), 6884–6888 (2011)
13. Porter, E., Hamdar, S.H., Daamen, W.: Pedestrian dynamics at transit stations: an integrated pedestrian flow modeling approach. Transp. A: Transp. Sci. **14**, 1–16 (2017)
14. Stillinger, F.H., Weber, T.A.: Computer simulation of local order in condensed phases of silicon. Phys. Rev. B **31**(8), 5262 (1985)
15. Tersoff, J.: Modeling solid-state chemistry: interatomic potentials for multicomponent systems. Phys. Rev. B **39**(8), 5566 (1989)

16. Voronoï, G.: Nouvelles applications des paramètres continus à la théorie des formes quadratiques. deuxième mémoire. recherches sur les parallélloèdres primitifs. Journal für die reine und angewandte Mathematik **134**, 198–287 (1908)
17. Zhang, J., Klingsch, W., Schadschneider, A., Seyfried, A.: Transitions in pedestrian fundamental diagrams of straight corridors and t-junctions. J. Stat. Mech: Theory Exp. **2011**(06), P06,004 (2011)

Defining the Pedestrian Fundamental Diagram

Ernst Bosina and Ulrich Weidmann

Abstract First introduced in vehicular traffic, the fundamental diagram is now also used widely in pedestrian transport to describe the relationship between speed, flow, and density. Various equations have been proposed, which often exhibit strong differences. So far, several parameters that influence the pedestrian fundamental diagram have been identified. These parameters do not, however, explain the differences in proposed representations of the fundamental diagrams.

Examining the literature, it becomes obvious that even though the concept is applied widely, a detailed and commonly accepted definition of the fundamental diagram for pedestrians is missing. Thus, the term "fundamental diagram" is used to describe different speed–density or flow–density relations. Without a proper definition, also the measurement and data evaluation methods differ strongly, which is then reflected in the resulting fundamental diagram curves.

This contribution aims at providing a definition for the pedestrian fundamental diagram. Starting from its origin as a model for pedestrian flow, its background and area of application are discussed. Based on these fundamental insights, a definition for the pedestrian fundamental diagram is proposed. An important aspect of the fundamental diagram concept is its stochastic nature. As the flow at a specific density is not constant, but shows certain variations over time, the fundamental diagram can either be described by its mean value or by using a probabilistic approach. In this contribution, an extension of the fundamental diagram to include its stochastic nature is discussed.

1 Introduction

Similar to the level of service concept, the pedestrian fundamental diagram model originates from vehicular traffic. In the 1920s the first studies were made to estimate the capacity of a single traffic lane (for a list see, for example, [6]). The work of

E. Bosina (✉) · U. Weidmann
ETH Zurich, Institute for Transport Studies and Systems (IVT), Zurich, Switzerland
e-mail: ernst.bosina@ivt.baug.ethz.ch; weidmann@ivt.baug.ethz.ch

S. H. Hamdar (ed.), *Traffic and Granular Flow '17*,
https://doi.org/10.1007/978-3-030-11440-4_42

Greenshield [9] is then considered the starting point of traffic flow theory and the fundamental diagram [16], even though the term fundamental diagram was only introduced several years later by Haight [10].

The first measurements of pedestrian density and walking speed were then published in the 1960s [18]. Some years later, Fruin [7] published his work on the pedestrian speed–density relation and the level of service, whose principles are still used in pedestrian transport planning. Even though the concept of the fundamental diagram was transferred from vehicular traffic, the first mentioning of the term "fundamental diagram" in the context of pedestrian transport can only be found in Weidmann [24]. In his work, a general fundamental diagram for pedestrian transport was proposed for walkways and walking up- and downstairs. In the last decades, many different fundamental diagrams have been measured and proposed in literature (Fig. 1). Among them, only a few references can be found which propose fundamental diagrams for different situation characteristics, for example, normal and emergency conditions, uni- and bidirectional flow, and different trip purposes [7, 18, 20, 23].

Apart from the free-flow walking speed [3], the different influence factors are likely to change the fundamental diagram curve [4]. For example, luggage can influence the free-flow walking speed, but it will also increase the individual space demand and hence the maximum density. Still, neither in car traffic nor in pedestrian traffic, a general definition and understanding of the fundamental diagram can be found. It can otherwise be observed that the term fundamental diagram is used for a vast amount of different relations, without discussing the validity or limitations of the approach [11].

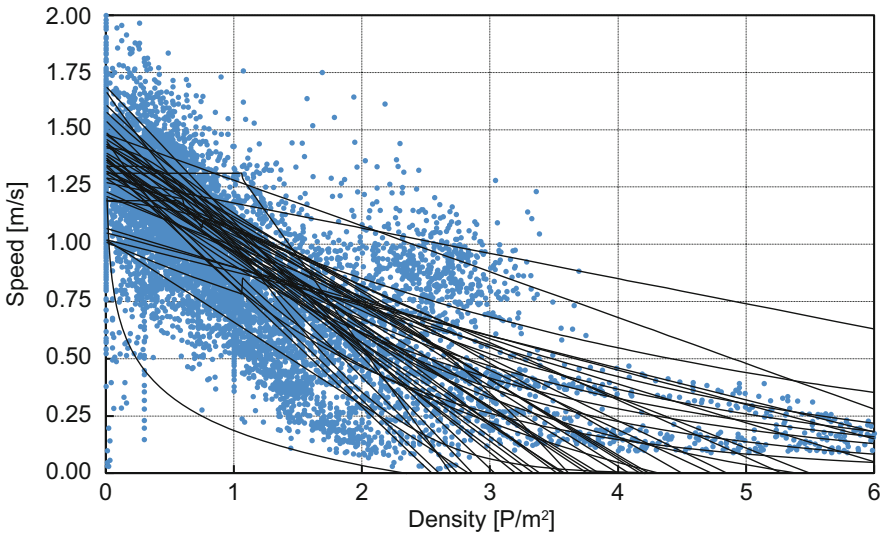

Fig. 1 Fundamental diagram curves for level walking proposed in literature in comparison with speed–density data found in literature [3]

2 Existing Definition of the Pedestrian Fundamental Diagram

Like for car traffic, the definitions of the pedestrian fundamental diagram found in literature vary considerably. Often, the fundamental diagram is solely described as the relation between density, flow, and speed. Nevertheless, the differences between theoretical considerations and measurement data are significant and show the need of a proper description of the fundamental diagram.

Generally, the pedestrian fundamental diagram describes a relation between walking speed, pedestrian density, and flow. Still, it can be argued that not all such measurements can be used to determine the fundamental diagram, as it aims at describing the general relation between these three traffic properties. In literature therefore stationary and homogeneous conditions [4, 17] or a stationary flow [13, 22] is mentioned as requirement. In addition, other factors like time and measurement area will influence the results [2].

Daamen [5] describes the fundamental diagram as statistical relation under similar average conditions. It is assumed that on average, pedestrians behave the same if the average conditions are similar. Therefore the fundamental diagram is also sometimes considered as the averages of flow and density, compared to local values [12]. The fundamental diagram thus represents the macroscopic characteristics [13, 23]. On the other hand, others state that the fundamental diagram contains the local density [1, 19].

Summarizing the literature, no detailed definition for the pedestrian fundamental diagram was found. Otherwise, several different v-D-F relations are named fundamental diagram although they are not comparable as, for example, the method used for calculating the density or the time intervals used differ considerably. Only a few authors provide a definition of the fundamental diagram, whereof some are contradictory. A specific definition including a consistent discussion of the aim of the fundamental diagram and therefore the essential properties of speed, flow, and density are lacking.

3 Aggregation Levels

For the classification of the fundamental diagram in terms of the aggregation level used, two different approaches can be distinguished. First, the different levels can be divided based on the usage, hence the outcome. Second, they can be classified using the aggregation level of the model.

Table 1 Usage based classification of speed–density relations at various levels

Level	Name	Pedestrian	Space
Macro	Network FD	Unknown number of flows	Area/network
Macro	Generalized FD	Multiple ped. flows	Single situation
Meso	Fundamental diagram	Pedestrian flow	Cross-section
Aggregated micro	Group v-D relation	Indiv. aggregated to groups	x–y position
Micro	Individual v-D relation	Individuals	x–y position

3.1 Usage Based Classification

For the usage based classification, the aggregation level of the result and the usage level of the outcome are relevant. In general, a division between microscopic, macroscopic, and mesoscopic can be made. A microscopic view provides data for the smallest unit; hence, single pedestrians and a macroscopic approach shows only aggregated values. A mesoscopic level will provide certain aspects on a macroscopic and others on a microscopic level. To categorize the fundamental diagram in relation to other speed–density relations according to this logic, Table 1 shows different levels and their corresponding main properties. The fundamental diagram considers pedestrian flows, hence a macroscopic aggregation, but at a cross-section location, which can be considered microscopic in terms of space. Hence it is argued here that the classic fundamental diagram is mesoscopic. The behavior of individual pedestrians cannot be described using this approach, but can be extended to also show variations in the flow, which will also support its mesoscopic nature.

3.2 Model Based Classification

In the model based classification, the aggregation of the model itself and not its output is considered. In microscopic models, the individual behavior of pedestrians and their individual characteristics are simulated using routines to describe the interaction between pedestrians and the environment. Macroscopic models use aggregated information; thus, the model framework considers aggregated features such as pedestrian flows or larger areas. In between, mesoscopic models show elements of both levels; thus, certain aspects are modeled in aggregated form, whereas others are modeled disaggregated. In this framework, the social force model is a microscopic model, and the Kladek formula [14] can be considered to be a macroscopic model.

The model based classification and the usage based classification are linked by the fact that the aggregation level of the model always has to be equal or lower that the results. Thus, a macroscopic model cannot be used to obtain individual speed–density relations but a microscopic model can be used to obtain a classic fundamental diagram. Until now, most fundamental diagrams are modeled using a

macroscopic model, hence providing a mostly linear relation between average speed and density. Nevertheless, especially for the validation of models, also fundamental diagrams are calculated from microscopic models [15]. Still, no approach was found to explicitly model the fundamental diagram using a microscopic model.

4 Defining of the Pedestrian Fundamental Diagram

To be useful for the design of pedestrian facilities, a basic definition of the fundamental diagram is needed which only reflects the pedestrian characteristics and thus is, for example, independent from the measurement method used to obtain the fundamental diagram [2]. The fundamental diagram, compared to other speed–density relations, therefore does not represent the characteristics of individual pedestrians, as it is done in microscopic models.

The purpose of the pedestrian fundamental diagram is to describe the properties of a pedestrian flow for a cross-section, thus at a mesoscopic level. Hence, the fundamental diagram will vary depending on the observed pedestrian characteristics (free-flow walking speed, shy away distance, etc.). For example, even if the average free-flow walking speed is the same, differences in the walking speed distribution among the group (i.e., the standard deviation) might result in differences in the fundamental diagram (assuming otherwise similar conditions). By default, the fundamental diagram represents a situation with solely unidirectional flow.

If different or no definitions of the fundamental diagram are used, the comparison between resulting data is of limited value. Therefore, and to summarize the characteristics of the fundamental diagram and to distinguish it from other speed–density relations, a detailed definition of the pedestrian fundamental diagram for unidirectional flow is proposed:

> The pedestrian fundamental diagram describes the (average) relation between speed, flow, and density of a set of pedestrians with defined properties at constant global density for infinite time and space. The individual characteristics of the pedestrians might vary, but they are randomly distributed over space and time.

In contrast to simulations, the constant state in the definition can hardly be reached in real-life situations. Still, based on the specific setting, techniques can be selected which minimize the deviation of the speed–density calculations from the proposed definition. This ensures a high comparability between measurements and reduces undesirable influences. Here, some of the requirements can be violated without a substantial influence on the results. For example, a finite measurement time and space is possible and small measurement areas can also be compensated

using long observation times and vice versa. In this case, the deviation between the definition and the method used and the expected effect on the results should be discussed.

5 Stochastic Variations in the Fundamental Diagram

Usually, the fundamental diagram only shows the average relation between density and speed or flow. Still, even for the same constant setting and global density, stochastic variations will be visible. Individual pedestrian will not always react the same in the same situation, as well as variations between different pedestrians exist. In addition, the pedestrian composition within a flow is statistically distributed. These differences will lead to variations in the local density, which itself will also influence the speed and direction of individual pedestrian and therefore the global average speed and flow.

In Fig. 2, an example for the influence of the stochastic variations on the fundamental diagram is shown. For this, it is assumed that the walking speed at a certain density shows a variation of $\pm 15\%$ around the mean value. For a given density, the fundamental diagram now shows a corresponding walking speed range as well as a range of flow values. Especially if the flow is known and it is in the range of the maximum average flow, this example will result in a wide range of corresponding densities.

These considerations are especially important for the design of pedestrian facilities. Usually the design of facilities is not done for mean values, which would imply that 50% of the time the design load is reached (assuming a normal

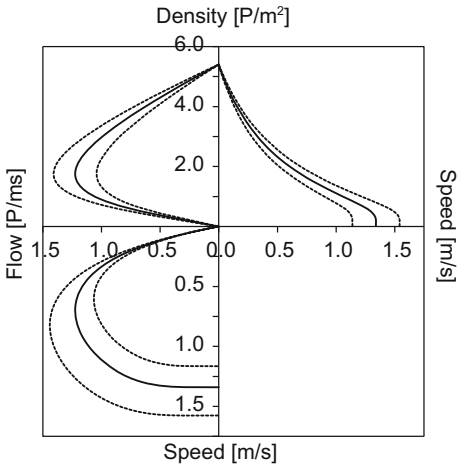

Fig. 2 Influence of parameter variation on the fundamental diagram (data: [24])

distribution) the facility is overloaded. Therefore, an exceedance probability is applied to integrate the stochastic nature of the variables into the calculation. As a reference for suitable probability values, data from similar situations can be used. For the pedestrian crossing speed, often the 15th percentile is used as a reference value [8]. To determine the design hourly volume of roads, the hourly value for the 30th to 100th yearly peak hour is used [21]. In addition, it has to be considered, if the values are used for the design for quality or design for safety.

6 Conclusions

Nowadays, the fundamental diagram concept is widely used to describe the relation between speed and density in pedestrian transport. Still, neither in car traffic, where the concept originates, nor in pedestrian transport, a commonly accepted definition beyond its three main properties, speed, density, and flow, can be found in literature. This led to the current situation, where a wide range of speed–density curves are named "fundamental diagram" which cannot be compared due to their differences in measurement and calculation processes.

Thus, a definition of the fundamental diagram for unidirectional flow was established for this work. It is based on the aim and application purposes found in literature. Based on this definition it shall also be possible to derive fundamental diagrams in different situations which can be compared in a meaningful way.

As, for example, the reaction of pedestrians to similar situation can vary, the fundamental diagram has some stochastic variations. The proposed definition thus allows an extension from a fundamental diagram representing the mean values to a stochastic fundamental diagram, which also includes these variations. Especially for the design of pedestrian facilities, this can enhance the quality of the results.

Further, the speed–density curves found in literature were shown. Although the differences in the creation pose difficulties for their comparison, they form a clear area within the speed–density plot. It can also be concluded that the widely used fundamental diagrams proposed by Weidmann [24] can still serve as an approximation of the mean curves. Using theoretical considerations about the physical properties of pedestrians, the range of the pedestrian fundamental diagram values can be narrowed down.

However, especially at the capacity values obtained from literature, considerable variations can be found. Apart from variation in the measurement settings, this can also reflect the walking behavior found in different setting. Here, like for the walking speed, several influences can be identified.

References

1. Bellomo, N., Piccoli, B., Tosin, A.: Modeling crows dynamics from a complex system viewpoint. Math. Models Methods Appl. Sci. **22**(suppl. 02), 1230004 (2012). https://doi.org/10.1142/S0218202512300049
2. Bosina, E., Weidmann, U.: Generic description of the pedestrian fundamental diagram. In: Song, W., Ma, J. Fu, L. (eds.) Proceeding of Pedestrian and Evacuation Dynamics 2016, pp. 548–555. University of Science and Technology of China Press, Hefei (2016)
3. Bosina, E., Weidmann, U.: Estimating pedestrian speed using aggregated literature data. Phys. A Stat. Mech. Appl. **468**, 1–29 (2017). https://doi.org/10.1016/j.physa.2016.09.044
4. Daamen, W.: Modelling passenger flows in public transport facilities. Trail Thesis Series, Netherlands TRAIL Research School, Delft (2004)
5. Daamen, W., Hoogendoorn, S.P., Bovy, P.H.: First-order pedestrian traffic flow theory. Transp. Res. Rec. J. Transp. Res. Board **1934**, 43–52 (2005). https://doi.org/10.3141/1934-05
6. Evans, H.K. (ed.): Traffic Engineering Handbook, 2nd edn. Institute of Traffic Engineers, New Haven (1950)
7. Fruin, J.J.: Pedestrian Planning and Design. Metropolitan Association of Urban Designers and Environmental Planner, New York (1971)
8. Gates, T.J., Noyce, D.A., Bill, A.R., Van Ee, N.: Recommended walking speeds for timing of pedestrian clearance intervals based on characteristics of the pedestrian population. Transp. Res. Rec. J. Transp. Res. Board **1982**, 38–47 (2006). https://doi.org/10.3141/1982-07
9. Greenshields, B.D.: A study of traffic capacity. In: Proceedings of the 14th Annual Meeting of the Highway Research Board, Washington, DC, vol. 14, pp. 448–477 (1935)
10. Haight, F.A.: Mathematical Theories of Traffic Flow. Mathematics in Science and Engineering, vol. 7. Elsevier Science, Amsterdam (1963)
11. Johansson, A.F.: Data-Driven Modeling of Pedestrian Crowds. Dissertation, Technische Universitaet Dresden, Dresden (2009)
12. Johansson, A., Helbing, D., Al-Abideen, H.Z., Al-Bosta, S.: From crowd dynamics to crowd safety: a video-based analysis. Adv. Complex Syst. **11**(4), 497–527 (2008). https://doi.org/10.1142/S0219525908001854
13. Kaakai, F., Hayat, S., El Moudni, A.: A hybrid Petri nets-based simulation model for evaluating the design of railway transit stations. Simul. Model. Pract. Theory **15**(8), 935–969 (2007). https://doi.org/10.1016/j.simpat.2007.05.003
14. Kladek, H.: Ueber die Geschwindigkeitscharakteristik auf Stadtstraßenabschnitten. Dissertation, Hochschule fuer Verkehrswesen "Friedrich List", Dresden (1966)
15. Kretz, T., Lohmiller, J., Schlaich, J.: The inflection point of the speed-density relation and the social force model. Collect. Dyn. **1**(0), 1–27 (2016). https://doi.org/10.17815/CD.2016.6
16. Kuhne, R.D.: Greenshields' legacy: highway traffic. In: 75 Years of the Fundamental Diagram for Traffic Flow Theory: Greenshields Symposium. Transportation Research E-Circular, vol. E-C149, pp. 3–10. Transportation Research Board, Woods Hole (2011)
17. Nikolic, M., Bierlaire, M., Farooq, B., de Lapparent, M.: Probabilistic speed-density relationship for pedestrian traffic. Transp. Res. Part B Methodol. **89**, 58–81 (2016). https://doi.org/10.1016/j.trb.2016.04.002
18. Oeding, D.: Verkehrsbelastung und Dimensionierung von Gehwegen und anderen Anlagen des Fussgaengerverkehrs. Dissertation, Technische Hochschule Carolo-Wilhelmina zu Braunschweig, Braunschweig (1963)
19. Parisi, D.R., Gilman, M., Moldovan, H.: A modification of the social force model can reproduce experimental data of pedestrian flows in normal conditions. Phys. A Stat. Mech. Appl. **388**(17), 3600–3608 (2009). https://doi.org/10.1016/j.physa.2009.05.027
20. Predtecenskij, W.M., Milinskij, A.I.: Personenstroeme in Gebaeuden: Berechnungsmethoden fuer die Projektierung, 1st edn. Verlagsgesellschaft Rudolf Mueller, Koeln-Braunsfeld (1971)
21. Sharma, S.C., Oh, J.Y.: Prediction of design hourly volume from road users' perspective. J. Transp. Eng. **115**(6), 646–660 (1989)

22. Steffen, B., Seyfried, A.: Methods for measuring pedestrian density, flow, speed and direction with minimal scatter. Phys. A Stat. Mech. Appl. **389**(9), 1902–1910 (2010). https://doi.org/10.1016/j.physa.2009.12.015
23. Venuti, F., Bruno, L.: Crowd-structure interaction in lively footbridges under synchronous lateral excitation: a literature review. Phys. Life Rev. **6**(3), 176–206 (2009). https://doi.org/10.1016/j.plrev.2009.07.001
24. Weidmann, U.: Transporttechnik der Fussgaenger - Transporttechnische Eigenschaften des Fussgaengerverkehrs (Literaturauswertung), 2nd edn. No. 90 in Schriftenreihe des IVT. Institut fuer Verkehrsplanung, Transporttechnik, Strassen- und Eisenbahnbau, ETH Zurich, Zuerich (1993). https://doi.org/10.3929/ethz-a-000687810

Part III
From Individual Interactions to Complex Systems: Airplanes, Bicycles, Mixed Flow, Particles and Traveler Behavior

Simulating Ground Traffic on Airports Using Cellular Automata: The CAMAT-Model

Florian Mazur and Michael Schreckenberg

Abstract Based on the Nagel–Schreckenberg cellular automaton model for freeway traffic (Nagel and Schreckenberg, J. Phys. I 2:2221–2229, 1992), a model for simulating ground traffic on airports, the CAMAT-model (cellular automaton model for airport traffic), was developed. The model was designed and calibrated by empirical research and presents the dynamic of airplanes from the point of touchdown on the runway to the gate or from the gate (including pushback if necessary) to the point of takeoff. For this purpose the behavior of airplanes was studied on the international airport of Duesseldorf, complemented by specific data provided by the German air traffic control (Deutsche Flugsicherung, DFS). The new model's main goal is to simulate the dynamics of all airplanes as realistically as possible and to give an airport planner the opportunity to simulate changes in layout or routing for improvement and optimization.

1 Introduction

Airplane traffic is the most increasing mode of transport [1, 2] due to the continuing trend toward long-distance travel and the increasing interdependence of international commerce. The expected growth rate in Germany is over 2.3% per year in contrast to 0.2% for motorized private transport, 0.3% for railway transport, and −0.1% for public road transport.

The increase of airplane traffic has created problems on most international airports in Germany. For instance, long queues of airplanes are waiting for takeoff in front of the runways because of the limited capacity of the runways. Therefore airport surface operations have to become more efficient in order to be able to handle the increasing number of airplanes and to reduce waiting times. Simulations are useful to evaluate suggestions in advance and to avoid poor planning.

F. Mazur (✉) · M. Schreckenberg
University of Duisburg-Essen, Physics of Transport and Traffic, Duisburg, Germany
e-mail: florian.mazur@uni-due.de; michael.schreckenberg@uni-due.de

S. H. Hamdar (ed.), *Traffic and Granular Flow '17*,
https://doi.org/10.1007/978-3-030-11440-4_43

1.1 Cellular Automata Models (CA)

Cellular automata models, being well known from road traffic and pedestrian traffic [4, 6, 9], are a very efficient method to simulate traffic in a microscopic way.

With regards to airplane traffic there are few models developed to simulate ground operations on airports. One is, for instance, the model of Mori et al. [7, 8], simulating ground traffic on the international airport of Tokyo (Narita). This model is specially tailored to this airport (e.g., the airport detection system, which is not used at airports in Germany) and does not use randomization. Therefore, a new cellular automaton model based on the CA model for road traffic [9] is developed for simulating ground traffic on airports like the international airport of Duesseldorf in Germany. The purpose is to reduce the airplanes' rolling times in order to reduce fuel consumption.

1.2 Duesseldorf Airport (EDDL)

The international airport of Duesseldorf (ICAO code EDDL) was opened in 1927. It consists of two parallel runways which are too close to each other to be operated independently (see Fig. 1). In 2016, 23.5 million passengers were processed and the airport handled 217,500 airplane movements [3]. The prognosis for 2017 is an exceedance of the 24 million passenger mark. There are lots of crossing situations due to the layout of the airport and the limited space.

The unique fact about the airport is the so-called Angerlandvergleich [10]. In 1965 the airport and the nearby towns reached a settlement for reducing noise pollution by limiting airplane movements. On the basis of the Angerlandvergleich the following relevant restrictions for using the second runway built in 1997 exist: first, the airport is allowed to use the second runway only half-time. Second, the local government determines the usage times one week in advance.

2 The CAMAT-Model

The newly developed cellular automaton model presented in this paper is called the CAMAT-model (cellular automaton model for airplane traffic). In the model, the main steps of the Nagel–Schreckenberg model for road traffic are adopted: the acceleration step, the breaking step, the randomization step, and the movement. It uses a parallel update and a cell size of 5 m. This is small enough to map all common types of aircrafts (e.g., a Cessna 152 needs 1 cell, an Airbus 320-200 and a Boeing 737-800 8 cells, an Airbus A330-200 12 cells, a Boeing 747-400 14 cells, and an Airbus 380-800 15 cells). The time discretization is 1 s due to the reaction time of human beings.

Fig. 1 Layout of Duesseldorf Airport (EDDL). The airport consists of two parallel runways (05R/23L and 05L/23R) and one main taxiway (M). Furthermore there is one passenger terminal with terminal parts A, B, and C and a main apron, the apron west, and the apron east. Source: OpenStreetMap contributors (Licence ODbL) [11]

The velocity of airplanes on the ground is limited to 2 cells per second (10 m/s) which is the maximum allowed speed for taxiing. On runways the maximum speed is unlimited, respectively, the specific takeoff and landing speed of the different airplanes.

Acceleration and deceleration depend on the airplanes' weight class, which are classified due to the maximum takeoff weight (MTOW) of the airplanes by the International Civil Aviation Organization (ICAO) [5]:

- Light (L) MTOW of 7000 kg (15,000 lb) or less
- Medium (M) MTOW of greater than 7000 kg, but less than 136,000 kg (300,000 lb)
- Heavy (H) MTOW of 136,000 kg (300,000 lb) or greater
- Super (J) refers only to the Airbus A380 and Antonov An225

In the CAMAT-model an airplane can accelerate one unit per 2 or 3 s (2 for L and 3 for M, H, and S). For deceleration it is important to distinguish between an airplane on the runway and an airplane on the taxiway. On the taxiway the deceleration is unlimited. On the runway the deceleration is one unit per 2–4 s (2 for L, 3 for M and H, and 4 for S).

Randomization is implemented as follows: arriving airplanes reduce their velocity one unit with a probability of 1% for the following 10 s, while departing airplanes reduce their velocity with a probability of 3% for the following 10 s. These values result from the analysis of empirical data collected at the airport of Duesseldorf.

Airplanes on ground adhere a minimum distance of 20 cells due to the jet blast and possible damages. To avoid unnecessary breaking the following airplane reduces its velocity to 1 cell per second if the distance gets closer than 150 cells between the airplanes.

In real life air traffic control (ATC) is responsible for all crossing situations on an airport. In the simulation the airplane arriving first at a crossing between two taxiways has the right of way. If they arrive at the same time the simulation has to dice. The crossing of runways with taxiways is very simple. The crossing of a runway is only possible if the runway is free of airplanes. Otherwise the airplane on the taxiway has to stop at the holding point (a line marked on the taxiway) in front of the runway.

The first action of a departing airplane is the pushback. The airplane has to be pushed backwards from the terminal onto the taxiway because it is not allowed to use the reverse thrust in this phase. The process of pushback normally takes 3–5 min (see Fig. 2) and depends on the position of the gate used by the airplane.

The actual used gate depends on air traffic control, the company which is responsible for the flight (due to strategic alliances aircrafts of all related companies use the same terminal if possible) and the destination (due to customs).

3 Calibrating the CAMAT-Model

Real-world data from the airport of Duesseldorf is very hard to obtain. Radar only provides pictures with lots of disturbances due to radar shadow. Also it is hard to distinguish between small airplanes and ground facilities, such as busses, without additional information. On the airport of Duesseldorf no automatic detection system is installed like on the airport of Tokyo. The identification by the airplanes' transponder is mostly not possible. A great number of airplanes power the transponder on just before line-up on the runway and not before pushback. As a result, the transponders' data for taxiing is not available and only visual observation is possible on the airport of Duesseldorf.

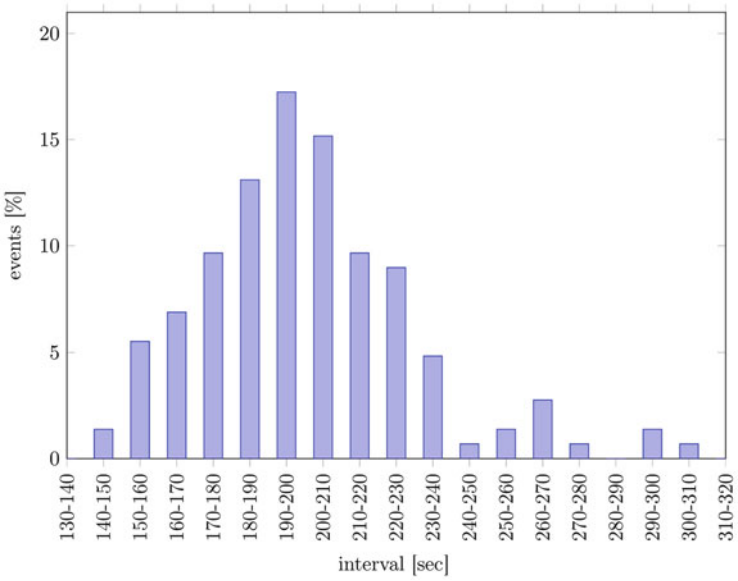

Fig. 2 Times needed for pushback at the airport of Duesseldorf. The average time of most airplanes amounts to 4 min

3.1 Concept of Collecting Data of Duesseldorf Airport

To obtain relevant information passing times are collected for airplanes at defined checkpoints (crossings of taxiways or taxiways with runways, see Fig. 3). As a result taxiing times are obtained for every section on taxiway and runway.

On each runway airplanes can take off and land in two directions depending on the direction of the wind. The data of each direction of operation has to be collected independently. Furthermore a differentiation between single-runway-operation (SRO), when only one runway is allowed to be used, and dual-runway-operation (DRO) is important to obtain relevant data.

This data is complemented by data of air traffic control like gates and routes used by the airplanes.

3.2 Comparison between Real-World Data and Simulation

A comparison between real-world data and simulation was realized on both runways. Data from each runway was compared for both directions of operation with the necessary distinction between single-runway-operation and dual-runway-operation. The following figures represent a selection of all comparisons.

Fig. 3 Checkpoints defined at Duesseldorf Airport (EDDL). The checkpoints on runways are named by letters, and the checkpoints on taxiways are named by numbers. Source: OpenStreetMap contributors (Licence ODbL) [11]

Figures 4 and 5 present the comparison for arriving airplanes on runway 05L in dual-runway-operation (in single-runway-operation runway 05L is not used), respectively, 23R in single-runway-operation. On the x-axis the distance starting at checkpoint M on the runway and on the y-axis the taxiing time starting when passing checkpoint M is plotted. In addition the position of all passed checkpoints is marked with green lines. The averaged trajectories of real and simulated data are very similar and differ only slightly. The slope of the trajectories shows the velocity of the airplanes. An increased slope indicates a decreased velocity.

Figures 6 and 7 show the same comparison but for departing airplanes on runway 05L, respectively, 23R. This runway is used for departing airplanes in single-runway-operation and dual-runway-operation. The direct comparison shows a lower taxiing time for airplanes in dual-runway-operation due to the higher capacity of the airport in this mode.

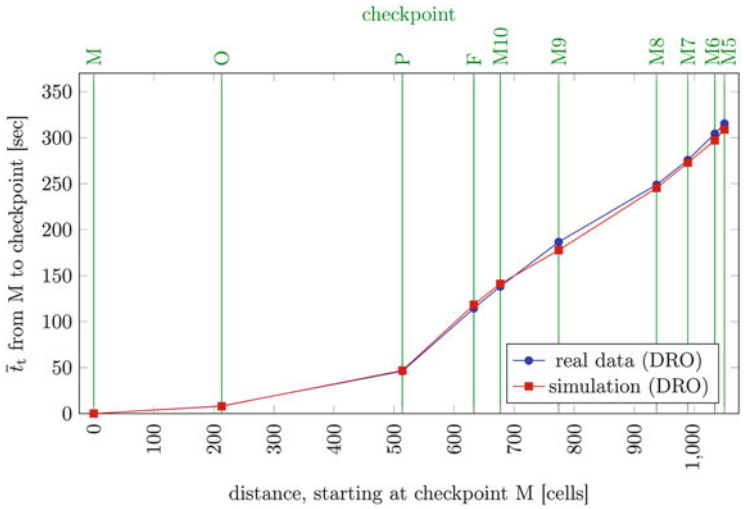

Fig. 4 Comparison between real-world data and simulation for arriving aircrafts on runway 05L (DRO) taxiing via K2 to checkpoint 5 on taxiway M at the airport of Duesseldorf

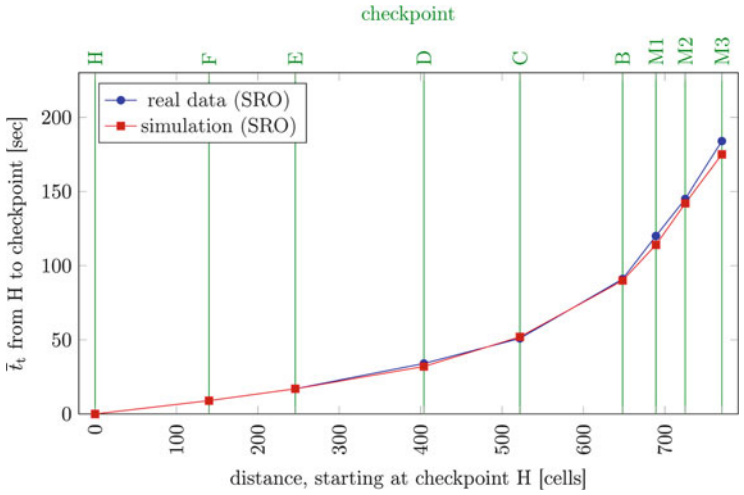

Fig. 5 Comparison between real-world data and simulation for arriving aircrafts on runway 23L (SRO) taxiing via L9 to checkpoint 3 on taxiway M at the airport of Duesseldorf

4 Summary and Outlook

In this paper the CAMAT-model (cellular automaton model for airplane traffic) is presented. The CAMAT-model offers an opportunity for microscopically simulating ground traffic of airplanes on an airport. The calibration is conducted by data of

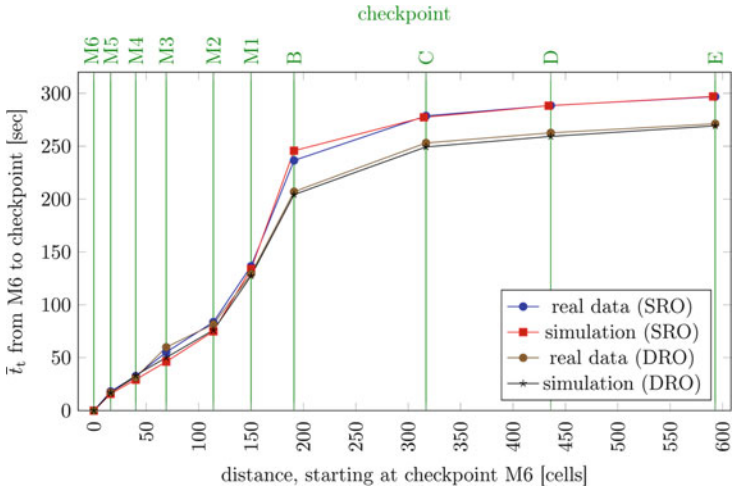

Fig. 6 Comparison between real-world data and simulation for departing airplanes on runway 05R (SRO and DRO) starting at checkpoint 6 on taxiway M at the airport of Duesseldorf

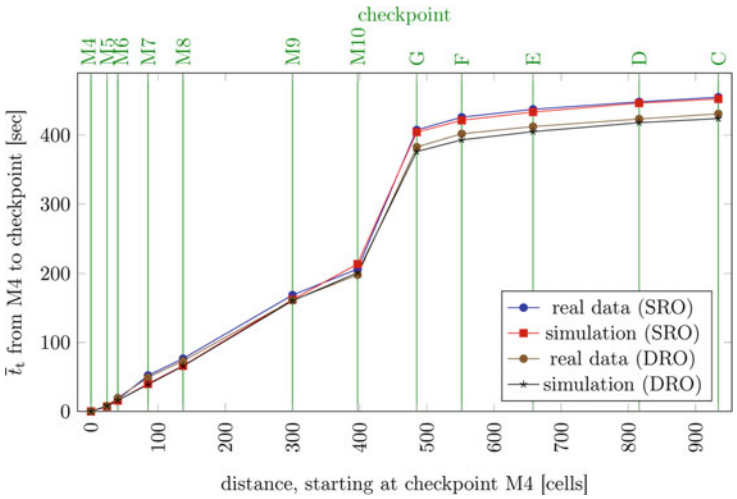

Fig. 7 Comparison between real-world data and simulation for departing airplanes on runway 23L (SRO and DRO) starting at checkpoint 4 on taxiway M at the airport of Duesseldorf

visual observations from the airport of Duesseldorf and data of air traffic control. As a result of the calibration the aberration of the CAMAT-Model is maximally 3% (typically 1–2%). By using the model it becomes possible to simulate new taxiing routes on the actual layout of an airport and to simulate new airport layouts in advance.

Further research will deal with the implementation of ground facility traffic, like fuelling vehicles, follow-me-cars, busses, etc., and the simulations of new airplane systems, like the break to vacate system (BTV) [12], which is a subset of the airplane's flight computer. It allows the computer to be programmed for a pre-selected stopping distance, indicating the required combination of brakes and thrust reversers to achieve that distance.

References

1. Bundesministerium für Verkehr und digitale Infrastruktur: Verkehrsverflechtungsprognose 2030. Internet, http://www.bmvi.de/SharedDocs/DE/Anlage/VerkehrUndMobilitaet/verkehrsverflechtungsprognose-2030-zusammenfassung-los-3.pdf (2014)
2. DFS Deutsche Flugsicherung: Luftverkehr in Deutschland - Mobilitätsbericht 2016. Internet, https://www.dfs.de/dfs_homepage/de/Presse/Publikationen (2017)
3. Düsseldorf Airport: Geschäftsbericht 2016. Internet, https://www.dus.com/~/media/fdg/dus_com/konzern/unternehmen/zahlen_und_fakten/geschaeftsbericht/dus_gb_2016_lr.pdf (2017)
4. Esser, J., Schreckenberg, M.: Simulation of city traffic with cellular automata: the city of Duisburg as an example. In: EUROMOTOR-Seminar 1996: Telematic, Vehicle and Environment, Aachen (1996)
5. International Civil Aviation Organization (ICAO): Air traffic management. Internet, www.navcanada.ca/EN/media/Publications/ICAO-Doc-4444-EN.pdf (2001)
6. Kretz, T.: Pedestrian traffic simulation and experiments. Ph.D. thesis, University Duisburg-Essen (2006)
7. Mori, R.: Aircraft taxiing model at congested airports. In: International Congress of the Aeronautical Sciences, vol. 28, pp. 1–9 (2012)
8. Mori, R.: Aircraft ground-taxiing model for congested airport using cellular automata. IEEE Trans. Intell. Transp. Syst. **14**(1), 180–188 (2013)
9. Nagel, K., Schreckenberg, M.: A cellular automata model for freeway traffic. J. Phys. I **2**, 2221–2229 (1992)
10. Oberwerwaltungsgericht des Landes Nordrhein-Westfalen: Protokoll eines Vergleichs (Angerlandvergleich). Internet, https://www.dus.com/~/media/fdg/dus_com/konzern/unternehmen/kapazitaetserweiterung/pdfs/angerlandvergleich.pdf (1965)
11. OpenStreetMap contributors: Openstreetmap (2017). http://www.openstreetmap.org
12. Tietze, S.E.: Airbus Series, vol. 1 (A318/A319/A320/A321), 1st edn. NBG EDV Handels und Verlags GmbH, Burglengenfeld (2016)

Investigating Passengers' Seating Behavior in Suburban Trains

Jakob Schöttl, Michael J. Seitz, and Gerta Köster

Abstract In pedestrian dynamics, individual-based models serve to simulate the behavior of crowds so that evacuation times and crowd densities can be estimated or the efficiency of public transportation optimized. Often train systems are investigated where seat choice may have a great impact on capacity utilization. Thus it is necessary to reproduce passengers' behavior inside trains. Yet there is surprisingly little research on the subject. In this contribution, we collect data on seating behavior in Munich's suburban trains, analyze it, and subsequently introduce a model that matches what we observe. For example, within a compartment, passengers tend to choose the seat group with the smallest number of other passengers. Within a seat group, passengers prefer window seats and forward-facing seats. When there is already another person, passengers tend to choose the seat diagonally across from that person. These and other aspects are incorporated in our model. We demonstrate the applicability of our model and present a qualitative validation with a simulation example. The model's implementation is part of the free and open-source VADERE simulation framework for pedestrian dynamics and thus available for cross-validation. The model can be used as one component in larger systems for the simulation of public transport.

1 Introduction

Pedestrian dynamics and crowd simulation is a wide field of research [3]. Microscopic, that is, individual-based models of human locomotion are used to simulate the behavior of crowds. The goal is often to improve safety by estimating evacuation times and crowd densities [1, 6, 9, 15] but also to optimize efficiency in public transport. For example, passenger exchange times are estimated by having virtual

J. Schöttl · M. J. Seitz · G. Köster (✉)
Munich University of Applied Sciences, Munich, Germany
e-mail: m.seitz@hm.edu; koester@hm.edu; gerta.koester@hm.edu

S. H. Hamdar (ed.), *Traffic and Granular Flow '17*,
https://doi.org/10.1007/978-3-030-11440-4_44

pedestrians leave and board trains. Thus it seems necessary to correctly reproduce passengers' behavior inside a train.

Simulation software can cope with common scenarios including gates, queues, stairs, and multiple floors (e.g., [10, 11, 28]). Research on people's spatial distribution during waiting times has also brought useful results (e.g., [12, 13, 23]). There are a number of publications on boarding schemes for airplanes [8, 17, 25], some of them providing simulations for the boarding process with the goal to reduce the boarding time. Some studies contain useful hints related to seating behavior, e.g., studies on the degree of capacity utilization [2], baggage in trains [16], passenger exchange times [14, 27], and train interior design [19]. Studies on seating layouts and passengers' seating behavior in trains are discussed by several authors: [26] investigated preferred facing directions in the Washington Metro, [18] surveyed preferred seat choices in inter-city trains, and [29] carried out a survey on passengers' valuation of seating layouts in public transportation. Others are concerned with the inflow process when people enter a room [5, 12, 13, 30]. While these studies conduct experiments where the subjects cannot sit down, some aspects are still interesting for this work. However, there is little research on people's seating behavior in trains that can be used to build a simulation model. This contribution aims at closing this gap.

In the following section, we present empirical data on how single passengers sit down in relation to other passengers. Other questions such as how groups sit together or how gender and age influence seat choices will have to wait for later studies. Then we build a seating model from our observations and implement it within the open-source VADERE simulation framework. See [21] and the website [28] for an introduction. Next we verify the model's implementation by comparing simulated data against real data. Then we qualitatively validate the model by demonstrating that the train fills up in a visually realistic manner. Both methods are based on a simulation run with real passenger counts. We conclude with a short summary, a discussion, and inspiration for future work in this field.

2 Field Observation

The first author used his own smart phone app, over a period of several weeks, to collect passenger data on his train ride to and from Munich University of Applied Sciences in Munich's suburban trains (S-Bahn). He observed single compartments (see Fig. 1) during train rides, logging relevant events such as sitting down, leaving, and placement of baggage. For more details we refer to his master thesis [20].

For all observed preferences, binomial tests are conducted, using the exact binomial test (`binom.test` from R's `stats` package), to see whether they are statistically significant. The significance level is set to $\alpha = 0.05$. We only report the significant results: Passengers prefer empty seat groups or, more generally, they prefer the seat group with the smallest number of occupants. See Figs. 2 and 3. Apparently passengers try to maximize the distance to other passengers which is in

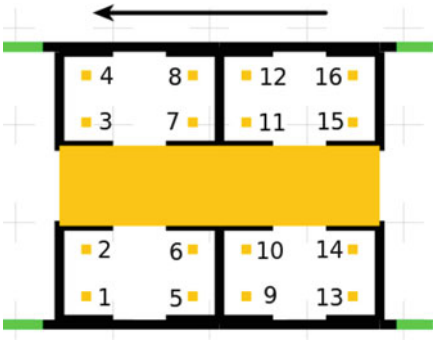

Fig. 1 Four seat groups, with four seats each. The black arrow on the top denotes the train's driving direction. The yellow dots mark the seats and the yellow area in the middle is the aisle connecting the entrance areas. The green bars are parts of the doors

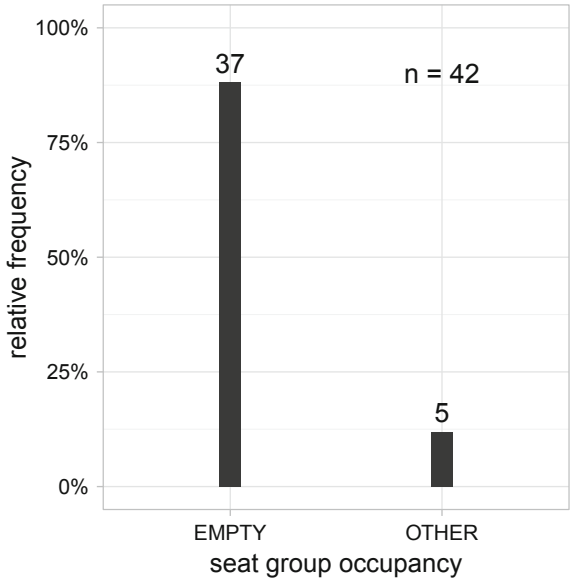

Fig. 2 There is a strong preference for empty seat groups

line with the phenomenon of personal space described in psychological studies [7]. When a seat group is empty forward seats win over backward seats, and windows win over aisles (Fig. 4). When one seat is already taken, the choice diagonally across wins (Fig. 5).

While we did not collect enough data to statistically investigate how passengers choose a compartment, we received the impression that passengers often choose one of the compartments next to their entrance area. Once they have chosen a direction, they rather proceed to the next compartment instead of turning around and going back. When they choose a compartment in a different train section they tend to directly walk to this section.

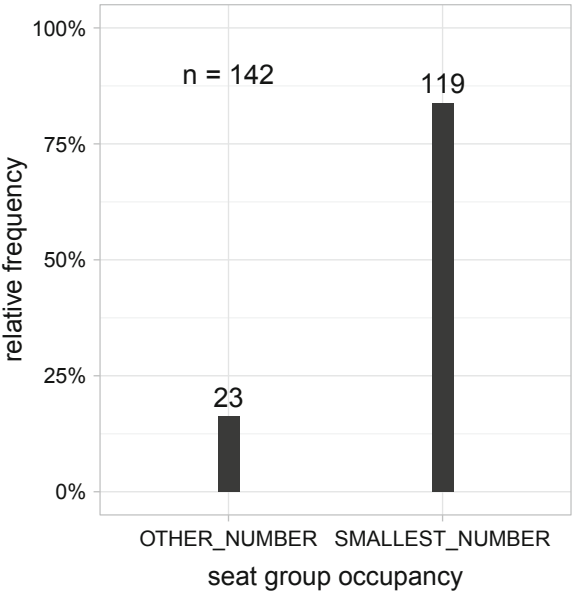

Fig. 3 There is a strong preference for the seat group with the smallest number of occupants

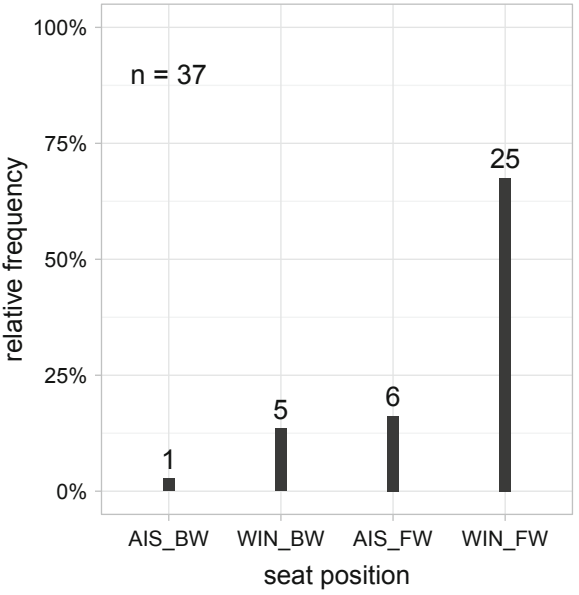

Fig. 4 When a seat group is empty forward seats win over backward seats, and windows win over aisles (AIS: aisle, WIN: window, FW: forward, BW: backward)

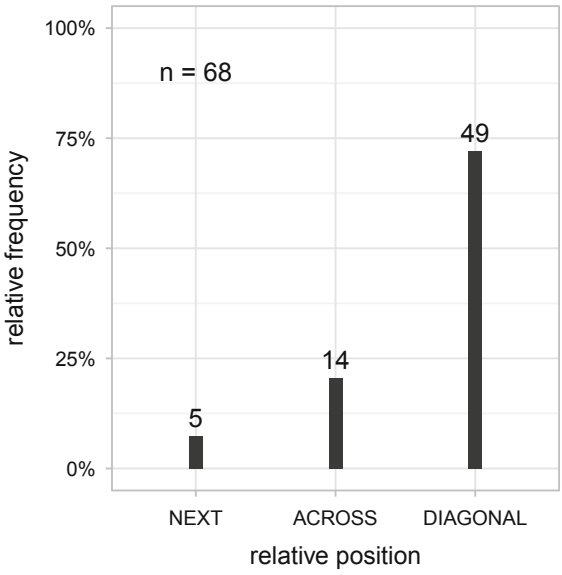

Fig. 5 When one seat is already taken, the choice diagonally across wins

3 The Seating Model: Algorithm and Test

For our seating model we use a combination of cognitive heuristics [22] and random assignment according to the empirical distributions. That is, we let the agents make true decisions based on the situation they are confronted with when entering the train, and base these choices on the empirical preferences. The algorithm's first decision is whether the passenger wants to sit at all. For this work we assume that all passengers wish to sit. The rest of the algorithm consists of three steps: choosing a compartment, choosing a seat group, and choosing a seat therein (see Fig. 6). We use a normal distribution to assign each agent a compartment where (s)he sits down. For the choices of seat group and seat, we only look at differences that we found statistically significant. Otherwise, we use a uniform distribution. The chosen seat is then assigned as target in the floor field-based navigation of the optimal steps model [21, 24] in the VADERE simulation framework. Alternatives would be the behavioral heuristics model [21], the gradient navigation model [4], or any other microscopic locomotion model that can deal with fine resolution of the geometry of Munich's ET-423 S-Bahn train. Some special cases, such as a full compartment or that another passenger snatches one's chosen seat, have to be handled. For this and for parameter choices we refer to [20].

We conduct simulation runs to test our implementation. Since we give the statistical distribution as an input, correct reproduction of the empirical data amounts to code verification. See Figs. 7 and 8. We achieve a qualitative validation by visually comparing simulation runs to our personal expectations as frequent users of the Munich S-Bahn.

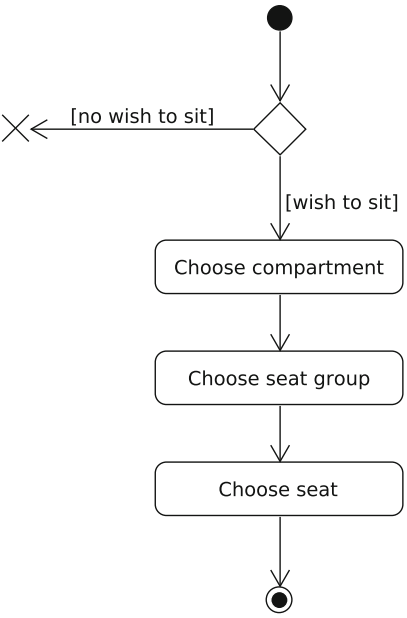

Fig. 6 The seating algorithm: passengers pick their seat according to the empirical preferences. They choose a compartment close to where they enter, following a normal distribution

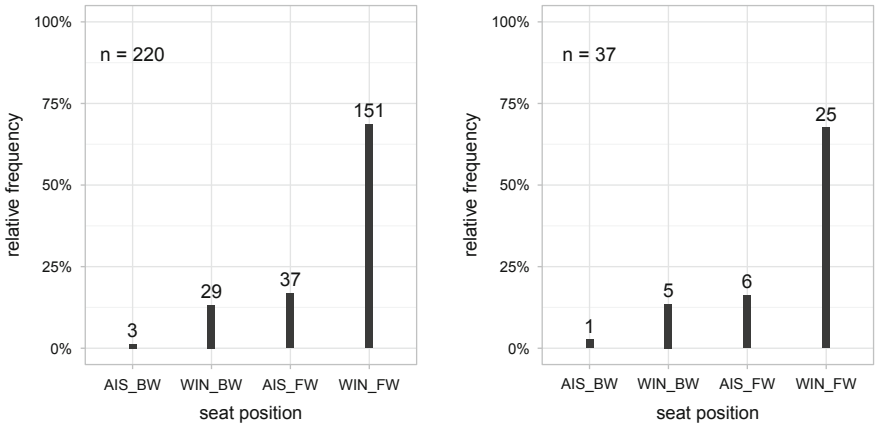

Fig. 7 Comparison of empirical data (right) to simulation outcome (left): choice of seat in an empty seat group

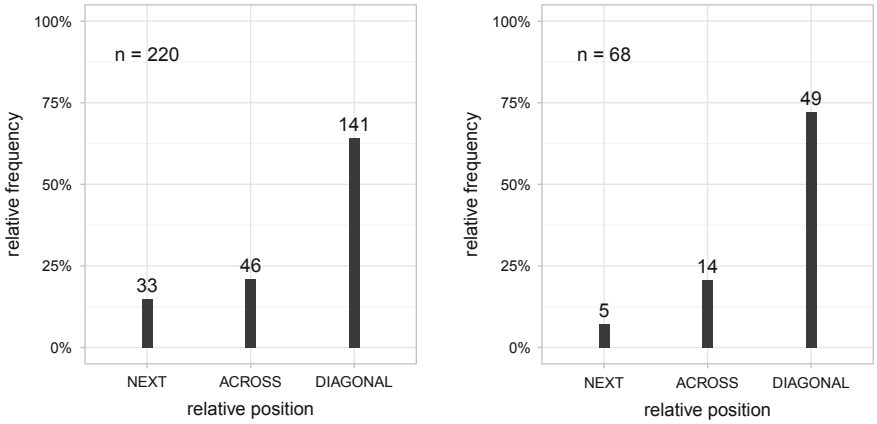

Fig. 8 Comparison of empirical data (right) to simulation outcome (left): choice of seat within a seat group when one seat is already taken

4 Conclusion

We designed a study on passengers' seating behavior in trains, developed a mobile app to support data logging, collected data, and processed and analyzed the data with respect to the choice of seating. Thus, we gained insights on where passengers prefer to sit down in a compartment and in a seat group. Based on the results of the data analysis, we designed a model for seating behavior and implemented it in the open-source crowd simulation software VADERE where it is available for cross-validation. The model can easily be included in larger simulation systems for public transport to make predictions of important control quantities such as flow, density, or passenger exchange times more realistic.

Our results are in line with psychological findings, namely the fact that people like to safeguard their personal space, keeping a distance from others. Other psychological questions, such as the influence of gender or age on the seat choice, or the behavior of groups, as well as the reasoning behind the choice of compartments, would be interesting follow-up studies.

References

1. Alizadeh, R.: A dynamic cellular automaton model for evacuation process with obstacles. Saf. Sci. **49**(2), 315–323 (2011). http://dx.doi.org/10.1016/j.ssci.2010.09.006. http://www.sciencedirect.com/science/article/pii/S0925753510002262
2. Cis, P.: Auslastungsgrad von Eisenbahnwagen in Abhängigkeit von individuellem Fahrgastverhalten. Diplomarbeit, Technische Universität Wien (2009). http://katalog.ub.tuwien.ac.at/AC07806180

3. Daamen, W., Duives, D.C., Hoogendoorn, S.P. (eds.): The Conference in Pedestrian and Evacuation Dynamics 2014 (PED 2014). In: Transportation Research Procedia, vol. 2, pp. 1–818. Elsevier, Delft (2014). www.sciencedirect.com/science/journal/23521465/2/
4. Dietrich, F., Köster, G.: Gradient navigation model for pedestrian dynamics. Phys. Rev. E **89**(6), 062801 (2014). http://dx.doi.org/10.1103/PhysRevE.89.062801
5. Ezaki, T., Ohtsuka, K., Chraibi, M., Boltes, M., Yanagisawa, D., Seyfried, A., Schadschneider, A., Nishinari, K.: Inflow process of pedestrians to a confined space (2016). Preprint. arXiv:1609.07884
6. Gao, Z., Qu, Y., Li, X., Long, J., Huang, H.J.: Simulating the dynamic escape process in large public places. Oper. Res. **62**(6), 1344–1357 (2014). http://dx.doi.org/10.1287/opre.2014.1312
7. Hall, E.T.: The Hidden Dimension. Doubleday, New York (1966)
8. Jaehn, F., Neumann, S.: Airplane boarding. Eur. J. Oper. Res. **244**(2), 339–359 (2015). http://dx.doi.org/10.1016/j.ejor.2014.12.008
9. Kirchner, A., Schadschneider, A.: Simulation of evacuation processes using a bionics-inspired cellular automaton model for pedestrian dynamics. Phys. A Stat. Mech. Appl. **312**(1), 260–276 (2002)
10. Köster, G., Zönnchen, B.: Queuing at bottlenecks using a dynamic floor field for navigation. In: The Conference in Pedestrian and Evacuation Dynamics 2014, Transportation Research Procedia, pp. 344–352. Delft (2014). http://dx.doi.org/10.1016/j.trpro.2014.09.029
11. Köster, G., Lehmberg, D., Dietrich, F.: Is slowing down enough to model movement on stairs? In: Knoop, V.L., Daamen, W. (eds.) Traffic and Granular Flow '15, 27–30 October 2015, pp. 35–42. Springer, Nootdorp (2016)
12. Liu, X., Song, W., Fu, L., Fang, Z.: Experimental study of pedestrian inflow in a room with a separate entrance and exit. Phys. A Stat. Mech. Appl. **442**, 224–238 (2016). http://dx.doi.org/10.1016/j.physa.2015.09.026
13. Liu, X., Song, W., Fu, L., Lv, W., Fang, Z.: Typical features of pedestrian spatial distribution in the inflow process. Phys. Lett. A **380**(17), 1526–1534 (2016). http://dx.doi.org/10.1016/j.physleta.2016.02.028. http://www.sciencedirect.com/science/article/pii/S0375960116001651
14. Panzera, N.: Die Haltezeit bei hochrangigen, innerstädtischen Verkehren–Einflussfaktoren und Optimierungspotenziale. Diplomarbeit, Fachhochschule St. Pölten GmbH (2014)
15. Pelechano, N., Badler, N.I.: Modeling crowd and trained leader behavior during building evacuation. Departmental Papers (CIS), p. 272 (2006)
16. Plank, V.: Dimensionierung von Gepäckablagen in Reisezügen. Diplomarbeit, Technische Universität Wien (2008). http://katalog.ub.tuwien.ac.at/AC05039323
17. Qiang, S.J., Jia, B., Xie, D.F., Gao, Z.Y.: Reducing airplane boarding time by accounting for passengers' individual properties: a simulation based on cellular automaton. J. Air Transp. Manag. **40**, 42–47 (2014). http://dx.doi.org/10.1016/j.jairtraman.2014.05.007
18. Rüger, B., Loibl, C.: Präferenzen bei der sitzplatzwahl in fernreisezügen. Eisenbahntechnische Rundschau (ETR) **59**(11), 774–777 (2010). http://www.eurailpress.de/etr
19. Rüger, B., Ostermann, N.: Der Innenraum von Reisezugwagen–Gratwanderung zwischen sinn und effizienz. Eisenbahntechnische Rundschau (ETR) (3), 38–44 (2015). http://www.eurailpress.de/etr
20. Schöttl, J.: Modelling passengers' seating behavior for simulations of pedestrian dynamics. Master's Thesis, Munich University of Applied Sciences (2016)
21. Seitz, M.J.: Simulating pedestrian dynamics: Towards natural locomotion and psychological decision making. Ph.D. Thesis, Technische Universität München, Munich (2016). https://mediatum.ub.tum.de/?id=1293050
22. Seitz, M.J., Bode, N.W.F., Köster, G.: How cognitive heuristics can explain social interactions in spatial movement. J. R. Soc. Interface **13**(121), 20160439 (2016). http://dx.doi.org/10.1098/rsif.2016.0439
23. Seitz, M.J., Seer, S., Klettner, S., Köster, G., Handel, O.: How do we wait? Fundamentals, characteristics, and modeling implications. In: Knoop, V.L. Daamen, W. (eds.) Traffic and Granular Flow '15, 27–30 October 2015, pp. 217–224. Springer, Nootdorp (2016). http://dx.doi.org/10.1007/978-3-319-33482-0

24. von Sivers, I., Köster, G.: Dynamic stride length adaptation according to utility and personal space. Transp. Res. B Methodol. **74**, 104–117 (2015). http://dx.doi.org/10.1016/j.trb.2015.01.009
25. Steiner, A., Phillipp, M.: Speeding up the airplane boarding process by using pre-boarding areas. In: Swiss Transport Research Conference. Ascona (2009)
26. Trinkoff, A.M.: Seating patterns on the Washington, DC Metro Rail System. Am. J. Public Health **75**(6), 657–658 (1985). http://www.ncbi.nlm.nih.gov/pmc/articles/PMC1646210/
27. Tuna, D.: Fahrgastwechselzeit im Personenfernverkehr. Master's Thesis, Technische Universität Wien (2008). http://katalog.ub.tuwien.ac.at/AC05036489
28. VADERE-Team: VADERE simulation framework (2016). www.vadere.org
29. Wardman, M., Murphy, P.: Passengers' valuations of train seating layout, position and occupancy. Transp. Res. A Policy Pract. **74**, 222–238 (2015). http://www.sciencedirect.com/science/article/pii/S0965856415000154
30. Xiao, Y., Gao, Z., Qu, Y., Li, X.: A pedestrian flow model considering the impact of local density: Voronoi diagram based heuristics approach. Transp. Res. C Emerg. Technol. **68**, 566–580 (2016). http://dx.doi.org/10.1016/j.trc.2016.05.012

How Long Does It Take to Board an Airplane?

Jevgenijs Kaupužs, Reinhard Mahnke, Eitan Bachmat, and Vidar Frette

Abstract A simple airplane-boarding model, introduced earlier by Frette and Hemmer, is considered. In this model, N passengers have reserved seats, but enter the airplane in arbitrary order. We are looking for an analytical expression, which describes the mean boarding time depending on the total number of passengers N. For this purpose, we first determine precise values of the exponents and expansion coefficients in the asymptotic expression at $N \to \infty$. It is reached by mathematical calculations and fitting the Monte Carlo simulation data for very large N, up to $N \sim 6 \cdot 10^8$. Finally, we compare the obtained analytical approximation to the simulation data for a realistic number of passengers $N \lesssim 500$ and find a good agreement.

J. Kaupužs
Faculty of Materials Science and Applied Chemistry, Institute of Technical Physics, Riga Technical University, Riga, Latvia
e-mail: kaupuzs@latnet.lv

Institute of Mathematical Sciences and Information Technologies, University of Liepaja, Liepaja, Latvia

R. Mahnke (✉)
Institute of Physics, Rostock University, Rostock, Germany
e-mail: reinhard.mahnke@uni-rostock.de

E. Bachmat
Department of Computer Science, Ben-Gurion University, Beer-Sheva, Israel
e-mail: ebachmat@cs.bgu.ac.il

V. Frette
Department of Engineering, Stord/Haugesund College, Haugesund, Norway
e-mail: vidar.frette@hsh.no

S. H. Hamdar (ed.), *Traffic and Granular Flow '17*,
https://doi.org/10.1007/978-3-030-11440-4_45

1 Introduction

As already discussed during the previous Traffic and Granular Flow conferences [10, 11], a significant part of the total transportation time in the air traffic (see [9] for a review) is related to the boarding of an airplane. A simple airplane-boarding model has been introduced by Frette and Hemmer [8], resulting in an interesting discussion in the following series of papers published in Physical Review [4–7].

In the simple model [8], N passengers have reserved seats, but enter the airplane in arbitrary order. Besides, there is only a single isle of rows and only one seat in each row. Each passenger occupies a place equal to the distance between rows. In this model, a passenger requires one time step to place carry-on luggage and get seated, the time for walking along the isle being neglected. However, a passenger must wait for a possibility to move forward to his/her seat if the motion is blocked by other passengers. The number of seats is equal to the number of passengers in this model.

One of the basic quantities of interest is the boarding time t_b of an airplane. The mean boarding time $\langle t_b \rangle$ scales as power law $\langle t_b \rangle \propto N^\alpha$ with $\alpha = 1/2$ for large N, as it has been proven analytically [2, 3] and later has been found also by numerical simulations [6, 7]. Interestingly, this scaling is described by a quite different effective exponent 0.69 ± 0.01 for small number of passengers $2 < N < 16$, as it follows from [8]. It means that corrections to the leading scaling behavior are very important. These are described by the correction-to-scaling exponent θ, i.e., $\langle t_b \rangle = cN^\alpha \left(1 + \mathcal{O}\left(N^{-\theta}\right)\right)$ at $N \to \infty$. As it is known from earlier analytical studies [2, 12], $\alpha = 1/2$ and $\theta = 1/3$ hold in a model with point-like passengers and, more generally, for $k < \ln 2$, where

$$k = \frac{\text{(personal space of a passenger)} \times \text{(number of passengers per row)}}{\text{distance between rows}} \tag{1}$$

is an essential control parameter of a generalized model. This parameter is $k = 1 > \ln 2$ for the particular model considered here. It means that θ is expected to be smaller than $1/3$, although $\alpha = 1/2$ always holds [2].

The aim of our present work is to determine numerically a precise value of θ and identify also the sub-leading correction terms in the asymptotic expansion of $\langle t_b \rangle$ at $N \to \infty$. For this purpose, Monte Carlo (MC) simulations up to $N \sim 6 \cdot 10^8$ have been performed. An important question is the applicability of the asymptotic theory to a realistic number of passengers. We have addressed this question by comparing the asymptotic formula to the simulation data for $N \lesssim 500$. A good agreement has been found.

2 Simulation Results and Analysis

Let us i-th passenger in the queue (where $i = 1$ stands for the passenger entering the airplane first) has the seat number j_i. In our analysis, it is convenient to represent the initial state of the queue by the two-dimensional scatter plot, where one point (q_i, r_i) with $q_i = i/N$ and $r_i = j_i/N$ is related to each passenger. Since passengers are randomly ordered in the queue, the points are uniformly distributed over the square $q \in [0, 1]$, $r \in [0, 1]$ for large N. As discussed in [10], the boarding time is equal to the number of nodes in the longest blocking sequence drawn by connecting points in such a scatter plot. The connected points correspond to passengers having certain blocking relation—see [10] for details. The longest blocking sequence is a fluctuating curve, which converges to a smooth line at $N \to \infty$ [2]. Under appropriate transformation [2, 3], i.e.,

$$x(q) = e^{kq} \ , \quad y(q, r) = \frac{(r-1)e^{-kq}}{k} \tag{2}$$

the longest blocking sequence becomes the longest increasing sequence. Moreover, the density of points remains uniform under this transformation, whereas the square $q \in [0, 1]$, $r \in [0, 1]$ transforms into another region $x \in [1, e^k]$, $y \in [-1/(xk), 0]$, as illustrated in Fig. 1.

The asymptotic longest increasing sequence at $N \to \infty$ is shown here by a thick solid line. It consists of two pieces. The first piece follows the lower border of the region up to the point (x_0, y_0), whereas the second piece is a straight line from (x_0, y_0) to the upper corner $(e^k, 0)$. This straight line is tangent to the lower border $xy = -1/k$ at $x = x_0 = e^k/2$ and $y = y_0 = -2e^{-k}/k$.

The number of points in the asymptotic longest increasing sequence, i.e., the length of the corresponding curve is well known [2]. It is equal to $d(k)\sqrt{N}$, where $d(k) = 2(k + 1 - \ln 2)/\sqrt{k}$ for $k \geq \ln 2$. Moreover, concerning the straight-line piece, we know not only its asymptotic length, but also the leading correction to

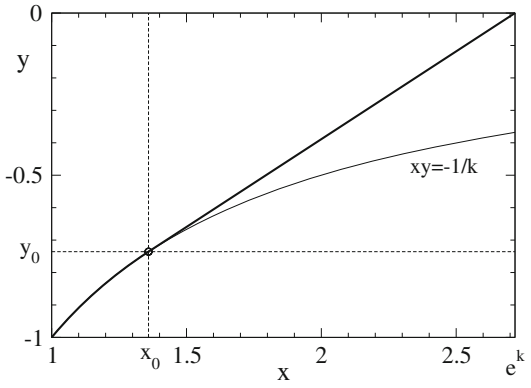

Fig. 1 The asymptotic longest blocking sequence at $N \to \infty$ (thick solid line) in new variables x and y after the transformation (2). The curve $xy = -1/k$ shows the lower border of the region for the transformed variables. The numbers on axes correspond to $k = 1$

scaling. According to [12], its length is $2\sqrt{\hat{N}}$, and the normalized to $\hat{N}^{1/6}$ deviations from this straight line is described by the Tracy–Widom distribution for large $\hat{N}$, where $\hat{N}$ is the number of points in the rectangle $x_0 < x < e^k$, $y_0 < y < 0$. Hence, omitting sub-leading correction terms, the straight line gives the contribution $2\sqrt{\hat{N}} + B\hat{N}^{1/6}$ to the mean boarding time, where $B \approx -1.771086807411$ is the mean value of the Tracy–Widom distribution. Note that the number of points above the curve $xy = -1/k$ is the number of passengers N, and we have $N = k\hat{N}$ at $N \to \infty$.

Corrections to the leading scaling behavior, which are related to the first (curved) piece of the longest increasing sequence in Fig. 1, are not known from analytical studies. This part disappears at $k < \ln 2$, therefore we have $\theta = 1/3$ in that case. In fact, a phase transition occurs when k is increased starting from 0 and reaches the critical value $\ln 2$. A contribution with different θ appears at $k > \ln 2$, which comes from the curved part of the longest increasing sequence in Fig. 1. We have performed MC simulations to determine this value of θ.

We have used the transformation (2) also in MC simulations. It allows us to perform simulations for much larger N than it would be possible in the original model owing to the fast algorithm, known as the patience sorting algorithm [1], which can be applied here. Our MC algorithm consists of the following steps:

1. In analogy with the original model, generate a scatter plot of uniformly distributed points over the rectangle $x \in [1, e^k]$, $y \in [-1/k, 0]$, corresponding to a random permutation (random queue) of length L;
2. Use the patience sorting algorithm to find the boarding time t_b as the length of the longest increasing sequence for the subset of $N \approx L\,k/(e^k - 1)$ points with $y > -1/(xk)$, where N is the number of passengers;
3. Make an averaging over M realizations to evaluate $\langle t_b \rangle$.

We have performed MC simulations at $k = 1$ for $L = 10^6, 1.4 \times 10^6, 2 \times 10^6, 2.8 \times 10^6$, and so on, up to $L = 1.024 \times 10^9$, as well as for smaller system sizes $L = 0.5 \times 10^6, 0.7 \times 10^6, 0.25 \times 10^6$, etc. In all cases $M = 10^4$ realizations have been used to determine the deviation of $\langle t_b \rangle / \sqrt{L}$ from its asymptotic value $\langle t_b \rangle^{as} / \sqrt{L} = 2(k+1-\ln 2)/\sqrt{e^k - 1}$, in accordance with the relations given before. We have subtracted from this deviation the already discussed correction to scaling $\propto BL^{-1/3}$, coming from the straight-line piece in Fig. 1, for a better estimation of the remaining unknown correction term. Namely, we have fit the data to the ansatz

$$(\langle t_b \rangle - \langle t_b \rangle^{as})/\sqrt{L} - B(e^k - 1)^{-1/6} L^{-1/3} = a_1 L^{-\theta} \tag{3}$$

to evaluate the correction-to-scaling exponent θ of this term. The results depending on the fit range $L \in [L_{\min}, L_{\max}]$ are listed in Table 1. The numbers in brackets indicate the magnitude of one standard deviation (error), e.g., 0.26165(74) means 0.26165 ± 0.00074. The quality of fit is characterized by the χ^2 per degree of freedom of the fit, i.e., χ^2/d.o.f., shown in the last column. The results apparently converge to a value somewhat smaller than 0.26 when the system sizes are increased.

Table 1 The exponent θ, obtained by fitting the MC data to the ansatz (3), depending on $L_{\min}$ and $L_{\max}$ of the fit range $L \in [L_{\min}, L_{\max}]$

$10^{-6}L_{\min}$	$10^{-6}L_{\max}$	θ	χ^2/d.o.f.
0.125	64	0.26165(74)	1.00
0.25	128	0.26171(70)	0.90
0.5	256	0.26079(67)	0.93
1	512	0.26050(64)	0.90
2	1024	0.25925(61)	0.86

The values of χ^2/d.o.f. of the fits are shown in column 4

Table 2 The exponent θ, obtained by fitting the MC data to the ansatz (4), depending on $L_{\min}$ and $L_{\max}$ of the fit range $L \in [L_{\min}, L_{\max}]$

$10^{-6}L_{\min}$	$10^{-6}L_{\max}$	θ	χ^2/d.o.f.
0.125	64	0.2630(34)	1.04
0.25	128	0.2556(36)	0.80
0.5	256	0.2535(35)	0.74
1	512	0.2512(34)	0.56
2	1024	0.2505(32)	0.45

The values of χ^2/d.o.f. of the fits are shown in column 4

If there is a correction $\propto L^{-\theta}$, the sub-leading correction of the kind $\propto L^{-2\theta}$ is also expected. We have included it in the refined ansatz

$$(\langle t_b\rangle - \langle t_b\rangle^{as})/\sqrt{L} - B(e^k-1)^{-1/6}L^{-1/3} = a_1 L^{-\theta} + a_2 L^{-2\theta}\ , \tag{4}$$

neglecting corrections of even higher orders. The fit results are collected in Table 2. As compared to the corresponding results in Table 1, the quality of fits is improved (χ^2/d.o.f. becomes smaller) and the estimated values of θ come very close to 0.25 for the largest $L_{\min}$ and $L_{\max}$. Hence, it is very plausible that $\theta = 1/4$ holds.

We have used this value in the following analysis and have determined the expansion coefficients $a_1 = -0.4495(12)$ and $a_2 = -1.393(90)$ in (4) by fitting the data over $L \in [2\times 10^6, 1.024\times 10^9]$ (as in the last row of Table 2) at a fixed $\theta = 1/4$. Finally, we have represented the corresponding asymptotic formula in terms of the number of passengers $N = L/(e-1)$ in the actual case of $k = 1$, i.e.,

$$\langle t_b\rangle \approx \sqrt{N}\left(2(2-\ln 2) + A_1 N^{-1/4} + B N^{-1/3} + A_2 N^{-1/2}\right), \tag{5}$$

where $B \approx -1.771086807411$, $A_1 = -0.5146(14)$ and $A_2 = -1.393(90)$.

3 A Test of Applicability and Final Conclusions

The asymptotic expression (5) has been established for very large L, up to $L = 1.024\times 10^9$, which corresponds to $N \approx 6\times 10^8$ passengers. We have tested the applicability of our approach to a realistic number of passengers $N \lesssim 500$ by

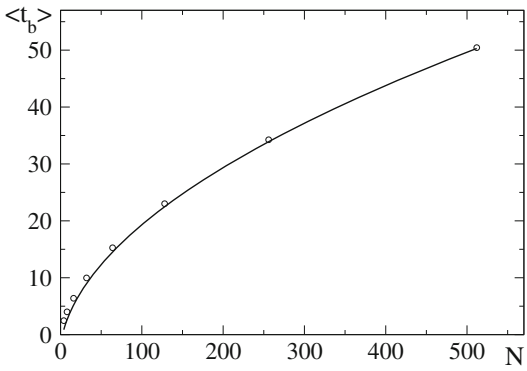

Fig. 2 The mean boarding time $\langle t_b \rangle$ depending on the total number of passengers N. The simulated in [7] values are shown by circles, whereas the solid line represents the asymptotic formula (5)

comparing $\langle t_b \rangle$ in (5) with the mean boarding times obtained earlier in [7], as shown in Fig. 2. The overall agreement is good.

Hence, we finally conclude that the correction-to-scaling exponent θ is $1/4$ or very close to $1/4$, as it follows from our simulation results for very large number of passengers. Moreover, the actual theoretical approach is valid also for description of airplane-boarding processes with realistic numbers of passengers $N \lesssim 500$.

Acknowledgements The airplane-boarding problem has been discussed by E. Bachmat, S. Erland, V. Frette, J. Kaupužs, and S. Neumann during a meeting at Technical College of Haugesund in August 2016. This work has been completed at Rostock University in October 2017. The authors acknowledge the use of resources provided by the Latvian Grid Infrastructure and High Performance Computing center of Riga Technical University.

References

1. Aldous, D., Diaconis, P.: Longest increasing subsequences: from patience sorting to the Baik-Deift-Johansson theorem. Bull. Am. Math. Soc. **36**, 413 (1999)
2. Bachmat, E., Berend, D., Sapir, L., Skiena, S., Stolyarov, N.: Analysis of airplane boarding via space-time geometry and random matrix theory. J. Phys. A **39**, L453–L459 (2006)
3. Bachmat, E., Berend, D., Sapir, L., Skiena, S., Stolyarov, N.: Analysis of airplane boarding times. Oper. Res. **57**, 499 (2009)
4. Bachmat, E., Khachaturov, V., Kuperman, R.: Optimal back-to-front airplane boarding. Phys. Rev. E **87**, 062805 (2013)
5. Baek, Y., Ha, M., Jeong, H.: Impact of sequential disorder on the scaling behavior of airplane boarding time. Phys. Rev. E **87**, 052803 (2013)
6. Bernstein, N.: Comment on 'Time needed to board an airplane: a power law and the structure behind it'. Phys. Rev. E **86**, 023101 (2012)
7. Brics, M., Kaupužs, J., Mahnke, R.: Scaling behavior of an airplane-boarding-model. Phys. Rev. E **86**, 042117 (2013)
8. Frette, V., Hemmer, P.C.: Time needed to board an airplane: a power law and the structure behind it. Phys. Rev. E **85**, 011130 (2012)
9. Jaehn, F., Neumann, S.: Airplane boarding. Eur. J. Oper. Res. **244**, 339 (2015)

10. Kaupužs, J., Mahnke, R., Weber, H.: Boarding of finite-size passengers to an airplane. In: Knoop, V.L., Daamen, W. (eds) Traffic and Granular Flow '15, pp. 597–604, Springer, Cham (2016)
11. Mahnke, R., Kaupužs, J., Brics, M.: Air traffic, boarding and scaling exponents. In: Chraibi, M. Boltes, M., Schadschneider, A., Seyfried, A. (eds.) Traffic and Granular Flow '13, pp. 305–314, Springer, Cham (2015)
12. Vershik, A.M., Kerov, C.V.: Asymptotics of the Plancherel measure of the symmetric group and the limiting form of Young tables. Dokl. Acad. Nauk SSSR **233**, 1024 (1977) [Sov. Math. Dokl. **18**, 527 (1977)]

Assessment of Pedestrian Fatality Risk at Unsignalized Crosswalks by Means of Simulation

Claudio Feliciani, Luca Crociani, Andrea Gorrini, Giuseppe Vizzari, Katsuhiro Nishinari, and Stefania Bandini

Abstract Unsignalized crosswalks are one of the most critical/risky traffic infrastructures in terms of safety, due to potentially vehicle–pedestrian conflictual interactions. Many accidents occur there and elderly pedestrians are among the most vulnerable victims. In a previous work, a simulation model has been developed with the aim of predicting traffic volumes and waiting times by reproducing the behavior of pedestrians and drivers during crossing attempts. Calibration and validation was performed based on experimental data gained through a field observation in an area with a significant population of elderlies. In this paper, we are focusing on safety issues and the simulation model has been adapted to include collisions between vehicles and pedestrians. The new simulation model presented here allows to compute the risk of an unsignalized crosswalk by considering both frequency and gravity of collisions. We consequently used the simulation model to evaluate the efficacy of particular policies. Simulation results show that while speed limit enforcement has an important effect in reducing pedestrian causalities, alternative and indirect solutions aiming at improving drivers' awareness are also effective to improve safety.

C. Feliciani (✉) · K. Nishinari
The University of Tokyo, Tokyo, Japan
e-mail: feliciani@jamology.rcast.u-tokyo.ac.jp

L. Crociani · A. Gorrini · G. Vizzari
University of Milano-Bicocca, Milan, Italy

S. Bandini
The University of Tokyo, Tokyo, Japan

University of Milano-Bicocca, Milan, Italy

S. H. Hamdar (ed.), *Traffic and Granular Flow '17*,
https://doi.org/10.1007/978-3-030-11440-4_46

1 Introduction

Traffic safety has seen a rapid improvement during the twentieth century and the number of road fatalities has constantly decreased in the developed countries [9]. However, improvements in terms of traffic victims and injuries are becoming minimal and with the aging of population, elderly are increasingly the most vulnerable among the different road users. The "World report on road traffic injury prevention" highlights "pedestrian safety as the main safety concern for the elderly," thus suggesting that pedestrians infrastructures need to be designed with a particular attention when elderly are the largest users. Among the several infrastructures making up the pedestrians environment, the crucial point where vehicles and cars interact in a direct way is represented by the case of unsignalized crosswalk, which is responsible for a comparatively high number of fatalities compared to other facilities.

Although there have been several studies considering experimental aspects of the behavior of both drivers and pedestrians on crosswalks, simulation models have been more limited in number. Some early studies considered crosswalks as purely mathematical model, allowing to determine, for example, the mean vehicle queue length, but were not able to consider the heterogeneity found in human behavior [5]. In the recent years, the popularity of computer simulation has brought some more sophisticated models which allows to consider more subtle aspects of crossing behavior, such as walking outside the zebra crossing [10]. In our previous work, we also proposed a simulation model which predicted with sufficient agreement the level of service (LOS) and traffic volumes [1, 3].

However, although some statistical models can be found in the literature [8], none of the simulation models presented so far consider collisions between vehicles and pedestrians, thus limiting their field of application to traffic engineering excluding safety issue. In this paper, we present a simulation framework (based on a validated model) which allows to consider collisions in a systematic way. Since microscopic data on traffic accidents are not available (usually only aggregated data for cities or countries are provided), we were not able to validate results for accidents, but qualitative nature of the results showed some agreement with real situations.

2 Simulation Model

2.1 General Architecture and Motion Rules

The simulation is based on a hybrid environment which employs different approaches for vehicles and pedestrians. A floor field cellular automata model is used to simulate pedestrians in their environment (sidewalk and crosswalk) and a modified Gipps model is used to account for the motion of vehicles (details are given in [3]). Figure 1 provides a schematic image providing details on the

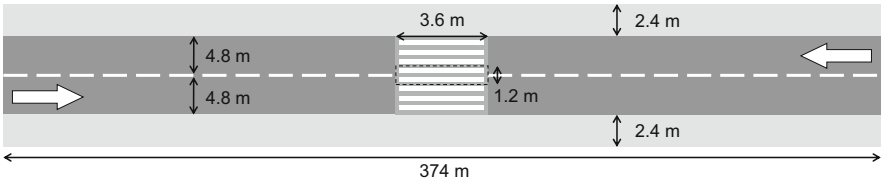

Fig. 1 Geometry considered in simulation and its size (midblock is given in dotted lines)

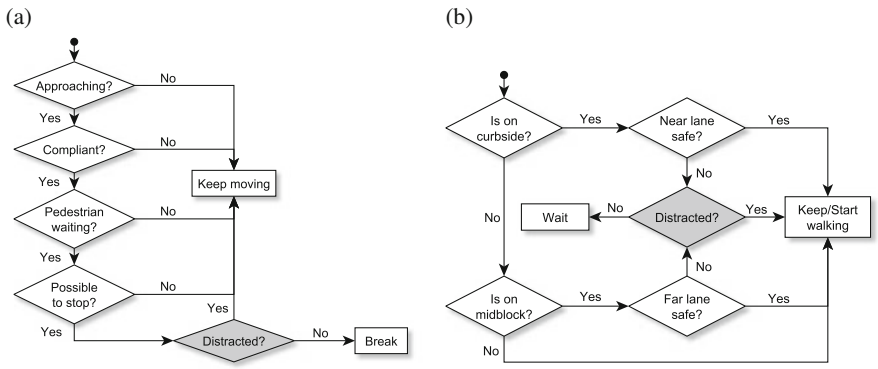

Fig. 2 Decision-making process for pedestrians and vehicles in relation with crosswalk. (**a**) Vehicle flowchart. (**b**) Pedestrian flowchart

geometry considered. Dimensions for the simulated scenario have been chosen equal to a crosswalk selected during an on-field observation carried out in the city of Milan (Italy) in an area characterized by a large elderly population and by a high number of pedestrian–car accidents in the past years [4].

Pedestrians are randomly generated from one of the four corners and get randomly assigned destinations which force them to cross the road. Cars move in a periodic environment along two lanes with opposite direction. The interaction between vehicles and pedestrians is modeled according to the logic of Fig. 2.

Drivers consider the possibility of breaking before the crosswalk only if they are leading a group of vehicles (i.e., approaching the crosswalk), they are compliant (i.e., the driver is willing to stop), and one or more pedestrians are waiting. Next, it is computed if the car can physically stop and this calculation is based on the kinetics law of the Gipps model. Pedestrians follow a similar behavior: when reaching the curbside they will check if a car is approaching and if it can stop. If the close lane is safe they will cross until the midblock (a virtual area in the middle of the road) and repeat the decision-making process again for the far lane. This crossing action was adopted after noticing a similar behavior during the on-field observations (i.e., appraising phase for evaluating the safety gap from oncoming vehicles).

To account for collisions, a given portion of drivers or pedestrians neglect the existence of the respective counterpart. This is to reproduce the risky behavior typically observed in case of collisions (or conflicts). For pedestrians, Hatfield and

Murphy [6] found that about 3% of the people crossing the road at unsignalized crosswalks were looking at their phone and did not pay attention to traffic conditions. We can assume that a similar proportion of users are distracted in our simulation.

It is important to notice that in our model there is a difference between *non-compliant* and *distracted* drivers. Distracted drivers do not break even if a pedestrian is on the road, while non-compliant ones will not stop when a pedestrian is on the curbside but will always stop if a pedestrian is already crossing.

With the aim to keep the simulation model relatively simple, we did not model the possible occurrence of accidents among vehicles; so, drivers have the ability to perceive other vehicles even if they are marked as distracted.

2.2 Estimation of Collision Gravity

Next, there is an additional important aspect which needs to be considered on collisions between vehicles and pedestrians and it is related with the fatality risk. It is known that collision speed has a strong relationship with the probability of resulting in pedestrian's death. Age of the pedestrians is also relevant, with elderly being more vulnerable than adults due to their body fragility. To quantify the relationship between collision speed, pedestrian age, and fatality risk, several authors collected data relative to traffic accidents and obtained a function describing this probability. Davis [2] presented a function which can be used to compute the risk of fatality as:

$$p_{fatality} = 1 - \frac{e^{a-b\cdot v}}{1 + e^{a-b\cdot v}} \tag{1}$$

where v is the collision speed (relative to the vehicle) and a and b empirical parameters obtained by fitting with statistical data for traffic accidents (in the case of Davis, data are relative to the 1970s when safety was rather poor compared to current standards). Different parameters have to be used depending on the age group of the pedestrian involved and Davis estimated them for children, adults, and elderly.

To measure pedestrian risk in a particular crosswalk using the simulation model, it is not sufficient to simply count the number of collisions occurring, but gravity of the accidents also needs to be accounted for. We therefore decided to include the above equation for pedestrian fatality in our model and evaluate each collision between vehicle and pedestrian using it. Our results will be therefore based on the combination between the frequency of collisions and the gravity of them, meaning that a crosswalk where collisions occur relatively often at low speed may be considered more safe than a crosswalk where collisions are rare but usually result in pedestrian death.

3 Results and Discussion

To reduce the number and relevance of accidents between vehicles and pedestrians, policies are an effective measure. The "World report on road traffic injury prevention" [9] estimated that serious and fatal road casualty reduction effects related to new policies account for 42% in the case of pedestrians, the highest percentage among road users. We want therefore to investigate which policy is the most efficient in reducing road casualties related to the specific case of pedestrians crossing unsignalized crosswalks. Our model allows to change different parameters related to traffic conditions and pedestrian/driver's attitude. The standard values used for the simulation results presented hereafter are given in Table 1.

For each simulation we varied the parameter which had to be investigated and kept the remaining ones constant. Since the case of elderly pedestrians is an important part of this work, three different scenarios were considered: adults only, a population consisting of adults and elderly in equal amount, and elderly only. If not provided in Table 1, values were taken from the on-field observation or from the literature (and are given in [3]). Pedestrian safety was estimated by computing the cumulative fatality risk over the total simulated time (360 h) and finally summarizing it in terms of fatalities per hour.

3.1 Driver's Attitude

We can start by considering driver's attitude, for which speed and non-compliance are given in Fig. 3. Logarithmic scale is used since fatality risk contains exponential terms and changes in fatality risk are extremely quick in a limited speed range.

A first look on both graphs should suggest that fatalities are intuitively high. Although it is not possible to provide a direct comparison with empirical data, from the graph for speed it is obtained that at 50 km/h one fatality occurs roughly about every 4 days (or almost 90 fatalities per year). To understand these results it is important to remark that parameters used refer to a moderate level of traffic from both vehicles and pedestrians and simulations were performed with the level

Table 1 Values used in the simulations presented in this work; in each case a single parameter was varied by keeping the remaining ones constant

Type	Variable	Value
Driver's attitude	Car speed	40.0 km/h
	Non-compliance	0.5
Traffic conditions	Car density	15.0 (km lane)$^{-1}$
	Pedestrian flow	5.0 min^{-1}
Distraction	Distracted pedestrians	0.02
	Distracted drivers[a]	0.00

[a]When the amount of distracted drivers was varied, distracted pedestrians was set at 0

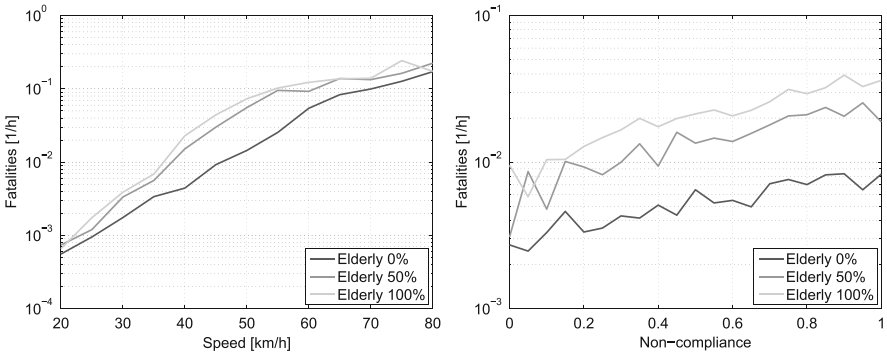

Fig. 3 Relationship between drivers' attitude (in terms of speed and compliance) and fatality risk for crossing pedestrians

of traffic unchanged for 360 h (i.e., constant during day and night). Also, parameters used for the fatality risk are relative to the 1970s. The results presented here are therefore intended for comparison between different policies and for qualitative considerations. Quantitative values are to be handled with care.

The graph for speed shows that velocity clearly has an influence on pedestrian fatality for all the populations considered. The ratio of elderly roughly has a linear relationship with frequency of fatality (consider that logarithmic scale is used). On the other side, non-compliance is seen as having only a marginal effect of pedestrian safety. Qualitatively it can be observed that pedestrians are able to recognize non-compliant drivers, thus preventing them from having a collision with them. In this regard, it can be concluded that compliance becomes important for LOS considerations, but its relation with safety is limited.

3.2 Traffic Conditions

Next we wish to consider volumes of traffic for both vehicles and pedestrians, whose simulation results are given in Fig. 4.

In the case of pedestrians, it is shown that fatalities grow with the volume of traffic, but a plateau is reached for around $6\,(\text{min})^{-1}$. This could be related with the fact that when the traffic of pedestrians grows, it is more often observed that people have to wait at the curbside. As a consequence even if a distracted pedestrian crosses without checking, it is more likely that cars already stopped to give way to other pedestrians, thus preventing him/her from suffering an accident. In the case of vehicular traffic (more precisely density), the situation is slightly different. At first the number of pedestrian fatalities grows with an increase in car density, but after reaching a maximum at about 20 cars/(km lane), it constantly decreases until the maximum density considered in simulations. This sudden change was created by

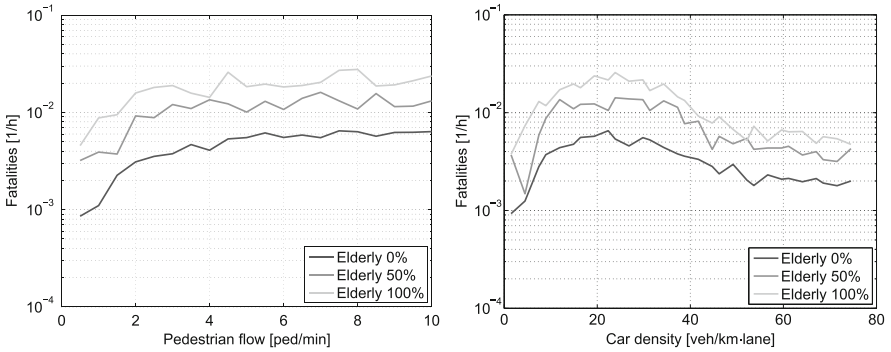

Fig. 4 Relationship between traffic volumes for vehicles and pedestrians and fatality risk for crossing pedestrians

the formation of traffic jams which reduced the driving speed for cars, consequently reducing the cumulative risk for pedestrians.

Considering traffic volumes of both pedestrians and vehicles altogether it can be concluded that a dense traffic is beneficial for pedestrian safety. This conclusions are in line to what is observed in the case of "shared spaces" (in which traffic signs are removed), where urban environment and traffic volumes create a reduction in speed, which is beneficial for the safety of pedestrian users. Karndacharuk et al. [7] reported for a shared space area in the city of Auckland (New Zealand) that vehicle speed increased with a decrease in the number of interactions, making the area more safe during the day (when the number of interactions is higher) but more dangerous at night.

3.3 Distraction

Finally, we wish to consider distraction and in particular we want to investigate which road user is most dangerous when not paying attention to the other type of entity. The results are shown in Fig. 5. In each case, distraction was set at zero for the road user which was not varied to allow a comparison under equivalent conditions.

The general behavior is similar for both drivers and pedestrians, although distraction in drivers results in a number of fatalities 3–4 times higher compared to distracted pedestrians (although victims are always pedestrians). These results show that reducing the amount of distracted drivers is more effective than increasing awareness among pedestrians. Being the most vulnerable users, pedestrians are somehow responsible for their own safety regardless of the behavior of drivers, but results show that policies increasing awareness on traffic accidents are more effective when directed on drivers. In this regard, the use of shared spaces may

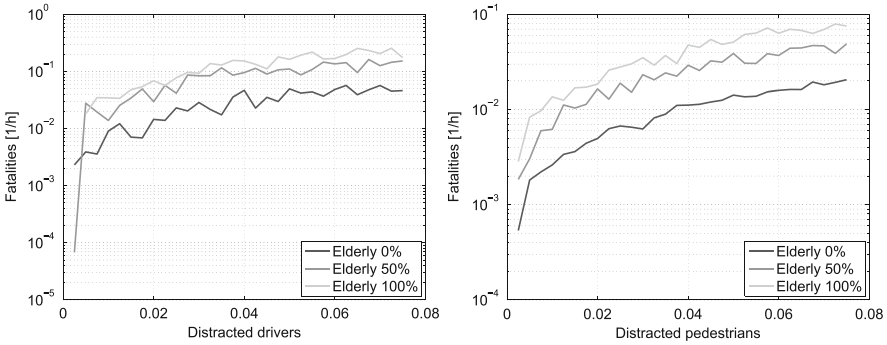

Fig. 5 Relationship between distraction in drivers and pedestrians and fatality risk for crossing pedestrians

help increasing the sense of responsibility among drivers, possibly reducing their distraction.

4 Conclusions and Discussion

Based on empirical results from a field survey, a simulation model for pedestrians crossing at unsignalized crosswalks was developed. Crossing mechanism of pedestrians has been modeled in a two-step fashion. A pedestrian attempting to cross will consider only the near lane first and later check the safety of the far one while walking on the crosswalk. The inclusion of distracted road users (not paying attention to traffic conditions) allowed to simulate accidents occurring between crossing pedestrians and incoming vehicles. Several scenarios were studied to investigate which factor is the most relevant in reducing fatalities and improving pedestrian safety. Speed limit was found being an effective measure to reduce fatality among pedestrians, since probability of surviving an accident is directly related to it. However, we also found that alternative solutions may have the same impact without specifically addressing only one road user. In particular, the shared space concept can automatically reduce traffic speed and, at the same time, decrease the number of distracted drivers, both leading to a safer pedestrian environment.

Acknowledgements This research was funded by the "AI*IA Incoming Mobility Grants 2016," the "University of Tokyo international students scholarship," and the SEUT-RA program.

References

1. Bandini, S., Crociani, L., Feliciani, C., Gorrini, A., Vizzari, G.: Collision avoidance dynamics among heterogeneous agents: the case of pedestrian/vehicle interactions. In: Proceedings of the Conference on AI*IA 2017 Advances in Artificial Intelligence, pp. 44–57. Springer, Berlin (2017). http://dx.doi.org/10.1007/978-3-319-70169-1_4
2. Davis, G.: Relating severity of pedestrian injury to impact speed in vehicle-pedestrian crashes: simple threshold model. Transp. Res. Rec. J. Transp. Res. Board **1773**, 108–113 (2001). http://dx.doi.org/10.3141/1773-13
3. Feliciani, C., Crociani, L., Gorrini, A., Vizzari, G., Bandini, S., Nishinari, K.: A simulation model for non-signalized pedestrian crosswalks based on evidence from on field observation. Intel. Artif. **11**(2), 117–138 (2017). http://dx.doi.org/10.3233/IA-170110
4. Gorrini, A., Vizzari, G., Bandini, S.: Towards modelling pedestrian-vehicle interactions: empirical study on urban unsignalized intersection (2016). Preprint. arXiv:1610.07892
5. Griffiths, J.: A mathematical model of a nonsignalized pedestrian crossing. Transp. Sci. **15**(3), 222–232 (1981). http://dx.doi.org/10.1287/trsc.15.3.222
6. Hatfield, J., Murphy, S.: The effects of mobile phone use on pedestrian crossing behaviour at signalised and unsignalised intersections. Accid. Anal. Prev. **39**(1), 197–205 (2007). http://dx.doi.org/10.1016/j.aap.2006.07.001
7. Karndacharuk, A., Wilson, D., Dunn, R.: Safety performance study of shared pedestrian and vehicle space in New Zealand. Transp. Res. Rec. J. Transp. Res. Board **2464**, 1–10 (2014). http://dx.doi.org/10.3141/2464-01
8. Pešić, D., Antić, B., Glavić, D., Milenković, M.: The effects of mobile phone use on pedestrian crossing behaviour at unsignalized intersections–models for predicting unsafe pedestrians behaviour. Saf. Sci. **82**, 1–8 (2016). http://dx.doi.org/10.1016/j.ssci.2015.08.016
9. World Health Organization: World report on road traffic injury prevention (2004)
10. Zeng, W., Chen, P., Nakamura, H., Iryo-Asano, M.: Application of social force model to pedestrian behavior analysis at signalized crosswalk. Transp. Res. C Emerg. Technol. **40**, 143–159 (2014). http://dx.doi.org/10.1016/j.trc.2014.01.007

Algebraic and Geometric Aspects of Flow Modeling and Prospects of Natural Science Applications

Valery V. Kozlov, Boris N. Chetverushkin, Alexander P. Buslaev, Alexander G. Tatashev, and Marina V. Yashina

Abstract Every modern applied direction of natural-scientific research has access to a lot of data of network information—big data. These trends make it possible to assume higher standards for information processing and quality of developing models. In addition to using in traffic modeling applications, models of particle flows on complex networks are applied in different areas. The areas are, for example, material science for design of new materials, study of biological processes (metabolism), medicine for the study of drug action , computing (supercomputers), etc.

We consider *regular* networks being *perturbation* of standard rectangular networks or other regular graphs, where vertices are replaced with contours as support of the local movement of particles. The movement rules are postulated. Qualitative and quantitative flow characteristics are studied.

The BML model of cellular automata on Manhattan network on a torus was considered. There are two types of particles moving in one direction. The particles of first type move along meridians, and the particles of second type move along parallels. *For the first time there was obtained an effect of self-organization* of the system, and collapse conditions were formulated. The BML authors *laid down the foundation of the spectral theory for the considered systems.*

We are developing models of flows in more general periodic symmetric structures. There are proved results about particles velocities. Conditions of self-organization and collapse of the system have been formulated.

V. V. Kozlov
Steklov Mathematical Institute of the Russian Academy of Sciences, Moscow, Russia

B. N. Chetverushkin
Keldysh Institute of Applied Mathematics of the Russian Academy of Sciences, Moscow, Russia

A. P. Buslaev · A. G. Tatashev · M. V. Yashina (✉)
Moscow Automobile and Road Construction State Technical University (MADI), Moscow, Russia
e-mail: yash-marina@yandex.ru

S. H. Hamdar (ed.), *Traffic and Granular Flow '17*,
https://doi.org/10.1007/978-3-030-11440-4_47

We consider a variant of general algebraic formulation for full graph with architecture of N-dial. The particle plans are given by recording of real number in N-ary number system. The results characterized by the quality behavior of the system have been obtained. We have developed approaches to evaluate the velocity of the plan implementation by the particle and value of intensity of the particle movement. Various generalizations of the considered statements are formulated. Interconnection of these problems with questions of classical branches of mathematics has been found, in particular, with the theory of Diophantine equations.

1 Introduction: Complex Systems, Big Data, Supercomputers, and Mathematical Models

Modern scientific research takes place in the environment of revolutionary change in information and communication technologies. This provides a qualitatively new level of field tests and experimental data. In other words, every major direction of natural science research, relevant to the application point of view, has at its disposal a large number of observed data—big data. In turn, this provides higher standards for information treatment and quality of models [12, 14]. It has been found by experimental way that powers of computation complexes, though fast developing, are not sufficient for investigations. The reason of this is a principally different scales of supercomputer possibilities and concrete problems (e.g., metabolism in system biology). Therefore, intensive searchers are carried out both in the development of new bases in the device of computers, and in the direction of modern mathematical models, which are in fact *intermediaries between the observed complex systems and existing technologies* for their research and controls forecasts [13].

2 Complex Systems, Geometry of Supporter, and Movement Rules

A complex system is a complex spatial network, which is a supporter of investigated subjects (particles) with local rules of movements (transformations). *The main purpose of the research is to predict the behavior of the system as a whole on the basis of information of the local behavior.* As a rule, in each concrete case, the network structure is unique, and therefore, passing to the limit in space and time (to continuous medium) is a very delicate problem and an attribute of mathematical models at the final stage of development. Therefore initially it is assumed that *the time is discrete and can time steps of any nonzero scale.* The mathematical model of the network is a graph with vertices in a linear finite dimensional space and edges, which interpolate vertices. Characteristic velocity of particles movement along edges and the time step value induce partition of the graph into sections,

and boundaries of these sections determine the discrete model of the graph. Thus the graph represents a sequence of vertices as *a matrix of neighbors* or in another classical equivalent form. The movement rules determine the behavior of particles set and, in concrete form, determine restrictions on the vertices capacity or on simultaneously movement of some particles in the same particles set. Delays appear because of given restrictions. In accordance with these restrictions more than one particles (or more than a given number of particles) cannot be located in the same cell simultaneously and cannot intersect the same nodes simultaneously. The restrictions can be given also in the following forms. The particles cannot move simultaneously to each other in opposite directions or more than one particle cannot move through the same channel, etc. If more than one particle tries to occupy a vacant common cell, then conflicts take place. If more than one particle tries to occupy a vacant common cell or intersect the same cell simultaneously, then conflicts take place. These conflicts are resolved in accordance with the given rules. Deterministic and stochastic conflict resolution rules are considered. In accordance with the deterministic rules, priorities of particles are assigned to particles. The particle with the highest priority wins the conflict. The egalitarian rule is an example of stochastic rule. In accordance with the egalitarian rule, particles win the conflict equiprobably. Steady states of the system are investigated. In particular, we consider steady fields of conflicts, the possibility to achieve free movement, self-organization, and full stop of the system. The main investigated characteristic is the velocity of particles in steady state.

3 Algebra of Complex Systems Models

Algebraic formulation of complex system modeling is the following. A sequence of cells is given. These cells are numbered. Indexes of cells are non-negative integer numbers $0, 1, \ldots, N-1$. There are logistical plans of M particles. The plans $L_i, i = 1, \ldots, M$, are defined by rational fractions. The representation of fraction is a periodic fraction $0.(k_{1i} \ldots k_{m_i,i})$ of nodes. Traffic rules are also given. We assume that the plan of particle is recorded on the tape, and the particle reads digits on its tape. The tape is shifted onto a position at every step if no delay of plan implementation takes place. *The plan implementation is characterized by the tape movement velocity.* The problem is to investigate the behavior of this dynamical system or, depending on restrictions, Markov process.

We use concepts, facts and approaches of the dynamic systems theory, theory of Markov processes, graph theory, function theory, algebra, number theory, approaches to give algorithmic representation of real numbers and to find the period of rational number representation, we develop visual geometric interpretations.

Thus, in accordance with traffic rules, a dynamical system (Markov process) with M subjects is defined on a semi-infinite lane $(L_1, L_2, \ldots, L_M)$ with periodic rows in positional system with ciphers $\{0, 1, \ldots, N-1\}$.

4 Regular Networks and Qualitative Behavior of Local Flows

Further we consider regular networks. These networks are *perturbations of standard regular networks and other regular graphs. In these graphs vertices are replaced by ring, which is the supporter of local movement of particles.* This approach simulates two characteristic types of displacements. These types are local displacements and cross migrations of particles.

Each contour consists of the same number of cells, and the number of neighbors is the same for each contour. This number is equal to two (necklace), three (honeycombs), four (chainmail). Neighborhood of two contours is determined by a common cell (*basic model*), or a common node, which is located between neighboring cells of the corresponding contour (*alternative model*). Respectively, more than one particle cannot be located in the same cell simultaneously, or particles of neighboring contours cannot intersect the same node simultaneously. We consider *deterministic* rules of movement, *deterministic–stochastic rules,* and *stochastic rules.* In the case of deterministic–stochastic rules, probabilistic behavior is shown only in the case of conflict, which appears if particles of neighboring contours try to occupy the common cell (intersect the common cell). In the case of stochastic rules the nature of movement on each contour is also probabilistic. Here we assume that, *on each contour, the same number of particles moves only along this contour (local migrations).*

Self-Organization *We have found the following. If the flow density (the number of particles related to the number of cells) is less than* $1/k$, *where* k *is the number of contour neighbors, then system self-organization is realized after a finite time and the free movement takes place after a finite moment.*

Boundary of Phase Transition *If* $\rho = 1/k$, *then, in the steady state, the velocity of particles movement depends on the initial state of the system, and, in the case of stochastic conflict resolution rule, the values of movement velocity can be different with positive values.*

In Fig. 1, we show a chainmail on a torus with boundary load. Vacant cells are shown in white. Occupied cells are shown in gray. Nodes, which are points of contours junctions, are shown as small black circles. On neighboring contours, particles move in opposite directions. We have the following specific properties of the considered systems:

(4.1) Behavior of deterministic–stochastic systems is deterministic after a time interval with finite expectation, though this time interval is greater than any fixed value with positive probability.

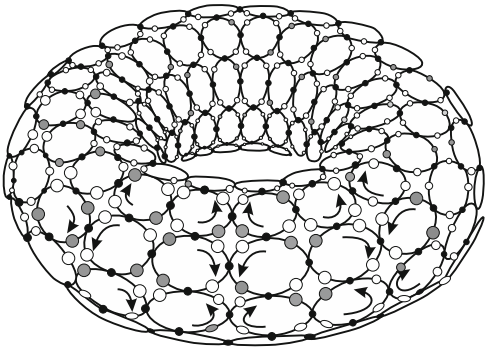

Fig. 1 Chainmail on torus

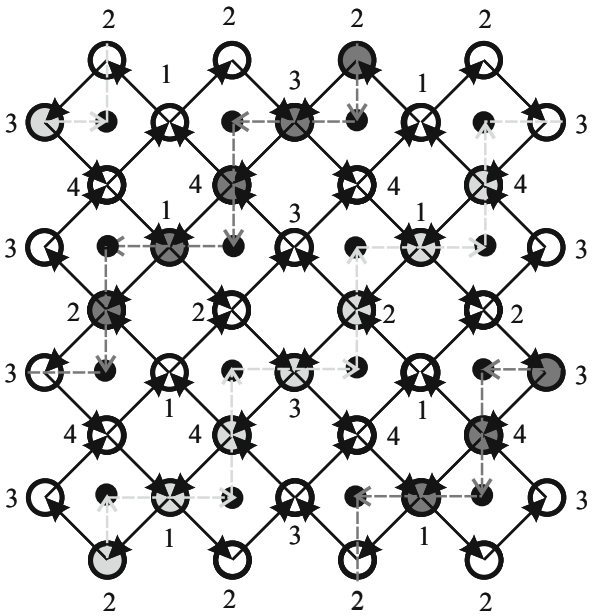

Fig. 2 Clusters of motionless particles on diagonals of chainmail, $k = 4$

(4.2) The considered dynamic system is a Markov chain. The space of this chain states is divided into communication classes of essential states and the set of inessential states. In general case, the velocity of particles depends on the communication class to which the initial state belongs. An absorbing state of the chain corresponds to a state of collapse.

(4.3) Steady state of movement on "chainmail" (two-dimensional toroid systems of rings). The set of contours is divided into subsets ("diagonals"), Fig. 2. The velocity of particles on all contours of each diagonal is the same. Consider the

set of particles such that these particles cannot move at current moment. This set shifts onto a position in the direction opposite to the direction of movement at each moment.

(4.4) We have that the nature of steady movement on the chainmail with particles flow density $\rho = \frac{1}{4}$ depends on whether particles of neighboring contours move in the same direction or in different directions. If the particles of all contours move counterclockwise, then the particle of each contour does not move (velocity is equal to 0) or moves at every moment (velocity is equal to 1). If the particles of the neighboring contours move in the opposite directions, then the spectrum of particles velocities contains values between 0 and 1 in general case.

(4.5) We use the theory of linear Diophantine equations in the investigation of self-organization on the discrete version of the model "flower" (systems of contours with a unique common point). Thus we use approaches of the number theory.

A condition for the system to be in the state of free movement is that there are no solutions of the corresponding Diophantine equations. The algorithm of calculation of particles velocities on flower with two contours deals with the analysis of solutions of linear Diophantine equations with two variables [8].

5 Rational Multipendulums

We consider a version of common algebraic formulation of problem for a full graph with abstract architecture N-dial. Each particle passes the distance between any cells for a step. The particles move in accordance with the plans. The plans are given by the representation of real numbers in N-ary positional system. Delays in particles movement take place in accordance with the given restrictions. The following types of restrictions are possible: *Simultaneous movement of particles to each other is forbidden. Simultaneous movement of particles along the same channel is forbidden (one-channel movement). More than fixed number of particles cannot be located in the same cell simultaneously (restriction on the cell volume).*

(5.1) *Bipendulum.* The simplest version is a dynamical system called bipendulum [23]. There are two cells (vertices) and two particles. Analysis of bipendulum with rational plans is related to unary algebras of proper fractions with fixed denominator with operation called Bernoulli shift (the fraction is multiplied by 2 and the integer part is excluded). Classical results of the number theory (Little Fermat theorem, Euler theorems, etc.) are useful in the analysis of Bernoulli algebras [9].

(5.2) *Multipendulum.* A generalization of bipendulum is real-valued pendulum, for which the numbers of vertices and particles are arbitrary. Generalized Bernoulli is related to real-valued pendulum [9].

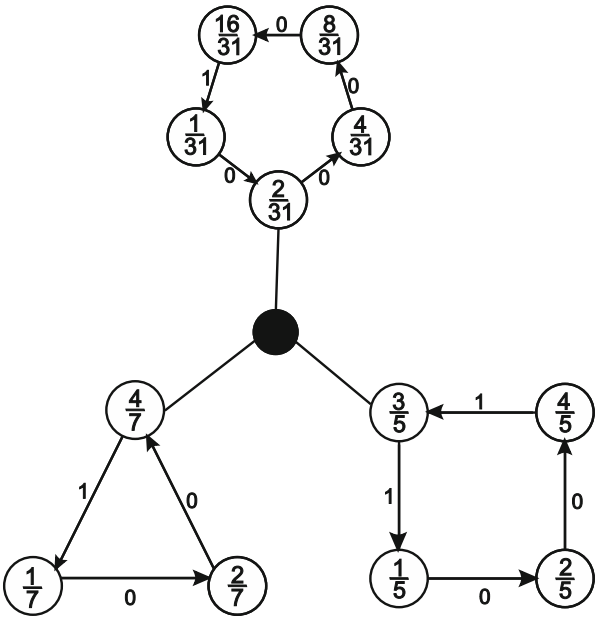

Fig. 3 Real-valued pendulum with orbits

In the model, shown in Fig. 3, rings, which turn when the tapes move, correspond to particles tapes. The reading head, shown in Fig. 3 in black color, reads tapes states at current moment. This representation shows how the real-valued pendulum and generalized Bernoulli algebras are related to each other. There are two vertices and three particles. The plans of particles are binary representations of numbers $\frac{1}{5}$, $\frac{1}{7}$, and $\frac{1}{31}$. In accordance with the given rules either the drum rotates and the particle realizes its plan for moving in the binary pendulum or there is a delay. Free movement of bipendulum is similar to the drum moving at each time step.

6 Cellular, BML Traffic Model and Processes on the Ring

(6.1) In a paper of Biham, Middleton, Biham [2], which has been published in 1992, a model of cellular automaton on Manhattan network on a torus. In this model, two types of particles are fixed. These particles move in the same direction upwards and to the right at alternating time moments or at each step but with random priority assignment. *A distinctive feature of the paper is that the system self-organization effect has been revealed. It has been found that conflicts disappear after a time interval for any admissible particles location.* It has been also revealed that, at certain network load, the system stops, i.e., the system comes to the state of collapse. **Thus it can be assumed that these**

authors have laid the first stone in the foundation of the theory which deals with the spectrum of the considered systems.

(6.2) In the subsequent papers, similar models in spaces of other dimensions were considered. However results were limited by computer modeling [1, 15]. There are a very few results in this theory.

(6.3) The models of flows on discrete graph of successive vertices on the ring are substantially more mathematized [3, 4]. However these results are in the periphery of our interest at this stage.

7 Mathematical Problems and Application Prospects

(7.1) In abstracts [18] of the conference TFG'13, we have formulated directions of our investigations in the scope of traffic flows modeling. The results of our investigations on discrete models have been published in papers [5–11, 17, 19–24]. Network models were introduced and investigated in [5, 6, 8, 11, 17, 19–22, 24]. In these models, particles move on contours of symmetrical periodic structures (necklace, chainmail, honeycombs, and flowers). The generalized traffic model was considered in [7, 9, 10, 23].

(7.2) Investigation of bipendulum and real-valued pendulum with irrational plans is related to problems of constructive representation of irrational numbers, the concept of normal number relative to positional system, calculation of fraction representation period, etc. It is known that sequences of digits in positional representation of well-known irrational constants behave chaotically (though proofs and even exact formulations of this statement are not known), and therefore, behavior of the considered system with irrational plans is similar to the behavior of a stochastic version of real-valued pendulum called random pendulum [10].

(7.3) Developed models can have applications not only in analysis and optimization of traffic flows but can be used for investigation of communication networks, physical and biological processes, in materials science, in computer science, etc. The experimental quantum computer of company D-Wave Systems [16] is based on the Ising model. *We note some analogies between the one-dimensional Ising model and the dynamical system "necklace," considered in [21].* The Ising model is represented as interacting vertices (atoms) of a crystal lattice, and each vertex can be divided into two states. A number called spin and equals to $+1$ or -1 ("field up"/"field down"). There are 2^N states of the system, where N is the number of vertices. Each vertex interacts with two neighboring vertices. The system state is characterized by the value of energy. The energy is sum, and the value of each term corresponds to a pair of vertices. This value is positive or negative depending on whether vertices of the pair are in the same or in different states. A necklace with alternance is a closed chain of N contours. There are 2^N states of the system. Each contour is at one of the two states at a fixed time. Namely, the contour is in

the top cell 1 or in the bottom cell −1. Each particle interacts with particles of two neighboring contours. The system state is characterized by the value of the variation function of the necklace state. The state of the system is characterized by the variation function of the necklace state. The value of variation characterizes the distance between the given state and the state of free movement, which is reached as a result of self-organization.

References

1. Austin, T.D., Benjamint, I.: For what number of cars must self organization occur in the Biham–Middleton–Levine traffic model, 2006, arXive:math/0607759 [math.CO]
2. Biham, O., Middleton, A., Levine, D.: Self-organization and a dynamical transition in traffic-flow models. Phys. Rev. A **46**, 10 (1992)
3. Blank, M.L.: Exact analysis of dynamical systems arising in models of traffic flows. Russ. Math. Surv. **55**(3), 562–563 (2000). http://dx.doi.org/10.1070/RM2000v055n03ABEH000295
4. Blank, M.: Metric properties of discrete time exclusion type exclusion time processes in continuum. J. Stat. Phys. **140**, 170–197 (2010)
5. Bugaev, A.S., Buslaev, A.P., Kozlov, V.V., Tatashev, A.G., Yashina, M.V.: Traffic modeling: monotonic total-connected random walk on a network. Matematicheskoye Modelirovanie **25**(8), 3–21 (2013) (In Russian)
6. Bugaev, A.S., Buslaev, A.P., Kozlov, V.V., Tatashev, A.G., Yashina, M.V.: Generalized transport-logistic problem as a class of dynamical systems. Matematicheskoye Modelirovanie **27**(12), 65–87 (2015) (In Russian)
7. Buslaev, A.P., Tatashev, A.G.: Generalized real numbers pendulums and transport logistic applications. New Developments in Pure and Applied Mathematics. New Developments in Pure and Applied Mathematics, pp. 388–392. Vienna (2015). www.inase.org/library/2015/vienna/bypaper/MAPUR/MAPUR-63.pdf
8. Buslaev, A.P., Tatashev, A.G.: Flows on discrete traffic flow. J. Math. Res. **9**(1), 98–108 (2016). http://dx.doi.org/10.5539/jmr.v9n1p98
9. Buslaev, A.P., Tatashev, A.G.: Bernoulli algebra on common fractions and generalized oscillations. J. Math. Res. **8**(3), 82–95 (2016) http://dx.doi.org/10.5539/jmr.v8n3p82
10. Buslaev, A.P., Tatashev, A.G.: On dynamical systems for transport logistic and communications. J. Math. Res. **8**(8), 195–210 (2016). http://dx.doi.org/10.5539/jmr.v8n4p195
11. Buslaev, A.P., Tatashev, A.G., Yashina, M.V.: Qualitative properties of dynamical system on toroidal chainmail. 11th International Conference of Numerical Analysis Mathematics 2013, ICNAAM 2013, Rhodes, Greece, 21–27 September 2013. AIP Conference Proceedings 1558, pp. 1144–1147 (2013)
12. Chetverushkin, B.N.: High-performance multiprocess systems: problems of using and personnel training. Vestnik RAN **72**(9), 786–794 (2000) (In Russian)
13. Chetverushkin, B.N.: Kinetic models for solving continuum mechanic problems on supercomputers. Math. Models Comput. Simul. **7**(6), 531–539 (2015)
14. Chetverushkin, B.N., Saveliev, V.I.: Kinetic models and High-performance calculations. Preprints of Keldysh Institute of Applied Mathematics. RAS, Moscow (2015), 079 (In Russian)
15. Ding, Z., Jiang, R., Wang, B.: Traffic flow in the Biham–Middleton–Levine model with random update rule. Phys. Rev. **83**(4) (2011)
16. Katzgraben, H.G., Hamse, F., Andrist, S.R.: Glassy chimeras could be blind to quantum speedup: designing better benchmakers for quantum speedup for quantum annealing machines. Phys. Rev. X. **4**, 1–8 (2014) http://dx.doi.org/10.1103/Phys.Rev.X.402.1008

17. Kozlov, V.V., Buslaev, A.P., Tatashev, A.G.: On synergy of totally connected flows on chainmails. Proceedings of the 13th International Conference on Computational and Mathematical Methods in Science and Engineering, CMSSE 2013, Cadiz, Spain, June 24–27 2013, vol. 3, pp. 861–873 (2013)
18. Kozlov, V.V., Buslaev, A.P., Tatashev, A.G., Yashina, M.V.: Mathematical problems and theorems on saturated flows on chainmail. Traffic and Granular Flow '13, 25–27 September 2013, Forschungzentrum, Julich, Germany. Book of Abstracts (2013)
19. Kozlov, V.V., Buslaev, A.P., Tatashev, A.G., Yashina, M.V.: Monotonic walks of particles on a chainmail and coloured matrices. Proceedings of the 14th International Conference on Computational and Mathematical Methods in Science and Engineering, CMSSE 2014, Cadiz, Spain, June 3–7 2014, vol. 3, pp. 801–805 (2014)
20. Kozlov, V.V., Buslaev, A.P., Tatashev, A.G.: Behavior of pendulums on a regular polygon. J. Commun. Comput. **11**, 30–38 (2014)
21. Kozlov, V.V., Buslaev, A.P., Tatashev, A.G.: Monotonic walks on a necklace and coloured dynamic vector. Int. J. Comput. Math. **92**(9), 1910–1920 (2015). http://dx.doi.org/1080/00207160.2014/915964
22. Kozlov, V.V., Buslaev, A.P., Tatashev, A.G.: A dynamical communication system on a network. J. Comput. Appl. Math. **275**, 247–261 (2015). http://dx.doi.org/10.1016/j.cam.2014.07.026
23. Kozlov, V.V., Buslaev, A.P., Tatashev, A.G.: On real-valued oscillations of a bipendulum. Appl. Math. Lett. **46**, 44–49 (2015) http://dx.doi.org/10.1016/j.aml.2015.02.003
24. Kozlov, V.V., Buslaev, A.P., Tatashev, A.G., Yashina, M.V.: Dynamical Systems on Honeycombs. Traffic and Granular Flow '13, pp. 441–452. Springer, Heidelberg (2015)

Crossing Behaviour of Social Groups: Insights from Observations at Non-signalised Intersection

Andrea Gorrini, Luca Crociani, Giuseppe Vizzari, and Stefania Bandini

Abstract Environmental, demographical and psychological factors have a demonstrated impact on risky crossing behaviour. In this work we focus on the potential influence of social factors on the considered phenomenon (i.e., *group crossing decision*). We present the results of a video-recorded observation about the crossing behaviour of singles and dyads at non-signalised intersections. The results showed that crossing behaviour is characterised by three distinct phases: (i) approaching, (ii) appraising (decision making) and (iii) crossing. Dyads walk slower than single pedestrians in all phases. The crossing behaviour of dyads is characterised by the emergence of a leader who takes the decision to cross first, followed by the companion. However, there is no difference between the accepted safety gap of singles and dyads. Understanding factors influencing the crossing decision of social groups represents an important result supporting the development of agent-based simulations of pedestrian–vehicle interactions.

1 Introduction

As highlighted by the WHO [16], road accidents represent the eighth leading cause of death in the world population: 1.2 million people are killed on roads every year. Despite recent efforts, the measures currently in place to reduce the phenomenon are mainly aimed at protecting car occupants. However, pedestrians are some of the most vulnerable road users, with a percentage of fatalities corresponding to 22% of the overall victims (26% in EU, 14% in USA).

A. Gorrini (✉) · L. Crociani · G. Vizzari
CSAI Research Center, University of Milano-Bicocca, Milan, Italy
e-mail: andrea.gorrini@disco.unimib.it; luca.crociani@disco.unimib.it; giuseppe.vizzari@disco.unimib.it

S. Bandini
CSAI Research Center, University of Milano-Bicocca, Milan, Italy

RCAST, The University of Tokyo, Tokyo, Japan
e-mail: stefania.bandini@disco.unimib.it

S. H. Hamdar (ed.), *Traffic and Granular Flow '17*,
https://doi.org/10.1007/978-3-030-11440-4_48

To effectively contrast the social costs of pedestrian–car accidents it is necessary to identify the determining factors of risky crossing decisions by means of a multi-disciplinary approach (e.g., traffic psychology, transportation engineering, safety science, computer science). This is aimed at supporting public institutions in the design of effective and safe infrastructures and traffic management solutions.

In this context, the results presented in [12, 15] highlighted, for instance, the impact of the physical features of the infrastructure on crossing behaviour (e.g., road width, traffic volumes, type of intersection). Other researches focused on the complex coordination of the motor and cognitive abilities involved in crossing behaviour, such as locomotion [15]; perception and attention [8]; attitude towards hazardous situations [3]. Other studies [2, 7] showed the impact of ageing on crossing behaviour, due to the progressive decline of these functions.

These works showed the relevant impact of environmental, demographical and psychological factors on risky crossing behaviour. However, there is still a lack of knowledge about the impact of social factors on the phenomenon, due to limited or controversial results. Urban cross-walks are characterised indeed by the presence of multiple pedestrians, and people often cross the street in the presence of other familiar or unfamiliar pedestrians.

The contributions about this topic can be classified according to two different approaches. On one hand, the results presented in [9, 13] showed that the presence of other pedestrians is associated with a reduction of cautiousness in crossing decision at signalised cross-walks. Moreover, the results presented in [4] showed that pedestrians imitate the behaviour of others to judge the gap from oncoming vehicles, with potentially dangerous crossing decisions due to an overestimation of crossing possibilities. This phenomenon is based on the power of group to cause a diffusion of responsibility [6], as each member feels that the responsibility for violating the norms and for taking risky crossing decisions is shared with the rest of the group.

On the other hand, the results collected by [1, 14] showed that people are more lax in risky crossing decisions standing by their own than when standing in groups. These findings can be explained considering the theory of social control [11], which describes the mechanism behind obedient behaviour as the motivation to be rewarded just for being conformist to the group norms.

Starting from these assumptions, the present work was focused on studying the crossing behaviour of social groups (groups composed of familiar pedestrians, such as relatives and friends) through a video-recorded observation at a non-signalised intersection. The research was aimed at comparing data about the crossing behaviour of single pedestrians and two-member groups (i.e., *dyads*): the simplest and most frequently observed type of group.

The methodology which sets the current work is presented in Sect. 2, with reference to data collection and data analysis. The results of the observation (e.g., traffic volumes, level of service, crossing phases, speeds, safety gap) are presented in Sect. 3. The paper concludes with remarks about the achieved results and their future use for the further development of a computer-based simulator of pedestrian/vehicles interaction in urban contexts [5].

2 Data Collection

The video-recorded observation [7] was performed in 2015 (from 10:45 a.m., 73 min in total) at a non-signalised intersection in Milan (Italy), which was selected by means of a preliminary analysis related to the localisation of road traffic accidents. The results showed that the area was characterised by a high number of pedestrian/car accidents in the past years.

A first phase of manual counting activity allowed to estimate and characterise the observed traffic volumes. An *ad hoc* designed checklist (see Table 1), comprising a set of locomotion and communication indicators, was used to support the annotators in the identification of social groups from the video images. Then, a time stamping activity allowed to measure the level of service in the observed intersection.

A second phase of data analysis was based on the use of the open source software Tracker Video Analysis and Modelling Tool (see Fig. 1). The tracker allowed to correct the distortion of the video images (due to the wide lens and the nearly zenith

Table 1 The checklist used by the coders for identifying social groups

Locomotion behaviour	High spatial cohesion and coordination while walking
	Waiting dynamics to regroup in case of separation
	Leader/follower dynamics in sudden changes of direction
Verbal behaviour	Talking while walking
Non-verbal behaviour	Physical contact
	Body and gaze orientation to each other
	Gesticulation while talking and/or indicating

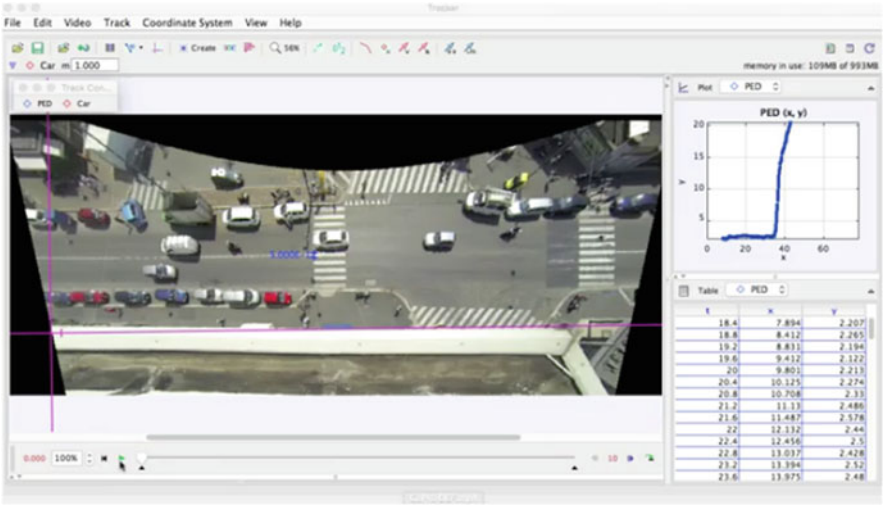

Fig. 1 A screenshot from the tracker tool used for data analysis

perspective of the camera), and to track a sample of pedestrians considering one frame every ten (every 0.4 s). The data set (including the X, Y coordinates and the associated frames t) was exported for data analysis.

3 Results

3.1 Traffic Volumes

The observed vehicular traffic volumes (1379 veh, 18.89 veh/min) were constituted for the majority by cars (67%). The direction of movements of vehicles was equally distributed. The majority of pedestrians (585 ped, 8.01 ped/min) were singles (65%). Dyads were a significant portion of the total counted pedestrians: 26% dyads; 8% triples; 1% other. A Cohen's Kappa analysis showed a moderate agreement between the two independent coders in the identification of social groups ($K = 0.47$).

3.2 Level of Service

The level of service (LOS) [10] describe the degree of efficiency of an intersection, by measuring the additional travel time experienced by drivers and pedestrians as they travel/walk through a road segment. At non-signalised intersections LOS E is the minimum acceptable design standard.

The LOS have been estimated by time stamping the delay of drivers due to vehicular traffic and crossing pedestrian flows (time for deceleration, queue, stopped delay, acceleration), and the delay of pedestrians due to drivers' non-compliance to their right of way on zebra (waiting, start-up delay). The results showed that the average delay of drivers (3.20 s/veh ± 2.73 sd) and pedestrians (1.29 s/ped ± 0.21 sd) corresponded to LOS A: nearly all drivers found freedom of operation; low risk-taking in crossing behaviour (Fig. 2).

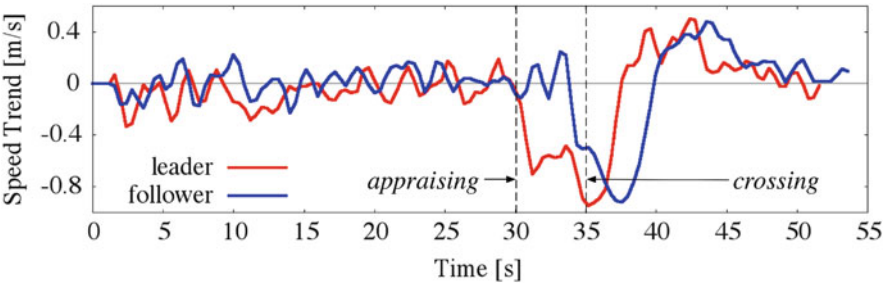

Fig. 2 An exemplification of the trend analysis performed on the time series of dyads' speeds

Table 2 The speed of singles and dyads among the crossing phases

Crossing phases	Speed of singles	Speed of dyads
Approaching speed	1.277 m/s ± 0.182 sd	1.123 m/s ± 0.155 sd
Appraising speed	0.943 m/s ± 0.214 sd	0.702 m/s ± 0.280 sd
Crossing speed	1.354 m/s ± 0.181 sd	1.127 m/s ± 0.131 sd

3.3 Speeds and Crossing Phases

A sample of 49 adult pedestrians (27 singles and 11 dyads, from about 18 y.o. until 65 y.o.) was selected for video-tracking analysis. The sample was selected avoiding situations such as platooning of vehicles on the roadway, the joining of pedestrians already crossing, and in general situations influencing the direct interaction between pedestrians and drivers. Part of the selected crossing episodes was characterised by the multiple interaction between the crossing pedestrian and two cars oncoming from the near and the far lane. Pedestrians' gender was balanced, but not considered for data analysis.

The speed of pedestrians has been analysed among the time series of video frames. The trend of speeds was analysed by calculating the difference between the moving average (MA, time period length: 0.8 s) and the cumulative average (CA) of the entire frames series. This allowed to smooth out short-term fluctuations of data and to highlight longer-term deceleration/acceleration trends. According to results, crossing behaviour is defined as composed of three distinctive phases:

1. *approaching phase*: the pedestrian travels on the side-walk with a stable speed (speed MA–CA $\simeq 0$);
2. *appraising phase*: the pedestrian approaching the cross-walk decelerates to evaluate the distance and speed of oncoming vehicles (safety gap). We decided to consider that this phase starts with the first value of a long-term deceleration trend (speed MA–CA < 0);
3. *crossing phase*: the pedestrian decides to cross and speed up. The crossing phase starts from the frame after the one with the lowest value of speed before a long-term acceleration trend (speed min).

A two-way ANOVA[1] showed a significant difference among the speeds of pedestrians while approaching, appraising and crossing [$F(2,146) = 66.981$, $p < 0.001$], and a significant difference between the speeds of singles and dyads [$F(1,146) = 40.652$, $p < 0.001$] (see Table 2 and Fig. 3). A series of post hoc Tukey test showed a non-significant difference between the speeds of all pedestrians while approaching and crossing ($p > 0.05$). The difference between the speeds of singles and dyads was significant among all the crossing phases ($p < 0.001$).

[1] All statistics have been executed by using *IBM SPSS Statistics 24*, at the $p < 0.01$ level.

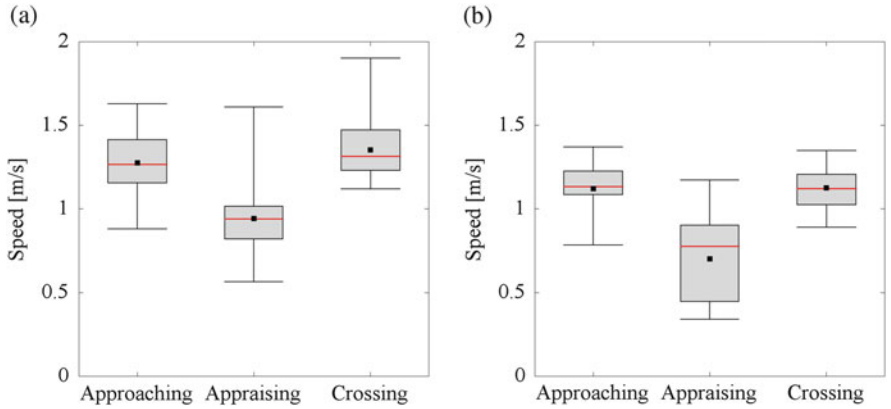

Fig. 3 The speed of (**a**) single pedestrians and (**b**) dyads among the crossing phases

Table 3 The safety gap accepted by singles, group leaders and followers

	Singles	Group leaders	followers
Safety gap	3.982 s ± 2.549 sd	4.355 s ± 2.491 sd	4.242 s ± 2.585 sd
Vehicle distance	16.399 m ± 7.753 sd	19.152 m ± 9.967 sd	17.325 m ± 9.583 sd
Vehicle speed	16.534 km/h ± 6.737 sd	16.525 km/h ± 5.662 sd	15.695 km/h ± 4.479 sd
Appraising time	2.785 s ± 1.474 sd	3.527 s ± 2.297 sd	3.164 s ± 1.682

The results showed that the crossing behaviour of dyads (see Fig. 2) is characterised by the emergence of a leader who completes the appraising first and takes the decision to cross, followed by the companion. An independent samples *t*-test analysis showed that the difference between the speeds of group leaders and followers was not significant among all the three crossing phases ($p > 0.05$).

The results demonstrated that the crossing behaviour of both singles and dyads is based on a significant deceleration in proximity of the curb to evaluate the distance and speed of oncoming vehicles to safely cross. Dyads walked in average 17% slower than singles among the three crossing phases, decelerating the 11% more than singles while appraising.

3.4 Accepted Safety Gap

The term *safety gap* denotes the ratio between the pedestrians's evaluation of the distance of an approaching vehicle and its speed (not taking into account acceleration/deceleration trends) to decide to safely cross avoiding collision.

A one-way ANOVA showed that the safety gap accepted by singles (3.982 s ± 2.549 sd), group leaders (4.355 s ± 2.491 sd) and followers (4.242 s ± 2.585 sd) was not significantly different ($p > 0.05$) (see Table 3). Moreover, a one-

way analysis of variance showed that the time duration of the appraising phase of singles (2.785 s ± 1.474 sd), group leaders (3.527 s ± 2.297 sd) and followers (3.164 s ± 1.682) was not significantly different ($p > 0.05$).

The results showed also that, compared to leaders, followers started appraising with a delay of 1.055 s (± 1.032 sd) and they decide to cross with a delay of 0.691 s (± 0.671 sd). Further analysis about the relative positions of group members showed that the large majority of group leaders preceded followers while appraising, and that all leaders preceded followers when they decided to cross. The results highlighted that the leaders were able to better evaluate the distance and speed of oncoming vehicles according to the position, and so they take the decision to cross first followed by the companion.

4 Final Remarks

A video-recorded observation was performed at a non-signalised intersection to study the crossing behaviour of social groups, comparing data among single pedestrians and dyads. Trend analyses on the speeds of the tracked pedestrians showed that crossing behaviour is characterised by three distinct phase: approaching, appraising and crossing. In particular, the appraising phase consists on a significant deceleration in proximity of the curb to evaluate the distance and speed of oncoming vehicle to safely cross (i.e., *decision making*).

The results showed that dyads walked in average 17% slower than singles among the three crossing phases, decelerating the 11% more than singles while appraising. Group crossing behaviour is based on the emergence of a leader who completes the appraising first and decides to cross, followed by the companion. However, followers did not merely imitate the crossing behaviour of the leaders in judging the safety gap from oncoming vehicles, since no significant difference was found in the time duration of the appraising phase between them. Finally, no significant difference was found in the safety gap accepted by singles and dyads.

Future works will be aimed at enlarging the sample of tracked pedestrians for data analysis, including also groups composed by unfamiliar pedestrians. Moreover, we consider the possibility to test the impact of social imitation among unfamiliar pedestrians on risky crossing behaviour, such as non-compliant jaywalking behaviour out of zebra-striped crossing.

While no significant difference has emerged in comparing the crossing decision of singles and dyads, the presented results could be of notable interest for those involved in modelling and simulation of urban interactions. In particular, the results of the observation will be used to support the further development of a computer-based simulator of pedestrian/vehicles interactions at non-signalised intersections [5], focusing on modelling heterogeneous crossing speed among pedestrians.

Acknowledgements The Italian policy was compiled in order to exceed the ethical issues about the privacy of the people recorded without their consent. The authors thank Fatima Zahra Anouar for her fruitful contribution in data analysis. The recorded video tape and the annotated data set are available for research purposes.

References

1. Dang, N.T., Cavallo, V., Thomson, J., Gorrini, A., Piwowarczyk, A., Vienne, F., Bandini, S., Pierre, G.S.: Crossing the street in dyads: social influence on pedestrian behavior in an immersive virtual environment. In: Proceedings of the International Conference on Road Safety and Simulation, Delft, Netherlands (in press, 2017)
2. Dommès, A., Le Lay, T., Vienne, F., Dang, N.T., Beaudoin, A.P., Do, M.C.: Towards an explanation of age-related difficulties in crossing a two-way street. Accid. Anal. Prev. **85**, 229–238 (2015)
3. Evans, D., Norman, P.: Understanding pedestrians' road crossing decisions: an application of the theory of planned behaviour. Health Educ. Res. **13**(4), 481–489 (1998)
4. Faria, J.J., Krause, S., Krause, J.: Collective behavior in road crossing pedestrians: the role of social information. Behav. Ecol. **21**(6), 1236–1242 (2010)
5. Feliciani, C., Crociani, L., Gorrini, A., Vizzari, G., Bandini, S., Nishinari, K.: A simulation model for non-signalized pedestrian crosswalks based on evidence from on field observation. Intel. Artif. (in press, 2017)
6. Festinger, L., Pepitone, A., Newcomb, T.: Some consequences of de-individuation in a group. J. Abnorm. Soc. Psychol. **47**(2S), 382 (1952)
7. Gorrini, A., Vizzari, G., Bandini, S.: Towards modelling pedestrian-vehicle interactions: empirical study on urban unsignalized intersection. In: Proceedings of the 8th International Conference on Pedestrian and Evacuation Dynamics, Hefei, China (in press, 2016)
8. Hamed, M.M.: Analysis of pedestrians' behavior at pedestrian crossings. Saf. Sci. **38**(1), 63–82 (2001)
9. Harrell, W.A.: Factors influencing pedestrian cautiousness in crossing streets. J. Soc. Psychol. **131**(3), 367–372 (1991)
10. Highway Capacity Manual: Highway Capacity Manual. Transportation Research Board, National Research Council, Washington (2010)
11. Hirschi, T., Gottfredson, M.R.: The Generality of Deviance. Transaction Publishers, New Jersey (1994)
12. Perumal, V., et al.: Study on pedestrian crossing behavior at signalized intersections. J Traffic Transp. Eng. **1**(2), 103–110 (2014)
13. Ren, G., Zhou, Z., Wang, W., Zhang, Y., Wang, W.: Crossing behaviors of pedestrians at signalized intersections: observational study and survey in China. Transp. Res. Rec. J. Transp. Res. Board (2264), 65–73 (2011)
14. Rosenbloom, T.: Crossing at a red light: Behaviour of individuals and groups. Transport. Res. F: Traffic Psychol. Behav. **12**(5), 389–394 (2009)
15. Sisiopiku, V.P., Akin, D.: Pedestrian behaviors at and perceptions towards various pedestrian facilities: an examination based on observation and survey data. Transport. Res. F: Traffic Psychol. Behav. **6**(4), 249–274 (2003)
16. WHO: Global Status Report on Road Safety 2015. World Health Organization, Geneva (2015)

Modeling and Solving of Multiple Conflict Situations in Shared Spaces

Chris Schiermeyer, Federico Pascucci, Nils Rinke, Volker Berkhahn, and Bernhard Friedrich

Abstract When streets are designed according to the shared space principle, road users tend to interact spontaneously and to negotiate priority with each other by adapting their trajectory and speed. Despite the success of this design principle in the recent years, traffic engineers still cannot rely on microsimulation tools for shared spaces, which would be extremely useful to compute performance indicators describing safety and quality of traffic. In view of this, in the previous research the authors have developed a three-layered social force-based model, capable to simulate the operation of shared space environments. The aim of the current work is to extend the model by including conflict solving strategies for multiple conflict situations, i.e., conflicts which involve more than two road users. A methodological approach based on aggregated probabilities is proposed to determine road users' behavioral strategy. The goodness of the model is shown by means of an observed situation involving multiple pedestrians and motorists.

1 Introduction

According to the shared space design principle, road users are encouraged to interact with each other on a continuously paved surface with no level difference. The minimized usage of road signs and markings, together with the reduced demarcation between the motorized and non-motorized area, makes road users more responsible for their own behavior. In conflict situations road users can freely choose whether

C. Schiermeyer (✉) · N. Rinke · V. Berkhahn
Leibniz Universität Hannover, Institute for Risk and Reliability, Hannover, Germany
e-mail: schiermeyer@irz.uni-hannover.de; rinke@irz.uni-hannover.de; berkhahn@irz.uni-hannover.de

F. Pascucci · B. Friedrich
Technische Universität Braunschweig, Institute for Transportation and Urban Engineering, Braunschweig, Germany
e-mail: f.pascucci@tu-braunschweig.de; friedrich@tu-braunschweig.de

S. H. Hamdar (ed.), *Traffic and Granular Flow '17*,
https://doi.org/10.1007/978-3-030-11440-4_49

to yield or take priority over each other, as well as whether to modify the preferred direction and speed in order not to collide.

However, the high diversification of human behavior and the heterogeneity of conflict solving mechanisms among them make it difficult to reproduce shared spaces in a microsimulation model. The challenge is also represented by the presence of different transport modes—namely vehicles, pedestrians, and cyclists—with different physical and mechanical characteristics, such as operational speed and movement constraints. These models would be extremely helpful in traffic engineering in order to estimate traffic quality and safety of these areas.

The challenge of the research project MODIS (Multi-mODal Intersection Simulation) is to build a microsimulation framework, capable of simulating the movements of road users in shared spaces. In the previous work [5, 7] the MODIS microsimulation model has been developed and tested against different traffic situations involving pedestrians, cars, and cyclists, and successively calibrated [8]. This paper deals with multiple conflict situations involving motorists and pedestrians, i.e., it addresses modeling of road user behavior when they encounter more than one road user at the same time. The challenge is to determine a conflict solving strategy which could resolve all current conflict situations, preventing any possible collision. Moreover, it must be ensured that this strategy does not induce additional conflict situations with other road users. In this paper we will provide a new modeling approach which is valid independent from the traffic modes and the number of simultaneous conflicts. To show its applicability, an observed situation is reproduced and tested.

2 Background

For an insight into the existing literature in the field of shared space microsimulation the authors recommend Anvari et al. [1], which introduces the characteristics of integrated street design and provides a full overview on the modeling techniques. The common idea is to extend the social force model by additional models or layers, e.g., methods for trajectory planning, to guide the road users in free-flow, or collision avoidance mechanisms, to address conflict situations. In addition to that, two issues are here briefly discussed with respect to previous literature.

The first issue regards the circumstances in which a road user would perform a behavioral change, i.e., a modification of their current direction and speed, caused by the presence of other users around. While investigating safety performances of shared spaces in New Zealand, Karndacharuk et al. [4] distinguished between two types of behavioral change: one taken by force of situation, referred to as *conflict*, and one as a choice or willingness, referred to as *interaction*. In accordance to this, a widely accepted definition of *conflict* by Gettman and Head [2] refers to "situations with a high risk of collision if the behavior of road users remains unchanged." Moreover Kaparias et al. [3], when analyzing the variety of actions that can be observed in shared spaces, referred to as *interactions* in case the movement taken

was not strictly of an "evasive" nature (as it would be in the specific case of a *conflict*).

The second issue concerns the mechanism of priority negotiation between motorists and pedestrians. Many approaches have been proposed in lane-based environments, i.e., where the behavior of road users is expected to be on a predefined trajectory, like at mid-block crossings or crosswalks [9, 11]. However in shared spaces, where pedestrians are modeled with two spatial degrees of freedom, possible evasive actions imply deviations as well as decelerations. Considering this, in the past research we have developed a discrete choice model to determine the behavior of pedestrians and motorists when encountering each other [6]. The model considers as an input simple variables related to the conflict, such as time to collision (TTC), or to the conflicting users, such as current speed and acceleration. It finally returns a set of probabilities for all types of reaction strategies, which are feasible in the respective situation, that are used to determine the most likely reaction.

3 Modeling Approach

In our previous work [5, 7, 8] different conflict solving strategies for situations involving two road users were investigated. For this purpose, only conflict situations according to the definition of Gettman and Head (see Sect. 2) were considered.

When dealing with multiple conflict situations, the aim is to find a strategy that resolves all concurrent conflict situations while at the same time the application of such a strategy should not induce new conflict situations with other road users. For this reason all road users in temporal and spatial proximity have to be regarded.

In [5] a concept for detecting conflicts based on the comparison of a safety distance with the predicted distance of two road users was introduced. For the detection of individual conflicts in multiple conflict situations this concept is still applicable, but is extended to cover the *umbrella term* "interaction," which does not imply a collision, but simply a high proximity of road users.

To determine which non-conflicting users may affect the decision process, the concept is extended by introducing an *interaction distance* d_{int} and an *interaction horizon* t_{int}. The extension is shown for a generic distance function in Fig. 1. If the distance function $d(t)$ is lower than d_{int} in the interval before t_{int}, these road users are defined as *interacting users*. Each other user within a user's perception range is analyzed following this definition and accordingly classified as conflicting, interacting, or non-interacting.

In case at least one conflicting and at the same time more than one interacting user is detected, a situation is classified as a multiple conflict situation. For the subsequent determination of a conflict solving strategy all conflicting and interacting users are considered with equal impact.

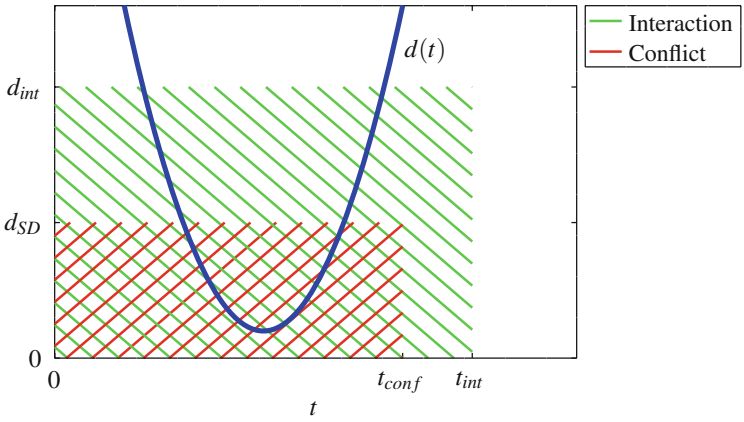

Fig. 1 Identification of interacting and conflicting users using the predicted distance function $d(t)$

3.1 Aggregation of Probabilities

As a first step, the probabilities for all possible reaction behaviors are calculated for all conflicting and interacting users using the decisional model by Pascucci et al. (see Sect. 2) independently as if they were in single conflict situations. Although on the first glance this approach contradicts the requirement to find a comprehensive strategy, it is noteworthy that the number of present road users already has an impact on the outcome of the decisional model. The result of this is a set of probabilities $P_i(B)$, where i denotes the interacting road user effecting the respective reaction and B the behavior type. An example is demonstrated in Fig. 2a, where a pedestrian in a conflict with two motorists has to decide between a prudent, an aggressive, or no reaction. Based on these single probabilities the aim is to find an aggregation $P_G(B)$ to determine the global probability for a behavior B considering all n_{int} interacting users.

Aggregating probabilities is a problem known, e.g., in the field of geoscience, where forecasts for natural events have to be combined from different sources. An intuitive and common way to calculate the aggregation is the *linear pooling* as proposed by Stone [10]:

$$P_G(B) = \sum_{i=1}^{n_{int}} w_i P_i(B), \tag{1}$$

where the aggregated probability $P_G(B)$ is expressed as a convex combination of the single probabilities.

For the test cases at hand (further covered in Sect. 4) currently equal weights w_i are used for all probabilities. In future work a variation of the individual weights will

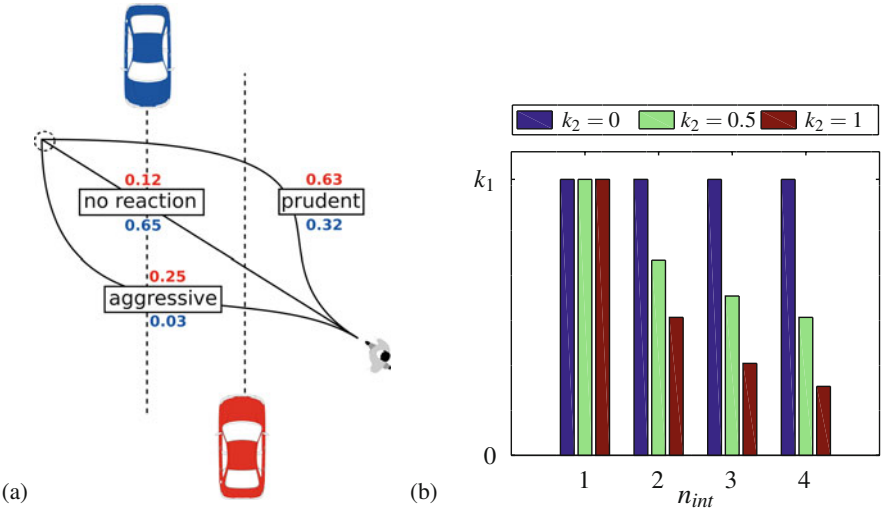

Fig. 2 **(a)** Conflict solving strategies in a pedestrian–car conflict with single probabilities, **(b)** Threshold function $T(n_{int})$ for different values of the shape parameter k_2

be investigated, in order to increase the influence of conflicting users in comparison to that of interacting users. To acquire plausible values for the weights an extensive calibration of the model using real world trajectories of multiple conflict situations is necessary.

3.2 Choice and Application of a Strategy

Starting from the aggregated global decision probabilities, it is possible to choose a strategy solely based on the probabilities using appropriate techniques, e.g., Monte Carlo simulation. Considering real world traffic situations, it can be assumed that especially vulnerable road users such as pedestrians show a higher tendency to choose the safest available strategy, the more unclear a situation seems. Furthermore the complexity of a situation increases with the number of road users involved. Thus, the likeliness to choose the prudent reaction increases with the number of road users present.

To incorporate this effect in the decision process, a threshold function $T(n_{int})$ is introduced as:

$$T(n_{int}) = \frac{k_1}{{n_{int}}^{k_2}}, \tag{2}$$

where n_{int} is the number of interacting users, k_1 is the initial threshold for $T(n_{int} = 1)$, and k_2 is a shape parameter describing the decrease of the function. The

exemplary curves of the threshold function in Fig. 2b show the influence of the shape parameter.

After the global probabilities $P_G(B)$ are calculated, the probability for the prudent reaction is compared to the respective threshold value T. If the probability for the prudent reaction is higher than the threshold value, the prudent reaction is chosen in any case. Otherwise, in the simulation the decision may be performed based on the global probabilities. Since the threshold function is decreasing for a higher number of interacting road users, the result of this approach is that with a higher number of interacting users a higher *perceived safeness* is required for choosing a non-prudent behavior.

Finally, the chosen strategy has to be applied to the social force model. The calculation of force-based long range conflict evasion strategies for single conflict situations was introduced in [7] and is adopted for multiple conflict situations. To calculate an overall reaction force, the respective forces for the chosen behavior are calculated for each interacting road user individually and subsequently combined additively with respect to the physical limitations of the regarded traffic mode, e.g., maximum acceleration. The consequence of this approach is that on one hand similar reactions amplify each other, on the other hand contradicting forces can partly compensate each other, resulting in deceleration. In real world scenarios, this effect can occur when a pedestrian has to wait for cars from both sides of the road to pass.

4 Application

In this section a real scene which was observed in a shared space street in Hamburg (D) is presented. The situation was chosen for the presence of multiple conflicts involving both vehicles and pedestrians. Five road users are involved in total, including three pedestrians (Ped_1, Ped_4, Ped_5) and two motorists (Mot_2, Mot_3). Two of them are examined, namely Ped_1 and Mot_3, since they have to deal with multiple conflict situations. Initially at time t_1 (Fig. 3a), Ped_1 decides to react

Fig. 3 Video footage. Multiple conflict situation for Ped_1 (**a**, **b**) and Mot_3 (**c**)

Table 1 Probabilities for conflict solving strategies

Time	User	Conflicting user	$p_{prudent}$	$p_{aggressive}$	$p_{noReaction}$
t_1	Ped_1	Mot_2	0.44	0.55	0.01
		Mot_3	0.27	0.57	0.16
		Aggregated	**0.36** (> 0.28)	0.56	0.08
t_2	Ped_1	Mot_2	0.21	0.70	0.09
		Mot_3	0.03	0.17	0.80
		Aggregated	0.12 (< 0.28)	0.43	**0.45**
t_3	Mot_3	Ped_1	0.64		0.36
		Ped_4	0.69		0.31
		Ped_5	0.47		0.53
		Aggregated	**0.60**		0.40

prudently, thus giving priority to the approaching motorists. Successively at time t_2 (Fig. 3b), Ped_1 retrieves her desired speed by reacting aggressively, thus taking priority over Mot_3. Finally at time t_3 (Fig. 3c), Mot_3 decides to brake to let all pedestrian cross the road. For the sake of clarity, the road users who have to take the decision are represented in blue, while the conflicting users in red.

The scene has been reproduced in MODIS with a focus on the decision taken at moments t_1 and t_2 for pedestrians, and moment t_3 for motorists. Consequently, we have simulated either pedestrians or motorist separately, and imposed the real spatio-temporal trajectory on the other traffic mode. Single probabilities are computed (with respect to all conflicting road users) and successively global probabilities according to Eq. (1). The values are then compared to threshold values to assign the corresponding behavior.

The results exposed in Table 1 demonstrate the validity of the developed approach. At every time, the road users take always the observed decision, whose combined probability is marked in bold, while the threshold values are in parentheses.

5 Conclusions

In this paper we have presented an approach for determining evasive strategies in multiple conflict situations using our previously developed decisional model. It was demonstrated that the aggregation of the probabilities for single conflict decisions yields realistic behaviors in multiple conflict situations. The proposed methodology further allows for the inclusion of uncertainties caused by complex situations.

The approach was developed and tested using the trajectories of selected real world situations involving pedestrians and cars, of which one was covered in detail in Sect. 4. In the future the parameters of the model, namely the aggregation weights and the parameters of the threshold function, have to be calibrated with regard to a

larger quantity of situations also involving the remaining traffic modes, especially cyclists. It is expected that the calibration will, similarly to single conflict situations in the past research, result in different parameter sets depending on the involved traffic modes.

Acknowledgements The scientific research published in this article is granted by the German Research Foundation (DFG) under the reference BE 2159/13-1 and FR 1670/13-1. The authors cordially thank the funding agency.

References

1. Anvari, B., Majumdar, A., Ochieng, W.: Mixed traffic modelling involving pedestrian dynamics for integrated street designs: a review. University of Science and Technology, Beijing (2016)
2. Gettman, D., Head, L.: Surrogate safety measures from traffic simulation models. Transp. Res. Rec. J. Transp. Res. Board (1840), 104–115 (2003)
3. Kaparias, I., Bell, M., Dong, W., Sastrawinata, A., Singh, A., Wang, X., Mount, B.: Analysis of pedestrian-vehicle traffic conflicts in street designs with elements of shared space. Transp. Res. Rec. J. Transp. Res. Board (2393), 21–30 (2013)
4. Karndacharuk, A., Wilson, D., Dunn, R.: Safety performance study of shared pedestrian and vehicle space in New Zealand. Transp. Res. Rec. J. Transp. Res. Board (2464), 1–10 (2014)
5. Pascucci, F., Rinke, N., Schiermeyer, C., Friedrich, B., Berkhahn, V.: Modeling of shared space with multi-modal traffic using a multi-layer social force approach. In: Transportation Research Procedia, vol. 10, pp. 316–326. Elsevier, London (2015). https://doi.org/10.1016/j.trpro.2015.09.081
6. Pascucci, F., Rinke, N., Schiermeyer, C., Berkhahn, V., Friedrich, B.: A discrete choice model for solving conflict situations between pedestrians and vehicles in shared space. Eprint arXiv: stat-AP/1709.09412 (2017)
7. Rinke, N., Schiermeyer, C., Pascucci, F., Berkhahn, V., Friedrich, B.: A multi-layer social force approach to model interactions in shared spaces using collision prediction. In: Transportation Research Procedia, vol. 25. Elsevier, London (2017). https://doi.org/10.1016/j.trpro.2017.05.144
8. Schiermeyer, C., Pascucci, F., Rinke, N., Berkhahn, V., Friedrich, B.: A genetic algorithm approach for the calibration of a social force based model for shared spaces. In: Proceedings of Pedestrian and Evacuation Dynamics, pp. 485–491 (2016)
9. Schroeder, B.J.: A Behavior-Based Methodology for Evaluating Pedestrian-Vehicle Interaction at Crosswalks. North Carolina State University, North Carolina (2008)
10. Stone, M., et al.: The opinion pool. Ann. Math. Stat. **32**(4), 1339–1342 (1961)
11. Sun, D., Ukkusuri, S., Benekohal, R.F., Waller, S.T.: Modeling of motorist-pedestrian interaction at uncontrolled mid-block crosswalks. Urbana **51**, 61801 (2002)

Vibration Driven Vehicles Flowing Through Bottlenecks

Germán A. Patterson, Federico Sangiuliano Jimka, Pablo G. König, Luis A. Pugnaloni, Angel Garcimartín, Iker Zuriguel, Pablo I. Fierens, and Daniel R. Parisi

Abstract In this work, we report the behaviour of an ensemble of self-propelled particles that flow through a bottleneck. In particular, we studied the emergent dynamics when mechanical vibration driven vehicles (VDVs) are placed in a hopper-like geometry on a horizontal plane. For this particular geometry, the particles present organized structures determining the size of the group of agents crowding at the exit door. Furthermore, we show that the latter has a strong influence on the distribution of time intervals between the exit of two consecutive vehicles. We found these results to be compatible with the *faster-is-slower* effect interpreting the term 'faster' as 'higher pressure'.

1 Introduction

The study of self-propelled particles has received considerable attention in the last decades, both in disciplines related to statistical physics and also in the development of specific applications. These investigations study the collective behaviour of

G. A. Patterson (✉) · P. I. Fierens · D. R. Parisi
Instituto Tecnológico de Buenos Aires, CONICET, Buenos Aires, Argentina
e-mail: gpatters@itba.edu.ar; pfierens@itba.edu.ar; dparisi@itba.edu.ar

F. S. Jimka · P. G. König
Instituto Tecnológico de Buenos Aires, Buenos Aires, Argentina
e-mail: fsangiul@itba.edu.ar; pkonig@itba.edu.ar

L. A. Pugnaloni
Departamento de Ingeniería Mecánica, Facultad Regional La Plata, Universidad Tecnológica Nacional, CONICET, La Plata, Argentina
e-mail: luis.pugnaloni@frlp.utn.edu.ar

A. Garcimartín · I. Zuriguel
Departamento de Física y Matemática Aplicada, Facultad de Ciencias, Universidad de Navarra, Pamplona, Spain
e-mail: angel@unav.es; iker@unav.es

S. H. Hamdar (ed.), *Traffic and Granular Flow '17*,
https://doi.org/10.1007/978-3-030-11440-4_50

microorganisms, flocks, herds, pedestrian dynamics, and transport systems, among other self-propelled agents [1, 3, 4, 10].

In this work, we study the collective dynamics of vibration driven vehicles (VDV) when flowing through a bottleneck, namely a narrow constriction in a hopper-like geometry. These agents have gained some attention recently because of their complex collective behaviour and similarities with active matter systems. Some of the advantages related to the VDVs are their simple mechanism, low cost, availability, and ease of use. They also allow to collect large amounts of data in comparison with other systems such as mice [8], sheep [5], and humans [6, 9].

We present results on the influence of both, the driving force and the spatial configuration on the dynamic of the egress of agents. By studying the distribution of time intervals between the exit of two consecutive VDVs, we show that the dynamic of the egress is very sensitive to the spatial arrangement of agents unlike the battery level charge. The former finding is in accordance with [11], where it was shown that a group of VDVs flowing through a narrow constriction experiences a transition from an unclogged to a clogged state when the number of the clogging agents is increased.

2 Experimental Setup

Experiments were carried out using 36 VDVs commercially available as Hexbug Nano. The dimensions of these are $43 \times 15 \times 18$ mm. The motion of the agents is based on an asymmetric bristle that rectifies vibrations originated by an internal eccentric motor. The VDVs are powered by a 1.5 V button cell battery. In order to trace positions and orientations, the agents were labelled on top with a white sticker and two colour dots.

The experimental setup consisted of a metal plate on which the hopper-like geometry was mounted as shown in Fig. 1. The relevant dimensions are specified in the caption of the figure. The hopper had an opening of width $L = 30$ mm where the VDVs evacuated. After the agents crossed the opening, they travelled through a feedback path which led them back to the opposite end of the hopper. The latter is indicated by yellow arrows in the figure. The experiments were recorded with a GoPro Hero3 camera and analysed with an ad hoc MATLAB routine that allowed us to determine the escape time of each agent and the spatial configuration of the remaining VDVs inside the hopper. The time resolution was given by the camera frame rate, that is, 29.97 fps.

Before starting the experiments, new batteries were installed in every agent. Under this experimental conditions, the charge of the batteries lasted $\approx$3600 s. After this time, some VDVs started to present signs of energy depletion as evidenced by a drastic decrease of their speed. Data were collected until 4 of 36 agents had their batteries drained. We performed two realizations under the same experimental conditions.

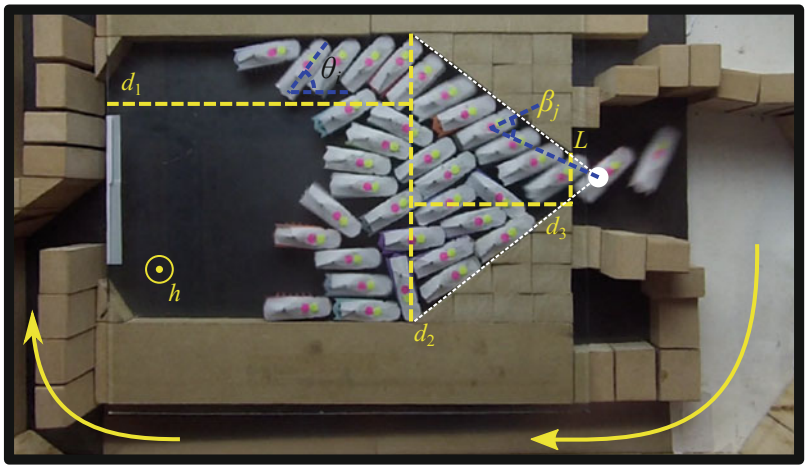

Fig. 1 Experimental setup. Relevant dimensions are: $d_1 = 200$ mm, $d_2 = 174$ mm, $d_3 = 100$ mm, and $L = 30$ mm. A sheet of glass was placed at $h = 18$ mm over the metal plate. The extensions of the inclined walls (white dashed lines) are used to determine the position of the putative apex. θ_i is the angle between the direction of agent i and the horizontal axis. β_j is the angle between the line joining the position of agent j and the putative apex and the long axis of the agent. Yellow arrows indicate the feedback path

3 Results

The system presented an intermittent flow of VDVs due to transient clogs occurring near the opening. We studied the time lapses Δt between the passage of two consecutive VDVs through the opening. Figure 2 shows the mean of time lapses $\langle \Delta t \rangle$ as a function of time. The average was computed with a sliding window of 200

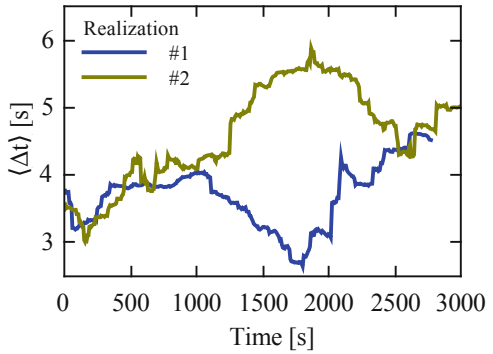

Fig. 2 $\langle \Delta t \rangle$ as a function of time for two different realizations of the same experiment. Data are the results of averages computed with a sliding window of 200 clogging events

clogging events. The results show different behaviours for each realization. While for realization #1 $\langle \Delta t \rangle$ experiences a minimum value around 1700 s, approximately at the same time, $\langle \Delta t \rangle$ of realization #2 reaches a maximum. As it will be explained later on, this heterogeneity of dynamics is related to the proximity of this system to a transition point.

In order to investigate the effect of different parameters on this behaviour, we first study the influence of the battery level on Δt. For this purpose, we built the complementary cumulative distribution function (CCDF) of times Δt. This function is the probability $P(\Delta t \geq \tau)$ for the duration of a certain clog Δt to be greater than or equal to a given duration τ. As the battery discharges continuously over time, we separated the data into two intervals of time $\approx$1800 s each. While the first interval corresponds to events with a high level of battery charge, the second corresponds to events with a low battery level.

Figure 3a shows results of CCDF for both high and low level battery charge for the experimental realization #1. We found that both sets of data present the same distribution function. Moreover, the tails of the distributions are compatible with a power-law (PL) function of characteristic exponent α, namely $P(\Delta t \geq \tau) \propto \tau^{-(\alpha+1)}$. This type of distributions was also found in other systems of clogging particles such as granular material, colloids, mice, sheep, and humans [5, 6, 8–10]. The PL hypothesis was put under test using the fitting procedure proposed by Clauset et al. [2]. The aforementioned technique not only provides α but also the accuracy and the range for which the fit is valid. The accuracy is measured by means of a p-value which is based on the distance between the distributions of the proposed model and the experimental data. According to [2], the permissive choice p-value < 0.05 is sufficient to reject the PL hypothesis. In all cases, we found a p-value > 0.2 which implies that the PL hypothesis is plausible for the evaluated data. Interestingly, we obtained very similar α values in both battery regimes showing that the clogging times are little affected by the battery charge level. Similar results were found for realization #2 despite the exponent obtained for low battery levels is slightly higher as it can be seen in Fig. 3b. Moreover, the exponents α are very

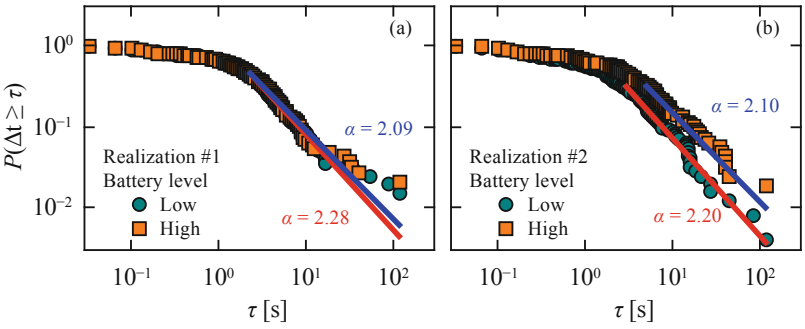

Fig. 3 CCDF of Δt for two battery levels. (**a**) and (**b**) show results for realizations #1 and #2, respectively. Solid blue (red) lines stand for PL fits regarding low (high) battery level data

similar for both realizations. This indicates that, from a statistical point of view, both realizations are equivalent and do not present an apparent dependence on the battery charge level.

We then study how the VDVs spatial arrangement could influence Δt. One of the usual tools to measure the relative alignment of agents is by means of the polarization parameter P defined as [12]

$$P = \sqrt{\langle \cos\theta_i \rangle^2 + \langle \sin\theta_i \rangle^2}\ , \tag{1}$$

where θ_i is the angle between the direction of agent i and the horizontal axis (see Fig. 1) and the operator $\langle \cdot \rangle$ is the average over all the agents. P measures the relative alignment of agents regardless of the spatial orientation of the total group of vehicles. In order to study the alignment of agents towards the escaping opening, we defined the A parameter as

$$A = \langle \cos(\beta_i) \rangle\ , \tag{2}$$

where β_i is the angle between the line joining the centre of agent i and the putative apex and the long axis of the agent (see Fig. 1). The position of the putative apex is determined as the intersecting point of the extension lines of the oblique walls of the hopper as shown in Fig. 1. In order to account simultaneously for both the relative alignment and the direction of agents towards the putative apex, we introduce the herding parameter H as

$$H = P \cdot A\ . \tag{3}$$

Note that high levels of H are obtained when both P and A are maximized. Figure 4a shows the probability distribution of H for the experimental realization #1. Under this approach, we have only considered the spatial configurations presented by the system every time an agent egressed from the hopper. Interestingly, we found that this distribution is bimodal showing that the system has two preferred configurations. This allows us to set a threshold to separate events of high H from events of low H. In particular, we choose a threshold value of 0.4 as indicated in Fig. 4a. Events of lower H are mainly associated to configurations where VDVs were divided into different groups. Figure 4c shows a typical configuration of low H where the VDVs are grouped in two different zones of the hopper. In this particular case, H is reduced because there is a large number of agents that are facing the lateral walls lowering the parameter A. On the other hand, Fig. 4d shows an example of a spatial configuration where the system presents high H. As most agents are crowding towards the opening, both P and A are expected to have a large value. The probability distribution of H for realization #2 has similar characteristics of the one for realization #1 as it can be seen in Fig. 4b.

Next, we filter Δt considering the spatial configuration of the remaining agents, that is, we separate Δt according to the H threshold. In this way, we obtained

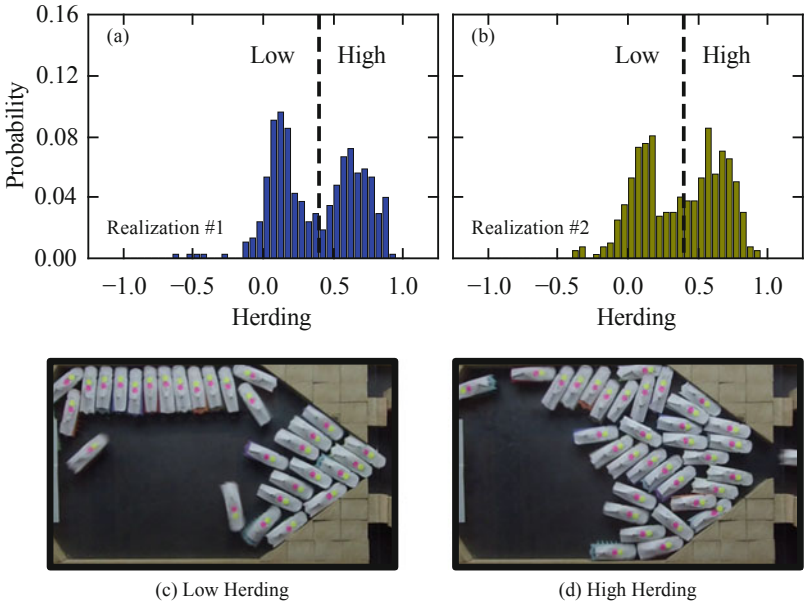

Fig. 4 (**a**) and (**b**) Probability distribution of the herding parameter for realizations #1 and #2. The dash line denotes the threshold used to filter events from high and low herding level. (**c**) and (**d**) show snapshots of the system configurations at low and high herding level, respectively

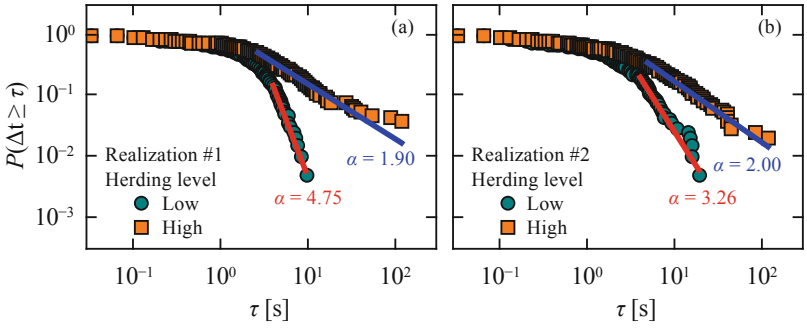

Fig. 5 CCDF of Δt for two herding levels. (**a**) and (**b**) show results for realizations #1 and #2, respectively. A high H level implies longer jams. Solid blue (red) lines stand for PL fits regarding low (high) H level

two sets of Δt associated with high and low H levels. We built the corresponding CCDF for both levels and found again results compatible with PL distributions. Figure 5a, b show these results for realizations #1 and #2, respectively. Surprisingly, unlike the influence of the battery level, there is a notorious difference between data from low and high H. The results show that spatial configurations with high H have larger probability to present longer Δt. The figure shows fitting values

for exponent α that quantify this difference. Data regarding low levels of herding present a higher exponent α than those with higher levels of H. Interestingly, for this experimental conditions, we observed that for high H the system is in a clogged state in accordance with the definition given by Zuriguel et al. [13]. In both realizations, #1 and #2, the mean clogging time diverges since $\alpha \leq 2$.

The effect of herding can be explained as follows. As a low H configuration implies VDVs crowding at different regions of the arena, there is a reduced number of agents around the opening. It is relatively easy for the VDV to destabilize a clog with few agents involved, thanks to their intrinsic vibration. In contrast, at high H configurations, most VDVs are crowding at the opening. In this situation they found very difficult to break possible entanglements since their vibration cannot overcome the pressure of the entire flock. This result can be related to the *faster-is-slower* effect observed in other active matter systems [6, 7, 10] where the flow rate is maximized for an intermediate value of the driving force. In this case, the term 'faster' should be interpreted in a more general way as 'higher pressure' produced by the number of VDVs crowding at the opening.

4 Conclusions

In this work, we studied the behaviour of self-propelled particles flowing through a narrow constriction. The system consisted of vibration driven vehicles and a hopper-like geometry that produce a net flow of particles out of the arena causing clogs around the opening. The time lapses Δt between the passage of two consecutive agents through the opening reveal a power-law tail which is compatible with other systems of clogging particles that interact with boundaries. In particular, we found that the PL distributions do not present a dependence on the battery charge level. We introduce a herding parameter H that not only accounts for the relative alignment of particles but also their direction towards the opening. Different PL exponents were found for different configurations of particles around the opening. The higher the H, the longer the duration of flow interruptions which implies a decrease of the flow rate. We found that in the case of high H, the system presents a distribution of clogs duration corresponding to a clogged state as defined in [13]. The results are compatible with the *faster-is-slower* effect, reinforcing the universality of this phenomenon for frictional particles flowing through bottlenecks.

Acknowledgements This work was funded by the following projects: ITBACyT-33 (Instituto Tecnológico de Buenos Aires, Argentina); PID2015-003 (Agencia Nacional de Promoción Científica y Tecnológica, Argentina); FIS2014-57325 (Ministerio de Economía y Competitividad, Spanish Government). GAP acknowledges Fundación Bunge & Born for financial support. The authors are also grateful to Martín Stortz and Carlos Stortz for their help with the experiments.

References

1. Buttinoni, I., Bialké, J., Kümmel, F., Löwen, H., Bechinger, C., Speck, T.: Dynamical clustering and phase separation in suspensions of self-propelled colloidal particles. Phys. Rev. Lett. **110**, 238301 (2013)
2. Clauset, A., Shalizi, C.R., Newman, M.E.J.: Power-law distributions in empirical data. SIAM Rev. **51**(4), 661–703 (2009)
3. Czirk, A., Vicsek, T.: Collective behavior of interacting self-propelled particles. Physica A **281**(1), 17–29 (2000)
4. Ferdinandy, B., Ozogny, K., Vicsek, T.: Collective motion of groups of self-propelled particles following interacting leaders. Physica A **479**(Suppl. C), 467–477 (2017)
5. Garcimartín, A., Pastor, J.M., Ferrer, L.M., Ramos, J.J., Martín-Gómez, C., Zuriguel, I.: Flow and clogging of a sheep herd passing through a bottleneck. Phys. Rev. E **91**, 022808 (2015)
6. Garcimartín, A., Parisi, D.R., Pastor, J.M., Martín-Gómez, C., Zuriguel, I.: Flow of pedestrians through narrow doors with different competitiveness. J. Stat. Mech. **2016**(4), 043402 (2016)
7. Helbing, D., Farkas, I., Vicsek, T.: Simulating dynamical features of escape panic. Nature **407**, 487–490 (2000)
8. Lin, P., Ma, J., Liu, T., Ran, T., Si, Y., Li, T.: An experimental study of the "faster-is-slower" effect using mice under panic. Physica A **452**(Suppl. C), 157–166 (2016)
9. Nicolas, A., Bouzat, S., Kuperman, M.N.: Statistical fluctuations in pedestrian evacuation times and the effect of social contagion. Phys. Rev. E **94**, 022313 (2016)
10. Pastor, J.M., Garcimartín, A., Gago, P.A., Peralta, J.P., Martín-Gómez, C., Ferrer, L.M., Maza, D., Parisi, D.R., Pugnaloni, L.A., Zuriguel, I.: Experimental proof of faster-is-slower in systems of frictional particles flowing through constrictions. Phys. Rev. E **92**, 062817 (2015)
11. Patterson, G.A., Fierens, P.I., Sangiuliano Jimka, F., König, P.G., Garcimartín, A., Zuriguel, I., Pugnaloni, L.A., Parisi, D.R.: Clogging transition of vibration-driven vehicles passing through constrictions. Phys. Rev. Lett. **119**, 248301 (2017)
12. Vicsek, T., Czirók, A., Ben-Jacob, E., Cohen, I., Shochet, O.: Novel type of phase transition in a system of self-driven particles. Phys. Rev. Lett. **75**, 1226–1229 (1995)
13. Zuriguel, I., Parisi, D.R., Hidalgo, R.C., Lozano, C., Janda, A., Gago, P.A., Peralta, J.P., Ferrer, L.M., Pugnaloni, L.A., Clément, E., et al.: Clogging transition of many-particle systems flowing through bottlenecks. Sci. Rep. **4**, 7324 (2014)

Conflict Model of Evacuees and Vehicles on Pedestrian Crossing in the Aftermath of Disaster

Kentaro Kumagai and Kenji Ono

Abstract Simulation which focuses on conflict between pedestrians and vehicles is important to assess evacuation safety of the pedestrians and drivers of the vehicles at a disaster. Although there were many researches in regular traffic conditions, conflict in the aftermath of disaster has not been discussed enough. Griffiths et al. developed a microscopic simulation model of pedestrians and vehicles on an unsignalized zebra crossing. In this contribution, we attempted to modify the conflict model of Griffiths et al. and applied it to a zebra crossing and an event of a tsunami evacuation drill. In the model proposed, we made assumptions that pedestrians are more reckless to cross a street in an emergency. As a result, it was found that the conflict model which takes into account the hypothesis about psychological state of pedestrians reproduced well the results of a field survey.

1 Introduction

Conflict between pedestrians and vehicles is one of the major issues which relate to a traffic safety in an unsignalized pedestrian crossing. Griffiths et al. [1] developed a microscopic simulation model of pedestrians and vehicles in the crossing with one lane of vehicle flow in each direction and with pedestrians able to cross from either side of the road (see Fig. 1).

Simulation which focuses on the conflict is important to assess evacuation safety at a disaster. Although there were researches of conflict on pedestrian crossing in a

K. Kumagai (✉)
Graduate School of Management, Kyoto University, Sakyo, Kyoto, Japan
e-mail: kumagai.kentaro.3e@kyoto-u.jp

Cooperating Faculty of DPRI, Kyoto University, Uji, Japan

K. Ono
Port and Airport Research Institute, Yokosuka, Kanagawa, Japan
e-mail: ono.kenji.5z@kyoto-u.jp

S. H. Hamdar (ed.), *Traffic and Granular Flow '17*,
https://doi.org/10.1007/978-3-030-11440-4_51

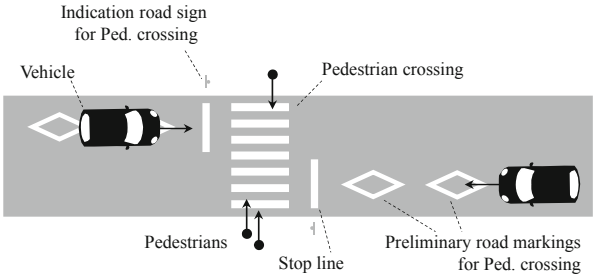

Fig. 1 Unsignalized pedestrian crossing, with one lane of vehicle flow in each direction and with pedestrians able to cross from either side of the road

regular traffic conditions with pedestrians of a low arrival rate [6], a conflict in the aftermath of disaster with high arrival rate has not been discussed enough.

In this contribution, we attempted to modify the conflict model of Griffiths et al., to validate the reproducibility of a field survey about the new model, and to apply the new model to an unsignalized pedestrian crossing under a hypothetical condition of tsunami evacuation in the aftermath of earthquake.

2 Numerical Simulation Model

2.1 New Model

A brief outline of the basic sequence of the program by Griffiths et al. [1] is as follows: The objective area is an unsignalized pedestrian crossing, with one lane of vehicle flow in each direction and with pedestrians able to cross from either side of the road (Fig. 1). The distribution of vehicle's inter-arrival times depends on the Poisson distribution. The speed of vehicles and pedestrians is distributed with a specified mean and a standard deviation. If a pedestrian arrives at a kerbside and there is a vehicle, the pedestrian must wait at the kerbside. If there is not enough interval before the next vehicle arrival in the right-to-left stream, the pedestrian will wait until the vehicle stops or passes through. If there is an enough interval before the next vehicle in the stream, the pedestrian will cross. The pedestrians will be prepared to stop again in the center of the road if there is a vehicle in the other stream. An approaching vehicle will always stop if it is able to do so.

According to empirical facts, it seems that this model involves two issues to be corrected. First, Fig. 2 is a snapshot of pedestrians around a kerbside, and they saw the left-hand side for their safety confirmation. One of them raised her hand in order to appeal to the driver of an approaching car in the left-hand side to request to slow down or stop. Once pedestrians started to cross, many of them kept crossing instead of stopping in the center of the road, if they find a vehicle approaching in the left-

Fig. 2 Pedestrian who saw the left-hand side for their safety confirmation and raised her hand in order to appeal to the driver of an approaching car

to-right stream. These facts suggest that pedestrians confirm their safety not only for an approaching car in the right-to-left stream but also for that in the left-to-right stream before starting to cross, instead of stopping in the center of the road to let a car in the left-to-right stream pass through. Second, in case pedestrians are waiting at the kerbside, approaching vehicles not always stop even if it is able to do so. Japan Automobile Federation [2] reported that only 7% of drivers stop when they found pedestrians waiting at the kerbside, according to their field survey in Japan. This fact suggests that proportion of drivers who find the pedestrian and are prepared to stop will vary depending on the location.

Based on these empirical knowledge, the model of Griffiths et al. should be modified. A new model was developed, including issues of modification as follows:

- Pedestrians confirm their safety not only for an approaching car in the right-to-left stream but also for that in the left-to-right stream before starting to cross, instead of stopping in the center of the road to let an approaching car in the left-to-right stream pass through, in conditions of left-hand traffic.
- Proportion of drivers who find the pedestrians waiting at the kerbside and are prepared to stop at crossing will vary depending on the location.

2.2 Simulation Cases

Basically, values proposed by Griffiths et al. [1] were adopted as parameters for the simulation. But some measureable parameters were derived from the results of a field survey which will be introduced in the following section. The parameters

categorized into this type were the length of the pedestrian crossing l_c (7.00 m), the mean time interval for arrival of pedestrians t_{ip} (4.4 s), the average speed of pedestrians v_p (1.11 m/s), and the mean time interval for arrival of vehicles t_{iv} (22.0 s). And some parameters and conditions were set hypothetically, since there was no explicit description by Griffiths et al. The parameters and conditions categorized into this type were the distribution of pedestrian's arrival time (the Poisson distribution), the maximum speed of vehicle v_v (8.33 m/s), a theory applied to successive vehicles (the car following theory), the values for the equation of response time which was proposed by Kometani and Sasaki [3] (1.0 s as the time for reaction of driver and 1.31 as the constant value in the equation), a length of a time step for simulations performed by an implicit method (0.1 s), and a percentage of pedestrians who will stop at kerbside for the purpose of waiting for the following colleagues (67% of pedestrians).

Let us now consider about how to model psychological state of evacuees. As they have to go to a safer place as quick as possible, it can be reasonable to assume their risk-taking and selfish attitude than usual. Based on this assumption, we introduced a hypothesis below to express risk-taking and selfish attitude of pedestrians:

Hypothesis Pedestrians are more reckless to cross a street in an emergency.

Table 1 shows parameters for two simulation cases. Both were for simulations which intended to reproduce the result of a tracking survey and to evaluate an accuracy of the simulation model. Case 2 was for a simulation with the hypothesis above. The other parameters and conditions were common between the two cases.

If a pedestrian arrives at a kerbside and there is an enough gap before the next vehicle, the pedestrian will cross. The minimum value of the gap, l_m, was determined by l_c, v_p, v_v, decelerate rate of vehicle a_v ($-1.961\,\mathrm{m/s^2}$), and width of the crossing w (4.0 m). For Case 1, pedestrians carefully consider about a risk that an approaching vehicle keeps its top-speed even if the driver finds the pedestrians at the kerbside:

$$l_m = \begin{cases} v_v \times \frac{l_c}{2v_p} + \frac{w}{2} & \text{for right-to-left stream} \\ v_v \times \frac{l_c}{v_p} + \frac{w}{2} & \text{for left-to-right stream} \end{cases} \quad (1)$$

Table 1 Simulation cases

Parameters		Case 1 (Regular mental state)	Case 2 (Risk-taking)
The minimum gap l_m for pedestrians to cross	For R-to-L stream	28 m	18 m
	for L-to-R stream	55 m	44 m

For Case 2, pedestrians will be risk-taking, and they expect the driver to avoid a collision by full-breaking if the driver finds the pedestrians crossing the street:

$$l_{\mathrm{m}} = \begin{cases} -\frac{{v_{\mathrm{v}}}^2}{2a_{\mathrm{v}}} & \text{for right-to-left stream} \\ v_{\mathrm{v}} \times \frac{l_{\mathrm{c}}}{2v_{\mathrm{p}}} - \frac{{v_{\mathrm{v}}}^2}{2a_{\mathrm{v}}} & \text{for left-to-right stream} \end{cases} \tag{2}$$

Proportion of drivers p who are prepared to stop when they find pedestrians waiting at the kerbside was set to 7% in both cases.

3 Results

3.1 Pedestrian Tracking

In 9 March 2014, a tsunami evacuation drill was conducted in Shimoda city. The residents of the Yamato community started walking to an evacuation site. In the middle of their route, there was a pedestrian crossing, which was 7 m in length, and has no signal and no central island. A video camera and two laser range-sensors were installed to track evacuees and vehicles. The equipment for this tracking was the same to the past research [4]. Figure 3 shows a bird-eye view of the measurement area. The evacuees walked through from the lower side of the figure, southeast, to the upper side, northwest. It was approximately 220 s, from the first evacuee arrived at the area until the last one left. Fifty pedestrians walked through from SE to NW, including forty-eight persons who joined in the drill and two who had no relation to the event. There are two more persons who walked in the inverse direction, from NW to SE, and two bicycles. But they were omitted because they had no effect on the main traffic. The number of cars and motorcycles in the main streams was 20.

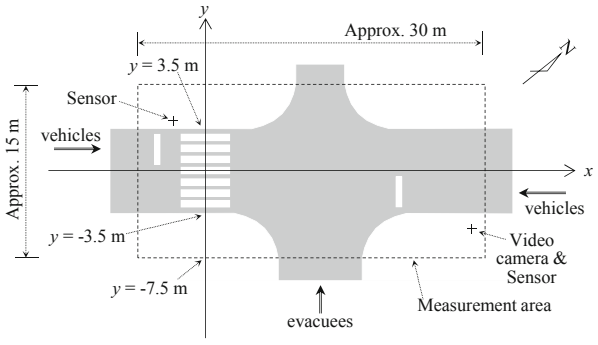

Fig. 3 Sketch of the measurement area: Pedestrian crossing of 7 m in length, no signal and no central island

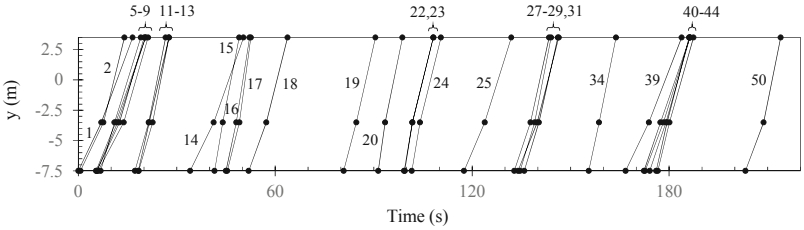

Fig. 4 Time-space diagram of pedestrians. Pedestrians walked from $y = -7.5$ m, passed through the kerbside, $y = -3.5$ m, and arrived at the opposite side of the street, $y = 3.5$ m. The Arabic number in the figure indicates ID number of the pedestrians, shown in column 1 of Table 2

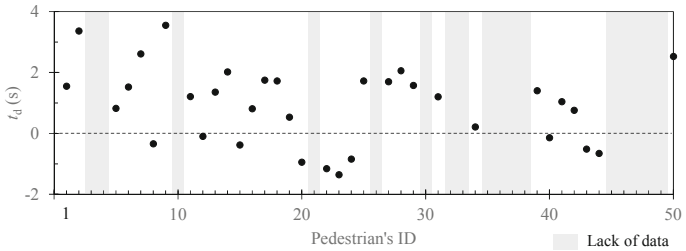

Fig. 5 Delay-time. Positive values in the vertical axis intended delay. Data in gray areas on this figure are not available because of lack of tracking data

Figure 4 is a time-space diagram of the 33 pedestrians, with time on the abscissa and y on the ordinate. Because of the limitation of measurement, it was impossible to draw points and lines for the other 17 pedestrians. The zero point of time was set to the time when the first pedestrian arrived at $y = -7.5$ m. The average speed in the sidewalk, from $y = -7.5$ m to $y = -3.5$ m, was 0.96 m/s, and that in the carriageway, from $y = -3.5$ m to $y = 3.5$ m, was 1.11 m/s. The reason why the former value was smaller than the latter one was that many pedestrians reduced their speed or waited at the kerbside in order to yield their way to vehicles.

On a hypothesis that a natural walking speed is equal to the speed observed in the carriageway (1.11 m/s), it is easy to calculate time t_n for passing through from $y = -7.5$ to $y = -3.5$ m in the natural speed. The difference between t_n and the observed value t_o was defined as an estimate delay-time t_d. Figure 5 draws t_d. The positive values in the vertical axis intended delay. Although some points were negative, the figure shows that the overall trend of t_d was positive. An average value of t_d was 0.56 s. Supposing that negative points were excluded from the data set, the average value of t_d of the remaining points was 1.61 s. Figure 6a is the frequency distribution of t_d.

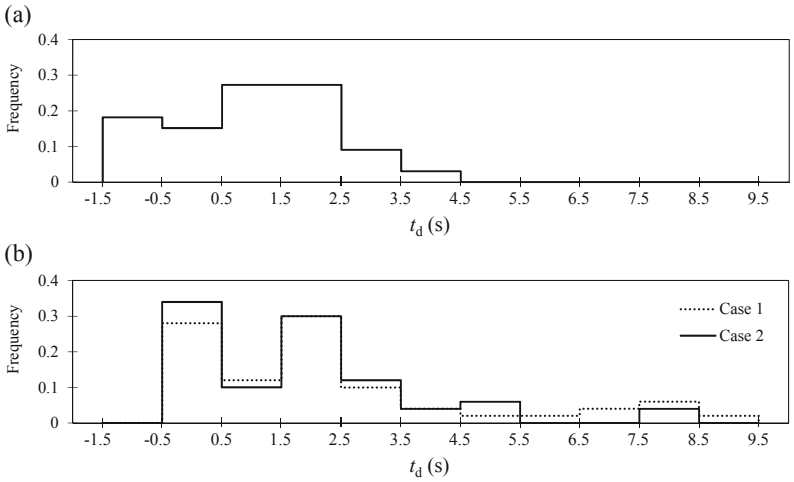

Fig. 6 Frequency distribution of delay-time t_d. (**a**) Observations of tracking survey (**b**) Results of numerical simulations

3.2 Simulation Results

Figure 6b is the frequency distribution of t_d for simulation results. According to the figure, in Case 1, t_d were within the range of values from 0 to 9 s. In comparison with Fig. 6a, the dotted line in Fig. 6b showed considerable discrepancies when t_d is equal to five or more. An average value of t_d was 2.30 s.

For Case 2, most values were distributed within the range of values from 0 to 5 s. Although there was a small peak at t_d equal to 8 s, it seems that the reproducibility of the distribution in Case 2 was improved compared to Case 1. The average of t_d was 1.85 s, and this shows a good agreement with the average of positive values of t_d in the tracking survey (1.61 s). As a result, it was found that the conflict model which takes into account the hypothesis about psychological state of pedestrians reproduced well the results of a field survey.

4 Discussion

An assessment of conflict is important not only for pedestrians but also for drivers of vehicles, because many people are expected to evacuate using cars. For example, 55% of people used their cars to evacuate in the event of the 2011 Tohoku tsunami [5]. It seems to be important to discuss about an impact of the mean time interval of arrival of vehicles, t_{iv}. In Case 2 of the previous chapter, the value of t_{iv} was set as 22 s. Because it was very low in frequency of arrival, it will be useful to simulate trial cases with t_{iv}, such as t_{iv} = 2, 3, …, 21 s. The results of simulations showed

that an average value of t_d for pedestrians was 30 s and more in cases that t_{iv} was equal to 4 s or less. In contrast, an average value of t_d for vehicles was almost 0 or at most 3 s in all cases. According to the results obtained, it was found that when the arrival rate of the vehicle increases, a large delay occurs for pedestrians, whereas almost no delay occurs for vehicles.

5 Conclusions

The purpose of this study is to modify the conflict model of Griffiths et al. and apply it to a zebra crossing under a hypothetical condition of tsunami evacuation in the aftermath of earthquake. In the model proposed, we made assumptions that pedestrians are more reckless to cross a street in an emergency.

- The conflict model which takes into account the hypothesis about psychological state of pedestrians reproduced well the results of a field survey.
- According to the simulation, when the arrival rate of the vehicle increases, a large delay occurs for pedestrians, whereas almost no delay occurs for vehicles.

Acknowledgements The authors would like to acknowledge Yamato community and City Office of Shimoda City, and Shimoda Branch Office of Shimizu Port Office, MLIT for their assistance in the tracking survey. The first author is a former senior researcher of National Institute for Land and Infrastructure Management, and the tracking survey was conducted as an activity of NILIM. The authors would like to acknowledge NILIM for utilizing the survey data. The authors also would like to express appreciation to Mrs. Yoko Nishikawa of DPRI for her assistance, and to Prof. Tomihiro Watanabe and Miss Misato Hiraoka, GSM, Kyoto University for discussions.

Appendix

Tracking data is shown in tables below. In Table 2, t_1, t_2, and t_3 are the time when a pedestrian passed through $y = -7.5$, -3.5, and 3.5 m, respectively. Sex and age were determined by subjective judgment based on video images. The character E in the sixth column indicates 65 years old and more, Y for 13 to 65, and Y^- for 12 or less. In Table 3, time is the arrival time when a vehicle reached at $x = 16$, $x = -4$, or $y = -7.5$ m. The character Y or N in the third column indicates that the vehicle stopped or not, respectively, when the driver of vehicle found evacuees at the kerbside.

Table 2 Pedestrians

ID	t_1 (s)	t_2 (s)	t_3 (s)	Sex	Age	ID	t_1 (s)	t_2 (s)	t_3 (s)	Sex	Age
1	0.0	7.0	16.5	F	Y	26	–	–	–	F	Y
2	0.7	7.7	14.0	M	E	27	132.8	137.8	143.4	F	Y
3	–	–	–	M	Y	28	134.0	139.8	146.4	M	Y
4	–	–	–	F	E	29	134.6	139.0	144.0	F	E
5	5.4	11.4	20.5	F	E	30	–	–	–	F	E
6	5.6	12.0	20.5	M	Y-	31	135.8	140.3	146.1	F	Y
7	5.6	12.5	20.0	F	E	32	–	–	–	F	E
8	6.8	11.0	19.0	M	E	33	–	–	–	F	E
9	6.0	13.8	21.3	M	E	34	155.5	158.7	163.8	M	Y
10	–	–	–	F	Y-	35	–	–	–	M	Y-
11	17.3	21.4	26.6	F	Y	36	–	–	–	F	Y
12	18.3	21.6	27.6	M	Y-	37	–	–	–	M	Y
13	18.4	22.6	27.6	M	Y-	38	–	–	–	F	Y-
14	34.1	41.3	50.3	M	Y	39	166.7	173.8	183.8	M	Y-
15	41.5	44.0	49.0	M	Y	40	172.3	177.3	186.3	F	E
16	45.0	48.1	52.2	F	Y	41	172.7	178.3	186.3	F	E
17	45.4	49.1	52.6	F	Y	42	174.1	179.0	186.3	M	E
18	51.9	57.3	63.7	M	Y	43	176.0	179.4	186.1	M	Y
19	80.8	84.7	90.5	F	Y	44	176.6	180.1	187.4	M	Y
20	91.4	93.5	98.7	F	Y	45	–	–	–	M	E
21	–	–	–	F	Y	46	–	–	–	F	Y
22	99.3	101.8	108.2	F	Y	47	–	–	–	M	E
23	99.5	101.8	108.2	M	Y	48	–	–	–	M	E
24	101.6	104.3	110.5	M	Y	49	–	–	–	F	Y
25	117.5	123.8	131.9	M	Y	50	203.3	208.8	214.0	M	Y

Table 3 Vehicles

ID	Time (s)	Stop	From/to
V-1	1.5	–	SE/NE
V-2	2.3	–	NE/SE
V-3	15.7	Y	NE/SW
V-4	34.2	–	SW/NE
V-5	35.0	–	NE/SW
V-6	40.8	–	SW/NE
V-7	46.4	Y	NE/SW
V-8*	57.0	N	SW/NE
V-9	69.5	–	NE/SW
V-10	76.0	–	SE/NE
V-11	76.3	–	SW/NE
V-12	119.6	–	SW/NE
V-13	128.5	N	NE/SW
V-14	133.3	N	NE/SW
V-15	143.0	Y	SW/NE
V-16	143.7	–	NE/SW
V-17	146.6	–	NE/SW
V-18	162.8	N	NE/SW
V-19	163.5	–	SW/NE
V-20	175.6	Y	NE/SW
V-21	185.5	–	SE/NE
V-22	195.3	–	NE/SW
V-23	198.3	N	NE/SW

*Motorbike, No asterisk: Automobiles

References

1. Griffiths, J.D., Hunt, J.G., Marlow, M.: Delays at pedestrian crossings. pt.2: the development and validation of a simulation model of a zebra crossing. Traffic Eng. Control **25**(10), 505–509 (1984)
2. Japan Automobile Federation: A survey on pedestrian priority in pedestrian crossing without traffic lights. http://www.jaf.or.jp/profile/news/file/2016_35.htm (2016). Accessed 1 Sept 2017
3. Kometani, E., Sasaki, T.: Car following theory and stability limit of traffic volume. J. Oper. Res. Soc. Jpn. **3**(4), 176–190 (1961)
4. Kumagai, K., Ehiro, I., Ono, K.: Numerical simulation model of group walking for tsunami evacuees. In: Proceedings of Pedestrian and Evacuation Dynamics 2016, pp. 348–358. USTC Press, Hefei (2016)
5. Ministry of Land, Infrastructure, Transport and Tourism: Arrangement of evacuation routes and facilities and evacuation guidance for tsunami, 3rd edn., pp. 32. https://www.mlit.go.jp/common/000233464.pdf (2013). Accessed 1 Sept 2017
6. Zhao, H., Yang, S., Chen, X.: Cellular automata model for urban road traffic flow considering pedestrian crossing street. Phys. A **462**, 1301–1313 (2016)

Social Force Model Describing Pedestrian and Cyclist Behaviour in Shared Spaces

Yufei Yuan, Bernat Goñi-Ros, Tim P. van Oijen, Winnie Daamen, and Serge P. Hoogendoorn

Abstract A simulation model capable of reproducing mixed-traffic operations in shared spaces is crucial for the design and management of such areas. Existing models focus on shared spaces where pedestrians and cars interact with each other. This contribution presents a social force model describing walking and cycling behaviour in shared spaces. The model assigns different physical shapes to pedestrian and cyclist agents, accounts for anisotropic interaction behaviour, and imposes turning-angle constraints. The face-validity of the model is tested by comparing simulation output data to empirical macroscopic traffic data derived from video recordings of a shared space in Amsterdam (the Netherlands).

1 Introduction

Shared space is an innovative urban design concept that is based on allowing pedestrians and vehicles of various sorts to simultaneously use a single-surface area with only basic priority rules. Space sharing aims to give equal priority to all road users and to improve traffic safety. The ability to realistically simulate traffic operations in shared spaces is crucial for the design and management of such areas. For this purpose, it is necessary to use a microscopic traffic model that can capture the complex interactions between different types of road users (e.g., pedestrians, cyclists, cars) arising in shared spaces. Most models reproducing the microscopic behaviour of single traffic modes (e.g., [1, 2, 7]) cannot capture those interactions, and thus they cannot be directly applied to shared spaces.

Models that aim to reproduce traffic operations in shared spaces usually use the force-based approach, which was first proposed by Helbing and Molnár [5] to model pedestrian dynamics. In this respect, Schönauer et al. [8] proposed a social force model including a tactical force to solve potential collisions between pedestrians and

Y. Yuan (✉) · B. Goñi-Ros · T. P. van Oijen · W. Daamen · S. P. Hoogendoorn
Delft University of Technology, Delft, The Netherlands
e-mail: y.yuan@tudelft.nl; b.goniros@tudelft.nl; t.p.vanoijen@tudelft.nl; w.daamen@tudelft.nl; s.p.hoogendoorn@tudelft.nl

S. H. Hamdar (ed.), *Traffic and Granular Flow '17*,
https://doi.org/10.1007/978-3-030-11440-4_52

cars using game theory. Anvari et al. [3] developed a rule-based social force model that takes into account car-following behaviour, steering behaviour, and long-range collision avoidance behaviour. Pascucci et al. [6] proposed a social force approach that pays special attention to modelling the long-range conflict avoidance behaviour of road users in different situations by means of a multi-layer modelling approach. The existing modelling approaches consider only pedestrians and cars; thus, they cannot be used to simulate traffic operations in situations where bicycles are present.

This contribution presents a social force model that reproduces walking and cycling behaviour in shared spaces. The model is based on the modelling framework proposed by Anvari et al. [3]. It assigns different shapes to the influencing areas of pedestrian and cyclist agents, accounts for anisotropic interaction behaviour, and imposes turning-angle constraints. A face-validation method is proposed to check the accuracy of the model and to identify a reasonable set of model parameter values. This method compares empirical traffic data (total outflows and average densities) collected at a shared space in Amsterdam (the Netherlands) with simulation output data obtained with different sets of parameter values. The simulation results have revealed some behavioural insights of the model: cyclists generally react to traffic conditions slower than pedestrians; and cyclists react to the presence of pedestrians within their radius of interaction more strongly than the other way around.

2 Social Force Model

The model considers two types of agents: pedestrians and cyclists. It is assumed that all agents move in a straight line towards their desired destinations at their desired speeds in the absence of other agents. This goal defines the so-called *driving force* of the agents. Furthermore, the model assumes that every agent that is within a certain distance of the target agent exerts a so-called *interaction force* (or repulsive force) on the latter. This repulsive force is greater if the neighbouring agent is closer to and in front of the target agent. Like the original social force model [5], our model assumes that the acceleration (magnitude and direction) of an agent at a certain time instant is determined by the sum of the driving force and all the repulsive forces exerted by neighbouring agents. At this stage, the model assumes that agents do not encounter any static obstacles while moving through shared spaces.

The mathematical formulation of the model is as follows: Let us denote the target agent by u (where u becomes α when considering a pedestrian and γ when considering a cyclist), and the neighbouring agents by s (where s becomes β when the neighbouring agent is a pedestrian and δ when it is a cyclist). The neighbouring agents of the target agent at a certain time step t are all agents located within a circle of radius R^u_{max} around the centre of agent u. The set of neighbouring pedestrians is denoted by $B(t)$, and the set of neighbouring cyclists is denoted by $D(t)$. Note that these sets are time-varying. Then, the acceleration of the target agent at time step t

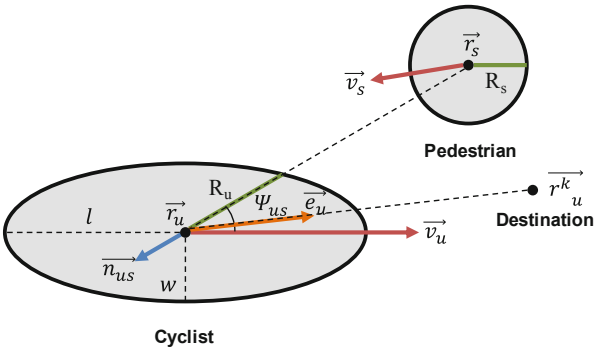

Fig. 1 Graphical representation of the variables and parameters needed to calculate the interaction force between a cyclist (target agent) and a pedestrian (neighbouring agent)

($\overrightarrow{f}_u(t)$) is defined as:

$$\overrightarrow{f}_u(t) = \overrightarrow{f}^0_u(t) + \sum_{\beta \in B(t)} \overrightarrow{f}_{u\beta}(t) + \sum_{\delta \in D(t)} \overrightarrow{f}_{u\delta}(t) \tag{1}$$

where $\overrightarrow{f}^0_u(t)$, $\overrightarrow{f}_{u\beta}(t)$, and $\overrightarrow{f}_{u\delta}(t)$ are the driving force and the interaction forces with the neighbouring pedestrians and cyclists at time instant t, respectively.

The driving force is defined as in [5]:

$$\overrightarrow{f}^0_u(t) = \frac{v^0_u \cdot \overrightarrow{e}_u(t) - \overrightarrow{v}_u(t)}{\tau_u} \tag{2}$$

where $\overrightarrow{v}_u(t)$ is the current velocity of the target agent; $\overrightarrow{e}_u(t)$ is the current direction to the destination; and v^0_u and τ_u are parameters that can be interpreted as the free speed of agent u and its relaxation time, respectively. The direction to the destination ($\overrightarrow{e}_u$ in Eq. (2)) is a normalized vector defined as follows (see also Fig. 1):

$$\overrightarrow{e}_u(t) = \frac{\overrightarrow{r}^k_u - \overrightarrow{r}_u(t)}{|\overrightarrow{r}^k_u - \overrightarrow{r}_u(t)|} \tag{3}$$

where $\overrightarrow{r}_u(t)$ is the current position of the centre of the target agent; and $\overrightarrow{r}^k_u$ is the position of the destination of agent u (which is predefined).

The interaction forces are defined based on the anisotropic exponential formulation proposed by Anvari et al. [3], which accounts for the distance and relative position between agents, and depends on the type of agents:

$$\overrightarrow{f}_{us}(t) = A_{us} \cdot \exp\left(\frac{R_u + R_s - d_{us}(t)}{B_{us}}\right) \cdot \overrightarrow{n}_{us}(t) \cdot F_{us}(t) \tag{4}$$

In Eq. (4), A_{us} and B_{us} denote the interaction strength and interaction range parameters, respectively. Note that these parameters are mode-specific: there are four A_{us} parameters ($A_{\alpha\beta}$, $A_{\alpha\delta}$, $A_{\gamma\beta}$, and $A_{\gamma\delta}$) and four B_{us} parameters ($B_{\alpha\beta}$, $B_{\alpha\delta}$, $B_{\gamma\beta}$, and $B_{\gamma\delta}$). Furthermore, $d_{us}(t)$ is the current distance between the centres of the target agent and the neighbouring agent ($d_{us}(t) = |\overrightarrow{r}_u(t) - \overrightarrow{r}_s(t)|$), and $\overrightarrow{n}_{us}(t)$ is the direction from the centre of agent s to the centre of agent u, which is a normalized vector defined as follows (see also Fig. 1):

$$\overrightarrow{n}_{us}(t) = \frac{\overrightarrow{r}_u(t) - \overrightarrow{r}_s(t)}{|\overrightarrow{r}_u(t) - \overrightarrow{r}_s(t)|} \tag{5}$$

In Eq. (4), $F_{us}(t)$ is the interaction form factor, which accounts for the anisotropic nature of interaction behaviour. $F_{us}(t)$ depends on the angle between two vectors: velocity of the target agent ($\overrightarrow{v}_u(t)$) and direction from the centre of agent u to the centre of agent s ($\overrightarrow{r}_s(t) - \overrightarrow{r}_u(t)$). This angle is denoted by $\Psi_{us}(t)$ (see Fig. 1):

$$F_{us}(t) = \lambda_u + (1 - \lambda_u) \cdot \frac{1 + \cos\Psi_{us}(t)}{2} \tag{6}$$

where parameter λ_u is the form factor constant. From Eq. (6), it follows that the highest value of F_{us} is achieved when $\Psi_{us}(t)$ is zero (i.e., the neighbouring agent is in front of the target agent), and the lowest value of F_{us} is achieved when $\Psi_{us}(t)$ is π rad (i.e., agent s is behind agent u).

Finally, R_u and R_s are the radii of the target agent and the neighbouring agent, respectively. Note that pedestrians are assumed to have a circular shape; thus, their radius (R_α and R_β) is constant. However, cyclists are assumed to have an elliptical shape. Therefore, for the purpose of calculating the interaction forces, the radius of a cyclist agent (R_γ or R_δ) depends on the angle between its direction of movement and the direction to the other agent ($\Psi_{\gamma s}(t)$ or $\Psi_{\delta u}(t)$), which is time-dependent. In general, the radius of an agent is defined as follows (see also Fig. 1):

$$R_u(t) = \frac{w_u}{\sqrt{1 - \frac{l_u^2 - w_u^2}{l_u^2} \cdot \cos^2\Psi_{us}(t)}} \tag{7}$$

where w_u and l_u are the width and length of the agent, respectively. For pedestrians, $w_\alpha = l_\alpha$, so the radius is constant and equal to w_α (see Eq. (7)). R_s can be calculated with the same equation after substituting $\Psi_{us}(t)$ by $\Psi_{su}(t)$, w_u by w_s, and l_u by l_s.

The velocities and positions of the target agent u are updated over time in accordance with the following two equations:

$$\overrightarrow{v}_u(t + \Delta t) = \overrightarrow{v}_u(t) + \overrightarrow{a}_u(t) \cdot \Delta t \tag{8}$$

$$\overrightarrow{r}_u(t + \Delta t) = \overrightarrow{r}_u(t) + \overrightarrow{v}_u(t + \Delta t) \cdot \Delta t \tag{9}$$

where Δt is the simulation time step length; and $\overrightarrow{a}_u(t)$ denotes the acceleration at time step t. The acceleration $\overrightarrow{a}_u(t)$ is calculated using Eq. (1), although its magnitude is constrained so that it is not greater than a maximum acceleration defined as a parameter ($a_u^{\max}$):

$$\overrightarrow{a}_u(t) = \min(a_u^{\max}, |\overrightarrow{f}_u(t)|) \cdot \frac{\overrightarrow{f}_u(t)}{|\overrightarrow{f}_u(t)|} \tag{10}$$

Furthermore, a constraint is imposed on the direction of vector $\overrightarrow{v}_u(t + \Delta t)$. If the angle between vectors $\overrightarrow{v}_u(t)$ and $\overrightarrow{v}_u(t + \Delta t)$ is higher than the maximum turning angle (a parameter denoted by θ_u) multiplied by Δt, then the direction (not the magnitude) of vector $\overrightarrow{v}_u(t + \Delta t)$ is changed so that this angle equals $\theta_u \cdot \Delta t$.

3 Model Face-Validation Methodology

The model presented in Sect. 2 was implemented in MassMotion (a crowd simulation software package). The face-validity of the model was tested by comparing simulation output data to empirical traffic data derived from video recordings of a shared space in Amsterdam (The Netherlands) in February 2016. The shared space is rectangular (36 × 20 m) and contains no static obstacles; it is mainly used by pedestrians and cyclists, who enter the rectangular area through any of its four sides and exit it through any of its four sides as well. Note that a few mopeds were observed in this area and they were treated as bicycles in this analysis. The main goals of the face-validation were to acquire a reasonable set of parameter values (as a first step towards extensive model calibration) and to determine whether the model can realistically reproduce traffic dynamics on a shared space.

Figure 2 shows a scheme of the face-validation methodology. Six scenarios were simulated using different parameter values. Every simulation scenario had a

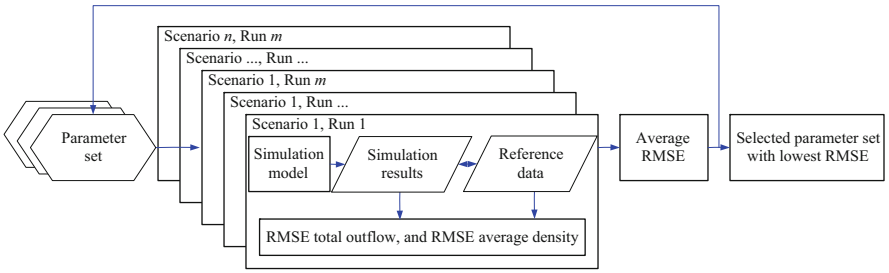

Fig. 2 Face-validation methodology, based on the concept presented in [4]. Note that, in this study, $n = 6$, and $m = 5$

different mode-specific dynamic OD matrix (which was derived from the video recordings) and was associated with a different set of reference data (which in this case were average density and total outflow estimates derived from the video recordings every 15 s). The scenarios covered situations with different demand levels and OD patterns; the layout of the shared space was the same in all scenarios. Every scenario was run five times for each set of parameter values in order to account for model stochasticity (which is due to small variations in the times and positions at which agents enter the shared space during simulation). The results derived from the simulation model were compared to the reference data by calculating the root mean square error (RMSE) of the total outflow and the RMSE of the average density in each scenario (averaging the simulation results of the five runs). These measures indicate the goodness of fit between simulated and empirical data. The sets of parameter values that were tested differed only in the values of interaction radii, strengths and ranges ($R^{\alpha}_{\max}$, $R^{\gamma}_{\max}$, $A_{\alpha\beta}$, $A_{\alpha\delta}$, $A_{\gamma\beta}$, $A_{\gamma\delta}$, $B_{\alpha\beta}$, $B_{\alpha\delta}$, $B_{\gamma\beta}$, $B_{\gamma\delta}$), and relaxation times (τ_{α}, τ_{γ}). These are the parameters that have a higher influence on the interaction behaviour of pedestrian and cyclist agents. The combinations of parameter values to be tested were generated by systematically changing the value of one of these parameters within a certain range while leaving the others unchanged (i.e., a grid search approach was used).

The grid search procedure (see Fig. 2) was implemented twice. First, a coarse grid search was carried out in order to identify reasonable parameter value ranges. The sets of parameter values given as input in this step were: 1, 2, …, 10 m for $R^{u}_{\max}$; 0.1, 0.2, …, 1.0 s for τ_u; 0.01, 1, 2, 3, …, 7 m/s^2 for A_{us}; and 1, 2, …, 5 m for B_{us}. Next, a fine grid search was carried out giving more precise parameter values as input (within the ranges identified in the previous step). Here, the main goal was to identify the set of parameter values that represent walking and cycling behaviour more realistically, which is the combination of parameter values leading to the lowest average RMSE (see Fig. 2). Note that the following parameters were

kept constant in both grid search steps: $v_\alpha^0 = 1.35\,\text{m/s}$, $v_\gamma^0 = 3.00\,\text{m/s}$, $\lambda_\alpha = \lambda_\gamma = 0.2$, $w_\alpha = l_\alpha = 0.5\,\text{m}$, $w_\gamma = 1.0\,\text{m}$, $l_\gamma = 2.0\,\text{m}$, $a_\alpha^{\max} = a_\gamma^{\max} = 3.0\,\text{m/s}^2$, $\theta_\alpha = \pi/4\,\text{rad}$, $\theta_\gamma = \pi/6\,\text{rad}$, and $\Delta t = 0.2\,\text{s}$. These values are considered reasonable given the authors' experience in traffic simulation.

4 Face-Validation Results

Figure 3 shows selected results of the coarse grid search that provide insights on walking and cycling behaviour (particularly on pedestrian–cyclist interactions). This figure shows the RMSE values associated with combinations of parameter values that differ only in the values of two parameters: the relaxation times of pedestrians and cyclists (τ_α and τ_γ) in Fig. 3a, and the intermodal interaction strengths of both types of agents ($A_{\alpha\delta}$, $A_{\gamma\beta}$) in Fig. 3b. In these figures, the values of the parameters that remain constant are similar to the values identified later in the fine grid search. Figure 3a shows that the relaxation time (τ_u) is generally higher for cyclists than for pedestrians (note the area with low RMSE at the upper-left corner of the plot). This implies that cyclists generally react to traffic conditions slower than pedestrians, possibly as a result of the manoeuvring constraints of bicycles. Figure 3b shows that the lowest RMSE values are obtained with low intermodal interaction strength values ($A_{\alpha\delta}$, $A_{\gamma\beta}$), at least within the considered range (note the area with low RMSE at the lower-left corner of the plot).

Table 1 provides the best set of parameter values identified in the fine grid search. Note that the relaxation times of pedestrians and cyclists (τ_α, τ_γ) are 0.28 s and 0.7 s, respectively, which is in line with the results plotted in Fig. 3a. Interestingly, the interaction strength of cyclists against pedestrians ($A_{\gamma\beta}$) is larger than the one of pedestrians against cyclists ($A_{\alpha\delta}$) (2.7 versus 0.1). This indicates that cyclists react to the presence of pedestrians within their radius of interaction more strongly than the other way around, possibly because cyclists can do more harm to pedestrians in case of collision. Note that the maximum interaction radii ($R_{\max}^{\alpha}$, $R_{\max}^{\gamma}$), the intramodal interaction strengths ($A_{\alpha\beta}$, $A_{\gamma\delta}$), and the interaction ranges ($B_{\alpha\beta}$, $B_{\alpha\delta}$, $B_{\gamma\beta}$, $B_{\gamma\delta}$) have similar values for both pedestrians and cyclists (see Table 1).

Figure 4a, b shows the total outflows and average densities over time generated by the simulation model in one of the scenarios (using the identified set of parameter values, see Table 1), and compares them to the reference data. As shown in those figures, the model can reproduce the empirical observations, which demonstrates the potential of the proposed modelling approach.

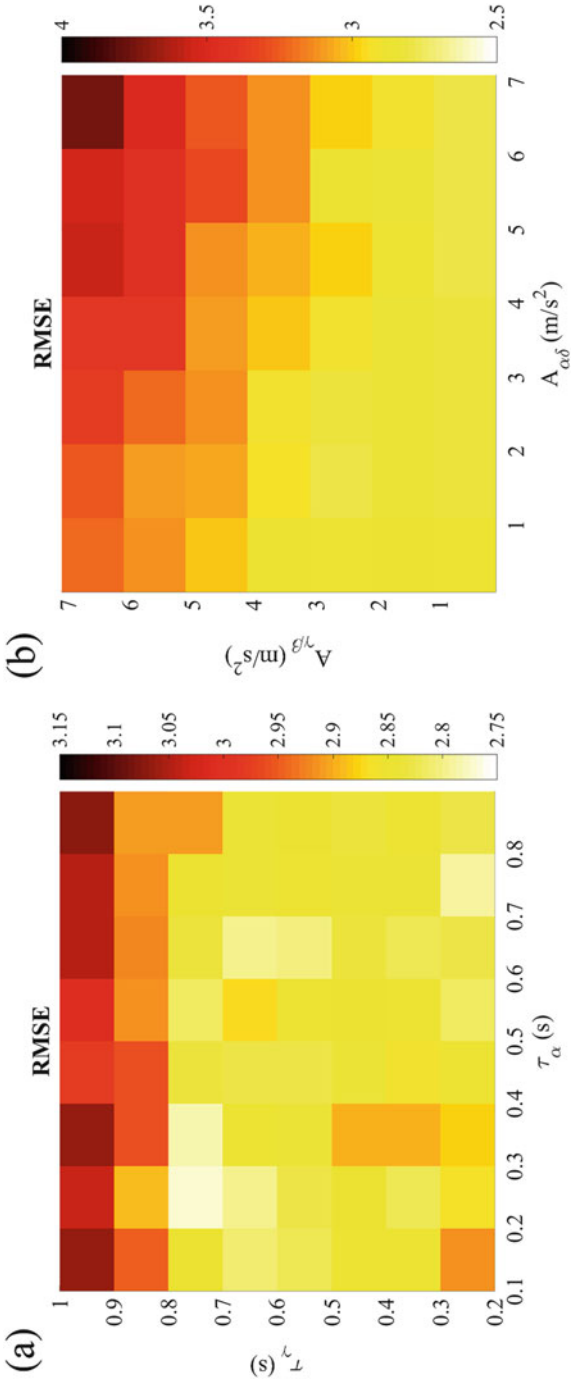

Fig. 3 Comparison of RMSE values (regarding average density in the shared space) associated with combinations of parameter values that differ only in the values of two parameters. (**a**) Relaxation times. (**b**) Intermodal interaction strengths

Table 1 Selected set of model parameter values after fine grid search.

Pedestrians						Cyclists					
$R^{\alpha}_{\max}$ (m)	τ_{α} (s)	$A_{\alpha\beta}$ (m/s^2)	$B_{\alpha\beta}$ (m)	$A_{\alpha\delta}$ (m/s^2)	$B_{\alpha\delta}$ (m)	$R^{\gamma}_{\max}$ (m)	τ_{γ} (s)	$A_{\gamma\delta}$ (m/s^2)	$B_{\gamma\delta}$ (m)	$A_{\gamma\beta}$ (m/s^2)	$B_{\gamma\beta}$ (m)
3.0	0.28	0.05	1.5	0.1	1.5	3.2	0.7	0.1	1.5	2.7	1.5

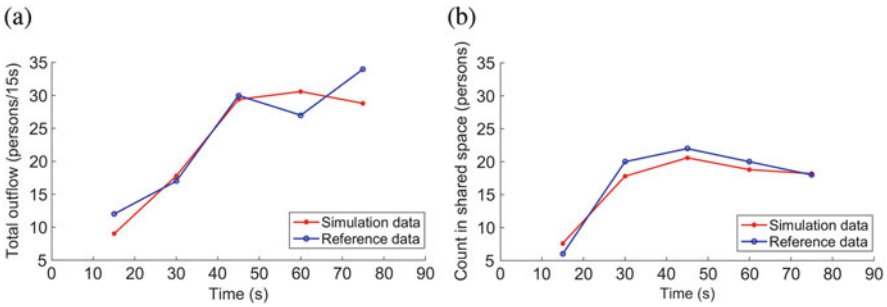

Fig. 4 Comparison of simulation data to reference data (total outflows and average densities). Note that the simulation results are the average of five simulation runs. (**a**) Total outflows. (**b**) Average densities (count/total area)

5 Conclusions and Outlook

This paper presented a social force model describing walking and cycling behaviour in shared spaces. The face-validity of the model was tested by comparing simulation output data to empirical traffic data collected at a shared space in Amsterdam. This led to the identification of a reasonable set of model parameter values. Furthermore, the face-validation results indicate that the model reproduces the macroscopic characteristics of traffic observed at the shared space in Amsterdam. Therefore we conclude that the model describes walking and cycling behaviour in a plausible way. Nevertheless, further research is necessary to improve the model. Firstly, it is necessary to include an anticipation term in the model to account for long-range collision avoidance behaviour. Also, other relevant types of forces (e.g., repulsive forces exerted by static obstacles, and drift forces) need to be included in order to model walking and cycling behaviour more realistically. Secondly, the acceleration and turning-angle constraints could be modelled together to account for the fact that cyclists compensate between the two. Finally, the model needs to be extensively calibrated and validated, preferably using individual trajectory data.

Acknowledgements This research was supported by the ALLEGRO project, which is funded by the European Research Council (Grant Agreement No. 669792), and a Stimulus project funded by the Amsterdam Institute for Advanced Metropolitan Solutions (AMS). The authors would like to thank I. Mackenzie and E. Morrow for their support in implementing the model in MassMotion.

References

1. Andresen, E., Chraibi, M., Seyfried, A., Huber, F.: Basic driving dynamics of cyclists. In: Behrisch, M., Krajzewicz, D., Weber, M. (eds.) Simulation of Urban Mobility, pp. 18–32. Springer, Berlin (2014)
2. Antonini, G., Bierlaire, M., Weber, M.: Discrete choice models of pedestrian walking behaviour. Transp. Res. Part B Methodol. **40**(8), 667–687 (2006)
3. Anvari, B., Bell, M., Sivakumar, A., Ochieng, W.: Modelling shared space users via rule-based social force model. Transp. Res. Part C Emerg. Techn. **51**, 83–103 (2015)
4. Campanella, M.C.: Microscopic modelling of walking behaviour. Ph.D. Dissertation, TRAIL Thesis series, Delft University of Technology (2016)
5. Helbing, D., Molnár, P.: Social force model for pedestrian dynamics. Phys. Rev. E **51**, 4282–4286 (1995)
6. Pascucci, F., Rinke, N., Schiermeyer, C., Friedrich, B., Berkhahn, V.: Modeling of shared space with multi-modal traffic using a multi-layer social force approach. Transp. Res. Proc. **10**, 316–326 (2015)
7. Schakel, W.J., Knoop, V.L., van Arem, B.: Integrated lane change model with relaxation and synchronization. Transp. Res. Rec. J. Transp. Res. Board **2316**, 47–57 (2012)
8. Schönauer, R., Stubenschrott, M., Huang, W., Rudloff, C., Fellendorf, M.: Modeling concepts for mixed traffic: steps toward a microscopic simulation tool for shared space zones. Transp. Res. Rec. J. Transp. Res. Board **2316**, 114–121 (2012)

Multi-Attribute, Multi-Class, Trip-Based, Multi-Modal Traffic Network Equilibrium Model: Application to Large-Scale Network

Mostafa Ameli, Jean-Patrick Lebacque, and Ludovic Leclercq

Abstract Transportation systems are dynamically driven not only by non-linear interactions between the different components but also by significant feedbacks between network state and user decision. In this work, we consider a trip-based multi-modal approach to network equilibrium. We assume that mode and path choice is carried out at the same level; therefore, travel time depends on the travel path and the mode attributes of travelers. First, we analyze the existing approaches in the literature to model users' heterogeneity. Second, we present a formulation for static traffic network equilibrium and propose a hybrid formulation of the cost function for trip-based traffic assignment. Third, we consider dynamic traffic assignment (DTA) and propose a variational inequality formulation of the trip-based fixed demand function for the multi-class dynamic traffic equilibrium problem. Finally, we analyze the equilibrium in a large-scale DTA test case (Lyon 6e + Villeurbanne) by a simulation-based approach. Moreover, we propose a novel trip-based algorithm to solve the discrete DTA problem and compare it with the gap function-based method.

M. Ameli (✉)
Universite Paris-Est, IFSTTAR, GRETTIA, Champs-sur-Marne, France

Université de Lyon, ENTPE, IFSTTAR, LICIT, Lyon, France
e-mail: mostafa.ameli@ifsttar.fr

J. P. Lebacque
Universite Paris-Est, IFSTTAR, GRETTIA, Champs-sur-Marne, France
e-mail: jean-patrick.lebacque@ifsttar.fr

L. Leclercq
Université de Lyon, ENTPE, IFSTTAR, LICIT, Lyon, France
e-mail: ludovic.leclercq@ifsttar.fr

S. H. Hamdar (ed.), *Traffic and Granular Flow '17*,
https://doi.org/10.1007/978-3-030-11440-4_53

1 Introduction

Network equilibrium is a situation of the traffic network in which all users' travel costs in all routes actually used are equal and less than those which would be experienced by a single user on any unused route. Generally, travelers consider different criteria in selecting their optimal properties of travel, including travel route and travel mode(s). Most multi-class flow models classify travelers by identifying traveler attributes. In the literature, this classification process identifies eight categories of information about travelers:

1. Choice model: Users are divided into different groups based on the behavioral model that they take into account to choose the route and mode(s) [6].
2. Cost function: Link cost or path cost can be different for each class of users, e.g., the toll of the links can be different for each class [2].
3. Economic attributes: Users are categorized into different classes based on their income [8].
4. General cost function: The goal of the generalized cost function is to present function which aggregates time and monetary cost. Typically, the general cost function (GC) integrates travel time (TT) and travel cost (TC). GC can take into account the class-dependent value of time (VOT) [10]:

$$GC = TC + \alpha_i . TT \tag{1}$$

   where α_i is VOT for class i.
5. Knowledge level of the network: Users can be classified by the ability to access the real-time traffic information (ATIS) [2].
6. Risk taking attitude: Risk is defined as the expected value of the unfavorable outcome. Travelers treat travel time variability as a risk in their travel choices because it introduces uncertainty for an on-time arrival at the destination [9].
7. Social class: To classify users into social classes cannot make difference in equilibrium calculation. The advantage is to estimate the demand in traffic assignment problems with variable demand [1].
8. Vehicle class: In multi-modal traffic network, vehicle classes are defined in order to calculate the travel time and cost based on mode attributes.

Traffic assignment mathematical models are divided into two main categories: flow-based and trip-based [6]. Here, we consider the trip-based approach to be more realistic for a large-scale traffic network. Therefore the path flow model will be discrete. Concerning the mathematical model, the problem is known as static traffic assignment (STA) when the origin–destination (OD) matrix and the link flows are assumed to be time-independent. On the other hand, if time dependence is considered, the problem becomes a dynamic traffic assignment (DTA). In this study, we apply the model to a real test case (Lyon 6e + Villeurbanne) by a simulation-based approach. In order to solve DTA model, we present a new heuristic approach to find equilibrium and compare it to one of the efficient approach based on method of successive average (MSA) by Lu et al. [4].

In the next section, the multi-class model is presented. The Wardrop condition for the network equilibrium model is discussed for STA and DTA in Sect. 2. Moreover, the uniqueness of the solution is also discussed in this section. The new algorithm to find the network equilibrium and the numerical experiment are explained in Sect. 3. Finally, we conclude this study by presenting the numerical results and discuss them in Sect. 4.

2 The Multi-Attribute, Multi-Class, Trip-Based, Multi-Modal Model

In order to describe the traveler behavior, a general cost function that takes into account four types of information (categories 2, 3, 4 and 7) defined in Sect. 1 is used. Typically the general cost function (GC) will take into account the class-dependent value of time (VOT) [10] denoted α_i for class i, and a vector β_i of economic and social class parameters. Hence the general cost of path p ($p \in P$: set of paths) is

$$GC_p(\alpha_i, \beta_i) = TC_p(\beta_i) + \alpha_i . TT_p \tag{2}$$

The vector of parameters β_i includes the mode(s) and social attributes of a traveler. For instance, one class in the network can be students who pay less to use the transit network and who have the specific value of time. The value of parameters and classes identification will be presented in Sect. 3. Each user is able to perceive the travel cost and travel time on a link. The demand of OD pair w ($w \in W$: set of OD pairs) is

$$d_w^i = \sum_{p \in P_w} \pi_p^i \quad , \quad d_w^i \geq 0 \tag{3}$$

where i is the user class index ($i \in 1, 2, ..., k$), P_w is a set of paths for w and π_p^i is the number of users of class i on path p. After assigning the user to the path between OD pair w, π_a (the number of users on link a) is

$$\pi_a^i = \sum_{p \in P} \pi_p^i \delta_{ap} \quad , \quad \pi_a = \sum_{i=1}^{k} \pi_a^i \tag{4}$$

where a is the link index ($a \in A$: set of links in the network), π_a^i is the number of users of class i on link a and $\delta_{ap} = 1$ if path p contains link a and 0, otherwise. The travel time/cost function depends on the congestion of the link. Therefore, the travel time and cost are calculated by the following formulas:

$$TT_a = TT_a(\pi_a) \quad , \quad TC_a^i(\beta_i) = TC_a^i(\beta_i, \pi_a) \tag{5}$$

Consequently, the link generalized cost function is calculated as follows:

$$GC_a(\alpha_i, \beta_i) = TC_a(\beta_i, \pi) + \alpha_i . TT_a(\pi) \tag{6}$$

2.1 STA equilibrium model

In the STA, the elastic OD demands are assumed to depend on averaged generalized OD travel costs via the OD demand functions. The OD demand functions are general and can depend not only on travel disutilities of each class on pair w, but also on other classes of users on other OD pairs. Therefore, the demand of class i for OD pair w is

$$d_w^i = \Delta_w^i(\overline{GC}_w^i) \tag{7}$$

where $\overline{GC}_w^i$ is averaged general cost of OD pair w. Δ_w^i denotes the demand function. The static traffic network equilibrium condition is defined as: For each class i, for all OD pair $w \in W$ and for all paths $p \in P_w$, the equilibrium conditions are

$$\begin{cases} GC_p(\alpha_i, \beta_i) = GC_w^{i\,*} & \text{if} \quad \pi_p^{i\,*} > 0 \\ GC_p(\alpha_i, \beta_i) \geq GC_w^{i\,*} & \text{if} \quad \pi_p^{i\,*} = 0 \end{cases} \tag{8}$$

$$\begin{cases} \Delta_w^i(GC_w^{i\,*}) = \sum_{p \in P_w} \pi_p^{i\,*} & \text{if} \quad GC_w^i > 0 \\ \Delta_w^i(GC_w^{i\,*}) \leq \sum_{p \in P_w} \pi_p^{i\,*} & \text{if} \quad GC_w^i = 0 \end{cases} \tag{9}$$

where $GC_w^{i\,*}$ is the minimum general cost of user in class i for travel between OD pair w and $\pi_p^{i\,*}$ is the optimal number of user class i on path p.

As presented in [5] the flow pattern π^* being the solution of this network equilibrium model is equivalent to solving the following finite-dimensional variational inequality formulation:

$$\begin{aligned} &\sum_{i=1}^{k} \sum_{a \in A} GC_a^i(\pi_a) \left(\pi_a^i - \pi_a^{i*}\right) - \sum_{i=1}^{k} \sum_{w \in W} GC_w^{i\,*}(d_w^i - d_w^{i\,*}) \\ &+ \sum_{i=1}^{k} \sum_{w \in W} \left(d_w^{i\,*} - \Delta_w^i(GC_w^{i\,*})\right) \left(GC_w^i - GC_w^{i\,*}\right) \geq 0 \quad \forall \pi \in \mathscr{H} \end{aligned} \tag{10}$$

where $(\pi_a^{i*}, d_w^{i*}) \in \mathscr{H}$ satisfy the equilibrium. $\mathscr{H}$ denotes the flow constraints (Eq. (3)); π^* must also be in $\mathscr{H}$. Equation (10) equivalently, in standard form:

$$\langle F(X^*)^T, X - X^* \rangle \geq 0 \quad \forall X \in \mathscr{H} \tag{11}$$

where $F \equiv (GC(), -GC()^T, d - \Delta(GC))$ and $X \equiv (\pi, d, GC)$.

2.2 DTA equilibrium model

Consider a network $G(N, A)$ with a finite set of nodes N and a finite set of directed links A. The demand is time-dependent. The period of interest (planning horizon) of duration H is discretized into a set of small time intervals indexed by τ ($\tau \in T = \{\tau_0, \tau_0 + \sigma, \tau_0 + 2\sigma, ..., \tau_0 + M\sigma\}$ and $\tau_0 + M\sigma = H$). σ is the duration of the time intervals. In an interval τ, travel time and traffic conditions do not change. The important notations to introduce the dynamic equilibrium model are as follows:

$P_{w,\tau}$: set of paths for w in departure time τ.
$P^*_{w,\tau}$: set of shortest paths for w in departure time interval τ.
p: index of path, $p \in P_{w,\tau}$.
p^*: index of shortest path, $p^* \in P^*_{w,\tau}$.
$GC_{p,\tau}(\alpha_i, \beta_i)$: general cost of path p for user class i in departure time τ.
$GC^{i}_{w,\tau}{}^*$: minimum general cost of OD pair w for user class i in departure time τ.

For each class i, for all OD pair $w \in W$ and for all paths $p \in P_w$, the dynamic traffic network equilibrium condition with fixed travel demands for the aforementioned traffic network equilibrium problem is

$$\begin{cases} GC_{p,\tau}(\alpha_i, \beta_i) - GC^{i}_{w,\tau}{}^* \geq 0 \\ \pi^i_{p,\tau}(GC_{p,\tau}(\alpha_i, \beta_i) - GC^{i}_{w,\tau}{}^*) = 0 \\ \pi^i_{p,\tau} \geq 0 \end{cases} \tag{12}$$

The solution of this problem is equivalent to finding the solution to the following variational inequality:

$$\sum_{w \in W} \sum_{\tau=1}^{T} \sum_{i=1}^{k} \sum_{p \in P(w,\tau)} GC^{i}_{w,p,\tau}{}^* \left(\pi^i_{w,p,\tau} - \pi^{i}_{w,p,\tau}{}^* \right) \geq 0 \tag{13}$$

Existence of solution(s) to Eq. (13) needs the continuity of the generalized cost functions of paths with respect to the numbers of users on paths. In this case, the uniqueness of the solution requires the strict monotonicity of the OD paths generalized cost functions with respect to OD path flows (i.e., number of cars). In

general urban transportation networks, these conditions are not guaranteed to hold. In the next section, we present a new heuristic algorithm to find a solution for the dynamic traffic network equilibrium model.

3 Trip-Based Solution Algorithm and Numerical Experiments

This simulation-based study works on trip-based DTA which transforms the solution space from continuous space to discrete space. The optimization process is executed for each departure time interval that contains two loops. The outer loop finds a new shortest path from origin to destination w and the inner loop finds a best assignment path for the path set of the current outer loop [7]. At the end of each outer loop, the best solution is kept and used to enter to the next outer loop. The optimization method updates the assignment plan in each iteration of inner loop. There is a convergence test for each loop. There are two differences between outer loop convergence test (OCT) and inner loop convergence test (ICT). First, in the outer loop we calculate the quality indicator (Eq. (14)), based on the new shortest path(s) but in ICT the path set is fixed during the inner loop and just the shortest path is updated in each iteration. Second, in ICT we calculate the difference of total gap between two iterations of the inner loop, but in OCT, we compare the total gap with a small reference value to check the convergence. The total gap as a quality indicator in time interval τ is

$$\text{Gap}(\pi, GC^*) = \sum_{w \in W} \sum_{i=1}^{k} \sum_{p \in P(w,\tau)} \pi^i_{w,p} (GC^i_{w,p} - GC^i_{w,p}{}^*) \tag{14}$$

The heuristic methods are path-swapping descent direction methods that decompose the problem into many (origin-destination, departure time interval) subproblems and solve each of them by adjusting time-varying OD flows between all non-shortest paths and the shortest path(s). Moreover, in this study, the optimization process is applied to each class of users.

To enable the deployment of large-scale (simulation-based) DTA models, [4] proposes a heuristic approach which we called "gap-based" method in this study. In iteration λ of this method, a fraction $\frac{1}{\lambda+1}$ of users on each non-shortest path swap to the one of the shortest path in current iteration. The new method which is called "probabilistic method" is a trip-based approach which is without step size for optimization. For each user the probability of swap to the shortest path(s) is calculated by the following formula:

$$\text{Swap indicator} = \frac{GC_p - GC^*_p}{GC_p} \tag{15}$$

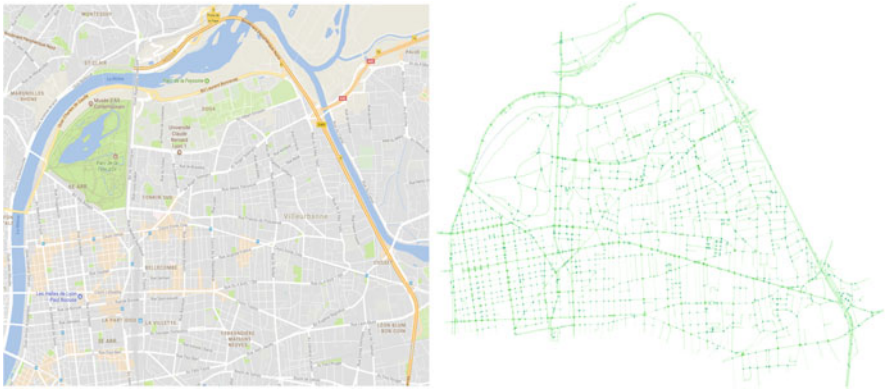

Fig. 1 Lyon 6e + Villeurbanne: Mapping data ©Google 2017 and the traffic network by using SymuVia

Table 1 User classes and their value of time for the Lyon 6e + Villeurbanne network

Percentage of trips (%)	Class name (job)	Value of time [euro/s]
44.7	Worker	0.01
8.2	Student	0.005
0.7	Worker–student	0.008
18.8	Retired	0.006
3.2	At home	0.004
8.2	Elementary school	0.004
10.3	Secondary school	0.005
5	Unemployed	0.004
0.9	Other	0.006

Then, we use a random number for taking a decision about swapping the user or not. If the random number is lower than indicator the user swaps to the shortest path and otherwise, the user keeps his/her path for the current iteration.

The model for multi-class DTA is applied to a large-scale network of Lyon 6e + Villeurbanne with 1883 nodes, 3383 links, 94 origins, 227 destinations and 54,190 trips. This network located in Lyon is described in Fig. 1. The trips are divided into 9 classes that are presented in Table 1.

In this work, we use SymuVia[1] as a trip-based simulator for calculating the needed variables in the network. SymuVia has been developed by the LICIT laboratory in IFSTTAR. It is a microscopic simulator based on a Lagrangian discretization of the LWR model [3]. It has a simulation time-step equal to 1 s and collects the information at the link level every 1 min. Note that the dynamic

[1]SymuVia is an open source simulator that will be available starting winter 2018.

simulator uses Eq. (6) to calculate the generalized travel cost on a link at each time interval.

The optimization process is executed for 9 outer loops that means we have 10 paths per OD. In each outer loop, 20 inner loops have been executed to find the best assignment pattern. Note that we have one more simulation per outer loop for keeping the best assignment pattern.

4 Numerical Results and Conclusion

The full optimization process is done for both methods and the quality of the solution at the end of each outer loop is evaluated by the following indicator that calculates the travel time gap per user in minutes:

$$\mathrm{Gap}(\pi,\ GC^*) = \frac{\sum_{w\in W}\sum_{\tau=1}^{T}\sum_{i=1}^{k}\sum_{p\in P(w,\tau)}\pi^{i}_{w,\,p,\,\tau}\left(GC^{i}_{w,\,p,\,\tau} - GC^{i}_{w,\,p,\,\tau}{}^{*}\right)}{\sum_{w\in W}\sum_{\tau=1}^{T}\sum_{i=1}^{k}\sum_{p\in P(w,\tau)}\pi^{i}_{w,\,p,\,\tau}} \tag{16}$$

The test results of two optimization methods on the multi-modal large-scale network are presented in Fig. 2. The total gap (Eq. (14)) and the quality indicator (Eq. (16)) are calculated for each outer loop with the updated shortest path. The average delay for each user by the gap-based method is around 30 s but this value for the probabilistic method is around 3 s. It shows that the new method obtains 10 times better quality than the gap-based method on this large-scale network.

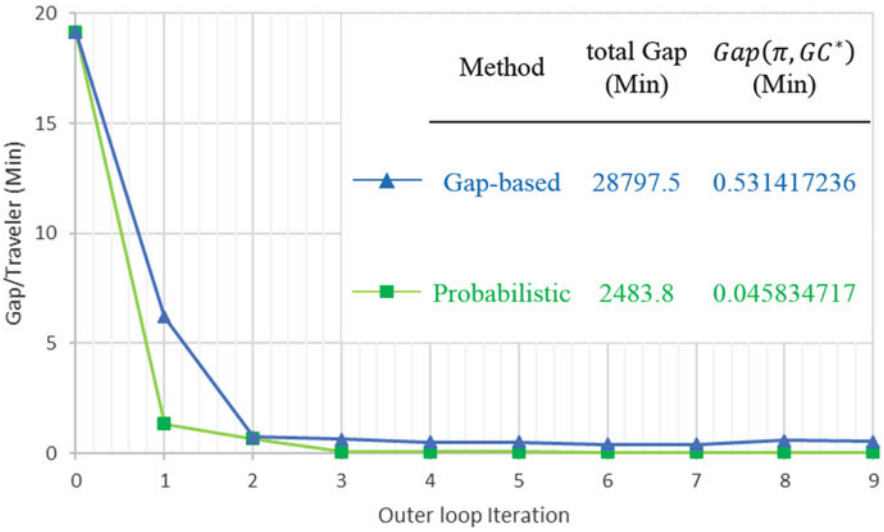

Fig. 2 Comparison of gap-based method and probabilistic method which is proposed by this study

The multi-attribute multi-class model and optimization process has a successful application on a multi-modal large-scale network. The new method (probabilistic) as a trip-based approach works significantly better than the gap-based method. It is free from step size and it converges faster in this study. The authors propose the following topics for the future works:

- Extend the multi-attribute, multi-class trip-based model to activity-based models in order to consider travel with activity chains;
- Compare and analyze the performance of the method in other large-scale networks with different topologies;
- Compare the other types of heuristic methods with the probabilistic method.

Acknowledgements This work has received funding from the European Research Council (ERC) under the European Union's Horizon 2020 research and innovation program (Grant agreement No. 646592—MAGnUM project).

References

1. Florian, M., Wu, J.H., He, S.: A multi-class multi-mode variable demand network equilibrium model with hierarchical logit structures. In: Transportation and Network Analysis: Current Trends, pp. 119–133. Springer, Boston (2002)
2. Huang, H.J., Li, Z.C.: A multiclass, multicriteria logit-based traffic equilibrium assignment model under ATIS. Eur. J. Oper. Res. **176**(3), 1464–1477 (2007)
3. Leclercq, L., Laval, J.A., Chevallier, E.: The Lagrangian coordinates and what it means for first order traffic flow models. In: Transportation and Traffic Theory 2007. Papers Selected for Presentation at ISTTT17 (2007)
4. Lu, C.C., Mahmassani, H.S., Zhou, X.: Equivalent gap function-based reformulation and solution algorithm for the dynamic user equilibrium problem. Transp. Res. B Methodol. **43**(3), 345–364 (2009)
5. Nagurney, A., Dong, J.: A multiclass, multicriteria traffic network equilibrium model with elastic demand. Transp. Res. B Methodol. **36**(5), 445–469 (2002)
6. Patriksson, M.: The Traffic Assignment Problem: Models and Methods. Courier Dover Publications, Mineola (2015)
7. Sbayti, H., Lu, C.C., Mahmassani, H.: Efficient implementation of method of successive averages in simulation-based dynamic traffic assignment models for large-scale network applications. Transp. Res. Rec. J. Transp. Res. Board **2029**, 22–30 (2007)
8. Yang, H., Zhang, X.: Multiclass network toll design problem with social and spatial equity constraints. J. Transp. Eng. **128**(5), 420–428 (2002)
9. Yu, J.G., Jayakrishnan, R.: Multiclass, multicriteria dynamic traffic assignment with path-dependent link cost and entropy-based risk preference. Transp. Res. Rec. **2667**(1), 108–118 (2017)
10. Zhang, K., Mahmassani, H.S., Lu, C.C.: Dynamic pricing, heterogeneous users and perception error: probit-based bi-criterion dynamic stochastic user equilibrium assignment. Transp. Res. C Emerg. Technol. **27**, 189–204 (2013)

Microscopic Cycling Behavior Model Using Differential Game Theory

Alexandra Gavriilidou, Yufei Yuan, Haneen Farah, and Serge P. Hoogendoorn

Abstract In order to develop design guidelines and assess the implications on traffic flow operations and safety, microscopic behavioral models are used. The increasing interest in cycling in cities necessitates the development of a model that captures the movement of cyclists. Given the fact that cyclists exert effort for their motion, the theory of effort minimization can be adopted from the micro-economic theory of subjective utility maximization. Also, due to their size and flexibility, close interactions between cyclists are possible, which can be resolved by solving a differential game. This solution determines the optimal control strategy of a cyclist and is, hence, a microscopic cycling model. In this paper we explain the derivation of such a model. Moreover, we demonstrate its plausibility by interpreting the derived equations and face validating the model. The results indicate the need to consider traffic rules and to collect bicycle trajectory data.

1 Introduction

Even though the interest in cycling in cities increases, research into the microscopic behavior of cyclists, i.e., how cyclists interact with other traffic participants and with the infrastructure, is still in its infancy. It is, therefore, important to study and understand the movements of cyclists and develop models that can capture their behavior. The model proposed in the present study focuses on interactions between cyclists, assuming no other modes and no effects from the infrastructure are present.

The outline of this paper is as follows: A literature overview of the microscopic modeling approaches is provided in Sect. 2, while in Sect. 3 the derivation of the cycling behavior model is described. Sect. 4 demonstrates the plausibility of the developed model. The main conclusions and recommendations of this study are discussed in Sect. 5.

A. Gavriilidou (✉) · Y. Yuan · H. Farah · S. P. Hoogendoorn
Delft University of Technology, Delft, The Netherlands
e-mail: a.gavriilidou@tudelft.nl; y.yuan@tudelft.nl; h.farah@tudelft.nl; s.p.hoogendoorn@tudelft.nl

S. H. Hamdar (ed.), *Traffic and Granular Flow '17*,
https://doi.org/10.1007/978-3-030-11440-4_54

2 Microscopic Modeling Approaches

The early microscopic cyclists' behavior models made use of the behavioral models developed for cars while adjusting their parameters to reflect the lower speeds of bicycles and their smaller size. Such vehicular modeling paradigms include the rule- and velocity-based models. In addition to these, force-based models, which stem from research on pedestrian dynamics, were developed to model the microscopic cycling behavior. The characteristics of each of these methods are described in this section, along with utility-based models which have not yet been used to represent cyclists' movements.

The most commonly used rule-based models are cellular automata (CA), proposed by Nagel and Schreckenberg [13]. They are discrete in time and space and vehicle movements are determined by a set of rules. The cell size was originally defined such that one vehicle fits per cell, allowing for the tracking of individual vehicles (i.e., microscopic level) through the grid of cells. However, modeling mixed traffic conditions (i.e., cycling on the road among motorized traffic) required adjustments to represent the difference in sizes and speeds between the modes. These adjustments concern the size of the cells and their occupancy in time. A nice example is the model developed in [12], where the cell occupancy is not only a function of the vehicle type but also of its speed. This way the model accounts for the variable lateral distance that bicycles keep from cars around them in order to maintain a sense of comfort and safety.

Velocity-based or longitudinally continuous models constitute a different modeling approach usually found in microscopic traffic simulation tools, such as VISSIM [4]. They are continuous in space and time and make use of separate models for the longitudinal and lateral control. The former is based on car-following models, while the lateral behavior is usually determined by a discrete choice model. Another alternative is the continuous lateral model of [3]. In this model, the lateral position is selected such that it maximizes the minimum time-to-collision (TTC) with surrounding traffic (i.e., time remaining for collision if no change in the position is made).

Force-based models assume agents to behave as particles that attract or repel each other. The most common method which stems from the modeling of pedestrian dynamics and was first proposed by Helbing and Molnar [5] is the social force models. They are continuous in space, allowing for movement in a two-dimensional plane in reaction to a set of forces acting on the individual by the surroundings. The forces represent the desire to follow a certain path and at the same time avoid bumping into obstacles and other road users. The former takes into account the desired speed and direction of each individual. The interaction force distinguishes between a psychological component, dependent on the distance from infrastructure and from other traffic participants, and a physical component, activated upon contact, to represent countering body compression and sliding friction [6].

Another modeling paradigm is based on utility theory. Utility-based models were introduced in economics to model market dynamics based on the assumption that

humans strive to maximize their benefits while behaving rationally. This concept of conscious decision making has been used in pedestrian research, but not yet to model cycling behavior. It encompasses two approaches, namely the discrete choice models [1] and models based on game theory [9]. The former are data-driven and use time and space discretization, but contrary to CA models the grid moves along with the individual instead of being fixed in space. In game theoretical approaches, the different agents are assumed to adopt strategies, like cooperating or not, to resolve conflicts and make decisions. Such a model is derived in the following section.

3 Cycling Behavior Model Derivation

Drawing a parallel from the utility maximization principle, it can be stated that since cyclists exert effort (physical as well as mental) for their motion, they move in a manner that minimizes this effort by applying optimal control and differential game theory. It is, therefore, important to define their objective cost (effort) function J_p, which, in optimal control theory, is generally determined by integrating the running cost L_p of cyclist p over the planning period $[t, t+T)$, where t and T denote the current and the terminal time, respectively [9]:

$$J_\mathrm{p} = \int_t^{t+T} \mathrm{e}^{-s} L_\mathrm{p}\, \mathrm{d}s \tag{1}$$

For the derivation of the model, it is assumed that the running cost comprises three components. The first describes the cost that is incurred by deviating from the desired path (defined by a desired speed ${v_\mathrm{p}}^0$ and direction ${\theta_\mathrm{p}}^0$). The second component refers to the application of control u_p, namely changing speed or direction. The third component captures the cost of approaching other cyclists q, while taking into account anisotropy with respect to the relative location of others. This anisotropic character of cyclist motion (i.e., cyclists in front have a bigger effect than those behind) is taken into account by the factor β proposed in [7]:

$$\beta = \psi + (1-\psi)\frac{1+\cos\phi_\mathrm{pq}}{2} \tag{2}$$

where ψ determines the level of anisotropy $\in [0, 1]$ and ϕ_pq denotes the angle between the direction of p and the position of q (Fig. 1).

Due to the fact that the change in direction is controlled by steering the bicycle, angular movements are more representative than lateral ones and this has led the authors to the choice of polar coordinates instead of Cartesian ones. The control u_p is then reflected by the longitudinal acceleration $\mathrm{a_p}$ and the angular velocity ω_p. It should be noted that a very simple model is assumed to describe bicycle kinematics, yet more complex models, such as those in [11], could also be used.

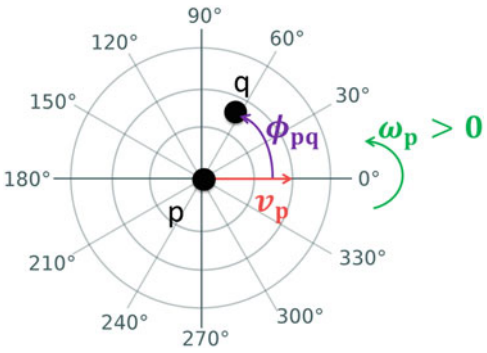

Fig. 1 Definition of (1) the angle ϕ_{pq} between the speed vector of cyclist p and the position of cyclist q and (2) the direction of positive steering ω_p

Given this, the running cost function is expressed by

$$L_p = \frac{1}{2}(v_p^0 - v_p)^2 + \frac{1}{2}(\theta_p^0 - \theta_p)^2 + \frac{1}{2}a_p^2 + \frac{1}{2}\omega_p^2 + \sum_q e^{-\frac{r_{pq}}{R}}\beta \tag{3}$$

where v_p and θ_p denote the current speed and direction of p, respectively, and r_{pq} the distance between cyclists p and q. R is the discount distance factor (i.e., the range of the repulsive interactions).

In order to solve the optimization problem, two assumptions are made. First, a non-cooperative behavior between agents is assumed which means that each person optimizes their own cost function while being aware that the opponents will do the same. Second, we assume zero-acceleration for the opponents, i.e., the opponents do not change their speed or direction during the prediction period.

The state of a cyclist can be fully described by the vector $\overrightarrow{\xi_p} = (x_p, y_p, v_p, \theta_p)$. Since the control variables (a_p and ω_p) are derivatives of state variables, the evolution of the system is governed by differential equations. This makes it a differential game [10], whose optimal strategy can be found using Pontryagin's principle [14].

First, the Hamiltonian function is defined as

$$H = L_p + \overrightarrow{\lambda}\frac{d}{dt}\overrightarrow{\xi_p} \tag{4}$$

where $\overrightarrow{\lambda}$ denotes the co-state or marginal cost vector.

The optimal control $u_p{}^*$ is then given by

$$u_p{}^* = \text{argmin}H(t, \xi_p, u_p, \lambda) \tag{5}$$

Once behavioral parameters are added as weights to the solution obtained from Eq. (5), the model is derived. The optimal longitudinal acceleration $a_p{}^*$ is described by Eq. (6) and the optimal angular velocity $\omega_p{}^*$ is given by Eq. (7).

$$a_p{}^* = \frac{v_p{}^0 - v_p}{\tau} - \sum_q e^{-\frac{r_{pq}}{R}} \left(A \frac{\cos \phi_{pq}}{R} \beta + B \frac{(1-\psi)}{2} \frac{\sin^2 \phi_{pq}}{r_{pq}} \right) \tag{6}$$

$$\omega_p{}^* = \frac{\theta_p{}^0 - \theta_p}{\zeta} - \sum_q e^{-\frac{r_{pq}}{R}} \left(C \frac{\sin \phi_{pq}}{R} \beta + D \frac{(1-\psi)}{2} \frac{\cos \phi_{pq} \sin \phi_{pq}}{r_{pq}} \right) \tag{7}$$

where A and B denote the interaction strength for longitudinal control. C and D denote the interaction strength for angular control. τ and ζ are the relaxation times for longitudinal and angular control, respectively.

The interpretation of these equations and their plausibility are demonstrated in the following section.

4 Model Plausibility Demonstration

Having derived the model, its plausibility is checked. The first step is to interpret the derived model (Eqs. (6) and (7)). Then the value ranges of the behavioral parameters are derived by face validating the model.

4.1 Model Interpretation

Equation (6) describes the optimal longitudinal acceleration and Eq. (7) the optimal angular steering. The first term in both equations reflects the urge to cycle with the desired speed and at the desired direction, while there is a relaxation time till the corresponding desired parameter is reached. The other two terms describe the behavior upon interaction with other cyclists.

Figure 2 visualizes these interaction terms with a cyclist q at every angle from cyclist p and at very close proximity (0.5 m) or further away (5 m). It can be seen that the reaction is much more intense for cyclists nearby than for those further away. The magnitude of these effects depends on the selection of parameters R and ψ. In the displayed case, the value of the distance discount factor comes from the face validation process described in Sect. 4.2 and is $R = 3$, while the level of anisotropy is set to $\psi = 0.2$, so that interactions beyond the vision field have little effect [2].

At the top part of the figure the acceleration is shown. The second term corresponds to reactions to cyclists in the front, i.e., 0–90° and 270–360° (braking to avoid collision) and in the back (slight acceleration). The third term captures the interaction with cyclists coming from the left (90°) or the right (270°) and since

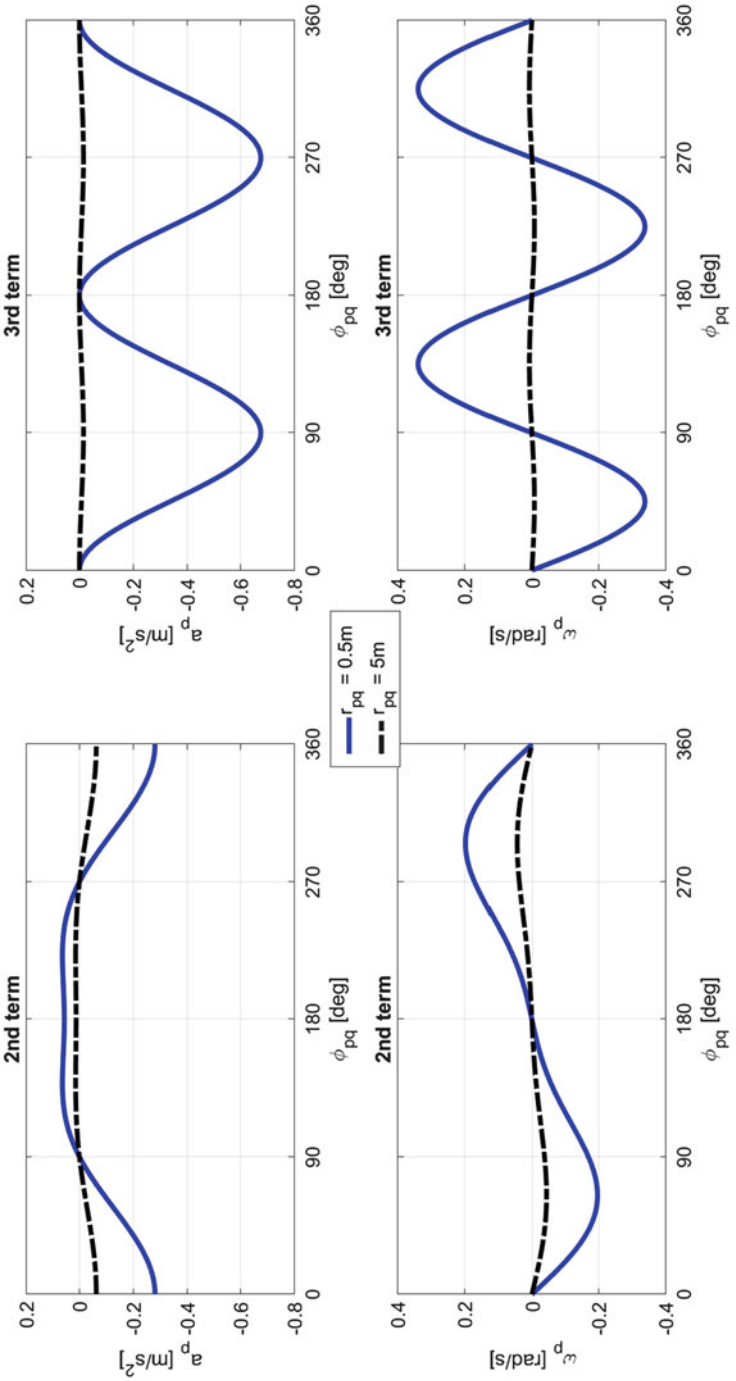

Fig. 2 Interaction terms of the optimal acceleration (top) and the optimal steering (bottom) for $R = 3$ and $\psi = 0.2$

no traffic rules have been introduced yet, both situations result in braking to avoid colliding.

The interaction terms of the optimal steering are depicted at the bottom part of the figure. Based on the definition of positive steering of Fig. 1, both terms result in steering to shy away from cyclists approaching vertically or diagonally.

4.2 Face Validation

The face validation examines a wide range of parameter values and aims to limit these ranges based on the resulting fundamental diagram and the cyclist trajectories. According to the literature, the critical density ranges between 0.05 and 0.14 bicycles/m, while the jam density between 0.27 and 0.45 bicycles/m [8]. Since there are literature findings concerning the fundamental diagram for cyclist traffic, it is the starting point for the face validation.

In order to obtain the fundamental diagram, it is assumed that equilibrium conditions have been reached. This means that there is no steering to switch lanes ($\omega_p{}^* = 0$) and no acceleration or braking ($a_p{}^* = 0$). Equation (6) can then be solved to give the equilibrium speed corresponding to a certain density (i.e., amount of cyclists). By varying the amount of cyclists, the speed–density relationship can be obtained. It should be noted that this step can only face validate parameters R, A, and τ, because in the described setup cyclists form a single file, thereby zeroing the term of parameter B.

First, coarse grids are examined and they become finer based on their performance. The initial ranges are $R \in [0.1, 10]$, $\tau \in [0.6, 1]$, and $A \in [0.1, 10^4]$, because of the physical interpretation of the corresponding parameter (R is distance in meters, τ is time in seconds, and A is the interaction strength). It is observed through the resulting fundamental diagram that R has an effect on the critical density, limiting its range to $R \in (2, 5)$, while τ and A have an impact on the jam density, which limits the range of A to (20, 50).

Following this step, parameter B is face validated by checking that cyclists brake to avoid colliding or riding through each other in case of a colliding crossing course. This leads to a range for $B \geq 10$.

The last step is to examine the steering behavior of non-colliding cyclists and get ranges for parameters C, D, and ζ. When cyclists are in close proximity, they steer away from each other. The effect of these parameters on the resulting cyclist trajectories is displayed in Fig. 3 for pairs of bi-directional cyclists who are initially separated by different vertical distances Δy. By changing the parameter values and looking at the resulting trajectory plots, it is observed that parameter C determines the magnitude of their steer-away movement, while D influences how far they deviate from each other. The value of ζ impacts the time it takes to return to the desired path. Since there is no literature studying this behavior, it becomes harder to draw quantitative conclusions regarding these parameters. This, however,

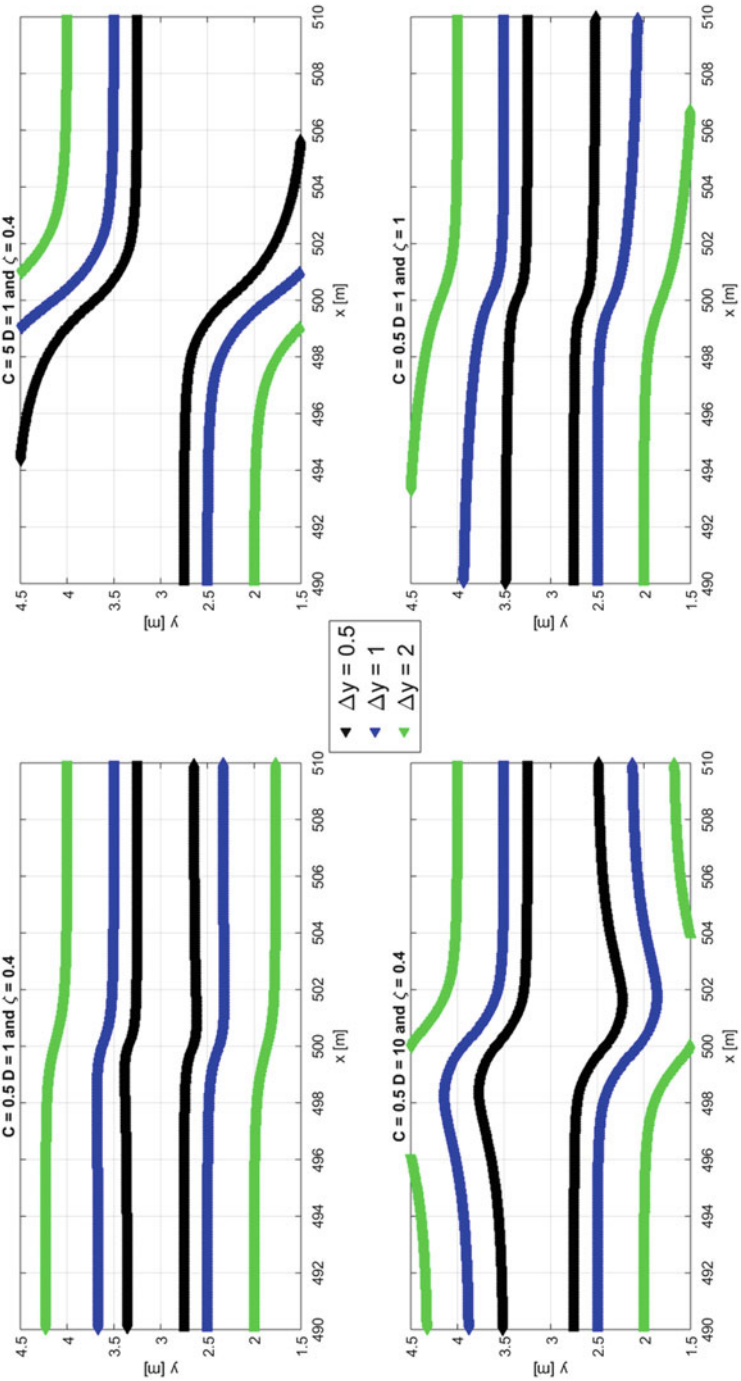

Fig. 3 Effect of changing parameters C, D, and ζ on the resulting cyclist trajectories for pairs of bi-directional cyclists who are initially separated by vertical distance Δy. The parameter set that is common for all cases is $R = 3$, $A = 35$, $\tau = 0.8$, and $B = 10$

demonstrates the plausibility of the model and highlights the need to collect and study bicycle trajectories.

5 Conclusions

In this paper a microscopic cycling behavior model has been derived based on effort minimization and differential game theory and its plausibility has been demonstrated. The developed model is, however, based on simple assumptions regarding the bicycle kinematics and the way cyclists anticipate the behavior of others. Moreover, the current model is not yet calibrated. These limitations create two directions for future research. One is to extend the model by considering more elaborate schemes, such as elliptical shape for the bicycles, the explicit reaction of other cyclists, and traffic rules. The other is the collection of bicycle trajectory data to calibrate and validate the model.

Acknowledgements This research was supported by the ALLEGRO project (no. 669792), which is financed by the European Research Council and Amsterdam Institute for Advanced Metropolitan Solutions.

References

1. Antonini, G., Bierlaire, M., Weber, M.: Discrete choice models of pedestrian walking behavior. Transp. Res. B Methodol. **40**(8), 667–687 (2006)
2. Anvari, B., Bell, M.G., Sivakumar, A., Ochieng, W.Y.: Modelling shared space users via rule-based social force model. Transp. Res. C Emerg. Technol. **51**, 83–103 (2015)
3. Falkenberg, G., Blase, A., Bonfranchi, T., Cossé, L., Draeger, W., Vortisch, P., Kautzsch, L., Stapf, H., Zimmermann, A.: Bemessung von radverkehrsanlagen unter verkehrstechnischen gesichtspunkten. Berichte der Bundesanstalt fuer Strassenwesen. Unterreihe Verkehrstechnik (103) (2003)
4. Fellendorf, M., Vortisch, P.: Microscopic traffic flow simulator VISSIM. In: Fundamentals of Traffic Simulation, pp. 63–93. Springer, New York (2010)
5. Helbing, D., Molnar, P.: Social force model for pedestrian dynamics. Phys. Rev. E **51**(5), 4282 (1995)
6. Helbing, D., Farkas, I., Vicsek, T.: Simulating dynamical features of escape panic. Nature **407**(6803), 487–490 (2000)
7. Helbing, D., Farkas, I.J., Molnar, P., Vicsek, T.: Simulation of pedestrian crowds in normal and evacuation situations. In: Pedestrian and Evacuation Dynamics, vol. 21(2), pp. 21–58. Springer, New York (2002)
8. Hoogendoorn, S., Daamen, W.: Bicycle headway modeling and its applications. Transp. Res. Rec. **2587**, 34–40 (2016)
9. Hoogendoorn, S., HL Bovy, P.: Simulation of pedestrian flows by optimal control and differential games. Optimal Control Appl. Methods **24**(3), 153–172 (2003)
10. Isaacs, R.: Differential Games: A Mathematical Theory with Applications to Warfare and Pursuit, Control and Optimization. Courier Corporation, New York (1999)

11. Kong, J., Pfeiffer, M., Schildbach, G., Borrelli, F.: Kinematic and dynamic vehicle models for autonomous driving control design. In: Intelligent Vehicles Symposium (IV), 2015 IEEE, pp. 1094–1099. IEEE, Piscataway (2015)
12. Luo, Y., Jia, B., Liu, J., Lam, W.H., Li, X., Gao, Z.: Modeling the interactions between car and bicycle in heterogeneous traffic. J. Adv. Transp. **49**(1), 29–47 (2015)
13. Nagel, K., Schreckenberg, M.: A cellular automaton model for freeway traffic. J. Phys. I **2**(12), 2221–2229 (1992)
14. Pontryagin, L.S.: Mathematical Theory of Optimal Processes. CRC Press, New York (1987)

Simulating Bicycle Traffic by the Intelligent-Driver Model: Reproducing the Traffic-Wave Characteristics Observed in a Bicycle-Following Experiment

Valentina Kurtc and Martin Treiber

Abstract Bicycle traffic operations become increasingly important and yet are largely ignored in the traffic flow community, until recently. We hypothesize that there is no qualitative difference between vehicular and bicycle traffic flow dynamics, so the latter can be described by reparameterized car-following models. To test this proposition, we reproduce bicycle experiments on a ring with the intelligent-driver model and compare its fit quality (calibration) and predictive power (validation) with that of the necessary-deceleration-model which is specifically designed for bike traffic. We find similar quality metrics for both models, so the above hypothesis of a qualitative equivalence cannot be rejected.

1 Introduction

In spite of its growing relevance, past research on bicycle traffic operations in experiments [3, 6, 7, 11] and models [1, 2, 4] is remarkably scarce. In contrast, there is a multitude of empirical and experimental investigations for vehicular traffic flow, as well as a plethora of models (for an overview see, e.g., [8]). Therefore, it is natural to ask whether there is a significant qualitative difference between vehicular and bicycle traffic flow at all. In other words, the question arises if one can use the well-developed car-following models for the simulation of bicycle traffic instead of creating new bicycle models.

In this paper, we test the intelligent-driver models (IDM) [10] as a typical representative of car-following models against the "ring-road" bicycle traffic experiments of Andresen et al. [1, 11]. In addition, we compare the IDM fit quality with that of a

V. Kurtc (✉)
Peter the Great St. Petersburg Polytechnic University, St. Petersburg, Russia

M. Treiber
Technische Universität Dresden, Institute for Transport and Economics, Dresden, Germany
e-mail: mail@martin-treiber.de

S. H. Hamdar (ed.), *Traffic and Granular Flow '17*,
https://doi.org/10.1007/978-3-030-11440-4_55

specifically designed "bicycle-following model," the necessary-deceleration-model (NDM) [1].

In the following two sections, we shortly describe the models and the experiments. Section 4 specifies the calibration procedure before we present our main calibration and validation results in Sect. 5 and conclude with a discussion in Sect. 6.

2 Models Under Investigation

Two microscopic car-following models are considered—the IDM [10] and the NDM [1]. Both of them are formulated as coupled ordinary differential equations and characterized by an acceleration function which depends on the actual speed $v(t)$, the approaching rate $\Delta v(t) = v - v_l$ to the leader, and the gap $s(t)$.

The IDM is defined by the acceleration function [10]

$$\dot{v}_{\mathrm{IDM}}(v, \Delta v, s) = a \left[1 - \left(\frac{v}{v_0} \right)^4 - \left(\frac{s^*(v, \Delta v)}{s} \right)^2 \right], \tag{1}$$

where $s^*(v, \Delta v) = s_0 + \max(0, vT + v\,\Delta v/(2\sqrt{ab}))$ is the dynamically desired gap. The IDM contains five parameters to identify via calibration—a, v_0, s_0, T, b. Recently, it has been found that stochasticity plays a significant role for low-speed traffic flow, so we have added the simplest form of white acceleration noise to the acceleration equation (see [9] for details) when simulating collective effects, cf. Sect. 5.4.

The NDM is originally formulated in terms of difference equations for the speed [1] which, in the limit of update times Δt tending to zero, is equivalent to a coupled differential equation with the acceleration function

$$\dot{v}_{\mathrm{NDM}}(v, \Delta v, s) = acc - \min(dec_1 + dec_2, b_{\max}), \tag{2}$$

where

$$acc = \begin{cases} 0 & s \le d(v) \\ \frac{v_0 - v}{\tau} & s > d(v), \end{cases} \tag{3}$$

$$dec_1 = \min \left(\frac{(\Delta v)^2}{2(s - l - s_0)}, b_{\max} \right), \tag{4}$$

$$dec_2 = \begin{cases} b_{\max} \frac{(s - d(v))^2}{(l - d(v))^2} & s \le d(v),\ \Delta v \le \epsilon \\ 0 & \text{otherwise.} \end{cases} \tag{5}$$

The safety distance $d(v) = s_0 + l + vT$ is a linear function of the cyclist's speed v, and l is a length of the cyclist. The NDM has five parameters to calibrate—τ, v_0, s_0, T, $b_{\max}$.

3 Ring-Road Experiment

Trajectory data of bicycle experiments were considered for calibration and validation. These experiments were conducted by the University of Wuppertal in cooperation with Jülich Forschungszentrum on 6th of May, 2012 [1]. Cyclists were moving one after another along the oval track of 86 m length. However the measuring area covered only a straight line of 20 m length. Group experiments were performed for several density levels—5, 7, 10, 18, 20, and 33 participants.

Recently, further experiments with up to 63 cyclists have been performed [3] giving essentially the same results and showing even more pronounced stop-and-go waves for the higher densities.

4 Methods

We have estimated the model performance by two approaches. One is based on trajectories, and the other on aggregated properties of scatter plots derived from stationary measurements (virtual detectors).

4.1 Calibrating and Validating Trajectories

Pairs of consecutive trajectories were used for calibration and validation according to the global approach [5, 8]. Specifically, the microscopic model was initialized with the empirically given speed $v^{\mathrm{sim}}(t=0) = v^{\mathrm{data}}(t=0)$ and gap $s^{\mathrm{sim}}(t=0) = s^{\mathrm{data}}(t=0)$, and the trajectory of the following cyclist for a given leader trajectory was calculated using the ballistic update (see Chapter 10.2 of [8]) with a time step $\Delta t = 0.04\,\mathrm{s}$. Afterwards, the simulated gaps $s^{\mathrm{data}}(t)$ were compared with the experimentally observed gaps by means of two objective functions, namely the absolute error measure

$$S^{\mathrm{abs}} = \frac{\sum_{i=1}^{n}(s_i^{\mathrm{sim}} - s_i^{\mathrm{data}})^2}{\sum_{i=1}^{n}(s_i^{\mathrm{data}})^2}, \tag{6}$$

and the relative error measure

$$S^{\mathrm{rel}} = \frac{1}{n}\sum_{i=1}^{n}\left(\frac{s_i^{\mathrm{sim}} - s_i^{\mathrm{data}}}{s_i^{\mathrm{data}}}\right)^2. \tag{7}$$

4.2 Comparing Microscopic Fundamental Diagrams

We used virtual stationary detectors at several positions of the ring and calculated

- the instantaneous speed v_i of cyclist i at passage time,
- the "microscopic density" ρ_i, i.e., the inverse space headway to the leader at passage time, and
- the microscopic flow $Q_i = \rho_i v_i$, i.e., the inverse (time) headway.

We combined these data to microscopic speed–density scatter plots both for the simulations and the experiments by defining the sets $\{[\rho_i^{\text{data}}, v_i^{\text{data}}]\}$ and $\{[\rho_i^{\text{model}}, v_i^{\text{model}}]\}$, respectively. In order to quantitatively compare the similarity, we create a partitioning of the data points by filtering them according to N equally spaced density intervals

$$V_j^{\text{src}} = \{v_i^{(src)} : \rho_i^{(src)} \in [\rho_j, \rho_{j+1}], i = 1, \ldots, M_{src}\}, \tag{8}$$

where $j = 1, \ldots, N$, src $=$ {data,model}. The key idea is to interpret V_j^{src} as a one-dimensional random variable. Now we calculate the (cumulative) distribution functions both for the experiment, $F_{V_j^{\text{data}}}(x)$, and the simulations, $F_{V_j^{\text{model}}}(x)$, and calculate the Kolmogorov–Smirnov distance

$$D_j = \sup_x |F_{V_j^{\text{data}}}(x) - F_{V_j^{\text{model}}}(x)|, \; j = 1, \ldots, N. \tag{9}$$

The distance D_j averaged over all density bins provides the quantitative metric which estimates the similarity of two data-clouds

$$D^* = \frac{1}{N} \sum_{j=1}^{N} D_j. \tag{10}$$

5 Results

5.1 Free Acceleration

First, we compare and calibrate the free acceleration profile against the experimental results (cf. Fig. 4 of [1]). After calibrating the relevant IDM parameters to the values $v_0 = 4.3\,\text{m/s}^2$ and $a = 1.0\,\text{m/s}^2$ and adding a small amount of white noise (intensity $Q = 0.02\,\text{m}^2/\text{s}^3$), we found a better agreement compared to the NDM (Fig. 1).

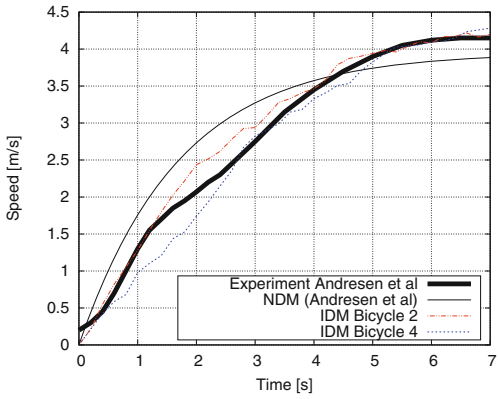

Fig. 1 First stage of the free acceleration of cyclists. Shown are a typical experimental profile and the NDM prediction taken from [1], and two realizations from the stochastic IDM

5.2 *Collective Driving Behavior*

Both models have been calibrated for all trajectory pairs and optimal parameter value distributions were obtained. Table 1 presents the calibration errors. For both error measures (Eqs. (6) and (7)) lower error values correspond to the IDM, whereas higher errors come from the NDM.

The use of several error measures can be interpreted as a benchmark for the robustness of the model calibration. Specifically, for a good model, the calibration results and the distribution of the calibrated parameters should not significantly vary with the chosen error measure. We compare the Kolmogorov–Smirnov distance

$$D_n = \sup \left| F_{1,n}(x) - F_{2,n}(x) \right| \tag{11}$$

of the distributions $F_{1,n}$ and $F_{2,n}$ of parameter n as obtained by calibrating the trajectories with respect to the absolute and relative error measure S^{abs} and S^{rel}, respectively. According to the results presented in Table 2, the IDM tends to be slightly more robust than the NDM.

Table 1 Calibration errors (%) for IDM and NDM

Model	$\sqrt{S^{\text{abs}}}$	$\sqrt{S^{\text{rel}}}$
IDM	2.86	3.01
NDM	4.85	5.05

Table 2 Kolmogorov–Smirnov distance (11) D_p of the parameter values for the two models

IDM	D_a	D_{v_0}	D_{s_0}	D_T	
	0.023	0.027	0.036	0.029	
NDM	D_τ	D_{v_0}	D_{s_0}	D_T	$D_{b_{\max}}$
	0.043	0.035	0.072	0.026	0.039

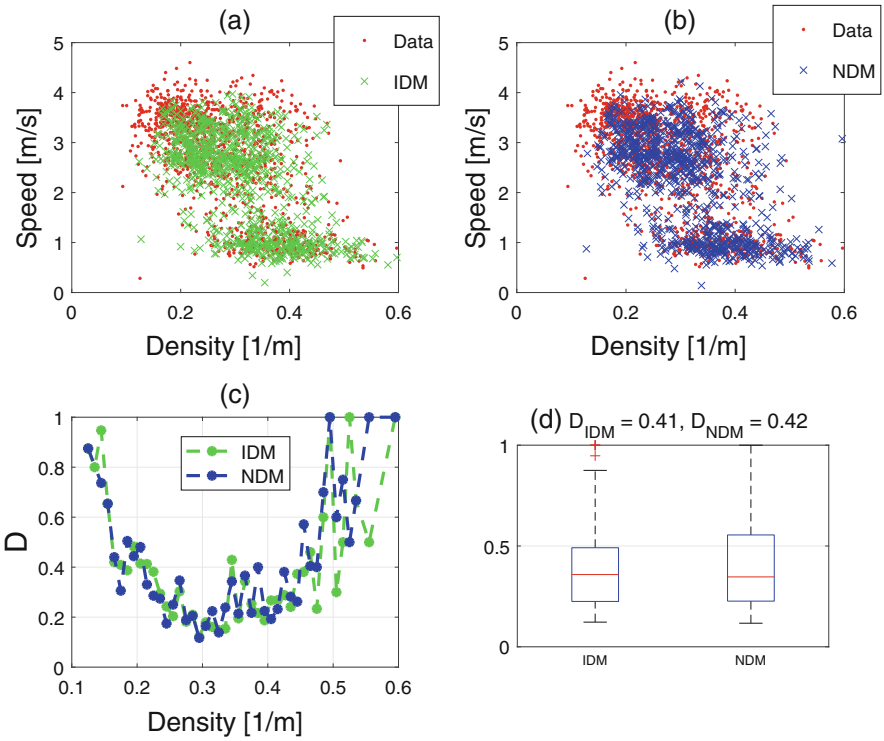

Fig. 2 Speed–density relation for the data, the IDM (**a**) and the NDM (**b**), (**c**) values of the metric D_j for jth density bin, (**d**) boxplots corresponding to the IDM (left) and the NDM (right)

5.3 Microscopic Fundamental Diagrams Comparison

We have calculated the microscopic fundamental diagram and the distance measures both for the real data and for the simulation of the two models with the optimal parameter values without noise. The results are shown in Fig. 2.

5.4 Stop-and-Go Waves

Besides calibrating the IDM by trajectory pair, we also tested if the IDM can produce collective effects such as the stop-and-go traffic observed in the experiments [1] and [3]. Figure 3 shows the result. Instead of using heterogeneous drivers, we simplified the investigation as much as possible by using a single parameter set for all drivers replacing the heterogeneity by white acceleration noise. In contrast to the free-flow simulation (Fig. 1), a higher amount of $0.1\,\mathrm{m}^2/\mathrm{s}^3$ was needed to approximatively reproduce the observed amplitude and frequency statistics of the traffic waves, while the free-flow parameters $v_0 = 4.3\,\mathrm{m/s}^2$ and $a = 1.0\,\mathrm{m/s}^2$ were

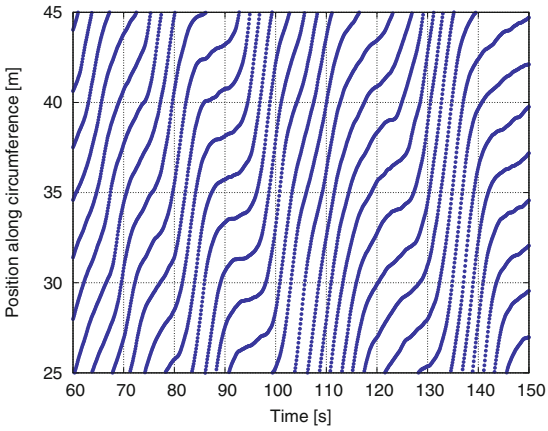

Fig. 3 Simulated trajectories of stop-and-go traffic appearing for the IDM for dense traffic (density 300 cyclists/km)

the same. The calibrated values $T = 0.85\,\mathrm{s}$, $s_0 = 0.4\,\mathrm{m}$, and $b = 1.3\,\mathrm{m/s^2}$ were near the median of the trajectory-by-trajectory calibration of Sect. 5.2.

5.5 *Inter-Driver Variation and Validation*

Validation by cross comparison implies determining the error measures for a certain test data set by simulating the model with the parameters calibrated to the disjunct "learning" data set [8]. For each experiment (5, 10, 15, 18, 20, and 33 participants, respectively), we have separately calculated the calibration-validation matrix whose elements M_{ij} give the error measure $\sqrt{S^{\mathrm{abs}}}$ for the trajectory pair j as obtained from the model calibrated to the trajectory pair i. The diagonal element M_{ii} are the calibration errors, whereas the off-diagonal elements M_{ji}, $j \neq i$, give a superposition of the validation error and the inter-driver variation of follower j with respect to follower i. The average validation error ϵ^{val} and calibration error ϵ^{cal} are given by

$$\epsilon^{\mathrm{val}} = \frac{1}{n(n-1)} \sum_{i=1}^{n} \sum_{\substack{j=1 \\ j \neq i}}^{n} M_{ij}, \tag{12}$$

$$\epsilon^{\mathrm{cal}} = \frac{1}{n} \sum_{i=1}^{n} M_{ii}, \tag{13}$$

where n is a number of trajectory pairs. Notice that a separation of these two causes would require using disjunct parts of the same trajectory for calibration and validation which is only viable for longer trajectories than the available ones. To obtain measures for the overall fitting quality and the predictive power plus inter-

Table 3 Calibration, validation errors (%), and averaged ratios for IDM and NDM

	$N = 5$	$N = 10$	$N = 15$	$N = 18$	$N = 20$	$N = 33$
IDM						
Calibration error	1.74	3.08	2.87	11.98	3.43	5.67
Validation error	32.23	26.37	22.53	32.79	26.6	32.63
Ratio	18.5	8.5	7.8	2.7	7.7	5.7
NDM						
Calibration error	1.28	6.39	3.49	3.54	5.78	7.43
Validation error	42.58	32.51	29.19	35.58	31.67	27.58
Ratio	33.2	5.1	8.3	10.0	5.5	3.7

driver variations, we have calculated the ratio of the average validation error to the calibration error (Table 3).

6 Discussion and Conclusions

According to the results presented in this paper, we conclude that the IDM, which has a similar underlying heuristics as the NDM, cannot only describe vehicular but also bicycle traffic, or, at least, "bicycle following." The IDM trajectories fit even better to the data than that of the NDM. The IDM calibration errors with absolute and relative error measures are 2.86 and 3.01%, whereas for the NDM they are 4.85 and 5.05%, respectively. The application of several objective functions indicates that the IDM calibration is also more robust in comparison to the NDM. Validation results show that the predictive power of the IDM is better than that of the NDM. However, the validation results are confounded by discrepancies from inter-driver variations, so further investigations to separate these factors are necessary.

The analysis of macroscopic characteristics such as speed–density relations provides more or less the same results for both models. Specifically, the averaged Kolmogorov distance D^* (Eq. (10)) is nearly the same. Furthermore, the stochastic IDM can well describe the statistical features of the amplitude and frequency of the observed stop-and-go waves. We conclude that the dynamics of bicycle traffic differs only quantitatively from vehicular traffic and reparameterized car-following models such as the IDM work at least as well as dedicated "bike-following" models.

References

1. Andresen, E., Chraibi, M., Seyfried, A., Huber, F.: Basic Driving Dynamics of Cyclists, pp. 18–32. Springer, Berlin (2014)
2. Gould, G., Karner, A.: Modeling bicycle facility operation: cellular automaton approach. Transp. Res. Rec. **2140**, 157–164 (2009)

3. Jiang, R., Hu, M.B., Wu, Q.S., Song, W.G.: Traffic dynamics of bicycle flow: experiment and modeling. Transp. Sci. **51**, 998–1008 (2016)
4. Jin, S., Qu, X., Xu, C., Ma, D., Wang, D.: An improved multi-value cellular automata model for heterogeneous bicycle traffic flow. Phys. Lett. A **379**(39), 2409–2416 (2015)
5. Kurtc, V., Treiber, M.: Calibrating the local and platoon dynamics of car-following models on the reconstructed NGSIM data. In: Traffic and Granular Flow'15, pp. 515–522. Springer, Cham (2016)
6. Navin, F.P.: Bicycle traffic flow characteristics: experimental results and comparisons. ITE J. **64**(3), 31–37 (1994)
7. Taylor, D., Davis, W.: Review of basic research in bicycle traffic science, traffic operations, and facility design. Transp. Res. Rec. **1674**, 102–110 (1999)
8. Treiber, M., Kesting, A.: Traffic Flow Dynamics: Data, Models and Simulation. Springer, Berlin. http://www.traffic-flow-dynamics.org (2013)
9. Treiber, M., Kesting, A.: The intelligent driver model with stochasticity-new insights into traffic flow oscillations. Transp. Res. B (2017). https://doi.org/10.1016/j.trb.2017.08.012
10. Treiber, M., Henneke, A., Helbing, D.: Congested traffic states in empirical observations and microscopic simulations. Phys. Rev. E **62**(2), 1805–1824 (2000)
11. Zhang, J., Mehner, W., Holl, S., Boltes, M., Andresen, E., Schadschneider, A., Seyfried, A.: Universal flow-density relation of single-file bicycle, pedestrian and car motion. Phys. Lett. A **378**(44), 3274–3277 (2014)

Large-Scale Modeling of VANET and Transportation Systems

Ahmed Elbery, Hesham A. Rakha, and Mustafa ElNainay

Abstract Intelligent transportation systems (ITSs) are key components of future smart cities. These systems attempt to enhance the transportation system efficiency. ITSs utilize vehicular ad hoc networks (VANETs) to collect and disseminate data to be used in ITS applications. Consequently, the performance of the communication network can significantly impact the performance of ITS applications. Consequently, in this paper, we develop a large-scale modeling framework that is capable of modeling large-scale transportation and communication networks. First, we develop and validate a communication model that estimates the packet drop probability and delay for a single hop communication system using a Markov chain and the M/M/1/K queuing model. Then, we integrate this model with a connected vehicle (CV) eco-routing navigation system within a microscopic traffic assignment and simulation software. The fully integrated vehicular and VANET tool is then used to model and evaluate the performance of the CV eco-routing application on a real large-scale road network with a realistic calibrated vehicular traffic demand.

A. Elbery
Department of Computer Science, Virginia Tech, Blacksburg, VA, USA
e-mail: aelbery@vt.edu

H. A. Rakha (✉)
Charles E. Via, Jr. Department of Civil and Environmental Engineering, Blacksburg, VA, USA

Bradley Department of Electrical and Computer Engineering, Blacksburg, VA, USA
e-mail: hrakha@vt.edu

M. ElNainay
Department of Computer and Systems Engineering, Alexandria University, Alexandria, Egypt
e-mail: ymustafa@alexu.edu.eg

S. H. Hamdar (ed.), *Traffic and Granular Flow '17*,
https://doi.org/10.1007/978-3-030-11440-4_56

1 Introduction

ITSs use networked sensors, microchips, and communication technologies to collect, process, and disseminate information about the state of the transportation system. Using these data, the traffic management center (TMC) can make better decisions to improve the performance of the overall transportation system and mitigate traffic congestion. These decisions are affected by the accuracy of the data collected, which is influenced by the communication system.

Vehicular ad hoc networks (VANETs) [8] are expected to constitute the ITS application communication infrastructure. Consequently, the performance of an ITS application is significantly influenced by the VANET communication performance. Consequently, it is imperative to study the impact of the VANET on the performance of transportation applications. It is well known that the communication network performance can also be affected by the mobility of the transportation system. This bidirectional interdependency creates a loop of mutual influence between the communication and transportation system that increases the complexity, and consequently, the analysis of these systems.

The feedback-based eco-routing (FB-ECO) navigation system is an ITS application that attempts to minimize vehicle fuel consumption and emission levels by routing vehicles through the most environmentally friendly routes. The FB-ECO system utilizes connected vehicle technology to gather real-time fuel consumption data from vehicles for use in real-time routing. However, studying and modeling such systems is challenging not only because of the interdependency of the communication and the mobility components, but also because of the scale in which these systems are applied which is covering a city level road network.

Consequently, in this paper, we propose a new scalable framework that is capable of modeling the mutual interaction of the communication and transportation systems in the vehicular environment. The proposed model is characterized by its scalability that supports thousands of concurrent vehicles in the network. Under the umbrella of this framework, we first develop a model for the medium access control (MAC) considering a finite buffer size in vehicular networks. This model utilizes a combination of Markov chain and the queuing theory to estimate the packet delay and drop probability. Second, this model is validated against benchmark simulated data. Third, to enable for the capturing of the mutual impact of the communication and transportation systems, this model is incorporated within the FB-ECO system in the INTEGRATION traffic simulation software [12]. Fourth, the developed simulation framework is used to quantify the impact of communication system on the FB-ECO application performance on a large-scale network.

The remaining of this paper is organized as follows: Sect. 2 gives an overview of VANET communication and the proposed communication model. Section 3 describes the transportation network modeling utilized and the eco-routing application. The simulation network and the results are then presented and discussed in Sect. 4 before the conclusions are presented in Sect. 5.

2 VANET Communication and the Medium Access Technique

According to the IEEE 802.11p [10] standard, the communicating station (vehicle) can support 4 data traffic access categories (AC). Every AC has its own enhanced distributed channel access (EDCA), which acts as a stand-alone virtual station that has its own queue and its own access parameters. Whenever any EDCA has a frame to send, it initializes its back-off counter to a random value within the range of the initial contention window CW (w_0). Then, when it detects that the medium is idle for a specific duration, it counts down the back-off counter. The station can send the frame only when the back-off counter becomes zero. When more than one EDCA count their back-off timers to zero and attempt to transmit at the same time, a virtual collision takes place within the same station, which is referred to as internal collision. In such cases, the access to the medium will be granted to the highest priority AC.

If two different stations start transmitting in the same time slot, an external collision takes place and both transmitted signals will be destroyed. Because the sender cannot detect the collision while transmitting, it has to wait for an acknowledgment (ACK). If an ACK was not received within a specified time, the sender assumes a collision occurred and increases its CW by a factor α, which has a typical value of 2 and backs off again. This process can be repeated until reaching a retransmission attempt threshold $(M + f)$, where M and f are the maximum number of retransmissions with and without increasing the CW, respectively.

2.1 The Proposed Medium Access Model Versus Previous Models

In this paper, we develop an analytical model for the medium access in the vehicular environment that supports only one AC. This assumption is validated, but because of space limitations the validation results are not presented. Our proposed model is characterized by: (1) unlike most of the previous models such as Bianchi's models [3, 14], as well as [9, 15], our proposed model considers the MAC layer queue size, so the model is capable of estimating both the average processing and queuing delay for each packet, (2) it works for both saturated and unsaturated cases, unlike many of the previous research efforts such as [3, 5, 9, 14, 15], and (3) it limits the number of retransmission attempts. When a packet reaches this limit, it will be dropped. These three characteristics are illustrated in Fig. 1.

2.2 Model Derivation

To build a model for the MAC layer, a two-dimensional Markov chain, shown in Fig. 1, is utilized. Due to space limitations, the model derivation will not be

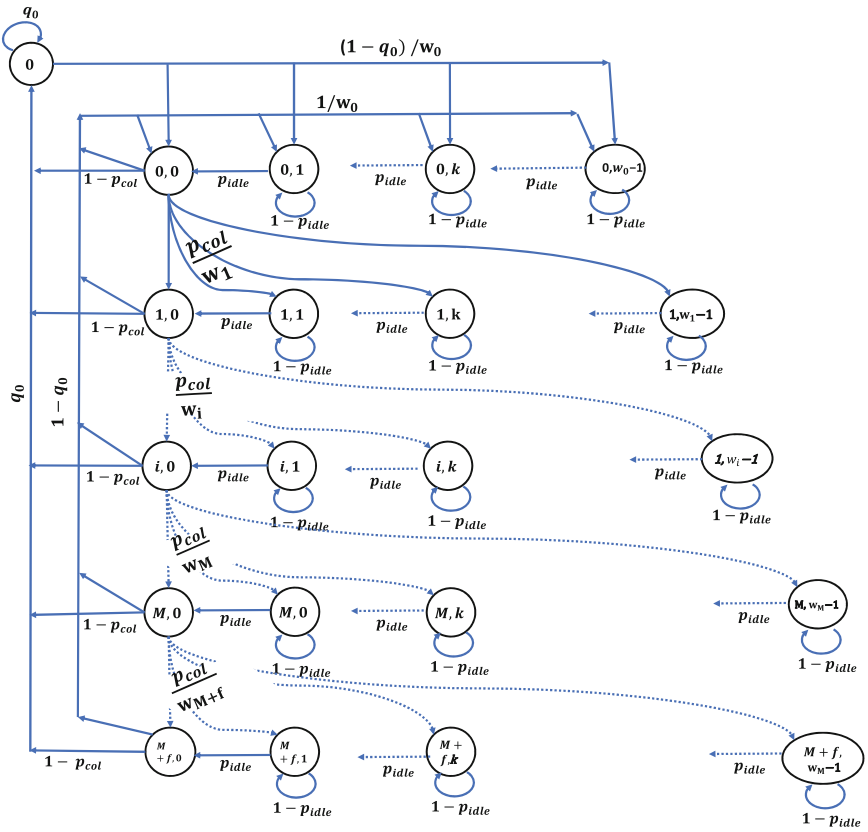

Fig. 1 Markov chain model for the medium access technique with only one AC. State 0 represents the system-empty state. Each of the other states is defined by (i, j), where i and j are the back-off stages and back-off counter value, respectively. w_i is the CW range for stage i. q_0 is the probability that the system becomes empty in any time slot. p_{col} is the packet collision probability. p_{idle} is the probability that the medium considered idle by a station

described. The general procedure is to derive all the state probabilities $P(i, j)$ in addition to $P(0)$ as functions of $P(0, 0)$. Subsequently, the summation of all these state probabilities should equal 1.0. Using this procedure results in Eq. (1) that is used to solve the model

$$P(0,0) = \left(\frac{q_0}{1-q_0} + \frac{1-{p_{col}}^{M+f}}{1-p_{col}} + \frac{w_0-1}{2\ p_{idle}} + \frac{1}{2\ p_{idle}} \Big[(\alpha^{M-1}\ w_0 - 1) \right.$$
$$\left. \frac{{p_{col}}^{M-1} - {p_{col}}^{M+f}}{1-p_{col}} + w_0 \frac{\alpha\ p_{col} - (\alpha\ p_{col})^{M-1}}{1-\alpha\ p_{col}} + \frac{p_{col} - (p_{col})^{M-1}}{1-p_{col}} \Big] \right)^{-1} \tag{1}$$

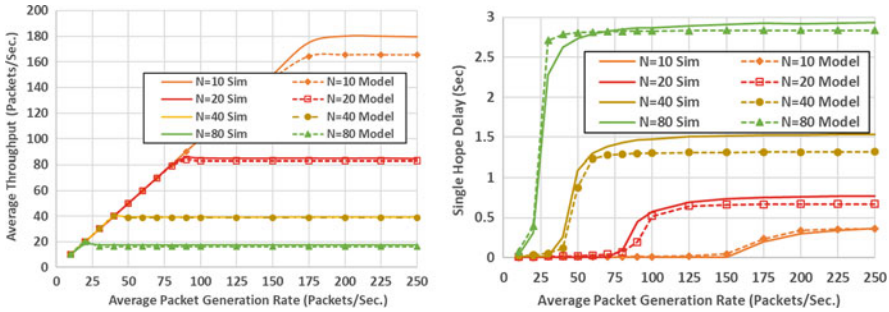

Fig. 2 Average throughput and delay, model versus simulation

where $p_{col} = 1 - (1 - p_{tran})^{N-1}$ and $p_{idle} = {p_{idle_{slot}}}^{AIFS}$. The probability that a station starts transmission in any time slot $p_{trans} = \sum_{i=0}^{M+f-1} P(i, 0)$, the probability that a medium is idle in any time slot $p_{idle_{slot}} = (1 - p_{tran})^N$, N is the number of vehicles in the communication range, and $AIFS$ is the arbitration inter-frame space communication parameter.

In solving Eq. (1) a relationship between q_0 and the state probabilities is derived. Utilizing the $M/M/1/K$ model, q_0 can be calculated as $q_0 = \frac{1-\rho}{1-\rho^{K+1}}$, where K is the queue capacity and ρ is the traffic intensity, which equals $\frac{packet\ arrival\ rate\ \lambda}{packet\ service\ rate\ \mu}$. λ is an input parameter that represents the background packet generation rate. μ can be calculated based on the communication parameter settings.

2.3 Communication Model Validation

To validate this communication model, we ran extensive simulations for different packet traffic rates and number of communicating stations considering V2I communication. We used the OPNET software [13], which is characterized by its trusted results because its implementations of the standard protocols are tested and validated before publishing. The results show an accurate estimation of both throughput and delay compared to the OPNET simulated results (Sim), as shown in Fig. 2.

3 Transportation Traffic Modeling

The transportation network is the environment where the vehicular communication takes place. Consequently, it is essential to integrate the proposed communication model into a scalable transportation simulation software. So, we implemented and incorporated the model within the INTEGRATION software [12] which is a trip-based microscopic traffic assignment, simulation, and optimization model.

INTEGRATION is capable of modeling networks with tens of thousands of cars concurrently on the network. It is characterized by its accuracy, which comes from its microscopic nature, and its small time granularity (0.1 s). This time granularity enables it to accurately track vehicles by modeling car-following, lane-changing, and gap acceptance behavior. The INTEGRATION simulation model provides 10 traffic assignment/routing options [12]. One important feature of INTEGRATION is its support for the FB-ECO traffic assignment. So, we use it to quantify the impact of the communication on the fuel consumption rate. By default, INTEGRATION assumes an ideal communication performance which means there is no drops or delay. So, to realistically model the FB-ECO we incorporated the communication model into the eco-routing model. The communication model can drop the packet or delay it based on the communication parameters and the vehicle density in the surrounding area. In this way, INTEGRATION can realistically model the impact of the communication on the EB-ECO performance.

3.1 Eco-Routing Application

Eco-routing navigation techniques were introduced to minimize fuel consumption and emissions. It utilizes the route fuel cost as a metric, based on which the most environmentally friendly route can be selected.

3.2 Eco-Routing in Literature

Eco-routing was initially introduced in 2006 and applied to the street network in the city of Lund, Sweden, to select the route with the lowest total fuel consumption and thus the lowest total CO_2 emissions [7]. This routing technique resulted in 4% average fuel consumption savings. Ahn and Rakha [1] showed the importance of route selection on the fuel and environment. They demonstrated that the emission and energy optimized traffic assignment based on speed profiles can reduce CO_2 emissions by 14–18%, and fuel consumption by 17–25% over the standard user equilibrium and system optimum assignment. Barth et al. [2] attempted to minimize the vehicle fuel consumption and emission levels by proposing a new set of cost functions that include fuel consumption and the emission levels for the road links. Boriboonsomsin et al. [4] developed an eco-routing navigation system that uses both historical and real-time traffic information to calculate the link fuel consumption levels and then selects the fuel-optimum route. To the best of our knowledge, the first work that considers the communication network and its impact on the eco-routing performance is our previous work [6]; however, the model presented in [6] is not scalable compared to the framework presented here.

4 Simulation and Results

To study the impact of the communication on the eco-routing system performance, We use the network shown in Fig. 3 which is the downtown area of the city of Los Angeles (LA). The modeled road network is shown by the red polygon in Fig. 3 which is about 133 Km^2. It has 1625 nodes, 3561 links, and 459 traffic signals. With regard to the car traffic demand, we use a calibrated traffic demand. The traffic calibration which uses data collected from multiple sources is described in detail in [11]. This traffic demand represents the morning peak hours in downtown area of the city of LA. In order to study the impact of different traffic origin–destination demands (ODs) levels, the calibrated traffic rates are multiplied by an OD scaling factors (ODSFs) 0.1–1 at step 0.1. So, we have 10 traffic demand levels.

In this paper, we use the V2I communication. So, we have to allocate the road side units (RSUs) in the network. The most economical method is to install the RSUs at the traffic signal locations since they are already equipped with the required connections and power sources. We used a greedy algorithm to select a subset of the 459 signals that achieves the maximum coverage with the minimum number of RSUs. Using 1000 m communication range, the algorithm selects only 42 signals to install RUSs as shown in Fig. 3. We run the network using different traffic demands levels in the case of the ideal communication model (which assumes no drops or delays) and the realistic communication modeling framework in which the packets can be dropped and/or delayed. For each of the ten scenarios in each

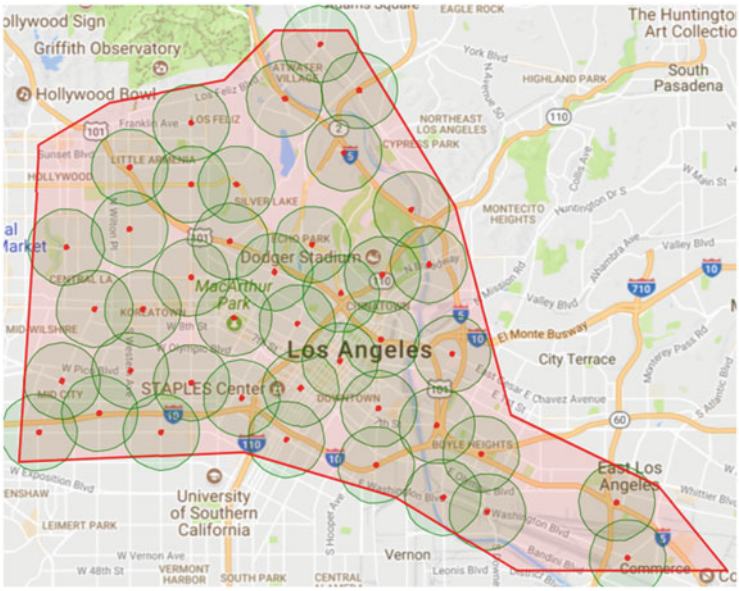

Fig. 3 The LA downtown area and coverage map

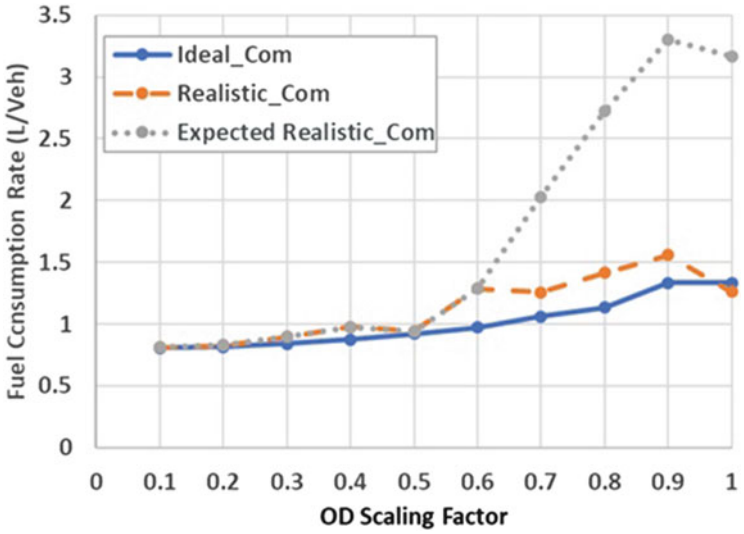

Fig. 4 Average fuel consumption per vehicle

case, the average fuel consumption per vehicle is calculated. The results shown in Fig. 4 demonstrate that for the low traffic demand levels, the difference between the realistic and ideal communication is not significant. However, for the higher demand levels, there are significant impacts of the realistic communication due to packet drop and delay.

As illustrated in Fig. 4, the difference in the fuel consumption rate decreases for the high traffic demand level. Analyzing the simulation outputs showed that when increasing the OD scaling factor to 0.7 or higher in the realistic communication case, the routing decisions become incorrect because of the high packet drop rate caused by the higher vehicle density. These incorrect routing decisions resulted in network gridlocks. Consequently, a large portion of the vehicles were not able to complete their trips and some of them were not able to enter the network because there were no free spots on their entrance links. The results show that at the 0.8 OD scaling factor, only 52% of the vehicles were able to complete their trips. This number decreased to approximately 40% at the full demand level. These vehicles are not accounted for when calculating the fuel consumption rate. This is the reason for the behavior of the Realistic_com curve in Fig. 4. Consequently, to account for those vehicles in the fuel consumption rate we assume that all the vehicles have already exited the network at the calculated rate so we can calculate the total fuel consumption. Then, the total fuel consumed is divided by the number of vehicles that completed their trips. This estimated rate is shown by the expected curve in Fig. 4, which shows that the expected fuel rate can reach approximately 2.5 times that of the ideal case.

5 Conclusions

In this paper, we introduce a framework to model and simulate the inter-connectivity of the vehicular and communication systems in large-scale networks. This framework is used to study the impact of the communication on the feedback-based eco-routing performance. The results show that for low traffic demands, the CV-based eco-routing system is not significantly affected by the communication performance. However, at high traffic demand levels, the performance of the CV-based eco-routing system is significantly degraded due to the incorrect routing decisions associated with packet delays and losses. As a result of the communication system degradation traffic gridlocks occur. These findings demonstrate the need to consider the realistic communication performance when realistically deploying such technologies.

References

1. Ahn, K., Rakha, H.: Field evaluation of energy and environmental impacts of driver route choice decisions. In: Intelligent Transportation Systems Conference, 2007. ITSC 2007. IEEE, pp. 730–735. IEEE (2007)
2. Barth, M., Boriboonsomsin, K., Vu, A.: Environmentally-friendly navigation. In: Intelligent Transportation Systems Conference, 2007. ITSC 2007. IEEE, pp. 684–689. IEEE (2007)
3. Bianchi, G.: Performance analysis of the IEEE 802.11 distributed coordination function. IEEE J. Sel. Areas Commun. **18**(3), 535–547 (2000)
4. Boriboonsomsin, K., Barth, M.J., Zhu, W., Vu, A.: Eco-routing navigation system based on multisource historical and real-time traffic information. IEEE Trans. Intell. Transp. Syst. **13**(4), 1694–1704 (2012)
5. Eichler, S.: Performance evaluation of the IEEE 802.11 p wave communication standard. In: Vehicular Technology Conference, 2007. VTC-2007 Fall. 2007 IEEE 66th, pp. 2199–2203. IEEE (2007)
6. Elbery, A., Rakha, H., Elnainay, M., Drira, W., Filali, F.: Eco-routing using v2i communication: system evaluation. In: Intelligent Transportation Systems (ITSC), 2015 IEEE 18th International Conference on, pp. 71–76. IEEE (2015)
7. Ericsson, E., Larsson, H., Brundell-Freij, K.: Optimizing route choice for lowest fuel consumption–potential effects of a new driver support tool. Transp. Res. Part C Emerg. Technol **14**(6), 369–383 (2006)
8. Hafeez, K.A., Zhao, L., Ma, B., Mark, J.W.: Performance analysis and enhancement of the DSRC for VANET's safety applications. IEEE Trans. Veh. Technol. **62**(7), 3069–3083 (2013)
9. Hajlaoui, N., Jabri, I., Jemaa, M.B.: An accurate two dimensional Markov chain model for IEEE 802.11n DCF. Wireless Networks, pp. 1–13 (2016)
10. IEEE standard for information technology– local and metropolitan area networks– specific requirements– part 11: Wireless LAN medium access control (mac) and physical layer (phy) specifications amendment 6: Wireless access in vehicular environments. IEEE Std 802.11p-2010 (Amendment to IEEE Std 802.11-2007 as amended by IEEE Std 802.11k-2008, IEEE Std 802.11r-2008, IEEE Std 802.11y-2008, IEEE Std 802.11n-2009, and IEEE Std 802.11w-2009) pp. 1–51 (2010). https://doi.org/10.1109/IEEESTD.2010.5514475
11. Jianhe Du Hesham, A. Rakha, A.E.M.K.: Microscopic simulation and calibration of a large-scale metropolitan network: Issues and proposed solutions. In: Annual Meeting of the Transportation Research Board, Washington, DC (2018)

12. Rakha, H.A., Ahn, K., Moran, K.: Integration framework for modeling eco-routing strategies: logic and preliminary results. Int. J. Transp. Sci. Technol. **1**(3), 259–274 (2012)
13. Riverbed modeler. https://www.riverbed.com/products/steelcentral/steelcentral-riverbed-modeler.html. Accessed: 2017-09-30
14. Tinnirello, I., Bianchi, G., Xiao, Y.: Refinements on IEEE 802.11 distributed coordination function modeling approaches. IEEE Trans. Veh. Technol. **59**(3), 1055–1067 (2010)
15. Weng, C.E., Chen, H.C.: The performance evaluation of IEEE 802.11 DCF using Markov chain model for wireless LANs. Comput. Stand. Interfaces **44**, 144–149 (2016)

Activity Location Recommendation Using a Decentralized Proportional Feedback Mechanism

Tim P. van Oijen, Winnie Daamen, and Serge P. Hoogendoorn

Abstract Numerous activity location recommendation strategies have been developed that recommend activity locations or points of interests to individuals. To the best of our knowledge, these strategies have always been designed from a user-optimal perspective. This paper contrariwise presents a recommendation strategy that aims for a system-optimal distribution of people over a set of locations. The task of generating recommendations is described as a control problem, in which the difference between a locally observed distribution of people over the locations and a desired distribution is minimized. We present a generic approach that uses feedback control laws to tackle this problem. Instead of modelling the effect of single recommendations on human behaviour, we follow a macroscopic approach and aim to determine optimal origin-specific destination choice distributions. The potential of the approach is illustrated by simulation of a simple scenario in a 3-node network.

1 Introduction

Crowd managers and large scale event organizers have always looked for methods to influence people's choice behaviour in order to have some control on the distribution of the crowd within a certain area. The recent advance of smartphones makes it feasible to communicate with the crowd on individual level and therefore offers a whole new range of possibilities to manage a crowd. One of these, which is already being applied in practice, is to provide visitors with descriptive information about current crowdedness-levels or waiting times at specific locations [3, 4]. This could potentially make people avoid highly crowded locations and therefore contribute in regulating the crowd distribution. A stronger regulation could be achieved when we consider prescriptive information as well and provide users with

T. P. van Oijen (✉) · W. Daamen · S. P. Hoogendoorn
Delft University of Technology, Delft, The Netherlands
e-mail: t.p.vanoijen@tudelft.nl; w.daamen@tudelft.nl; s.p.hoogendoorn@tudelft.nl

S. H. Hamdar (ed.), *Traffic and Granular Flow '17*,
https://doi.org/10.1007/978-3-030-11440-4_57

context-specific location recommendations. The concept of the so-called context-aware recommender systems already exists for many years [1], but studies have always adopted a user-optimality perspective. Although system-optimality has been studied for related topics, like pedestrian evacuation [2, 5] and road-traffic routing [6], to the best of our knowledge, there are no studies yet that look into activity location recommendation from a system perspective. Therefore, in this paper, we describe a location recommendation strategy that actively aims for a system-optimal distribution of people over a set of activity locations.

Section 2 describes a location-choice model of a single agent, which serves as the basis for our control formulation, which is outlined in Sect. 3. Finally, a simple case is described in Sect. 4, showing the potential of the strategy.

2 Model for the Uncontrolled System

This section describes a model of the uncontrolled system dynamics with respect to the occupation of a set of activity locations. First, a simple location-choice model for a single agent is introduced. The aggregated system dynamics are derived afterwards.

Single Agent Model We consider a system that contains n activity locations, denoted by the set $N = \{1, \ldots, n\}$. Time is discretely defined according to $t_k = k\,\Delta t$, with some fixed interval Δt and $k \in \{0, 1, \ldots\}$. $\Theta_{d,o}$ denotes the free travel time from origin o to destination d, expressed as the number of discrete-time slots. During each time slot, an agent i is either located at an activity location in N, or he is travelling towards a new location. The state of agent i at time instant t_k, denoted by $s_i[k]$, is represented by the 2-tuple $(d_i[k], \tau_i[k])$, where $d_i[k] \in N$ is the location of agent i at time instant t_k, or the location he is travelling towards, and $\tau_i[k]$ is the remaining time period needed to reach this location. Obviously, $\tau_i[k] = 0$ in case agent i is located at an activity location at time instant t_k.

Agents do not change their intended destination while travelling. If currently at a location, we assume that an agent chooses a next destination according to an origin-specific probability distribution, and will start travelling towards this destination at the start of the next time slot. The next destination might be equal to the agents' current location, in which case the agent simply stays at this location during the next time slot. The latter implicitly allows us to specify the average activity duration for the different locations, by selecting proper 'stay probabilities' for the given discretization interval Δt.

The origin-specific probabilities to choose a next location are defined by a left stochastic matrix $\overline{P}$, where element $\overline{p}_{d,o}$ represents the probability that an agent currently located at o chooses destination d as his next location. See Fig. 1b for an example of such a location-choice matrix $\overline{P}$. We assume that $\overline{P}$ is irreducible (each location is reachable, regardless of an agent's initial location) and aperiodic

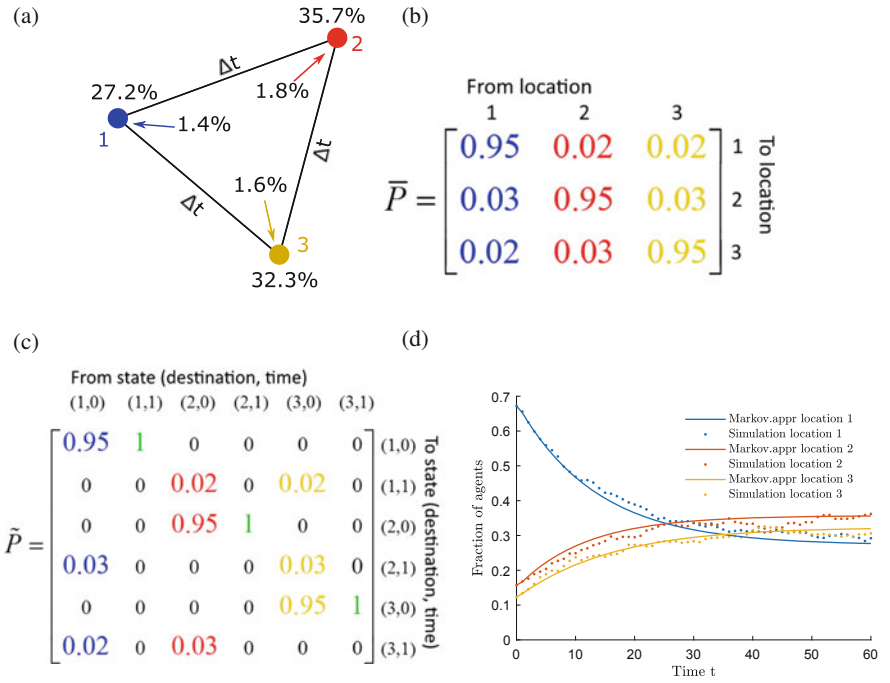

Fig. 1 (**a**) Example of network, having three locations and a travel time of $1\Delta t$ between all locations. The stationary agent distribution is shown for the location-choice matrix as shown in (**b**), the arrow percentages denote the fraction of agents travelling towards the specific activity location. (**b**) Location-choice matrix $\overline{P}$. On average, agents stay at a location for a duration of 20 time slots (5% chance to leave during each time slot). (**c**) State transition matrix $\widetilde{P}$. Notice the analogy with the location-choice matrix $\overline{P}$. (**d**) Simulated time evolution of the fractions $\widetilde{v}$ of 1000 agents, together with the Markov approximation according to (2)

(all possible return time durations for all locations are not a multiple of a common period greater than 1 time step). Both conditions hold for a matrix with only strictly positive entries.

System Dynamics The 2-tuple state representation does not allow for a direct evaluation of the system dynamics. Therefore, we first describe the range of a single agent's state $s_i[k] = (d_i[k], \tau_i[k])$ as a finite ordered set $S = (s_1, s_2, s_3, \ldots)$, according to:

$$S = \Big((1,0), (1,1), \ldots, \Big(1, \max_o(\Theta_{1,o})\Big), \ldots, (n,0), (n,1), \ldots, \Big(n, \max_o(\Theta_{n,o})\Big)\Big). \tag{1}$$

The ordered set S covers all activity locations and travelling states (the remaining travel time is larger than zero) that are reachable, given the travel times between locations. Next, we introduce $\widetilde{\mathbf{v}}[k]$, being the distribution of all agents over the states S at time t_k. The j-th element of $\widetilde{\mathbf{v}}[k]$, denoted as $\widetilde{v}_j[k]$, equals the fraction of all agents that are in state s_j at time instant t_k. The time evolution of the expectation of $\widetilde{\mathbf{v}}[k]$ can now be written as a discrete-time Markov chain:

$$\mathbf{E}(\widetilde{\mathbf{v}}[k+1]) = \widetilde{P}\,\mathbf{E}(\widetilde{\mathbf{v}}[k]). \tag{2}$$

The state transition matrix $\widetilde{P}$ contains the probabilities to transit from a given state to another state. The transition probabilities when located in an activity location state are already given by the agent's location-choice probabilities, which are defined by matrix $\overline{P}$. Since travelling choices are assumed deterministic, the travelling state transition probabilities are either 1 or 0. Figure 1b, c shows the trivial transformation from $\overline{P}$ into $\widetilde{P}$.

The assumption of irreducibility and aperiodicity of location-choice matrix $\overline{P}$ makes that $\widetilde{P}$ is an irreducible and aperiodic stochastic matrix as well. This implies that the uncontrolled system has a unique stationary distribution $\widetilde{\mathbf{v}}^*$, which is also the limiting distribution, satisfying

$$\widetilde{\mathbf{v}}^* = \widetilde{P}\,\widetilde{\mathbf{v}}^*, \quad 0 \leq \widetilde{v}_i^* \leq 1, \quad \sum_i \widetilde{v}_i^* = 1. \tag{3}$$

Example Figure 1a shows an example of a 3-node network with travel times equal Δt. Figure 1b shows an arbitrary location-choice matrix $\overline{P}$ and the corresponding state transition matrix $\widetilde{P}$ is shown in Fig. 1c. The stationary agent distribution (solution of Eq. (3)) is shown in Fig. 1a. The simulated time evolution of $\widetilde{\mathbf{v}}[k]$, starting in a non-stationary distribution, together with the Markov approximation according to (2) is shown in Fig. 1d.

3 Controller Design Problem Formulation

By influencing the activity choice process of individual agents, the collective system dynamics can be altered. By providing adequate recommendations, we might be able to (1) shift the uncontrolled stationary distribution towards a desired reference distribution, which from now on will be denoted with $\widetilde{\mathbf{v}}_{\mathbf{ref}}$, and (2) improve the disturbance behaviour of the system.

Human compliance plays an important role in the design of a recommendation strategy. In this paper we will not look into this behavioural aspect, which usually comes with lots of assumptions. Instead, we model our control at the level of the aggregated location-choice distributions, regardless of compliance. More precise, we define our control strategy as a modification of the location-choice matrix $\overline{P}$. Future studies are needed to find out which advice should be provided to people at

specific locations, such that their collective choice behaviour is in accordance with the location-choice matrix as demanded by our controller. Intuitively, we would argue that a lower compliance rate requires a higher rate of recommendations, though this will not be further discussed in this paper.

Our proposed location-choice control strategy can be subdivided into three parts. The first part comprises a constant modification of the location-choice matrix, which we call the feedforward strategy. By applying this feedforward strategy, we are able to shift the stationary distribution to another desired distribution $\widetilde{\mathbf{v}}_{\mathbf{ref}}$. The second part is a feedback strategy, where the error of the currently observed distribution with respect to the desired distribution is used to modify the location-choice matrix such that this error is reduced. The third part is a correction term which ensures that the location-choice distributions always contain values between 0 and 1. Formally, we write:

$$\overline{P} = \overline{P}_0 + \overline{P}_{ff} + \overline{P}_{fb}(\widetilde{\mathbf{v}}[k], \widetilde{\boldsymbol{\epsilon}}[k]) + \overline{P}_{corr}(\widetilde{\boldsymbol{\epsilon}}[k]), \tag{4}$$

where

- $\overline{P}_0$ denotes the predefined left stochastic location-choice matrix for the uncontrolled case (previous section).
- $\overline{P}_{ff}$ is a static feedforward control term, whose columns should sum to 0. The problem of finding $\overline{P}_{ff}$, given $\widetilde{\mathbf{v}}_{\mathbf{ref}}$, is underdetermined, which allows us to solve for $\overline{P}_{ff}$ and simultaneously optimize some objective function. One typical example is to minimize the total distance of the 'forced' location-choice adjustments.
- $\overline{P}_{fb}(\widetilde{\mathbf{v}}[k], \widetilde{\boldsymbol{\epsilon}}[k])$ is a feedback control term, which depends on the current distribution $\widetilde{\mathbf{v}}[k]$ and the error $\widetilde{\boldsymbol{\epsilon}}[k]$ $(= \widetilde{\mathbf{v}}[k] - \widetilde{\mathbf{v}}_{\mathbf{ref}})$. See Sect. 3.1 for an in-depth discussion.
- $\overline{P}_{corr}(\widetilde{\boldsymbol{\epsilon}}[k])$ is a correction term that ensures that $\overline{P}$ only contains values between 0 and 1. For small $\widetilde{\boldsymbol{\epsilon}}[k]$, $\overline{P}_{corr}(\widetilde{\boldsymbol{\epsilon}}[k])$ is supposed to be a zero matrix.

3.1 Feedback Control

In this study, we limit ourselves to feedback functions of the following form:

$$\overline{P}_{fb}(\widetilde{\mathbf{v}}[k], \widetilde{\boldsymbol{\epsilon}}[k]) = \left(\frac{\overline{B}_1}{\widetilde{v}_1[k]} \widetilde{\boldsymbol{\epsilon}}[k] \middle| \frac{\overline{B}_2}{\widetilde{v}_2[k]} \widetilde{\boldsymbol{\epsilon}}[k] \middle| \ldots \middle| \frac{\overline{B}_n}{\widetilde{v}_n[k]} \widetilde{\boldsymbol{\epsilon}}[k] \right), \tag{5}$$

where $\overline{B}_j$ denotes an arbitrary feedback gain matrix for location j. Equation (5) actually states that the feedback control term at location j is governed by an origin-specific time-invariant feedback gain matrix ($\overline{B}_j$), scaled by the current fraction of all agents at that specific location $\widetilde{v}_j[k]$. Notice that Eq. (5) cannot be evaluated if

$\widetilde{v}_j[k] = 0$. Fortunately, this is not necessary since in this case there is no agent whose location choice needs to be modelled.

Parameterization of Gain Matrices Several constraints have to be taken into account when selecting element values of $\overline{B}_j$. First, to ensure that the controlled location-choice matrix stays left stochastic for small errors (see Eq. (4)), the column-sums of $\overline{B}_j$ should be 0. Second, in a real-world application some state occupations might be unobservable, which further reduces the set of allowed gain matrices. To deal with these constraints, we write in the general case that $\overline{B}_j = \overline{B}_j(\boldsymbol{\beta})$, where $\boldsymbol{\beta}$ is a vector that parameterizes (a subset of) all gain matrices that satisfy the given set of constraints.

Although an infinite number of parameterizations exist that satisfy the imposed constraints, this study is limited to two particular parameterizations (see Fig. 2). Parameterization 1 assumes that travelling agents cannot be observed and uses a single parameter ($\boldsymbol{\beta} = (\beta)$) to specify the strength of counter-acting a certain crowd distribution disturbance. The key mechanism here is that for each location, a certain fraction of agents is either attracted from or pushed towards all other locations, depending on the sign and magnitude of the error at that specific location. Parameterization 2 assumes that the destinations of travelling agents can be observed and uses a second 'decay' parameter to also allow for gain-factors that depend on observed travelling state fractions. For this parameterization, $\boldsymbol{\beta} = (\beta_0, \gamma)$.

Optimization In order to find optimal values for $\boldsymbol{\beta}$, we introduce a quadratic function that expresses the 'cost' of an initial disturbance $\widetilde{\boldsymbol{\epsilon}}_0$ in terms of future state errors and control inputs (similar to LQR optimization):

$$J_0(\boldsymbol{\beta}, \widetilde{\boldsymbol{\epsilon}}_0) = \sum_{t=0}^{\infty} \left(\mathbf{E}\left(\widetilde{\boldsymbol{\epsilon}}[k]\right)^T Q \mathbf{E}\left(\widetilde{\boldsymbol{\epsilon}}[k]\right) + \sum_{i \in N} \mathbf{E}\left(\widetilde{\mathbf{u}}_i[k]\right)^T R \mathbf{E}\left(\widetilde{\mathbf{u}}_i[k]\right) \right), \widetilde{\boldsymbol{\epsilon}}[0] = \widetilde{\boldsymbol{\epsilon}}_0, \tag{6}$$

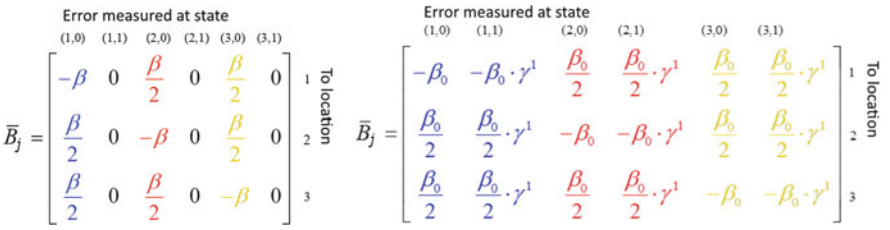

Fig. 2 Two examples of feedback matrix parameterizations. The left case (parameterization 1) assumes that agents can only be observed at locations. The matrix is parameterized with a single parameter β. The right matrix (parameterization 2) observes travelling agents as well and adds a 'decay' factor γ to allow for remaining travel time dependent gains

where $\widetilde{\mathbf{u}}_i[k] = \widetilde{B}_i(\boldsymbol{\beta})\,\widetilde{\boldsymbol{\epsilon}}[k]$. The matrices Q and R specify the weights on state errors and control inputs, respectively. They are assumed to be symmetric and positive definite. Next, we define $J_{fb}(\boldsymbol{\beta})$ as the largest possible value of $J_0(\boldsymbol{\beta}, \widetilde{\boldsymbol{\epsilon}}_0)$, where we restrict the disturbance $\widetilde{\boldsymbol{\epsilon}}_0$ to have a fixed norm $\alpha \ll 1$:

$$J_{fb}(\boldsymbol{\beta}) = \max_{|\widetilde{\boldsymbol{\epsilon}}_0|=\alpha\ll 1} J_0(\boldsymbol{\beta}, \widetilde{\boldsymbol{\epsilon}}_0). \tag{7}$$

Finally, the grand optimization problem is defined as

$$\underset{\boldsymbol{\beta}}{\text{Minimize}}\; J_{fb}(\boldsymbol{\beta}). \tag{8}$$

A direct calculation of the cost function $J_{fb}(\boldsymbol{\beta})$ (Eq. (7)) can be derived by assuming an infinite number of agents and infinitely small disturbances. However, due to limited space, we will not elaborate on this.

4 Simulation of a 3-Node Network

For a 3-node network with travel times equal to $3\Delta t$ and a location-choice matrix as in Fig. 1, the collective behaviour of 10,000 agents has been simulated for different feedback control strategies (see Fig. 3). The results show that applying optimal single-gain feedback (parameterization 1) can largely increase the convergence rate. Observation of travelling states combined with the 'decay' factor (parameterization

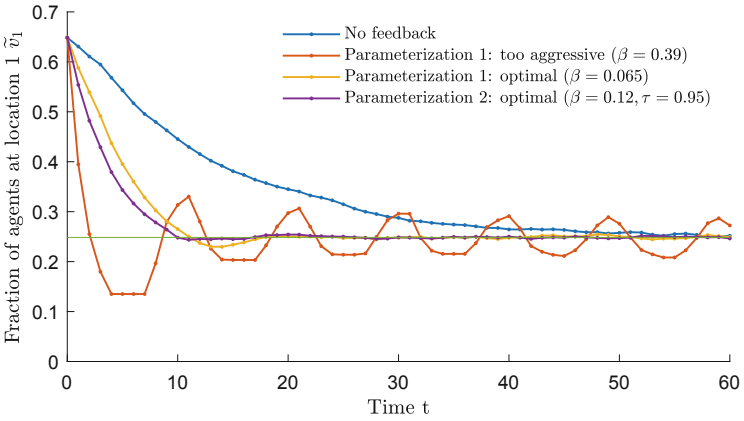

Fig. 3 Simulated response for network and location-choice matrix as in Fig. 1 and travel times equal to $3\Delta t$, using different types of feedback control. Notice the oscillations when using too aggressive gains and the overshoot reduction when applying the single gain with 'decay' strategy (parameterization 2)

2) further increases the convergence rate and also reduces the overshoot. We also looked into the system's behaviour when choosing larger gains than the computed optimal ones. Figure 3 shows that oscillatory responses can occur in these cases. A linearized stability analysis indicates that the system becomes locally unstable in these situations, although at a global level the magnitude of the error seems to be upper bounded. More research is needed to better understand these phenomena.

5 Conclusions and Outlook

In this paper, an activity location recommendation strategy has been explored with a focus on system-optimality. A simulation of agents moving through a network with three activity locations has shown that the distribution of agents over multiple locations can be largely improved if the error with respect to a desired distribution is used to modify the location-choice distributions. How to translate such a collective strategy into local recommendation strategies (from the perspective of a single agent) has deliberately not been addressed, since this would require us to involve many assumptions on human behaviour. If we would assume a fixed compliance rate, which often occurs in similar studies, a translation from the collective strategy into local strategies would be straightforward. In this case, we could exploit a local strategy in which local recommendations would be provided based on probabilities that can be computed such that the collective behaviour would be as prescribed by the collective strategy. More research is needed to find out whether and in which cases such simple behavioural assumptions can be used when implementing local strategies. Looking for methods in which human compliance factors are adaptively learned can be another direction to continue this work.

Acknowledgement This research was supported by the ALLEGRO project, which is funded by the European Research Council (Grant Agreement No. 669792).

References

1. Adomavicius, G., Tuzhilin, A.: Context-aware recommender systems. In: Ricci, F., Rokach, L., Shapira, B., Kantor, P.B. (eds.) Recommender Systems Handbook, pp. 217–253. Springer, Boston (2011)
2. Albi, G., Bongini, M., Cristiani, E., Kalise, D.: Invisible control of self-organizing agents leaving unknown environments. SIAM J. Appl. Math. **76**(4), 1683–1710 (2016)
3. Franke, T., Lukowicz, P., Blanke, U.: Smart crowds in smart cities: real life, city scale deployments of a smartphone based participatory crowd management platform. J. Internet Serv. Appl. **6**(1), 27 (2015)
4. Google: Popular times, wait times, and visit duration. https://support.google.com/business/answer/6263531?hl=en (2017)

5. Hoogendoorn, S., Daamen, W., Duives, D., Van Wageningen-Kessels, F.: Optimal crowd evacuation. In: 93rd Annual Meeting Transportation Research Board, Washington, 2014, pp. 1–19 (2013)
6. Mahmassani, H., Peeta, S.: Network performance under system optimal and user optimal assignments: implications for advanced traveler information systems. Transp. Res. Rec. **1408**(August 2015), 183–193 (1993)